

Growth and Structure of CaCO_3

Johannes Friedrich Ihli

Submitted in accordance with the requirements for the degree of
Doctor of Philosophy

The University of Leeds
Faculty of Mathematics and Physical Sciences
School of Chemistry

October, 2014

Author's Declaration

The candidate confirms that the work submitted is his own, except where work which has formed part of jointly-authored publications has been included. The contribution of the candidate and the other authors to this work has been explicitly indicated below. The candidate confirms that appropriate credit has been given within the thesis where reference has been made to the work of others.

Permission from the respective publisher was obtained before reproduction here in part or total. If not stated explicitly the work in jointly-authored publications is attributable to the candidate.

“Chapter 3: Amorphous Calcium Carbonate” is based on the following publication:

- Ihli J, Kim Y-Y, Noel EH, Meldrum FC. The Effect of Additives on Amorphous Calcium Carbonate (ACC): Janus Behavior in Solution and the Solid State. *Adv Funct Mater* 2013, **23**(12): 1575-1585.

Transmittance and parts of electron microscopy were performed by Kim Y-Y

- Ihli J, Kulak AN, Meldrum FC. Freeze-drying yields stable and pure amorphous calcium carbonate (ACC). *ChemComm* 2013, **49**(30): 3134-3136.

Kulak, AN provided guidance in experimental setup.

- Ihli J, Wong WC, Noel EH, Kim Y-Y, Kulak AN, Christenson HK, Duer MJ, Meldrum FC. Dehydration and crystallization of amorphous calcium carbonate in solution and in air. *Nat Commun* 2014, **5**.

SSNMR analysis and acquisition was performed by Wong WC and Duer MJ. Noel EH, Kim Y-Y and Kulak AN performed preliminary experiments.

- Ihli J, Wang Y-W, Cantaert B, Kim Y-Y, Bomans PHH, Sommerdijk NAJM, Meldrum FC. On the Possibility of Amorphous Calcium Oxalate Precursor Phases. *To be Submitted*

Wang Y-W, Cantaert B and Kim Y-Y performed initial experiments in confined geometries. Wang Y-W performed wedge geometry experiments. Bomans PH H and Sommerdijk NAJM perormed low dose elctron microscopy.

“Chapter 4: Characterisation of Diffusion Methods” is based on the following paper:

- Ihli J, Bots P, Kulak A, Benning LG, Meldrum FC. Elucidating Mechanisms of Diffusion-Based Calcium Carbonate Synthesis Leads to Controlled Mesocrystal Formation. *Adv Funct Mater* 2013, **23**(15): 1965-1973.

Bots P obtained ion chromatography results. Kulak AN assisted with the experimental setup.

- Kim Y-Y, Schenk AS, Ihli J, Kulak AN, Hetherington NBJ, Tang CC, Schmahl WW, Griesshaber E, Hyett G, Meldrum FC. A critical analysis of calcium carbonate mesocrystals. *Nat Commun* 2014, **5**.

The candidate performed initial experiments of the surface area analysis.

“Chapter 5: Bragg Coherent Diffraction Imaging - Calcite” is a reproduction of manuscripts accepted or in preparation for publication.

- Clark JN[†], Ihli J[†], Schenk AS, Kim Y-Y, Kulak AN, Campbell JM, Nesbit G, Meldrum FC, Robinson IK. Three-dimensional imaging of dislocation propagation during crystal growth and dissolution. *Nature under review*
- Ihli J[†], Clark JN[†], Côté AS, Kim Y-Y, Schenk AS, Kulak AN, Comyn TP, Chammas O, Harder RJ, Duffy DM, Robinson IK, Meldrum FC. The Role of Strain in Controlling Crystallisation at Soft Interfaces. *To be Submitted*

Experimental work, sample preparation, data analysis, acquisition, manuscript production and project design were performed in parts or total by the candidate. Data acquisition, phasing and visualization of diffraction pattern along with analysis and manuscript production was done in parts or total by Clark JN. Simulation work was performed by Côté AS and Duffy DM. Schenk AS, Kim Y-Y, Kulak AK assisted in secondary sample characterisation. Comyn TP assisted with pole figure acquisition. Chammas O assisted with atomic force microscope operation.

This copy has been supplied on the understanding that it is copyright material and that no quotation from the thesis may be published without proper acknowledgement.

© 2014 The University of Leeds and Johannes Friedrich Ihli

Acknowledgements

“No, no! The adventures first, explanations take such a dreadful time.”

Lewis Carroll

Fiona

Alex

Jesse

Yi-Yeoun

Bram

Anna

Thank you.

Abstract

Organisms often employ non-classical crystallisation mechanisms to create the remarkable materials that are biominerals. These materials often surpass their synthetic counterparts in terms of physical properties, morphologies and structural organisation. The non-classical mechanisms employed include the controlled formation, transition and release of amorphous precursor material, and the oriented attachment/ nucleation of nano sized particulates. Combined, these strategies are capable of generating hierarchically ordered superstructures. Both of these mechanisms operate under ambient conditions in a physically delimited environment of body fluids, which enables precise regulation of the solution composition.

This thesis describes a range of biomimetic studies which have investigated key aspects in the formation and structural organization of calcium carbonate. Of interest were the influence of additives and physical confinement on the formation and transformation of amorphous calcium carbonate (ACC). The studies revealed that both of these factors play key roles in controlling ACC crystallisation. Additives which inhibit crystallisation in solution can accelerate transformation of ACC in the solid state. This effect was observed for all of the larger molecules examined, while the small molecules retarded crystallisation in both solution and the solid state. Investigation of ACC crystallisation in confinement, in turn, demonstrated that ACC dehydrates prior to crystallizing even in solution, and that nucleation of the first crystal phase in solution must occur by dissolution/ reprecipitation.

Studies were also performed to characterise the “ammonia diffusion method” which is widely used in the precipitation of calcium carbonate. Despite this, virtually nothing is known about the changes in solution conditions which occur during this process. The analysis showed that the supersaturation remains relatively high and constant throughout most of the process, which potentially enables multiple nucleation events to occur in a single experiment. These results were then used to develop a one pot method which offers comparable reaction conditions.

Finally, Bragg coherent diffraction imaging (BCDI) was used to characterise calcite crystals precipitated on self-assembled monolayers (SAM), where these provide a mimic of the organic matrices used to control crystallisation in organisms. Initial observations of the growth and dissolution of calcite by BCDI allowed the visualization of the 3D dislocation network present within a single crystal. Examination of crystals grown on SAMs, in contrast, showed that a build-up strain causes the formation of a single dislocation loop, where this is correlated with the morphological development of the crystal.

Table of Contents

Author's Declaration	i
Acknowledgements	iii
Abstract	v
Table of Contents	vii
List of Tables	xiv
List of Figures	xv
Introduction to the Thesis	1
Chapter 1: General Introduction	3
1.1: Biomineralization	4
1.2: Amorphous and Crystalline Solids.....	7
1.2.1: Crystalline Solids.....	7
1.2.1.1: A Crystal.....	7
1.2.1.2: Crystallographic Reference System	8
1.2.1.3: Indexing Crystal Faces and Directions	8
1.2.1.4: Types of Crystalline Material	9
1.2.1.5: Polymorphism	10
1.2.2: Amorphous Solids	11
1.3: Solution Crystallisation	13
1.3.1: Supersaturation and Metastable Solutions.....	13
1.3.2: Classical Crystallisation Theory	16
1.3.2.1: Nucleation	16
1.3.2.2: Crystal Growth	19
1.3.2.3: Crystal Dissolution.....	21
1.3.3: Crystal Defects.....	22
1.3.4: Crystal Morphology and Additives.....	24
1.3.4.1: Thermodynamic Morphology	24
1.3.4.2: Kinetically Governed Crystal Morphologies.....	25
1.3.5: Non Classical Crystallisation	27
1.3.5.1: Multi Step Nucleation Theories	27
1.3.5.2: Crystal Growth by Oriented Attachment and Mesocrystal Formation.....	31
1.4: Calcium Carbonate.....	34

1.4.1	General Information.....	34
1.4.2:	Calcium Carbonate Polymorphism and Morphology	34
1.4.3:	Calcite	38
1.4.4:	Amorphous Calcium Carbonate	40
1.4.4.1:	Amorphous Calcium Carbonate and Biominerals	40
1.4.4.2:	Structure and “life-cycle” of Amorphous Calcium Carbonate.....	42
1.4.4.3:	The Stabilization of ACC or Polymorph Growth Retarder	45
1.4.5:	Calcium Carbonate in Aqueous Solution.....	48
Chapter 2:	Experimental Methods and Analysis	53
2.1:	Glassware and Substrate Preparation.....	54
2.1.1:	Cleaning Procedures.....	54
2.1.2:	Substrate Preparation	54
2.2:	General Precipitation Methods	56
2.2.1:	Direct Combination of Reagents.....	56
2.2.1.1:	Precipitation in the Presence and Absence of Soluble Additives.....	56
2.2.1.2:	Precipitation in the Presence of Sodium Silicate.....	56
2.2.1.3:	Coating of Precipitates with Phosphatidylcholine	57
2.2.2:	Kitano Method	57
2.2.3:	Diffusion Methods and Alternatives	58
2.2.3.1:	Ammonia Diffusion Method	58
2.2.3.2:	Slow Addition of Reagents	58
2.2.3.3:	Enzymatically Driven Precipitation	58
2.2.4:	Precipitation in Track-etch Membranes	59
2.2.5:	Precipitation from Saturated Solutions by Freeze Concentration.....	59
2.3:	Microscopy	61
2.3.2:	Optical and Florescence Microscopy.....	61
2.3.2.1:	Visible Light Microscopy.....	61
2.3.2.2:	Fluorescence Microscopy.....	62
2.3.3:	Electron Microscopy	63
2.3.3.1:	Scanning Electron Microscopy	63

2.3.3.2: Transmission Electron Microscopy	64
2.3.4: Scanning Probe Microscopy	65
2.3.4.1: Atomic Force Microscopy	65
2.4: Spectroscopy Techniques	67
2.4.1: Ultraviolet–Visible Spectroscopy	67
2.4.2: Atomic Absorption Spectroscopy	68
2.4.3: Energy-dispersive X-ray spectroscopy	68
2.4.4: Fourier Transform Infrared Spectroscopy	69
2.4.5: Raman Spectroscopy	70
2.4.6: Solid-state Nuclear Magnetic Resonance Spectroscopy	71
2.5: Electrochemical Techniques	72
2.6: Dynamic Light Scattering	73
2.7: Surface Area Determination	74
2.8: Thermo Gravimetric Analysis and Differential Scanning Calorimetry	76
2.9: Diffraction	78
2.9.1: X-Ray Diffraction	78
2.9.2: Diffraction Techniques	80
2.9.2.1: Powder X-Ray Diffraction	80
2.9.2.2: Electron diffraction	84
2.9.2.3: Bragg Coherent Diffraction Imaging	85
2.10: Winterbottom Reconstructions	87
Chapter 3: Amorphous Calcium Carbonate	89
3.1: Abstract	91
3.2: Additives and Amorphous Calcium Carbonate	92
3.2.1: Introduction	92
3.2.2: Experimental	94
3.2.3: Results	99
3.2.3.1: Characterisation of “Pure” Amorphous Calcium Carbonate	99
3.2.3.2: Effect of Additives in Solution	101
3.2.3.3: The Effect of Additives in the Solid State	108
3.2.4: Discussion	122
3.2.5: Conclusion	127
3.3: Dehydration and Crystallisation of ACC	128

3.3.1: Introduction.....	128
3.3.2: Dehydration and Crystallisation of ACC in Solution.....	130
3.3.2.1: Synthesis and Dehydration of ACC – Silica Coated Particles.....	130
3.3.2.2: Synthesis and Dehydration of ACC – Bilayer Coated Particles.....	139
3.3.3: Dehydration and Crystallisation of ACC in the Solid State.....	141
3.3.4: Mechanism of ACC Dehydration	150
3.3.5: Discussion	156
3.3.6: Conclusions.....	159
3.4: ACC by Freeze Concentration.....	160
3.4.1: Introduction.....	160
3.4.2: Experimental	161
3.4.3: Results	163
3.4.3.1: Characterisation	163
3.4.3.2: Crystallisation of Freeze Dried ACC in Atmosphere.....	167
3.4.4: Translation to Amorphous Calcium Phosphate	169
3.4.5: Discussion and Conclusion	171
3.5: Amorphous Calcium Oxalate.....	172
3.5.1: Introduction.....	172
3.5.2: Results and Experimental.....	175
3.5.2.1: Bulk Precipitation.....	175
3.5.2.2: Precipitation in the Presence of Additives	177
3.5.2.3: Precipitation in Confined Volumes.....	179
3.5.2.4: Precipitation via Freeze Concentration.....	184
3.5.3: Discussion.....	187
3.5.4: Conclusion.....	188
Chapter 4: Characterisation of Diffusion Methods Towards an understanding of Mesocrystal formation	190
4.1: Abstract	192
4.2: Introduction.....	193
4.3: Characterising the ADM: Experimental and Results.....	196
4.3.1: General Description of the Ammonia Diffusion Method..	196
4.3.2: Experimental	201
4.3.3: Carbonate Addition Rate	205

4.3.4: Influence of Reaction Variables.....	208
4.3.4.1: Initial Mass of Ammonium Carbonate	208
4.3.4.2: Calcium Concentration	210
4.3.4.3: Solution Surface Area	212
4.3.4.4: Secondary Diffusion Barrier	214
4.3.4.5: Solution Agitation	215
4.4: Reproduction of the Ammonia Diffusion Method	217
4.4.1: Mechanically Driven Slow Addition of Reagents	217
4.4.2: Enzymatic Hydrolysis of Urea	222
4.5: CaCO ₃ Mesocrystals	227
4.5.1: Introduction - What Characterizes a Mesocrystal	227
4.5.2: Elevated Surface Area	228
4.5.3: Crystallinity	230
4.6: Discussion	232
4.7: Conclusion	235
Chapter 5: Bragg Coherent Diffraction Imaging of Calcite Single Crystals	237
5.1: Abstract	239
5.2: Fundamentals of Bragg Coherent Diffraction Imagings.....	240
5.2.1: Introduction	240
5.2.2: Experimental	243
5.2.3: Retrieving the phase information from a BCDI pattern ...	245
5.2.4: Sensitivity of the Method to Lattice Deformation	247
5.2.5: Data Visualisation.....	249
5.3: Crystal Growth, Dissolution and Dislocations.....	250
5.3.1: Introduction	250
5.3.2: Experimental	252
5.3.2.1: Mineralisation	252
5.3.2.1: Coherent Diffraction Imaging.....	255
5.3.3: Results	256
5.3.3.1: Crystal Growth and Dissolution	256
5.3.3.2: Screw Dislocations and Dislocation Network	260
5.3.3.3: Overall Strain Effect	265
5.3.4: Discussion.....	267
5.4: Heterogeneous Nucleation on a Soft Interface.....	269
5.4.1: Introduction	269

5.4.2: Experimental	272
5.4.3: Results	275
5.4.3.1: Nucleation and Growth of Calcite on SAMs.....	275
5.4.3.2: BCDI Reconstructions of Calcite Nucleated on SAMs.....	279
5.4.3.3: Surface Cusps and Dislocation Loops.....	283
5.4.3.3: Overall Strain Effect	286
5.4.4: Discussion.....	288
5.4.5: Conclusion.....	290
5.5: Outlook.....	291
Chapter 6: Conclusions and Outlook	293
6.1: Conclusions.....	294
6.2: Outlook.....	297
List of References	299
Nomenclature	324
Abbreviations.....	324
Symbols.....	327
Appendix	331
Appendix A: Reference FTIR- , Ramen- and PXRD Spectra.....	332
Appendix B: Solution Activity Coefficients	336
Appendix C: CaCO ₃ Equilibrium Constants and Solubility Products	337
Appendix D: BCDI Image Reconstruction Details.....	339
Appendix E: Calcite Dissolution by Acetic Acid	347
Appendix F: Supporting Movie Captions	348
Index.....	350

List of Tables

Table 1: The seven crystal systems	8
Table 2: Properties of the anhydrous crystalline calcium carbonate and ACC, and their utilization in biomineralizing organism. Reproduced from (1, 42, 86, 87).....	35
Table 3: Reagent starting concentrations and pH as used for experiments.(152).....	96
Table 4: Activation energies, crystallisation peak temperatures (T_p) given heating rate and water/ additive percentage of ACC samples precipitated in the presence and absence of selected additives: Mg^{2+} , SO_4^{2-} , Aspartic acid (Asp), poly(aspartic acid) (PAsp), poly(styrene sulphonate) (PSS) and bis(2-ethylhexyl)sulfosuccinate (AOT) obtained by DSC and TGA.(152).....	115
Table 5: Key information extracted from the thermal analysis of uncoated ACC.(95)	149
Table 6: Summary of ADM crystallisation parameters under different experimental conditions, where (k_1) is the carbon accumulation rate in solution, (k_2) is the crystallisation rate, (dC_T/dt) the total carbon addition rate, (dCO_3/dt) the carbonate addition rate, (t_{ind}) the induction time and (S_{ind}) is the supersaturation with respect to ACC at the induction point.(169).....	207
Table 7: Key enzymatic parameter of urea-urease hydrolysis obtained at 24°C in a free drift pH setup.....	224
Table 8: “Strain parameters and coherence lengths derived from line profile analysis of powder synchrotron XRD spectra of calcite crystals.”(327).....	231
Table 9: “Strain parameters and coherence lengths derived from line profile analysis of powder synchrotron XRD spectra of three different batches of calcite PSS-MA mesocrystal after <i>in situ</i> heating to 300°C, <i>ex situ</i> heating to 400°C and aging in air.” (327) Altered after (327).....	231

List of Figures

Chapter 1

- Figure 1 - 1: (a) Illustration of a generic cubic unit cell (a). Given in (b) is the idealized equilibrium shape expression of a single crystal of halite (NaCl, cubic). Shown in (c) are the crystal structure and relative atomic position of Na (●), Cl (●) in halite. A cubic unit cell is outlined in red.....9
- Figure 1 - 2: Schematic illustration of Ostwald's rule of stages. That details the possible crystallisation pathways under either thermodynamic control route A (Without any intermediate phases, high activation energy and slow reaction kinetics -red) or kinetic control route B (Sequential precipitation via metastable polymorph occurrence and associated lower activation barriers and faster reaction kinetics -blue). Which route is followed depends on the degree of precipitation pressure present, the activation energy associated with the formation of a polymorph (ΔG) and formation kinetics. Intermediate amorphous precipitates as a potentially precipitating phase have been added for coherence reasons. It is noted that amorphous phases do not represent an additional polymorph. Reproduced from (28).....12
- Figure 1 - 3: Solution states as a function of ion activity product and temperature. Outlined are stable solution/ undersaturated solution area bounded by the solubility curve (- - - -), the metastable solution state/ zone - crystallisation is activated externally and the unstable supersaturated solution state – crystallisation occurs spontaneously(- - -). Shown is the system response of crystallising an equilibrium solubility determined amount (Δc) of a solution compound, upon the increase of solute concentration (Δc_i) exceeding the equilibrium concentration of said compound. Modified from (33).....15
- Figure 1 - 4: Total free energy change as a function of nucleation cluster size. Interfacial energy (G_S) opposes nucleation and nuclei formation whereas the secondary phase formation (G_V) promotes nucleation. As the cluster increases in size the interfacial term is outweighed by the volumetric term ($r \geq r_{crit}$) leading to the formation of a stable nucleolus.(36).....18
- Figure 1 - 5: Possible building block adsorption sites on a growing crystal surface. In order of decreasing free energy (i) face, (ii) step and (iii) kink site. Highlighted in grey are the connecting “surfaces” of elementary building blocks (pink) to a crystal surface (blue). Reproduced after (37).....21
- Figure 1 - 6: AFM images of SiO_4 demonstrating the dominating growth and dissolution mechanism as function of super/ undersaturation. Scale bars $1\mu m$. Taken from (38).
.....22

- Figure 1 - 7: Illustration of spiral growth by screw dislocation. Shown is the progression from dislocation surface outcrop (a) to complete growth spiral (d). Orange arrow shows the direction of applied shear stress, Black arrow the direction of lattice displacement and Blue arrow the step direction. d (l) is equal to one lattice spacing of step height. Reproduced after (40).23
- Figure 1 - 8: Changes in crystal morphology and rate determining step with increasing supersaturation. Shown is the transition from kinetic control at low supersaturation (thermodynamic morphology) to diffusion controlled conditions (kinetic oriented morphology) at high supersaturation. From left to right single crystal near equilibrium, hopper crystal, single-crystalline ordered symmetric dendrite, partially disordered dendrite having a single-crystalline ordered trunk and disordered polycrystalline side branches, polycrystalline dendrite. Reproduced after (51).26
- Figure 1 - 9: An idealized sequential overview of calcium carbonate phase precipitation from supersaturated solution prior to crystalline calcium carbonate formation in the context of non-classical multi step nucleation theory. Shown is the position of PNC / DOLLOP and following liquid crystalline phases (LCP) e.g. PILP or liquid amorphous phases as a result of two phase segmentation of the crystallizing solution in the context of non-classical nucleation mechanism. The formation of secondary solid amorphous and crystalline phases is omitted. Further given are assumed relative activation barriers for phase transition. Reproduced from (64).29
- Figure 1 - 10: Schematic phase diagram of the $\text{CaCO}_3\text{-H}_2\text{O}$ system assuming spinodal decomposition and liquid-liquid phase coexistence e.g. two or multi step nucleation. The olive line represents a constant temperature slice through the phase diagram as the saturation is increased. (SL) single solubility line for a given solid phase (calcite, aragonite, vaterite, and ACC). Blue undersaturated region. "Indirect nucleation of the solid phases occurs to the high supersaturation of the dashed black liquid-liquid coexistence line (L-L). The bright yellow phase field bounded by the L-L line and the dashed red spinodal line (SP) indicates the conditions in which nucleation of the dense liquid phase is possible. In the region bounded by the spinodal line, the solution is unstable to fluctuations, and liquid-liquid separation proceeds."(33) Image taken from (33).30
- Figure 1 - 11: Classical and non-classical crystal growth mechanisms. Given are growth mechanism alternatives after nucleation of the primarily nanoparticles (~10-100 nm). (a) Represents the classical ion by ion growth pathway of nanoparticle amplification. (b) Oriented attachment of primary nanoparticles to form an oriented crystal, where the nanocrystalline building units can lock and fuse. (c) Mesocrystal formation primary nanoparticles covered by an additive (assembly enhancer/ enabler) undergo a mesoscale assembly (mesocrystal). The nucleation step may or may not involve the

formation of an amorphous precursor liquid or solid and utilization of pre-existing nucleation cluster. Reproduced from (12).....	31
Figure 1 - 12: Illustration of the calcite crystal structure and its morphological expression. Shown is a side view (a) and top down projection (b) of relative atomic positions and crystallographic directions in relation to the crystallographic c axis. Calcium (●), Carbonate (◆) and Oxygen (●). A hexagonal unit cell is outlined in red. Presented in (c) are Wulff reconstructions highlighting the morphological expression of homo – and hereto ionic facets of interest.(111-113)	39
Figure 1 - 13: (a) Scheme of ACC formation in the course of sea urchin spine mineralization. (1) Uptake of precipitating ions. (2) Ion-sequestering and (3) transport to specialized vesicles. (4) ACC formation inside of vesicles. (5) Transport of ACC vesicles into the syncytium and to the crystallisation fringes(6). (7 & 8) Transformation of ACC into more ordered phases and attachment to / growth of the crystalline spicule. Taken from (117). (b) Component micrographs of developing spicules. (i) XANES-PEEM image at the Ca L-edge. (ii) RGB map displaying the results of component mapping corresponding to a particular mineral phase. (iii) Zoomed section of (ii). (iv) XANES spectral differences between calcite and ACC used for colour component mapping. Taken from (118).....	41
Figure 1 - 14: (a) Monte Carlo refined X-ray total scattering based structural model of hydrated ACC. Ca-rich framework is given in red. Calcium deficient channels in blue (4 Å separation from any Ca centre). A box dimension of ~ 40 Å is presented. Taken from (127).....	44
Figure 1 - 15: Carbonate species distribution in solution as a function of solution pH from 0 to 100%	48
Figure 1 - 16: Solution concentrations of calcium and carbonate species as a function of carbon dioxide partial pressure. Reproduced from (168).	50

Chapter 2

Figure 2 - 1: Schematic to Bragg's law of diffraction. Given is the geometrical derivation for constructive interference from a crystal. The lower X-ray beam must travel an extra distance AB + BC to continue to be in phase with the upper beam.....	78
Figure 2 - 2: 1D PXRD Calcite diffraction pattern and its structural relation to atomic arrangement. 2 theta position are given in respect to cu radiation	79
Figure 2 - 3: Schematic displaying the acquisition principle behind pole figures (a) and its translation to given pole figure representation. Illustrated are rotating sample angle φ and tilt angle ψ . Reproduced after Kagami, 2011.(195)	83

Chapter 3

Figure 3 - 1: Characterization data of “high pH” ACC using (a) IR-, (b) Raman spectroscopy, (c) TEM and (d) SED, where the inset in (c) shows the electron micrograph corresponding SEAD pattern. Finally given in (e) is a PXRD pattern collect from an ensemble of “high pH” ACC.(152)100

Figure 3 - 2: (a) Plotted is the transmittance recovery as a function of time after mixing two solutions of 1 M CaCl₂ and 1 M Na₂CO₃/ 30 mM NaOH containing 200 ppm of the additives, poly(styrene sulphonate) (PSS), Aspartic acid (Asp), poly(aspartic acid) (PAsp), bis(2-ethylhexyl)sulfosuccinate (AOT) or 10 mM of Mg²⁺, 2 mM SO₄²⁻ divided into 3 discreet stages of precipitation - (i) formation of ACC, (ii) onset of transmittance recovery and associated crystallisation of ACC and (iii) complete transmittance recovery as crystallisation and sedimentation progresses. Presented in (b) and (c) are IR spectra aquired of isolated precipiate at distinct stages (i to iii) of pure ACC and addive incorporating/ occluding ACC. Stage (i) coresonds to the inital ACC formation – broad band at 711 cm⁻¹. (ii) crystallisation of pure ACC to vaterite -emerging band at 743 cm⁻¹, no crystalline phases of calcium carbonate were observe at this stage for the addtive containing ACC. (iii) detection of calcite (711 cm⁻¹) and vaterite across all samples.(152)103

Figure 3 - 3: Dissolution behaviour of “high pH” ACC samples prepared in the presence of different types and amounts of additives: Mg²⁺, SO₄²⁻, Asp, PAsp, PSS and AOT. Presented are averaged dissolution profiles of three repeats given with positionally selected standard deviation.(152).....105

Figure 3 - 4: Shown are dissolution progress – time profiles of calcium carbonate precipitates prepared by different methods. Dissolution profiles were recorded in an undersaturated solution of 250 ml with respect to the most stable polymorph (calcite ~10 mg l⁻¹) given added mass of 1 mg. Profiles are shown for ammonia diffusion method (ADM calcite) (5-10 µm in diameter), ACC precipitated by direct precipitation (direct ACC), ACC precipitated at high pH (“high pH” ACC), ACC precipitated using the ammonia diffusion method (ADM ACC) and commercial nano-sized calcite (nano calcite) all with an apparent diameter of 50-150 nm. Presented are averaged dissolution profiles of three repeats given with positionally selected standard deviation.(152)107

Figure 3 - 5: Electron micrographs and SEAD pattern of (a) pure ACC after heating at 10°C min⁻¹ to 70°C followed by an annealing period of 12 hours at 70°C and (b) pure ACC after heating at 10°C min⁻¹ to 350°C followed by an annealing period of 3 hours at 350°C. (c) ACC formed in the presence of 200 ppm PSS (25°C) and (d) after heating at 10°C min⁻¹ to 70°C followed by an annealing period of 12 hours at 70°C.(152).....109

Figure 3 - 6: Given are IR spectra of (a) pure ACC and (b) ACC prepared in the presence of PSS and AOT before and after heating. The samples were heated at a rate 10°C min⁻¹

to 70°C or 350°C, followed by an isothermal annealing period at 70°C for 12 hours or 350°C for 3 hours.(152).....	111
Figure 3 - 7: TGA (a)/ DSC (b) profiles of ACC synthesized by mixing 1 M CaCl ₂ with 1 M Na ₂ CO ₃ / 30 mM NaOH in the presence or absence of selected additives. The profiles were obtained at a heating rate of 25°C min ⁻¹ under nitrogen flow. Additive spiked samples reveal a shift in crystallisation temperature. Identical amounts of sample (~ 10 mg) were used in all runs. A tabular overview of key parameter and starting additive concentration is given in Table 5.	113
Figure 3 - 8: Shown are sections of DSC scans obtained from the analysis of pure and additive retaining “high pH” ACC samples showing the peak corresponding to the transition from ACC to calcite. DSC scans were obtained at a heating rate of 15°C min ⁻¹ .(152, 205).....	117
Figure 3 - 9: Plotted is recorded crystallisation progress of ACC samples formed in the presence of Mg ²⁺ , SO ₄ ²⁻ , Aspartic acid (Asp), poly(aspartic acid) (PAsp), poly(styrene sulphonate) (PSS), poly(aspartic acid) (PAsp) and bis(2-ethylhexyl)sulfosuccinate (AOT), versus temperature as obtained by DSC. Crystallisation progress was calculated by crystallisation associated exothermic peak integration and following normalisation (0-1). DSC scans were performed with an applied heating rate of 15°C min ⁻¹ .(152).....	118
Figure 3 - 10: Plotted are the progress of crystallisation versus temperature of ACC prepared by mixing 1 M CaCl ₂ with 1 M (NH ₄) ₂ CO ₃ / 30 mM NaOH in the absence or presence of PAsp, PSS and Mg ²⁺ . The progress of crystallisation was estimated based or recorded intensity changes of the [104] peak of calcite (I ₀) with respect to the maximum intensity measured after complete crystallisation (I _{max}) measured by PXRD analysis of samples heated <i>in situ</i> .(152).....	121
Figure 3 - 11: Characterisation of prepared silica-coated ACC (ACC-SiO ₂). Given in (a) and (b) are transmission electron micrographs of ACC-SiO ₂ encapsulates as formed and after dissolution of the calcium carbonate core. (c) IR spectrum and (d) TGA of ACC-SiO ₂ encapsulates as prepared. Further provided are PXRD pattern acquired from of ACC-SiO ₂ encapsulates after heating to (e) 220°C and (f) 550°C. B-Belite.(95).....	132
Figure 3 - 12: TGA of silica shells formed by leaching the calcium carbonate from ACC-SiO ₂ particles. Dissolution of the calcium carbonate core was realized by immersing ~500 mg of prepared ACC-SiO ₂ encapsulates in 250 mM HCl (50 ml) for 24 hours. A heating rate of 15°Cmin ⁻¹ was applied.(95).....	133
Figure 3 - 13: Summary detailing the crystallisation/ dehydration of ACC-SiO ₂ encapsulates upon re-suspension. Given in (a) and (b) are scanning electron micrographs of ACC-SiO ₂ after incubation in solution for 0 mins and 500 mins. (c) IR spectra and (d) TGA of ACC-SiO ₂ encapsulates, showing the structural and compositional changes in encapsulates with incubation in solution.(95)	135

Figure 3 - 14: Characterization of pure ACC particles coated with a porous silica shell, formed by the delayed addition of sodium silicate and their dehydration in solution. Scanning electron micrographs collected with increasing time in solution (a-d) demonstrate clearly that the silica shell is not completed on all ACC particles allowing a rapid dissolution and formation of calcite. (a) Initially prepared particles identical in appearance to ACC-SiO₂ encapsulates. (b) Silica-coated ACC by delayed addition after 180 minutes in solution, showing the presence of (c) empty silica shells and (d) calcite. Observations are supported by ex-situ collected IR spectra. Formed calcite presents a constant background in IR spectra (e). Collected TGA profiles show a similar dehydration behaviour as seen for ACC-SiO₂ encapsulates (f).(95).....136

Figure 3 - 15: Shown is the observed crystallisation and dehydration of ACC-Asp-SiO₂ encapsulates prepared by combining equal volumes of 10 mM Na₂CO₃/ 6 mM Na₂SiO₃ and 10 mM CaCl₂/ 5 mM aspartic acid in comparison with Asp-ACC and pure ACC-SiO₂ encapsulates. (a) TGA and (b) IR spectra of ACC-Asp-SiO₂ after different incubation times in solution. Performed identical to ACC-SiO₂ encapsulates. Emerging vibrational band at $\approx 714 \text{ cm}^{-1}$ is selective to crystalline calcium carbonate observed in given IR spectra after 18 hours, with the first hint of crystallinity appearing after ≈ 5 hours. Provided in (c) and (d) are IR spectra of ACC-SiO₂ (–), ACC-Asp (–) and ACC-Asp-SiO₂ (–) after incubation in solution for (c) 0 mins and (d) 60 mins. Revealing the emergence of vibrational bands of vaterite and or calcite selective for the ACC-Asp particles after 60 mins of incubation, while coated ACC specimen still remain amorphous at this time.(95)138

Figure 3 - 16: Summary detailing the crystallisation of ACC particles coated with lipid bilayers upon re-suspension. Provided in (a) and (b) are laser scanning confocal micrographs of ACC bilayer aggregates taken directly after preparation and after 4 days of re-suspension in water respectively. (c) IR spectra and (d) TGA profiles of ACC coated with lipid bilayers isolated and characterized after certain incubation periods in solution.(95).....140

Figure 3 - 17: Overview showing the crystallisation of uncoated ACC particles with increasing temperature exposure. Given in (a) is the total observed change in weight percent of water (Total wt%) and corresponding molecular composition of ACC (CaCO₃: xH₂O) upon heating to and isothermal storage at a predefined temperature as obtained by TGA shown for a temperature range of 25°C to 400°C. Provided in (b) and (c) are electron micrographs of uncoated ACC after isothermal annealing at 30°C and 200°C respectively. (d) IR spectra of ACC particles after the exposure to a heating procedure involving a ramp (15°C min⁻¹), followed by isothermal annealing (100 min) and a second ramp (15°C min⁻¹) step.(95)143

Figure 3 - 18: TGA (a) and DSC (b) profiles obtained from uncoated ACC particles undergoing a full heating cycle i.e. from dehydration to anhydrous ACC, crystallisation

(b) and eventual decomposition to calcium oxide. Uncoated ACC was prepared by the direct combination and immediate isolation of formed precipitate of equal volumes of (0.5-1.5 ml) of 1 M $(\text{NH}_4)_2\text{CO}_3$ (pH 9.15) with 1 M CaCl_2 (pH ~6.8) at 4°C. A heating rate of 15°C min⁻¹ with a single isothermal annealing period (for 100 min at 55, 95 or 115°C) was used.(95)144

Figure 3 - 19: Profiles provided in (a) detail the crystallisation progress of uncoated ACC samples under heating with an intermediate annealing period (135°C for 100 min), as derived from DSC scans performed with applied heating rates of 10, 15, 20 and 25°C min⁻¹. Stated progress of crystallisation, 0-1, is obtained by integration of the crystallisation associated exothermic peak area in obtained (b) Corresponding Boswell plot.(95)145

Figure 3 - 20: Given are scatter plots presenting calculated dehydration activation energies (E_A) as a function of the degree of dehydration (α) (bottom scale) and molecular composition of ACC $\text{CaCO}_3 \cdot x\text{H}_2\text{O}$ (all water) (top scale). (a) uncoated ACC and (b) ACC-SiO₂ encapsulates. The standard deviation of measurements is represented in the error bars given.(95).....148

Figure 3 - 21: Categorizing the progress of ACC dehydration. Presented are dehydration cures of ACC and ACC-SiO₂ encapsulates as a function of temperature (T) or time (t) (Single data points). Presented alongside with best fits to the common solid state reaction models given in Table 1 (continuous lines). Given in (a) is the general dehydration profile of uncoated ACC upon heating shown over the range of 20 - 220°C, freed from kinetic drag as a result of constant heating. (b) and (c) provided specific, normalized ranges of this dehydration process. (b) representing the range 40 - 140°C, fitted by a geometric contraction model and (c) shows the range 140 - 220°C, fitted by a second order nucleation model. Depicted in (d) is the dehydration of uncoated ACC by isothermal annealing (40°C). Provided in (e) the dehydration of ACC-SiO₂ encapsulates as a function of time on incubation in solution (25°C). Experimental dehydration curves – each given point corresponds to average observed weight loss during a series (x3) of separate isothermal/solution annealing experiments. Stated weight loss was obtained from the end point of isothermal/ solution annealing periods. α is equal to the total fraction of water (Figure 3-20); α_N refers following to the normalized weight fraction of water lost over a specified temperature range (0 - 1).(95)152

Figure 3 - 22: Depicted in given schematic are the idealized succeeding stages of ACC dehydration. Starting from hydrated, wet ACC (a) to the loss of surface-bound water (b). Continuing from (b) to (c) water is lost from the inner of the ACC concurring with particle compaction. Further dehydration leads to the expulsion of deeply located water and hydroxyl ions (d) and the crystallisation to calcite (e).(95).....153

Figure 3 - 23: Provided are ^1H solid state NMR spectra of (a) uncoated ACC particles and (b) ACC - SiO_2 particles isolated from the process at specific known degrees of dehydration as determined in reference by TGA. ACC- SiO_2 particles were isolated from solution, uncoated ACC particles were prepared by means of isothermal heating. Samples for SSNMR were kept at 40°C for one hour prior to the measurements.(175).(95)155

Figure 3 - 24: Schematic representation of the production of ACC by freeze concentration. Illustrated in (a) are the particular phase changes of used solvent during the production process from liquid to solid upon freezing (red arrow) and solid to gas during sublimation i.e. vacuum application (blue arrow). (b) Illustrates the formation process of ACC upon the selective crystallisation of present solvent. (1) Saturated CaCO_3 solution is (2) plunged into LN_2 (3) upon which the solvent begins to freeze, creating localized environments of increasing supersaturation, (4-5) leading to ACC precipitation and (6) followed by final solvent solidification and ACC stabilization. (c) provides line plots with suggested changes in supersaturation and solution volume accompanying the freezing of present solution. Reproduced and altered after (175).162

Figure 3 - 25: (a) TEM, and (b) SEM images of ACC produced via freeze-drying. The inset in (a) provides an EDX spectra of formed ACC. TEM - sample is supported by a nickel grid. (c) Particle size distribution of produced ACC measured using DLS of particles suspended in ethanol.(175)164

Figure 3 - 26: (a) Raman-, (b) IR spectra,(c) PXRD pattern and (d) TGA acquired of ACC obtained via freeze concentration and by direct combination. The inset in (a) shows a comparison of the peak widths of both samples 1088 cm^{-1} .(175)166

Figure 3 - 27: Raman spectra of ACC obtained via freeze concentration, held under ambient atmospheric conditions. Shown is a series of spectra collected over a time frame of 6 weeks.(175)167

Figure 3 - 28: IR spectra of ACC obtained via freeze concentration, held under ambient atmospheric conditions. Shown is a series of spectra collected over a time frame of 6 weeks.168

Figure 3 - 29: Electron micrograph and example EDX spectra of ACP obtained via freeze concentration of saturated calcium phosphate solution.(175)169

Figure 3 - 30: (a) Raman and (b) IR spectra of ACP obtained via freeze concentration and by direct combination of 200 mM CaCl_2 and 200 mM $\text{Na}_2\text{HPO}_4 \cdot 7\text{H}_2\text{O}$. (c) PXRD of ACP obtained via freeze concentration. (d) TGA of ACP obtained via freeze concentration. (175).....170

Figure 3 - 31: (a-c) Examples of calcium oxalate crystals used as active defence structures in plants. (a) A living raphide idioblast, (b) an idioblast after pressure is applied, the cell tip is cracked and the raphide crystals are forcibly expelled. (c) SEM of the

raphide crystals displaying the sharp tips and grooves (→).(122) (d) Schematic depicting the idealized formation of calcium oxalate crystals in idioblasts. Calcium is actively accumulated with the xylem and is distributed among cells in the leaf via the cell wall, crystal idioblasts accumulate Ca via ion pumps. Oxalate can be generated from ascorbate in crystal idioblasts directly and transferred to the vacuole along with imported calcium. In this particular model, calcium and oxalate are transferred across the crystal chamber membrane and added to the growing facets. Crystals of particular length do no longer add Ca and oxalate, proteins interacting at the growing crystal facet may regulate precipitation or shape in this regard. The “mechanisms for transfer of Ca and oxalate to the vacuole and into the crystals have not been identified”(122).
 Reproduced after (122).....174

Figure 3 - 32: Electron micrographs of calcium oxalate precipitates extracted from bulk experiments. Samples were obtained by the direct equimolar combination of 10 ml CaCl_2 and 10ml $\text{Na}_2\text{C}_2\text{O}_4$. Starting concentrations are given on the left hand side. Samples prepared by Yun-Wei Wang.....176

Figure 3 - 33: (a-d) Electron micrographs of calcium oxalate precipitates extracted from bulk experiments in the presence of PAA fixed at $50 \mu\text{g ml}^{-1}$. Samples were obtained by the direct equimolar combination of 10 ml CaCl_2 and 10ml $\text{Na}_2\text{C}_2\text{O}_4$. Stating concentrations are given on the left hand side.177

Figure 3 - 34: Micrographs of calcium oxalate thin films formed on the crystallisation substrate (glass). Presented in (a) is an optical micrograph of found film. Given in the inset is the sample under cross polarizers. (b) the film after heating to 180°C for 3 hours under crossed polarizer. Presented in (c) and (d) are electron micrographs of thin films as found present and after heating to 180°C for 3 hours. Precipitates were prepared by the direct combination of equimolar (5 mM) combination of 10 ml CaCl_2 and 10ml $\text{Na}_2\text{C}_2\text{O}_4/ 50 \mu\text{g ml}^{-1}$ PAA.178

Figure 3 - 35: Calcium oxalate precipitation in wedge geometry. Provided is a schematic of experimental set-up, depicting the increasing surface separation/ decreasing 2D confinement away from the contact point of TEM grid and half cylinder.179

Figure 3 - 36: Calcium oxalate precipitation in wedge geometry. (a-f) provide electron micrographs of precipitates present at decreasing surface separation between the TEM grid and the cylinder. The surface separation for a given precipitate is provided on the left hand side of the respective image. Further provided is an electron diffraction pattern as inset in (f), which demonstrates the amorphous nature of present precipitates close to the contact point of TEM grid and crossed cylinders. Starting concentrations of 2 mM CaCl_2 and $\text{Na}_2\text{C}_2\text{O}_4$ were used. Experiment was performed by Yun-Wei Wang.181

Figure 3 - 37: Calcium oxalate precipitated in track-etch membranes. (a) schematic of experimental set-up used. Further provided are (b) scanning – and (c)

transmission electron micrographs. (d) TEM corresponding electron diffraction patterns obtained from rod shaped precipitate after 12 hours (i) in solution and after 2 weeks (ii). (ii) Diffraction pattern is corresponding to COM. Starting concentrations of 2mM CaCl_2 and $\text{Na}_2\text{C}_2\text{O}_4$ / (PAA 50 $\mu\text{g}/\text{ml}$) were used.....183

Figure 3 - 38: Amorphous calcium oxalate prepared by rapid freezing of saturated solutions. Presented in (a) are scanning and transmission micrograph of the obtained ACO. (b) SEAD diffraction pattern. Further given are structural and compositional information of the formed ACO. The acquired Raman and IR spectra are given in (c) and (d) respectively, together with their spectra after atmospheric crystallisation to COM (ACO in red, COM in black). Raman spectra were collected on a glass substrate. TGA is presented in (f), a heating rate of $15^\circ\text{C min}^{-1}$ was used. Data was collected under N_2 flow.186

Chapter 4

Figure 4 - 1: Schematic diagram of the experimental set-up and methods used to determine the concentrations of aqueous Ca^{2+} and CO_3^{2-} ions. Aliquots were removed with time and quenched with ethanol, the $[\text{Ca}^{2+}]$ was determined using atomic absorption (AA), and the $[\text{CO}_3^{2-}]$ using ion-chromatography (IC). Image taken from (169).....195

Figure 4 - 2: Time-resolved profiles of calcium carbonate precipitation using the ADM, with reaction conditions: 25 mM CaCl_2 , 70 ml, 3 g ammonium carbonate, 2.6 l reaction chamber, no additional diffusion boundaries. The data shown are averages of three experiments, and the error bars show the standard deviation in the values. (a) Transmission, (b) pH, (c) supersaturation, (d) calcium activity, (e) carbonate activity, (f) crystallisation progress. Image taken from (169).....199

Figure 4 - 3: (i) Time-resolved transmittance profile showing the change in transmittance occurring during CaCO_3 precipitation using the ammonia diffusion method (70 ml, 25 mM CaCl_2 , $A = 48 \text{ cm}^2$, 3 g ammonium carbonate, 2.6 l head space, no additional diffusion boundaries). (ii) IR analysis of samples isolated at key times in the reaction were (a) ACC, (b) vaterite and (c) calcite. Here, the peak at 748 cm^{-1} is a fingerprint for vaterite, while the peak at 712 cm^{-1} identifies calcite. Image taken from (169)....200

Figure 4 - 4: A typical pH profile for an ADM experiment (70 ml, 25 mM CaCl_2 , $A = 48 \text{ cm}^2$, 3 g ammonium carbonate, 2.6 l head space, no additional diffusion boundaries) which shows the establishment of a constant solution pH (9.25) after 20 hours. Image taken from (169).....200

Figure 4 - 5: Surface plot of the equilibrium $\text{pH} = f(P_{[\text{NH}_3]}, P_{[\text{CO}_2]})$ in a calcium-carbonate-ammonia system.204

- Figure 4 - 6: Comparison of Total Carbon addition rates, (a) experimental, (b) theoretical (c) theoretical k_1 only, (d) experimental pure diffusion no calcium chloride. Image taken from (169).....206
- Figure 4 - 7: Time-resolved profiles of calcium carbonate precipitation experiments using the ammonia diffusion method, studying the influence of changes in initial amounts of ammonium carbonate added (1.5g, 3g and 5g). Experimental conditions 70 mL of 25 mM CaCl_2 , 48 cm^2 surface area, 2.6 l head space, no additional diffusion barriers). — 1.5 g, --- 3 g, -•- 5g, ▲ 1.5g, •3g, ■ 5g $(\text{NH}_4)_2\text{CO}_3$. Image taken from (169).....209
- Figure 4 - 8: Time-resolved profiles of calcium carbonate precipitation experiments using the ammonia diffusion method studying the influence of initial CaCl_2 concentration (10 mM, 25 mM and 50 mM). Experimental conditions 70 mL of x mM CaCl_2 , 3 g $(\text{NH}_4)_2\text{CO}_3$, 48 cm^2 surface area, 2.6 l head space, no additional diffusion barriers). —10mM, --- 25mM, -•- 50mM, ▲ 10mM, • 25mM, ■ 50mM CaCl_2 . Image taken from (169).211
- Figure 4 - 9: (i) SEM images and corresponding (ii) Raman spectra of calcium carbonate precipitates obtained via the ADM after 100 minutes under reaction conditions of 70 ml, 3 g ammonium carbonate, 48 cm^2 , 2.6 l head space, no additional diffusion boundaries and (a) 25 mM CaCl_2 , no agitation (Calcite+Vaterite), (b) 25 mM CaCl_2 and 100 rpm agitation (Calcite+Aragonite), (c) 50 mM CaCl_2 , no agitation (Calcite), (d) 10 mM CaCl_2 , no agitation (Vaterite+Calcite). The CaCO_3 polymorphs can be identified based on characteristic peaks, where peaks at 1085, 711, 281 and 155 cm^{-1} identify calcite, peaks at 1085, 705, 208 and 155 cm^{-1} aragonite and peaks at 1093, 1066, 753, 713 and 300 cm^{-1} vaterite.(169, 309).....212
- Figure 4 - 10: Time-resolved profiles of calcium carbonate precipitation experiments using the ammonia diffusion method studying the influence of solution surface areas (13 cm^2 , 48 cm^2 , 58 cm^2). Experimental conditions 70 ml of 25 mM CaCl_2 , 3 g $(\text{NH}_4)_2\text{CO}_3$, x cm^2 surface area, 2.6 L head space, no additional diffusion barriers). —13 cm^2 , --- 48 cm^2 , -•- 58 cm^2 , ▲ 13 cm^2 , • 48 cm^2 , ■ 58 cm^2 . Image after (169).....213
- Figure 4 - 11: Time-resolved profiles of calcium carbonate precipitation experiments using the ammonia diffusion method studying the effect of solution agitation (100 rpm). Reaction conditions 70 ml of 25 mM CaCl_2 , 48 cm^2 surface area, 3g ammonium carbonate, 2.6 liter head space, no additional diffusion barriers). — Stirring 100 rpm, - - Stagnant, ■ Stirring 100 rpm, •Stagnant. Image taken from (169).....216
- Figure 4 - 12: Schematic of the mechanically driven slow addition setup used for mesocrystal and thin film replication.218
- Figure 4 - 13: Electron micrographs of produced mesocrystal. (a) 1.25 mM CaCl_2 ADM, (b) 1.25 mM CaCl_2 Slow Addition, (c) 5 mM CaCl_2 ADM, (d) 5 mM CaCl_2 Slow Addition. Image taken from (169).....219
- Figure 4 - 14: Characterization data of pseudo-octahedral CaCO_3 mesocrystals obtained in the presence of PSS-MA, and spectra of rhombohedral calcite crystals as reference.

(a) Raman and (b) IR spectra. (c) TGA spectra of pseudo-octahedral CaCO ₃ mesocrystals produced in the presence of PSS-MA by slow addition of reagents. A heating rate of 5°C min ⁻¹ was applied.(169)	220
Figure 4 - 15: CaCO ₃ thin film formed via (a) ADM (80ml 10 mM CaCl ₂ , 50 mgml ⁻¹ PAA, 48 cm ² and 0.6 cm ² diffusion boundary pore surface area.) and via (b) via slow addition (20ml 175 mM (NH ₄) ₂ CO ₃ , 0.0148mlmin ⁻¹ , 80ml 10 mM CaCl ₂ , 50 after heat treatment (400°C, 300min).	221
Figure 4 - 16: (a) Typical conductance urea/ urease calibration curve. Stated are final conductance values recorded, a urease/ urea ratio of 0.178 mg/mM was used throughout. (b) Michaelis-Menten and (c) Hanes–Woolf plot of urea/ urease hydrolysis obtained at 24°C a fixed amount of 22 µg ml ⁻¹ urease was used.	224
Figure 4 - 17: (a) Theoretical total inorganic carbon (C _T) addition rates required for the production of CaCO ₃ -PSS MA mesocrystals based on mechanical reagent addition (- - -) and C _T addition rates based on enzymatic hydrolysis of urea at 24°C and free pH drift with varying urease/ urea ratios (continuous). (b) Experimentally obtained pH - time profiles of mechanical slow addition -20 ml of 250 mM (NH ₄) ₂ CO ₃ added at 0.0057 ml/min to a 80 ml of solution containing 325 ppm PSS-MA and 5 mM CaCl ₂ -, and enzymatic hydrolysis of urea from a 70 ml solution of 5 mM CaCl ₂ , 40 mM urea, 1 mg urease and 325 ppm PSS MA.	225
Figure 4 - 18: (a) Scanning electron micrograph of CaCO ₃ -PSS MA mesocrystals obtained after 48 hours of incubation from a 70 ml solution of 5 mM CaCl ₂ , 40 mM urea, 1 mg urease and 325 ppm PSS MA. (b) Raman and (c) IR-spectra of CaCO ₃ -PSS MA mesocrystals obtained by the controlled enzymatic hydrolysis of urea.	226
Figure 4 - 19: (a) Scanning electron micrographs of CaCO ₃ PSS-MA mesocrystals retrieved from the mineralizing solution after 12 hours, 14 days and 28 days given from left to right. (b) Measured surface area, (c) polymer “occlusion” and (d) fractal index changes with aging in solution. Mesocrystals were prepared by adding a carbonate containing reagent solution (20 ml of either 250 mM (NH ₄) ₂ CO ₃) at 0.0057 mlmin ⁻¹ to a 80 ml of solution containing 325 ppm PSS-MA and 5 CaCl ₂ , under agitation at 70 rpm.....	229

Chapter 5

Figure 5 - 1: Principle of Bragg Coherent Diffraction Imaging. 1. Experimental acquisition of coherent 3D diffraction pattern. Diffracted beams (aqua) emitted by an isolated specimen (green) exited by a spatially coherent wave (blue) exceeding the specimen size and undergoing rocking motion are collected by an area detector (2D) and are then stacked (3D). 2. The collected 3D pattern (1) is passed to a phase retrieval algorithm moving between real space and reciprocal space (1 ⇌ 4) till autocorrelation between measured amplitude and retrieved amplitude with an evolving phase is

established. This yields a complex function of amplitude (electron density) and phase (lattice displacement) as a product of scattering vector Q (h,k,l) and lattice displacement field u . (3) Fourier transformation of the now known phase and amplitude returns a 3D, tomographic representation of the crystal. An example is shown of a calcite rhombohedron nucleated in solution 1 μm in diameter. Schematic reproduced and extended after (197) and (196).....242

Figure 5 - 2: Illustration of a basic phase retrieval algorithm. This starts from a collected 3D CDX pattern to which a phase is guessed and inverse Fourier transformed (F^{-1}). A support constraint (opaque box) is then applied and a Fourier transformation carried out. A modulus constraint with the measured intensity is enforced next. The process is then repeated under evolution of guessed phase till a self-consistent solution is found. Image taken from (196).....246

Figure 5 - 3: Illustration highlighting the relationship between the local lattice displacement and the alteration in real space phase carried over into the CXD pattern. Shown is a generic lattice arrangement (blue) in which a block of material is displaced from its ideal position (pink) by a vector or $u(r)$. The phase of X-rays scattered by the displaced block is therefore shifted relative to the material in perfect register (highlighted in green), with the total amount given by $\phi(r) = k_f \cdot u(r) - k_i \cdot u(r) = Q \cdot u(r)$. $\phi(r)$ is equal to the phase. k the incoming and scattered wave vector and Q the scattering vector, set to a Bragg condition. In the Bragg condition every part of the perfect crystal scatters in phase – with areas of displacement and phase shift becoming a region of complex density with the same amplitude as the rest of the crystal but with a phase $\phi(r)$. The scattering vector Q is given by $Q = 4\pi \sin\theta / \lambda$. 2θ the angle between the incident wave and the detector. Illustration reproduced after (196, 340).....248

Figure 5 - 4: Schematic illustrating the formation (a), overgrowth (b) and repeated partial dissolution (c) of calcite formed on hydroxyl terminated SAMs. From left to right given in (a) is the urea-urease hydrolysis based nucleation and deposition of calcite rhombohedra. (b) Overgrowth of the formed rhombohedra is achieved by addition of calcium bicarbonate solution and subsequent solvent evaporation. (c) Repeated partial dissolution of the calcite crystals is achieved by the repeated addition of acetic acid solution onto the substrate, followed by its removal and a washing step.254

Figure 5 - 5: Summary of BCDI observations. Presented are separately reconstructed images of a calcite rhombohedra sitting on a (104) facet as formed (i), after secondary overgrowth (ii), and (iii & iv) after consecutive dissolution steps. Shown are from left to right, top - down, side and bottom - up perspectives. Given in (a) is the electron density (reconstructed amplitude) and in (b) projected displacement (phase). These highlight the shape transition during growth (prominent surface advance, \rightarrow) towards steady state and equilibrium shape adoption - dissolution (\rightarrow). The primary screw

dislocation identified is marked (→). The beam enters along the z - axis, with the y axis vertical to z. Crystal and substrate are located at a set scattering angle towards the beam direction (z) and spanned plane (x-z).(199).....258

Figure 5 - 6: Electron micrographs of calcite rhombohedra as deposited (i), after secondary overgrowth (ii), and (iii & iv) after consecutive dissolution steps. Evident is the initial increase in particle volume with crystal overgrowth (ii). This is followed by shrinkage, etch pit formation, surface roughening (iii) and a porous “spherical” isometric appearance of the calcite crystal (iv).(199)259

Figure 5 - 7: Central cut slices through the imaged crystal’s electron density (amplitude) – top row - and projected displacement – bottom row. Central sections are shown of the initial crystal after growth (ii) and repetitive dissolution steps (iii & iv). Provided are two viewing directions top down (a) and side (b) not corrected for the set scattering angle. Pointed out are the initially detected regions, possessing both a low-amplitude core (white arrows) and spiral deformation (circular blue arrow).(199)261

Figure 5 - 8: Provided is a comparison between a simulated screw dislocation at atomic resolution (top) and a simulated screw processed by BCDI scripts applied (bottom). (a) simulated screw, (b) simulated screw Fourier transformed and BCDI processed. (c) and (d) simulated screw with given resulting displacement respectively rendered on top. (e) and (f) secondary viewing angle revealing the retention of both hollow core and spiral displacement after BCDI processing of the simulated screw.(199)262

Figure 5 - 9: Given are iso-surface renderings of defects within calcite. Presented are dislocations (hollow core + spiral displacement) identified by BCDI in deposited calcite (i) after growth (i-ii) and dissolution (ii-iv) within overall crystal shape – transparent electron density. From left to right given are top-down, side and bottom up perspectives. Dislocations are primarily identified near crystal surfaces, observed to actively grow in addition to one predominant screw dislocation present. Later being substrate normal present across the whole crystal height (o). Falsely identified dislocation (o).(199)264

Figure 5 - 10: The total displacement measured over the course of an applied growth/dissolution cycle (i-iv) vs fractional crystal size. The centre of the crystal is equal to 0 and the crystal surfaces are equal to 1. The total displacement was calculated based on measured mean root means square displacement over increasing shell sizes. The presented line plot highlights the diminishing/ increasing relevance of surface effects with growth and dissolution with respect to the crystal size/ volume. Notable are the unequal starting strain percentages at low fractional sizes (centre of the crystal). These can be explained by the anisotropic growth of the crystal, which induces a shift in the centre of mass i.e. fractional size 0 shifts.(199).....266

Figure 5 - 11: Electron micrographs of the inner nacreous layer of an *Atrina rigida* mollusc shell. (a) Cross-sectional view of oriented aragonite tablets, (b) top – down view of

stacked layers. Images taken from (372). (c) Schematic illustrating the formation of sheet nacre. (i) This starts from the formation of an organic scaffold and initial oriented nucleation of aragonite tablets. (ii) Growth of aragonite tablets is limited in the c-axis direction by secondary layers of organic matrix. (iii) Continued lateral growth of tablets. (iv) Primary nacre layer completion. (v) Nucleation of secondary tablet layer directed by mineral bridges connecting primary and secondary layer. Schematic after (386).....271

Figure 5 - 12: (a) Schematic showing an Organothiol molecule adsorbed on gold (111) in upright configuration. (b) SAM monolayer formation (i) “physisorption” of Organothiol on gold, (ii) lying down phase, (iii) standing up process, (iv) completed monolayer. Schematics after (387). (c) Scanning tunnelling microscope image of a 2D hexanethiol lattice- SAM on Au. The bright spots indicate the position of the thiol molecules. Image taken from (387).....273

Figure 5 - 13: Texture of calcium carbonate (calcite) precipitated onto carboxylate terminated organothiol SAMs supported on a thin gold film (111) deposited on glass. Presented are pole figures derived from powder diffraction data sets with a (113), (012), and (104) substrate normal (ND - normal direction, RD – rolling direction, TD – transverse direction). Evident is the presence of two highly oriented populations (012) and (113) exposing homoionic substrate facing facets. No crystals oriented with ({104} faces parallel to the substrate could be detected. Diffractograms were collected for samples deposited on glass substrates -in contrast to the silicon waver supported crystals used in BCDI experiments - in order to avoid interference related to silicon or gold scattering277

Figure 5 - 14: Morphological progression of calcite nucleated on COOH terminated SAMs. Given are schematic (top), experimental observation –micrographs- (centre) and expected equilibrium morphologies (bottom) depicting the formation of preferentially oriented calcite nucleated on carboxylate-terminated SAM supported by a thin gold film. (a) Diffusion of CO₂ and NH₃, into CaCl_{2(aq)} causes ACC formation (●) and deposition onto the substrate in inverted droplets. (b) Precursor depletion yields oriented tetrahedral calcite exposing three smooth 104 facets. (c) Further growth leads to long axis vertex truncation and development of an additional facet. (d) Further crystal growth, results in the complete transition of calcite tetrahedron to rhombohedral calcite. Winterbottom reconstructions are of identical volume with stepwise increasing relative surface energy (γ_s ; 0.1 - 0.9). Crystal/ water interfacial energy values used were taken from Duffy.(110) Further provided is a geometrical overview of terms used throughout.....278

Figure 5 - 15: Summary of BCDI reconstructions. Presented are 3 reconstructions obtained from 3 different crystals of calcite (i-iii) nucleated on a carboxylate-terminated SAM. (a) Reconstructed crystal shapes from BCDI amplitude measurements, and (b) the

projected displacements ($-d/2$ blue lattice dilation and $+d/2$ red contraction). Substrate normal central cut slices through retrieved electron density (c) and projected displacement (d). Given are cuts along the short axis (top) and the long axis truncated vertex direction through the isoperimetric point. Surface cusps are highlighted (o). The beam direction is along the z - axis, with the y axis oriented vertically. The sample/ substrate is located at a set scattering angle towards the beam direction (z) and plane (x-z).280

Figure 5 - 16: Atomic force micrographs of gold film deposited on silicon wafer. AFM measurements returned surface roughness of 1.4 nm (Rq) / 6.61 (Rmax).282

Figure 5 - 17: Electron micrographs of a sample prepared using FIB. (a) SEM of oriented, “tetrahedral” calcite nucleated on a gold film supported SAM eventually cut. (b) Selectively thinned tip of prepared lamella, morphologically originally located central beneath the long axis directly under the truncated vertex onset. (c) Presents a higher magnification of the front end of the tip. Apparent is an area of peculiar phase contrast difference (decreased electron density) $\sim 85 \times 15$ nm.283

Figure 5 - 18: Iso-surface rendering of defects present within oriented calcite crystals. Highlighted are defects present in oriented calcite which display both a low electron density core and surrounding spiral deformation field. Evident is the defect accumulation (i) and singular dislocation loops (ii & iii) in the direction of the initial, elongated pyramidal axis (\rightarrow).285

Figure 5 - 19: Projected displacement in the direction of the truncated vertex. Shown is the recorded increase in projected displacement present on the substrate facing facet, with increasing fractional distance away from the suspected nucleation site (0) towards the newly-formed 104 facet (1) i.e. in the direction of that dislocation loop. The recorded increase in projected displacement is shown for all three reconstructions presented previously (i-iii). The stars indicate the approximate location of the major dislocations (helical – black, dislocation loops – red and blue).287

Introduction to the Thesis

This thesis investigates the formation and structural evolution of calcium carbonate in consideration of biomineralization strategies. Biomimetic studies revealed how changes in physical and chemical environment can not only influence the resulting mineral but also regulate the crystallisation pathway. Results are discussed in view of classical and non-classical crystallisation theories. A special emphasis is placed on the crystallisation of amorphous calcium carbonate (ACC).

This thesis consists of six chapters. **Chapter 1** introduces the concepts of classical and non-classical crystallisation in reflection to biomineralization and calcium carbonate. **Chapter 2** provides an overview of cleaning, experimental and analytical techniques used throughout the thesis. This is followed by three experimental chapters.

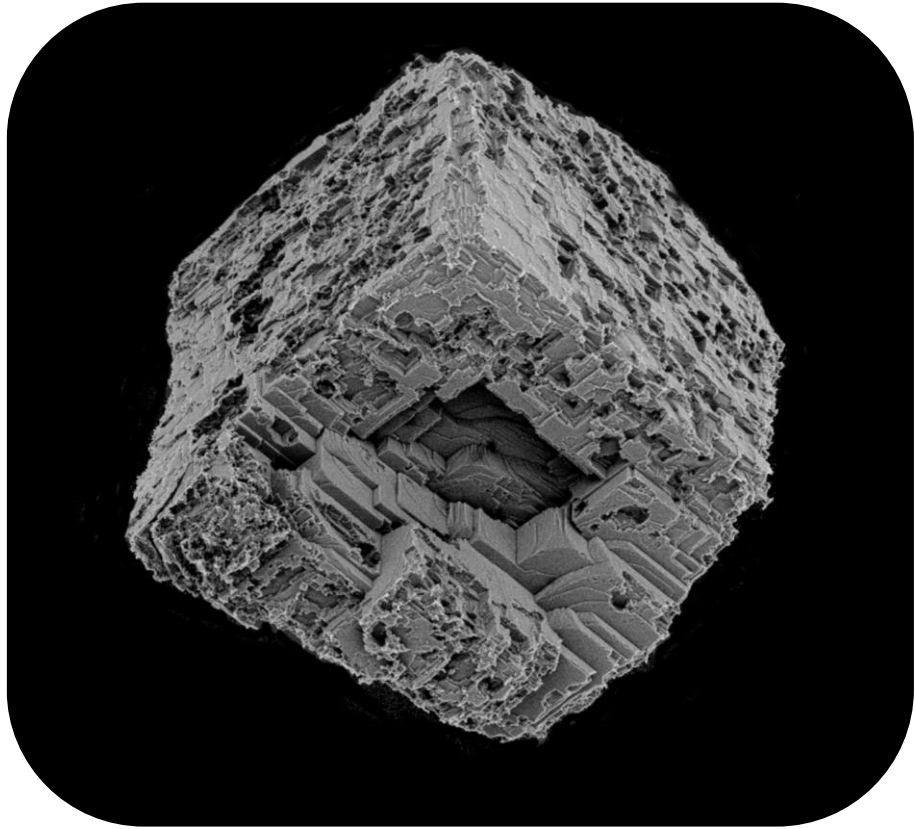
Chapter 3 investigates the crystallisation behaviour of ACC and is divided into five parts. First given is the current stand on the matter e.g. importance, formation, transitioning mechanism along with general characterisation and structural composition of ACC. Followed by a study examining the effect a range of additives have on the crystallisation behaviour in solution and atmosphere. The amorphous to crystalline transition in physical confinement in solution and its similarities to solid state transition are discussed next. Concluded by the development of a one-step synthesis method for ACC and its successful translation to secondary mineral systems.

Chapter 4 focuses on the characterisation of commonly used vapour diffusion methods in the biomimetic synthesis of calcium carbonate. Further discussed is its relevance to CaCO₃ based mesocrystal formation. Lastly given is an enzymatically driven true one pot synthesis alternative to common diffusion methods. Allowing in situ inquiries into the formation process of CaCO₃ based mesocrystal and polymer induced liquid precursor phases.

Chapter 5 concentrates on the utilization of Bragg coherent diffraction imaging (BCDI) in visualisation and analysis of morphology corresponding strain motives in calcite. After introducing the fundamental concept and limitations of coherent diffraction 2 case studies are presented. First study highlights the fundamental notion of strain energy towards crystal growth and dissolution, following the growth and dissolution of a single crystal of calcite. The second study investigates the effect of interfacial strain during mineral templating of calcite on functionalized self-assembled monolayer.

Chapter 6 Concludes presented body of work briefly summarizing important aspects, addressing open questions and future challenges.

Chapter 1: General Introduction



1.1: Biomineralization

The controlled assembly of materials at the nanoscale and their integration/translation into macroscopic devices is considered to be one major bottleneck in the advancement of material science and technology. Harnessing properties emerging from the assembly on the nanometre level, enhanced surface and confinement effects and the “geometric” freedom in the design of crystalline materials among others bears great potential. As of yet material scientist struggle with the necessary level of control and understanding of assembly process to make use of this potential at the necessary length scales. That such levels of control are feasible is known, as set by the many examples found in nature.

Biominerals in particular are a great example of this, where they are formed at ambient conditions in vertebrates and invertebrates alike. By gentle manipulation of their constituents, they can produce oriented arrays of small crystallites purposely tuned for a particular function that are in combination harder and more fracture resistant than their synthetic mineral cousins.(1) The prime example of an organism exerting this level of control down to the nano-scale and nucleation of the mineral phase can be found in any ocean. Sea urchins are capable of forming “single crystalline” spicules from the larval stage, making up their endoskeleton, in a way that defies the common physical constraints imposed on single crystals. The spicules are flexible, with curved facets, their axes are not crystalline axes and their outer morphology does not resemble any crystal structure. Yet, on a macroscopic level they behave as a single crystal.(2-4)

Biomineralization is a process where living organisms convert elementary building units actively taken from the environment into a solid mineral phase. It occurs in all 6 taxonomic kingdoms and dates back to the Neoproterozoic age.(5, 6) One of the earliest scientific advances in the area was D’Arcy Thompson’s work “On Growth and Form” which was first published in 1917. Using a geometrical approach Thompson described the beauty of shape and functionality of biominerals down to a microscopic level.(4)

Biominerals are known to serve a wide range of functions in organisms, such as skeletal support in vertebrates and invertebrates, cutting and grinding in teeth and environmental protection.(7, 8) Biominerals further supply the structures organism use to orient in gravitational or magnetic fields or even provide the actual optical lens as for example in brittle stars.(9, 10) The latter represents an immense

Chapter 1: General Introduction

feat in crystal orientation as each single crystal lens is aligned along its crystallographic c-axis to generate a lens which minimizes spherical aberration and birefringence.

That biominerals can adopt this breadth of functionality and show an assortment of shapes and physical properties which exceeds what is synthetically possible, is not only based on their specific compositions. Biominerals are intrinsically composite materials of an inorganic mineral phase and an organic matrix. It is the tremendous level of control that an organism exerts during crystal formation and growth which is seen to be the key factor in generating this degree of versatility.

Control is generally achieved through mineralization in localized zones in the organism. Those zones provide the ability to maintain high enough levels of supersaturation to induce nucleation through physical delimitation (cellular vesicles) or diffusion limitations found on an extra-, inter- and intra-cellular level. In all cases, biomineralization needs active promotion from the organism in the form of uphill diffusion or modifications in ion activity or pH in those compartments to induce, or temporarily prevent the mineralization process. The actual control of the process can generally be divided into (i) biologically induced and (ii) biological controlled mineralization. Biologically induced mineralization refers to heterogeneous nucleation due to interactions between biological activity with its environment; cell surfaces act as nucleation promoters. Biological controlled mineralization relies on organic matrix mediated cellular activity to direct nucleation, growth and transport, such that the assembly of mineral units can create the observed complex shaped hierarchically ordered materials.(11)

In the course of deriving this knowledge, four non-exclusive overarching mechanisms were identified. These are the (i) oriented nucleation/ growth, through the interaction with templates and or other developing entities, (ii) the use of spatial confinement, (iii) the time resolved incorporation/ removal of additives present in the mineralizing solution and most central to the work presented here, (iv) the utilization of non-classical crystallisation mechanism such as oriented attachment of nanoparticles and the use of amorphous precursor phases.(12-14) In combination, these mechanisms allow the creation of the purpose-optimised properties of biominerals, where these are influenced by their composition at the atomic scale and structural orientation from the nano scale, to the macro scale.

Biomimetic crystallisation studies try to capture the essence of biomineralization mechanisms and apply the obtained knowledge to the synthesis of novel functional

Chapter 1: General Introduction

materials. On a first level physical and chemical approaches are used to mirror the structure, shape and orientation obtained in biominerals. Crystallisation in confinement reproduces the small volumes in which biominerals are formed, and chemical assisted templating can be used to mimic the effect of surface functionalized cell and membrane surfaces. The mirroring of chemical composition of biominerals, using additives, can generate similar composite structures and induce changes in morphology.(15-18) This thesis follows in the footsteps of those studies and nurtures our understanding of how biomineralizing organisms achieve those levels of control in their mineral formation mechanism. More specifically - what are the factors contributing to mineralisation control? Are the proposed mechanisms really the ones that operate? A special interest is placed on the crystallisation of amorphous calcium carbonate and oriented attachment. On a fundamental level these studies allow us to take a step closer to answering the question “how do crystals grow?”

1.2: Amorphous and Crystalline Solids

Crystalline materials are a continuous presence in our everyday lives. They traverse the disciplines of physics, chemistry, biology and material science. They find applications as pharmaceuticals, life science products, ceramics and electronics.

Crystallography - the study of the geometric arrangement of a crystals primary building blocks, has led to many scientific breakthroughs and Nobel laureates over the last century and will continue to do so. As for amorphous materials, it is the renewed promise to obtain crystalline materials free from their geometrical confines that drives studies and inspiration forward.

1.2.1: Crystalline Solids

1.2.1.1: A Crystal

A crystal is a finite body exhibiting periodic order in its elementary building blocks (atoms, molecules), i.e. conserving a long range order across its building blocks. Building blocks are positioned in a repetitive three-dimensional pattern, with each block bonded to his nearest-neighbour.⁽¹⁹⁾ The smallest unit of repeated 3D structural motive is defined as the unit cell. Amplification of the former under certain symmetry operations (translation, rotation and reflection) will always return the crystal structure in its entirety.

On exploitation of this concept the position of each building block in any crystal can be defined according to Equation 1, given a particular structural motive, where r is equal to the translational vector of a building block. a , b and c are the basis vectors of the unit cell and α , β and γ the angles of a structural motive. In combination, this makes up the basic crystallographic reference system, **Figure 1a**, where u , v and w are natural integers.

$$\vec{r} = (r_0) + u \cdot \vec{a} + v \cdot \vec{b} + w \cdot \vec{c} \quad (1)$$

1.2.1.2: Crystallographic Reference System

Seven distinct crystallographic reference or symmetry classes exist, where these are defined by their symmetry axes and unit cell vectors, listed in **Table 1**. On a fundamental level only those 7 classes can possibly achieve the highest packing density of considered building blocks (atoms, molecules). This is tangible - imagine the possible shapes that a milk carton can possess while achieving simultaneously the maximum number of milk cartons stored in a fridge.

On a smaller level each unit cell can and will have a distinct arrangement of its building blocks. In combination with symmetry classes, this makes up the 14 unique structural arrangements of building blocks given by Bravais. (20, 21)

Crystal System	Lattice System	Axial Length and Angles	
Cubic	Cubic	$a=b=c$	$\alpha=\beta=\gamma=90^\circ$
Tetragonal	Tetragonal	$a=b\neq c$	$\alpha=\beta=\gamma=90^\circ$
Orthorhombic	Orthorhombic	$a\neq b\neq c$	$\alpha=\beta=\gamma=90^\circ$
Monoclinic	Monoclinic	$a\neq b\neq c$	$\alpha=\gamma=90^\circ; \beta>90^\circ$
Triclinic	Triclinic	$a\neq b\neq c$	$\alpha\neq\beta\neq\gamma\neq90^\circ$
Hexagonal	Hexagonal	$a=b\neq c$	$\alpha=\beta=90^\circ; \gamma=120^\circ$
Trigonal	Rhombohedral	$a=b=c$	$\alpha=\beta=\gamma\neq90^\circ$

Table 1: The seven crystal systems

1.2.1.3: Indexing Crystal Faces and Directions

Application of Equation 1 with a given atomic motif (Axial Length and Angles) creates a perfect crystal structure. “A deduced geometric property of such a structure is that any straight line of arbitrary direction passing through the crystal will be divided by the atoms/spheres that it cuts through, or is tangent to, into finite segments recurring endlessly at regular intervals. In the special case when such lines coincide with the directions of the vectors, a ,b or c the lines are referred to as the lattice.”(22) The plane a particular set of lattice intercepts spans – a lattice plane – is commonly used to describe crystallographic directions, set or family of planes or the morphologically expressed crystal facet. The facets are the outer morphologically represented flat surfaces. Miller indices are conventionally used to do this. Miller indices h, k, and l are the fractional reciprocal intercepts that the plane in question creates with the crystallographic axis a, b and c.(21) A notation of Miller indices in round brackets (h, k, l) refers to the specific plane while notation in square brackets [h, k, l] refers to the specific direction normal to the lattice plane.

Chapter 1: General Introduction

For a family of symmetry related planes $\{h, k, l\}$ or a family of directions $\langle h, k, l \rangle$ the notation is extended as given. If one or more of these indices (h, k, l) is equal to 0 it means this particular plane does not intersect the crystallographic axis. An illustration based on the cubic structure of sodium chloride (Halite) is given in **Figure 1**.

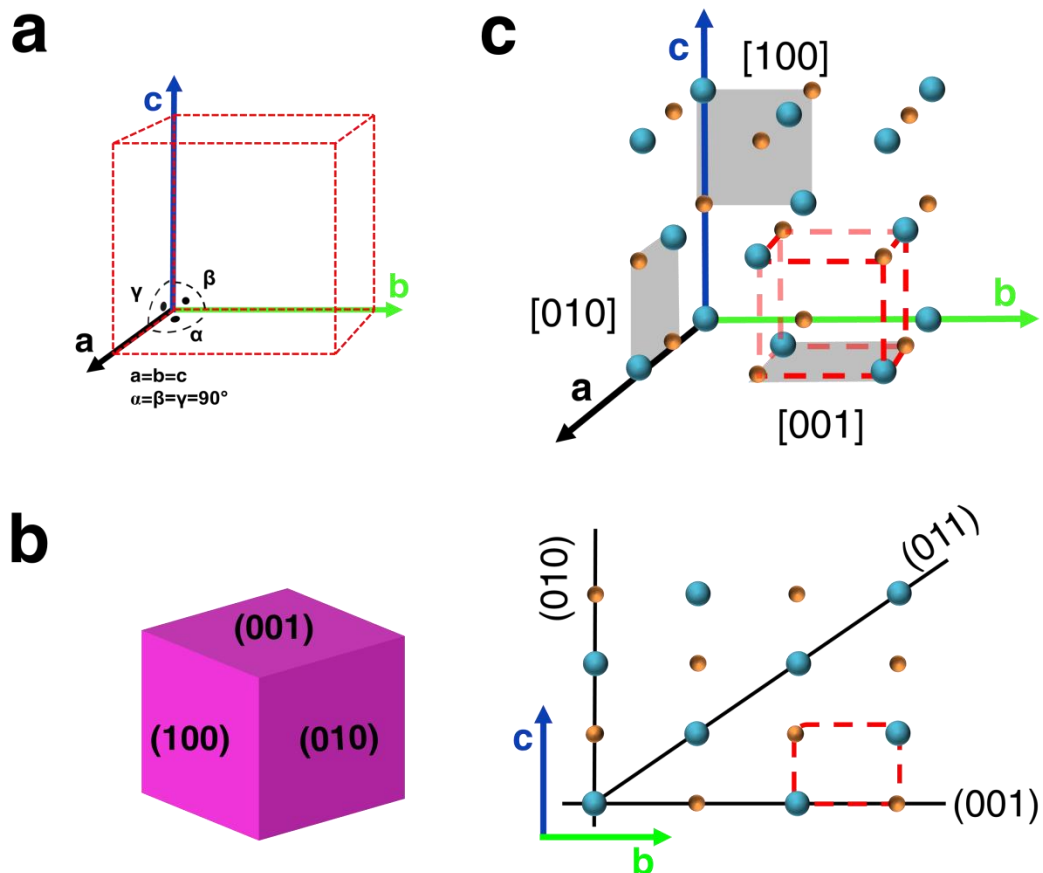


Figure 1 - 1: (a) Illustration of a generic cubic unit cell (a). Given in (b) is the idealized equilibrium shape expression of a single crystal of halite (NaCl, cubic). Shown in (c) are the crystal structure and relative atomic position of Na (\bullet), Cl (\bullet) in halite. A cubic unit cell is outlined in red.

1.2.1.4: Types of Crystalline Material

A further distinction between two types of crystalline material, with identical crystal structures and compositions, is generally made. Materials can be either single crystalline or polycrystalline.

Single crystalline materials are defined by the absence of any grain boundaries or secondary grains in what on the outside appears to be, and ultimately is, a single finite body. These materials exhibit a coherence length equal to macroscopic

Chapter 1: General Introduction

dimensions and diffract as a perfect three-dimensional alignment of its building blocks (molecules, ions), Chapter 2.9.(23)

Perfect single crystal materials rarely exist, due to crystallographic defects and impurities in the crystal structure. The arrangement of building block is as a result distorted. If the distortion moves past a critical threshold, a polycrystalline material is obtained. **Polycrystalline materials** - in contrast to a single crystal are composed of a number of smaller crystals referred to as grains or crystallites. Grain boundaries are the interfaces between two grains. The particular degree of miss-orientation in lattice planes between adjoining grains is what results in the analytical distinction from single crystal materials, and the grains diffract as separate entities. It has to be said what is and what is not considered a single crystal is somewhat fluid depending on degree of miss-orientation between grains/crystallites and the method of observation.

1.2.1.5: Polymorphism

Polymorphism describes the ability of a material of identical composition to occupy a different crystal structure depending on the crystallisation conditions. Each possibility is referred to as a polymorph and has its own set of physical parameters including thermodynamic stability and formation kinetics. Since most solution crystallisation processes are governed by precipitation kinetics it is common to observe the successive formation and dissolution of multiple polymorphs. This polymorphic cascade start with the least stable or metastable polymorphs and ends eventually in the most stable polymorph given certain constrains. This is highly dependent on the given precipitation pressure, where this concept is summarized in Ostwald's rule of stages, as shown schematically in **Figure 1-2**.(24)

1.2.2: Amorphous Solids

Amorphous matter – a material without defined shape and structure – is characterized by the absence of any long range order and mostly the absence of translational symmetry of its components. This basically implies that the ideal amorphous material can be imagined to be a body in which all of its components are “ordered” in complete randomness.

Due to physical constraints we know that the ideal case seldom reflects what is commonly considered an amorphous material. Most glasses, polymers, forms of iron oxides, carbonates, phosphates, ice and most liquids have been considered amorphous in the past.(16, 22, 25-27) This comes with good reason - they do not possess any long range order. But are they totally randomly arranged? No. Short range order does exist, but is frequently limited to the second coordination shell.

From a material science perspective an amorphous material is defined by the absence of any crystallinity. This is confirmed through calorimetric techniques, with X-ray diffraction producing an “amorphous halo” and spectroscopic methods determining the present/ absence of specific bond correlations.(22) With this in mind, it is obvious that determination of whether a particular material is amorphous is method-dependent and the distinction between amorphous matter or nano-crystalline (defect rich) particles can therefore be blurry (Chapter 2.9.2.1).

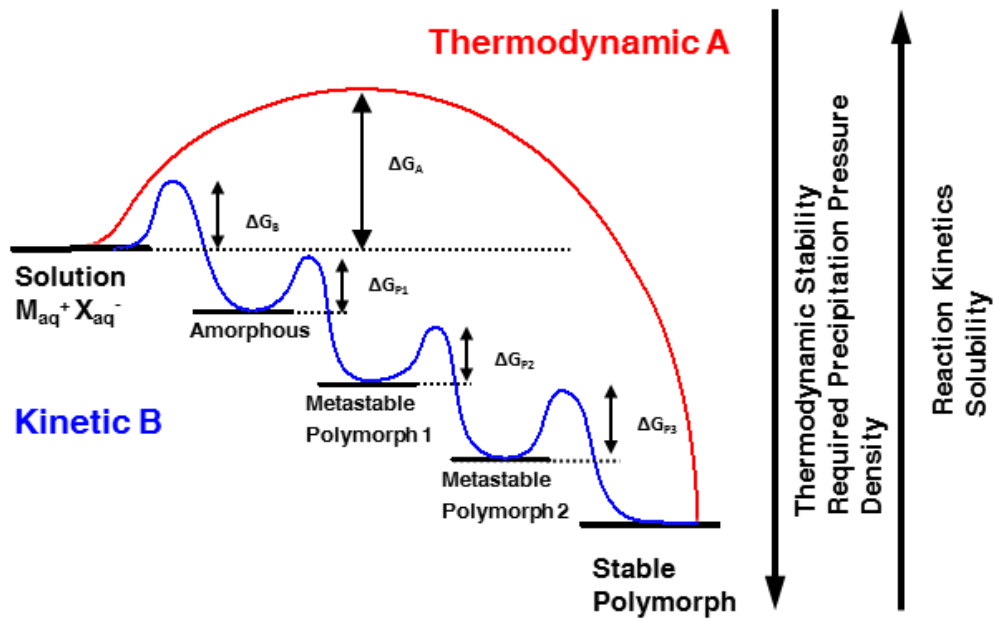


Figure 1 - 2: Schematic illustration of Ostwald's rule of stages. That details the possible crystallisation pathways under either thermodynamic control route A (Without any intermediate phases, high activation energy and slow reaction kinetics -red) or kinetic control route B (Sequential precipitation via metastable polymorph occurrence and associated lower activation barriers and faster reaction kinetics - blue). Which route is followed depends on the degree of precipitation pressure present, the activation energy associated with the formation of a polymorph (ΔG) and formation kinetics. Intermediate amorphous precipitates as a potentially precipitating phase have been added for coherence reasons. It is noted that amorphous phases do not represent an additional polymorph. Reproduced from (28).

1.3: Solution Crystallisation

Solution crystallisation is a first order phase transformation process describing the abrupt phase transformation of solutes, which can be dissolved ions or molecules, to a long range ordered crystalline structure – a crystal. Crystallisation can be described in wider terms as the one-sided competition of a system in minimizing its free energy or chemical potential (Δc), while retaining a maximal state of entropy. It occurs only under the prerequisite of a thermodynamically unstable solution state. Crossing the phase boundary from liquid to solid occurs to return the system back to an equilibrium state.

Classically, crystallisation is considered to be a two-step process consisting of nucleation and crystal growth. Nucleation, the primary step in the formation of a new solid phase, is followed by crystal growth – the amplification of the formed nuclei by addition of basic building blocks (atoms, molecules).(29)

The following presents current and classical concepts describing the formation and growth of crystals.

1.3.1: Supersaturation and Metastable Solutions

Any crystallisation or precipitation process is driven by the fact that the original state of the system is thermodynamically unstable. The degree of this instability is determined by how far the present chemical potential of the system (μ_i) deviates from its equilibrium position (μ_{equ}), Equation 2.

$$\Delta\mu = \mu_i - \mu_{equ} \quad (2)$$

For solution crystallisation this is equal to the difference between the Activity Product (AP) present – the actual solute concentration – and the equilibrium solute concentration given by a phase or polymorph specific solubility product (K_{sp_i}). This difference in solute concentrations is commonly referred to as supersaturation (S).(30) Equations 3-6 highlight those relationships for the example of calcium carbonate crystallisation.

$$AP = [Ca^{2+}] [CO_3^{2-}] \quad (3)$$

$$K_{sp_i} = \frac{[Ca^{2+}][CO_3^{2-}]}{[CaCO_3]} \quad (4)$$

$$S = \frac{AP}{K_{sp_i}} = \frac{[Ca^{2+}][CO_3^{2-}]}{K_{sp_i}} \quad (5)$$

$$\Delta\mu_i = -k_B T \ln(S) = -k_B T \ln\left(\frac{[Ca^{2+}][CO_3^{2-}]}{K_{sp_i}}\right) \quad (6)$$

The **supersaturation** – the amount of solute exceeding equilibrium concentration - determines the rate of crystallisation, the first phase or polymorph formed, and nucleation and growth mechanism of any crystallisation. It also provides a quantification of the chemical potential of a solution.

Solutions can be classified into 3 distinct states according to the concentration of the solutes present. A solution can be either unstable-supersaturated, metastable or unstable-undersaturated. **Undersaturated solutions** have a negative chemical potential with respect to the crystallizing compound and will not form any new material. Rather, they will attempt to assimilate species of the crystallizing compound or dissolve any present crystallizing compound until an equilibrium solubility is reached.

If a system exceeds the metastable chemical potential through temperature or pH variation, solvent removal or compositional changes (Δc) the solution becomes unstable-supersaturated and crystallisation starts to occur rapidly. Alternatively, it may freeze temporarily in an amorphous state if the increase in supersaturation is relatively large and too abrupt.(31)

In the metastable region, crystallisation can and does occur, but is time delayed. The delay or the induction time – that is the time taken to form the first “detectable” nuclei as compared to an unstable supersaturated solution, is much longer and depends on variables such as species, solvent and most prominently heterogeneous nucleators.(32) Heterogeneous nucleators can shorten the metastability of a solution such that a potential spinodal decomposition mechanism is rarely observed (Chapter 1.3.5.1). **Figure 1-3**, visualizes the above described solution states.

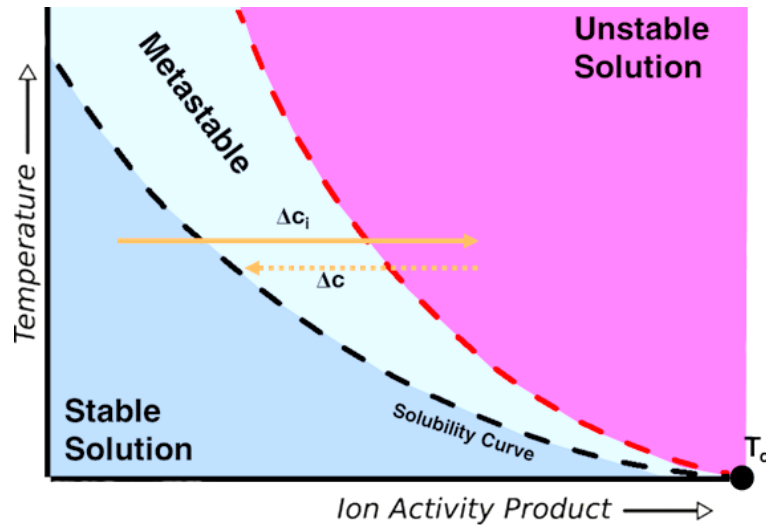


Figure 1 - 3: Solution states as a function of ion activity product and temperature. Outlined are stable solution/ undersaturated solution areas bounded by the solubility curve (- - - -), the metastable solution state/ zone - crystallisation is activated externally and the unstable supersaturated solution state – crystallisation occurs spontaneously(- - - -). Shown is the system response of crystallising an equilibrium solubility determined amount (Δc) of a solution compound, upon the increase of solute concentration (Δc_i) exceeding the equilibrium concentration of said compound. Modified from (33).

1.3.2: Classical Crystallisation Theory

1.3.2.1: Nucleation

Nucleation is the first irreversible step in the formation of a new phase. A nucleus is the smallest possible stable entity of the forming phase. The classical nucleation theory (CNT) was in part formulated by Volmer and is based on his observations of vapour condensation.(34)

CNT states that nucleation occurs as a result of stochastically addition/ aggregation of elemental building blocks (cluster) and is based on collision theory and local concentration fluctuations in an otherwise homogeneous supersaturated medium.

Concentration fluctuations are inherently unstable and “dissolve” rapidly beneath a critical cluster size in solution. Past this critical spatial dimension, the addition of elementary units to the formed “nuclei” is energetically more favourable than the subtraction of one.(34) Fluctuations can be imagined to be a result of Brownian motion or random walks of solutes in a solution. These occur independently of solution state. The probability of such fluctuations leading to a nucleus exceeding the critical size, naturally increases the more solutes are present and are out on a walk. Hence, nucleation is dependent on supersaturation.(35)

Josiah Willard Gibbs laid the mathematical and physical foundations for such a description. He defined the free energy change associated with cluster formation as the sum of decreasing free energy as a new phase of volume x and decreased chemical potential ($\Delta\mu$) is formed ($G_V(r^3)$) and the increase in surface free energy owing to the creation of the solid-liquid interface surrounding the formed cluster ($G_S(r^2)$), Equation 7-12. Here n is equal to the number of atoms associated with a cluster, Ω the atomic volume of solute inside the cluster, A the surface area and γ the interfacial energy of a cluster.(36)

$$\Delta G = G_V + G_S \quad (7)$$

$$G_V = n \Delta\mu \quad (8)$$

$$G_S = \gamma A \quad (9)$$

$$\Delta G = n \Delta\mu + \gamma A \quad (10)$$

Spherical cluster of radius (r).

Chapter 1: General Introduction

$$\Delta G = \frac{4\pi r^3}{3\Omega} \Delta\mu + 4\pi r^2 \gamma \quad (11)$$

Substituting ($\Delta\mu$) with Equation 6.

$$\Delta G = -\frac{4\pi r^3}{3\Omega} k_B T \ln(S) + 4\pi r^2 \gamma \quad (12)$$

From Equation 12, which is graphically represented in **Figure 1-4** two observations spring to mind. The volumetric term drives the reaction towards its energy minimum and scales with the degree of supersaturation. The interfacial term destabilizes the forming cluster / nuclei increasing the total Gibbs free energy solely depended on cluster radius.

Based on geometrical constraints, as cluster volume is proportional to r^3 and surface area to r^2 there has to exist a supersaturation dependent critical cluster radius (r_{crit}) above which the volume associated gain in free energy outweighs surface - associated cost. Beyond this point, nuclei growth is self-perpetuating until a solution equilibrium state is re-established. The growth of nuclei can be controlled through either growth kinetics, or diffusion limitations rather than the thermodynamic driving force.(30)

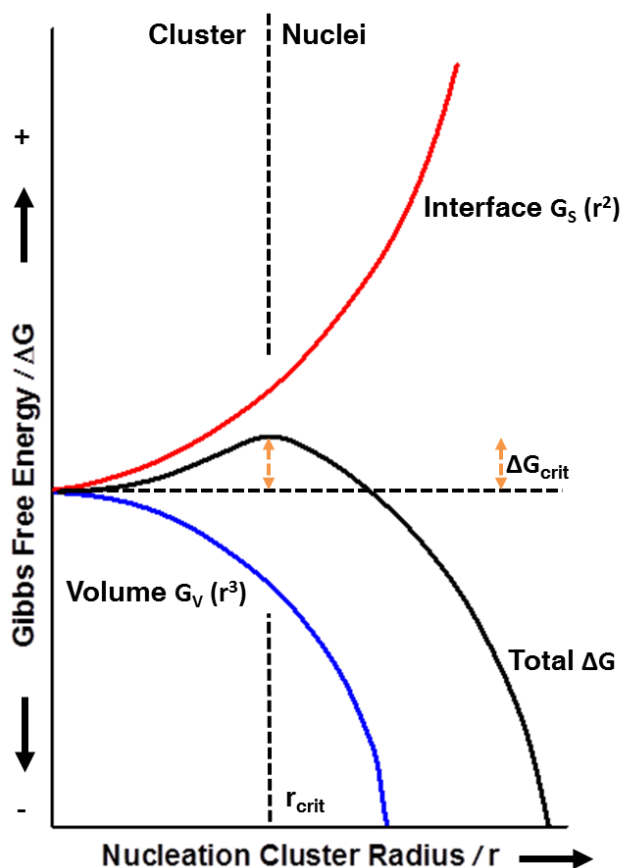


Figure 1 - 4: Total free energy change as a function of nucleation cluster size. Interfacial energy (G_s) opposes nucleation and nuclei formation whereas the secondary phase formation (G_v) promotes nucleation. As the cluster increases in size the interfacial term is outweighed by the volumetric term ($r \geq r_{crit}$) leading to the formation of a stable nucleus.(36)

The above describes the general concept of homogeneous nucleation. This refers to nucleation in the absence of any secondary interfaces, such as substrate surfaces or suspended particles, that reduce the activation barrier for nucleation. Of course this rarely occurs in practice. Nucleation in the presence of a catalysing interface is termed **heterogeneous nucleation**.(36) The reduction in activation energy or barrier for heterogeneously formed nuclei compared to homogenous formed nuclei is a result of the stronger interaction between the nucleating phase with the secondary interface than the bonds of solvation. As a result, a distinction has to be made between surfaces based on the degree of interaction with the nucleating phase, being either heterogeneously nucleating or crystallisation inert surfaces. On a macroscopic scale this is relatable to the wetting capability and contact angle of a solvent on specific substrates. Substrates that wet are likely to be good heterogeneous nucleators, whereas substrates with high contact angles are not expected to be.

1.3.2.2: Crystal Growth

Crystal growth is defined as the addition of elementary building blocks to an existing lattice structure after a crystalline nucleus has been formed. The conditions (most prominently the present degree of supersaturation, and agitation) under which crystal growth occurs determine not just the final particle size and/ or the number of crystals formed. Conditions may alter the limiting reaction steps and potentially change the underlying growth process altogether. This can have a direct influence over the final crystal morphology (Chapter 1.3.4).

The overall growth process can be broken down into the following successive steps.

- I. Transport to and diffusion of building blocks through the diffusion boundary layer surrounding the growing crystal. The diffusion layer thickness is determined by the system's Reynolds number.
- II. Adsorption of building blocks onto the crystal surface (partial desolvation).
- III. Building block surface diffusion to energetically favourable incorporation sites, from face to step to kink sites if kinetically feasible.
- IV. Integration into the existing lattice structure, including complete desolvation of the building blocks.
- V. Removal of the heat of crystallisation.

Each of these steps (I-V) has its own specific activation energy and kinetic factor, and is strongly dependent on the local surface and bulk supersaturation levels. As a general rule of thumb, the slowest process – which is generally associated with the highest activation energy - defines the growth rate, mechanism and type of crystal formed. In this manner, a distinction can be made between growth based on bulk kinetic limitations (i.e. a “shortage” of material supply to the crystal from the solution, where this takes place at low supersaturation levels and leads to steady-state crystal morphologies) and growth limited by building block integration and diffusion along the crystal surface (this occurs at high supersaturation levels and results in morphologies resulting from the imperfect incorporation of building blocks as material is supplied too fast from the solution). At even higher supersaturation values, crystal growth is offset by further nucleation events and polycrystalline materials can be obtained.(30)

Chapter 1: General Introduction

On a crystal surface not all incorporation sites for new building blocks are equal. A differentiation between favourable and less favourable incorporation sites is based on the deduction that a 3D crystal can present up to 3 distinct environments to an incoming building block. Environments are based on the degree of interaction of a building block with the crystal surface. These are in increasing order of accessible neighbouring lattice units - "unsaturated bonds" - face, edge and kink sites. See **Figure 1-5** for a graphical illustration. As systems tend towards a state of lowest free energy, sites that maximize the interaction between elementary building blocks (offering the highest number of unsaturated bonds -kink sites) are energetically most favourable and will therefore be filled first, if reaction kinetics are sufficiently slow. In turn, those positions require the least amount of energy (supersaturation) to be filled and on this basis the differentiation between occurring growth mechanism is made.

In order of increasing supersaturation these crystal growth mechanism are:

- I. Layer by layer or 1D growth. Growth units are added to a surface layer one by one. During the integration process blocks move from their original points of adsorption to energetically favourable position till a layer is completed and a new layer is nucleated by (III).
- II. Screw dislocation driven growth. Dislocation provides self-perpetuating new kink sites for the integration of building blocks. Bypassing the need of nucleating a new layer by (III).
- III. 2D island nucleation or birth and spread model. New layers are created on top of each other. Nucleation occurs on face sites, where this requires an elevated level of activation energy/ supersaturation. New layers are formed before the layer beneath is completed (insufficient surface diffusion kinetics).

The switch in the dominant crystal growth mechanism at a given supersaturation is similar to the formation of metastable polymorphs, and is a result of kinetic limitations in relaxing the supersaturation.

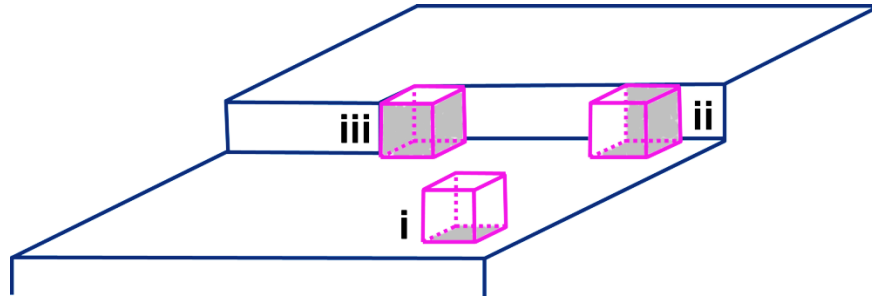


Figure 1 - 5: Possible building block adsorption sites on a growing crystal surface. In order of decreasing free energy (i) face, (ii) step and (iii) kink site. Highlighted in grey are the connecting “surfaces” of elementary building blocks (pink) to a crystal surface (blue). Reproduced after (37).

Oswald ripening, the growth of a larger crystal at the expense of smaller ones is another option of crystal growth. The presence of fewer larger crystal as compared to an equal volume of smaller crystals provides an energetically lower state of the system. This originates from the increasing surface to volume ratio as particles decrease in size, and the corresponding increasing number of unsaturated bonds across a given particle interface. If placed in equivalent solution the smaller particles dissolve while the already larger particles increase in volume by common crystal growth mechanisms.

1.3.2.3: Crystal Dissolution

Dissolution, the gradual release of elementary building blocks back into the solution in the form of solutes only occurs if a particular solution is unstable – undersaturated with respect to the dissolving phase. This originates from a negative state in chemical potential ($\Delta\mu$). In analogy to the criterion for crystal growth, dissolution can be described as a direct reversal of crystal growth.(38) This also applies to the actual dissolution mechanism as seen in **Figure 1-6**. With increasing undersaturation the dissolution mechanism changes from 1D step (layer) retreat to etch pit formation above, or in the vicinity of, crystallographic defects/ dislocations. A further increase in undersaturation results in the 2D nucleation of vacancy islands. This is analogous to the growth mechanism – dissolution mechanisms requiring an enhanced degree of undersaturation are associated with faster reaction kinetics.

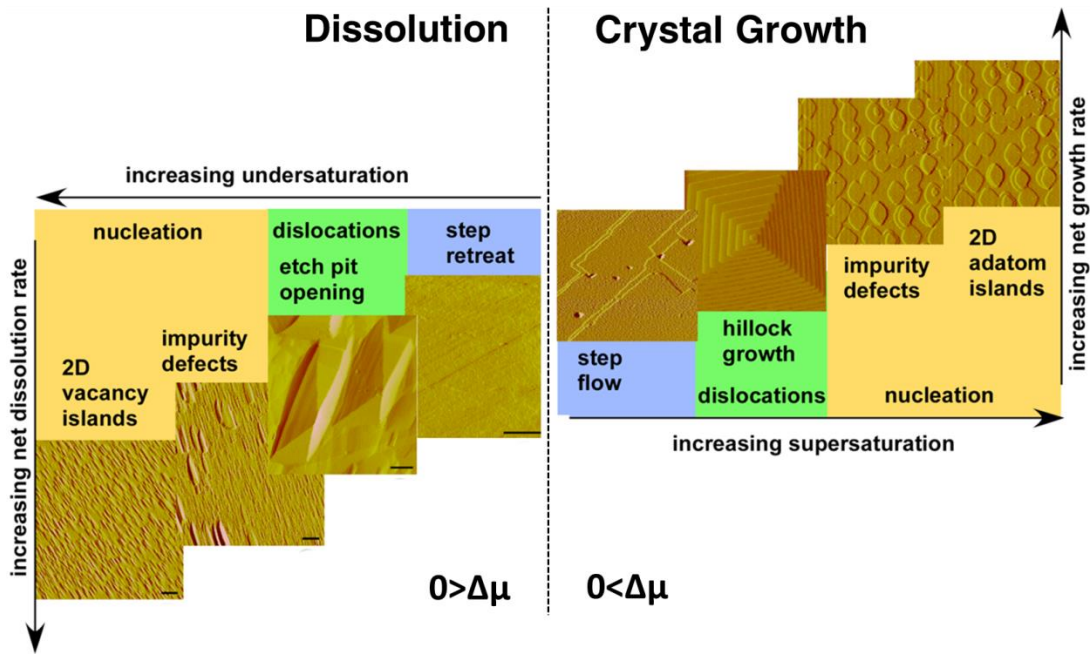


Figure 1 - 6: AFM images of SiO_4 demonstrating the dominating growth and dissolution mechanism as function of super/undersaturation. Scale bars $1\mu\text{m}$. Taken from (38).

1.3.3: Crystal Defects

Most crystals do not possess a perfect repetitive atomic or molecular arrangement, and are defined by their defects. A detailed description of the myriad of crystallographic defects known can be found elsewhere (39). The formation of screw dislocations due to their inherent importance to crystal growth and dissolution is described below. The detection of screw dislocations single handily reconciled experimental deviations from the above stated growth theory as offering a “low cost” option for crystal growth which avoids the need of 2D nucleation altogether.

A screw dislocation is one form of line defect. Quite literally, this means that one part of the crystal lattice is dislocated with respect to the rest of the crystal, due to an applied shear stress. On an elementary scale, a line of building blocks are out of their ideal lattice position. The lattice is therefore strained and the degree of strain is equal to the displacement of building blocks from their ideal positions.

For **edge dislocations**, which are another form of line defect, the displacement of building blocks from their ideal positions is commonly visualized by an extra half plane of blocks parallel to the applied shear stress. The dislocation moves one step at a time with the shear stress, which allows for the plastic deformation of crystalline material beneath its theoretical strength.

Chapter 1: General Introduction

In a **screw dislocation** the displacement and hence the dislocation propagates perpendicular to the applied shear stress. An exposed end is created when the end of a screw dislocation intersects a crystal surface. Crystal growth now occurs preferentially on this step, due to the increased number of unsaturated bonds. This continuously self-propagates as a new displaced step relative to bulk lattice is created throughout, as shown in Figure 1-7. This results in the formation of a growth spiral with a displacement of one lattice spacing (d) per 360° . The displacement is naturally maximal at the centre of the dislocation line – the dislocation core – and has a lower bulk density. The displacement takes the form of a propagating, decaying spiral, which is maximal at the core and traverses into the ideal lattice position with increasing radial distance from the core.

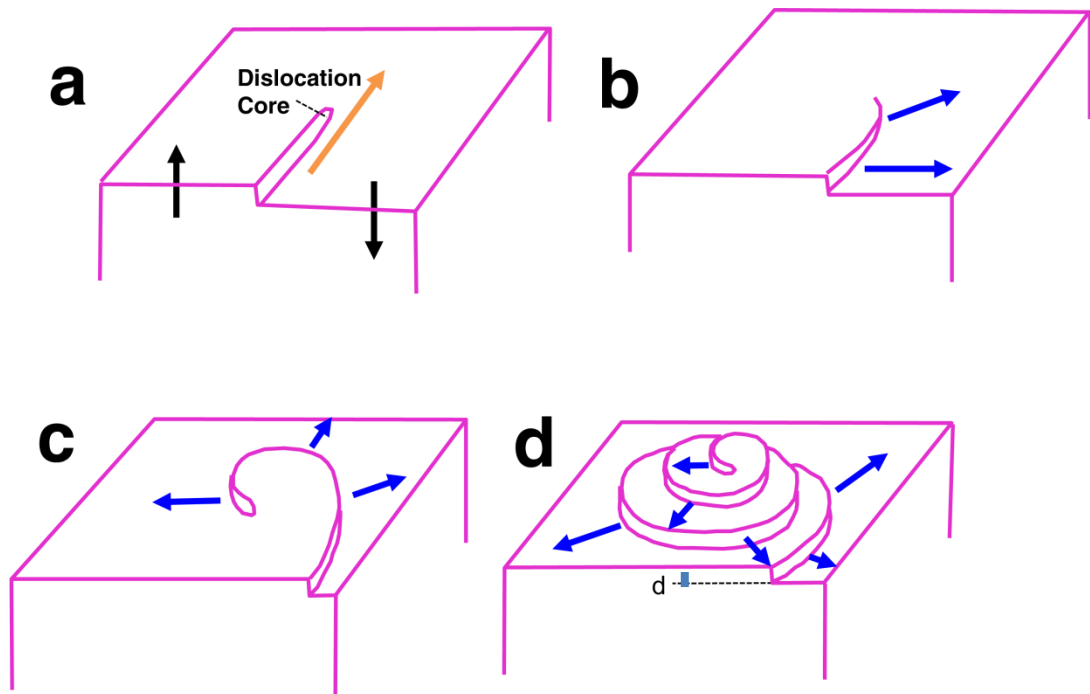


Figure 1 - 7: Illustration of spiral growth by screw dislocation. Shown is the progression from dislocation surface outcrop (a) to complete growth spiral (d). Orange arrow shows the direction of applied shear stress, Black arrow the direction of lattice displacement and Blue arrow the step direction. d (l) is equal to one lattice spacing. Reproduced after (40).

1.3.4: Crystal Morphology and Additives

The morphology a crystal adopts i.e. the sum of crystal habit (area ratio of faces present) and *Kristalltracht* (external facets presented by the crystal) is controlled either thermodynamically according to Wulff's rule or kinetically (high precipitation pressure).

1.3.4.1: Thermodynamic Morphology

Wulff's rule basically states that crystals of the same polymorph and of equal volume possess one equilibrium shape under thermodynamic constraints, corresponding to the minimal Gibbs free energy (ΔG_{\min}). This is achieved through the minimization of the total free surface energy across a crystal. This law and the associated ΔG_{\min} can be expressed as the product of crystal facet area (A_i) and interfacial energy (γ_i) across all crystal faces, Equation 13. See also Chapter 2.10.

$$\Delta G = \sum_i A_i \gamma_i \quad (13)$$

Different facets which exhibit different atomic arrangements do possess different surface energies. This is a result of the number of available surface bonds and the interaction of solvent and facet terminating atomic arrangement. In the case of calcite, for example, polar facets have higher interfacial energies. Hence, the addition of growth units is favourable and faster in polar crystallographic directions. Polar facets therefore reduce in size over time, leaving the developing morphology to be dominated by slow growing non-polar, lower interfacial energy facets.(41)

This balance in interfacial energies is not set in stone and relative interfacial energy changes between facets do occur for numerous reasons. With them the expressed crystal morphology adjusts. Factors include the type of solvent, environmental conditions and chemical potential. Most importantly for the work discussed, the crystal morphology adjusts based on crystallographic defects and due to the presence of additives (impurities) in solution or if the crystal is grown on a nucleating template.(42)

A range of different mechanisms have been proposed to describe how **additives** affect crystal growth and nucleation. The most reported (which is independent of the particular type of additive be it ionic, low or high molecular weight compounds) is the change in interfacial energies and growth kinetics due to selective surface adsorption and blockage of incorporation sites on specific crystallographic facets. It

Chapter 1: General Introduction

is also possible that additives become incorporated into or occluded in the crystal.(43, 44)

Additives also have a significant effect on the polymorphic transition of minerals, where they display not just facet selective interactions but also preferential interaction between different polymorphs. As a result they can stabilize a metastable phase either directly against the polymorphic transition or indirectly by retarding/ inhibiting the formation of the next stable polymorph. An example of the former is the stabilization of vaterite by the delayed addition of poly(acrylic acid).(45) The latter includes the hindrance of calcite formation at elevated levels of magnesium ions present in solution, which results in the formation of aragonite at room temperature.(46-48)

Other means of morphological control involve, for example, the restriction of crystal habit development to a physically confined geometry. This has been demonstrated to be synthetically successful by confining crystal morphology in the pore space of track etch membranes or colloidal templates.(49, 50)

1.3.4.2: Kinetically Governed Crystal Morphologies

That crystal morphologies can be governed by precipitation kinetics is primarily a result of increased precipitation pressure/ supersaturation. This is fundamentally determined by the insufficient velocity of one or more crystal growth steps (Chapter 1.3.2.2) in achieving the lowest possible free energy minimum and is consistent with the change in governing crystal growth mechanism with supersaturation. **Figure 1-8**, shows the general trend in morphological development with increasing supersaturation. These change from thermodynamic single crystal morphologies at low supersaturation levels to diffusion limited polycrystalline dendritic structures at high supersaturation level. Diffusion - limited here refers to the surface diffusion of growth units into the most favourable positions. Kinetic - limited describes when the supply of growth units to the growing crystal surface is the rate determining factor.(36)

Chapter 1: General Introduction

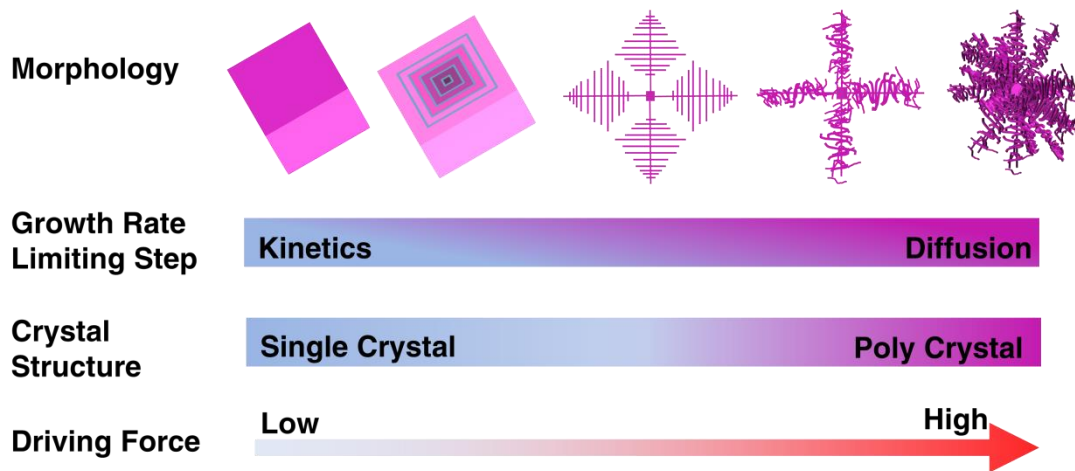


Figure 1 - 8: Changes in crystal morphology and rate determining step with increasing supersaturation. Shown is the transition from kinetic control at low supersaturation (thermodynamic morphology) to diffusion controlled conditions (kinetic oriented morphology) at high supersaturation. From left to right single crystal near equilibrium, hopper crystal, single-crystalline ordered symmetric dendrite, partially disordered dendrite having a single-crystalline ordered trunk and disordered polycrystalline side branches, polycrystalline dendrite. Reproduced after (51).

1.3.5: Non Classical Crystallisation

1.3.5.1: Multi Step Nucleation Theories

The classical theory proposed by Gibbs describes nucleation on a phenomenological level. Its goal is to describe the phase transition or nuclei formation by means of macroscopic properties e.g. surface tension and density. Local, short-lived temperature fluctuations induce the formation of nucleation clusters in a stochastic manner. At a given point, a cluster or fluctuation overcomes a certain size at which point energy is gained by forming a secondary phase. This outweighs the associated interfacial cost which limits the stability of smaller cluster.(33)

Over the years various shortcomings of this theory have come to light.(52) These include the overestimation of nucleation rates at low and high supersaturation and more troublesome inconsistencies between the formation of local periodic structure and density were detected. New microscopic nucleation theories were therefore proposed, including the **density fluctuation theory** (DFT). DFT basically describes a nucleus as a function of two structural parameters, namely a critical structured size and coinciding density. It does so by treating any nucleating system as having an inhomogeneous structure.(53)

Two Step nucleating theories work on those postulations. Here, density changes occur first, before a periodic structure develops in the crystallizing unit.(54) This can be imagined as a combination of two distinct steps, (1) the formation of short-lived, highly dense, disordered liquid droplets/ nucleation clusters and (2) internal rearrangement of those clusters to form the actual nuclei. The short-lived, liquid droplets formed in solution, with their high density of solute molecules and elevated local supersaturation levels therefore present a more favourable environment for nucleation to occur. The actual formation of a nucleus is concomitantly occurring through a reorganization of the cluster entities to give a structured object.(13, 55) Further, it is clear that we have here a process involving two energy barriers, corresponding to cluster formation and rearrangement. The critical free energy requirement for the phase transformation is divided into two quantities. The total energy requirement for a reaction can be assumed to be route-independent and is thus equal in both scenarios. The two-step nucleation theory should therefore predict higher nucleation rates than the CNT on a thermodynamic basis, and a cascading or catalytic effect can be imagined considering that a time deferred energy requirement is present. Experimental evidence for this theory on a

Chapter 1: General Introduction

macroscopic scale was provided by Zang and Liu (56-58) who used an alternating electric field to induce colloidal particle precipitation via a two-step mechanism.

Going one step further, in recent experimental history two observations were made in mineralizing solutions of calcium carbonate - the detection of stable pre-nucleation clusters (PNC) and polymer induced liquid precursor phases (PILP) - which suggest that further alterations to, or a better description of the governing nucleation mechanism behind calcium carbonate nucleation is required.(59, 60)

The reported existence of stable **pre-nucleation clusters** (PNC) compared to the short-lived clusters described above is currently suggested for a variety of organic and inorganic systems.(55, 59, 61-63) PNC refer to amorphous clusters of atoms ~ 1-2 nm in diameter, which are present in any solution prior to any nucleation event, even in undersaturated solutions. They are different to ion pairs in that they exhibit a particular meta-stability in solution, and sit in an ambiguous potential well. A refined view in the case of calcium carbonate mineralizing solutions refers to PNC as dynamically-ordered liquid-like oxyanion polymer (DOLLOP). These undergo constant change and thus remain in thermodynamic equilibrium with the surrounding solution, which suggests meta stability.(64) It has been suggested that PNC may provide a starting point in the formation chain of amorphous and crystalline calcium carbonate, **Figure 1-9**. Direct evidence of this or the involvement in any form of crystallisation has not as yet been obtained.

PNC and applicable experimental techniques for phase identification and compositional analysis are necessary limited in their ability to resolve short-lived species. Future studies will have to provide a conclusive answer as to the significance of the observations made.

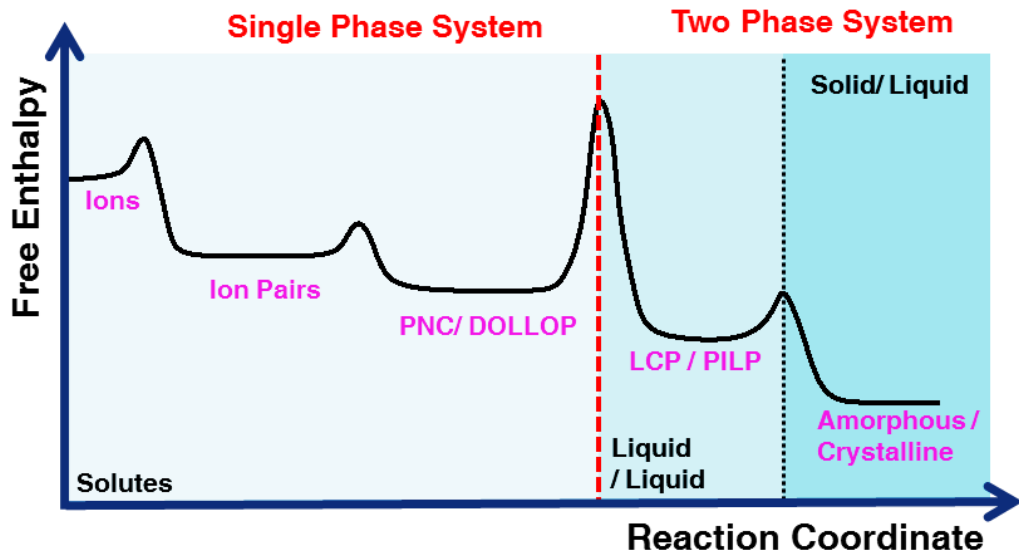


Figure 1 - 9: An idealized sequential overview of calcium carbonate phase precipitation from supersaturated solution prior to crystalline calcium carbonate formation in the context of non-classical multi step nucleation theory. Shown is the position of PNC / DOLLOP and following liquid crystalline phases (LCP) e.g. PILP or liquid amorphous phases as a result of two phase segmentation of the crystallizing solution in the context of non-classical nucleation mechanism. The formation of secondary solid amorphous and crystalline phases is omitted. Further given are assumed relative activation barriers for phase transition. Reproduced from (64).

The detection of a polymer induced liquid precursor phases (PILP), and the subsequent identification of liquid–liquid phase separation in the absence of polymers brings a 2-step nucleation mechanism by means of spinodal decomposition into the picture.(25, 26, 33, 64, 65)

Spinodal decomposition. For reasons of entropy, a solution at a given composition is thermodynamically stable only at a particular composition. Away from this the solution splits into coexisting phases. Spinodal decomposition describes that process. **Figure 1-10** provides a schematic representation of this, and shows the decomposition into a low and high density phase from an unstable solution past the binodal or coexistence curve (---) and the region of 2 phase liquid-liquid coexistence between spinodal (- - - -) and binodal. The area in which the nucleation of liquid CaCO_3 / PILP is thought to occur is highlighted. Detailed formation of crystalline or solid amorphous phases following spinodal decomposition is omitted here for simplicity. See Figure 1-2 for the eventual phase/ polymorph transformations.

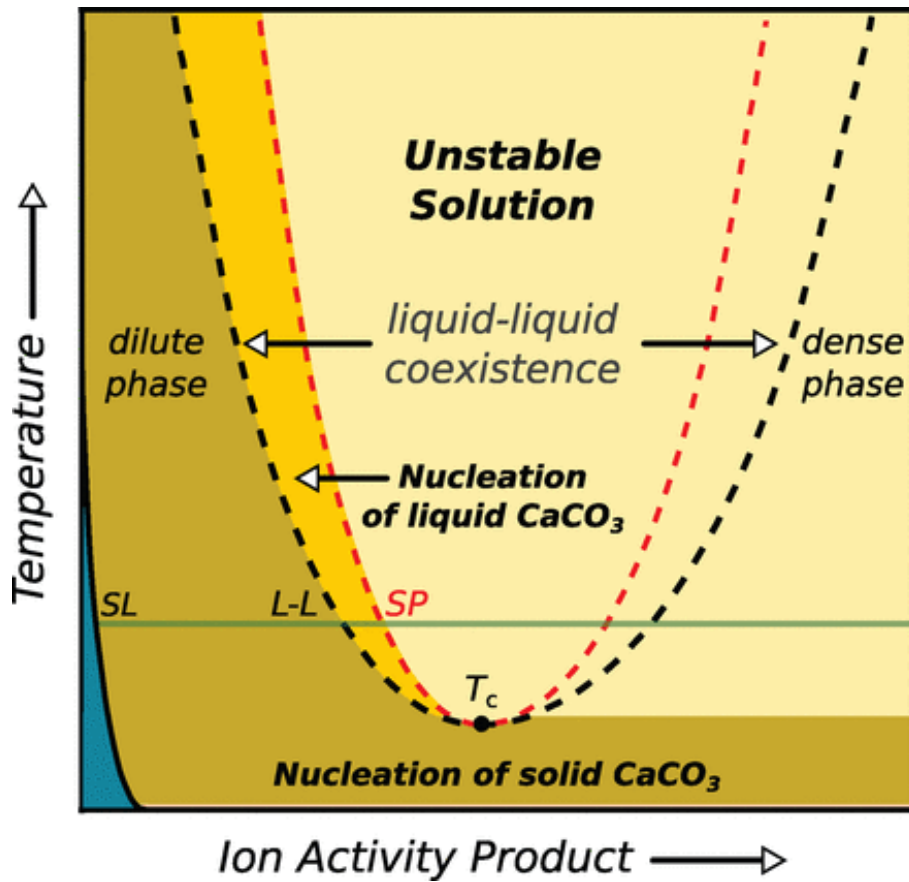


Figure 1 - 10: Schematic phase diagram of the $\text{CaCO}_3\text{-H}_2\text{O}$ system assuming spinodal decomposition and liquid-liquid phase coexistence e.g. two or multi step nucleation. The olive line represents a constant temperature slice through the phase diagram as the saturation is increased. (SL) single solubility line for a given solid phase (calcite, aragonite, vaterite, and ACC). Blue undersaturated region. "Indirect nucleation of the solid phases occurs to the high supersaturation of the dashed black liquid-liquid coexistence line (L-L). The bright yellow phase field bounded by the L-L line and the dashed red spinodal line (SP) indicates the conditions in which nucleation of the dense liquid phase is possible. In the region bounded by the spinodal line, the solution is unstable to fluctuations, and liquid-liquid separation proceeds."(33) Image taken from (33).

1.3.5.2: Crystal Growth by Oriented Attachment and Mesocrystal Formation

Over the last two decades numerous crystal growth studies have revealed that certain observations of the growth mechanism were not reconcilable with the classical ion by ion crystal growth mechanism, **Figure 1-11** (a). This eventually lead to the proposition of two alternative, yet somewhat interchangeable, growth mechanisms in the formation of what commonly appear to be single crystals, (b) oriented attachment, or (c) polymer guided self-assembly of crystallites - Mesocrystals.(28, 66) The latter has recently been modified to refer to a structure classification rather than a formation mechanism per se.(67)

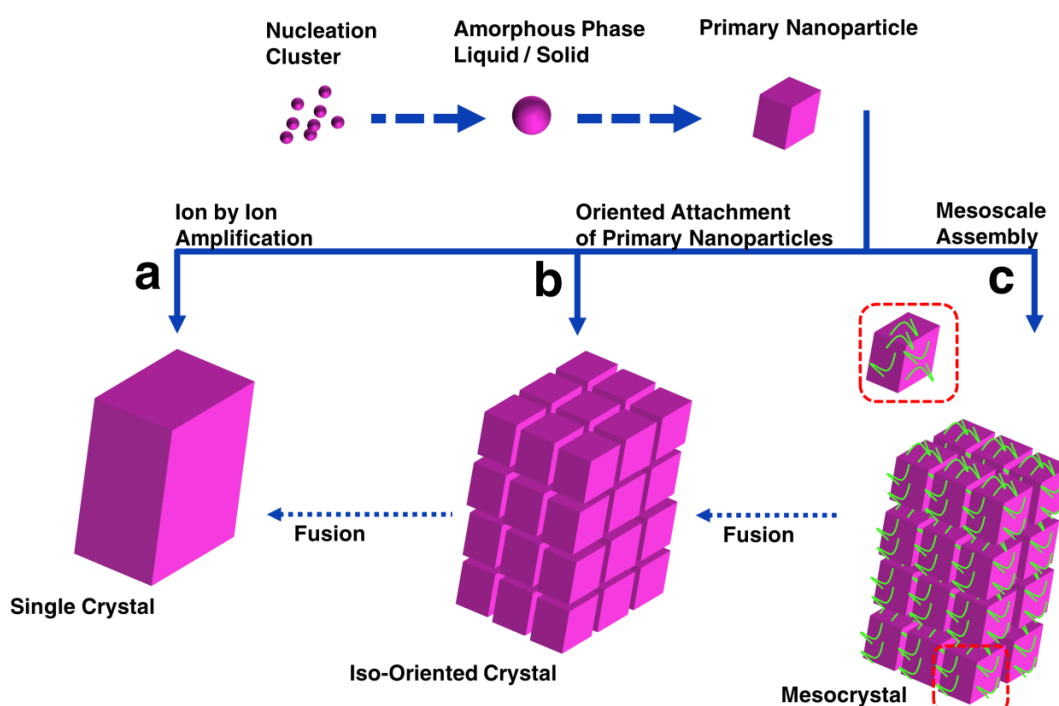


Figure 1 - 11: Classical and non-classical crystal growth mechanisms. Given are growth mechanism alternatives after nucleation of the primarily nanoparticles (~10-100 nm). (a) Represents the classical ion by ion growth pathway of nanoparticle amplification. (b) Oriented attachment of primary nanoparticles to form an oriented crystal, where the nanocrystalline building units can lock and fuse. (c) Mesocrystal formation primary nanoparticles covered by an additive (assembly enhancer/enabler) undergo a mesoscale assembly (mesocrystal). The nucleation step may or may not involve the formation of an amorphous precursor liquid or solid and utilization of pre-existing nucleation cluster. Reproduced from (12).

The **oriented attachment** driven crystal growth mechanism is founded on observations made by Banfield of the self-assembly of iron oxide and titania nanoparticles in solution.(66, 68) Growth by oriented attachment describes the spontaneous self-assembly of amorphous and/ or crystalline nuclei (primarily

Chapter 1: General Introduction

nanoparticles) into superstructures with a common crystallographic orientation.(69) The result are “iso-oriented crystals” – which on the macroscopic level diffract ideally as single crystals, such as those found in biominerals such as nacre or sea urchins spines.(67, 70) Observations of such assembly at the nano-scale are currently limited to two dimensional observations synthetically.(71) A study of iron oxyhydroxide nanoparticle self-assembly revealed that particles undergo a continuous rotation and interaction until they find a corresponding lattice match. At this point direct interfacial contact is established and solidified via ion by ion addition around the contact point between the two nanoparticles.

Oriented attachment depends foremost on the existence of a metastable period of the nanoparticles in solution, which is sufficient to allow assembly to take place. The assembly process in itself can be a result of intra-molecular forces such as van-der-Waals forces, the isotropic structure of nanoparticles and statistical particle collision, and subsequent grain rotation.(72) The ultimate driving force underlying oriented attachment is assumed to be the minimization of surface free energy, as inferred from the phenomenon of Ostwald ripening. During oriented attachment, two particles/ nuclei fuse together causing two high energy crystal faces to disappear. In common with Ostwald ripening, oriented attachment must not be limited to supersaturated solutions, but can potentially also occur in saturated solutions.

Mesocrystals and the idea of mesocrystal formation is itself a sub classification of the oriented attachment growth mechanism.(37, 56) The initially, idealized mesocrystal formation concept introduced for calcium carbonate relied on the presence of nanoparticle stabilizing and self-assembly enabling factors such as dipole-dipole interactions, epitaxial growth (mineral bridge formation between two adjoining particles) or a constrained volume mediated by surface absorbed polymer species such as poly(styrenesulfonate) or poly(styrenesulfonate) maleic acid. The latter introduced the structural classification of a mesocrystal,(67) and states that mesocrystals are colloidal crystals made up of many particles which are ordered in a common crystallographic register. They therefore behave as highly ordered single crystals.(73-75)

So far, the only quantities used to define a mesocrystal are the total free surface area and scattering coherence length. The surface area should be significantly larger for a mesocrystal than for a single crystal of identical volume due to the internal surfaces between the singular building units. The coherence length

Chapter 1: General Introduction

is expected to be much smaller than for a single crystal. Differentiation between iso-oriented crystals, mesocrystals and true single crystals is difficult as determination of crystalline coherence length is error prone and often not even considered, leaving judgement to be based on appearance and increased surface area.

1.4: Calcium Carbonate

1.4.1 General Information

Calcium carbonate (CaCO_3) was selected as the principal material for investigation for multiple reasons. Firstly it is of geological **importance**. CaCO_3 mineral deposits make up to 7% of earth crust. Deposits play a key role in the global carbon dioxide cycle and hence global warming.(76) Secondly, CaCO_3 has many industrial applications. Currently, CaCO_3 is used as a filler and coating pigment in the manufacturing of paint and paper. Other uses include CaCO_3 as a tableting and carrier material in life science products. Most interesting for us here is the fact that CaCO_3 is the most abundant and documented of all biominerals. It seemingly indulges in most non-classical crystallisation concepts and assembly/ incorporation strategies. This ranges from the utilisation of “solid” amorphous precursor and polymer induced liquid precursor phases to the shaping of complex morphologies by means of oriented attachment.(2, 3, 14, 67, 77, 78) Preferred orientation and enhanced structural properties occur as a result of mineral facet specific template interactions and preferential impurity incorporation.(15, 23, 79-83) This width and associated spread in morphologies and applications make it the ideal model system to increase our understanding of mechanisms guiding nucleation, growth, orientation and polymorph selection.

1.4.2: Calcium Carbonate Polymorphism and Morphology

Calcium carbonate is a rock-forming mineral which exhibits 3 known **polymorphs**, multiple hydrates and multiple amorphous phases under ambient conditions.(42, 84, 85) In order of decreasing solubility these are amorphous calcium carbonate (ACC), calcium carbonate hexa-hydrate, calcium carbonate monohydrate, vaterite, aragonite and calcite. A summary of the structural parameters of the 3 most stable polymorphs and ACC is given in **Table 2** alongside their utilization in particular biomineralizing organisms.

Chapter 1: General Introduction

Phase		ACC	Vaterite	Aragonite	Calcite
Composition		CaCO ₃ : H ₂ O	CaCO ₃	CaCO ₃	CaCO ₃
Crystal System		-	Hexagonal	Orthorhombic	Trigonal
Lattice Constants [Å]	a	-	4.13	4.95	4.99
	b	-	4.13	7.96	4.99
	c	-	8.48	3.73	17.06
Angles [°]	α	-	90	90	90
	β	-	90	90	90
	γ	-	120	90	120
Density [g/cm³]		2.59	2.66	2.93	2.71
Habit		-	Needle Disk	010,011	104
Solubility Product pK_{sp}		6.22-6.60	7.60-7.91	8.22-8.34	8.42-8.48
Organism		Crustaceans	Gastropods	Molluscs	Molluscs
Utilisation		Mechanical Strength	Exoskeleton	Exoskeleton	Exoskeleton
Organism		Plants	Ascidians	Fish	Mammals
Utilisation		Calcium Store	Protection	Gravity Sensor	Gravity Sensor
Organism					Trilobites
Utilisation					Optical Focus

Table 2: Properties of the anhydrous crystalline calcium carbonate and ACC, and their utilization in biomineralizing organism. Reproduced from (1, 42, 86, 87).

The most common polymorph of calcium carbonate in biominerals by mass is calcite. Control over the precipitated polymorph is determined either by kinetic or thermodynamic constrains. The transition of polymorphs in solution follows Ostwald's empirical rule of stages.(24) In the case of calcium carbonate a phase transition can occur from ACC via vaterite to aragonite and/ or calcite.(88) However, not all intermediates will necessarily be exhibited. The relative thermodynamic stabilities of these polymorphs can be modified using additives or changes in environmental conditions as shown by Nan (89) who used PAM and CTAB to transform calcite, the commonly thermodynamically most stable polymorph to aragonite at elevated temperatures. That the higher solubility polymorph is precipitated before a less soluble polymorph can be based on drastic differences in precipitation kinetics between the respective polymorphs.(9, 90)

Chapter 1: General Introduction

An overview of the activation energy and corresponding solid state activation temperatures for the non-hydrated polymorphs was given by Wolf and Radha.(91, 92) The latter also includes data concerning ACC phase transformations. The **transformation mechanism** between the crystalline species is thought to occur through dissolution and reprecipitation, where the reprecipitation process is thought to be rate-limiting in most cases.(88) The transformation mechanism of ACC to a crystalline polymorph is not particularly clear at this moment.(93-97)

The dedicated experimental precipitation of a particular polymorph of calcium carbonate is more hit and miss, despite certain ground rules. This is due to the myriad of experimental procedures, environmental conditions, additives used throughout the literature and the varying metastable polymorph stabilizing mechanism under this multitude of conditions.

Vaterite, for example, is found to be stabilized by the use of surfactant mixtures.(98, 99) Surfactants are believed to hinder a particle-mediated growth mechanism. Similar observations were made in the presence of ammonia which seemingly also extends the existence of vaterite in solution. Another route to gain control over the precipitating polymorph is through simple variation of the ethanol/water ratio used as a precipitating solvent.(100-102) As the ratio increases, a transition from rhombohedral calcite via spherical vaterite to dendritic vaterite is observed. An explanation for this transition can be found in the energetically more favourable interaction of the calcium carbonate surface with ethanol than with the water molecules present. This leads to an increased kinetic stability of the polymorphs present in solution,(103, 104) which can be utilized in the stabilization of ACC.

Aragonite is seldom precipitated under atmospheric crystallisation conditions, and generally forms at elevated temperatures (>50°C) and under slow precipitation kinetics.(105) If precipitated at room temperature, the presence of magnesium ions as a crystallisation additive is commonly involved. Magnesium ions bind/ incorporate preferably into certain crystal faces present only in calcite not aragonite. This elevates the solubility of calcite and thus induces a shift in thermodynamic stability from calcite to aragonite.

The **morphologies** of the calcium carbonate polymorphs precipitated varies greatly depending on the crystallisation conditions, and therefore cannot always be used as a reliable indicator of particular polymorphs. A range of techniques have therefore been used to identify CaCO₃ polymorphs and secondary co-precipitated minerals. The most simple and therefore the most used here include Powder X-ray diffraction (PXRD), Raman and IR-Spectrometry. Examples of the polymorph specific spectra

Chapter 1: General Introduction

can be found in Appendix A. Common precipitates of calcite display as rhombohedra, aragonite as single crystalline bundles of needles and vaterite as spherical objects.(106) ACC is composed at the primary level of non-crystalline spherical particles, 50-400 nm in diameter.(86)

An overview of CaCO_3 polymorph crystallography can be found in (107). Provided below and extended in experimental chapters are structural information regarding calcite and ACC.

1.4.3: Calcite

The most stable polymorph of calcium carbonate is calcite. It is commonly described using an elementary hexagonal unit cell for simplicity, but actually possesses a rhombohedral unit cell. This is well reflected in the macroscopic rhombohedral shape of synthetic calcite crystals. The unit cell can be further imagined as a modification of the face centred cubic unit cell of sodium chloride,⁽¹⁰⁸⁾ where Na^+ and Cl^- ions are replaced by groups of Ca^{2+} and CO_3^{2-} . Due to the size difference and anisotropy of the CO_3^{2-} anion compared to the Cl^- anion, the unit cell distorts. This gives rise to a face-centred rhombohedral unit cell, where a stretch in the c axis occurs to accommodate the carbonates.

The spatial arrangement of ions in a calcite crystal is given in **Figure 1-12**, which provides a side view (a) and top down projection (b) of the atomic arrangement with respect to the crystallographic c axis. The alternating, homoionic layers of CO_3^{2-} (royal, orange) and Ca^{2+} (turquoise) can be seen normal to the crystallographic c axis. The carbonate groups adopt an equilateral triangular shape within the plane and are rotated in the plane by 60° from one layer to the next. 6 alternating layers form a hexagonal unit cell – encircled in red – and each calcium ion is surrounded by 6 carbonate groups with each oxygen being paired to two calcium ions one in the layer above and one in the layer below.⁽¹⁰⁹⁾

Also shown here are common crystallographic directions and planes seen in the research presented in this thesis (c). Important is the distinction between homoionic and heteroionic facets/ directions. Homoionic or polar crystallographic facets such as (001) or (012) consist only of carbonate or calcium ions in one layer. They are therefore high energy facets and possess relatively high interfacial energies as compared to heteroionic facets. They thus grow fastest and are present as smaller facets (if at all) in the final morphology.⁽¹¹⁰⁾ Polar or heteroionic facets such as {104} possess an alternating structure of carbonate or calcium ions in the same layer. These ultimately determine the idealized equilibrium shape expected of a growing calcite rhombohedron.

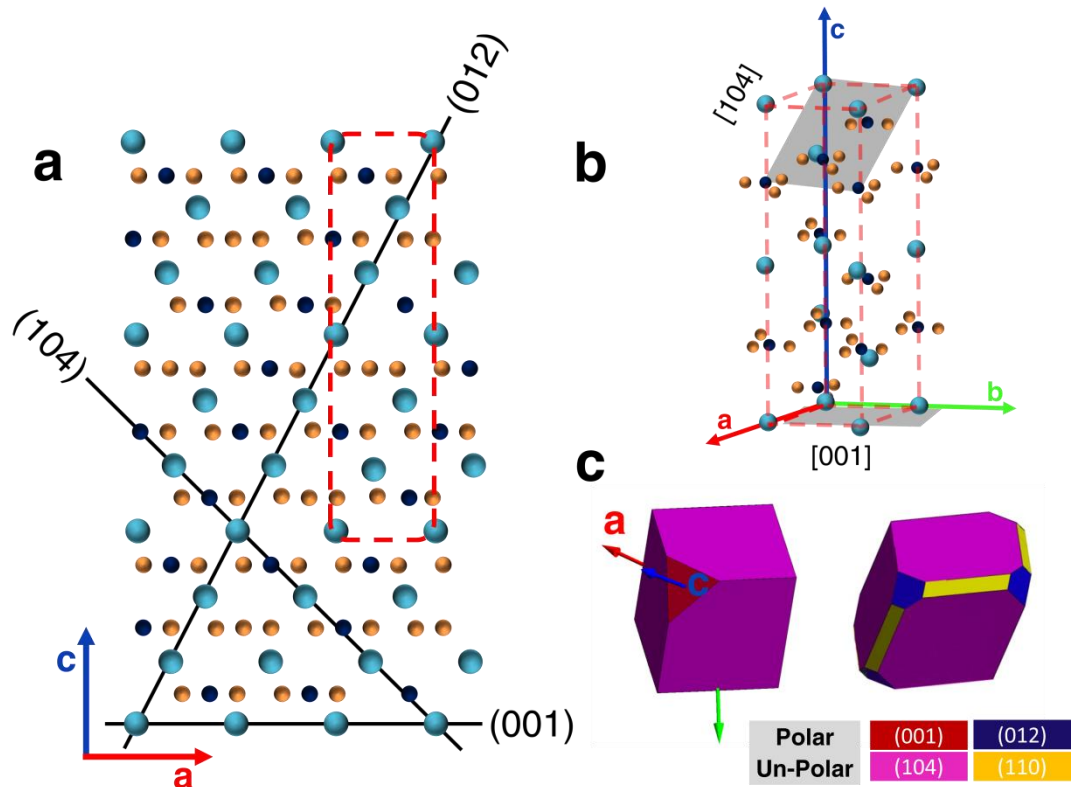


Figure 1 - 12: Illustration of the calcite crystal structure and its morphological expression. Shown is a side view (a) and top down projection (b) of relative atomic positions and crystallographic directions in relation to the crystallographic c axis. Calcium (●), Carbonate (●) and Oxygen (●). A hexagonal unit cell is outlined in red. Presented in (c) are Wulff reconstructions highlighting the morphological expression of homo – and hereto ionic facets of interest.(111-113)

1.4.4: Amorphous Calcium Carbonate

1.4.4.1: Amorphous Calcium Carbonate and Biominerals

Amorphous calcium carbonate (ACC), the amorphous precursor to the crystalline CaCO_3 polymorphs, was first mentioned in the literature over 100 years ago, where it was reported as a mineral deposit that did not diffract X-rays. However, it became forgotten soon afterwards.(114) A particular interest in this phase arose much later and is founded in the observations of how biomineralizing organisms utilize such amorphous precursor to form their respective biominerals.(14)

The prime example of such control is the formation of spicules in sea urchin larvae.(18) Formation of ACC and subsequent utilization in biomineral formation is postulated to occur in membrane-delineated compartments which may be further functionalized and contain soluble organic additives.(97, 115, 116)

This process is shown in detail, **Figure 1-13a**. Precipitating ions are actively taken up from the environment (seawater) by the organism/ cell and are subsequently sequestered and actively transported inside the cell and pumped against a concentration gradient into specialized delimited vesicles in which the formation of ACC occurs. Precursor bearing vesicles are next transported to the site of utilization. In the case of a sea urchin spicule this is the syncytium which is a multicellular compartment with minimal water and space between the growing spicule mineral and the syncytial membrane. Once delivered, the precursor ACC undergoes an amorphous to crystalline transformation. The spicule therefore grows one step at a time.(117) Visual evidence of the latter stages of this mechanism has been provided by photo emission electron microscopy (PEEM), **Figure 1-13b**, which shows the presence of ACC at the growth fringes of the calcitic spicule.(118, 119)

ACC in general appears to fulfil three major roles in biominerals. It can act as a transient, shapeable precursor to crystalline CaCO_3 biominerals as discussed above,(120) as a dense ion storage phase which readily dissolves upon request to meet e.g. calcium deficiencies.(121, 122) It can also act as a structural material due to its ability to incorporate high concentrations of trace elements and its isotropic nature.(23) Saying that, it has been shown that ACC is not ultimately required for the formation of complex-shaped, single crystalline structures.(50)

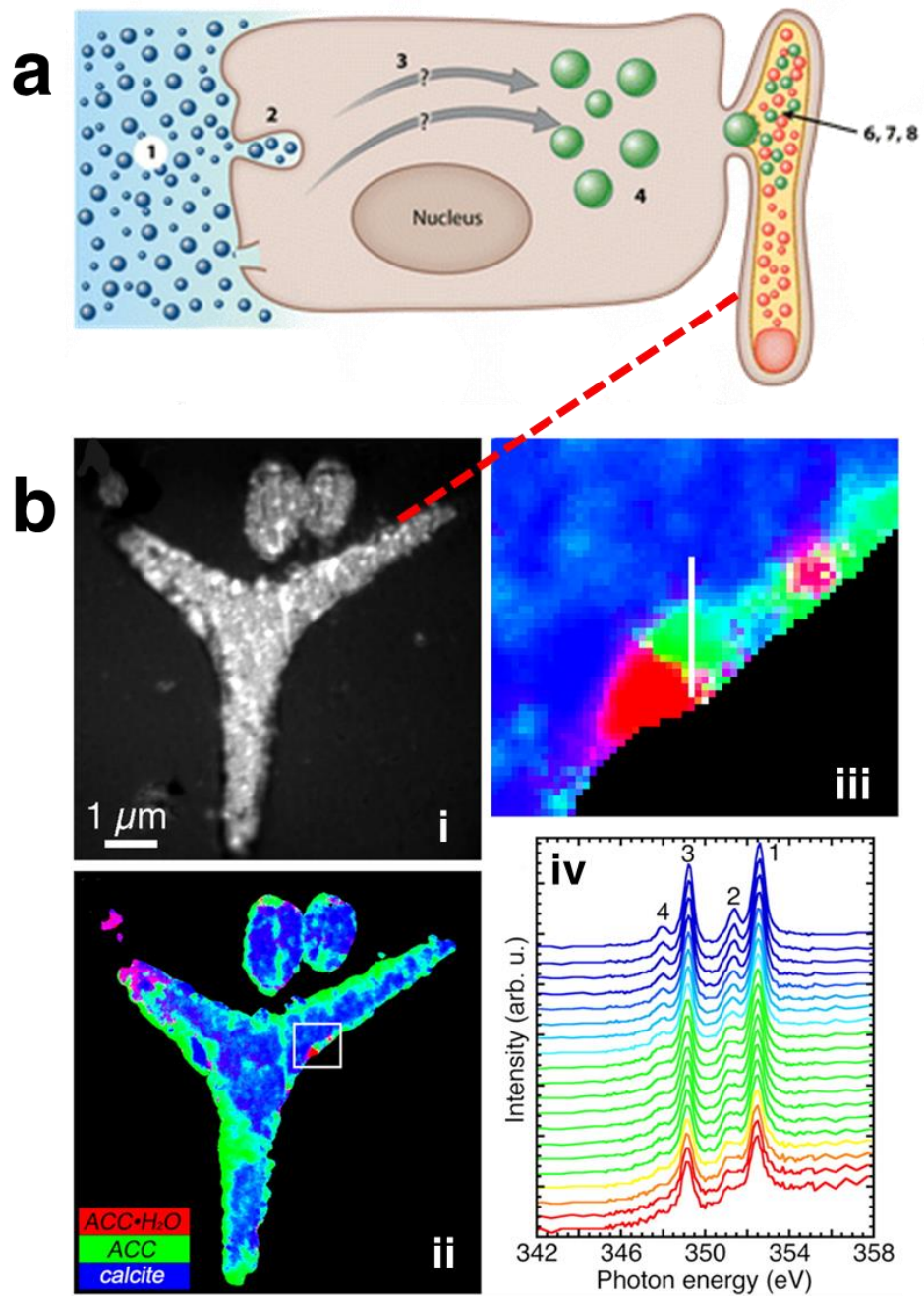


Figure 1 - 13: (a) Scheme of ACC formation in the course of sea urchin spine mineralization. (1) Uptake of precipitating ions. (2) Ion-sequestering and (3) transport to specialized vesicles. (4) ACC formation inside of vesicles. (5) Transport of ACC vesicles into the syncytium and to the crystallisation fringes(6). (7 & 8) Transformation of ACC into more ordered phases and attachment to / growth of the crystalline spicule. Taken from (117). (b) Component micrographs of developing spicules. (i) XANES-PEEM image at the Ca L-edge. (ii) RGB map displaying the results of component mapping corresponding to a particular mineral phase. (iii) Zoomed section of (ii). (iv) XANES spectral differences between calcite and ACC used for colour component mapping. Taken from (118).

The formation and transformation of biogenic ACC occurs as a result of intricate control and complex interactions. There are many open questions, some of which

Chapter 1: General Introduction

will be touched upon in Chapter 3. These include; "how is the inherently unstable amorphous phase stabilized?" "What is the role of the physical environment and the organic soups it's mineralizing in", and finally, "what is driving force behind the amorphous to crystalline transition, what is the mechanism?"

1.4.4.2: Structure and "life-cycle" of Amorphous Calcium Carbonate

ACC, having the highest solubility, precipitates before any polymorphs at high supersaturation levels according to Ostwald rule of stages.(93) Potential reasons for this have been discussed and include a decrease in activation barrier for "nucleation" and an increase in growth rates, as was postulated by Gale, 2010.(123) ACC exhibits fewer spatial constraints than the crystalline polymorphs benefitting its "nucleation" and has rough atomic surfaces. The latter reduces the activation barrier for ACC growth/ coalescence due to easier disturbance of the solvation layers. Altogether, this results in faster precipitation kinetics as compared to polymorphs, even at nominal supersaturations.

How ACC **forms** is still a question of interest, especially in consideration of the pre-nucleation steps introduced earlier. Faatz (65, 124) tried to visualize the process using a hypothetical phase diagram based on Gower's observations of the formation of a polymer induced liquid CaCO_3 precursor phase (PILP) prior to ACC formation.(60) He suggested that the mineralizing solution undergoes a spinodal liquid-liquid phase segregation (i.e. the solution splits into two separate phases with different physical characteristics and unequal chemical potential spread uniformly throughout the solution; this does not require specific nucleation sites) – Chapter 1.3.5.1. The formation of the spherical amorphous particles occurs as the carbonate/ calcium concentrations in solution exceeds a certain threshold concentration. The system then divides into a bulk phase of low calcium and carbonate concentration and a minor highly concentrated liquid droplet phase (liquid ACC). Finally, the liquid ACC phase eventually undergoes "gelation"/ water expulsion and subsequently forms a solid amorphous phase in the form of spherical droplets, for energy minimization reasons, Figure 1-9. The diameter of these spheres was also later found to depend on experimental variables such as temperature, and pH. Therefore, a generalized size range cannot be given as literature values vary from 10-400 nm and information regarding early stage investigations i.e. the initial liquid ACC, is limited.(64, 121)

Chapter 1: General Introduction

This scheme was experimentally confirmed by Wolf and Wallace,(26, 33) who investigated the formation of various carbonate metal complexes. They reported the formation of a liquid-liquid phase separation in the absence of any polymer additives, where this leads to liquid-like amorphous intermediates that behave like classical emulsions. It is believed that the stabilization of the liquid-like amorphous intermediates can be explained through ideas from classical emulsion theory including steric, electrostatic- and depletion stabilization. This in turn implies that liquid-liquid phase segregation may be the general way ACC forms in solution. Consequently, the presence in solution of a polymer such as poly(acrylic acid) in the initial work of Gower does not induce phase separation, but it rather facilitates access to/ extends the lifetime of the liquid precursor as a precursor to solid ACC, as found in biominerals. A follow-up study (Gower (64)) proposed that stable CaCO_3 pre-nucleation clusters might be the starting point of the ACC formation chain.(59)

Structure wise, ACC is often described as a family of phases which exhibit various degrees of short range order ($<15 \text{ \AA}$) and hydration levels, depending upon the formation conditions e.g. pH-level, additives present, precipitation method and confinement.(14, 121, 125-127) In this sense, it was discovered that ACC phases exhibit short-range atomic order around the calcium ion in the first and second coordination shells, which appears to reflect the structure of the eventually formed polymorph.(84) Proto calcite and proto vaterite short range structures were reported in ACC by Gebauer.(85) Michel (128) opposes this view and reported that similarities exist, but that no short range structure comparable to other polymorphs was observed. As far as an experimental review of this topic goes, it seems that ACC formed at low supersaturation levels and/ or in the presence of additives has “more order” at atomic length scales comparable to crystalline polymorphs, than ACC formed at high supersaturation. This goes hand-in-hand with Koga’s (129) thermo-gravimetric observations of ACC precipitated at different pH and supersaturation levels. This study showed an increase in the atomic disorder as pH and supersaturation were increased, as shown by the shift in crystallisation temperature (330-370°C) and exothermic release. Consistent with this, a range of differing activation energies required to induce the solid state transformation of ACC can be found in the literature.(91)

Synthetic ACC is commonly obtained experimentally in hydrated form (exceptions noted,(95, 96, 130)) with a composition of $\text{CaCO}_3 \cdot \text{H}_2\text{O}$. A general distinction can be made in the case of biogenic ACC, containing additives, which is either hydrated ($\text{CaCO}_3 \cdot \text{H}_2\text{O}$) and stable or transient and non-hydrated.(131, 132)

Chapter 1: General Introduction

Various structural models of solid ACC have been considered where these range from an array of disordered unit cells,(133) to a porous, charge-separated calcium ion rich framework. The latter, **Figure 1-14**, is the currently most accepted one, and states that ACC in its hydrated or thermally induced dehydrated state consists of a calcium ion rich framework (red) containing channels in which water, carbonate and small additives are embedded (violet).(96, 134) Since the calcium ion packing density in this model for hydrated ACC is similar to crystalline CaCO_3 the rearrangement to a crystalline polymorph is likely to occur via relocation of the carbonate ions from the channels into the calcium framework. Structural water is concomitantly expelled from the framework. This first dehydration step in the transformation process of ACC is readily observed in biominerals (Figure 1-13) but was previously elusive in solution in experimental investigations.(97, 126)

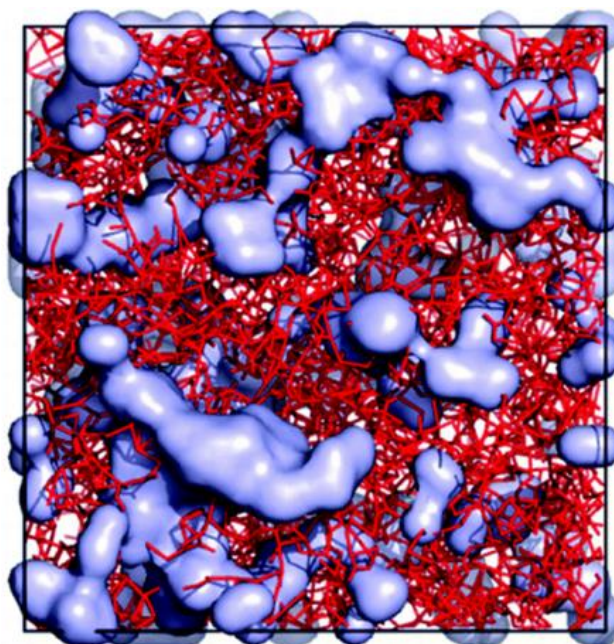


Figure 1 - 14: (a) Monte Carlo refined X-ray total scattering based structural model of hydrated ACC. Ca-rich framework is given in red. Calcium deficient channels in blue (4 \AA separation from any Ca centre). A box dimension of $\sim 40 \text{ \AA}$ is presented. Taken from (127).

The “**life-cycle**” of ACC seems to progress stepwise from the gelation of the liquid ACC to solid hydrated ACC. This then undergoes dehydration and structural rearrangement to give anhydrous ACC.(87, 91, 135) The final transformation of the anhydrous ACC into a crystalline polymorph (representing the most exothermic step in the transition series) is not completely understood. It is known from thermo gravimetric analysis and differential scanning calorimetry that a solid-state transformation of ACC is clearly possible upon heating to $\sim 310\text{-}370^\circ\text{C}$ (depending

Chapter 1: General Introduction

on experimental conditions). However, whether a solid state transformation is also the dominating mechanism in solution, rather than a dissolution/ reprecipitation mechanism similar to the transformation of vaterite into calcite (93) or a particle-mediated agglomeration process, has not yet been answered. All mechanisms have been considered in the literature e.g. (86, 136) for dissolution and reprecipitation and (93, 94, 137, 138) for an internal structural reorganization of ACC. The latter presents compelling visual evidence for a combination of both mechanisms.(93) The initial nuclei of vaterite/ calcite may well form via the solid state transformation of ACC, while subsequent growth certainly occurs via dissolution/ reprecipitation of the surrounding ACC, as ACC depletion zones are observed around the crystalline vaterite and calcite nuclei (139).

It is to be noted that a full dissolution/ reprecipitation of ACC to calcite would run counter to the discussion of the short-range structure of ACC acting as a blueprint for the structure of the transformation polymorph, as clearly all order would be lost on dissolution. The presence of short range order similar to the subsequently formed polymorph might just be coincidental in this regard.

The **growth** of ACC particles is another topic of interest. Does it occur by ion addition? Or does growth occur solely through particle-mediated pathways i.e. aggregation/ coalescence of basic spherical units until the critical stability diameter, ~100nm, is exceeded.(137) The stated critical size limit of the metastable ACC spheres can be thought to result from the offset of the entropic penalty at such a size scale, which can reverse the order of the thermodynamic stability of the polymorphs. The defining factor in determining the transformation is the Gibbs free energy, which is the sum of the changes in enthalpy and entropy. The entropy is negligibly small at that size scale, so the phase stability is only determined by changes in the enthalpy and following surface free energy. That becomes smaller as the phase decreases in density, due to a lower packing density of surface atoms and increasing hydration. This leads to a lower density of uncompensated charge which results in the observed stabilization of ACC (91, 140).

1.4.4.3: The Stabilization of ACC or Polymorph Growth Retarder

The fact that **impurities/ additives**, even if present at low concentrations, have a dramatic effect on crystallisation and crystal morphology is well known. Additives do not necessarily retard or inhibit crystallisation.(138, 141) In fact, it has been shown that aspartic acid assists anion desolvation on specific calcium carbonate crystal faces at low concentrations.(142) The reported effects of some of the

Chapter 1: General Introduction

principal additives associated with biogenic ACC, or used experimentally to control ACC crystallisation are described below.

Magnesium is found in nearly all biogenic ACC and crystalline biominerals.(131) It is thought to promote aragonite formation through calcite growth retardation, based on adsorption to specific calcite faces, followed by eventual incorporation. This results in a higher solubility of calcite due to differences in cation solvation energies.(46, 143, 144) Biogenic calcite can contain up to 40 % mol magnesium, which far exceeds the thermodynamically stable value of 10 % mol. This has been explained through calcite formation via ACC which incorporates Mg^{2+} ions much more easily.(145). How this occurs is as yet unknown, but what is observed is that magnesium containing ACC is much more crystallisation resistant.(145-147) The mechanism by which magnesium kinetically stabilizes ACC in solution has yet to be fully determined.

Molecules containing **phosphate** and **aspartic acid** groups have also been identified as having an effect on the formation of different calcium carbonate polymorphs, including ACC.(90, 148) The stabilization or growth retardation effects observed are not limited to macromolecules rich in these groups as commonly found in biominerals.(80, 82) Ions or short molecules containing phosphate or aspartic acid can also have a similar effect. Over the last decade, evidence has been obtained which shows that low molecular weight compounds can have a more pronounced effect than single ions or macromolecules at similar concentrations.(7, 149) This stabilizing effect of ACC is similar to magnesium and is only of a temporary nature.(150) Reviewing the literature, the effects of phosphates and aspartic acid on crystallisation inhibition or ACC stabilization may well be a combination of surface adsorption onto ACC and retardation/ inhibition of the formation of the crystalline polymorphs. Which of those is the dominating mechanism is not yet known. Further, the degree of stabilization also clearly depends on the type of phosphates or amino acids present in solution.(7, 137, 148, 151, 152)

The specific interest in **macromolecules** rich in anionic groups as additives/ inhibitors of calcium carbonate crystallisation is rooted in their similarity to many bio-macromolecules found within $CaCO_3$ biominerals. Taking nacre as an example, acidic macromolecules are required in addition to the insoluble organic matrix framework to induce the formation of an oriented crystalline layer. Crystal formation is believed to occur via an amorphous precursor depositing on the organic matrix

Chapter 1: General Introduction

present. The ACC layer then transforms into a specific polymorph depending on the active groups (e.g. hydroxyl, primary amine groups) on the organic matrix and the soluble macromolecules present in solution.(153, 154) Macromolecules are apparently more effective in the latter stages of crystallisation e.g. retarding inhibiting crystallisation rather than stabilizing the ACC.(90, 152, 155)

The **spatial confinement** of a forming mineral has been identified as another factor assisting the stabilization of metastable phases, such as vaterite (156) and ACC (157) in the case of calcium carbonate. It is also been seen for amorphous calcium phosphate, (16) – sulphate (158) and oxalate (Chapter 3.6). As for carbonates, a range of different physical confinement strategies were proven to successfully extend the lifetime of a metastable phase. These include the precipitation in between angular geometries,(157) in isolated small volumes e.g. pico-litre droplets (159) or liposomes (160). Growth arrest in the pore space of track etch membranes,(49) in silica (161) or ATP shells (162) come to mind for direct spatial confinement methods leading to a temporary stabilization of ACC.

1.4.5: Calcium Carbonate in Aqueous Solution

The composition of a calcium carbonate mineralizing solution, the supersaturation and the solubility can be controlled by several external factors such as the addition of an anti-solvent, actively directing reaction kinetics, pH adjustments and temperature regulation.

The aqueous solution chemistry of calcium carbonate is rather simple, and yet distinct. First of all, it is a multi-component precipitation system, unlike for example simple sugar systems (undergoing mutarotation of its enantiomers), and precipitation limitations are either based on carbonate and/ or calcium ion shortage. Secondly, carbonate or total inorganic carbon (TIC) is a diprotic species present either in the form of carbon dioxide (CO_2), bicarbonate (HCO_3^-) and carbonate (CO_3^{2-}), depending on solution pH, **Figure 1-15**. Precipitation of calcium carbonate (CaCO_3) “only” occurs by the direct reaction of calcium with carbonate ions. That means precipitation only occurs above a certain pH level as indicated by the dotted line.

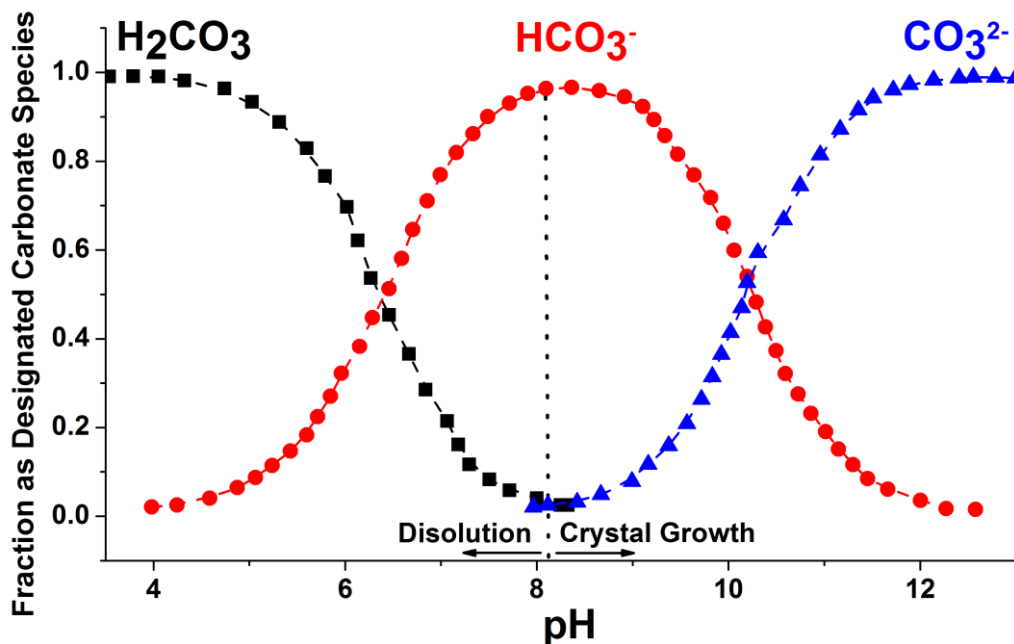


Figure 1 - 15: Carbonate species distribution in solution as a function of solution pH from 0 to 1.

Thirdly, the reaction involves a soluble gas in the form of carbon dioxide, as we can see from Equations 14-19. Knowledge of the exerted partial pressure (P_{CO_2}) in addition to knowledge of equilibrium constants (K), Henry (k_{H}) and carbonic acid-dissociation constants (K_{A}) is sufficient to determine the equilibrium composition of

Chapter 1: General Introduction

a calcium carbonate solution. Equilibrium constant expressions and solubility products are provided in Appendix C.(86, 163-167). This is possible as the partial pressure directly dictates the solution pH and in turn with it the carbonate species distribution. A graphical representation of this relationship is found in Bohn and is presented in **Figure 1-16**.(168)

The equilibrium solution composition is calculated using the underlying charge balance, Equation 14, and solved via Newton's method for pH as a function of P_{CO_2} .

$$2[Ca^{2+}] + [H^+] + [HCO_3^-] = [OH^-] + [HCO_3^-] + 2[CO_3^{2-}] + [Cl^-] \quad (14)$$

$$0 = [H^+]^4 \cdot \left(\frac{2 \cdot K_{sp} \cdot k_{HCO_2}}{K_{A1} \cdot K_{A2} \cdot P_{CO_2}} \right) + [H^+]^3 + [H^+]^3 \cdot \left(\frac{K_{sp} \cdot K_{CaHCO_3}}{K_{A2}} \right) - [H^+]^2 \cdot [Cl^-] - [H^+] K_w - [H^+] \cdot \frac{P_{CO_2} \cdot K_{A1}}{k_{HCO_2}} - 2 \cdot \left(\frac{K_{A1} K_{A2} P_{CO_2}}{k_{HCO_2}} \right) \quad (15)$$

$$[H_2CO_3^*] = \frac{P_{CO_2}}{k_{HCO_2}} \quad (16)$$

$$[HCO_3^-] = \frac{P_{CO_2} k_{HCO_2} K_{A1}}{[H^+]} \quad (17)$$

$$[CO_3^{2-}] = \frac{P_{CO_2} k_{HCO_2} K_{A1} K_{A2}}{[H^+]^2} \quad (18)$$

$$[Ca_i^{2+}] = \frac{K_{sp_i}}{[CO_3^{2-}]} \quad (19)$$

In the case of an unknown partial pressure or determining the present supersaturation i.e. obtaining knowledge the dynamic state of the system, secondary expressions need to be considered. These comprise of solution pH, calcium concentration and total inorganic carbon (TIC), Equations 20-23. (169)

$$[C_{TS}] = [CO_3^{2-}] + [HCO_3^-] + [H_2CO_3] \quad (20)$$

$$[CO_3^{2-}] = \frac{[C_{TS}] K_{A1} K_{A2}}{[H^+]^2 + K_{A1}[H^+] + K_{A1} K_{A2}} \quad (21)$$

$$[\text{HCO}_3^-] = \frac{[\text{C}_{\text{TS}}] K_{\text{A1}} [\text{H}^+]}{[\text{H}^+]^2 + K_{\text{A1}} [\text{H}^+] + K_{\text{A1}} K_{\text{A2}}} \quad (22)$$

$$[\text{H}_2\text{CO}_3^*] = \frac{[\text{C}_{\text{TS}}] [\text{H}^+]^2}{[\text{H}^+]^2 + K_{\text{A1}} [\text{H}^+] + K_{\text{A1}} K_{\text{A2}}} \quad (23)$$

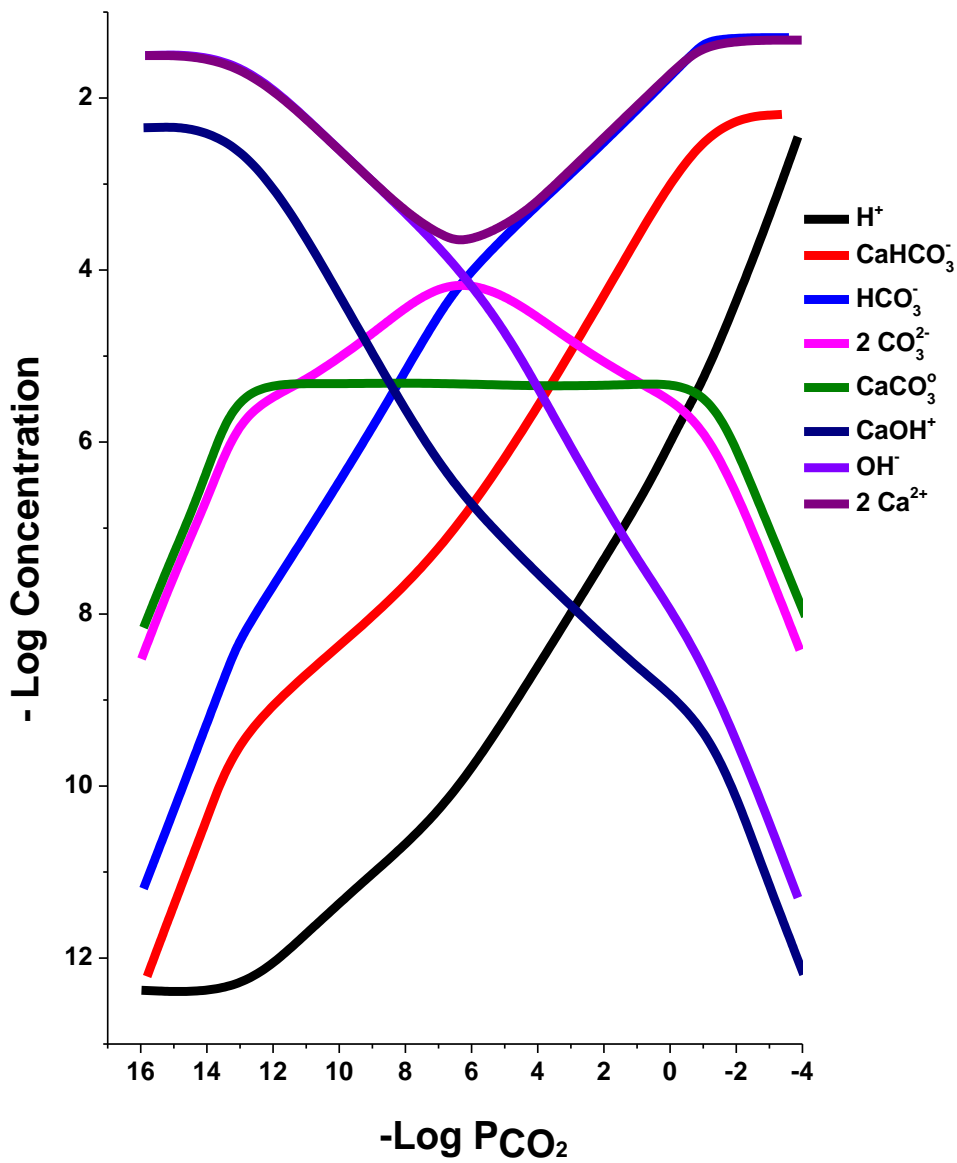


Figure 1 - 16: Solution concentrations of calcium and carbonate species as a function of carbon dioxide partial pressure. Reproduced from (168).

Chapter 1: General Introduction

From Figure 1-16 it can be clearly seen that a decrease in P_{CO_2} will result in an increase in pH. This will result in a gradual reversal in the bicarbonate/ carbonate ion ratio, and an increased availability of carbonate ions at elevated pH levels. This explains the more rapid precipitation of CaCO_3 at elevated pH levels under equivalent starting concentrations. (129, 170)

Chapter 1: General Introduction

Chapter 2: Experimental Methods and Analysis



Chapter 2: Experimental Methods and Analysis

This chapter provides information on the preparation of glass and gold substrates and crystallisation dishes. In addition, brief descriptions of precipitation methods used are provided. This is followed by basic information regarding sample characterisation and analysis techniques. A certain overlap with experimental chapters is intended for clarity.

2.1: Glassware and Substrate Preparation

2.1.1: Cleaning Procedures

Two cleaning procedures were employed, depending on the subsequent use of the glassware. These were primarily performed to ensure that no or a minimal quantity of heterogeneous nucleator or impurities were introduced into mineralising solutions. Reagent-containing glassware e.g. ball flasks, *Shott* bottles, volumetric cylinders were soaked overnight with 10 w/v% sodium hydroxide. They were then rinsed with diluted hydrochloric acid and were finally washed with water (Milli-Q Standard 18.2 MΩcm at 25°C).

Crystallisation substrates e.g. microscope slides or silicon wafers were cut to size (1 cm²) and were then placed in Piranha solution (70:30 %wt sulphuric acid : hydrogen peroxide) for two hours. They were then washed with Milli-Q water and dried under nitrogen. Substrates were either used directly or stored in Milli-Q water. The cleaning effect due to immersion into Piranha solution is twofold. Hydrogen peroxide is a strong oxidizer by itself, removing oxygen and hydrogen from the organic residues present. The vigorous reaction of hydrogen peroxide with sulphuric acid, and the associated release of elemental oxygen, enhances this oxidizing capability, promoting the removal of elemental carbon. A secondary cleaning effect is due to piranha solution's acidic nature, which allows the dissolution of certain mineral deposits, Equation 24.



2.1.2: Substrate Preparation

The templating work described in Chapter 5 required the heterogeneous nucleation of calcite on functionalized self-assembled monolayers (SAM). Functionalized organothiol self-assembled monolayers were prepared on freshly deposited noble metal films.⁽¹⁷¹⁾ Thin films were deposited either on Piranha cleaned silicon

Chapter 2: Experimental Methods and Analysis

wafers or glass slides using a Mantis Qprep 250 deposition system at a base pressure below 10^{-6} mbar. 2 nm of Cr were initially deposited to promote substrate adhesion, followed by the evaporation of 30-50 nm of Au or Ag at ≤ 0.1 nms⁻¹. Monolayer formation on the metal substrate was initiated by immersion in 1 mM thiole/ ethanol solution (11-Mercaptoundecanoic acid, 11-Mercapto-1-undecanol). The prepared SAMs were thoroughly rinsed with ethanol and Milli-Q water, and were subsequently dried under nitrogen.

2.2: General Precipitation Methods

The principal methods used for the precipitation of calcium carbonate, calcium phosphate and calcium oxalate are discussed here with further information being given in subsequent chapters where necessary.

2.2.1: Direct Combination of Reagents

2.2.1.1: Precipitation in the Presence and Absence of Soluble Additives

In this method, precipitation is induced by the rapid combination of equimolar solutions of two highly soluble reagents (for example CaCl_2 and Na_2CO_3 or 1 M $(\text{NH}_4)_2\text{CO}_3$ (0.01-1 M)). This results in the precipitation of a sparingly soluble species, here CaCO_3 based on the common ion effect or Le Chatelier's principle. A new equilibrium is re-established by precipitating CaCO_3 due to the shift in chemical potential upon combination of both reagents. This method is generally employed to obtain bulk sample quantities of crystalline CaCO_3 or to obtain ACC if employing starting reagent concentrations greater than 10 mM.(172) Slight variations in experimental procedures involve the adjustment of the initial solution pH and/ or ionic strength by the addition of sodium hydroxide and sodium chloride respectively. The resulting slurry is either filtered directly through a 0.45- μm membrane filter and washed with ethanol before being left to dry, or left to incubate for certain periods of time in the mineralizing solution. Additives studied were added either to the calcium (Mg, Asp, PSS-MA and Poly-Asp) or carbonate solution (PAA, SO_4 , PO_4 and SiO_4).

2.2.1.2: Precipitation in the Presence of Sodium Silicate

Calcium carbonate, specifically ACC, was encapsulated in silica shells based on the methodology given by Kellermeier *et al.*(161) Here, 125 ml of 10-50 mM CaCl_2 was mixed with 125 ml of 10-50 mM $\text{Na}_2\text{C}_2\text{O}_4$ / 10-25 mM Na_2SiO_3 solution, and the precipitates generated were incubated in the reaction solution for 20 min to allow the formation of a silica shell around the initially formed ACC units. The solution was then filtered using a 0.45- μm membrane filter and washed with ethanol before being left to dry. Confirmation of encapsulation was obtained by leaching the calcium carbonate from the silica shell by immersing ~500 mg of encapsulates in 1 M HCl (50 ml) for 24 h.(95)

2.2.1.3: Coating of Precipitates with Phosphatidylcholine

Synthesis of ACC particles coated with lipid bilayers (95) was achieved by precipitating ACC particles according to 2.2.1.1, and then covering them with bilayers of L- α phosphatidylcholine (PC) and dihexadecyl phosphate (DHP) according to the method of Bugni.(173) 5-25 mg of ACC were dispersed in 1 ml of ethanol and briefly sonicated, before depositing them on a glass slide and leaving them to dry at 40 °C. Approximately 0.2 ml of a lipid stock solution (100 mg PC & 10 mg DHP per ml chloroform) was then applied drop-wise to the ACC film, before rapidly evaporating the solvent under nitrogen. Subsequently, the resulting ACC-bilayer aggregates were placed in 100 ml of Milli-Q Water and were gently agitated to displace them from the glass support. The lipid-bilayer coating on the ACC was confirmed using confocal fluorescence microscopy, where particles were coated using a lipid stock solution containing PC labelled with a fluorescent group - (1 wt% NBD labelled PC(1-Oleoyl-2-[12-[(7-nitro-2-1.3-benzoxadiazol-4-yl)amino]dodecanoyl]-sn-glycero-3 phosphocholine).

2.2.2: Kitano Method

The term Kitano Method refers to a precipitation method publicised by Kitano, Park and Hood.(105) Here, CaCO_3 is precipitated from an enriched solution of “ CaHCO_3 ” open to the atmosphere. Calcium bicarbonate solutions are prepared by adding an excess amount of solid CaCO_3 (~100 mg) to one litre of Milli-Q water through which $\text{CO}_{2(g)}$ is then bubbled for three hours. The slurry is then filtered through a 200 nm membrane to remove any undissolved species. The resulting solution is slightly acidic with a pH of ~6.4 compared to the natural basic pH of a solution saturated in calcium carbonate. Enriching a solution with CO_2 reduces the pH of the solution in question and subsequently shifts the species distribution away from the Ca^{2+} reactive CO_3^{2-} towards HCO_3^- and $\text{CO}_{2(g)}$, thereby creating a temporarily enhanced solubility of initially present solid calcium carbonate. This enhanced solubility slowly decreases as the CO_2 source is removed and CO_2 starts outgassing from the solution. This is due to the enforced CO_2 partial pressure imbalance between the atmosphere and the liquid, which ultimately leads to a pH shift back to its original position. This in turn forces a reversal in species distribution back towards CO_3^{2-} and the original solubility, creating a gradual increase in supersaturation. The main advantage of the method and the reason why it is often used is the absence of secondary “counter-ions” in the precipitate. Further precipitation occurs at a low pH.

2.2.3: Diffusion Methods and Alternatives

2.2.3.1: Ammonia Diffusion Method

Please refer to Chapter 4 for a detailed description.(169) In brief, the ammonia diffusion method (ADM) is based on a slow increase in supersaturation in a crystallizing calcium solution, through vapour diffusion of NH_3 and CO_2 into the crystallizing solution. The vapours of NH_3 and CO_2 are a result of the decomposition of solid $(\text{NH}_4)_2\text{CO}_3$, which is located separately with the crystallizing solution in a hermetically sealed environment. The diffusing ammonia initially raises the solution pH up to ~ 9.25 and subsequently works as a buffer, stabilizing the pH thereafter. This enables the transformation of infusing carbon dioxide to bicarbonate and eventually carbonate, creating the required supersaturation with calcium ions present.

2.2.3.2: Slow Addition of Reagents

The mechanically driven addition of a concentrated reagent (either ammonium- or sodium carbonate) to a diluted reservoir of calcium chloride solution (47, 169) was primarily employed to mimic the gradual increase in supersaturation present in diffusion methods, Chapter 4.2. In detail, carbonate solutions were drawn into glass syringes and were transferred at a fixed rate via mechanical syringe pumps into an atmospherically sealed calcium solution, which was kept under constant agitation by means of an orbital shaker.

2.2.3.3: Enzymatically Driven Precipitation

A second way to mimic the ADM was investigated, Chapter 4.3, which utilizes the enzymatic hydrolysis of urea by urease in aqueous calcium solution.(174) The controlled hydrolysis of urea by urease into carbonate and ammonium – with variation of substrate (urea) and enzyme (urease) concentrations – allows the direct replication of the ADM. This provides also a slow increase in supersaturation, as is required to obtain unstrained calcite crystals with sufficient high number densities, where this occurs by providing a homogenous diffusional spread in solution. The primary advantage was deemed to be the fact that it is a true one pot method. This can facilitate studies concerning the formation of either CaCO_3 - based mesocrystal or polymer-induced liquid precursor phases (PILP) in situ, using techniques such as

DLS, SAXS and or liquid cell TEM without manually interfering with the ongoing formation process.

2.2.4: Precipitation in Track-etch Membranes

Precipitation of calcium oxalate within the 200 nm pore space of polycarbonate track-etch membranes was employed as a strategy to temporarily stabilize any potentially present amorphous precursor phase as demonstrated in the case of calcium carbonate and phosphate, Chapter 3.5.(16, 49)

Membranes were degassed in water at reduced pressure to ensure complete filling of the membrane pores with solution. In the Double Diffusion (U-tube) method, wetted membranes are mounted between two U-tube arms which are then filled with solutions of CaCl_2 (2-10 mM) and $\text{Na}_2\text{C}_2\text{O}_4$ (2-10 mM) / PAA ($50 \mu\text{gml}^{-1}$). Intra-membrane particles are isolated either after 12 hours or 2 weeks by dissolution of the membranes in dichloromethane. Previous to dissolution, the membranes are rinsed with ethanol and their surfaces are scraped with a cover glass to remove the majority of surface-bound crystals. After brief sonication of the membranes in ethanol, the membranes are then subjected to 3 cycles of sonication in dichloromethane, centrifugation and exchange of the solvent. The isolated precipitates were finally washed with methanol to remove residual dichloromethane, and were then washed with ethanol before being pipetted onto a TEM grid/ glass for analysis.

2.2.5: Precipitation from Saturated Solutions by Freeze Concentration

Please refer to Chapter 3.4 for a detailed description.(175) In brief, precipitation by means of freeze concentrating a saturated solution of the precipitate in question relies on the selective solvent removal during plunge freezing of a saturated solution in liquid nitrogen. The subsequent continuous decrease in free solution volume as more and more liquid is transformed into crystalline ice results in the “molecular crowding” of the ions present into the remaining, shrinking solvent pockets. This in turn leads to an increasing precipitation force. The product precipitate is then stabilized against possible transformation as the solution completely solidifies and is returned for sample analysis upon solvent sublimation.

Precipitates produced by freeze concentration require the production of “counter-ion free”, saturated solutions and hence pure bulk precipitate as starting

Chapter 2: Experimental Methods and Analysis

material. This is either obtainable by repeated precipitation and dissolution, Chapter 2.2.1, or by commercial acquisition. Saturated solutions are then prepared by adding, e.g. 20 mg of “pure” CaC_2O_4 to 500 ml H_2O , stored for 24 hours at room temperature, before centrifuging to remove the majority of any remaining undissolved calcium oxalate. This saturated solution is then either heated (CaC_2O_4) or cooled (CaCO_3) to remove possible ghost nuclei, and filtered through a 200 nm filter membrane. Freezing of the prepared saturated solutions is achieved by plunge immersion into a liquid nitrogen bath, followed by a 10 minute annealing period to strengthen the ice structure. Subsequent sublimation (Labcono FreezeZone 1, 50 mBar, -49°C) of the excess solvent delivers the freeze-dried precipitate.

2.3: Microscopy

Microscopy is the use of a microscope to magnify objects beyond the resolution limit of the human eye. Microscopes can broadly be cast into 3 categories based on signal acquisition and or resolution: Optical, Electron and Scanning Probe Microscopy. Microscopy was utilized in the presented work to determine the morphological effects that additives and crystallisation conditions had on formed minerals.

2.3.2: Optical and Florescence Microscopy

2.3.2.1: Visible Light Microscopy

A **visible light microscope (VLM)** uses the interaction of a sample with visible light (390 to 700 nm), either by transmission through or reflectance by the sample to magnify and resolve smaller morphological features. In simple compound microscopes the magnification is achieved in two separate successive steps. The illuminated sample transmits or reflects light towards a static objective lens of a magnification factor x . The objective gathers and focuses the beam into the microscope column by a single lens or a set of lenses. Focused light is subsequently passed through an ocular (~ 10 fold magnification) or a secondary readout for observation. Due to the static position of the objectives used, varying the focal depth is achieved by modifying the distance between lens and sample. The magnification achievable for a single lens is determined by the distance of the lens to the sample (d_0) and the focal depth (f) according to Equation 25. Focal depth is the distance at which collimated light is brought into focus.

$$\text{Magnification} = \frac{f}{f - d_0} \quad (25)$$

Most commonly, the bottleneck is not the magnifying capability of a microscopy technique but rather its inherently limited resolution capabilities, which is the minimal distance (d) between two objects that can identified as separate objects. The fundamental resolution limit of light microscopes was determined by Abbe and Zeiss, Equation 26.(29, 176) The maximal obtainable resolution is given by the ratio of the wavelength of electromagnetic radiation, used for illumination, and the numeral aperture (N_A). N_A is the product of the refractive index (N) of the immersion medium (1 for Air) and alpha is the apparent half opening angle of the lens with respect to the focal point. The resolution limit of VLM is ~ 200 nm.

$$d = \frac{\lambda}{2 N_A} \quad (26)$$

$$N_A = N \sin(\alpha) \quad (27)$$

Due to the many interaction possibilities of light with matter VLM was extended to identify if precipitates formed were crystalline or amorphous in character. This is made possible by placing precipitates in-between two crossed polarizers. A polarizer blocks all but “one orientation” of light passing through. Two, successive crossed polarizers hence block all incidental light towards an observation piece. As amorphous matter is isotropic in comparison to, for example, crystalline anisotropic calcite (material with different properties in different directions) the observed image of amorphous matter between cross polariser remains dark. Calcite, on the other hand, re-scrambles initial uniaxial oriented light upon transmission, letting a certain fraction pass through the second polarizer. This makes it visible in the observed image, where this is due to different relative travelling velocities in the anisotropic material, due to different refractive indices.(177) Optical microscope images were collected using a Nikon eclipse LV100 microscope at 20, 50 or 100 fold magnification.

2.3.2.2: Fluorescence Microscopy

Fluorescence describes the combined process of atoms or molecules becoming excited by absorption of electromagnetic radiation and the relaxation of species back to their ground states. Relaxation leading to the emission of light commonly occurs at a longer wavelength than the excitation radiation.(178)

In contrast to VLM, **Fluorescence microscopy** detects radiation that is directly emitted by a sample when it is irradiated with primary radiation. Fluorescence microscopy is generally used to highlight particular areas of interest in a complex sample by specifically labelling objects of interest with a fluorophore. Objects of interest can be specific ions or, as studied here, phospholipids, Chapter. 3.3.

Fluorescence microscopy and in-situ crystal growth observations were made using an Inverted Olympus IX-70 confocal microscope equipped with a 60x magnification lens. Image analysis was performed using Zeiss Zen lite or Image J software packages.(179)

Confocal microscopy refers to an extension of the general VLM and removes the detrimental effect of stray light on image resolution. This is achieved by specific area illumination and the blockage of stray light.

2.3.3: Electron Microscopy

2.3.3.1: Scanning Electron Microscopy

Scanning electron microscopy (SEM) returns magnified images of the specimen, currently up to 1 nm resolution, by scanning the specimen with a high energy beam of electrons. Electrons are accelerated in a field emission gun using electric current and are focused on a sample spot by the use of condenser lenses. A vacuum is commonly required to avoid air scattering of the electrons. The bombarding electrons (primary electrons) interact in a multitude of ways with the specimen. Here, mostly of interest is the inelastic scattering of primary electrons by the sample atoms. This leads to the emission of secondary electrons from specified locations in the sample as scanning with the primary electrons progresses. The secondary electrons are then amplified and directed to a scintillation detector for signal readout. The obtained image is reconstructed by integration of the scanned position intensities, which results in a surface topographical sample representation. The obtained image is a surface topographical representation of the sample as the intensity per scanned area is “equal” to the measured electron density. The particular magnification is dependent on two factors, namely the applied raster size and the resolution on screen, Equation 28.

$$\text{Magnification} = \frac{\text{Screen Resolution}}{\text{Raster Size}} \quad (28)$$

Secondary and tertiary interactions provide further sample information. Backscattered primary electrons are electrons reflected by atoms at the sample surface, and provide information regarding elemental sample composition. Heavier elements provide a better reflection “mirror” for backscattered primary electrons, due to increased electron density. Reflection from those areas will therefore appear brighter due to the increased intensity registered by the detector. A tertiary interaction involves the release of element specific x-rays as discussed in Chapter 2.5.3.(180)

Samples for SEM investigation were initially dried (desiccator filled with moisture adsorbent) for 30-60 minutes before they were sonicated (~3 minutes) in ethanol.

Chapter 2: Experimental Methods and Analysis

Droplets of the ethanolic sample slurry were then placed onto cleaned glass slides or silicon wafers and were left to dry, before being mounted on a SEM stub covered with sticky carbon tape. Finally, SEM samples were either used as prepared or coated with 10-15 nm of Pt/ Pd (80/ 20) prior to analysis.

Scanning electron micrographs of uncoated specimens were obtained using a FEI Nova NanoSEM 650. Micrographs of coated specimen were obtained using LEO 1530 Gemini FEGSEM operating at 2 kV or a NeoScope JCM-5000 SEM operating at 10 kV.

2.3.3.2: Transmission Electron Microscopy

Transmission electron microscopy (TEM) operates on the same principle as transmission VLMs, but provides an increased resolution (~0.1 nm) by utilizing electrons as an irradiation source, and imaging a thin specimen (<100 nm) in a vacuum. The electron intensity is recorded by a CCD. The increased resolution is thanks to the short wavelength (λ) of electrons at a particular energy (E), Equation 29.(181) The difference between ideal subatomic resolutions based on electron wavelength, at for example 100 kV (0.004 nm), and the practical resolution is partially a result of imperfect electron lenses.

$$\lambda = \frac{1.22}{\sqrt{E}} \quad (29)$$

Basic image generation and acquisition proceeds as follows: electrons are generated from and accelerated by a field emission gun (FEG) towards the thin sample. Intermediate electromagnetic lenses are used to focus the electrons onto the sample. After specimen interaction, the electron beam is passed through an objective lens and finally projected onto the CCD for readout. Sample visibility on the CCD is a result of electrons scattered by the atomic columns or electron cloud of the sample. Thus thicker/ denser sample areas or areas composed of heavy elements will appear darker on screen as fewer electrons hit the CCD.

A substantial problem associated with the use of electrons for microscopy is the possibility of beam damage to the sample. To avoid the introduction of image artefacts of this origin, Cryo-TEM and **low dose imaging** procedures were developed.(181) Imaging with a low electron dose was required for the work on calcium oxalates described in Chapter 3.5.

Chapter 2: Experimental Methods and Analysis

Samples for TEM investigations were prepared by depositing droplets of the prepared mineral/ ethanol slurry onto carbon-coated, formvar-coated copper or gold TEM grids. Samples were used for microscopy after total solvent evaporation. Secondary investigation of thicker specimens was possible by preparing thin cut sections via focused ion beam milling (FIB).⁽¹⁸²⁾

Focused ion beam samples were prepared as follows. In the first step, the sample region of interest (lamella) was covered with a protective film of platinum 50 nm thick and 200 nm wide and 2 μ m long. The second step involved the excavation of the lamella by creating two angular trenches into the substrate on each side of the protective layer. This is achieved using a Ga⁺ beam operating at 5 nA. The lamella was then welded onto a transportation tip before the remaining connection between substrate and lamella prepared was removed by ion milling. The cut lamella was then lifted out and welded onto a TEM grid before undergoing a secondary milling step to ensure electron transparency. FIB sample preparation was performed using an FEI Nova200 Dual Beam FIB/SEM. The ion beam was operated at 30 kV and at beam currents between 0.1 and 5 nA. Lift-out was performed in situ using a Kleindiek micromanipulator.

TEM images and electron diffraction patterns were acquired using a FEI Tecnai F20 -200 kV FEG-TEM fitted with an Oxford Instruments INCA 350 EDX system/80mm X-Max SDD detector and a Gatan Orius SC600A CCD camera. Low dose TEM work was performed by P.H.H. Bomans and N.A.J.M. Sommerdijk at the Eindhoven University of Technology using a TU/e CryoTitan (FEI) -300 kv FEG-TEM. Images were recorded on a 2k x 2k Gatan CCD camera.

2.3.4: Scanning Probe Microscopy

2.3.4.1: Atomic Force Microscopy

Atomic force microscopy (AFM) was performed to obtain information regarding surface roughness and the gold island size of prepared thin films on silicon wafer substrates. The latter were used as substrates for SAM deposition. Surface roughness is either reported in terms of average measured surface roughness or in terms of the surface fractal dimension. Fractal dimensions were obtained by applying the lake/ island perimeter-area method as given by Williams.⁽¹⁸³⁾ Substrates were characterized using a Bruker Dimensions 3100 AFM in tapping

Chapter 2: Experimental Methods and Analysis

mode (Brucker Tespa; resonance frequency 345-385 kHz, K 20-80 N/m) at a scan rate of 1.98 Hz with pixel dimension of 512 x512.

In simplistic terms, basic AFM in tapping mode provides images of surface topography by “feeling” the surface with a mechanical probe. In the used setup an “atomically” sharp tip is located at the free end of a cantilever and is scanned over the sample surface. A feedback loop ensures that the “flexible” tip is maintained at a constant force during the scanning process of the surface. During this process the cantilever is deflected by the sample contour. An optical detection system is used to readout the degree of tip deflection and hence returns information concerning surface topology. The optical detection system consists of a diode laser focused on the back side of the cantilever and a dual element photodiode collecting the reflected beam. The degree of cantilever deflection and the resulting light intensity difference between the upper and lower photo detectors are subsequently reinterpreted as height displacements in the sample. Tapping mode refers to the fact that the tip is not in constant contact with the surface. Rather, the tip and cantilever is oscillated near the cantilever's resonant frequency where it is maintained during the scanning process. The non-permanent surface contact inherently prevents the tip from sticking to the surface. This reduces the risk of damaging the sample and or tip during scanning.

2.4: Spectroscopy Techniques

Spectroscopic characterisation techniques are based on the interaction of matter with radiation energy. Recorded is the interaction degree (changes in intensity and or frequency) as a function of radiation frequency/ wavelength. In the presented study this is based on changes in resonance frequency due to structural differences in molecular and or atomic order/ local environment/ excitation level. Generally, changes in intensity provide quantitative information while shifts in the position of “resonance” frequencies are used for qualitative phase, element or species identification. The techniques utilized are presented based on the particular type of interaction (Absorption, Emission, Inelastic scattering and coherent interaction) and subsequently the length scale of interaction (Atoms, Molecules, amorphous and crystalline materials).(178)

2.4.1: Ultraviolet–Visible Spectroscopy

Ultraviolet–visible spectroscopy (UV-VIS) and secondary radiation absorption and emission techniques are based on the Beer-Lambert Law, Equation 30. The Beer-Lambert law relates the absorption (A) of a certain molecular characteristic or ionic species at a specific wavelength to the analyte (c) concentration. This is based on the absorbance intensity measured at a particular wavelength (Quantitative information) given a constant extinction coefficient (ϵ) and measurement path length (L). A sweep across a certain wavelength (λ) interval and the obtained absorbance spectra give rise to qualitative information such as polymorph identification, level of hydration or elemental composition. The difference between the analytical techniques is primarily based on the range of electromagnetic radiation used for probing. This results in different physical interactions and consequently different information about the specimen studied. Probing of a liquid sample with a light source in the **UV-VIS** range (10^{-9} - 10^{-7} m) leads to the excitation of “ π -electrons or non-bonding electrons” from the ground state in the sample. This is in contrast to fluorescence measurements, which register the transition from excited to ground states.

$$\log_{10} \left(\frac{I_0}{I} \right) = A = \epsilon * c * L \quad (30)$$

UV-Vis spectroscopy was performed here for kinetic studies of mineralization. The mineralizing solution was irradiated at a constant λ and the “absorption” recorded

with time. Changes in measured “absorption” allowed the extraction of information regarding mineralization reaction progress and foremost onset of mineral formation (induction point) given certain resolution limitations. This is based on the light scattering behaviour of formed mineral particles reducing the radiation intensity at the detector (I) compared to sample incoming radiation (I_0) –“absorption”, Equation 31. A Perkin Elmer lambda 35 UV/VIS Spectrometer, $\lambda = 500$ nm, in time-drive mode was employed in transmission mode to estimate the induction point and the progress of the reaction.

$$\log_{10} \left(\frac{I_0}{I} \right) = A \quad (31)$$

2.4.2: Atomic Absorption Spectroscopy

Atomic absorption (AA) refers to the absorption of radiation by free atoms in the gaseous state. As stated above, absorption at a particular wavelength provides qualitative information, which are here element specific. Absorption is fundamentally based on the electronic transition of outer shell electrons (valence electrons) to higher orbitals through the absorption of a defined energy quantity, which is specific to a particular electron transition. Elements - specifically Ca and Mg - were transformed to an ionic gaseous state by first dissolving the mineral sample in 5 %wt nitric acid and then atomized using a Perkin Elmer AA Analyst 400 spectrometer. A second irradiation source sitting normal to the flame direction (“ionisation source”) supplies the transition-specific energy quantity. Spectroscopy was performed at, $\lambda = 422.67$ nm, Slit width 2.7/ 0.69 mm, Flow rate ($L\text{min}^{-1}$) Oxidant/Acetylene =10/ 2.7 for Ca and $\lambda = 285.2$ nm, Slit width 2.7/ 0.7 mm, Flow rate ($L\text{min}^{-1}$) Oxidant/Acetylene =10/ 2.7 for Mg.

2.4.3: Energy-dispersive X-ray spectroscopy

Energy-dispersive X-ray spectroscopy (EDX) utilized in scanning and transmission electron microscopes provides information regarding the elemental composition of the sample, and is studied in the microscope by means of emission spectroscopy. This is achieved by exciting the sample with the electron beam. This causes core electrons to be expelled, created gaps which are then filled by electrons from a higher orbital. The associated energy difference between changes in orbital is released in the form of X-rays. Emitted X-rays are element-specific as

Chapter 2: Experimental Methods and Analysis

only a number of specific transitions are possible in consideration of unique atomic structures (as described by Moseley's Law Equation 32). Recorded are intensity patterns with increasing energy, where a combinatorial match of peak positions provides information concerning the elements present. The peak intensity (number of x-ray photons with a particular energy) is roughly equal to the abundance of the element in question.

$$f_{k\alpha} = (2.47 \cdot 10^{15}) (Z - 1)^2 \quad (32)$$

In simplest terms, Moseley's law states that the frequency ($f_{k\alpha}$) of emitted X-rays (i.e. the $K\alpha_{(1 \text{ or } 2)}$ lines) are directly relatable to the elements specific atomic number (Z) in Bohr's atomic model, where frequency (f) is related to wavelength (λ) and energy (E) according to Equation 33.

$$\frac{E}{h} = f = \frac{c}{\lambda} \quad (33)$$

2.4.4: Fourier Transform Infrared Spectroscopy

Fourier transform infrared spectroscopy (FTIR) which uses a lower energy, longer wavelength (10^{-6} - 10^{-4} m) as compared to UV-VIS, is another type of absorption spectroscopy. Recorded is the absorption at structural or molecular resonant frequencies or vibrations. For a vibrational mode to be IR active, the radiation must be able to induce a shift in the dipole moment. The vibration frequencies of certain IR active bonds changes based on the local environment they are exposed to, and they resonate at a particular wavelength, according to their local environment. This is important for the work undertaken here as it allows the identification of the polymorph or hydration state of the sample. Polymorphs differ in crystal structure and local environments around the IR active group. This results in a shift/ occurrence of polymorph specific absorption peaks. Rather than utilizing a dispersive approach (scanning with monochromatic radiation) as the methods stated above, FTIR collects spectral data in a wide spectral range simultaneously. The resulting interferogram is then subjected to a discreet Fourier transformation (FT). FT returns the wavelength – intensity profile. FTIR spectroscopy was carried out using a Perkin Elmer Spectrum 100 FT-IR Spectrometer equipped with a universal ATR sampling accessory. ATR

accessories allow the direct sampling of the prepared powder. The spectra are all presented after subtraction of the atmospheric background.

2.4.5: Raman Spectroscopy

Raman spectroscopy was used in tandem with FTIR in compositional/ structural analysis of the formed precipitates. Raman spectroscopy is based on the inelastic scattering of incoming coherent radiation by a “molecule”. Incoming photons emitted from a monochromatic IR source induce a transition in vibrational states of molecules in the sample from their ground state to a virtual, non-discrete excited level. The vibrational state transition is dependent on the local environment of the molecule, and can be sensitive to polymorph or structural changes. The non-discrete excitation results in a returning vibrational ground state which is different in energy as compared to the initial ground state. The associated emitted photon from the sample has therefore a different frequency compared to the incoming radiation. This difference is reported as the Raman characteristic signal, from which the Raman spectrum is constructed in terms of vibrational or Raman shift. The effective Raman vibration in crystals is only active when equivalent atoms e.g. a structure exhibiting long range order, are vibrating in phase. Therefore, if a sample does not possess long range order, as in an amorphous or nano crystalline material, broadening of the signal peaks is observed due to the heterogeneity present in vibrational modes. Raman spectroscopy was performed using a Renishaw inVia Raman Microscope equipped with a 785 nm diode laser as excitation source, focused onto the sample using a 5 or 50 x (NA $\frac{1}{4}$ 0.75) objective.

2.4.6: Solid-state Nuclear Magnetic Resonance Spectroscopy

Solid State Nuclear Magnetic Resonance (**SSNMR**) spectra were obtained on a Bruker 9.4 Tesla Avance-400 wide bore spectrometer, at frequencies of 400.1 MHz (^1H). One-dimensional datasets were acquired on samples spun at 10 kHz using MAS (^1H $\pi/2$ pulse length 2.5 μs , contact time 2.5 ms, at a ^1H field strength of 100 kHz) and a repetition time of 2 s was employed in all experiments. The number of scans acquired depended on the quantity of available sample, and was generally between 256 and 512. Experiments were performed by Wei Ching Wong at the University of Cambridge.

2.5: Electrochemical Techniques

Knowledge of the **pH** level in solutions was required to determine the distribution of carbonate species. pH was measured using a Mettler Toledo S20 SevenEasy™ pH meter equipped with a 3 in 1 pH electrode InLab 431 Premium Metler Toledo and logged via serial port communication (RS-232) into a remote computer using a simple RS-232 data logger (Eltima Software 2.7). The electrode used was calibrated before every run to correlate the voltage/ electromotive force (EMF) registered to the pH scale using pH 4 and pH 9 standards. EMF arises from the potential difference between the hydrogen ion sensitive electrode and a reference electrode according to the Nernst equation, Equation 34 which basically, measures the galvanic cell potential (178).

$$E_{Cell} = E^0 + \frac{RT}{zF} * \ln(a_{H^+}) \quad (34)$$

Conductivity (κ) was measured in solution to record the mineralization progress and secondly to determine the total fraction of carbonate present in an isolated solution. A Mettler Toledo MC 226 conductivity meter equipped with an InLab 731 conductivity electrode was used for measurements. The change in current (I) across the immersed “anode/cathode” was recorded as the ion concentration in solution decreases due to progressing mineralization, once a voltage is applied inducing an electric potential (U), Equation 35.

$$I = \left(\kappa + \frac{A}{L} \right) U \quad (35)$$

A Dionex **ion chromatography (IC)** system was used to determine the total inorganic carbon content present in the mineralizing solution. Inorganic carbon ions were separated from the remaining solution species using an Ion Pac AS 15 column with KOH as eluent (pH >10), separating ions on the basis of their columbic charge. KOH was used as an eluent in order to convert all of the present inorganic carbon in the solution to carbonate. A conductivity detector (Dionex EG50) was used to derive the total activity of the carbonate present by measuring the change in conductivity in the mobile phase as the former passes into the solution. Knowledge of the initial solution pH in conjunction with the total inorganic carbon present allows the recalculation of carbonate species distribution present in a mineralizing solution.

2.6: Dynamic Light Scattering

Dynamic light scattering (DLS) was carried out using a Malvern Zetasizer Nano to obtain information regarding the particle size distribution of already formed precipitates or to monitor particulate growth. Size determination is based on the dissimilar Brownian motion velocities of differently - sized particles (r). Particle size measurement depends on the diffusion velocities (D) and is obtained according to the Stokes Einstein relationship, Equation 36 at low Reynolds numbers. In simplified terms, two or more pictures are taken at a certain time interval (~10ms), from which the distance travelled by the imaged particles is evaluated to obtain the particle size. In reality, the subject is more complicated as we find a particle ensemble which scatters the incoming radiation ideally according to Mie theory which produces a scattering pattern. Continuous fluctuations in intensity, position and size are used to evaluate the size distribution present.(184)

$$D = \frac{k_B T}{6\pi\eta r} = \mu k_B T \quad (36)$$

2.7: Surface Area Determination

Surface area measurements (Micrometrics ASAP 2020, Nitrogen Sorption) were primary required to investigate the formation of mesocrystals. The Brunauer–Emmett–Teller theory (**BET**) used for surface area determination is in itself an extension of the Langmuir theory of monolayer adsorption to multilayer adsorption for gases onto solid surfaces. The surface area is determined by measuring the gas quantity adsorbed onto a solid surface (V) over a certain vapour (P)/saturation pressure (P_0) range, which results in an adsorption isotherm from which in turn the volume of a monolayer of adsorbed gas (V_m) can be extracted ($1/(\text{slope} + \text{intercept})$), Equation 37. A detailed derivation is given in Brunauer.(185) The total sample surface area (S_T) is obtained according to Equation 38 under consideration of molecular volume ($M_v = 22,414$ ml) and specific surface area ($A_m = 0.162$ nm²) of adsorbed gas molecules. The specific surface area (S_i) is obtained in relation to the sample mass (m) present after degassing, Equation 39. Here, samples were degassed at reduced pressure for 2 hours at 100°C to remove any previous absorbed material, including pore water. The surface area was calculated from the linear part of the BET plot (10 data points).

$$\frac{1}{V \left[\left(\frac{P_0}{P} \right) - 1 \right]} = \frac{C - 1}{V_m C} \left(\frac{P_0}{P} \right) + \frac{1}{V_m C} \quad (37)$$

$$S_T = \frac{V_m N_a A_m}{M_v} \quad (38)$$

$$S_i = \frac{S_T}{m} \quad (39)$$

Acquired BET data sets could further be used to extract sample surface topography information by means of extracted surface fractal dimensions (D_s). Fractal dimensions present a relative measurement of surface roughness, where this ranges from a perfectly smooth surface with a $D_s = 2$ to a totally rough surface $D_s = 3$. Fractal dimensions were extracted based on nitrogen absorption curves collected according to the Frankel–Halsey–Hill method,(186) and were calculated based on Equation 40-42. Only data points in the region of statistical multilayer adsorption were considered for fractal analysis.

$$\ln\left(\frac{V}{V_m}\right) = \text{const.} + \frac{1}{s} \ln\left(\ln\left(\frac{P_0}{P}\right)\right) \quad (40)$$

$$s > 3; \quad \frac{1}{s} = \frac{(3 - D_s)}{3} \quad (41)$$

$$s < 3; \quad \frac{1}{s} = 3 - D_s \quad (42)$$

2.8: Thermo Gravimetric Analysis and Differential Scanning Calorimetry

Thermo gravimetric analysis (TGA) (TA Instruments STD Q600, 100ml min⁻¹ Air/ N₂) and **Differential scanning calorimetry (DSC)** (TA Instruments DSC Q200, 100ml min⁻¹ N₂) were applied to determine sample composition and the activation energies of dehydration and crystallisation respectively. TGA registers changes in sample mass as a function of time and/ or temperature. A microbalance is used for TGA readout, from which thermal decomposition temperatures and molar compositions can be calculated based on externally - obtained knowledge of starting and end products. DSC measures the change in heat flow compared to an internal standard as the sample undergoes incremental heating/ cooling cycles. The change in heat flow (dQ/dt or dQ/dT) is due to alterations in sample heat capacity (cp) upon temperature variation and or atmospheric decomposition. Changes in heat capacity occur for various reasons. Firstly, they can occur due to sample decomposition and removal of volatile substances which alter the sample composition. Secondly, changes can be a result of phase transformations, which can be endothermic e.g. water evaporation or exothermic e.g. crystallisation events. Recorded is the difference in energy supplied to the internal reference and the sample to maintain them at equal temperature. The measured energy difference or equivalent temperature difference is then reinterpreted as the change in heat flow according to Ohm's law, Equation 43 this is when a readout in the form of a thermocouple is used.

$$\Delta U = RI = R \frac{dQ}{dT} \quad (43)$$

$$cp = \frac{dQ}{dT} \quad (44)$$

Phase transformations and the associated "latent heat" results in peaks in the obtained heat flow profile which can be used to derive the associated enthalpy through peak area integration. The integration of the present peak area also provides a secondary option of tracking the reaction progress (0-1).

Crystallisation activation energies (E_a) can be obtained graphically from a series of experimental runs performed at distinct heating rates.(129) The resulting shifts in the phase transition peak position associated with an applied heating rate can be related to crystallisation activation energies according to the method given by

Chapter 2: Experimental Methods and Analysis

Boswell, Equation 45.(187) β is equal to the applied heating rate for a particular run and T_p is the central peak position. For a graphical representation please refer to Chapter 3.3.

$$\ln\left(\frac{\beta}{T_p}\right) = -\left(\frac{E_a}{RT_p}\right) + c \quad (45)$$

The activation energies associated with liberation of different water fractions (E_a) were derived by iso-conversion methods based on sets of isothermal TGA curves collected at increasing isothermal hold temperatures (40 - 280°C in 5°C steps and hold times of 100- 200 minutes.).(188) **Dehydration activation energies** are acquired according to Equation 46. Here, α (as defined in Equation 47) represents the dehydration progress. $(d\alpha/dt)_T$ the reaction velocity at a given isothermal temperature (T), A is a pre-exponential factor and $f(\alpha)$ describes the underlying unknown reaction model. W_{max} , W_{min} and W_t are the fractions of H_2O present at the beginning, end and time (t) during an isothermal dehydration event.

$$\ln\left(\frac{d\alpha}{dt}\right)_T = \ln[Af(\alpha)] - \frac{E_a}{RT} \quad (46)$$

$$\alpha = \frac{(W_{max} - W_t)}{(W_{max} - W_{min})} \quad (47)$$

The activation energy associated with the liberation of a particular water fraction can be obtained based on recorded overlapping α values present in experimentally flanking isotherms, such as runs performed with isothermal periods at 85, 90 and 95°C. A plot of $\ln(d\alpha/dt)_\alpha$ versus $1/T$, where the value of $(d\alpha/dt)_\alpha$ is determined for each isothermal dehydration event and temperature T , returns a straight line of gradient E_a/R for one particular dehydration step.(95)

2.9: Diffraction

2.9.1: X-Ray Diffraction

X-Ray diffraction (XRD) is a non-destructive elastic scattering technique which is used to analyse solid matter. XRD is able to provide information regarding structural and physical properties of crystalline sample including but not exclusive to phase identification, crystal size (coherently scattering domains), lattice deformation, atomic arrangement and crystal orientation. XRD utilizes atomic long rang order present in a crystal to extract this information based on the principles of destructive and constructive interference of X-rays scattered/ diffracted by the specimen.

Father and son Bragg observed that crystals irradiated by X-rays only exhibited constructive interference at certain X-ray incident angles.(189) From these observations they inferred that direct information of the crystal structure could be gained. Bragg’s law, Equation 48, states the condition of constructive interference and a graphical illustration is given in **Figure 2-1**.

$$2d \sin(\theta) = n\lambda \quad (48)$$

Coherent interference and in turn scattering of X-rays occurs only if the wavelength (λ) or a natural number multiple of the incident X-rays wavelength ($n\lambda$) is equal to $2d\sin(\theta)$. That is the distance (d) between two scattering planes of atoms at a set diffraction angle (θ). In geometry terms, the path length difference marked red in Figure. 2-1 is equal to $n\lambda$.

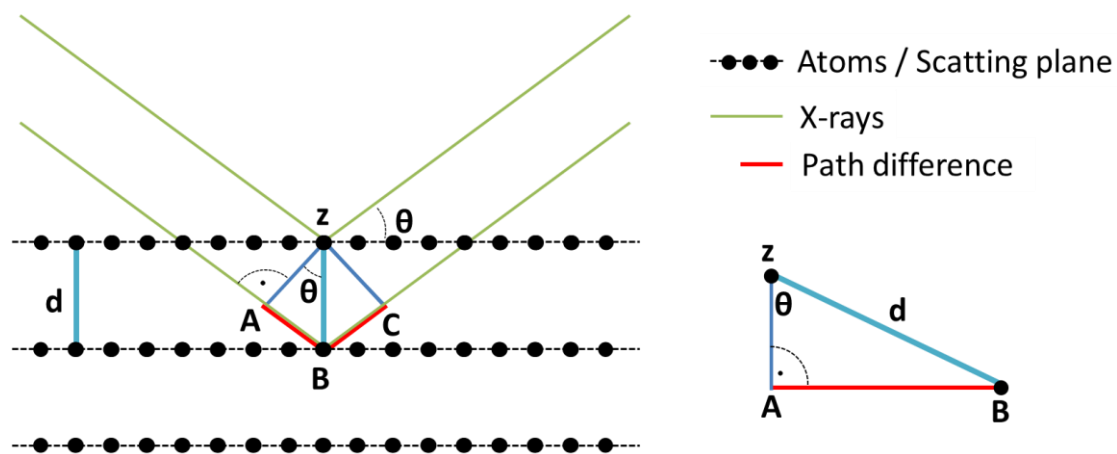


Figure 2 - 1: Schematic to Bragg’s law of diffraction. Given is the geometrical derivation for constructive interference from a crystal. The lower X-ray beam must travel an extra distance $AB + BC$ to continue to be in phase with the upper beam.

Chapter 2: Experimental Methods and Analysis

A change in effective scattering angle follows as a result of the interaction with different scattering planes/ directions of separation d . This combined with knowledge of possible scattering angles eventually allows the reconstruction of the irradiated crystal's atomic arrangement. A list of the obtained scattering angles and lattice spacings is used for phase identification, where this is specific to a crystal of composition y and structure x . (189, 190)

A one dimensional pattern obtained by PXRd is shown for calcite in **Figure 2-2**. Visible are the Bragg peaks as a function of 2θ (Cu source) and the lattice planes (hkl) d spacing in relation to the atomic arrangement of calcite normal to the c - axis.

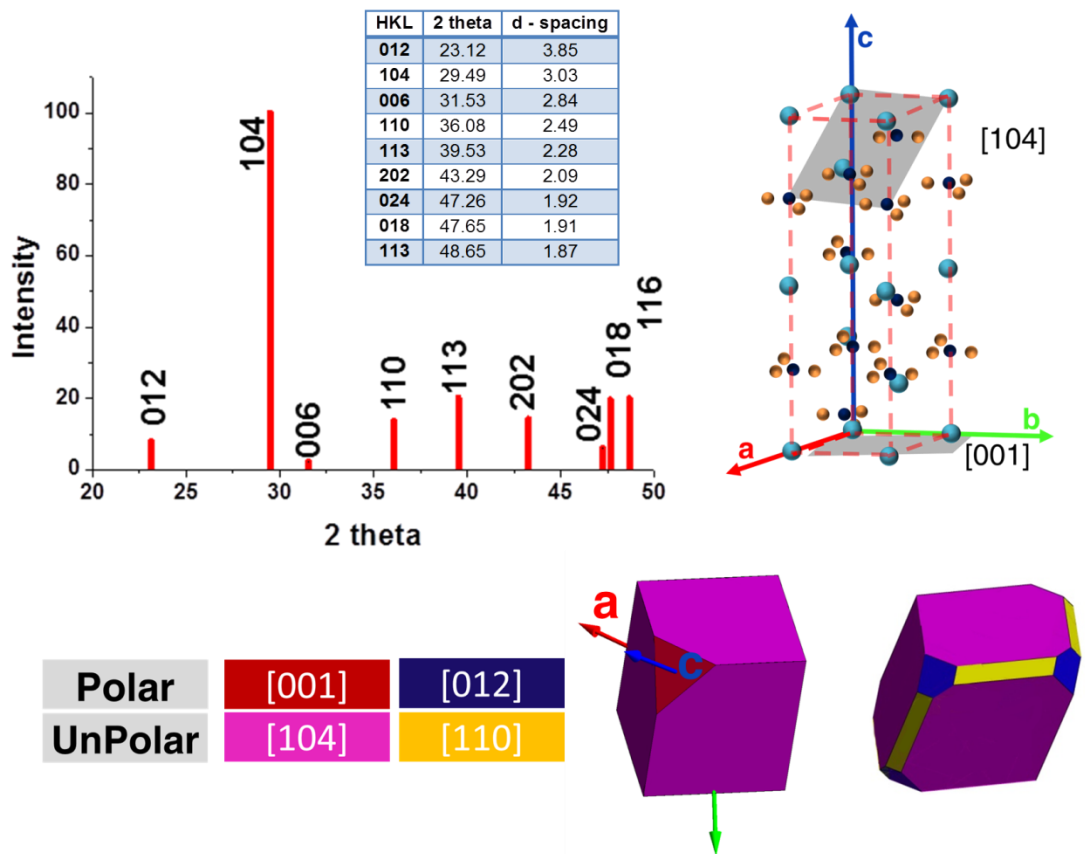


Figure 2 - 2: 1D PXRd Calcite diffraction pattern and its structural relation to atomic arrangement. 2θ position are given in respect to cu radiation.

2.9.2: Diffraction Techniques

2.9.2.1: Powder X-Ray Diffraction

Powder X-ray diffraction (PXRD) is an extension of single crystal diffraction and structure refinement. Instead of a single crystal, diffraction patterns are obtained from an ensemble or powder of crystals, where this avoids the difficulty of having to obtain large, defect free crystals for analysis. In a general laboratory $\theta/2\theta$ setup, a powder sample - located here on a low background holder - is placed between an X-ray source and a one dimensional detector. X-rays are emitted from an X-ray tube, in which a tungsten filament/ cathode is subjected to a high voltage which accelerates electrons towards the anode. When this electron beam hits the anode, the inner electrons of the anode material are ejected and an electron from the higher orbital falls back to fill the hole. As there is a difference between the energetic levels of these orbitals, X-rays specific to the anode material are emitted (2.4.3: *Energy-dispersive X-ray spectroscopy*). The coherently scattered X-rays are detected by scintillating material which converts the number of X-ray photons detected at a particular irradiation angle to a displayed intensity.

Data is collected while both the X-ray source and detector move around the sample at a rate of θ°/min in a uniaxial motion. This generates a pattern as given in Figure 2.2., which can be used to extract several structural and physical parameters. This is achieved by fitting the pattern with respect to a known “ideal” atomic structure of the phase in question by Rietveld refinement.(191) Singular Bragg peak profile fitting can also be performed.(192) Given below are sample characteristics of interest for the work presented, and the methods used to derive them.

Crystallite size (τ) or the coherently scattering domain size was obtained by profile fitting of the most prominent peak present in the given spectra or through the fitting of multiple peaks (Rietveld refinement – Pseudo Voigt Peak shape, size and strain). For single peak line profiles the extracted FWHM (B) was used to calculate the crystallite size using the Scherer equation, Equation 49 after subtracting instrumental broadening. A shape factor (K) of 1 was used.

$$\tau = \frac{K\lambda}{B \cos \theta} \quad (49)$$

Chapter 2: Experimental Methods and Analysis

For Rietveld, the following relationships were used (Equations 50-51), where (u) carries information regarding strain broadening and (w) information about size peak broadening.

$$FWHM = \sqrt{(u \tan^2 \theta + v \tan \theta + w)} \quad (50)$$

$$\tau = \left(\frac{180}{\pi}\right) \frac{\lambda}{\sqrt{w}} \quad (51)$$

Peak broadening is related to crystal size by means of the constructive interference/diffraction criterion. I.e. diffracted beams must be in phase which in a perfect infinite crystal ideally results in infinitely narrow sharp peaks as all atoms scatter at only this condition. Now as crystals are limited in size a number of interfacial atoms are present which fulfil slightly different constructive interference criteria. The peak therefore broadens with decreasing crystal size.(193) Instrumental broadening is a result of imperfect optical devices among others.

Strain or lattice distortions have to be further classified as either **homogenous** (global uniform strain) or **inhomogeneous** (microstrain). Homogeneously strained crystals are a result of, for example, a uniform applied stress field or due to the uniform incorporation/ lattice substitution in the crystal. An example of the latter is the calcium ion substitution by magnesium in calcite crystals. As internal or external stress and the resulting strain are uniform, the spacing between particular planes (direction and species dependent) changes to a certain degree. The strain is therefore identified by a shift in scattering angle. Tensile stress generally results in a shift to higher d spacing, while compressive stress leads to a lower d spacing. The associated changes in unit cell are expressed as given in Equation 52.

$$\% = \frac{\Delta c}{c_{initial}} = \frac{(c - c_{initial})}{c_{initial}} \quad (52)$$

Micro strain (ϵ) as a result of crystallographic defects is perceived by peak broadening (as for crystallize size). Both factors can be separated as strain broadening is length-scale independent and therefore results in different peak shape profiles than size broadening.(192) This was carried out here by Rietveld refinement according to Equation 53.

$$e = \frac{\sqrt{(u-w)}}{\left(\frac{180}{\pi}\right) 4\sqrt{2 \ln 2}} \times 100 \quad (53)$$

Knowledge of texture or the degree of **crystal orientation** with respect to a substrate, as required for the experimental work presented in Chapter 5, was obtained by collecting rocking curves or acquiring pole figures.

Rocking Curves provide information about the degree of orientation present in a sample with respect to crystallographic directions or the substrate. This is achieved by determining the changes in peak width of a Bragg reflection as the sample is gradually rocked through the reflection. The rocking motion can be achieved in two ways. The sample holder can be independently rocked from one side of the peak to the other while the detector and source are kept fixed at the peak maximum, corresponding to the 2θ value. Alternatively, the sample holder is fixed and the source/ detector are moved to emulate the sample holder rocking motion. The width of the peak is correlated with the degree of orientation such that a range of constructive scattering conditions can be tested. A sharper peak width correlates with a higher degree of orientation.(194)

If applied to the measurement of single crystals, as used in Bragg coherent diffraction imaging, (Chapter 5) additional information can be gathered including the detection of secondary grains (peak shoulders) and dislocations where this is achieved by “sectioning” the crystal as in tomographic techniques.

Pole Figures are acquired in a similar manner to rocking curves for powdered specimens. That is, measurements are collected at fixed scattering angles (2θ) and differences in diffraction intensity are recorded as the sample is tilted (ψ 0- 90°) and rotated around the sample surface normal axis (ϕ 0-360°). This is done step-wise, which means that the sample is rocked a certain degree in psi and the intensity is collected as phi is varied (0-360°). This is repeated for further increments in psi. A pole figure is generated from the obtained intensity profiles. Pole figures are a stereographic projection of pole density (diffraction intensity) as a function of pole orientation. $\psi = 0^\circ$ is the centre of the pole figure e.g. the lattice plane to set scattering condition 2θ , is parallel to the substrate surface. Intensities recorded at $\psi = 90^\circ$ have then to come from a scattering plane normal to set scattering condition that is perpendicular to the sample surface, **Figure 2-3**. The intensity variation in

the ψ direction at a fixed ϕ is due to the tilting motion while variation in the ϕ direction at fixed ψ corresponds to the in- plane distribution i.e. if the crystal sits epitaxially on the substrate or with preferred orientation.(195)

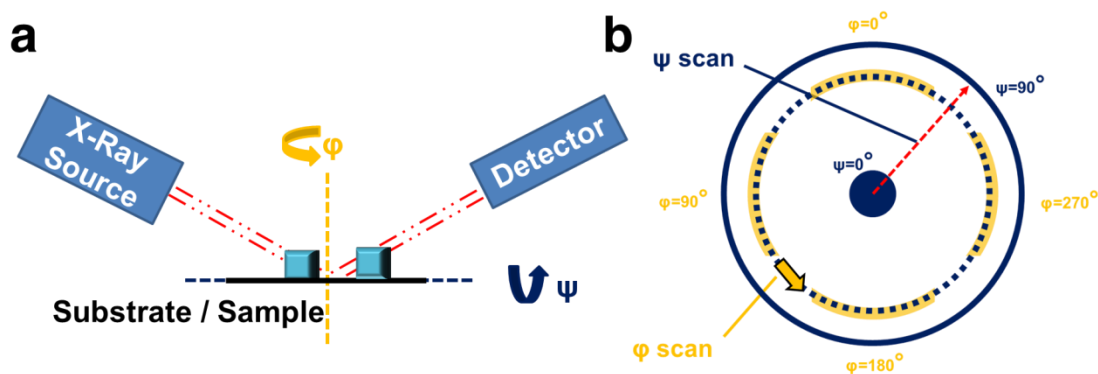


Figure 2 - 3: Schematic displaying the acquisition principle behind pole figures (a) and its translation to given pole figure representation. Illustrated are rotating sample angle ϕ and tilt angle ψ . Reproduced after Kagami, 2011.(195)

PXRD data were collected using a Bruker D8 Advanced diffractometer equipped with an X-ray source emitting Cu $K_{\alpha 1}$ radiation. XRD data were collected in an angular range between 10° and 120° in intervals of 0.033° with a scan rate of 2° min^{-1} . Programmable divergence slits were used during the measurement, with an irradiated area of $10 \times 10 \text{ mm}$. The data were subsequently corrected, utilizing the software HighScore Plus (Almelo, The Netherlands) for analysis. Crystal orientation was inferred from the same equipment in pole configuration, with a step size of 1.5° at 2.5 seconds (Psi 0-90, Phi 0-360).

2.9.2.2: Electron diffraction

Electron diffraction (ED) as carried out in TEM provides fundamentally identical information as X-ray diffraction, but differs in 3 key aspects. The use of electrons rather than X-rays allows the rapid on-screen readout of the diffraction pattern. The second and third differences are a result of the TEM setup – from which it is easily possible to obtain 2D diffraction patterns and the third is due to the ease of focus and magnification variation. It is therefore possible to extract diffraction patterns from a particular area of a specimen or a small single crystal as described by the term selected area electron diffraction (SAED).

2.9.2.3: Bragg Coherent Diffraction Imaging

Bragg Coherent Diffraction Imaging (BCDI) is a form of X-ray phase contrast microscopy, which generates strain-sensitive image reconstructions from 3D diffraction patterns collected from an isolated crystalline specimen illuminated by a spatial and temporal coherent light source. Reconstructions are obtained by applying phase retrieval algorithms to the collected intensity patterns.(196)

Experiments were performed in collaboration with Jesse N. Clark and Ian K. Robinson from University College London. The former performed the image reconstructions presented in Chapter 5. Presented below are in brief technical and experimental details of the data collection and analysis methods. A general description of the working principle is given in Chapter 5.1. Explicit details can be found here (197, 198), Chapter 5 and Appendix G.

Experiments were conducted at Beamline I-16 at the Diamond Light Source (DLS) UK and at Beamline 34-ID-C of the Advanced Photon Source (APS) USA. Synchrotron radiation or “Bremsstrahlung” is electromagnetic radiation of high brilliance and broad spectral width, where this is emitted by charged particles at relativistic velocities under radial acceleration. Synchrotron radiation in synchrotron sources is generated by previously accelerated electrons, which are kept in circular motion in a storage ring through application of bending magnets or undulators. These enforce a continued circular motion.

BCDI Setup and Data Acquisition: An undulator produced X-rays which were monochromatized using a silicon (111) double-crystal monochromator to an energy of 8 keV (APS) or 9 keV (DLS). Calcite crystals on a substrate were placed on a diffractometer which had its rotation center aligned with the X-ray beam. Slits were used to aperture the X-rays to reduce the illuminated area. An X-ray sensitive charge-coupled device (Medipix3) with 256 x 256 square pixels of side length 55 μm or a (Princeton instruments) with 1300 x 1300 square pixels of side length 22.5 μm was positioned at the desired diffraction angle for an off-specular (104) reflection at a distance of 2.5 m from the sample. To measure its full 3D diffraction patterns, the crystal was rotated by 0.3 degrees with 0.003 degrees step size. At each rotation angle, a two-dimensional slice of the 3D far-field diffraction pattern was recorded. By stacking all of these two-dimensional diffraction frames together, a complete 3D diffraction pattern was obtained, from which real-space images can be reconstructed (see Reconstruction Algorithm). Due to the small size of the

Chapter 2: Experimental Methods and Analysis

crystals, 1-2 μm , the illumination can be considered to be almost completely coherent.(199)

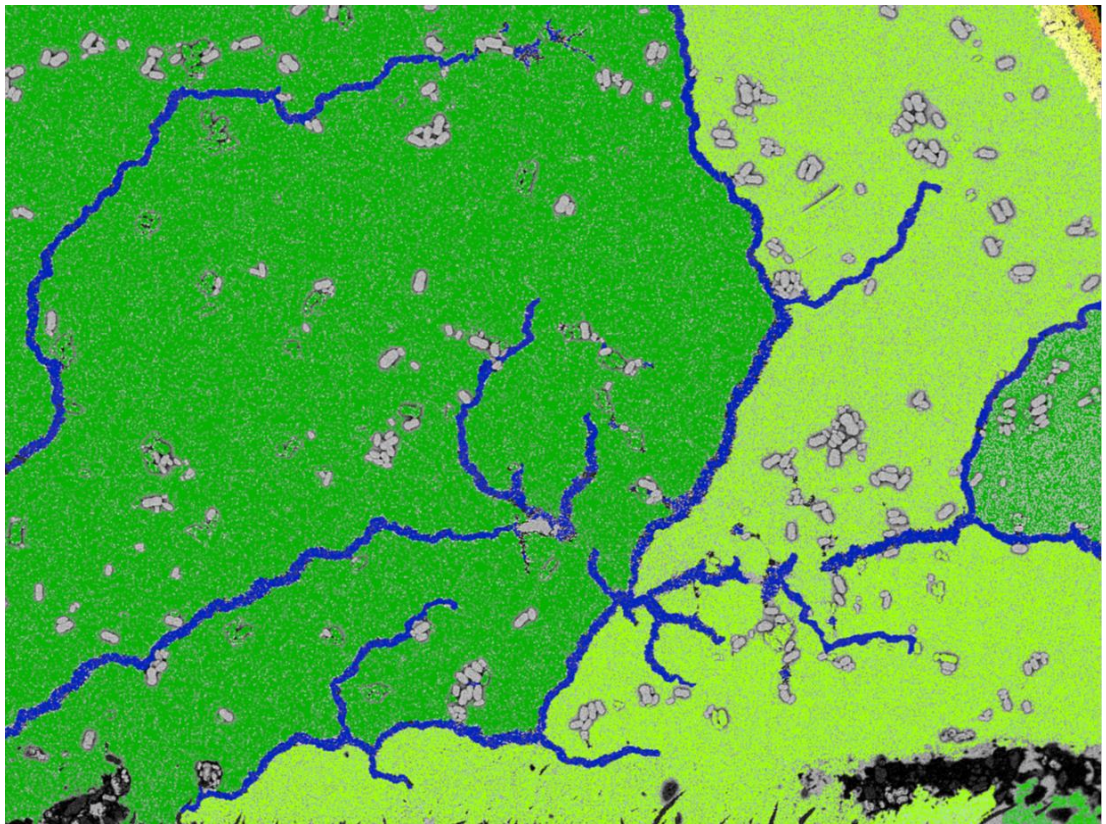
Reconstruction Algorithm: Images were obtained by performing iterative phase retrieval (200) on the three-dimensional coherent diffraction patterns. Complete knowledge (both amplitude and phase) of the diffracted wavefield allows an image to be obtained via an inverse Fourier transform. Provided that the diffraction data is oversampled, that is, the sample has its Fourier transform sampled at least twice the Nyquist frequency (or alternatively its auto-correlation is sampled at least at the Nyquist frequency) and the crystal is isolated, phase retrieval can be performed. The basic phase retrieval process begins with a guess for the diffracted phase before applying an inverse Fourier transform to yield a first estimate of the crystal. After enforcing the constraint that the crystal is isolated (the 'support constraint') this new crystal iterate is Fourier transformed to yield an estimate for the three-dimensional diffracted wavefield. Consistency with the measured intensity (the 'modulus constraint') is enforced while retaining the current estimate of the phase. This process is repeated until a self-consistent solution is reached using combinations of current and previous estimates for the crystal.

For this work, a novel approach was used which combined guided phase retrieval (201) with low to high resolution (or multi-resolution) reconstructions (202). The combination of a guided approach with low to high resolution reconstructions allows objects with non-negligible phase to be reconstructed. 50 estimates were initially reconstructed using a combination of error reduction (ER) and hybrid input output (HIO) (alternating between 10 ER and 100 HIO for a total of 1000 iterations) at a reduced resolution, which was achieved by multiplying the data by a Gaussian function with standard deviation equal to 10% of the array size. After this initial phase retrieval, 50 new low-resolution iterates were generated by combining the best estimate with the remaining 49 estimates. Further reconstructions were then performed using the 50 low-resolution iterates as seeds for reconstructions at the full resolution of the diffraction pattern to yield 50 new estimates. The 5 best estimates were then averaged to produce the final estimate. The best iterates were selected based on their agreement with the data. The final 50 estimates during the reconstruction were averaged to produce the output estimate which takes into account the slight variations in similar solutions. Partial coherence was taken into account (198) with only a small departure from full coherence observed.(199)

2.10: Winterbottom Reconstructions

Winterbottom reconstructions are an extension of the Wulff reconstruction and are used to determine the shape of a crystal in thermodynamic equilibrium which is sitting on a hard substrate. The shape which provides the minimal surface energy for a fixed volume is constructed by plotting the direction-specific surface energies as a function of the orientation normal and subsequently drawing the tangent through each end point of any given orientation. The resulting enclosed body is equal to the equilibrium or Wulff shape. Winterbottom reconstructions were obtained using Wulffmaker.(111)

Chapter 3: Amorphous Calcium Carbonate



Chapter 3: Amorphous Calcium Carbonate

Chapter 3 is a reproduction of the following publications. Images are provided in reproduction in parts or total with the respective source acknowledged.

Ihli J, Kim Y-Y, Noel EH, Meldrum FC. The Effect of Additives on Amorphous Calcium Carbonate (ACC): Janus Behaviour in Solution and the Solid State. *Adv Funct Mater* 2013, **23**(12): 1575-1585.

Ihli J, Wong WC, Noel EH, Kim Y-Y, Kulak AN, Christenson HK, Duer MJ, Meldrum FC. Dehydration and crystallisation of amorphous calcium carbonate in solution and in air. *Nat Commun* 2014, **5**.

Ihli J, Kulak AN, Meldrum FC. Freeze-drying yields Stable and pure Amorphous Calcium Carbonate (ACC). *Chem. Commun.* **49**, 3134-3136, (2013)

Ihli J, Wang Y-W, Cantaert B, Kim Y-Y, Bomans PHH, Sommerdijk NAJM, Meldrum FC. On the Possibility of Amorphous Calcium Oxalate Precursor Phases. *To be Submitted*

3.1: Abstract

The mechanisms by which amorphous precursors transform into crystalline materials are poorly understood. One amorphous precursor of interest is amorphous calcium carbonate (ACC). Its crystallisation is a key intermediate step in the formation of crystalline calcium carbonate in synthetic, biological and environmental systems. By investigating this process in detail - studying the effects that additives, confinement and the synthesis method each have on the stability and transformation mechanism of ACC in solution and in the solid state – a number of contrasting and apparently contradictory views in the literature are unified. This reveals that additives primarily affect the nucleation of a crystalline phase rather than stabilizing ACC and that this affect occurs in a “Janus-like” behaviour, where they retard the crystallisation of ACC in solution, but yet accelerate crystallisation in the solid state. Confinement studies show that ACC can dehydrate prior to transforming to calcite, both in solution and in air. This suggests that it is highly unlikely that ACC crystallizes by means of a solid state transition in solution, and that a catalyst in the form of surface water is required to overcome the high activation energy of full dehydration and crystallisation. In recognition of the importance of water in ACC synthesis, methods and secondary treatment steps were evaluated to elucidate their influence. This led to the development of a simple synthetic method based on freeze-drying saturated, counter ion free CaCO_3 solutions. The developed method returns ACC with minimal surface water and extended atmospheric stability in a single step. Finally, the developed synthesis method was applied to test the generality of amorphous precursor formation in solution across a range of known biominerals. This proved successful in the preparation of amorphous calcium phosphate and amorphous calcium oxalate. The latter provides the first evidence of an amorphous calcium oxalate precursor phase in aqueous solution.

3.2: Additives and Amorphous Calcium Carbonate

3.2.1: Introduction

Biominerals are single crystal composites with remarkable morphologies and properties, which are formed by living organisms. The organisms exert an extraordinary control over the crystallisation processes in terms of regulating mineralisation and guiding the supersaturation profile, spatial dimensions and bodily fluid composition.⁽⁵⁾ All this is achieved under ambient reaction conditions and many studies have tried to identify the strategies employed by nature and then translate them to synthetic systems.⁽²³⁾ The first and most readily identified of nature's strategies is the use of soluble **additives** in controlling calcite, aragonite and vaterite crystallisation, and this has been particularly well-studied. These studies demonstrated that organic macromolecules extracted from biominerals have a direct effect on the morphology, the polymorph precipitated and the mechanical properties of crystals obtained from bulk solution experiments.⁽²⁰³⁾ While these studies have yielded valuable information on the interaction between bio-macromolecules and calcium carbonate crystals, the finding that many biominerals may form via **amorphous precursor** phases rather than by ion-by-ion growth, (Chapter 1.4.4),^(117, 204) raises questions concerning the mechanisms by which additives participate in the crystallisation of the amorphous phase.

The most studied among the amorphous precursor phases is amorphous calcium carbonate (ACC). ACC will therefore be the focal point of our investigations in this chapter. Across Chapter 3.2 we will introduce the general identification criteria of "pure" ACC and its structural variation with chosen synthesis method, while simultaneously tackling the question of "how do additives affect the stabilization of the amorphous phase?"

ACC is typically very short-lived when precipitated in the absence of additives, while it can be indefinitely stable in biominerals. As a transient precursor phase, ACC can and eventually will undergo a sequential transition from hydrated ACC, to anhydrous ACC, to the final crystal polymorph when crystallising.^(78, 118) The extended stability of biogenic ACC is commonly attributed to the organic and inorganic additives present within the mineral phase (occluded/ incorporated). Major organic and inorganic additives found associated with ACC and or the resulting crystalline biominerals include magnesium, phosphate, silicate and

Chapter 3: Amorphous Calcium Carbonate

glycoproteins rich in glutamic acid and hydroxyamino acids.(18, 205) Further metabolic intermediates of crustaceans in the form of low molecular weight phosphoenolpyruvate and 3-phosphoglycerate, have also been identified to be effective in stabilizing the ACC.(7)

More and more additives, inspired from nature's strategy, have been tested to determine whether they affect ACC, and in particular whether they stabilize it. Successful candidates in extending the lifetime of ACC **in solution** in synthetic systems include highly carboxylated species such as poly(acrylic acid),(206) a poly(ethylene oxide)-*b*- poly(acrylic acid) block copolymer,(207) poly(aspartic acid)(60, 78), poly(allylamine hydrochloride) (PAH),(208), poly(styrene sulfonate) (PSS),(206) and ovalbumin(25). Others include the more biomineral relevant magnesium, phosphate and silicate ions.(147, 205, 209, 210)

It is important to point out that prior research studies have predominantly focused on the effects of additives have on the crystallisation of ACC in solution. However, this actually might not be the case for ACC crystallizing in biominerals. The crystallisation of ACC may well occur via a **solid-state** transformation in biology as is demonstrated in the case of the sea urchin spine formation.(97, 211) The ACC precursor in this case is encapsulated within a membrane - bound compartment, such that it effectively crystallizes in the absence of bulk water. This potentially prohibits any dissolution/ recrystallisation mechanism which would dominate if ACC was crystallising in solution, Chapter. 3.3.

It is therefore surprising, given the importance of a solid-state crystallisation mechanism to the transformation of ACC to crystalline CaCO₃ biominerals, that the ability of additives to direct this process has received such little attention.(49, 95, 157, 161, 206, 212) The following addresses this problem and compares the crystallisation/ stabilization profiles of ACC precipitated in the presence and absence of different additives, in solution and in the solid state. This resulted in a surprising observation that some additives exhibit a "Janus-like" behavior in which they retard the crystallisation in solution yet accelerate a heat-induced solid-state crystallisation. Explanations for this observation are sought by exploring the effects of the additives in detail, and making attempts to characterize the individual stabilization mechanism as either direct (altering the stability of the ACC) or indirect (suppressing/ retarding the formation of the emerging polymorph).

3.2.2: Experimental

The influence of a range of additives on the crystallisation of amorphous calcium carbonate (ACC), both in solution and in the solid state (i.e. when the ACC was dry) was investigated, where ACC was co-precipitated with the additives Mg^{2+} , SO_4^{2-} , L-aspartic acid, poly(styrene sulphonate) (M.W. 70.000), poly-(α,β)-DL-aspartic acid sodium salt (M.W. 2.000-11.000) and sodium bis(2-ethylhexyl)sulfosuccinate (Na-AOT). Reference nano-calcite (≈ 100 nm in diameter) was obtained from American Elements.

ACC synthesis. ACC was synthesized using three methods based on those introduced in Chapter 2.2. This was done to determine the effects that different synthesis methods have on the formed ACC. Two direct precipitation methods, as described in Chapter 2.2.1, were used (direct ACC and high pH ACC), where these provide the bulk of the experimental observations. Additionally, ACC was synthesized using the ammonia diffusion method, Chapter 2.2.3.1 (ADM-ACC). (93, 169)

Direct ACC and high pH ACC were prepared by combining equal solution quantities of 1 M Na_2CO_3 / (30 mM NaOH,- high pH ACC only), and 1 M $CaCl_2$ at 4°C (pH~6.8). The resulting ACC slurry was immediately separated from the remaining solution by filtration (0.22 μm Isopore GTTP membrane filter), prior to washing with ethanol. Selected additives were added either to the initially prepared calcium or carbonate solutions. The addition of sodium hydroxide to the reacting carbonate solution leads to an increase in carbonate solution pH from 11.4 to 12. This change in pH directly influences reaction kinetics and co-precipitate formation upon combination of calcium and carbonate solution.

ADM-ACC was prepared by placing a calcium chloride solution (10 mM, 25 ml) into a hermetical sealed container which was previously loaded with 3 g of solid ammonium carbonate. Precipitates were removed from solutions at appropriate times to obtain specific "polymorphs". ACC < 30 minutes, calcite > 120 minutes. In this method, the initial neutral pH of the calcium solution is raised slowly by diffusing carbon dioxide and ammonia to a pH~ 9, providing thusly a low pH alternative, with even slower reaction kinetics in forming ACC then compared to either high pH or direct ACC.

Samples for analysis were isolated according to the description given for direct ACC and high pH ACC. $CaCO_3$ precipitates for TEM analysis were collected on formvar/ carbon-coated Cu TEM grids by immersing the grids in 10 ml of the ACC carrying solutions for two seconds before rinsing them with ethanol.

Chapter 3: Amorphous Calcium Carbonate

The **ionic strength** (I) of the combined solutions (no precipitation) was calculated using Visual Minteq. In the case of ACC prepared by direct precipitation methods, and in the absence of additives this returned a value of $I = 1.21-1.22$. Only minor differences in ionic strength were calculated based on the addition of most additives under the conditions tested (PAsp,-Asp,-AOT,-PSS a 200 ppm; 10 mM Mg^{2+} or 2 mM SO_4^{2-}). A notable exception is the difference in ionic strength which arises upon the addition of 200 mM Mg^{2+} or SO_4^{2-} . Reference experiments in which NaCl (2-200 mM) was added to the initial solutions to achieve identical ionic strengths showed no difference in the observed trends in additive behaviour.

A summary of the reaction space investigated, together with the measured starting solution pH values is given in Table 3.

Chapter 3: Amorphous Calcium Carbonate

Reagent 1	Reagent 2	Reagent 3	Concentration 1	Concentration 2	Concentration 3	Concentration 1	Concentration 2	Concentration 3	pH
			[ppm]	[ppm]	[ppm]	[mM]	[mM]	[mM]	[-]
High pH ACC									
CaCl ₂	-	-	-	-	-	1000	-	-	6.83
CaCl ₂	MgCl ₂	-	-	-	-	1000	200	-	6.25
CaCl ₂	Na-Asp	-	-	200	-	1000	1.5	-	5.87
CaCl ₂	Na-PAsp	-	-	200	-	1000	1.5	-	5.37
CaCl ₂	Na-PSS	-	-	200	-	1000	0.97	-	5.78
CaCl ₂	Na-AOT	-	-	200	-	1000	0.45	-	6.82
Na ₂ CO ₃	-	NaOH	-	-	-	1000	-	30	11.98
Na ₂ CO ₃	Na ₂ SO ₄	NaOH	-	-	-	1000	200	30	11.87
ADM-ACC									
CaCl ₂	-	-	-	-	-	1000	-	-	6.83
CaCl ₂	MgCl ₂	-	-	-	-	1000	200	-	6.25
CaCl ₂	Na-PSS	-	-	200	-	1000	0.97	-	5.78
CaCl ₂	Na-AOT	-	-	200	-	1000	0.45	-	6.82
(NH ₄) ₂ CO ₃	-	NaOH	-	-	-	1000	-	30	9.56
Turbidity measurements									
CaCl ₂	MgCl ₂	-	-	-	-	1000	10	-	
Na ₂ CO ₃	-	-	-	-	-	1000	-	-	
Na ₂ CO ₃	Na ₂ SO ₄	-	-	-	-	1000	2	-	

Polymer concentrations were calculated based on the number of functional groups and independent of given solution pH

Table 3: Reagent starting concentrations and pH as used for experiments. (152)

Chapter 3: Amorphous Calcium Carbonate

ACC stabilization/ crystallisation in solution. The effect of additives on the crystallisation and stabilization of ACC in solution was investigated by means of turbidimetry and conductometry, where these provide estimates of the onset of crystallisation of the different ACC samples, and by determining their dissolution profiles from conductivity measurements.

Turbidity measurements were carried out as described in Chapter 2.4.1. In detail, ACC was precipitated by direct combination of solutions (0.5 ml), 1 M $\text{CaCl}_2 \cdot 2\text{H}_2\text{O}$ with 1 M Na_2CO_3 / 30 at 4°C. Experiments were performed directly in spectrophotometer cuvettes. Additives were added to the calcium solution or carbonate solution prior to mixing, depending on the nature of the additive in question, with a final additive concentration of 100 ppm (Asp, PAsp, AOT, PSS) or 1-5 mM (Mg^{2+} , SO_4^{2-}). SO_4^{2-} was added to the carbonate solution to avoid the precipitation of calcium sulphate.

The dissolution behaviour of ACC which had been precipitated in the absence, and in the presence of additives, was investigated below the calcite solubility limit of $< 5.73 \text{ m g l}^{-1}$, 25°C.(166) Experiments were performed according to the procedure given by Meiron, 2011.(213) Here 1 mg of dried ACC was added to a closed Schott bottle filled with 250 ml deionized water and equipped with a conductivity probe. The dissolution progress was recorded, under constant agitation (100 rpm). Working beneath the calcite solubility limit ensures that no precipitation of the crystalline polymorphs of CaCO_3 can occur during dissolution. This allowed the direct stabilization of ACC by additives incorporated within its structure to be investigated.

ACC crystallisation in the solid state. Solid state crystallisation was studied by annealing, through TGA and DSC, and by performing in situ PXRD analysis while heating the ACC precipitates. This allows us to obtain direct information regarding the phase transformation.

TGA and DSC measurements provide information regarding crystallisation activation energy and the degree of additive incorporation. Combined TGA/ DSC measurements were performed under air flow in the temperature range from 25°C to 400°C with heating rates of 10°C min⁻¹, 15°C min⁻¹ and 20°C min⁻¹. Identical amounts of sample (~ 10 mg) were used in all runs.

PXRD was used to monitor the crystallisation progress and to determine the onset temperature of ACC crystallisation. ACC samples were heated in situ on the diffractometer. A heating rate of 5°C min⁻¹ was applied, and scans were carried out over the interval $2\theta = 28 - 32^\circ$ (Cu source), monitoring the emergence of the [104] - calcite or [112] – vaterite selective reflections.

3.2.3: Results

3.2.3.1: Characterisation of “Pure” Amorphous Calcium Carbonate

Before describing the effects the additives magnesium, sulfate, aspartic acid (Asp), poly(styrene sulphonate) (PSS), poly(aspartic acid) (PAsp) and sodium bis(2-ethylhexyl)sulfosuccinate (Na-AOT) have on the crystallisation/ stabilization of ACC in both solution and in the solid state, the properties and appearance of pure ACC will be described. Most of the ACC in this study was synthesized by mixing equal volumes of solutions of 1 M Na_2CO_3 / 30 mM NaOH and 1 M CaCl_2 at 4°C, where this is termed “high pH” ACC. ACC samples prepared were characterized using a combination of IR- and Raman spectroscopy, TGA, DSC, PXRD, SAED and SEM or TEM to confirm their amorphous character and general characteristics.

Typical data of prepared “high pH” ACC is shown in **Figure 3-1**. IR spectroscopy of this ACC (a) showed broad vibrational bands centred around 1476 / 1414 cm^{-1} (ν_3), 1075 cm^{-1} (ν_1) and 865 cm^{-1} (ν_2), which, in addition to peaks due to the vibration of water molecules at 1651 cm^{-1} ~3300 cm^{-1} are characteristic of ACC. The absence of a ν_4 vibrational band centred around 750-700 cm^{-1} in acquired spectra is the ultimate descriptor of ACC. The ν_4 vibrational band is specific to crystalline calcium carbonate.(214)

Raman spectroscopy (b) yields a more plain spectrum. Only a very broad peak at 1085 cm^{-1} is visible, where this corresponds to the internal CO_3^{2-} symmetric stretch. Notable in the spectra obtained is the absence of any secondary peaks, and in particular the ν_4 peak centred around 700 cm^{-1} , which is similar to the IR ν_4 and is unique to crystalline calcium carbonate.(215)

The obtained TEM (c) and SEM (d) images presented in Figure 3-1 demonstrate that the prepared ACC consists of spherical particles of approximately 50 - 80 nm in diameter. A range of synthesis and extraction time dependent sizes from 10 - 500 nm have been reported.(94, 216) Presented in the inset (d) is a SAED pattern corresponding to the presented electron micrograph. This confirms the amorphous character of the ACC prepared through the complete absence of any bright spots or rings, and the presence of the classic amorphous halo. The acquired PXRD pattern (e) supports this observation by showing an amorphous background of low intensity and the absence of any sharp peaks. An overview of the IR-, Raman- and PXRD spectra/ pattern obtained from amorphous and crystalline calcium carbonate is provided in Appendix A-C.

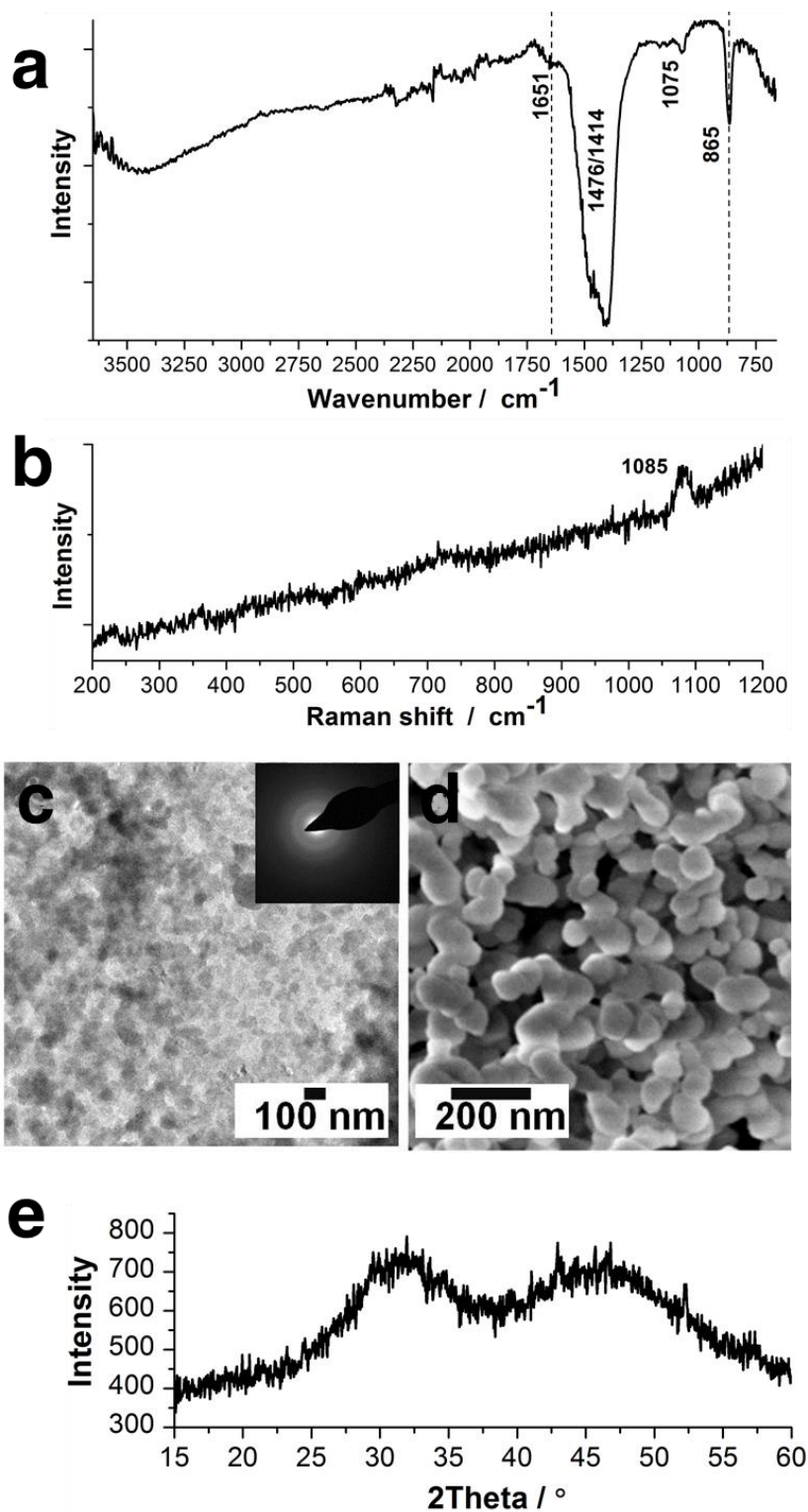


Figure 3 - 1: Characterization data of “high pH” ACC using (a) IR-, (b) Raman spectroscopy, (c) TEM and (d) SED, where the inset in (c) shows the electron micrograph corresponding SEAD pattern. Finally given in (e) is a PXRD pattern collect from an ensemble of “high pH” ACC.(152)

3.2.3.2: Effect of Additives in Solution

The effect of additives on the stabilization and crystallisation of ACC in solution was investigated first. This was achieved by recording the changes in the solution **turbidity** with time using UV-Vis spectroscopy in the presence and absence of selected additives. The chosen method provides an effective yet simple method for observing the early stages of calcium carbonate precipitation in solution. This is achievable as the recorded changes in light transmission/ turbidity with time can be related to either the formation and aggregation of ACC (decrease in transmission) or its subsequent crystallisation and sedimentation of the growing crystals (increase in transmission).(217)

Presented in **Figure 3-2a** are the acquired transmittance - time profiles in the absence and in the presence of the additives studied. As a result of the highly concentrated starting solutions (1 M), ACC formation occurs instantaneously upon the combination of reagents, where this drops the transmittance to 0% across all experiments (i). This decrease and the resulting baseline in transmittance, are solely associated with the formation of ACC (Figure 3-2b i), and was taken as the starting point of our observations. The graphs then show a S-shaped transmission recovery. The observed increase in transmittance with time, which is seen in all samples, is associated with the crystallisation of the ACC and the subsequent sedimentation of the crystalline particles (ii & iii).(217) These regions therefore provide us with information regarding the stability of the formed ACC, when comparing profiles obtained in the presence and absence of additives.

Figure 3-2a shows that all of the additives studied retarded the onset of crystallisation (onset of transmission increase), thereby increasing the lifetime of ACC in solution. Pure “high pH” ACC samples showed a measured induction time of ~ 300 sec, while crystallisation onsets between 320 and 500 sec were recorded for ACC precipitated in the presence of additives. The measured retardation effect was in the order AOT > PSS > PAsp > Asp for 200 ppm additives. The profiles shown for Mg^{2+} and SO_4^{2-} correspond to concentrations of 10 mM Mg^{2+} and 2 mM SO_4^{2-} . These deviate from the additive concentration used for ionic additives throughout the study as 200 mM Mg-ACC failed to crystallize within 1 day, and $CaSO_4$ co-precipitated with the ACC.

Confirmation that the decrease and increase in turbidity corresponds to the formation of ACC and calcite respectively was obtained by ex-situ IR measurements on precipitates isolated at different time-points on the turbidity curves (i-iii). Acquired IR spectra are shown for pure ACC in Figure 3-2b (i-iii) and of Mg-ACC and PSS-ACC in Figure 3-2c (ii). The spectra presented in (b) show the transformation of ACC to calcite and vaterite as the transmittance recovers. This is

Chapter 3: Amorphous Calcium Carbonate

evident by the emergence of the ν_4 band. The spectra given in (c) highlights the extended lifetime of ACC prepared in additive presence when compared to pure ACC. This is again evident from the emergence of the ν_4 band, which is delayed in the presence of the additives.

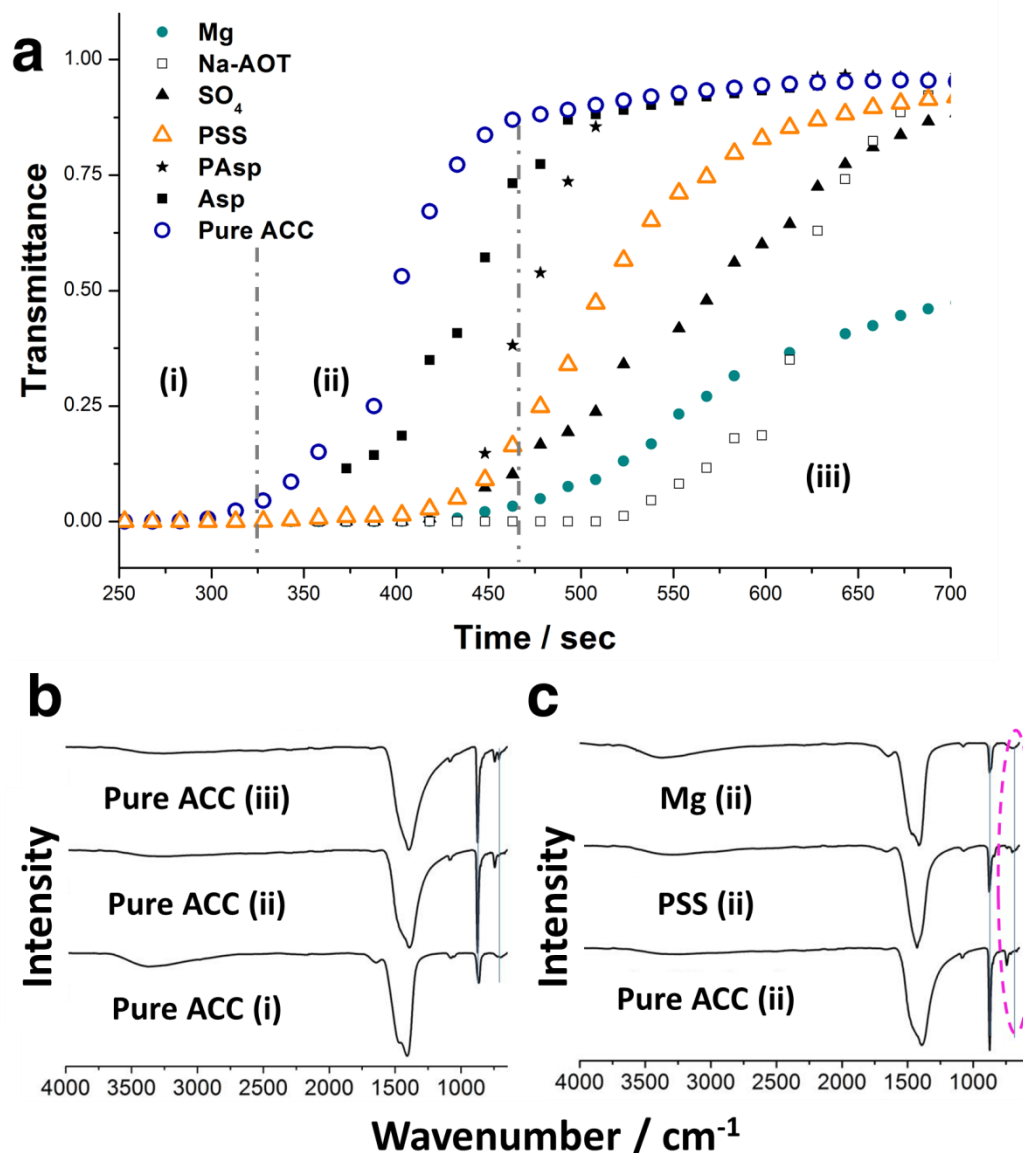


Figure 3 - 2: (a) Plotted is the transmittance recovery as a function of time after mixing two solutions of 1 M CaCl₂ and 1 M Na₂CO₃/ 30 mM NaOH containing 200 ppm of the additives, poly(styrene sulphonate) (PSS), Aspartic acid (Asp), poly(aspartic acid) (PAsp), bis(2-ethylhexyl)sulfosuccinate (AOT) or 10 mM of Mg²⁺, 2 mM SO₄²⁻ divided into 3 discrete stages of precipitation - (i) formation of ACC, (ii) onset of transmittance recovery and associated crystallisation of ACC and (iii) complete transmittance recovery as crystallisation and sedimentation progresses. Shown is the average transmittance recovery of 3 repeats. Presented in (b) and (c) are IR spectra acquired of isolated precipitate at distinct stages (i to iii) of pure ACC and additive incorporating/ occluding ACC. Stage (i) corresponds to the initial ACC formation – broad band at 711 cm⁻¹. (ii) crystallisation of pure ACC to vaterite - emerging band at 743 cm⁻¹, no crystalline phases of calcium carbonate were observed at this stage for the additive containing ACC. (iii) detection of calcite (711 cm⁻¹) and vaterite across all samples. (152)

Chapter 3: Amorphous Calcium Carbonate

Having seen that additives can stabilize ACC in solution, the next obvious question to address is, "how do additives induce this **increased stability?**" Is the extended lifetime a result of ACC with enhanced stability i.e. do additives directly stabilize the formed ACC? Or is the extended lifetime a side-effect of mere growth poisoning i.e. the stabilization is indirect, where additives retard the formation of the crystalline calcium carbonate?

To test this, experiments in bulk solution were performed, taking direct advantage of ACC's meta-stability. In bulk solution, the formation of ACC and its subsequent crystallisation is commonly accompanied by dissolution of the ACC.(139, 209, 218-220) To gain insight into whether the additives affect this process by directly stabilizing the ACC in solution, or via an indirect effect, **dissolution profiles** of ACC formed in the presence and absence of additives beneath the calcite solubility limit were measured and compared. By staying far beneath the solubility limit, the re-precipitation of added ACC in the form of vaterite, aragonite or calcite can be excluded, and with it the option of indirect stabilization can be discarded. Any difference in acquired dissolution profiles has therefore to result from a direct stabilization mechanism.

The time-resolved, normalized dissolution profiles for "high pH" ACC samples precipitated with and without additives are presented in **Figure 3-3**. Dissolution progress refers to the normalized measured conductivity difference between the point of ACC addition and complete dissolution of ACC i.e. final constant conductivity value. The dissolution profiles reveal only minor differences in the dissolution behaviour of the different samples. Complete dissolution of all ACC samples was accomplished after ~ 300 seconds. Magnesium was quite distinct from all other additives and displayed a tendency to increase the dissolution rate of ACC in agreement with the higher solubility of Mg-calcite as compared with pure calcite.(221) Considering the minor differences observed in acquired dissolution profiles it seems that the stabilization of ACC in solution is a result of indirect stabilization.

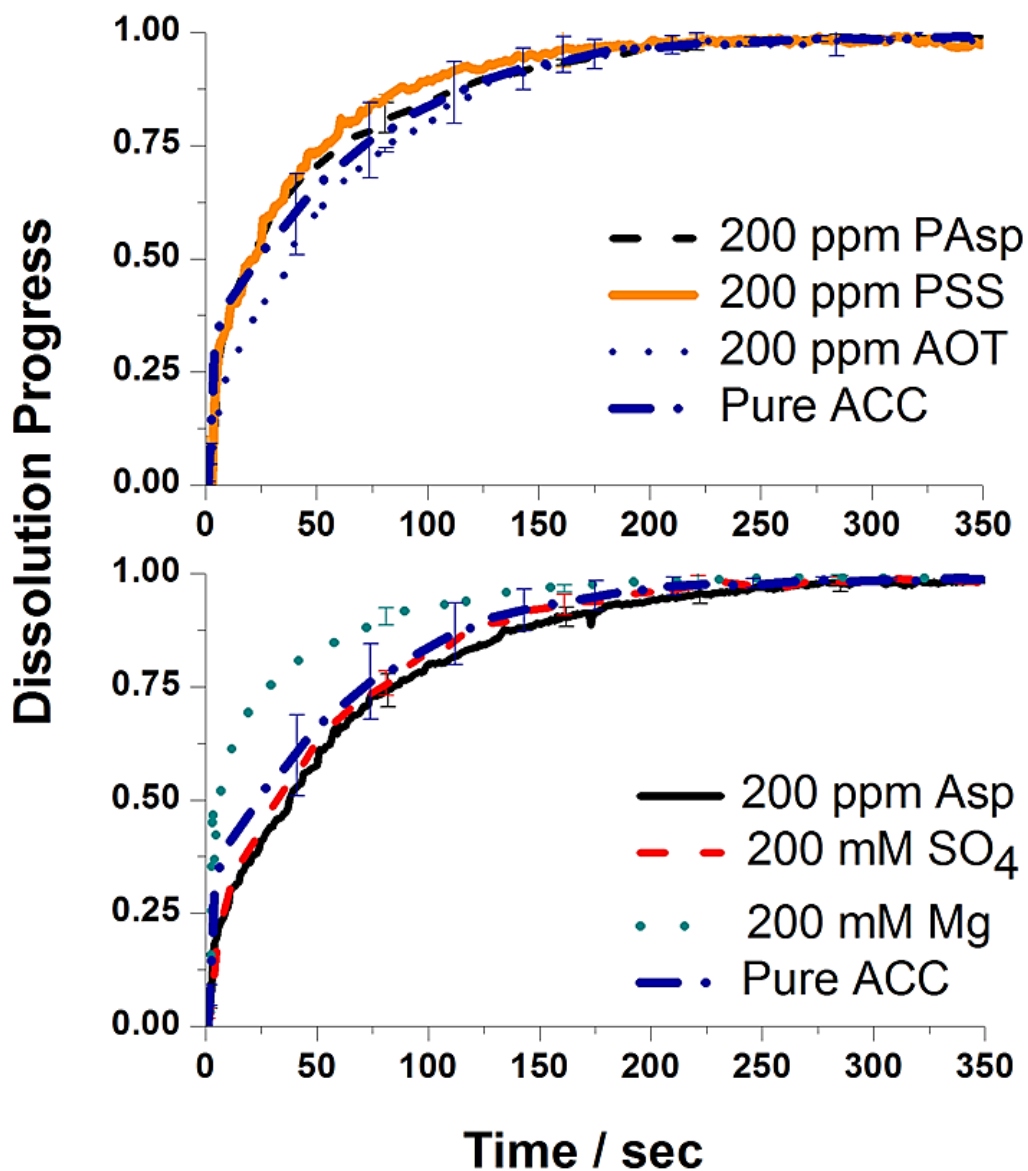


Figure 3 - 3: Dissolution behaviour of “high pH” ACC samples prepared in the presence of different types and amounts of additives: Mg²⁺, SO₄²⁻, Asp, PAsp, PSS and AOT. Presented are averaged dissolution profiles of three repeats given with positionally selected standard deviation.(152)

Chapter 3: Amorphous Calcium Carbonate

The applied methodology of recording dissolution profiles of a known, added sample quantity, was further used to highlight differences in the stability of ACC produced by a number of synthesis methods. This was realized by collecting the dissolution profiles of ACC prepared by a number of different methods, and comparing them with nano- and micron- sized calcite crystals. ACC was precipitated by a direct precipitation route (direct ACC – combining 1 M NaCO₃ with 1 M CaCl₂), at high pH (“high pH” ACC – combining 1M NaCO₃/30 mM NaOH with 1 M CaCl₂) and using the ammonia diffusion method. Nano - calcite was ≈100 nm in size and calcite precipitated using the ammonia diffusion method was 10 μm in size.

The obtained dissolution profiles are shown in **Figure 3-4**, and clearly reveal differences in the dissolution behaviour of the samples according to the ACC synthesis method and the size of the calcite crystal. As intuitively expected, the more thermodynamically stable calcite dissolved slower than the prepared ACC samples. The nano-calcite dissolved faster than the micron-sized calcite crystals. Interestingly, however, the ACC precipitated using the ammonia diffusion method dissolved significantly more slowly than that precipitated using any of the other methods (all ACC had a similar size 50-150 nm). ACC obtained by the ammonia diffusion method approached full dissolution after ~ 700 seconds, while other ACC samples achieved a similar level after ~ 300 seconds. The high pH ACC dissolved slightly faster than the direct ACC formed in the absence of sodium hydroxide.

The increasing dissolution rates with decreasing particle size, as seen for the two types of calcite tested, can be easily explained by the increase in surface to volume ratio as particles decrease in size. The increase in dissolution rate with increasing pH/ supersaturation (solution pH determines the carbonate species distribution), as observed for ACC of similar sizes but of different methodology, has to have a different origin. ACC formed at the lowest pH (ADM-ACC) dissolves the slowest and thus has to have the highest stability among formed ACC. The origin of this stability can potentially be related to a more rigid “ordered” structure of ACC formed at low pH levels. An argument that can be raised at this point is that all ACC is not equal. Rather, ACC which does not diffract X-rays is best described as a family of phases, such that direct comparison of the behaviour of ACC prepared by different methods should be made with caution.(129)

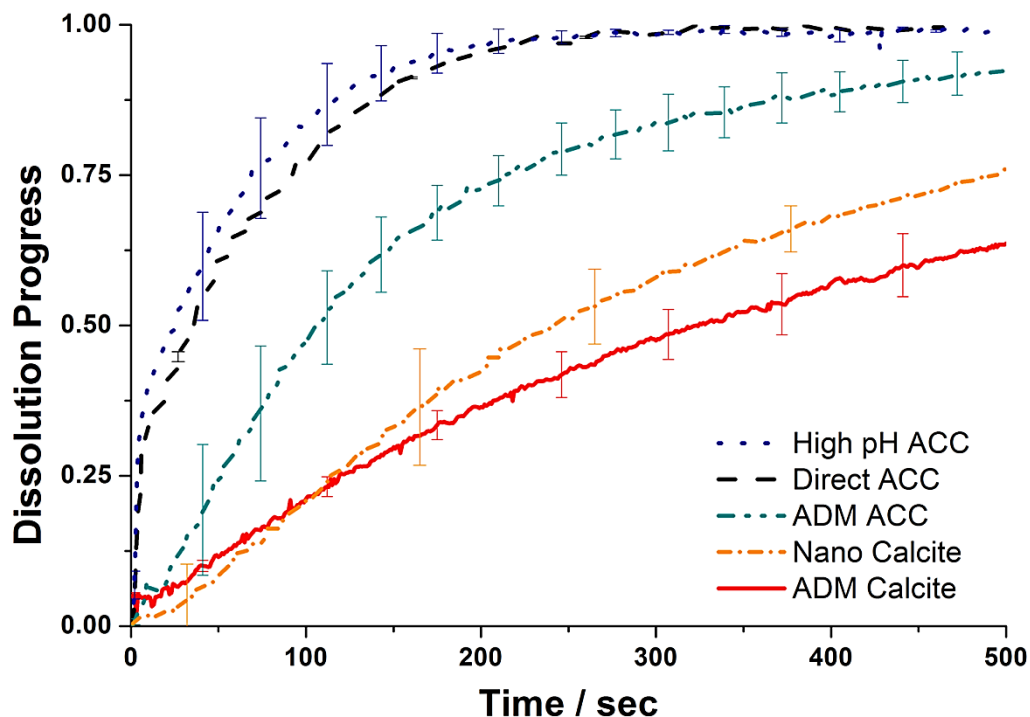


Figure 3 - 4: Shown are dissolution progress – time profiles of calcium carbonate precipitates prepared by different methods. Dissolution profiles were recorded in an undersaturated solution of 250 ml with respect to the most stable polymorph (calcite $\sim 10 \text{ mg l}^{-1}$) given added mass of 1 mg. Profiles are shown for ammonia diffusion method (ADM calcite) (5-10 μm in diameter), ACC precipitated by direct precipitation (direct ACC), ACC precipitated at high pH (“high pH” ACC), ACC precipitated using the ammonia diffusion method (ADM ACC) and commercial nano-sized calcite (nano calcite) all with an apparent diameter of 50-150 nm. Presented are averaged dissolution profiles of three repeats given with positionally selected standard deviation.(152)

3.2.3.3: The Effect of Additives in the Solid State

After observing a uniform behavioural trend in the crystallisation/ stabilization of ACC precipitated in the presence of additives in solution (they all retard ACC crystallisation), now turn to original query - how do additives affect the solid-state transition of ACC to crystalline calcium carbonate? This question was again evaluated using a number of different approaches, including annealing samples at moderate temperatures, through thermal analysis, and by performing in situ PXRD analysis in air while heating the ACC precipitates.

We started with the examination of ACC samples by electron microscopy and SAED after **annealing** at 70°C for 12 hours. Pure ACC, **Figure 3-5a**, did not crystallize under these conditions as is evident by the presence of an amorphous halo in the SAED pattern. The same behaviour was observed for ACC precipitated in the presence of 200 mM Mg²⁺, SO₄²⁻ or 200 ppm Asp. “Pure” ACC and ACC precipitated in the presence of the stated additives only crystallised after continued heating and above a temperature of 250°C. Evidence of this crystallisation is presented in Figure 3-5b, which shows an electron micrograph and the corresponding SAED pattern of pure ACC heated to a temperature of 350°C. The SAED pattern is recognizable as calcite.

In contrast to pure ACC and ACC prepared in the presence of low molecular weight additives, ACC formed in the presence of 200 ppm AOT, PSS or PAsp crystallized readily after heating to 70°C and isothermal storage. This is shown for the example of PSS in Figures 3-5 c and d. The SAED pattern inset in Figure 3-5(c) was acquired from ACC formed in the presence of PSS at 25°C and shows an amorphous halo, while the SAED pattern in Figure 3-5 (d), which was acquired after heating to 70°C, presented a diffraction pattern of calcite. Examination of the ACC particles before and after heating further revealed that while the pure ACC particles sintered together on heating to 70°C and after crystallisation at 350°C, there was little change in the original spherical form of the particles. Additives-containing ACC, in contrast, transformed to partially sintered singular rhombohedral calcite crystals on annealing at 70°C.

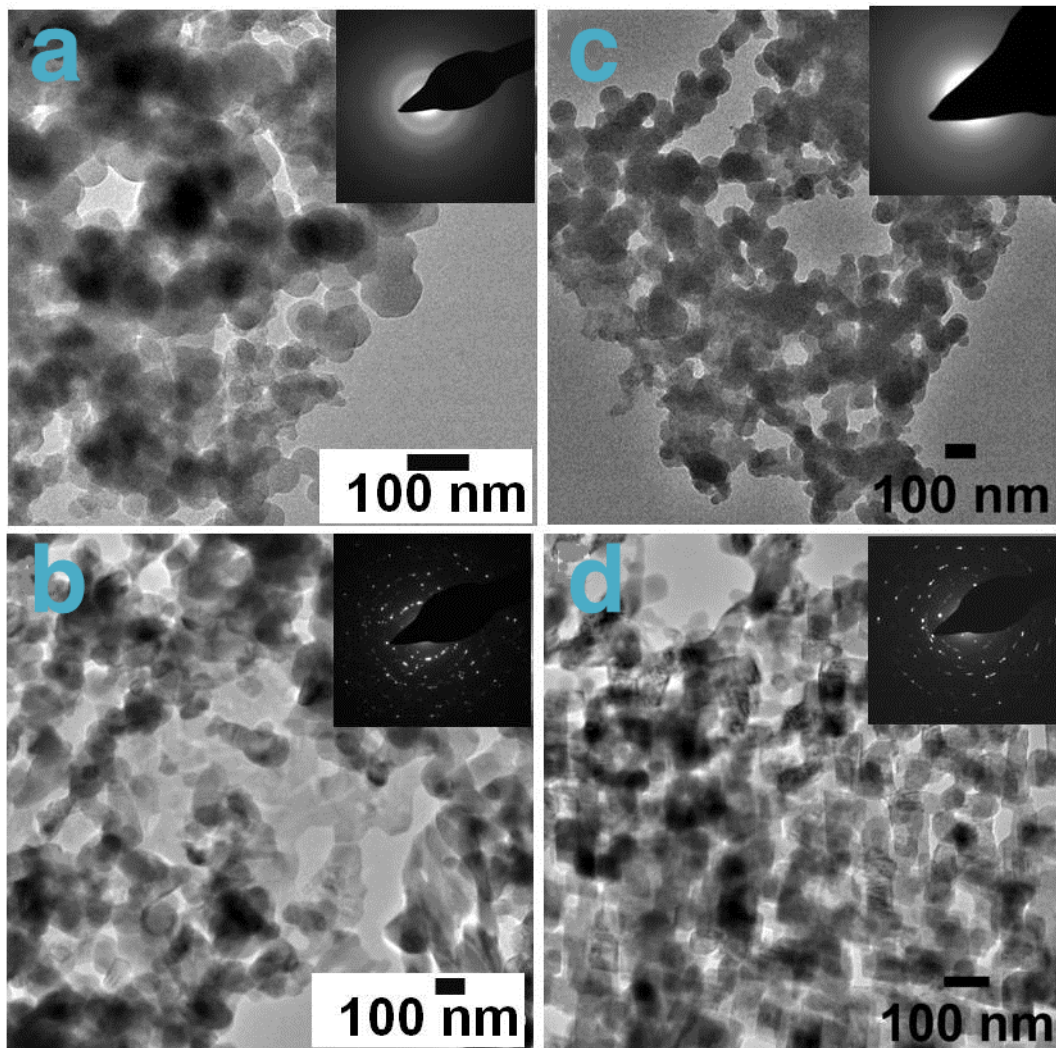


Figure 3 - 5: Electron micrographs and SEAD pattern of (a) pure ACC after heating at $10^{\circ}\text{C min}^{-1}$ to 70°C followed by an annealing period of 12 hours at 70°C and (b) pure ACC after heating at $10^{\circ}\text{C min}^{-1}$ to 350°C followed by an annealing period of 3 hours at 350°C . (c) ACC formed in the presence of 200 ppm PSS (25°C) and (d) after heating at $10^{\circ}\text{C min}^{-1}$ to 70°C followed by an annealing period of 12 hours at 70°C .(152)

Chapter 3: Amorphous Calcium Carbonate

The differences seen in additive behaviour in the “solid state” crystallisation of ACC, where some additives accelerate crystallisation (200 mM Mg^{2+} , SO_4^{2-} or 200 ppm Asp) while others either do not affect it, or retard it (200 ppm AOT, PSS or PAsp), is somewhat perplexing. Indeed, they all showed a crystallisation retarding effect of ACC in solution. To ensure that the observations made were not a result of the small sample size analysed or technique introduced, IR spectroscopy on a heated, larger sample mass was performed. The acquired IR spectra are presented in **Figure 3-6a** (pure ACC) and **b** (PSS-ACC and AOT-ACC). These spectra show a behaviour which is consistent with the observations made by TEM and SAED analysis, where the ACC formed in the presence of PSS and AOT showed bands at $875\text{ cm}^{-1}(\nu_2)$ and $713\text{ cm}^{-1}(\nu_4)$, confirming the formation of crystalline precipitates upon heating to and storage at 70°C , while pure ACC only showed those bands upon heating to 350°C .(214)

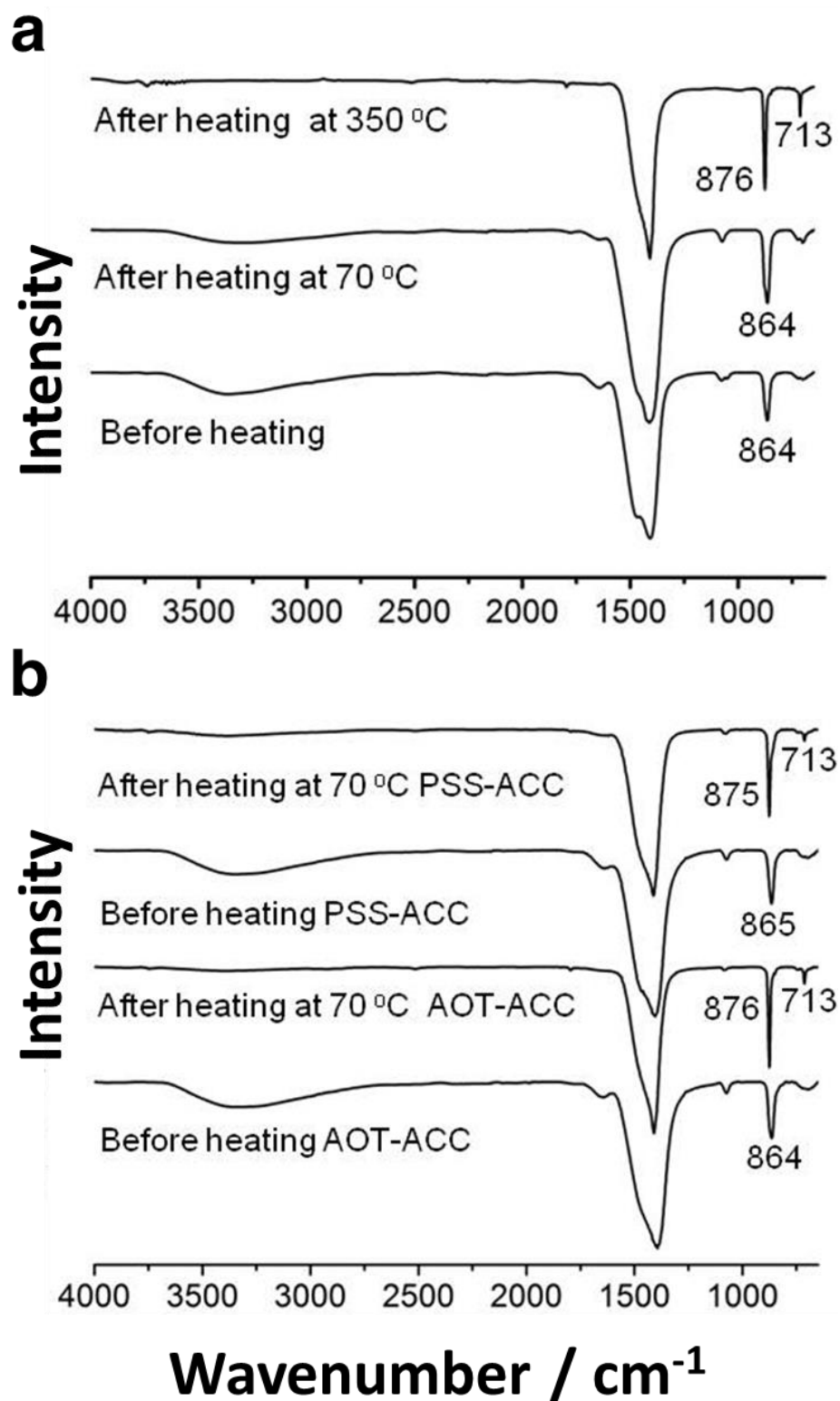


Figure 3 - 6: Given are IR spectra of (a) pure ACC and (b) ACC prepared in the presence of PSS and AOT before and after heating. The samples were heated at a rate $10^{\circ}\text{C min}^{-1}$ to 70°C or 350°C , followed by an isothermal annealing period at 70°C for 12 hours or 350°C for 3 hours.(152)

Chapter 3: Amorphous Calcium Carbonate

In search of an explanation for these observations (contrasting behaviour in solid state) the crystallisation of ACC prepared in the presence of a range additives was studied by TGA and DSC. This was done in particular to determine if there are any changes in the hydration of the ACC and to assign a specific crystallisation temperature/ activation energy to each additive.

The graphs shown in **Figure 3-7** are typical **TGA** (a) and **DSC** (b) profiles obtained for pure ACC and ACC prepared in the presence of additives. The weight or sample mass loss profiles given in (a) obtained by TGA show a gradually decreasing release of “surface bound” water and the subsequent loss of structural water, upon heating to ~ 200°C. The identification of two distinct water environments is made possible thanks to the simultaneously acquired DSC profiles (b), which show two endothermic events present beneath 200°C, as highlighted in pink.

The total water loss accumulates to ~ 22-24 wt% of the total sample weight. “Surface bound” water accounts to ~ 4-6 wt% of the total weight loss, lost upon heating to ~ 50-70°C. Structural water accounts for the remaining 14-18 wt% and is lost until about 200°C. This amount of structural water corresponds to a composition of ~ 1 H₂O : 1 CaCO₃. Past this water loss, at temperatures >200°C, a weight stabilization sets in, demonstrating the transition from hydrated ACC to stable anhydrous ACC, which is still amorphous as the subsequently recorded exothermic peak at ~ 330°C in the DSC profile demonstrates. This is particularly evident for pure ACC. The recorded exothermic peak is characteristic of an amorphous to crystalline transition and results from the latent energy or the heat of crystallisation. If heated further, above 550°C, the now crystalline calcium carbonate decomposes into calcium oxide and carbon dioxide.

The final weight ratio between the amount of dry CaCO₃ in the sample and the formed CaO after decomposition, can be used to calculate the purity of the ACC prepared. More specifically, it allows us to determine the amount of additive occluded/ incorporated within the ACC.

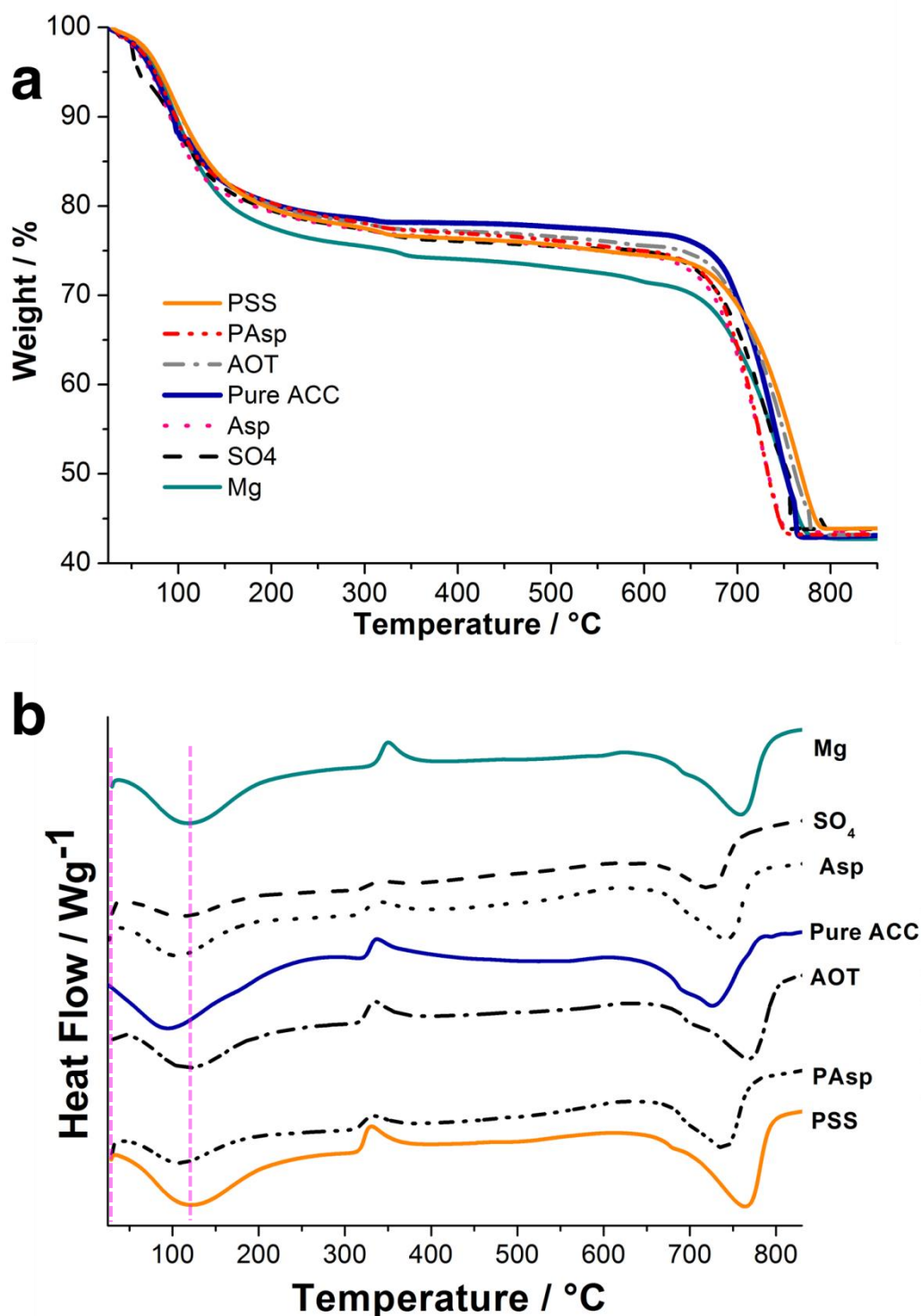


Figure 3 - 7: TGA (a)/ DSC (b) profiles of ACC synthesized by mixing 1 M CaCl_2 with 1 M Na_2CO_3 / 30 mM NaOH in the presence or absence of selected additives. The profiles were obtained at a heating rate of $25^\circ\text{C min}^{-1}$ under nitrogen flow. Additive spiked samples reveal a shift in crystallisation temperature. Identical amounts of sample (~ 10 mg) were used in all runs. A tabular overview of key parameter and starting additive concentration is given in Table 5.

Chapter 3: Amorphous Calcium Carbonate

Turning now our attention to the effect that additives have on the transformation of ACC in the solid state, as revealed in the TGA/ DSC profiles.

TGA in a first instance provides us with estimates of the amount of additives occluded/ incorporated within the ACC. This information can be obtained from the TGA profiles in two ways. This information is obtainable by looking at the sample weight lost in the region of 250°C - 550°C; the organic additives associated with the ACC decompose across this temperature range. A second more precise option is a comparison of the recorded final weight ratio of the sample before decomposition and after decomposition. This can be compared with the idealized or expected ratio of calcium carbonate decomposition to calcium oxide if a pure sample was analysed. Any discrepancy between these two ratios can be directly related to either, the sample contained “fully” decomposable matter – organic additives - (the experimental ratio is higher) or the sample contained non decomposable matter – inorganic additives – (the experimental ratio is lower).

The latter method was applied here and demonstrated that small quantities (\approx 1–2 wt%) of the organic additives Asp, PAsp, PSS, and AOT were associated with ACC, while the inorganic additives SO_4^{2-} and Mg^{2+} were retained to a higher degree of 3 wt% and 6 wt% respectively. TGA further revealed no significant difference in the total amount of water associated with the ACC samples, with values ranging between 19.4 and 21.3 wt% H_2O . Mg-ACC contained the somewhat higher amount of 23.6 wt% H_2O . A tabular summary of these observations is provided in Table 4.

Chapter 3: Amorphous Calcium Carbonate

	Additives						Pure ACC
	Group 1 $M_w < 400 \text{ g mol}^{-1}$			Group 2 $M_w > 400 \text{ g mol}^{-1}$			
	Mg	SO ₄	Asp	AOT	PAsp	PSS	
Additive Conc. at Formation ^{a)} [mM]	200	200	1.5	0.5	1.5	0.9	-
wt% Additives	6	3	1.5	0.9	1.4	1.7	-
wt% H ₂ O	23.6	20.7	19.4	20.5	19.4	21.3	20.2
10 °C min ⁻¹ T _P [°C]	332.66	330.49	328.66	325.98	324.86	323.57	328.10
15 °C min ⁻¹ T _P [°C]	344.63	339.49	336.97	332.85	331.02	326.39	335.63
25 °C min ⁻¹ T _P [°C]	351.22	342.67	339.27	334.80	334.83	332.26	337.48
Approximate E _A [kJ mol ⁻¹]	351	291	271	228	207	206	246

^{a)}Additive concentrations based on functional group

Table 4: Activation energies, crystallisation peak temperatures (T_P) given heating rate and water/ additive percentage of ACC samples precipitated in the presence and absence of selected additives: Mg²⁺, SO₄²⁻, Aspartic acid (Asp), poly(aspartic acid) (PAsp), poly(styrene sulphonate) (PSS) and bis(2-ethylhexyl)sulfosuccinate (AOT) obtained by DSC and TGA.(152)

Chapter 3: Amorphous Calcium Carbonate

The **DSC** profiles acquired, Figure 3-7b, reveal the major influences that additives have on the crystallisation/ stabilization of ACC in the solid state, where these are shifts in the crystallisation temperature as given by the crystallisation associated exothermic peak position, and the variation in peak shape.

Figure 3-8 provides a closer examination of the region surrounding the crystallisation of ACC (exothermic peak), shown for all additives tested. A change in peak shape and most prominently a change in peak position can be seen, with crystallisation peak temperatures (T_p) ranging between 326°C and 344°C for ACC precipitated in the presence of 200 ppm (<2 mM) of the organic additives or 200 mM of the “inorganic ions”.

Pure ACC had a crystallisation peak temperature of 336°C. DSC profiles were collected at a heating rate of 15°C min⁻¹. Moreover, the most-significant increase in crystallisation temperature occurred with magnesium ions (344°C), while PSS lowered the crystallisation temperature the most (326°C). This is in agreement with the observations made earlier using low temperature annealing. Considering that crystallisation occurs from an anhydrous state, we can further exclude now that water or the hydration state of the ACC plays a critical role in this behavioural trend in the solid state crystallisation of ACC. Some additives retard the crystallisation, while others accelerate it.

In making this statement, however, we emphasize that the concentrations of the additives employed necessarily affect the magnitude of their effect on the crystallisation temperature, but not the direction of the temperature change. On a simple mole-per-mole basis, the functional groups on the polymers have much larger effects on ACC crystallisation than the inorganic ions. Recorded crystallisation peak temperatures are within the wide variety of reported crystallisation temperatures of pure ACC (320 – 350°C).^(91, 100, 129) Indeed, the pH at which the ACC is formed has been recognized to alter the crystallisation temperature, with a value as low as ~210°C having been reported for ACC precipitated at pH 11.2.⁽¹²⁹⁾ The crystallisation temperature of ACC is therefore synthesis and isolation dependent, Chapter 3.4.

Closer examination of the effect additives have on the crystallisation of ACC, as is evident in the given DSC profiles, showed that it was possible to separate them into **two categories**: those which increase the crystallisation temperature (Mg^{2+} , SO_4^{2-} , and, to a lesser, extent Asp) as compared with pure ACC, and those which lower it (AOT, PSS, and PAsp). With the most obvious shared attribute being “similar”

Chapter 3: Amorphous Calcium Carbonate

molecular weights, high-molecular-weight additives lower the apparent crystallisation temperature, whereas the smaller additives exhibit the reverse behaviour.

However, although similarity in molecular weight is one possible commonality (the most obvious) across additives in each category, this does not say that changes in the molecular weight of additives is the source of them acting as either crystallisation inhibitors or promoters for ACC in the solid state.

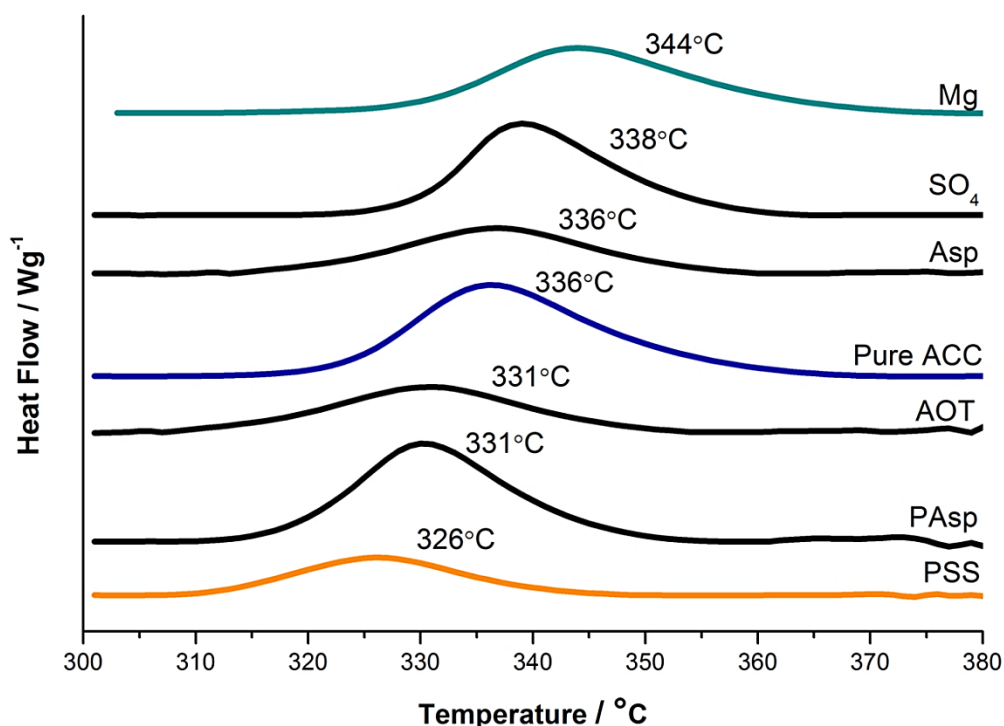


Figure 3 - 8: Shown are sections of DSC scans obtained from the analysis of pure and additive retaining “high pH” ACC samples showing the peak corresponding to the transition from ACC to calcite. DSC scans were obtained at a heating rate of 15°C min⁻¹. (152, 205)

Crystallisation peaks as seen in the DSC profiles can further be used to extract information regarding the **crystallisation progress** with increasing temperature. This is achieved by replotting the obtained peak profiles, assuming Johnson-Mehl-Avrami transformation behaviour, Chapter 2.8.(222) Doing this, one obtains plots of crystallisation progress versus temperature. **Figure 3-9**, presents such plots generated from the DSC profiles shown in Figure 3-8. The trends seen in the crystallisation progress plots are largely in keeping with the recorded crystallisation temperature trends, such that the curve for the Mg-ACC sample appeared at the highest temperature and the PSS-ACC sample the lowest. The curves for the ACC precipitated with the three high-molecular-weight additives were shifted to lower temperatures as compared with the ACC associated with the low molecular weight additives.

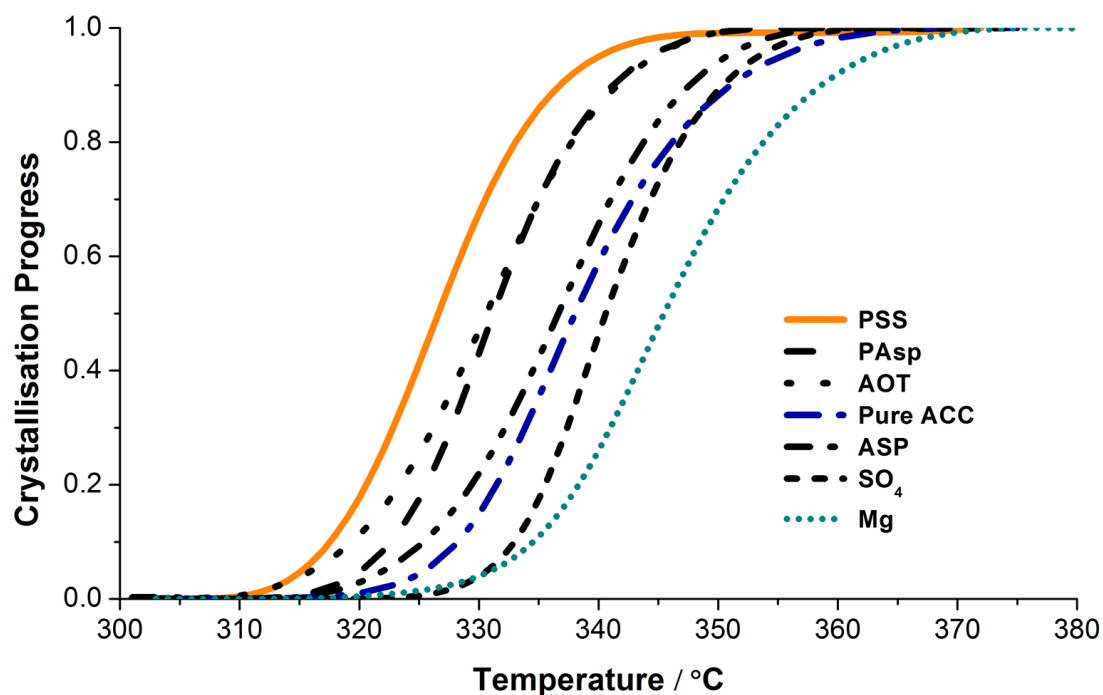


Figure 3 - 9: Plotted is recorded crystallisation progress of ACC samples formed in the presence of Mg^{2+} , SO_4^{2-} , Aspartic acid (Asp), poly(aspartic acid) (PAsp), poly(styrene sulphonate) (PSS), poly(aspartic acid) (PAsp) and bis(2-ethylhexyl)sulfosuccinate (AOT), versus temperature as obtained by DSC. Crystallisation progress was calculated by crystallisation associated exothermic peak integration and following normalisation (0-1). DSC scans were performed with an applied heating rate of $15^{\circ}C\ min^{-1}$.(152)

Chapter 3: Amorphous Calcium Carbonate

Final bits of information that can be extracted from the acquired TGA and DSC profiles are a number of thermodynamic quantities, such as estimates of the enthalpies of crystallisation (ΔH_{cryst}) and the activation energy of crystallisation (E_A).

Estimates of the **enthalpies of crystallisation** (ΔH_{cryst}) of the different ACC samples can be obtained by crystallisation peak area integration (DSC), given the known sample mass (TGA).⁽⁹¹⁾ All ΔH_{cryst} values, except the Mg-ACC, fell within the range -18 to -31 kJ mol^{-1} where the errors in the data were such that no statistical difference was recorded as compared with the value of $\Delta H_{\text{cryst}} = -21.93 \pm 6.13$ kJ mol^{-1} for the pure ACC. The analysed Mg-ACC sample exhibited a higher enthalpy of crystallisation $\Delta H_{\text{cryst}} = -58.59 \pm 6.44$ kJ mol^{-1} .

The **activation energy** (E_A) associated with the transformation of anhydrous ACC to calcite was derived from multiple DSC scans carried out at different heating rates, Chapter 2-8. Heating rates of $10^\circ\text{C min}^{-1}$, $15^\circ\text{C min}^{-1}$, and $25^\circ\text{C min}^{-1}$ were applied. The calculated activation energies (207 - 352 kJ mol^{-1}) were in agreement with those of Koga et al. ⁽¹²⁹⁾ for pure ACC precipitated at different pH values (152 - 304 kJ mol^{-1}) and followed the same trend as seen for the shift of crystallisation peak temperatures. A summary of calculated activation energies is given in Table 4. High molecular weight additives decrease the crystallisation temperature and activation energy, while magnesium and sulphate or low molecular weight additives increase the crystallisation temperature and activation energy.

Chapter 3: Amorphous Calcium Carbonate

To ensure that the observed classification of additives as either crystallisation promoters or retarders in the solid state was based on the molecular weight of the additive, further analysis was performed using **PXRD**.

PXRD patterns of ACC samples prepared in the presence and absence of additives were collected during in situ heat treatment. This was achieved by performing rapid scans around the angular range of $2\theta = 28-32^\circ$ to monitor the emergence of the [104] calcite reflection from the amorphous background, while the sample was continuously heated.

Although the trends in the crystallisation temperature shifts as determined by DSC are maintained for all ACC samples by PXRD analysis, the observations made vary slightly in numerical terms - a result of the increased sensitivity of PXRD and the “direct ACC” used for PXRD analysis as compared to the “high pH” ACC used for DSC studies, **Figure 3-10**. All samples showed a broad crystallisation event, which took place over a temperature range of 150°C with a typical onset temperature of ~ 220°C.

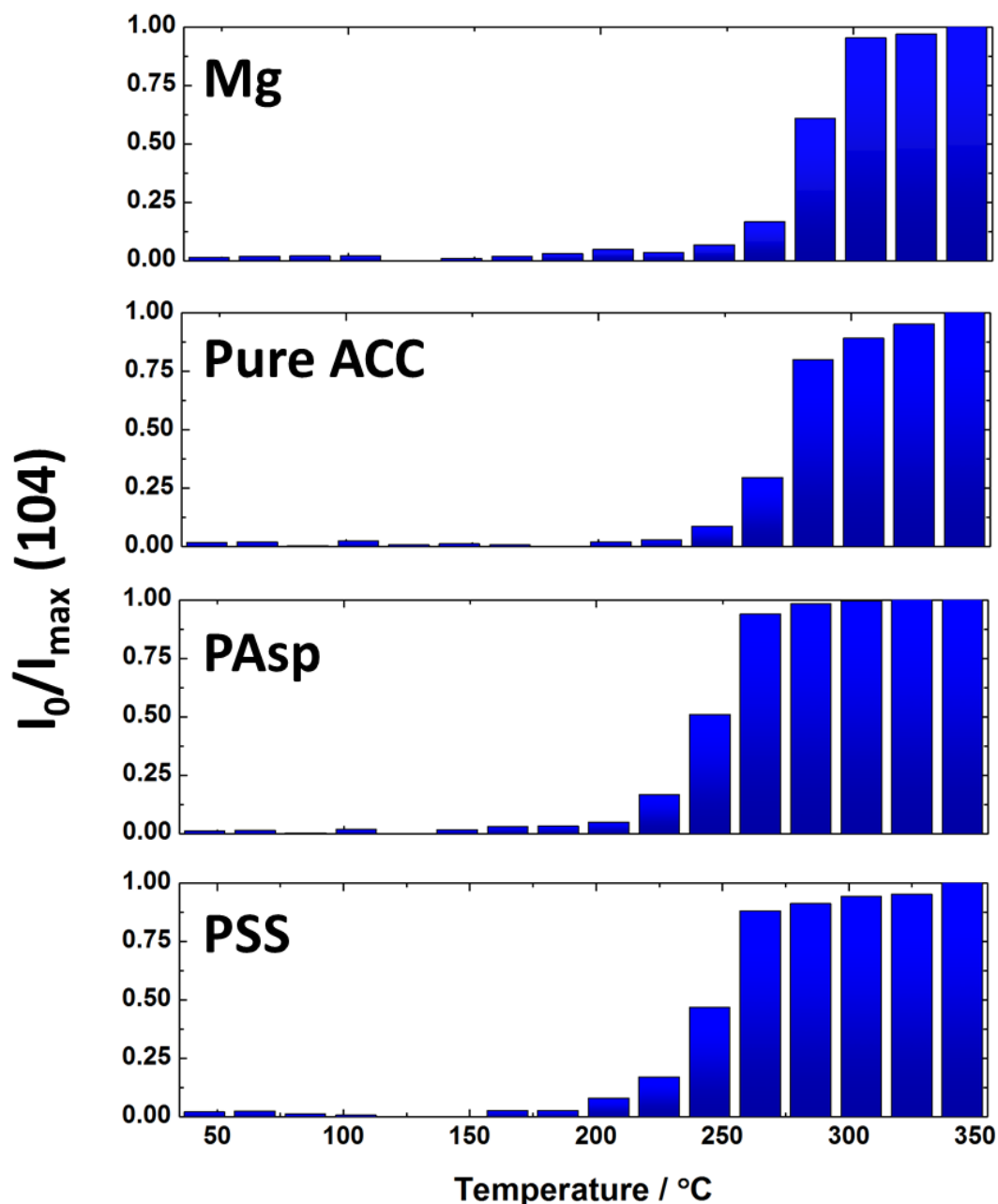


Figure 3 - 10: Plotted are the progress of crystallisation versus temperature of ACC prepared by mixing 1 M CaCl_2 with 1 M $(\text{NH}_4)_2\text{CO}_3$ / 30 mM NaOH in the absence or presence of PAsp, PSS and Mg^{2+} . The progress of crystallisation was estimated based on recorded intensity changes of the [104] peak of calcite (I_0) with respect to the maximum intensity measured after complete crystallisation (I_{max}) measured by PXRD analysis of samples heated *in situ*.(152)

3.2.4: Discussion

This study investigated the effects that a range of additives incorporated/ occluded within ACC have on the crystallisation of this phase, depending on whether crystallisation occurred in solution or via a heat-induced solid state phase transition. The differences observed in the crystallisation behaviour of ACC in solution and the solid state, due to the presence of additives, clearly demonstrate that additives can display different patterns of behaviour in directing crystallisation in these two contrasting environments. These different patterns of behaviour provide some insight into the possible mechanisms of ACC crystallisation, and, in doing so, challenge some common ideas regarding the role of additives in stabilizing ACC.

Sets of experiments following the crystallisation of additive incorporating/ occluding ACC **in solution** revealed that all of the studied additives retarded the crystallisation of ACC to some degree. The formation of a new crystalline phase in solution from ACC follows a two-step process – the nucleation of the new phase and its subsequent growth. The latter step, crystal growth, is generally accompanied by the dissolution of the ACC. Thus, zones depleted of ACC particles have often been observed adjacent to calcite crystals growing on solid substrates from suspensions of ACC.(139, 219) Based on combined SAXS/ WAXS studies of the transformation of ACC we also know that dissolution of ACC as a result of polymorph formation and growth also occurs in the bulk solution.(220) During this process (ACC dissolution to vaterite/ calcite formation) it was further shown that the solution composition i.e. the ion activity product of calcium and carbonate remains at the solubility level of ACC.(86, 209) The solution is therefore supersaturated with respect to calcite and vaterite during crystallisation of the ACC to these phases, which demonstrates that the rate-determining step is the growth of the crystalline phases rather than dissolution of the ACC. In simple terms, the formation of the crystalline phase drives the process. This observation is supported by the dissolution studies performed here, which tested the stabilization of additive incorporating/ occluding ACC in reference to pure ACC. The obtained dissolution experiments show that there was negligible change in the ACC dissolution profile when additives were occluded within the ACC.

This indicates that in solution, rather than directly stabilizing the ACC, the additives either retard the growth of the new crystalline phase, and/ or they inhibit nucleation

Chapter 3: Amorphous Calcium Carbonate

of the new polymorph altogether. That additives can retard the growth of crystalline calcium carbonate above a certain threshold concentration is well-documented and is kinetic and thermodynamic in origin (Mg,(143, 223, 224) phosphate,(224, 225) Asp,(226) poly(aspartic acid),(227) sulfate,(224, 228) and poly(styrene sulfate)(206)). No structural or compositional change occurs in the ACC which inhibits its dissolution, a process which occurs concomitantly with the formation of the new crystal phase.

Magnesium and sulfate ions are incorporated within the calcite lattice, which causes a change in lattice parameters, an increase in solubility, and a reduction in thermodynamic stability as compared with pure calcite.(143, 147, 229) The effect of additives on growing crystals can also be considered in terms of their interaction with step edges and kink sites, where, for example, blocking of a kink site by an additive would give rise to kinetic inhibition of growth.(230) The influence of ACC occluded additives on nucleation would depend on whether nucleation of the polymorph occurs from solution i.e. by dissolution of the ACC and reprecipitation or if it takes place within the existing ACC particles. This is still under debate and the mechanism is likely to vary according to the experimental conditions,(93, 137, 160, 218) - as further discussed in Chapter 3.3. Arguments and experimental evidence for both mechanisms is in part provided in Chapter 1.4.4.

Chapter 3: Amorphous Calcium Carbonate

A different, and interesting, pattern of behaviour was seen for the crystallisation of ACC in the **solid state**. Unlike in solution, where all additives retarded the crystallisation of ACC, additives in the solid state either retarded or accelerated the crystallisation, depending on the type of additive. This trend was first evident on annealing pure ACC samples at moderate temperatures (70°C) for 12 hours. No crystallisation was observed in this case, while in contrast, ACC co-precipitated with 200 ppm AOT, PSS, and PAsp crystallized under the same conditions. These additives therefore effectively promoted crystallisation of ACC in the solid state, while inhibiting it in solution.

More detailed analysis of this observation was carried out by heating the respective samples at different rates up to and past the phase transformation temperature and confirmed this behaviour. This again showed that the additives could be divided into two distinct groups based on their action. The low molecular weight compounds (Mg, Asp and SO₄) stabilized the ACC against crystallisation in the solid state, while the high molecular weight compounds (Na-AOT, PSS and PAsp) promoted crystallisation. It is noted that PSS has been reported -in one instance- to stabilize ACC against crystallisation in the solid state, as shown by an increase in crystallisation temperature registered by DSC.(206) The origin of this discrepancy is unknown and could lie in differences in the polymer.

The data therefore suggests that additives with low and high molecular weights may affect ACC crystallisation by different mechanisms. Assuming that additives are truly occluded in the ACC such that they are mixed at a molecular level and not occluded in the void space of a larger ensemble of ACC particles, the **larger additives** may increase the free volume present in the ACC, enhancing the molecular mobility of the ACC constituents i.e. the system internal diffusivity. This would reduce the activation barrier and increase the crystallisation kinetics. This is consistent with the reduced activation energies derived from the DSC analyses. The recorded destabilisation may also be due to the concentrated number of functional groups in high molecular weight additives compared to “smaller” additives. This may induce the formation of short-range order in the ACC, reducing the number of assessable conformations required until the perfect crystal structure is obtained.(216, 231)

Chapter 3: Amorphous Calcium Carbonate

The introduction of short range order around occluded additives could also, of course, apply to **smaller additives**. These may also induce local ordering in the ACC on a smaller scale, and maybe even provide nucleation sites. This has been in part confirmed experimentally through the observation (using EXAFS) of short-range order resembling vaterite in PAsp-ACC. The same technique also suggests that Mg-ACC may have short range structures most similar to aragonite.(126) Indeed, a range of studies using techniques including NMR(85) and EXAFS(116, 232) have indicated that ACC can exhibit different short-range orders according to the presence of occluded additives, and the precipitation conditions.

Magnesium ions were the most effective in raising the crystallisation activation energy as compared to pure ACC, an effect which may derive from the higher hydration energy of Mg^{2+} as compared with Ca^{2+} , as the water must necessarily be lost before crystallisation can occur.(147) As an additional effect, the product Mg-calcite is also thermodynamically less stable than pure calcite. Sulfate ions again retarded the crystallisation, where the reduction in thermodynamic stability of calcite on incorporation of sulfate is likely to be a significant factor.(164)

Given the experimental uncertainties in studying nucleation phenomena is it not possible to determine conclusively the origin of additive induced changes in the crystallisation behaviour of ACC in the solid state. Frankly, we don't know the origin of the observed behavioural trend between low and high molecular weight additives in the solid state.

Disregarding the origin of this behaviour, if nucleation of the product crystalline phases is indeed homogeneous, and occurs within ACC particles **in solution and in the solid state**, the influence of the additives on nucleation would be expected to be identical in the solid state and solution. The fact that it is not and a different pattern of behaviour was observed in the solid state as compared with solution for the larger additives (PAsp, AOT, and PSS) demonstrates that the additives must also significantly affect the growth of the new crystalline phase in solution. We suggest that additives are released from ACC particles into solution during their dissolution, which inhibits the growth of the new crystalline phase and that this is the main stabilization mechanism for the remaining ACC in solution.

Chapter 3: Amorphous Calcium Carbonate

The relevance of these observations to **biological calcification** via an ACC precursor phase is intriguing. Referring again to the formation of the sea urchin larvae, crystallisation of ACC effectively occurs in an aqueous environment, in the absence of bulk water. This suggests that the ACC crystallises by a solid state transition via sequential ACC dehydration and secondary nucleation.(97, 118, 211) With no water access what is then the role of the macromolecules associated with this mineral phase? The experiments performed to-date have all examined the effects of organic molecules extracted from biogenic ACC phase on the crystallisation of ACC in solution. In contrast, our results show that this does not necessarily provide a good test for their behaviour in the solid state, where they can actually promote crystallisation, depending on their size. Notably, however, biogenic ACC also typically contains magnesium ions, which significantly inhibit the crystallisation of ACC both in solution and in the solid state. It is therefore foreseeable that biomineralizing organisms utilize a combination of organic macromolecules and magnesium to tailor the stability of the ACC, which would allow control over its lifetime, and crystallisation pathway. That is – of course – if crystallisation does indeed proceed via a solid state transformation mechanism.(146)

3.2.5: Conclusion

In conclusion, the experiments performed show that the additives investigated can display a “Janus behaviour”, retarding the crystallisation of ACC in solution while promoting the solid state transition. This was observable for all larger molecules explored here (poly(aspartic acid), poly(styrene sulfonate) and Na-AOT). Smaller additives (magnesium and sulfate ions) hampered the crystallisation both in solution and the solid state. This potentially provides insight into the different stabilization mechanisms of ACC in the presence of the selected additives. In solution, the stabilization of ACC due to additives is dominated by an inhibition of the growth of the crystalline phase by additives present in solution, or additives newly released into the solution as the ACC dissolves. This is supported by the observation that the dissolution of ACC itself is little affected by the composition of the ACC. This implies an indirect stabilization mechanism rather than a direct stabilization based on additive induced changes in the structure/ stability of the ACC itself. The solid state transformation of ACC to calcite on the other hand is apparently dominated by the effects that additives have on the nucleation of the new phase. As additives may induce a change in the structure of the resulting ACC, this is consistent with suggestions that the short-range structure of ACC can determine the structure of its crystalline transformation product, both in synthetic and biogenic systems.(85, 232)

Future work could investigate the effects a range and/ or combination of additives have on the crystallisation of ACC, by means of high throughput screening procedures. Screening procedures utilizing automated, sample preparation, % additive inclusion determination, reaction kinetic acquisition and resulting particulate imaging are currently being developed in a project which is using high throughput screening to determine the incorporation of amino acids into a range of minerals. A goal of this project is to obtain an understanding of how individual additives (type and concentration) affect ACC, and indeed, how they affect mineralisation itself.(233, 234)

3.3: Dehydration and Crystallisation of ACC

3.3.1: Introduction

Having established an understanding of the effects additives have on the stabilization and crystallisation of ACC. The focus of our studies turned towards a second effect contributing to the stabilization of ACC - confinement. How does confinement stabilize ACC?

That this question is asked is thanks to observations which showed that biogenic ACC can be indefinitely stable in a biomineralizing organism.⁽¹⁴⁾ The next question is obvious, “how does the biomineralizing organism achieve this stability?” and this is the point where confinement comes into play. The crystallisation/transport of ACC in biominerals (sea urchin embryo) occurs in membrane-bound vacuoles. These vacuoles provide an environment of **limited size** (confinement) that is virtually free of bulk water. The phase transition of ACC in this specialized environment proceeds from hydrated ACC to anhydrous ACC, before subsequently crystallizing via a “solid state” mechanism.^(17, 97, 118, 120, 211)

The necessity to understand this phase transition in solution, from hydrated, amorphous precursor to crystalline phase, resembling a solid state transition at room temperature, is not due to the fact that it is not well understood. It is more that we need an understanding of this transformation process to force mineralization to occur by this option.

Biomineralizing organisms show us that ACC can be used as a mouldable, space-filling starting material, which can be delivered on-demand for the rapid, yet controlled production of structurally and morphologically-complex crystalline materials.^(14, 23, 78, 235, 236) There are some success stories in which ACC has been used in synthetic systems in this fashion ^(78, 155, 208, 237-241), but most attempts end up with the carefully prepared ACC simply dissolving.

Chapter 3: Amorphous Calcium Carbonate

Bio-inspired strategies were therefore employed here to study the crystallisation of ACC encapsulated in a porous silica shell or coated by a lipid bilayer membrane in aqueous environments. This was carried out in an effort to mimic the specialized, spatially-confined environments found in biomineralizing organisms. The results were then compared to the crystallisation behaviour of ACC in the solid state. When heated, ACC shows a comparable stepwise transformation as found in nature, from hydrated to anhydrous precursor to the crystalline phase. (91, 129, 132, 152, 242)

The encapsulation of ACC particles within porous silica shells did indeed provide an effective inorganic mimic of the spicule environment of the sea urchin in solution, which retarded the crystallisation of ACC sufficiently to allow characterization of the transformation process. In combination with the analysis of ACC samples with well-defined water contents, which were generated by annealing at different temperatures, this revealed that an identical dehydration processes does occur both in air and in solution. Despite this, nucleation must differ between these environments as ACC crystallisation in solution must be initiated by a local dissolution – reprecipitation mechanism, considering the here measured high activation barrier for ACC dehydration.

3.3.2: Dehydration and Crystallisation of ACC in Solution

3.3.2.1: Synthesis and Dehydration of ACC – Silica Coated Particles

ACC was encapsulated in silica shells using a **procedure** given by Kellermeier, 2010.(161) This encapsulation creates isolated environments analogous to the environments present during biomineral formation. The stability and crystallisation of the silica-coated ACC particles was investigated. This was achieved by re-suspending these particles in solution and analysing the changes in structure that occur with progressing incubation time.

Specifically, ACC silica encapsulates (ACC-SiO₂) were obtained by the direct combination of 125 ml of 10 mM CaCl₂ with 125 ml of 10 mM Na₂C₂O₄/ 6 mM Na₂SiO₃ solution, and the formed precipitates were incubated in the reaction solution for 20 minutes to allow the formation of a silica shell around the initially formed ACC units. Silica shell formation is postulated to occur as a result of the formation and subsequent growth of ACC particles in an alkaline solution, which induces a pH gradient at their surfaces due to the consumption of free carbonate ions and the subsequent conversion of the bicarbonate ions present. The reduction in pH is then assumed to cause the precipitation of amorphous silica via the condensation of silanol groups between saturated Si(OH)₄ molecules, forming siloxane bonds on the surface of the particles ACC. This creates a porous membrane covering the ACC particle.

Chapter 3: Amorphous Calcium Carbonate

The **successful formation** of a porous silica shell around each of the ACC particles was determined by TEM (**Figure 3-11**). Presented in (a) are the ACC-SiO₂ particles as prepared, which are ~100 nm in diameter, while (b) shows the ACC-SiO₂ particles after leaching out the calcium carbonate core by immersion in HCl. This demonstrates the presence of a continuous ~5 - 10 nm thick silica shell around each ACC particle.

IR spectra of the ACC-SiO₂ particles (c) confirmed the formation of ACC and an amorphous silica shell based on the presence/ absence of vibrational bands at 1425 cm⁻¹ (ν_3), 1075 cm⁻¹ (ν_1) and 863 cm⁻¹ (ν_2) which are due to the carbonate groups. Bands at ~3300 cm⁻¹ and 1641 cm⁻¹ ($\nu_{\text{H}_2\text{O}}$) are associated with water in the encapsulate and the silica at 1038 cm⁻¹ (ν_{SiO_2}). Notable is the absence of the (ν_4) bands at 747 cm⁻¹ and 714 cm⁻¹, which are characteristic of vaterite and calcite respectively. Surface area (BET) measurements of the ACC-SiO₂ particles both before and after removal of the ACC yielded values of $\approx 40 \text{ m}^2 \text{ g}^{-1}$ and $\approx 400 \text{ m}^2 \text{ g}^{-1}$.

TGA of ACC-SiO₂ particles (d) showed that the encapsulates exhibited different TGA profiles from the regular ACC. This can be related to the change in sample composition. The TGA profile shows an 18 – 20 wt% loss below 200°C due to the dehydration of the ACC and SiO₂. This is similar in magnitude to pure ACC. An additional 7 – 10 wt% loss between 200°C – 550°C is then seen for the ACC-SiO₂ particles, where this is as a result of CO₂ release on reaction of the SiO₂ shell with the CaCO₃.

The PXRD patterns acquired during in-situ heating of ACC-SiO₂ particles, helped to clarify this secondary weight loss. The amorphous encapsulates (e) transformed upon heating to Ca₂SiO₄ (Belite) (f), which was readily detectable above a temperature of 400°C.

The formation of calcium silicate also explains the gradual weight loss of 18 – 20 wt% above 550°C in the TGA profile. A sharp transition is typically observed in uncoated, regular ACC on conversion of CaCO₃ to CaO.

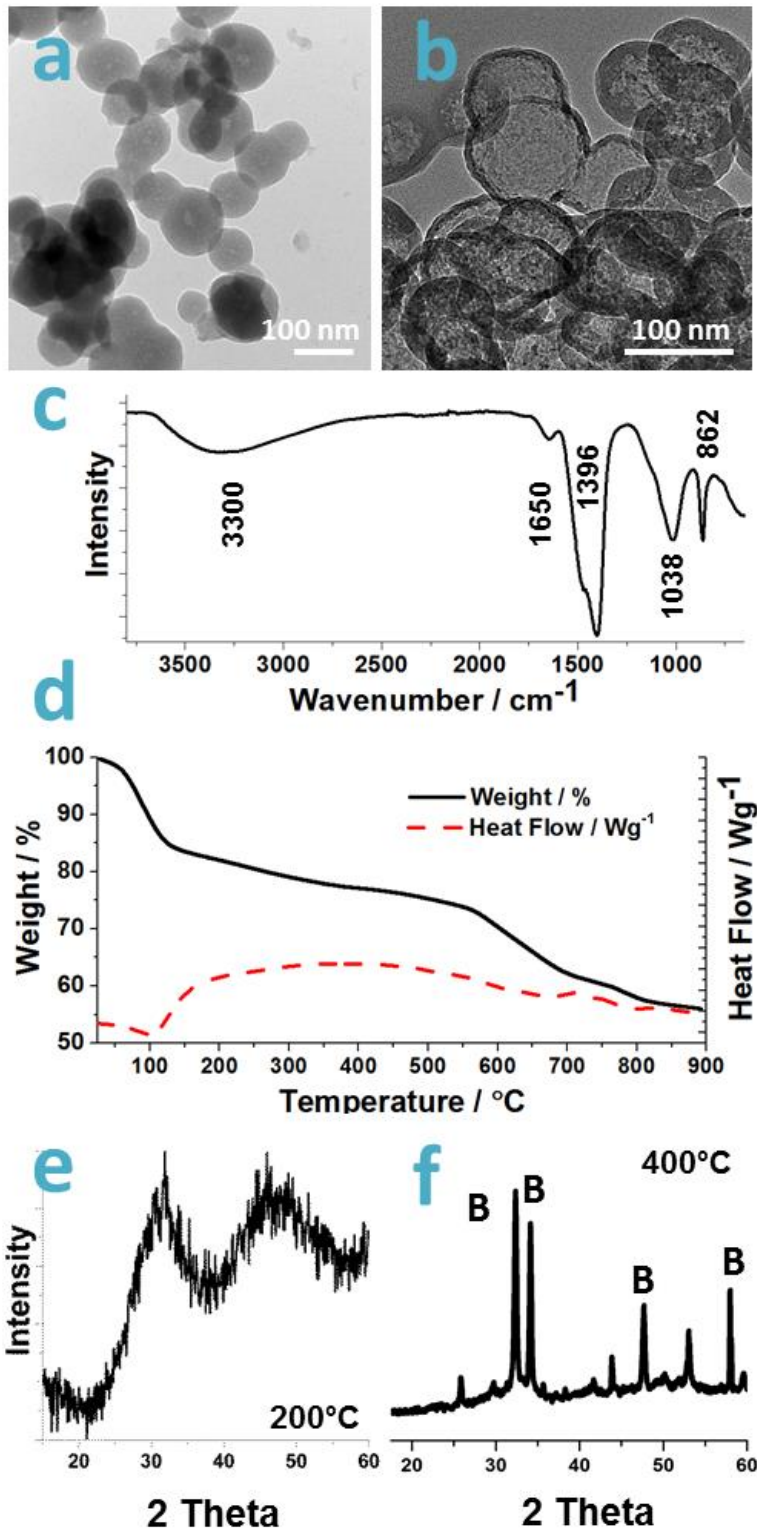


Figure 3 - 11: Characterisation of prepared silica-coated ACC (ACC-SiO₂). Given in (a) and (b) are transmission electron micrographs of ACC-SiO₂ encapsulates as formed and after dissolution of the calcium carbonate core. (c) IR spectrum and (d) TGA of ACC-SiO₂ encapsulates as prepared. Further provided are PXRD pattern acquired from of ACC-SiO₂ encapsulates after heating to (e) 220°C and (f) 550°C. B-Belite.(95)

Chapter 3: Amorphous Calcium Carbonate

TGA of the silica shells alone (that is, after leaching out the ACC) revealed that they comprise ~20 wt% water, **Figure 3-12**. Considering then the formation of encapsulates of 100 nm in diameter with a 5 nm thick silica shell, and taking the densities of ACC and hydrated silica ($\text{SiO}_2 \cdot \text{H}_2\text{O}$) to be 1.62 gcm^{-3} ,⁽²⁴³⁾ and $\sim 1.9 \text{ gcm}^{-3}$ respectively, the ACC- SiO_2 particles have compositions of ~22 wt% $\text{SiO}_2 \cdot \text{H}_2\text{O}$ and ~78 wt% $\text{CaCO}_3 \cdot \text{H}_2\text{O}$. Given that the unheated ACC- SiO_2 particles comprise 20 wt% water, ~4-6 wt% H_2O is associated with the SiO_2 component and ~14-16 wt% with the ACC.

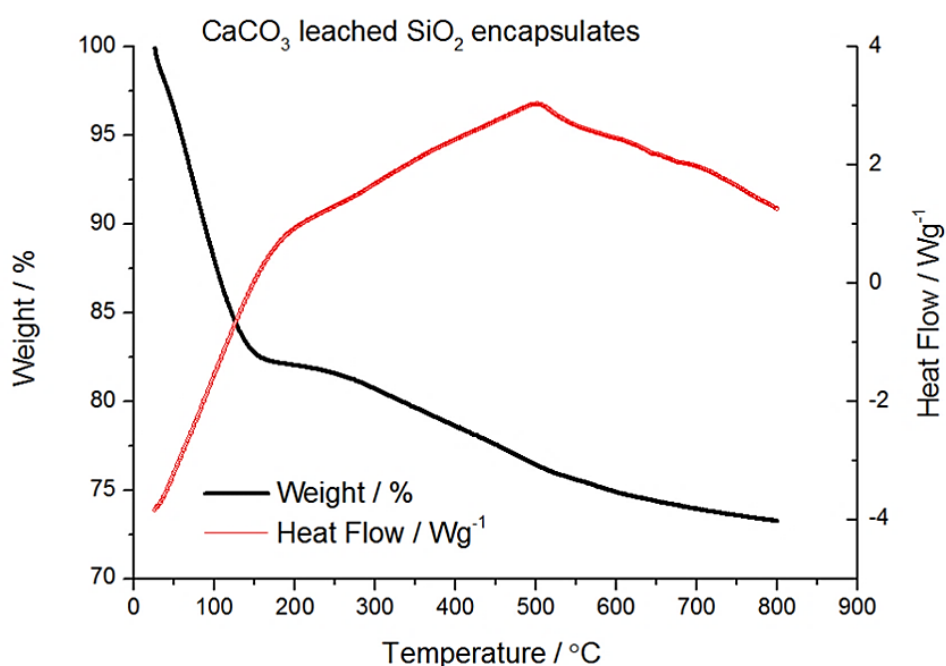


Figure 3 - 12: TGA of silica shells formed by leaching the calcium carbonate from ACC- SiO_2 particles. Dissolution of the calcium carbonate core was realized by immersing ~500 mg of prepared ACC- SiO_2 encapsulates in 250 mM HCl (50 ml) for 24 hours. A heating rate of 15°Cmin^{-1} was applied.⁽⁹⁵⁾

Chapter 3: Amorphous Calcium Carbonate

Having established the formation and characterisation of ACC-SiO₂ encapsulates, their **stability and transition** behaviour **in solution** was observed. 15 mg of ACC-SiO₂ particles were transferred to 100 ml Milli-Q water and were analysed with time, for changes in their structures and compositions. A summary of the observations made is provided in **Figure 3-13**.

Electron micrographs (a) of the ACC-SiO₂ particles as prepared and after 500 minutes in solution, demonstrate the structural stability of the particles and show that they aggregate during incubation. The collected IR spectra (c) and TGA profiles (d) demonstrate a negligible change in the silica content of the encapsulates. The latter is evident in the IR spectra, when comparing the relative silica band intensities across spectra. Compared are the ratios of ν_3/ν_{SiO_2} with increasing time in solution.

Addressing changes that occur in the ACC during their incubation in water, time-dependent IR measurements (c) revealed a structural rearrangement, as was apparent from a narrowing of the ν_3 band, a reduction in intensity of the ν_1 band and a shift in the ν_2 band. Importantly, this was accompanied by dehydration of the ACC, which occurs before any evidence of crystalline phases is detected. The onset of crystallisation occurs after ~8 hours, as shown by the appearance of a characteristic calcite peak at 714 cm^{-1} (ν_4).

TGA confirms the detected dehydration and structural reorganisation. TGA of ACC-SiO₂ particles incubated in solution for different times clearly showed a decrease in the water-associated weight loss under 200°C from 20 wt% to a constant 6 wt% (SiO₂:H₂O phase). The structural reorganisation with time in solution is observable by the gradual appearance of a sharp CaCO₃ to CaO transition above 550 °C and a reduction in the weight loss in the intermediate range (200 – 500°C) for longer incubation times. Both of these phenomena demonstrate reduced calcium silicate formation in ACC samples with greater degrees of dehydration. The decreased calcium silicate formation can be explained by the fact that co-precipitation of ACC in the presence of silicate also results in the occlusion of the silicate ions within the ACC, which results in an increase in its thermal stability. During dehydration/restructuring of the ACC, silicate ions are likely to be expelled, resulting in reduced calcium silicate formation. The expelled silicate ions might subsequently support the aggregation behaviour observed by electron microscopy.

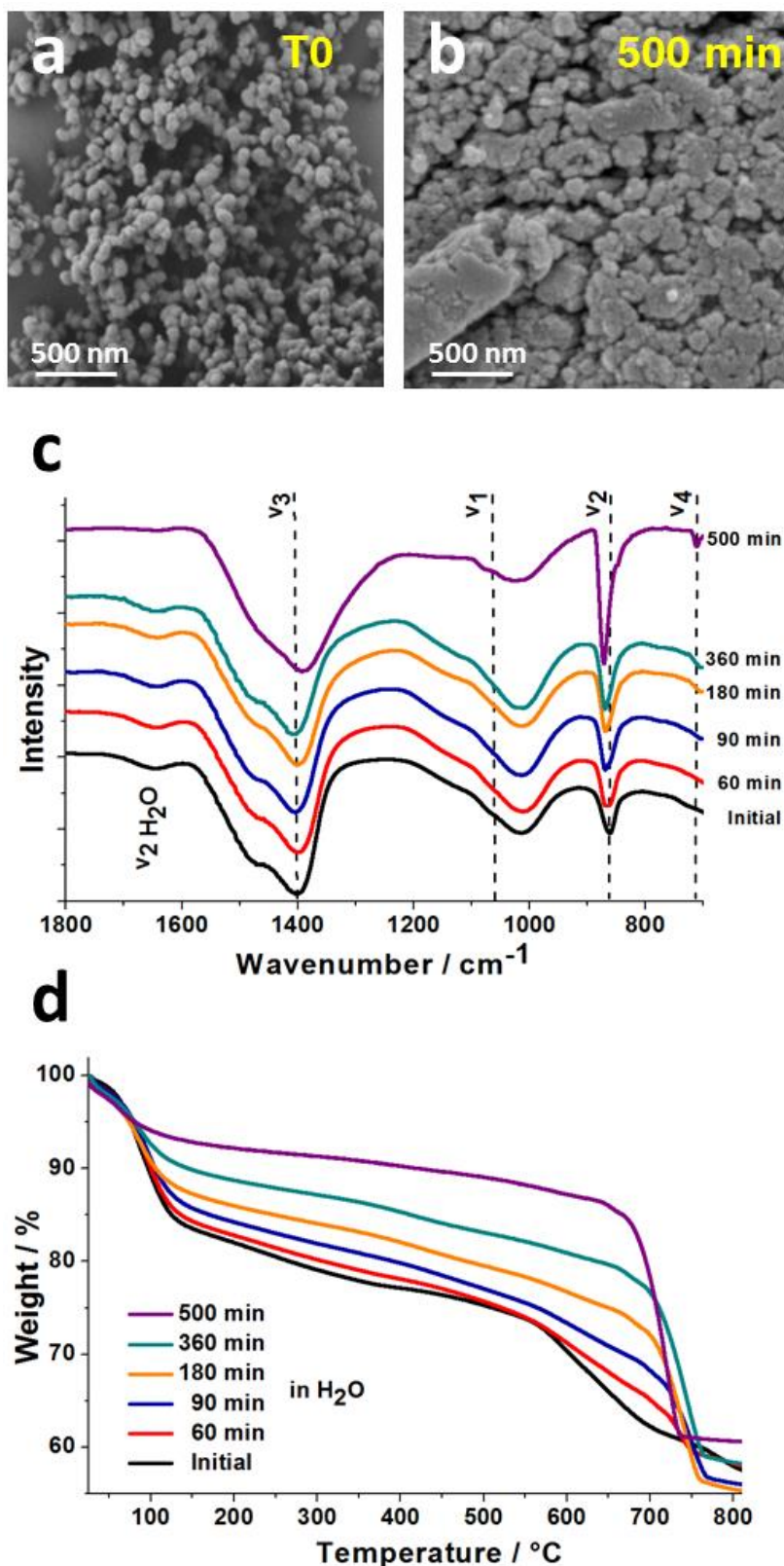


Figure 3 - 13: Summary detailing the crystallisation/ dehydration of ACC-SiO₂ encapsulates upon re-suspension. Given in (a) and (b) are scanning electron micrographs of ACC-SiO₂ after incubation in solution for 0 mins and 500 mins. (c) IR spectra and (d) TGA of ACC-SiO₂ encapsulates, showing the structural and compositional changes in encapsulates with incubation in solution.(95)

Chapter 3: Amorphous Calcium Carbonate

While the degree to which occluded silica ions contribute to the extended stability in ACC is difficult to judge, that they do contribute has been clearly shown.⁽²⁰⁵⁾ Confirmation that the presence of silicate ions within the ACC does not change the pathway by which it crystallizes (dehydration) was obtained by monitoring the crystallisation in water of ACC particles, which were precipitated in the absence of silicate, and then coated with a silica shell, **Figure 3-14**. Silica shell formation on the preformed ACC particles (direct combination of 0.5 ml of 20 mM $\text{CaCl}_2 \cdot 2\text{H}_2\text{O}$ with 0.5 ml of 20 mM Na_2CO_3) was possible by the delayed addition of sodium silicate, four seconds after initiating ACC precipitation (1 ml of 12 mM NaSiO_2). This method never succeeded in coating all of the ACC particles present completely (a to d), such that there was a constant calcite background during analysis (e, v_4). However, the data clearly demonstrates that the pure ACC particles (ie not containing any silica) also dehydrate before recrystallisation (f).

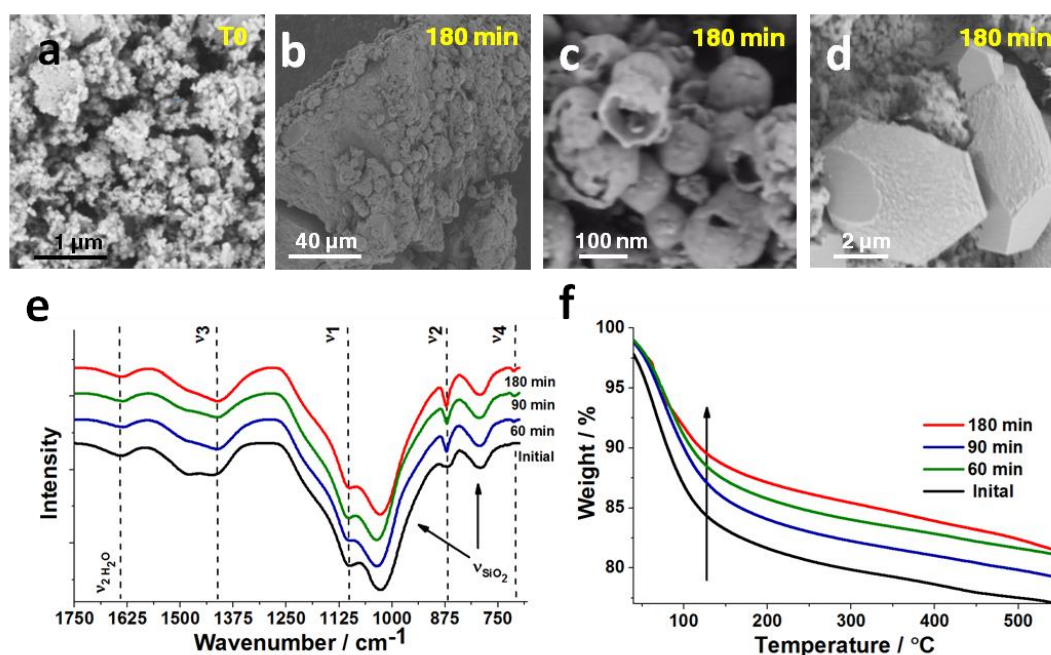


Figure 3 - 14: Characterization of pure ACC particles coated with a porous silica shell, formed by the delayed addition of sodium silicate and their dehydration in solution. Scanning electron micrographs collected with increasing time in solution (a-d) demonstrate clearly that the silica shell is not completed on all ACC particles allowing a rapid dissolution and formation of calcite. (a) Initially prepared particles identical in appearance to ACC-SiO₂ encapsulates. (b) Silica-coated ACC by delayed addition after 180 minutes in solution, showing the presence of (c) empty silica shells and (d) calcite. Observations are supported by ex-situ collected IR spectra. Formed calcite presents a constant background in IR spectra (e). Collected TGA profiles show a similar dehydration behaviour as seen for ACC-SiO₂ encapsulates (f).⁽⁹⁵⁾

Chapter 3: Amorphous Calcium Carbonate

Realizing that the occlusion of silicate ions in the ACC-SiO₂ particles, on a basic level, is nothing else than the **combined use** of a soluble **additive** and **confinement** in directing mineralisation, we explored this route further. It is well recognized that soluble macromolecules and ions, such as magnesium, silicate, sulphate and phosphate, contribute to the extended lifetime of biogenic ACC.(7, 17, 244) However, this alone cannot provide the stability observed for biogenic ACC. As we've just seen above, the environment of the ACC also makes a significant contribution to its stability.

We therefore precipitated ACC as before with a silica shell, but also in the presence of the crystallisation inhibitor aspartic acid. Its crystallisation behaviour was then studied. ACC-Asp-SiO₂ particles crystallized by an identical pathway to ACC-SiO₂ (dehydration followed by crystallisation) where a small band at $\approx 700\text{ cm}^{-1}$ corresponding to crystalline CaCO₃ was observed in the IR spectra after 18 hours. This compares with the appearance of an equivalent peak at 8 hours for ACC-SiO₂ and under 1 hour for uncoated ACC-Asp.(152) The soluble additive and confinement therefore appear to act synergistically in retarding ACC crystallisation.

Viewing the system now from a slightly more abstract angle, what we actually have is a potentially non-toxic core-shell particle, in which the core can be loaded with an active ingredient. The release rate of this encapsulated active ingredient upon re-suspension can be controlled simply by changing the initial sodium silicate concentration. This has a direct influence on the resulting silica shell porosity. Current investigations are encapsulating water soluble fluorescent molecules, quantum dots and gold nano crystals into the ACC-SiO₂ particles, by simply adding the "active ingredient" to the calcium solution prior to the formation of ACC-SiO₂ particles.

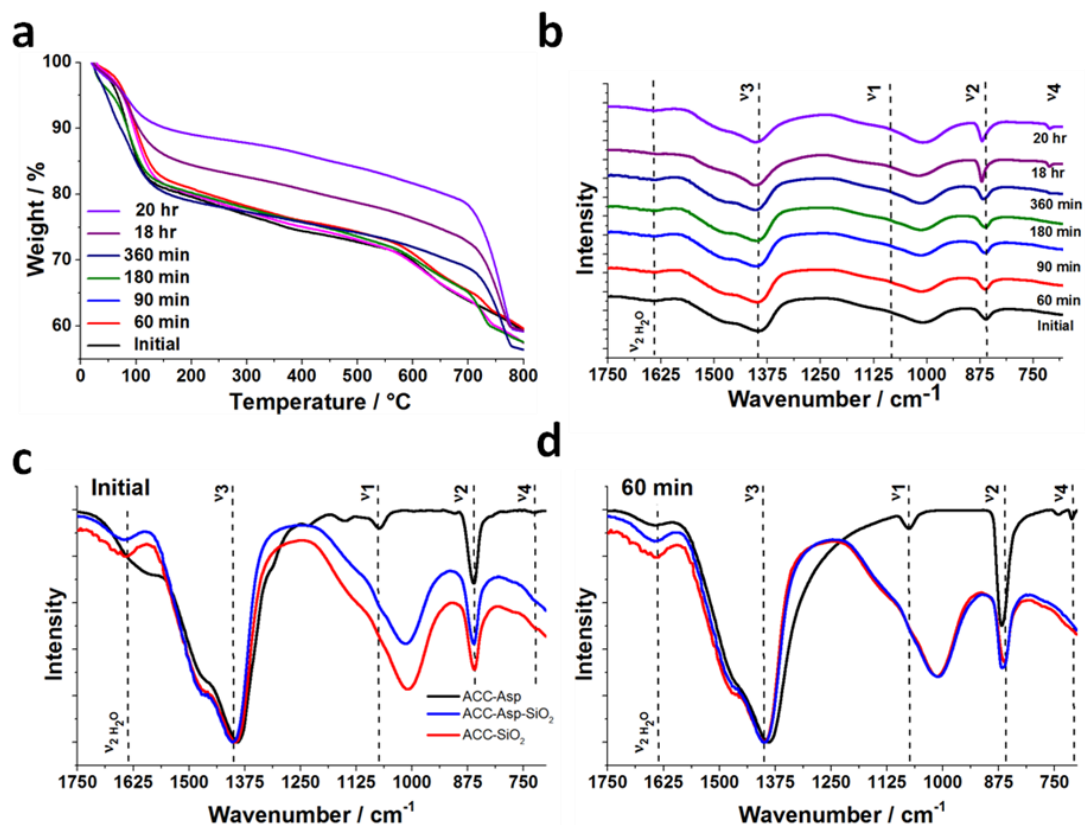


Figure 3 - 15: Shown is the observed crystallisation and dehydration of ACC-Asp-SiO₂ encapsulates prepared by combining equal volumes of 10 mM Na₂CO₃/ 6 mM Na₂SiO₃ and 10 mM CaCl₂/ 5 mM aspartic acid in comparison with Asp-ACC and pure ACC-SiO₂ encapsulates. (a) TGA and (b) IR spectra of ACC-Asp-SiO₂ after different incubation times in solution. Performed identical to ACC-SiO₂ encapsulates. Emerging vibrational band at $\approx 714 \text{ cm}^{-1}$ is selective to crystalline calcium carbonate observed in given IR spectra after 18 hours, with the first hint of crystallinity appearing after ≈ 5 hours. Provided in (c) and (d) are IR spectra of ACC-SiO₂ (—), ACC-Asp (—) and ACC-Asp-SiO₂ (—) after incubation in solution for (c) 0 mins and (d) 60 mins. Revealing the emergence of vibrational bands of vaterite and/or calcite selective for the ACC-Asp particles after 60 mins of incubation, while coated ACC specimen still remain amorphous at this time.(95)

3.3.2.2: Synthesis and Dehydration of ACC – Bilayer Coated Particles

Having demonstrated that encapsulation of ACC within a porous silica shell reduces the rate of ACC crystallisation in solution, we extended our approach to explore whether ACC encapsulation within a lipid membrane - as in biological systems - may act in an analogous way.(120, 211) ACC particles were coated with phosphatidylcholine-dihexadecyl phosphate (DHP) membranes using standard methods (Chapter 2.2.1.3) (173), and their stability in Milli-Q water was investigated by isolating and characterizing the coated particles at different times.

Laser scanning confocal microscopy, made possible by addition of a fluorescent phosphocholine (PC) molecule to the lipid mixture, demonstrated that the ACC particles were coated by lipid membranes and that they agglomerated with time, **Figure 3-16a**. Figure 3-16 a and b provide laser scanning confocal micrographs (LSCM) of the formed encapsulates directly after formation and after 4 days of incubation.

Notably, structural changes in the ACC comparable to those seen during the transformation of ACC-SiO₂ were observed on incubation in solution, as shown by a reduction in intensity of the ν_1 absorption band and a shift in the ν_2 band, IR spectra Figure 3-16c. No bands at 714 cm⁻¹ (calcite) or 747 cm⁻¹ (vaterite) were detected even after day 4 of re-suspension. Noteworthy is also the reduction in the intensity of the bands associated with the PC membrane,(245) (2923 cm⁻¹ (ν_{CH}) and 1234 cm⁻¹ ($\nu_{PO_2^-}$)). This indicates that the membrane coatings are unstable over longer incubation times.

TGA of freshly prepared samples showed a weight loss due to lipid decomposition of ~30 wt% between 230 and 530 °C Figure 3-16 d. This compares with ~20 wt% loss, estimated for 100 nm ACC spheres coated with single bilayers,(246) which suggests the presence of multilamellar coatings or additional vesicles. Importantly, the TGA analysis also demonstrated that the coated ACC particles underwent a very slow dehydration during incubation in solution, as shown by the loss of water below 230°C. Indeed, the water content decreased from an initial ~18–20 wt% to 10–13 wt% after two days, although the particles were still ACC, as judged by IR. The mass loss associated with decomposition of organic materials, which occurs at 230–530°C, also decreases from ~30 wt% to 16 wt% over 2-4 days incubation. The TGA data are in agreement with IR and therefore indicate that the lipid coating of the ACC particles is lost/ reorganizes with time in solution.

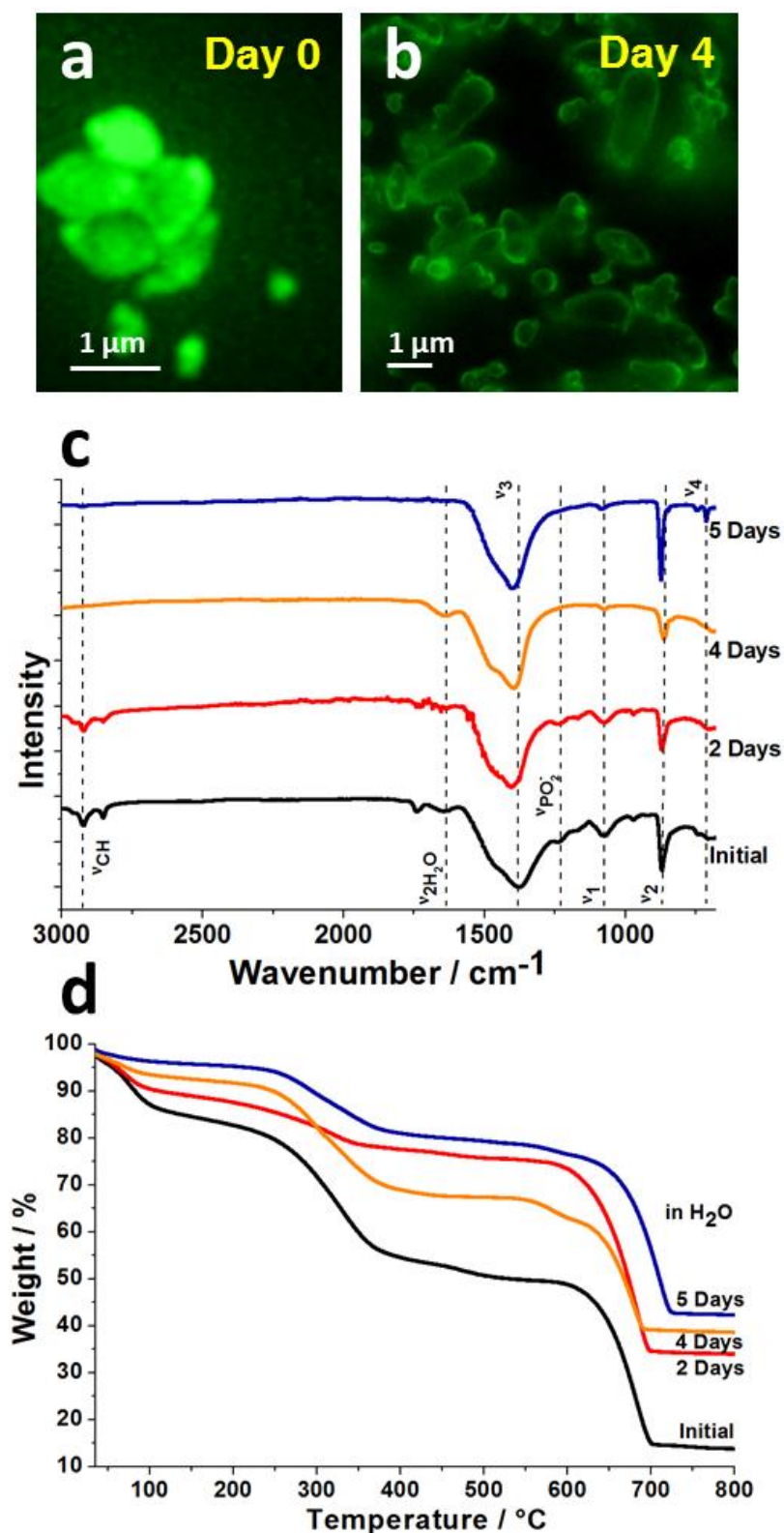


Figure 3 - 16: Summary detailing the crystallisation of ACC particles coated with lipid bilayers upon re-suspension. Provided in (a) and (b) are laser scanning confocal micrographs of ACC bilayer aggregates taken directly after preparation and after 4 days of re-suspension in water respectively. (c) IR spectra and (d) TGA profiles of ACC coated with lipid bilayers isolated and characterized after certain incubation periods in solution.(95)

3.3.3: Dehydration and Crystallisation of ACC in the Solid State

After observing the gradual dehydration of ACC-SiO₂ particles in solution and bearing in mind our goal of comparing its apparent solid state transition in solution with a known solid state transition - to elucidate the underlying mechanism - we studied a known solid state transition of ACC. Detailed studies of the transformation from hydrated ACC to anhydrous ACC to crystalline calcite were therefore carried out by annealing ACC samples at specific temperatures. Annealing ACC samples at specific temperatures leads to the formation of ACC with different hydration levels, thereby allowing us to gain some insight into the reaction mechanism.

ACC containing different amounts of structural water was obtained by the simple heating and subsequent isothermal storage of ACC particles. Samples were heated in a nitrogen atmosphere at a rate of 15°C min⁻¹ and were then maintained at the desired temperature until the weight stabilized, as judged by <1 wt% change over 100 minutes. The isothermal annealing was carried out at 5 °C intervals in the temperature range 25 – 200°C. It is important to stress that these steps were carried out in a TGA/ DSC system, such that data concerning the structural transition are recorded constantly. The annealing is important as it removes the kinetic drag from the TGA profiles, which occurs when the sample temperature is ramped up continuously.

The ACC used for analysis was prepared by combining equal volumes (0.5-1.5 ml) of 1 M (NH₄)₂CO₃ (pH 9.15) with 1 M CaCl₂ (pH ~6.8). TGA/ DSC revealed the formation of ACC containing ~20 wt% water. ~15 wt% water is structurally associated with the ACC, which is consistent with the commonly reported molecular composition of ~CaCO₃:H₂O.

Chapter 3: Amorphous Calcium Carbonate

Following the transformation of ACC while annealing at specific temperatures by TGA and DSC proved to be hugely informative. This provided information regarding the amount of water lost at each temperature, the water fraction remaining and the crystallisation onset temperature. **Figure 3-17a**, shows representative TGA profiles that clearly demonstrate that ACC can be systematically dehydrated by application of defined heating cycles. Extended TGA profiles showing the decomposition to calcium oxide and DSC detected crystallisation are provided in **Figure 3-18**.

Figure 3-17 b & c , provides electron micrographs of ACC particles before (30°C) and after heating (200°C). Aggregation of ~50 nm sized ACC particles occurs during dehydration/ heating. Figure 3-17 d presents IR spectra which were acquired ex-situ. These show that the ACC particles remain amorphous after isothermal annealing up to 250°C. This is evident by the absence of the ν_4 vibrational band. The dehydration of ACC as observed by TGA and IR (decreasing $\nu_{\text{H}_2\text{O}}$), was accompanied by a structural rearrangement of the ACC. The structural rearrangement is apparent based on a reduction in intensity of the ν_1 absorption band, and a slight shift in the ν_2 band to higher frequencies, in common with observations made for ACC samples undergoing dehydration/ crystallisation in solution. DSC showed that the crystallisation of ACC only occurred above a temperature of 290°C, regardless of whether samples were continuously heated or annealed at different temperatures.

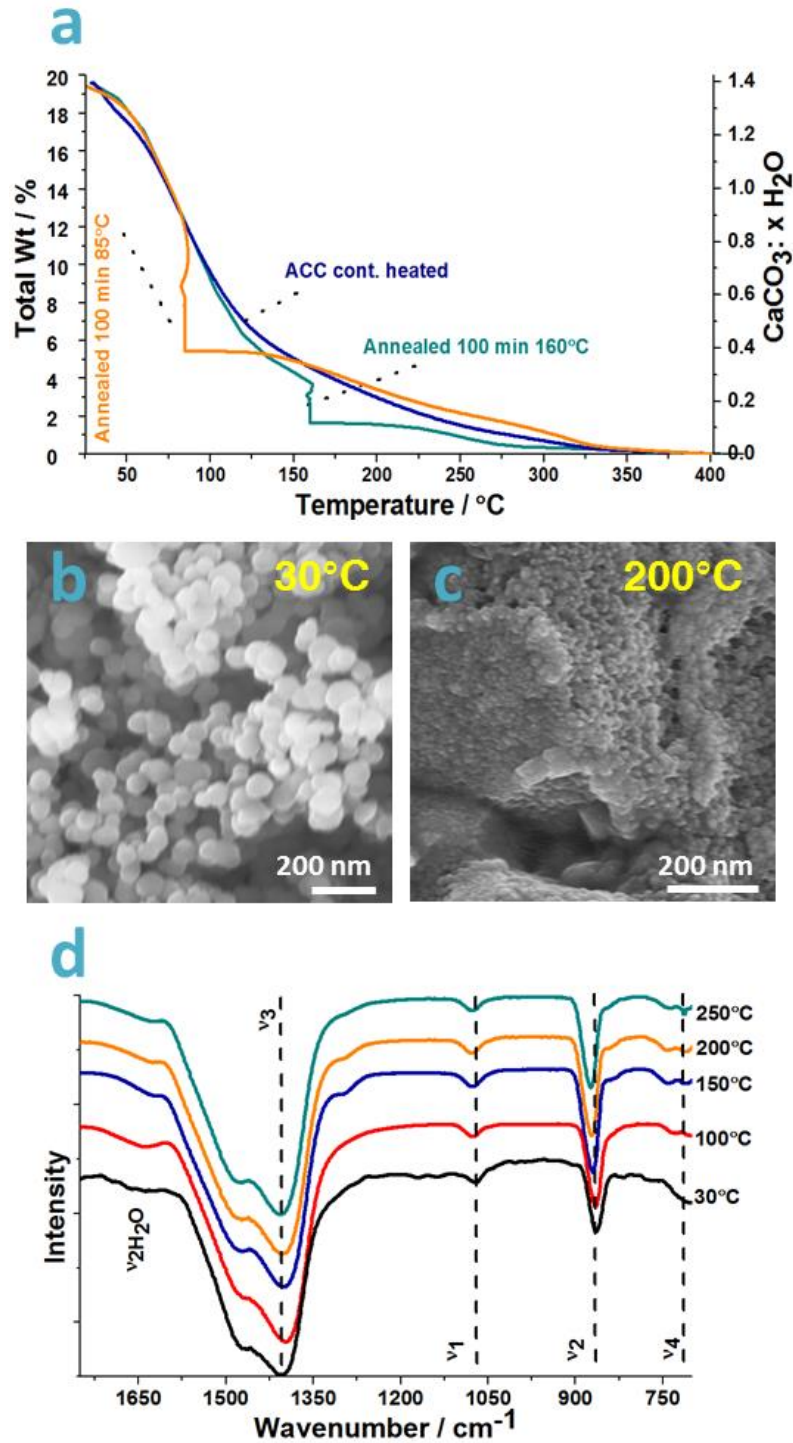


Figure 3 - 17: Overview showing the crystallisation of uncoated ACC particles with increasing temperature exposure. Given in (a) is the total observed change in weight percent of water (Total wt%) and corresponding molecular composition of ACC ($\text{CaCO}_3 \cdot x\text{H}_2\text{O}$) upon heating to and isothermal storage at a predefined temperature as obtained by TGA shown for a temperature range of 25°C to 400°C. Provided in (b) and (c) are electron micrographs of uncoated ACC after isothermal annealing at 30°C and 200°C respectively. (d) IR spectra of ACC particles after the exposure to a heating procedure involving a ramp ($15^\circ\text{C min}^{-1}$), followed by isothermal annealing (100 min) and a second ramp ($15^\circ\text{C min}^{-1}$) step.(95)

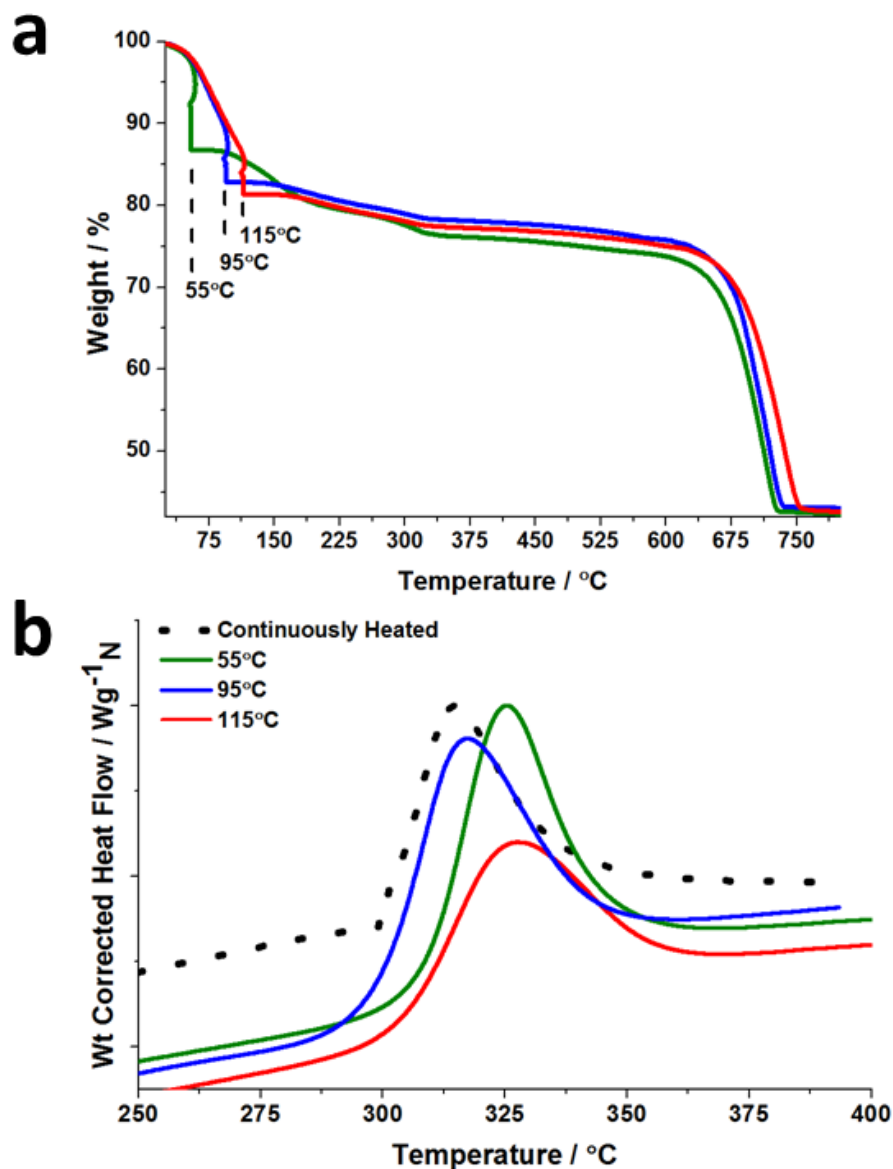


Figure 3 - 18: TGA (a) and DSC (b) profiles obtained from uncoated ACC particles undergoing a full heating cycle i.e. from dehydration to anhydrous ACC, crystallisation (b) and eventual decomposition to calcium oxide. Uncoated ACC was prepared by the direct combination and immediate isolation of formed precipitate of equal volumes of (0.5-1.5 ml) of 1 M $(\text{NH}_4)_2\text{CO}_3$ (pH 9.15) with 1 M CaCl_2 (pH ~6.8) at 4°C. A heating rate of $15^\circ\text{C min}^{-1}$ with a single isothermal annealing period (for 100 min at 55, 95 or 115°C) was used.(95)

Chapter 3: Amorphous Calcium Carbonate

The **DSC** data could further be used to calculate the crystallisation activation energies of the ACC to calcite transition, and its reaction progress with increasing temperature. This was done using the method developed by Boswell, which was introduced in Chapter 2.8. Crystallisation activation energies of $\sim 100 \text{ kJ mol}^{-1}$ were derived in all cases.(187) **Figure 3-19** (a) shows example crystallisation progress profiles, which were obtained from ACC annealed 135°C for 100 minutes and heated at different rates. Presented in (b) is the corresponding Boswell plot used to calculate the crystallisation activation energy (E_a) of ACC annealed 135°C for 100 minutes (a). β is the applied heating rate, and T_p corresponds to the temperature at crystallisation peak maximum in the DSC profile.

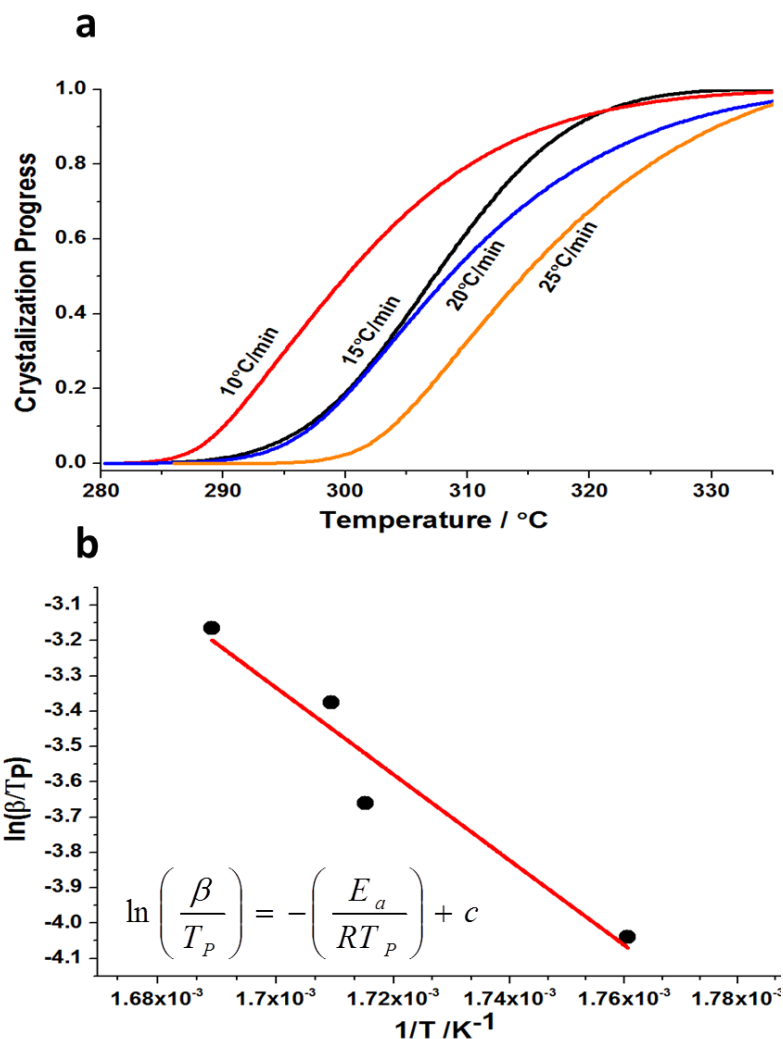


Figure 3 - 19: Profiles provided in (a) detail the crystallisation progress of uncoated ACC samples under heating with an intermediate annealing period (135°C for 100 min), as derived from DSC scans performed with applied heating rates of 10, 15, 20 and $25^\circ\text{C min}^{-1}$. Stated progress of crystallisation, 0-1, is obtained by integration of the crystallisation associated exothermic peak area in obtained (b) Corresponding Boswell plot.(95)

Chapter 3: Amorphous Calcium Carbonate

From the DSC scans we know that the systematic dehydration of ACC does not affect the activation energy of ACC crystallisation. A question that is still open, however, is “what is the **cost of dehydrating the ACC?**”

The acquired TGA profiles, help us to answer this question. The activation energies associated with the liberation of different water fractions occurring in the ACC, were derivable by iso-conversion methods (Chapter 2.8). This was achieved by calculating the activation energies as averages of at least six isothermal measurements using Equation (22). (188)

Here, α (as defined in Equation (23)) represents the degree of dehydration, A is a pre-exponential factor, $f(\alpha)$ describes the reaction model and W_{max} , W_{min} and W_t are the fractions of H_2O present at the beginning, end and time t during an isothermal dehydration event. T is the temperature of an isothermal dehydration event.

$$\ln\left(\frac{d\alpha}{dt}\right)_T = \ln[Af(\alpha)] - \frac{E_a}{RT} \quad (22)$$

$$\alpha = \frac{(W_{max} - W_t)}{(W_{max} - W_{min})} \quad (23)$$

The **average** dehydration activation energy of all of the structural water in ACC can be calculated by plotting the dehydration rate $\ln(d\alpha/dt)$ of the different isothermal dehydration events versus $1/T$. T is equal to the annealing temperature of the corresponding dehydration event. The average dehydration activation energy can then be obtained from the slope of the generated line, Equation 22.

More informative is the dehydration activation energy of a particular **water fraction** i.e. the energy required to partially dehydrate the ACC, say from a composition of $CaCO_3 : 0.8 H_2O$ to $CaCO_3 : 0.4 H_2O$. This information can be obtained as neighbouring isothermal dehydration events, i.e. ACC annealed at “near identical” temperatures, contain both information of the same degree of dehydration. This allows us to plot the measured dehydration rate of the same degree of dehydration across multiple annealing temperatures. A plot of $\ln(d\alpha/dt)_\alpha$ versus $1/T$, where the value of $(d\alpha/dt)_\alpha$ is determined for each isothermal dehydration event and temperature T , then returns a straight line of gradient— E_a/R for a particular degree of dehydration α .

Chapter 3: Amorphous Calcium Carbonate

Repeating this process in incremental steps of α , i.e. from fully hydrated ACC $\alpha=0$ to anhydrous ACC $\alpha=1$, allows us then to generate a plot of dehydration activation energy vs the degree of dehydration.

Such plots for pure ACC and ACC-SiO₂ particles are presented in **Figure 3-20 a** and **b** respectively. The plots show a general increase in the activation energy with increasing dehydration. Further, they indicate the existence of three apparent dehydration regimes. The first shows an increase in E_a up to $\alpha \sim 0.2 - 0.3$, which corresponds to the loss of the surface water, while the second corresponds to a plateau regime from 40°C to $\sim 85^\circ\text{C}$ ($0.3 \leq \alpha \leq 0.6$). The E_a then increases further to a regime from 140–260°C ($0.85 \leq \alpha \leq 1$) which is characterized by high activation energies of $\sim 245 \text{ kJ mol}^{-1}$ (a). Estimates of the weight loss and activation energies (E_a) of each of the dehydration regimes are summarized in Table 5. The dehydration of the silica-coated ACC particles in air also shows the activation energies to increase as dehydration progresses. The derived activation energies were somewhat higher than for the uncoated ACC in air, which demonstrates that the silica coating can retard ACC crystallisation by providing a barrier to water loss.

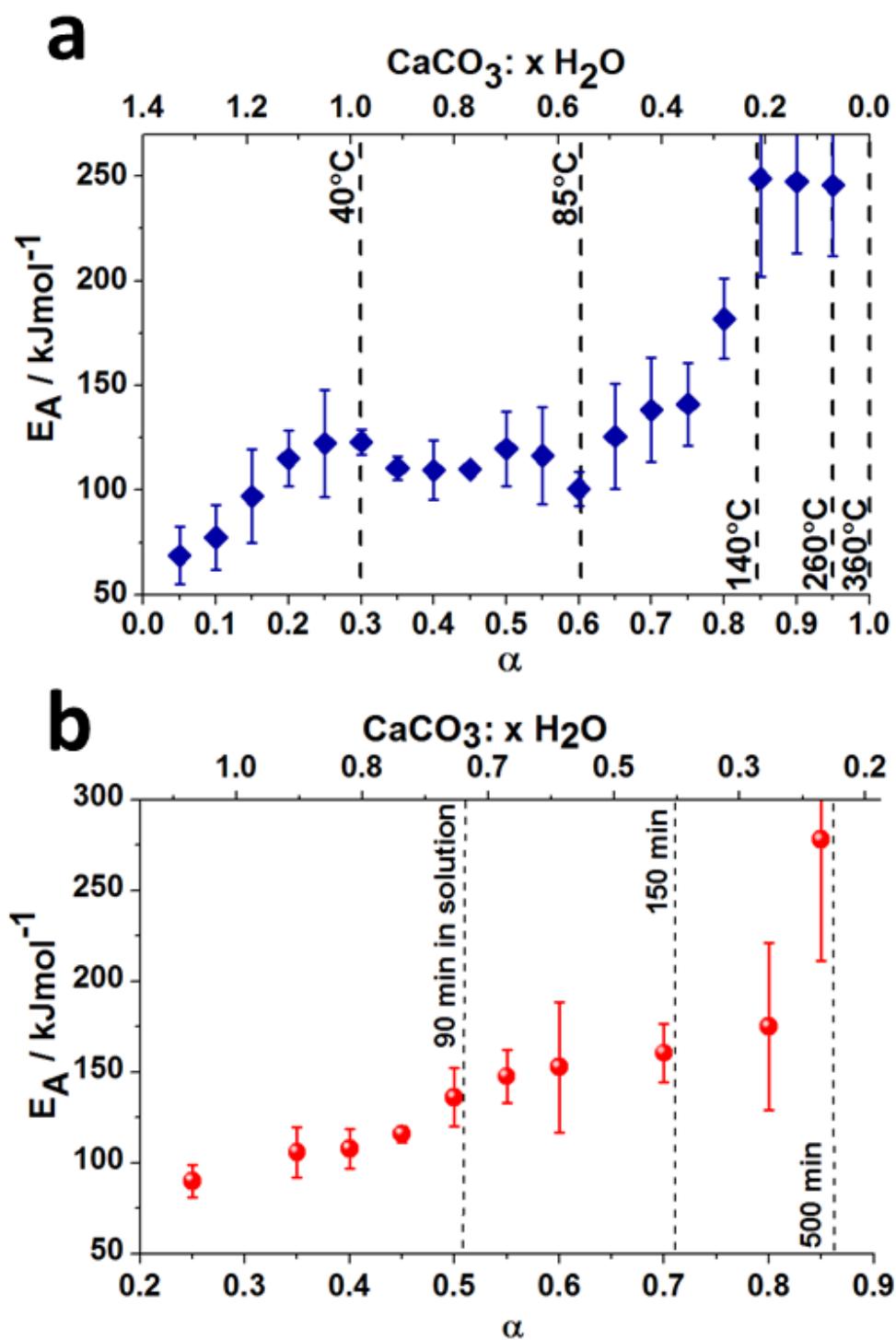


Figure 3 - 20: Given are scatter plots presenting calculated dehydration activation energies (E_A) as a function of the degree of dehydration (α) (bottom scale) and molecular composition of ACC $\text{CaCO}_3 \cdot x \text{H}_2\text{O}$ (all water) (top scale). (a) uncoated ACC and (b) ACC-SiO₂ encapsulates. The standard deviation of measurements is represented in the error bars given.(95)

Chapter 3: Amorphous Calcium Carbonate

	~Wt% Range	α	CaCO ₃ :xH ₂ O	E _a [kJ mol ⁻¹]	Dehydration Model			
					Type	f(α)=kT	R ²	k [°C ⁻¹]
25-40°C	20-14	0.0-0.3	~1.4-0.98	80	2 ^{ed} order reaction	[1/(1- α)]-1	0.98	0.153*
40-140°C	14-3	0.3-0.85	~0.98-0.25	140	Contracting volume	1-(1- α) ^{1/3}	0.92	0.0042
140-260°C	3-0.5	0.85-0.95	~0.25-0.08	245	2 ^{ed} order nucleation	α ^{1/2}	0.85	0.0031
25-260°C	-	-	-	125	Contracting volume	1-(1- α) ^{1/3}	0.92	0.0038

α ; degree of dehydration

CaCO₃:xH₂O ; number of moles of water associated with 1 CaCO₃ formula unit

E_a ; average activation energy associated with water loss for a given temperature range

Dehydration Model ; best-fit solid state reaction models (f(α)=kT) , coefficient of determination R² , rate constant k

* f(α)=k[min^{-1}]t

Table 5: Key information extracted from the thermal analysis of uncoated ACC.(95)

3.3.4: Mechanism of ACC Dehydration

Provided in **Figure 3-21** are scatter plots of the gradual dehydration of ACC observed over a temperature range 25 – 220°C. Plots were derived using α values obtained at the end of each annealing period. By doing so we remove the kinetic drag of continuous heating experiments, such that the plots provide a true reflection of the dehydration profile with temperature. Kinetic drag refers to the underestimation of weight/ mass lost at a particular temperature, where the latter is due to mass loss being slower than commonly applied heating rates.

Figure 3-21, shows that the rate of dehydration decreases at higher temperatures, which demonstrates that it becomes increasingly difficult to remove water as the limit of anhydrous ACC is reached. This is in keeping with the activation energy measurements. The dehydration curve also provides further insight into the mechanism of dehydration of ACC in air by considering fits to common solid-state reaction models ($f(\alpha)$) (247). The insights gained are summarized in Table 5. It should be noted that the validity of such analysis is still debated due to the mathematical interdependence between activation energy, pre-exponential factor and chosen model.(248, 249)

The full dehydration curve (Figure 3-21a) is best described by a geometric contraction model, in which the reaction rapidly initiates on the particle surface and then proceeds towards its centre. The intermediate temperature range (40 – 140°C), which represents ~ 65 % of the total water fraction, can also be described by the same model (b). In both cases, a contracting sphere provided a slightly better fit than a contracting cylinder, with R^2 values of 0.92 and 0.89, respectively, as compared with 0.90 and 0.85. The final dehydration at 140 – 220°C, which represents less than 15 wt% of the initial water content, is in contrast best described by a second-order nucleation model (c). Removal of the last water is therefore not diffusion limited but is determined by the barriers to water release.

The dehydration regime from $0 \leq \alpha \leq 0.3$ (~ 40°C) is best described by an isothermal process following a second-order rate equation, as is consistent with loss of surface water and common adsorption isotherms (d).

Chapter 3: Amorphous Calcium Carbonate

The dehydration of the ACC-SiO₂ particles in solution as a function of time (Figure 3-21 e) showed that the overall behaviour from $0.3 \leq \alpha \leq 1$ obeys an identical three-dimensional model (contracting sphere, $R^2=0.94$) as for the dehydration of uncoated ACC in air. A graphical summary of those observations is presented in **Figure 3-22**.

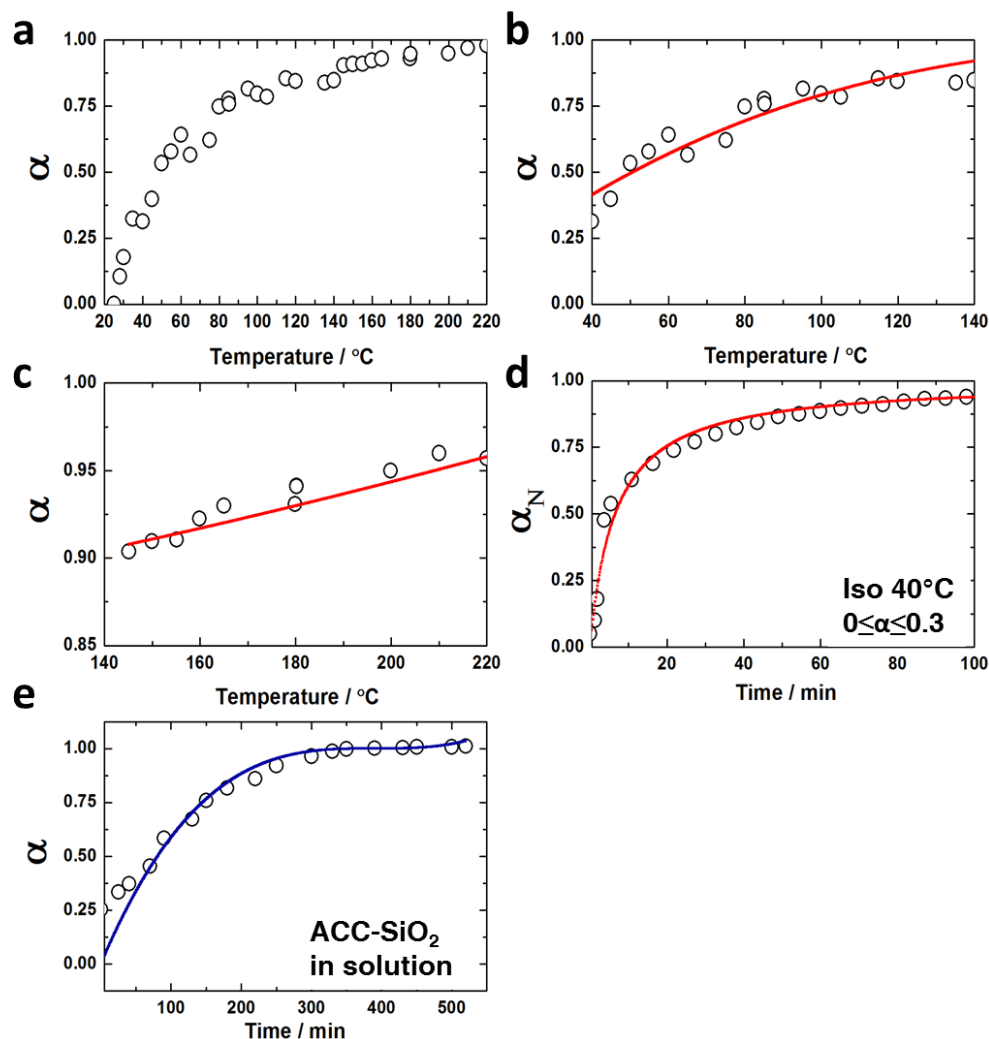


Figure 3 - 21: Categorizing the progress of ACC dehydration. Presented are dehydration cures of ACC and ACC-SiO₂ encapsulates as a function of temperature (T) or time (t) (Single data points). Presented alongside with best fits to the common solid state reaction models given in Table 1 (continuous lines). Given in (a) is the general dehydration profile of uncoated ACC upon heating shown over the range of 20 - 220°C, freed from kinetic drag as a result of constant heating. (b) and (c) provided specific, normalized ranges of this dehydration process. (b) representing the range 40 - 140°C, fitted by a geometric contraction model and (c) shows the range 140 - 220°C, fitted by a second order nucleation model. Depicted in (d) is the dehydration of uncoated ACC by isothermal annealing (40°C). Provided in (e) the dehydration of ACC-SiO₂ encapsulates as a function of time on incubation in solution (25°C). Experimental dehydration curves – each given point corresponds to average observed weight loss during a series (x3) of separate isothermal/solution annealing experiments. Stated weight loss was obtained from the end point of isothermal/ solution annealing periods. α is equal to the total fraction of water (Figure 3-20); α_N refers following to the normalized weight fraction of water lost over a specified temperature range (0 - 1).(95)

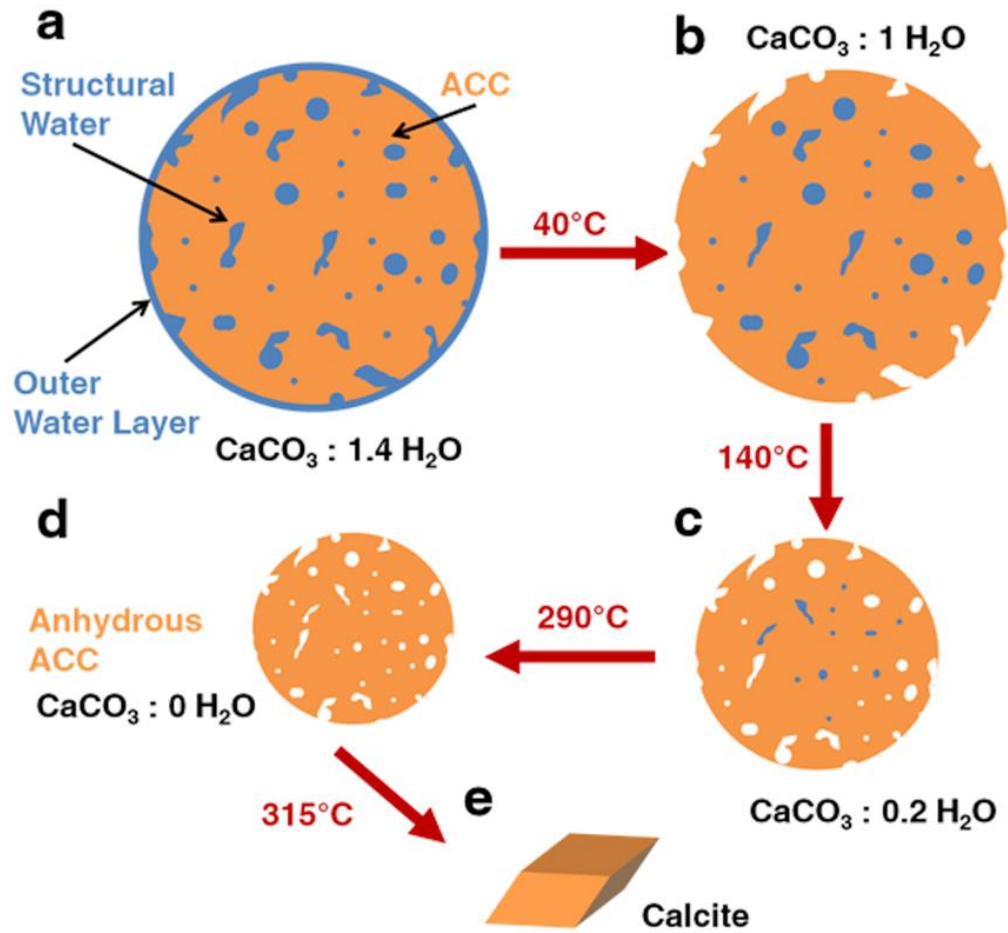


Figure 3 - 22: Depicted in given schematic are the idealized succeeding stages of ACC dehydration in the form of a cross section through an ACC particle. Starting from hydrated, wet ACC (a) to the loss of surface-bound water (b). Continuing from (b) to (c) water is lost from the inner of the ACC concurring with particle compaction. Further dehydration leads to the expulsion of deeply located water and hydroxyl ions (d) and the crystallisation to calcite (e).(95)

Chapter 3: Amorphous Calcium Carbonate

Further insight into the nature of the water environments in hydrated ACC was gained from ^1H **solid-state NMR** (SSNMR) measurements of ACC samples that had been isothermally annealed to different levels of dehydration.

The measured spectra are given in **Figure 3-23**. Analysis of the uncoated samples presented in (a) reveal the presence of five different proton environments in its fully hydrated state. These are a rigid structural phase associated with Ca^{2+} (two types of OH^- at 0.9 and 3.4 ppm), two partially mobile phases due to H_2O (4.9, 5.7 ppm) and a signal due to CO_3^{2-} (H^+) framework components (7 ppm).(250) With progressing dehydration, little change is observable in the OH^- signal, while the ^1H signal from H_2O and HCO_3^- decrease progressively.

Heating of the samples resulted in coalescence of the ^1H signals, which gave a broader signal centred at 5.2 – 5.5 ppm. This is a weighted average of the 4.9 and 5.7 ppm signals and is due to the exchange of protons between the two environments. This shows that they are in physical contact. The ^1H signal from HCO_3^{2-} shifts downfield (~6.7 ppm) when the dehydration temperature is increased, suggesting that the ^1H in these sites also exchange with water ^1H . Its chemical shift therefore becomes a weighted average of that for the HCO_3^- site (~7 ppm) and the water sites (4.9, 5.7 ppm).

(b) ACC- SiO_2 particles, with different water contents were also characterized (dehydrated in solution). This revealed the presence of different proton environments within the ACC, as in the case of uncoated ACC, which behaves similarly with dehydration. In addition, signals originating in the hydrated SiO_2 shell were detected.(251)

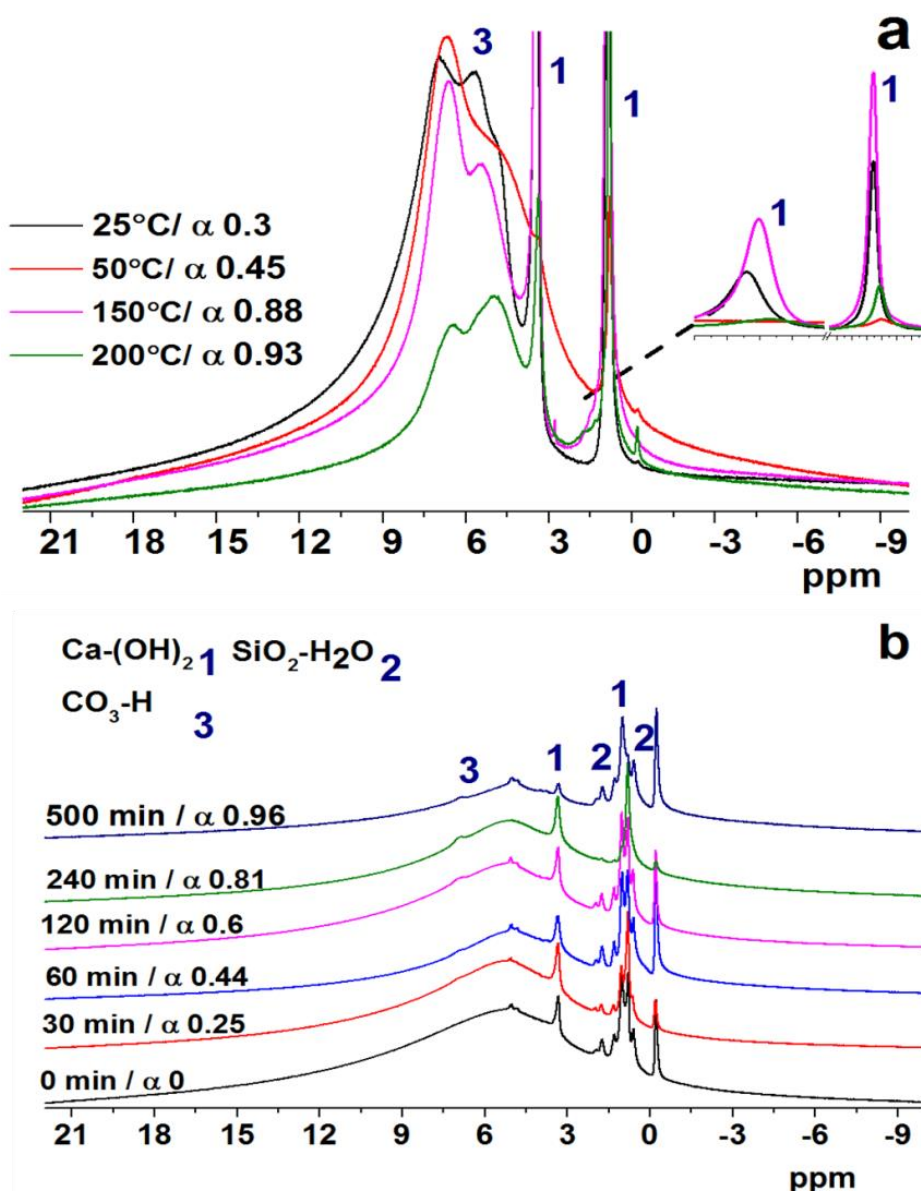


Figure 3 - 23: Provided are ^1H solid state NMR spectra of (a) uncoated ACC particles and (b) ACC-SiO₂ particles isolated from the process at specific known degrees of dehydration as determined in reference by TGA. ACC-SiO₂ particles were isolated from solution, uncoated ACC particles were prepared by means of isothermal heating. Samples for SSNMR were kept at 40°C for one hour prior to the measurements(175).(95)

3.3.5: Discussion

By employing a bio-inspired strategy, where encapsulation of ACC particles within silica shells retards crystallisation, we here show that in common with biomineralization processes and the transformation of ACC in air, synthetic ACC also dehydrates at room temperature in an aqueous environment. This process is driven by the generation of a more stable, low water content ACC phase.(91)

Characterisation of this dehydration process demonstrated a strong dependence of the activation energy required to remove water on the degree of dehydration. The activation energies required to remove the first water fractions (up to 0.3 H₂O) are close to the hydration energy of calcite crystal faces.(252) This is as expected if the first stage of dehydration removes more accessible water of hydration. Note that this is far more than monolayer coverage of water on the outer surface of the ACC particles, and undoubtedly includes water condensed around the contact points of adjacent particles as well as some more deeply located water.(253) The higher activation energies measured for the remaining fractions may reflect the increasingly hindered escape of water molecules in low humidity environments.

The mechanistic interpretation of the magnitudes of activation energies for solid-state reactions is open to some debate.(248, 249, 254) Nevertheless, the obtained results are in good agreement with current modelling studies of ACC dehydration. These predict an increasing hydration energy with progressing dehydration. This is explained by the formation of stronger hydrogen-bond network interactions with surrounding/ neighbouring Ca²⁺ and CO₃²⁻ ions.(87) The latter is potentially reflected in the experimentally-observed structural reorganization of the ACC towards calcite-like fingerprint spectra during heating.

One particular model of ACC dehydration obtained from combined computer simulations and structural studies of synthetic ACC (CaCO₃:H₂O) suggests that the water molecules in hydrated ACC are located, along with carbonate ions, within a network of nanoporous channels in a Ca²⁺-rich framework.(134) It is those channels that are foreseen to facilitate the loss of water during dehydration, where this process would also be accompanied by a structural rearrangement in which CO₃²⁻ ions relocate from the channels into the calcium framework.

Chapter 3: Amorphous Calcium Carbonate

Focusing on the actual crystallisation process, the crystallisation of dry ACC (i.e. out of solution and in the absence of any surface water) is only observed at temperatures of $\sim 300^{\circ}\text{C}$, where this is triggered by/ coincides with the loss of the final water fraction of the initially hydrated ACC. In the absence of any water the phase transition of anhydrous ACC to calcite must proceed by a solid-state transformation. This is supported by the measured high activation energy of $\sim 245 \text{ kJmol}^{-1}$ of the final dehydration step and the subsequent crystallisation activation barrier of $\sim 100 \text{ kJmol}^{-1}$. The final high dehydration energy associated with the last water fraction is more likely to be associated with the removal of hydroxyl ions and trapped water as activation energies of dehydration of crystalline solids are typically of the order of 100 kJmol^{-1} , which corresponds to the intermediate fraction of water lost from the ACC.(96, 254)

Bearing in mind the magnitude of the measured activation barriers, while recollecting the fact that ACC crystallizes very rapidly in solution or when wet, an alternative mechanism with a lower energy barrier must occur. Indeed, when isolated, ACC only shows extended stability when washed with solvents such as ethanol which can substitute for much of the surface water or by the direct removal of the latter in the form of freeze drying.(104, 175) Even then, the rate of crystallisation is dependent on the ambient humidity.

These data, and in particular the observations made in confined volumes here, strongly suggest that while ACC can certainly dehydrate at room temperature in and out of solution, the energy barrier to nucleation is such that the formation of the first crystalline nuclei can only occur via a partial dissolution/ reprecipitation. It needs to be stressed that it is not proposed that the ACC particles fully dissolve and then re-precipitate. Rather, it appears more likely that this occurs locally within a domain on the surface of an ACC particle, or within aggregates of ACC particles which may contain pockets of entrapped water.(162) The progressing crystallisation of the ACC particle can therefore occur by a “solid state” transformation, which has previously been termed secondary nucleation (255). The crystal nucleus then induces structural changes in its adjacent surrounding,(97) catalysing the further dehydration of the ACC. Such a transformation is supported by the observed structural changes which accompany dehydration of the ACC observed here and during biomineral formation.(119)

Chapter 3: Amorphous Calcium Carbonate

The transition of ACC to calcite at room temperature therefore seems to be defined/decided by a balance between the rates of dehydration and dissolution/reprecipitation. ACC in bulk solution would therefore be predicted to transform via a full dissolution/ reprecipitation route, while ACC with limited water access or minimal surface water would be anticipated to convert via a “solid state” mechanism.

As stated in the discussion of the effects additives have on ACC crystallisation (Chapter 3-2), the suggested mechanisms are consistent with the data presented in the literature. Studies investigating the precipitation of calcium carbonate from concentrated solutions by in-situ SAXS/WAXS have suggested that initial dehydration and subsequent reorganization of ACC is followed by a direct transformation to vaterite, before changing to a dissolution/ reprecipitation mechanism which leads to calcite formation.(93, 256) Further evidence for a “solid state” transition comes from cryo-TEM studies of ACC. These have reported the direct transformation of ACC into vaterite as well, revealed by the development of a crystalline nucleus within the ACC particles.(94) Further evidence for nucleation of the new crystal phase within ACC comes from observations that ACC typically aggregates prior to direct transformation into a crystal,(218) that ACC particles crystallize more slowly in small volumes with few particles present,(157, 160) and that small ACC particles show greater stability.(137) Once initial nuclei of vaterite or calcite are established, further growth principally occurs by dissolution of the surrounding ACC.(86, 93, 139, 209, 219, 220, 256)

Moving away from calcium carbonate, observations of stepwise transformation mechanisms in solution have been made in many other natural and synthetic instances including the transformation of amorphous titania to anatase or rutile, or ferrihydrite to goethite or haematite.(257) These hydrated, metastable, amorphous or nano-crystalline phases have been shown to transform only after an initial dehydration.(258) In particular, the transformation of ferrihydrite to haematite or goethite has been considered analogous to calcium carbonate, and may occur via a dissolution/ recrystallisation mechanism or a solid-state transformation.(257) Other examples include the dehydration of crystal hydrates, where these often proceed via an intermittent amorphous phase which dehydrates i.e. the removal of structural water often destroys the pre-existing crystal lattice.(254) As in the case of ACC, the nature of the transformation mechanisms are still debated.

3.3.6: Conclusions

Thermal analysis combined with solid-state NMR spectroscopy following the transformation of ACC to crystalline calcium carbonate in air and in solution by application of bio-inspired strategies provides a first insight into the mechanism of ACC transformation. It demonstrates that ACC undergoes parallel dehydration and structural changes both in air and in solution prior to crystallisation, if dissolution/ recrystallisation processes are hindered. In both cases, the water in ACC – which exists in different environments - is gradually lost. Mobile water is lost first, followed by rigid water, and hydroxyl ions and trapped water are lost last. The loss of the final component then appears to trigger or coincide with the crystallisation of the dehydrated ACC. This last step was determined to be associated with a high free energy barrier $> 150 \text{ kJmole}^{-1}$, which implies that at room temperature and in solution the first crystal nucleus can only form via a dissolution/ reprecipitation mechanism, mediated by water present on particle surfaces or in solution.

Through application of bio-inspired strategies, we further reveal that confinement stabilizes ACC by retarding dissolution/ reprecipitation based nucleation, and by limiting ACC aggregation in solution. This is further enhanced in the presence of crystallisation inhibitors, which primarily affect the formation of a crystalline phase at this stage. This suggests that nature employs both biomacromolecules and confinement to tailor the stability of ACC in organisms.

The majority of the structural water in ACC seems of little importance to the stability of ACC itself. However the water present plays a key role in the initial precipitation of ACC, where this lowers the energy barrier towards the formation of this hydrated phase as compared with the anhydrous polymorphs.

3.4: ACC by Freeze Concentration

3.4.1: Introduction

As established in the discourse above, ACC, and to some extent, amorphous calcium phosphate (ACP) are widely utilized in biomineralizing organisms to produce their intricate structures.(14, 117, 120, 236) The most prominent examples of amorphous precursor utilization include the collagen/ hydroxyapatite composite that is bone (ACP) and by the controlled, and yet rapid crystallisation of spicules in sea urchins.(259, 260) To fully utilize the enormous potential of amorphous precursor phases in material synthesis, with their promise of superior control over nucleation, crystal growth, and the access to rapid growth rates and “non-crystalline” morphologies, there is a requirement to obtain pure amorphous precursors.(49, 239)

As yet, we have not discussed the challenges associated with the production of pure ACC in a reproducible way using common synthesis methods. This will be done here, where I describe a synthesis method that can produce exactly this – pure, dry ACC. Currently, the principal methods used to prepare ACC are the ammonia diffusion method (261), synthesis at high pH, as introduced by Koga and co-workers (129, 261) and the rapid mixing of highly concentrated (1M) calcium and carbonate solutions (93),(172). Further, ACC appears to represent a family of phases whose structures and compositions are dependent on the particular synthesis method and solution conditions (e.g. temperature, pH).(129, 152) Treatments following precipitation such as drying or washing with agents such as ethanol can also make significant changes to the ACC and its crystallisation behaviour.(104) Consequently, synthetic ACC can vary considerably in terms of stability,(161, 212), co-precipitated ions, and the amount of structural and surface water,(130) which makes characterization of the mechanism of its crystallisation difficult. Indeed, synthetic ACC with long-term stability in air or solution is only typically reported on precipitation from ethanol,(104) or in the presence of Mg^{2+} .(210)

A method was therefore developed based on freeze concentration of saturated counter ion free calcium carbonate solutions, where this avoids some problems associated with the common ACC synthesis methods. The ACC is generated in the absence of any counter-ions, contains little surface-bound water and shows an extended atmospheric stability. The generality of this approach for the synthesis of amorphous phases is then demonstrated by extension to ACP.

3.4.2: Experimental

The production of ACC by freeze concentration of an aqueous, saturated, “counter ion” free calcium carbonate solution, is possible, thanks to the selective crystallisation of water during a freezing process. The gradual transformation of water to ice during freezing creates local environments (water pockets) which gradually decreases in free volume but simultaneously increase in the concentration of the reacting ions. This eventually leads to the formation of ACC, in a very similar way to the method by which fruit juices are concentrated.

A schematic diagram of the experimental process and the idealized formation and stabilisation process of ACC is given in **Figure 3-24**. In the developed method, ACC is suggested to form during the freezing process of a saturated solution (a, red arrow). Subsequent application of a vacuum leads to sublimation of the ice (solvent), which frees the ACC formed during the freezing process (a, blue arrow) Figure 3-24 (b and c). On placing a solution of calcium carbonate into liquid nitrogen, rapid freezing occurs, During this process the reacting ions, calcium and “carbonate”, are pushed away from the ice front into smaller and smaller liquid reservoirs as freezing progresses, creating highly supersaturated environments in which ACC ultimately precipitates. The ACC is stabilised against crystallisation due to the low temperature and complete solidification of the solvent. The subsequent sublimation of the frozen solvent then releases the as-formed ACC.(262, 263) That ACC is formed during the freezing process itself is supported by the fact that if slow freezing rates are employed, calcite is obtained rather than ACC.

To obtain pure ACC, the synthesis method necessitates the use of a counter ion free starting solution. This solution is ideally prepared by the dissolution of pure $\text{CaCO}_3(\text{s})$ in double distilled water. “Pure” solid CaCO_3 was obtained by the repeated dissolution and re-precipitation of CaCO_3 which had been obtained by combining 1 M CaCl_2 and 1 M Na_2CO_3 . Saturated solutions were then prepared by adding 25 mg of “pure” CaCO_3 to 500 ml doubled distilled water and they were then stored for 24 hours before the bulk of the remaining un-dissolved calcium carbonate was removed. The prepared saturated solution was then cooled to 4°C to remove any possible ghost nuclei, and was then filtered through a 0.2 μm membrane. Freezing of the prepared, saturated solutions (1 – 400 ml) was achieved by immersion into a liquid nitrogen bath, followed by a 10 minute annealing period to strengthen the ice structure. Specifically, 30 ml of saturated CaCO_3 held in a 10x2.5 x 2.5 cm Teflon holder was immersed into LN_2 at a fixed rate, visual

solidification was achieved in ≤ 15 min. Subsequent sublimation of the excess solvent (3 days) under vacuum delivers the pure, dry ACC.

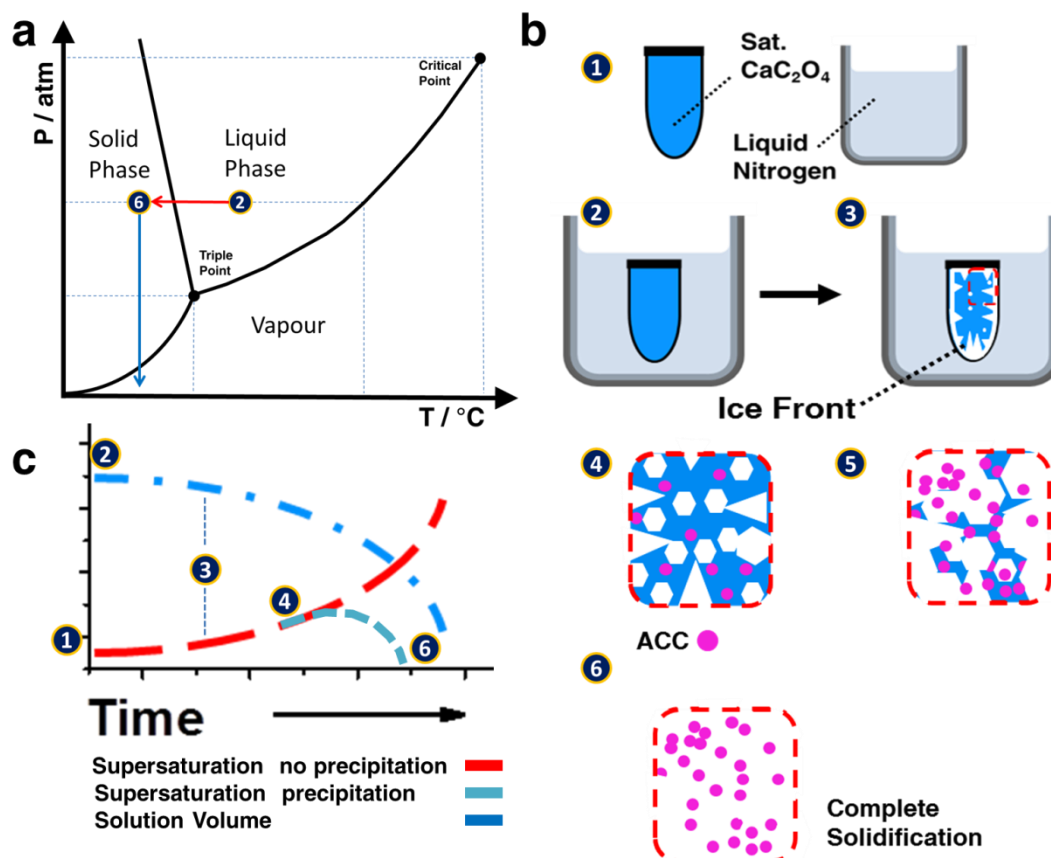


Figure 3 - 24: Schematic representation of the production of ACC by freeze concentration. Illustrated in (a) are the particular phase changes of used solvent during the production process from liquid to solid upon freezing (red arrow) and solid to gas during sublimation i.e. vacuum application (blue arrow). (b) Illustrates the formation process of ACC upon the selective crystallisation of present solvent. (1) Saturated CaCO_3 solution is (2) plunged into LN_2 (3) upon which the solvent begins to freeze, creating localized environments of increasing supersaturation, (4-5) leading to ACC precipitation and (6) followed by final solvent solidification and ACC stabilization. (c) provides line plots with suggested changes in supersaturation and solution volume accompanying the freezing of present solution. Reproduced and altered after (175).

3.4.3: Results

3.4.3.1: Characterisation

Confirmation that the precipitate obtained by freeze concentration of a saturated solution is indeed ACC was established by characterising it using a range of techniques. The obtained spectra were compared with references from the literature (Appendix A) and *standard* ACC produced here by the direct mixing of equimolar (1 M) solutions of CaCl_2 and Na_2CO_3 , Chapter 2.2.1. The latter *standard* ACC was isolated after 5 minutes of incubation by filtration and was washed with ethanol and air-dried.

Presented in **Figure 3-25** are electron micrographs (a) and (b) of ACC obtained by freeze concentration which demonstrates the formation of spherical particles ~100 nm in diameter. This was further confirmed using dynamic light scattering (c). The inset in (a) provides an EDX spectra of ACC obtained by freeze concentration, which demonstrates the major absence of secondary ions commonly present in ACC including Na^+ and Cl^- when precipitated from a high solution pH <12.

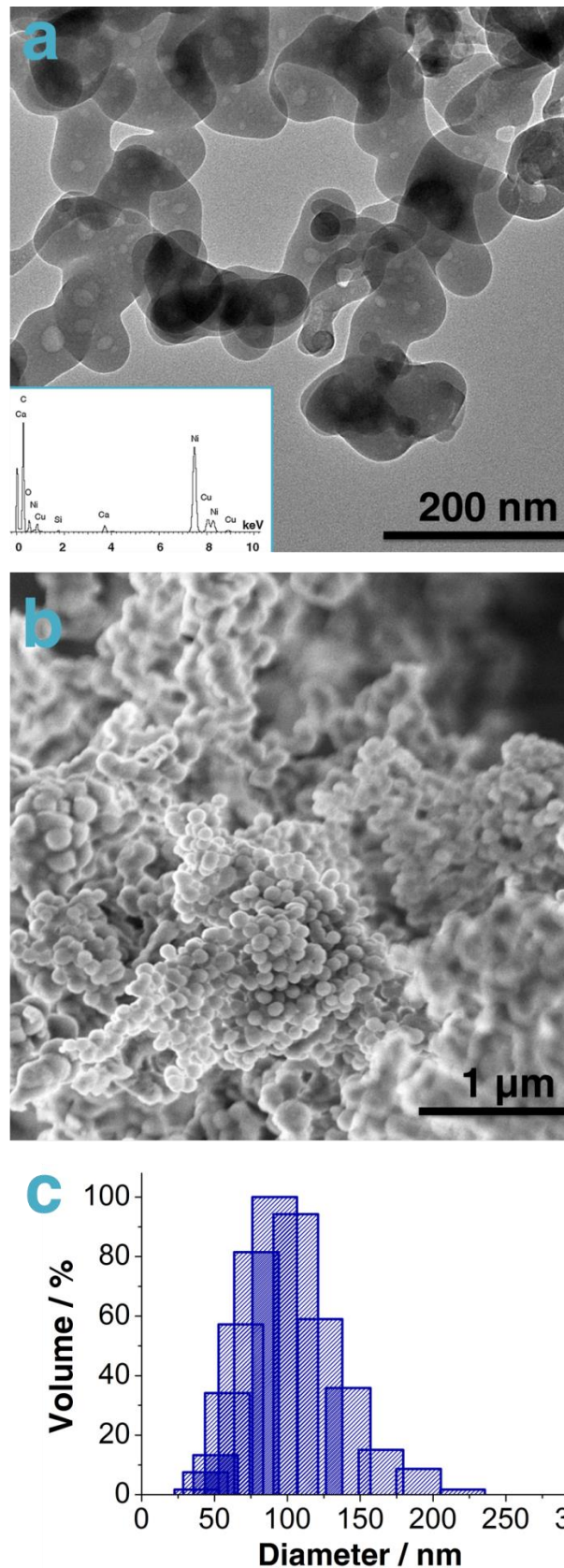


Figure 3 - 25: (a) TEM, and (b) SEM images of ACC produced via freeze-drying. The inset in (a) provides an EDX spectra of formed ACC. TEM - sample is supported by a nickel grid. (c) Particle size distribution of produced ACC measured using DLS of particles suspended in ethanol.(175)

Chapter 3: Amorphous Calcium Carbonate

Analysis of the prepared ACC is presented in **Figure 3-26**. (a) Comparison of the Raman spectra of the ACC samples prepared by freeze-drying and direct precipitation showed an increase in peak broadening of the ν_4 (1088 cm^{-1}) band of $>20\%$ at full width half maximum (FWHM) for the freeze-dried ACC, which is indicative of a higher degree of disorder between the two.(264) More importantly, no secondary peaks could be detected and only a very broad peak centred at the ν_4 position (corresponding to the internal CO_3^{2-} symmetric stretch) could be detected in both spectra. This confirmed the successful formation of ACC in both cases.

(b) The acquired IR spectra support this conclusion, where the freeze-dried ACC exhibits a much stronger symmetric-stretch ν_1 peak.(14) IR spectroscopy yielded spectra characteristic of ACC with broad peaks centred around $1473/1406\text{ cm}^{-1}$ (ν_3), 1130 cm^{-1} (ν_1) and 868 cm^{-1} (ν_2), in addition to peaks due to the vibration of water molecules at 1651 cm^{-1} . The notable absence of the ν_4 peak around 700 cm^{-1} further demonstrated the formation of ACC.(214) (c) PXRD of CaCO_3 precipitated by freeze-drying revealed the presence of a broad amorphous background and the complete absence of any sharp peaks. (d) TGA was used to investigate the composition of the ACC produced. The heating/ weight profile of freeze-dried ACC which had been stored in a laboratory atmosphere for 2 weeks demonstrated a loss of $10\text{ wt}\%$ below 200°C , where this corresponds to adsorbed surface and structural water. This was followed by a continuous weight loss due to CO_2 release, before decomposition to CaO above 550°C . This suggests a composition of $\sim 1\text{ CaCO}_3 : 0.7\text{ H}_2\text{O}$. This can be compared with the ACC produced by direct combination which exhibits a loss of $\sim 20\text{ wt}\%$ below 200°C and a composition of $\sim \text{CaCO}_3:\text{H}_2\text{O}$, which is typical of ACC synthesised in aqueous solution.(152, 172)

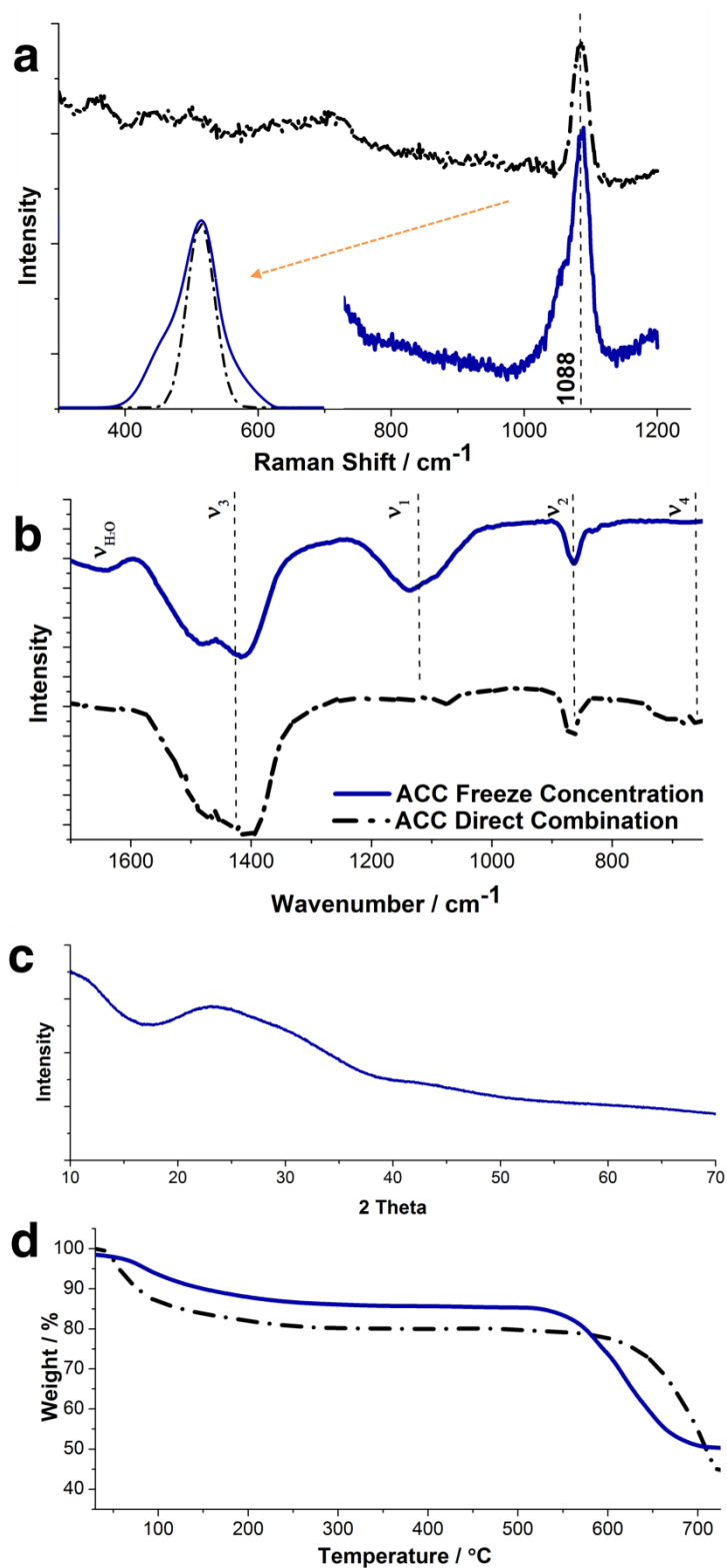


Figure 3 - 26: (a) Raman-, (b) IR spectra, (c) PXRD pattern and (d) TGA acquired of ACC obtained via freeze concentration and by direct combination. The inset in (a) shows a comparison of the peak widths of both samples 1088 cm^{-1} . (175)

3.4.3.2: Crystallisation of Freeze Dried ACC in Atmosphere

Based on the reduced water content of ACC prepared by freeze concentration and the observation of ACC dehydration in the case of coated ACC particles (Chapter 3.3.2), the structural transition of ACC prepared by freeze concentration under atmospheric conditions was investigated by IR and Raman spectroscopy. TGA was not possible due to the low sample quantities produced per experiment. ACC obtained after solvent sublimation was transferred onto glass slides, and analysed at regular intervals. In between analyses the sample was stored in a petri dish sealed with punctured Parafilm.

In the first instance, ACC obtained by freeze concentration showed a notable stability against crystallisation in ambient atmospheric conditions, crystallizing only after 6 weeks of storage (precipitation) as evident from Raman spectra in **Figure 3-27**. This is remarkable given that the reaction was not quenched using an ethanol wash, which partially replaces the surface water. ACC prepared by the direct combination of 1 M CaCl_2 / Na_2CO_3 and washed with isopropanol generally crystallizes within 24-48 hours.(93)

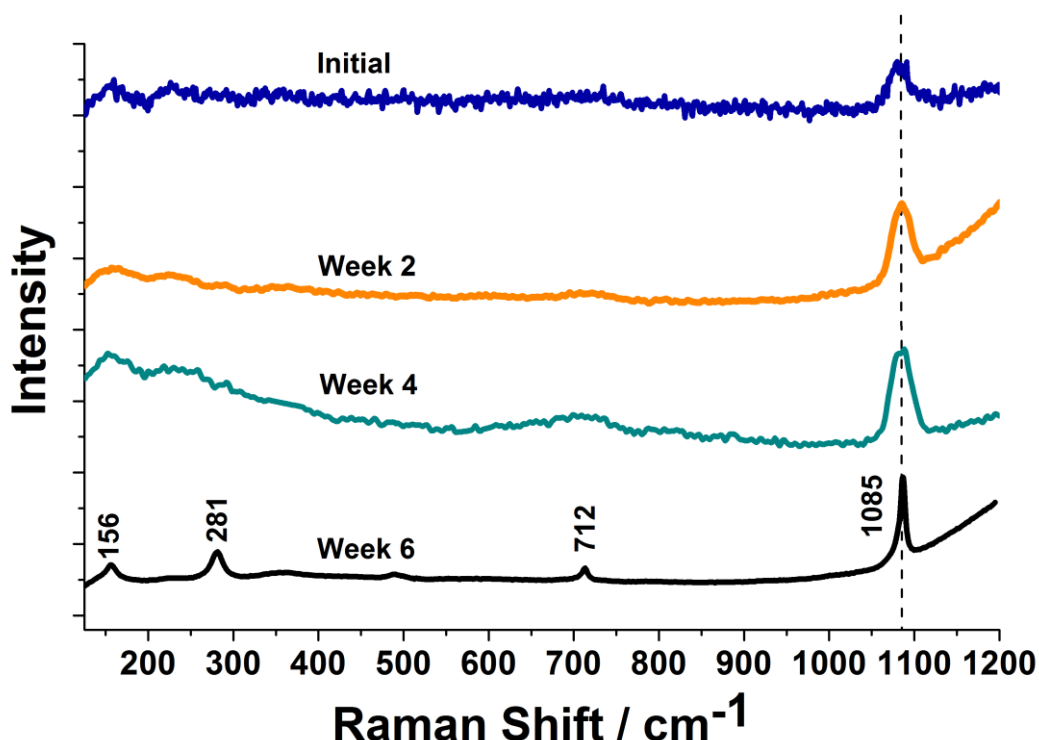


Figure 3 - 27: Raman spectra of ACC obtained via freeze concentration, held under ambient atmospheric conditions. Shown is a series of spectra collected over a time frame of 6 weeks.(175)

Figure 3-28, shows IR spectra which were in agreement with the observation made by Raman spectroscopy. They clearly show the transition of hydrated ACC to anhydrous ACC and eventually calcite/ vaterite. Importantly, they provide evidence of a gradually decreasing intensity in the vibrational band at 1641 cm^{-1} (highlighted in grey) which is associated with water, a shift in the ν_2 band and the appearance of calcite and vaterite selective (ν_4) bands with increasing storage time in atmosphere.

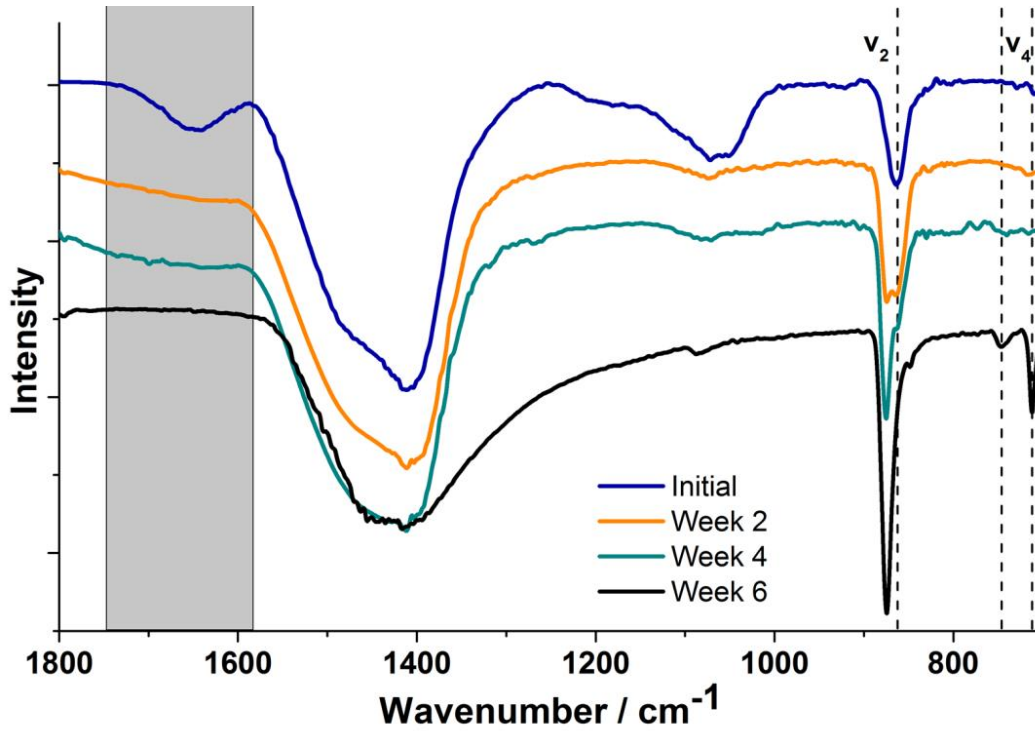


Figure 3 - 28: IR spectra of ACC obtained via freeze concentration, held under ambient atmospheric conditions. Shown is a series of spectra collected over a time frame of 6 weeks.

3.4.4: Translation to Amorphous Calcium Phosphate

Having established that ACC can be obtained by freeze concentration of saturated solutions, experiments were performed to test the generality of the developed method to form amorphous precursor phases. Studies were conducted to precipitate amorphous calcium phosphate and amorphous calcium oxalate (Chapter 3.5) by freeze concentration of saturated, aqueous solutions. Calcium phosphate was chosen as the primary target due to its importance and because the existence of an amorphous precursor phase (ACP) is well known and “structurally” defined.(236, 265, 266)

The required saturated “counter ion free” solution of calcium phosphate was generated by processes analogous to those used for calcium carbonate. The saturated solution of calcium phosphate was prepared by repeated dissolution and re-precipitation of calcium phosphate formed by mixing 200 mM $\text{CaCl}_2 \cdot 2\text{H}_2\text{O}$ with 200 mM $\text{Na}_2\text{HPO}_4 \cdot 7\text{H}_2\text{O}$.

Figure 3-29, provides an electron micrograph and an example EDX spectra of the precipitate generated by freeze-drying of the prepared calcium phosphate solution. Elementary units have an apparent diameter of ~50 nm, and consist primarily of calcium and phosphate.

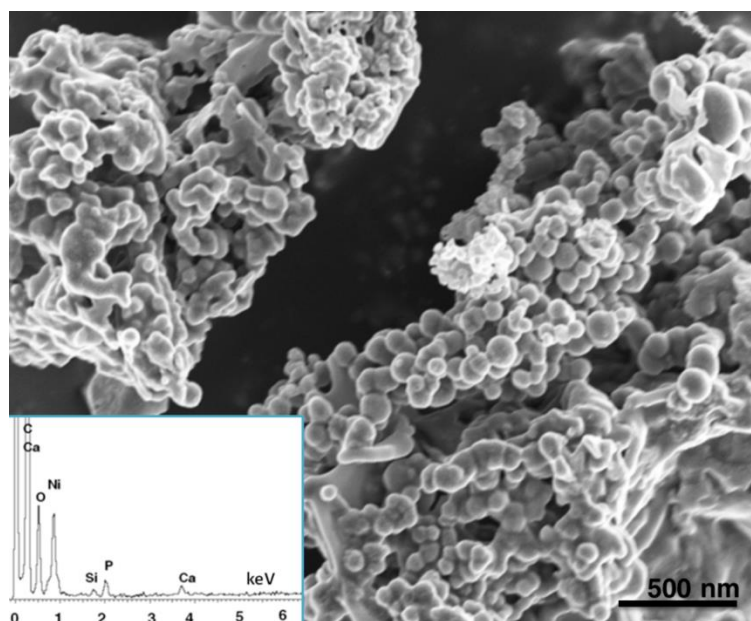


Figure 3 - 29: Electron micrograph and example EDX spectra of ACP obtained via freeze concentration of saturated calcium phosphate solution.(175)

Chapter 3: Amorphous Calcium Carbonate

Figure 3-30, shows Raman- (a), IR-spectra (b) and PXRD (c) patterns obtained from the generated calcium phosphate precipitate by freeze concentration. These confirm the formation of ACP based on comparison with the literature, and reference spectra of ACP prepared by a direct precipitation method (combination of equimolar of 200 mM CaCl_2 and $\text{Na}_2\text{HPO}_4 \cdot 7\text{H}_2\text{O}$). (266, 267) These comparisons confirm the formation of ACP by the presence of a single broad peak in the Raman spectra and the absence of bands associated with crystalline calcium phosphate in the IR spectra (Appendix A). The PXRD pattern reveals that the prepared sample is not 100% amorphous calcium phosphate. (d) The TGA of the obtained precipitate revealed a Ca/P ratio of ~ 1.70 which suggests a precipitate of composition $\text{Ca}_{1.7}(\text{PO}_4)_1(\text{OH})_{0.4}$ which resembles hydroxyapatite. (268)

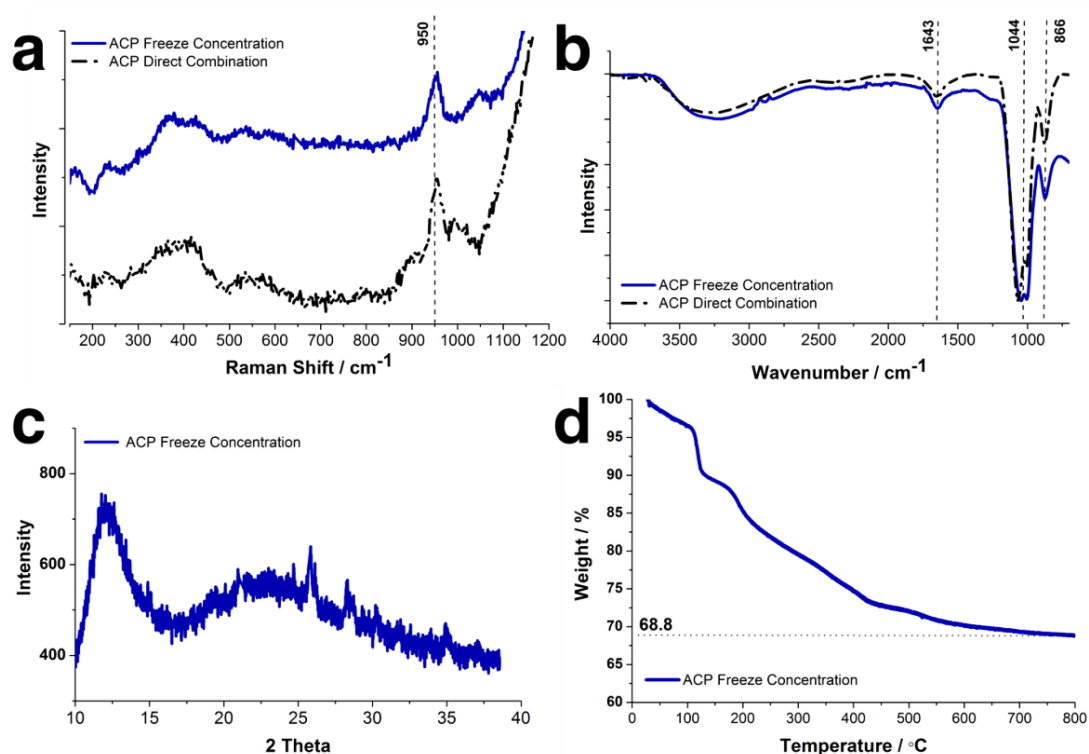


Figure 3 - 30: (a) Raman and (b) IR spectra of ACP obtained via freeze concentration and by direct combination of 200 mM CaCl_2 and 200 mM $\text{Na}_2\text{HPO}_4 \cdot 7\text{H}_2\text{O}$. (c) PXRD of ACP obtained via freeze concentration. (d) TGA of ACP obtained via freeze concentration. (175)

3.4.5: Discussion and Conclusion

In conclusion, a method was developed based on the freeze concentration of a counter-ion free solution of a mineral to reproducibly produce “pure”, amorphous mineral phases. The developed method was used here to produce amorphous solids of calcium carbonate, phosphate and oxalate (Chapter 3.5) which exhibited low levels of physisorbed and structural water.

In the case of ACC, this was shown to extend the atmospheric stability of the otherwise short-lived ACC. This indicates that the rapid atmospheric crystallisation observed for ACC precipitated from aqueous solution derives from excessive surface water, and that routine variations in the amounts of bound water and ethanol (from washing) may be the origin of many of the problems in obtaining ACC with reproducible properties.

The “one touch” procedure developed here overcomes some of the problems associated with common amorphous precursor syntheses, and may provide an effective route for determining the existence of amorphous precursor phases. The method has some downsides, which include the fact that the formation mechanisms of the amorphous precursor phase cannot be studied. Secondly, due to the inherently low starting concentration – which is equal to the solubility of the most stable polymorph – the method has a fixed maximal yield. The excessive volume to product ratio makes the process prone to the introduction of impurities if not handled carefully. Despite these negatives, however, the method is currently used by two independent research groups in the production of amorphous reference compounds.

Future work utilizing the developed method might include the combination of counter-ion free ACC with the general idea of ice templating/ freeze casting to form structured porous scaffold materials.(269-271) Here, freeze casting/ unidirectional freezing of an ACC precursor solution could be envisioned to provide a new route to the formation of minerals with complex shapes, and an alternative to existing methods such as negatively templated polymer structures.(50) Particularly interesting is that the amounts of secondary constituents e.g. occluded additives can be controlled based on alteration of the starting concentration. If successful in producing porous scaffold materials, the procedure could be used in the production of layered complex hereto-structures, where this could eventually result in the formation of composite materials currently generated using gel approaches.(272) First trials in this direction are currently under way.

3.5: Amorphous Calcium Oxalate

3.5.1: Introduction

The use of amorphous precursor phases of calcium carbonate and calcium phosphate by bio-mineralizing organism is now commonly accepted.(14, 23, 236, 265, 273) Utilized in vertebrates, invertebrates and embryophytes alike,(235, 274, 275) precursor phases offer themselves as dense ion storage phases and foremost as a transient, shapeable precursor to crystalline biominerals. Calcium oxalate biominerals, the next prominent biomineral within some plants (Embryophyta or Metaphyta) fulfil identical functions as to those seen for carbonates and phosphates and are shaped and assembled by similar mechanisms.(276) This starts from the active accumulation of reacting ions in specified cells, to the formation of mineral deposits in confined spaces to the transport and release at a particular destination.(122, 276, 277) Vascular bundles and epidermal cells use calcium oxalate deposits to harden protective tissues or to provide structural support as calcium carbonate is used in the sea urchin spine.(260, 278, 279) Another example is the exploitation of the mineral for simple protection against predators by means of calcium oxalate styloid and raphide crystals, whose functions resemble those of the protective spines in sea urchins. **Figure 3-31**, shows these raphide crystals (a-c) and the suggested mechanisms by which they form (d). This closely resembles sea urchin spine formation Chapter 1.4, Figure 1-13 In view of those similarities, the question arises as to whether calcium oxalate biomineralization follows the same path as calcium carbonate and phosphate – taking advantage of an amorphous precursor phase.

The mechanism of calcium oxalate precipitation in aqueous solution was investigated here, with the goal of determining whether an amorphous precursor phase is present in the early stages of precipitation. A range of methods that are known to kinetically stabilize amorphous precursor phases in solution (including the freeze-concentration method of saturated solutions and precipitation within the confines of track etch membrane pores and wedge geometries) were used to stabilize any possible amorphous phase formed, and thus aid its identification and characterization.(49, 157, 175)

Chapter 3: Amorphous Calcium Carbonate

In common with recent experiments which generated amorphous calcium oxalate (ACO) in ethanolic solution,(280) the confinement methods used here demonstrated that ACO particles ~10 - 50 nm in diameter can be formed in aqueous solution. ACO has an apparent composition of $\text{Ca}_2\text{C}_2\text{O}_4\cdot\text{H}_2\text{O}$. When crystallised in confinement, ACO or more specifically the resulting calcium oxalate crystal adopts to the confinement geometry. Studies of the precipitation of calcium oxalate in bulk solution and in the presence of crystal growth inhibitors rich in anionic groups performed here have indicated the presence of an amorphous precursor in solution.(157, 158, 281-284) It was not however not possible to isolate a homogenous amorphous precipitate from bulk experiments. These results suggest that organisms may use a combination of strategies to stabilize amorphous calcium oxalate in vivo, relying on limited contact of the ACO with bulk water and the presence of soluble crystallisation additives.

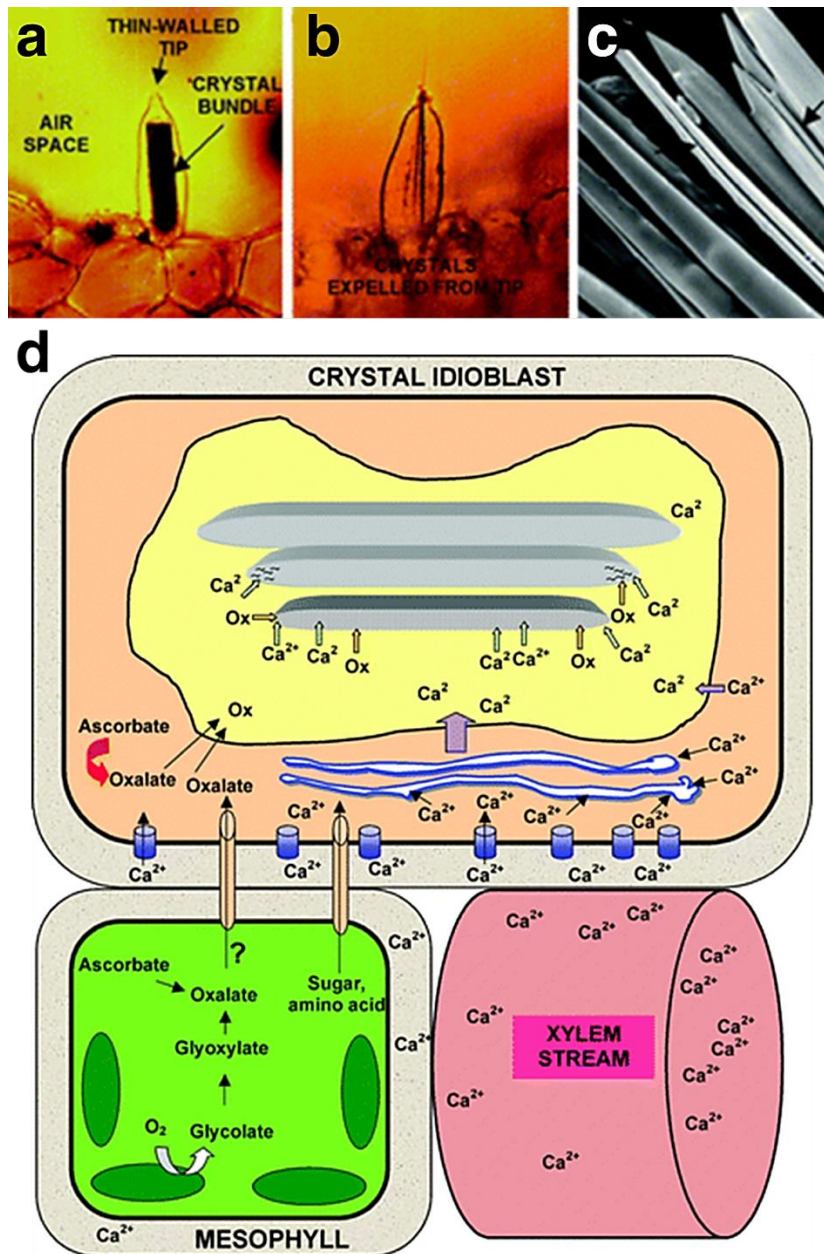


Figure 3 - 31: (a-c) Examples of calcium oxalate crystals used as active defence structures in plants. (a) A living raphide idioblast, (b) an idioblast after pressure is applied, the cell tip is cracked and the raphide crystals are forcibly expelled. (c) SEM of the raphide crystals displaying the sharp tips and grooves (→). (122) (d) Schematic depicting the idealized formation of calcium oxalate crystals in idioblasts. Calcium is actively accumulated with the xylem and is distributed among cells in the leaf via the cell wall, crystal idioblasts accumulate Ca via ion pumps. Oxalate can be generated from ascorbate in crystal idioblasts directly and transferred to the vacuole along with imported calcium. In this particular model, calcium and oxalate are transferred across the crystal chamber membrane and added to the growing facets. Crystals of particular length do no longer add Ca and oxalate, proteins interacting at the growing crystal facet may regulate precipitation or shape in this regard. The “mechanisms for transfer of Ca and oxalate to the vacuole and into the crystals have not been identified”(122). Reproduced after (122).

3.6.2: Results and Experimental

3.6.2.1: Bulk Precipitation

Calcium oxalate was initially precipitated in bulk across a range of supersaturation levels by the direct combination of equimolar solutions of NaC_2O_4 and CaCl_2 (0.25 - 100 mM). Solutions were degassed with nitrogen for 2 hours prior to usage to avoid the possible formation of calcium carbonate. Initial experiments were performed in the expectation of obtaining a homogeneous, nano-sized amorphous precipitate within 5 - 45 min of incubation in solution. This procedure is consistent with those used in the preparation of ACC and ACP.⁽¹⁷²⁾

This was not achievable here for calcium oxalate. Analysis of isolated samples prepared at different supersaturation levels after 15 minutes of incubation revealed the presence of a mixture of calcium oxalate polymorphs. At elevated supersaturation levels, the prominent polymorph in the sample was calcium oxalate monohydrate (COM), where this formed at starting concentrations greater than 10 mM. With decreasing supersaturation the prominent polymorph in the sample shifted towards calcium oxalate dihydrate (COD). Closer examination of the lower supersaturation range employed (which used starting concentrations of 5-0.25 mM), by scanning and transmission electron microscopy, **Figure 3-32(a-d)**, emphasizes this transition in polymorph precipitation.

The interesting aspect in the provided figure, where the goal was to identify and characterise ACO, is magnified in the inset in Figure 3-32(b). Visible in the inset are nano-sized precipitates of ill-defined shape, sitting on top a COD surface. The known amorphous precursor phases of calcium carbonate and calcium phosphate look exactly like this, a nano-sized precipitate of ill-defined shape. Sadly, due to sample heterogeneity - nano-sized precipitate sitting on top of crystalline calcium oxalate – characterisation techniques e.g. PXRD, IR - and Raman spectroscopy were inconclusive in determining the presence of an amorphous calcium oxalate phase (ACO).

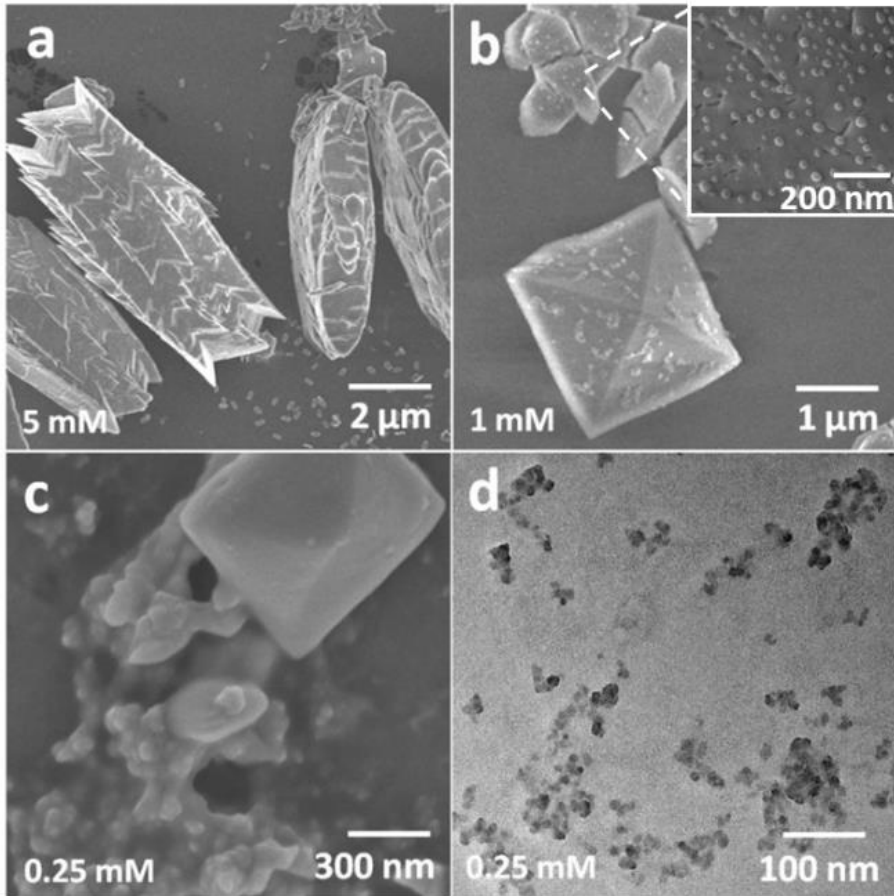


Figure 3 - 32: Electron micrographs of calcium oxalate precipitates extracted from bulk experiments. Samples were obtained by the direct equimolar combination of 10 ml CaCl_2 and 10ml $\text{Na}_2\text{C}_2\text{O}_4$. Starting concentrations are given on the left hand side. Samples prepared by Yun-Wei Wang.

3.5.2.2: Precipitation in the Presence of Additives

In an effort to stabilize ACO in bulk experiments, poly acrylic acid (PAA) was added to the $\text{Na}_2\text{C}_2\text{O}_4$ solution. PAA was chosen as an additive due to its similarity to the macromolecules present in biomineralizing organisms, in this it is rich in anionic groups and is a proven crystal inhibitor for calcium oxalate.(283, 285, 286) Provided in **Figure 3-33** are micrographs obtained from precipitates generated from solutions of composition 0.5-5 mM $\text{CaCl}_2/ \text{Na}_2\text{C}_2\text{O}_4/ (50\mu\text{g ml}^{-1})$ PAA). Evident is a particular change in precipitate morphology compared to the calcium oxalate formed in the absence of PAA.

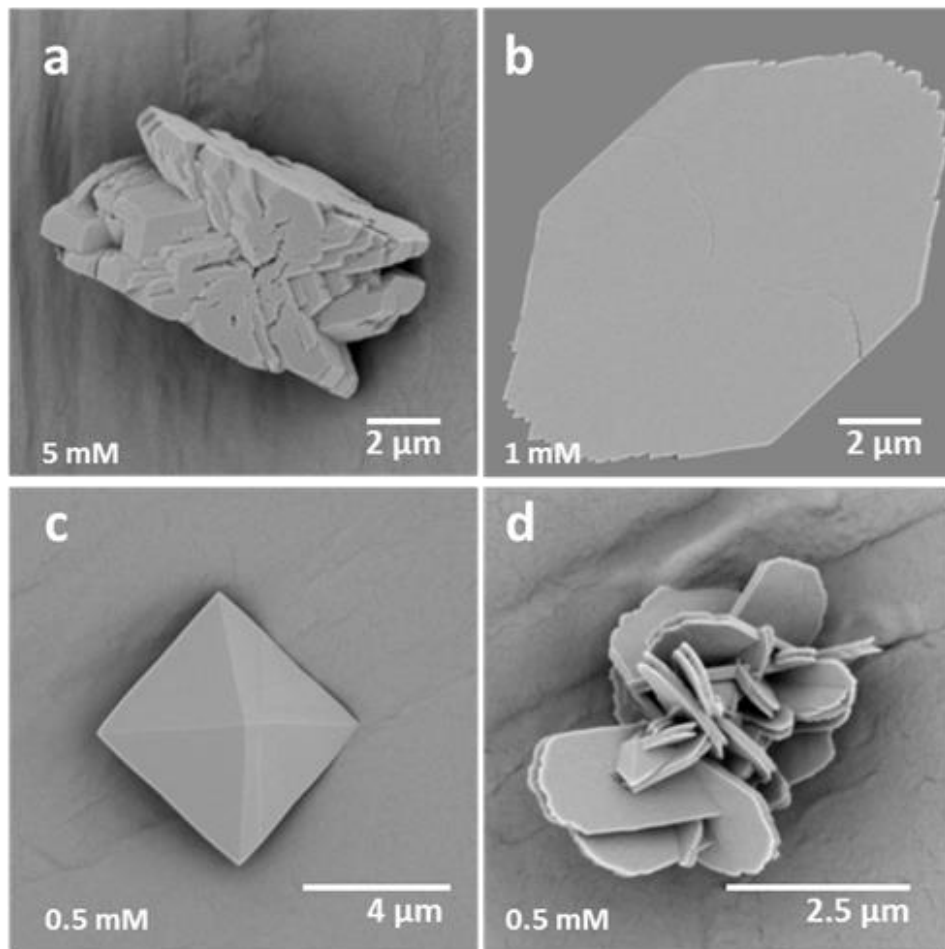


Figure 3 - 33: (a-d) Electron micrographs of calcium oxalate precipitates extracted from bulk experiments in the presence of PAA fixed at $50 \mu\text{g ml}^{-1}$. Samples were obtained by the direct equimolar combination of 10 ml CaCl_2 and 10ml $\text{Na}_2\text{C}_2\text{O}_4$. Stating concentrations are given on the left hand side.

Chapter 3: Amorphous Calcium Carbonate

Pure ACO could not be extracted from experiments performed in the presence of PAA. Instead, amorphous thin films, **Figure 3-34**, were detected on the mineralizing substrate in addition to small single crystals of calcium oxalate. The amorphous character was recognised as they were not visible under cross polarizers, inset (a). Upon heating the sample to 180°C, polycrystalline films are observable (b). Electron micrographs are provided in (c) and (d) respectively. The thin films of calcium oxalate obtained resemble thin films identified in calcium carbonate/ PAA precipitates.(60) These are generally associated with polymer induced liquid precursor phases, which are suggested to provide a precursor step to solid amorphous precursor formation.(33, 64, 208)

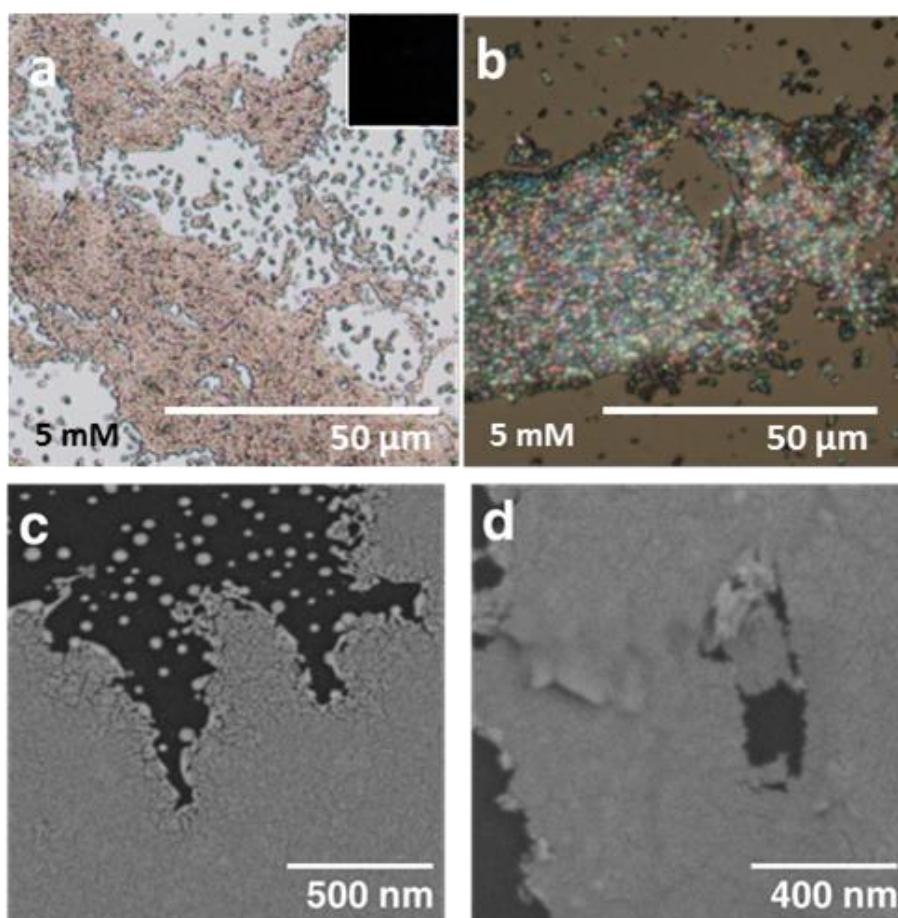


Figure 3 - 34: Micrographs of calcium oxalate thin films formed on the crystallisation substrate (glass). Presented in (a) is an optical micrograph of found film. Given in the inset is the sample under cross polarizers. (b) the film after heating to 180°C for 3 hours under crossed polarizer. Presented in (c) and (d) are electron micrographs of thin films as found present and after heating to 180°C for 3 hours. Precipitates were prepared by the direct combination of equimolar (5 mM) combination of 10 ml CaCl_2 and 10ml $\text{Na}_2\text{C}_2\text{O}_4$ / $50 \mu\text{g ml}^{-1}$ PAA.

3.5.2.3: Precipitation in Confined Volumes

In further efforts to temporarily stabilize ACO, calcium oxalate precipitation was confined to small volumes, which were previously shown to be successful in stabilizing ACC and ACP.

Initial confinement studies kinetically arrested the precipitation of calcium oxalate within 20 µl droplets of 2 mM CaCl₂/ Na₂C₂O₄ placed in the confines of an **annular wedge**,⁽¹⁵⁷⁾ formed around the contact point of two crossed half cylinders (Glass tubes with diameters of 25 mm were cut to produce half-cylinders). Experimentally, the cylinders were mounted on Teflon holders to hold them in place. A TEM grid was placed between the two cylinders before they were brought into contact with the curved surfaces facing each other, a schematic of the experimental set-up is given in **Figure 3-35**. As is evident from the schematic, the set-up used provides a mean of investigating how 1D confinement affects crystallisation. This is achieved given the annular wedge configuration, which provides a continuously decreasing surface separation between the TEM grid and the half cylinder towards their contact point. The particular surface separation (h) or 1D confinement between the crossed cylinder and TEM grid or crossed cylinder halves can be estimated according to Equation 54.⁽¹⁵⁷⁾ R is equal to the radius of the half cylinder used and x equal to the distance away from the contact point at surface separation (h).

$$h = R - \sqrt{R^2 - x^2} \approx x^2/2R \quad (54)$$

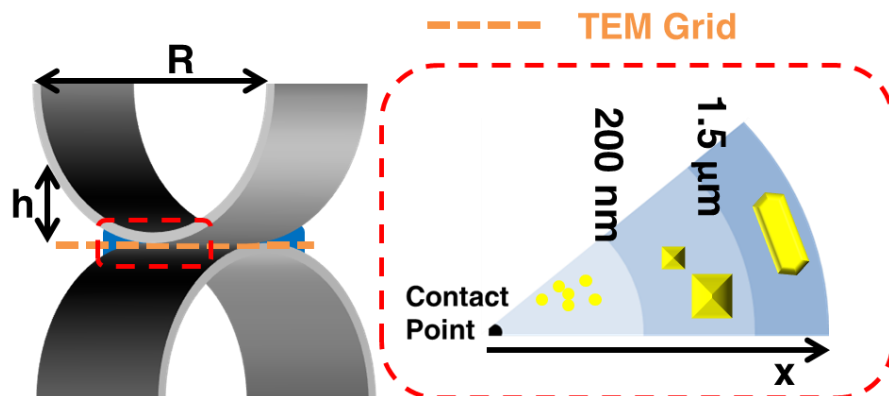


Figure 3 - 35: Calcium oxalate precipitation in wedge geometry. Provided is a schematic of experimental set-up, depicting the increasing surface separation/ decreasing 2D confinement away from the contact point of TEM grid and half cylinder.

Chapter 3: Amorphous Calcium Carbonate

Observations for the calcium oxalate experiments in wedge geometry are summarized in **Figure 3-36**. The 3 previously detected precipitate types COM, COD and ACO were detected here as well, where these appeared at different distances away from the contact point of the crossed cylinders (equivalent to different surface separations). Up to a surface separation of 1.5 μm COM is observed (a) where this is replaced by ill-defined COD as the surface separation decreases to 0.2 μm (c). Below this value, small spherical “amorphous” particles \sim 10-50 nm are detected (d) where these decrease in number density towards the contact point (e).

The occurrence of only one type of precipitate at a given surface separation allowed the analysis of individual precipitate types. Analysis was carried out by means of TEM and SAED. Electron diffraction patterns obtained from precipitates close to the contact point at a surface separation of $< 0.1 \mu\text{m}$ (f) returned an amorphous halo indicative of ACO. Continued beam exposure led to specimen decomposition rather than yielding a crystalline electron diffraction pattern. The radiation sensitivity of calcium oxalate is well known,⁽²⁸⁷⁾ where this contributes to the fact that despite the extensive literature of calcium oxalate, the presence of an amorphous calcium oxalate precursor (ACO) was until recently not explicitly stated.

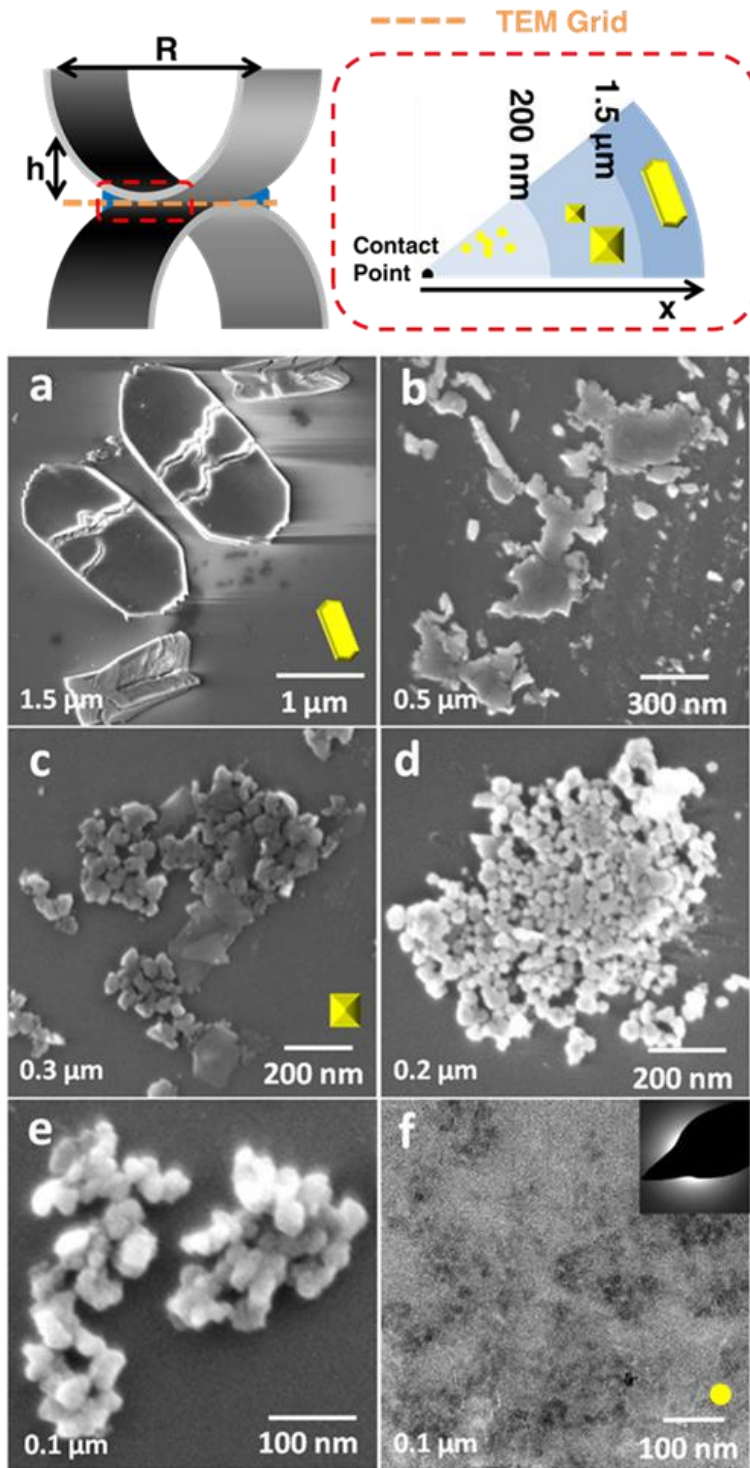


Figure 3 - 36: Calcium oxalate precipitation in wedge geometry. (a-f) provide electron micrographs of precipitates present at decreasing surface separation between the TEM grid and the cylinder. The surface separation for a given precipitate is provided on the left hand side of the respective image. Further provided is an electron diffraction pattern as inset in (f), which demonstrates the amorphous nature of present precipitates close to the contact point of TEM grid and crossed cylinders. Starting concentrations of 2 mM CaCl_2 and $\text{Na}_2\text{C}_2\text{O}_4$ were used. Experiment was performed by Yun-Wei Wang.

Chapter 3: Amorphous Calcium Carbonate

To avoid the problems associated with artefacts generated by continued beam exposure, calcium oxalate was precipitated in confinement within the **pores of a track etch membrane** to stabilize the ACO.

In the U-tube set-up used, (**Figure 3-37a**) solutions of CaCl_2 (2 mM) and $\text{Na}_2\text{C}_2\text{O}_4$ (2 mM/ PAA ($50 \mu\text{g ml}^{-1}$)) were added separately, each to one arm, of a U-tube between which a track etch membrane of 200 nm pore size (polycarbonate track-etch membranes Isopore, Millipore) had been mounted. In this way it was possible to force the precipitation of calcium oxalate to occur inside the pore spaces by cross diffusing ions from the respective U-tube arms.

Experimentally, membranes were initially plasma cleaned and were then degassed in water at reduced pressure to ensure complete filling of the membrane pores with solution. The wetted membranes were mounted between two U-tube arms which were then filled with solutions. Intra-membrane particles were then isolated either after 12 hours or 2 weeks by dissolution of the membranes in dichloromethane. After precipitation, membranes were rinsed with ethanol, their surfaces were scraped with a cover glass and they were then wiped with filter paper to remove the majority of surface-bound crystals. After brief sonication of the membranes in ethanol, they were subjected to at least 3 cycles of sonication in dichloromethane/ centrifugation and exchange of the solvent for fresh. The isolated precipitates were rinsed with methanol to remove residual dichloromethane, and were finally washed with ethanol before being pipetted onto a TEM grid/ glass piece for analysis.

The resulting rod-shaped calcium oxalate crystals were removed from the membrane pores by dissolution of the membrane material either after 12 (i) hours or after 2 weeks (ii). SEM and low dose TEM images, of the calcium oxalate “rods” are presented in Figure 3-37 (b) and (c) respectively.

Confining the precipitation of calcium oxalate to a fixed location, as done here, offers one great advantage as compared to confinement in an annular wedge geometry. One can be sure that the “same” precipitate can be located at the same place, independent of incubation time. The extraction of such an “immobile” deposit after various incubation times in solution, and the subsequent comparison of initially obtained SAED pattern with a pattern obtained at a later time (d), allows the differentiation between what was an initially amorphous deposit (ACO) (i) and is now crystalline calcium oxalate (ii). These analyses clearly demonstrated that the “mature” rods were single crystals of COM. The initial amorphous calcium oxalate rods (i) displayed an apparent average length of $\sim 2 \mu\text{m}$, while the crystalline rods (ii) were slightly longer on average $\sim 4 \mu\text{m}$.

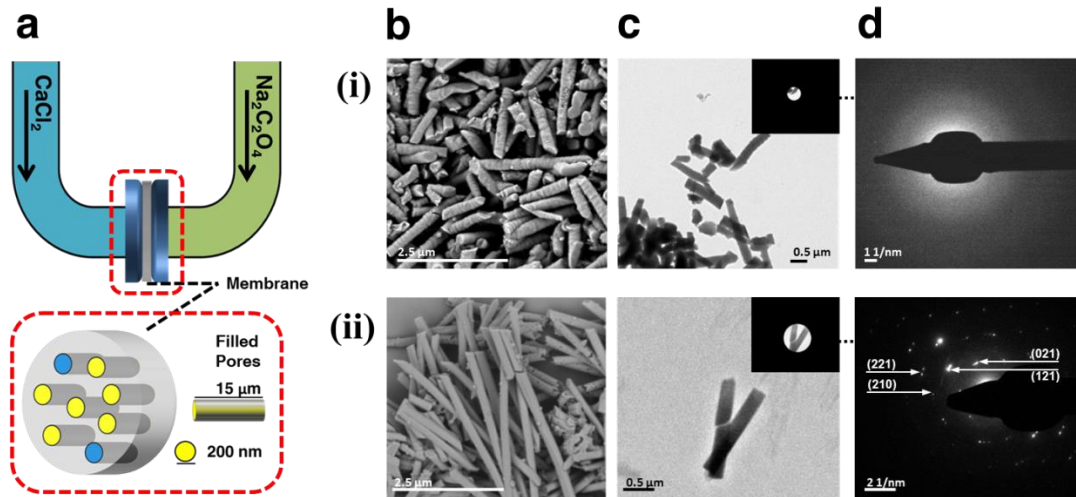


Figure 3 - 37: Calcium oxalate precipitated in track-etch membranes. (a) schematic of experimental set-up used. Further provided are (b) scanning – and (c) transmission electron micrographs. (d) TEM corresponding electron diffraction patterns obtained from rod shaped precipitate after 12 hours (i) in solution and after 2 weeks (ii). (ii) Diffraction pattern is corresponding to COM. Starting concentrations of 2mM CaCl_2 and $\text{Na}_2\text{C}_2\text{O}_4$ / (PAA 50 $\mu\text{g}/\text{ml}$) were used.

3.5.2.4: Precipitation via Freeze Concentration

Having established that ACO can form in an aqueous mineralizing solution, an effort was made to obtain structural and compositional information.

Pure ACO was obtained by rapid freezing and sublimation of saturated, counter ion free calcium oxalate solutions, **Figure 3-38**.(175) Selective solvent removal during plunge freezing of a saturated solution in liquid nitrogen forces the precipitation of ACO and/ or crystalline polymorphs to occur (depending on the freezing rate). Precipitation occurs as a result of increasing superstition as the free solution volume decreases. Total solution solidification temporarily stabilizes the formed precipitate, while subsequent ice sublimation releases formed precipitate for analysis.

The experimentally-required counter-ion free, saturated CaC_2O_4 solutions were produced from solid CaC_2O_4 (Sigma, 99.999 % trace metals basis). Saturated solutions were then prepared by adding 20 mg of “pure” CaC_2O_4 to 500 ml DI water, and were stored for 24 hours at room temperature before centrifuging to remove the majority of any remaining un-dissolved calcium oxalate. This saturated solution was then heated to remove possible ghost nuclei, and was then filtered through a 0.2 μm membrane filter. Freezing of the prepared saturated solutions (5-40 ml) was achieved by plunge immersion into a liquid nitrogen bath, followed by a 10 minute annealing period to strengthen the ice structure.

Electron micrographs of the precipitate, after sublimation are given in Figure 3-38 (a). The precipitate appears similar in appearance and size (~40 nm) to ACO obtained by mineralisation in bulk and the ACO found in annular wedge experiments. Presented in (b) is a featureless electron diffraction pattern obtained from ACO prepared by this method. This confirms the amorphous nature of the precipitate.

Provided in (c) are Raman spectra of ACO as prepared and after 2 weeks stored in air. Evident is the transformation of the initially present ACO to COM. The spectra of ACO is different from COM based on peak broadening and the resulting peak amalgamation of asymmetric and symmetric stretching modes (C=O) located around ~ 1475 cm^{-1} and ~ 505 cm^{-1} (deformation of CO_2), as recently observed for ethanolic ACO.(280) Both broadening and peak mergence are indicative of increased structural disorder.

Chapter 3: Amorphous Calcium Carbonate

Presented in (d) are IR spectra of the produced ACO and COM, which reveal a transition from structurally disordered H₂O (~3300 cm⁻¹) present in the ACO, to ordered H₂O as COM is formed. The re-organisation of H₂O molecules into a structured order is evident in the more defined appearance of the ~3300 cm⁻¹ “peak”, which reveals the presence of multiple vibration bands. Reference “spectra” of calcium oxalate are also provided in Appendix A.

Thermo gravimetric analysis of prepared ACO (e) revealed a stepwise decomposition of the formed precipitates. The decomposition starts with the gradual loss of structural and surface water (~ 14.4 wt%) up to 220°C, beyond which the classical sequential decomposition of calcium oxalate to calcium carbonate (470°C - 15.5 wt%) and calcium oxide (630°C – 29.2 wt%) is observed.⁽²⁸⁸⁾ Based on the amount of calcium carbonate formed and the observed weight loss associated with H₂O, a molecular composition of ~ CaC₂O₄:H₂O was calculated. It has to be noted that simultaneously performed differential scanning calorimetry (DSC) did not register an amorphous to crystalline transition of ACO upon heating. Further, the observed weight loss associated with the transition of calcium oxalate to calcium carbonate formation does not correspond to the theoretical value of this transition. One reason for this discrepancy may be the presence of impurities in the sample. A second reason could be that formed ACO has a different stoichiometry, different from a 1 to 1 ratio (Ca:C₂O₄).

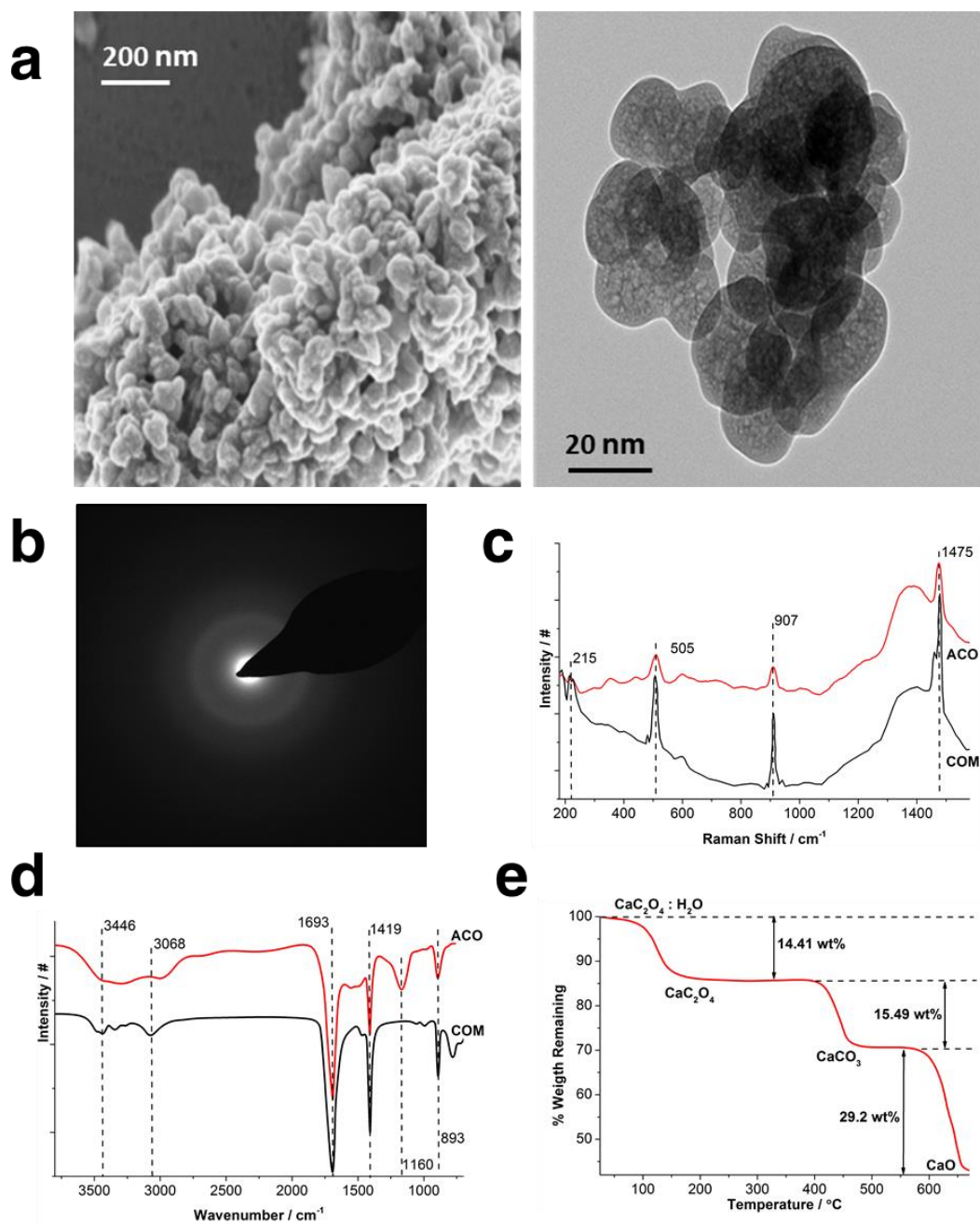


Figure 3 - 38: Amorphous calcium oxalate prepared by rapid freezing of saturated solutions. Presented in (a) are scanning and transmission micrograph of the obtained ACO. (b) SEAD diffraction pattern. Further given are structural and compositional information of the formed ACO. The acquired Raman and IR spectra are given in (c) and (d) respectively, together with their spectra after atmospheric crystallisation to COM (ACO in red, COM in black). Raman spectra were collected on a glass substrate. TGA is presented in (f), a heating rate of $15^\circ\text{C min}^{-1}$ was used. Data was collected under N_2 flow.

3.5.3: Discussion

The detection and characterisation of ACO in mineralizing solutions is not unexpected. It also suggests that an amorphous phase may play a role in the formation of calcium oxalate kidney stones or oxalate bodies in certain plants.(276, 289) A question that needs addressing, however, is why ACO is so difficult to observe and isolate from solution as compared with ACC and ACP.

One factor clearly associated with the difficulty of ACO observation is its beam/radiation sensitivity. Despite similarities in the reacting anion ($C_2O_4^{2-}$ vs CO_3^{2-}) and final solubility ($\sim 10 \text{ mg l}^{-1}$ for Calcite, $\sim 6 \text{ mg l}^{-1}$ Whewellite (COM)) a second factor contributing to the difficulty in observation can be that the solubility of ACO and its formation kinetics are much closer to the next polymorph than they are for ACC and vaterite, for example. The system therefore has less to gain by forming an amorphous precursor phase (the driving force for forming a more stable crystalline force is similar).. A third explanation could lie in the apparent size limit of the particles, which is $< 50 \text{ nm}$ for ACO and $> 100 \text{ nm}$ for ACC.(137, 216) Assuming these size limits are defined by the particles' surface energy, species with a smaller critical size relative to the next stable phase nucleating in solution will destabilize faster as the particle continues to growth. This results in a faster dissolution of particles with a smaller critical size.(140)

The observed stabilization of ACO within membrane pores and a wedge geometry can be thought to arise due to kinetic factors. Limited access to the bulk water delays a potential dissolution/ reprecipitation mechanism.(95, 162) Why ACO forms in the first place in confined volumes is a completely different question and this is currently under investigation.(156)

3.5.4: Conclusion

The work presented here provides initial evidence for the existence of amorphous calcium oxalate in aqueous solution. Amorphous precursor units of ~10-50 nm with an apparent composition of $\sim \text{CaC}_2\text{O}_4 \cdot \text{H}_2\text{O}$ could be kinetically stabilized in confined geometries < 200 nm. A pure phase in bulk or in the presence of additives has not yet been isolated. Despite this, isolated ACO could be detected together with crystalline polymorphs at reagent concentrations of 1 mM. This is indicative of a reduced kinetic precipitation advantage and a size-dependent stability of ACO. Continuing investigations will try to confirm the presence of ACO in biominerals.

Chapter 3: Amorphous Calcium Carbonate

Chapter 4: Characterisation of Diffusion Methods Towards an understating of Mesocrystal formation



Chapter 4: Characterisation of Diffusion Methods

Chapter 4 is primarily a reproduction of the following publication.

Ihli J, Bots P, Kulak A, Benning LG, Meldrum FC. Elucidating Mechanisms of Diffusion-Based Calcium Carbonate Synthesis Leads to Controlled Mesocrystal Formation. *Adv Funct Mater* 2013, **23**(15): 1965-1973.

Supplemented by results obtained from a succinctly published study and work performed concurrently.

Kim Y-Y, Schenk AS, Ihli J, Kulak AN, Hetherington NBJ, Tang CC, Schmahl WW, Griesshaber E, Hyett G, Meldrum FC. A critical analysis of calcium carbonate mesocrystals. *Nat Commun* 2014, **5**.

4.1: Abstract

Calcium carbonate is arguably the most-studied inorganic mineral, due to its environmental and industrial importance and because it provides an excellent model system for developing methods for controlling nucleation and crystal growth. However, despite being widely studied, CaCO_3 is frequently precipitated using diffusion-based techniques which are poorly-characterized and offer low reproducibility. Utilization of these methods is founded on the observation that diffusion methods give rise to crystals with complex morphologies thought to be built on aggregation-based crystal growth. These morphologies are supposedly not attainable by other means, particularly for crystals grown in the presence of organic additives.

In the following work, advantage was taken of this feature of diffusion methods to develop a one-pot method capable of generating crystal morphologies that are considered characteristic of aggregation-based growth. This was achieved by characterization of the widely used ammonia diffusion method (ADM) currently used as a “black box”. Identifying the solution and supersaturation conditions which accompany CaCO_3 precipitation allowed us to gain insight into the nucleation and growth processes which generate those morphologies. The study reveals a number of features that are specific to the method studied. This includes a prolonged period of “constant” supersaturation past the initial nucleation event, which is at levels well above the threshold for amorphous calcium carbonate formation. New material is therefore potentially nucleated over the entire course of an experiment, a feature which appears to be fundamental to the formation of complex morphologies. The power of this understanding is then demonstrated by using the identified carbonate and supersaturation profiles to successfully replicate the formation of CaCO_3 “mesocrystals”, which had previously been limited to the ADM method, through slow addition of reagents to a bulk solution and the enzymatic hydrolysis of urea. These approaches overcome many of the inherent problems of the ADM by offering excellent reproducibility, enabling the synthesis of such CaCO_3 structures in large-scale and continuous-flow systems, and ultimately facilitating in situ studies of assembly-based crystallisation mechanisms. Initial studies using this method revealed - in conjunction with high resolution PXRD studies - that the classification of CaCO_3 “mesocrystals” may be incorrect.

4.2: Introduction

Significant efforts have been made to synthesize crystals with defined sizes, morphologies and structures for applications in areas as wide-ranging as pharmaceuticals, biomaterials and nanomaterials.(23) In order to achieve control over these features it is necessary to understand the mechanisms by which crystals form. At one end of the spectrum, the classical picture of crystallisation from solution envisages crystal growth to occur via ion-by-ion, or molecule-by-molecule addition to an established nucleus to give a single crystal product.(290) At the other, if growth of the individual nuclei is slow, then aggregation can dominate, leading to the formation of polycrystalline particles. Importantly, such aggregation-based processes often lead to crystalline particles with unusual morphologies, such as fibers,(291, 292) and “microtrumpets”(293) which cannot be accessed through classical growth processes.

Aggregation-based crystal growth is currently receiving considerable interest.(290, 294-296) While the formation of polycrystalline particles based on non-oriented aggregation of nanoparticles has been recognized for a long time, single crystal formation through the oriented aggregation of precursor nanoparticles is a rather new finding.(297) One prominent example of this is the work of Banfield and co-workers which showed the formation of single crystal titania through nanoparticle aggregation,(298) a phenomenon they also observed in iron oxide systems,(66) and recently in the calcium sulfate system.(299) It is now well-established that many crystals grow by aggregation under appropriate experimental conditions, and that a number of mechanisms can operate, ranging from the oriented aggregation of crystalline nanoparticles to the aggregation and then subsequent crystallisation of amorphous nanoparticles.(294) While these processes can lead to single crystals indistinguishable from those formed by classical growth mechanisms, the crystals produced can also retain a memory of the precursor particles from which it forms. In this case, the crystal is classified as a mesocrystal, which ideally comprises a 3D array of iso-oriented single crystal particles of size 1–1000 nm.(67) The ultrastructure of such a mesocrystal clearly contributes to defining its properties, as exemplified by sea urchin spines. These calcium carbonate single crystal biominerals have recently been classified as “mesocrystals”, where the nanoparticulate sub-structure and residual amorphous calcium carbonate may contribute to their remarkable mechanical properties.(67, 300)

Chapter 4: Characterisation of Diffusion Methods

Although aggregation-based growth promises the ability to produce crystals with unique morphologies and internal structures, this can only be achieved by elucidating the mechanisms by which aggregation occurs. Moving towards this goal, we here focus on calcium carbonate as an important mineral,(23, 78) which grows apparently by aggregation under appropriate experimental conditions. Our approach is based upon the common observation that diffusion-based methods, including the double diffusion,(49, 136) the Kitano(105) and the ammonium carbonate diffusion method(301, 302) often generate unusual crystal morphologies which cannot be accessed by other methods. This appears to be particularly true for additive-directed crystal growth, as exemplified by polymers such as poly(styrene sulfonate) or poly(4-styrenesulfonate- maleic acid) (PSS-MA), which have to-date only yielded calcium carbonate mesocrystals when using diffusion methods.(303-305)

This work characterizes the physico-chemical changes in solution which accompany CaCO_3 precipitation by the most widely used of these diffusion-based methods – the ammonium diffusion method (ADM) – where CaCO_3 precipitation is induced by exposing a solution of calcium ions to the vapor released on the decomposition of solid ammonium carbonate in a hermetically-sealed container (**Figure 4-1**).(301, 302) This was achieved by performing time-resolved measurements of solution pH, carbon and calcium ion concentrations, and identifying how these are determined by key variables including the Gas-Liquid interfacial area, the CaCl_2 concentration, the initial mass of ammonium carbonate, the stirring rate and the presence of a secondary diffusion barrier. A unique insight into the ADM is therefore generated by (i) identifying the variables which principally dictate the precipitation products and (ii) determining for the first time the carbon addition rates, the supersaturation and reaction profiles.

To demonstrate the power of this understanding, we then use the identified carbon addition rates to reproducibly precipitate CaCO_3 mesocrystals in the presence of PSS-MA, by secondary and tertiary means. The ability to prepare such CaCO_3 mesocrystals using alternative synthetic methods opens the door to industrial scale and potentially one-pot syntheses,(65) and will ultimately facilitate *in situ* studies of mesoscale assembly. A first step in this direction was taken here, which revealed that the bulk analysis of formed CaCO_3 mesocrystals may not be the way to go. This work ultimately questioned the validity of CaCO_3 mesocrystals, and more specifically the measured characteristics which can be used to distinguish mesocrystals from classical crystals.

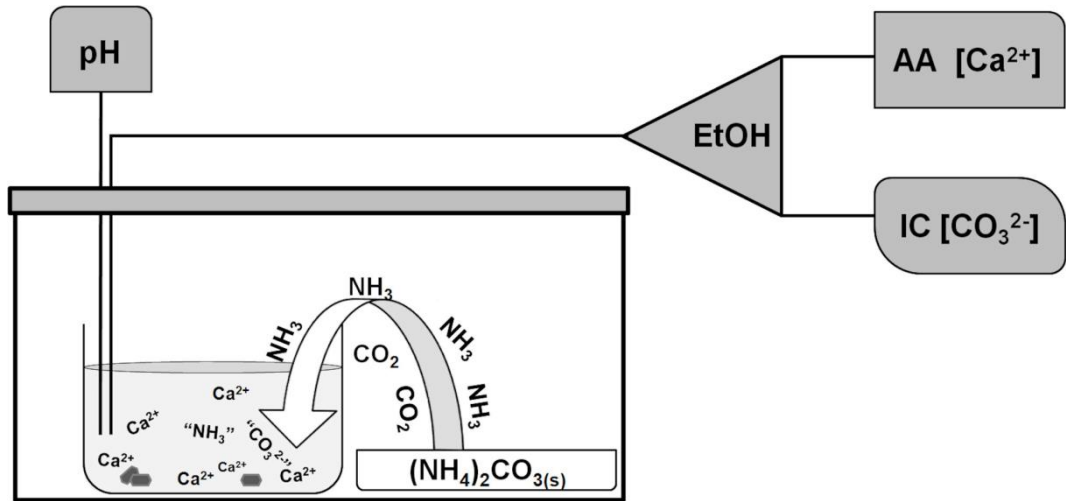
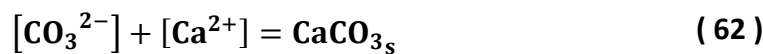
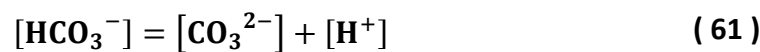
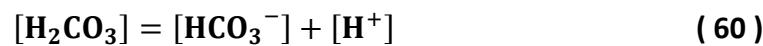
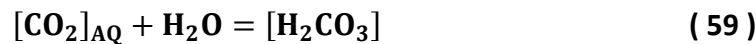
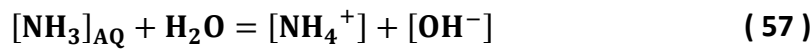
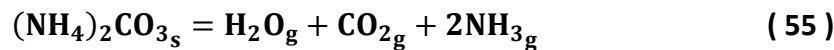


Figure 4 - 1: Schematic diagram of the experimental set-up and methods used to determine the concentrations of aqueous Ca^{2+} and CO_3^{2-} ions. Aliquots were removed with time and quenched with ethanol, the [Ca^{2+}] was determined using atomic absorption (AA), and the [CO_3^{2-}] using ion-chromatography (IC). Image taken from (169).

4.3: Characterising the ADM: Experimental and Results

4.3.1: General Description of the Ammonia Diffusion Method

The ammonium diffusion method is characterized by two distinct steps, the first being the rapid saturation of the gas phase with CO₂ and NH₃ and the subsequent diffusion of the CO₂ and NH₃ molecules across the gas-liquid interface into the solution. In the slower, second step, the aqueous carbon dioxide reacts with the solution water to form carbonic acid, which in turn deprotonates to give both carbonate and bicarbonate ions, where the ratio of these species is defined by the solution pH. The dissolved NH₃, in turn, increases the pH of the solution. In combination with the calcium ions present, a solution that is supersaturated with respect to CaCO₃ is generated. The equations describing the solution equilibria are given in Equation 55--62.



The ADM was initially characterized from a standard set-up using 70 ml of 25 mM CaCl₂, with an air/solution surface area of 48 cm², 3 g of uncovered (NH₄)₂CO_{3s} and 2.6 L free volume in the reaction chamber. Time-resolved measurements were made of the key solution variables (namely the pH and the calcium and carbonate concentrations), which together yielded the carbon addition rates and underlying supersaturation profiles. Typical graphs showing the time-resolved changes in (a) turbidity (transmittance), (b) pH, (c) supersaturation, (d) calcium activity, (e) carbonate activity and (f) crystallisation progress are presented in **Figure 4-2**. The turbidity measurements show a rapid decrease at ~15 mins (Figure 2A). This is likely caused by the formation of detectable amounts of calcium carbonate

Chapter 4: Characterisation of Diffusion Methods

precipitate, which reveals an induction period of 15 mins. The rapid drop in transmission after 15 min is associated with the formation of amorphous calcium carbonate (ACC) which subsequently transforms to vaterite and ultimately calcite, as confirmed by Raman and IR spectroscopy (**Figure 4-3**). The small increase in transmission at around 20 mins is observed in almost all experiments, and may result from the transition of ACC to a crystalline phase. (136, 256)

The turbidity measurements are also consistent with the pH data (Figure 4-2b). Knowledge of the solution pH is critical to understanding the ammonia diffusion method as it governs the distribution of aqueous carbonate speciation, and is required to determine the fraction of carbonate in the total carbon content measured. (168) A higher pH is associated with an increase in the concentration of carbonate at the expense of bicarbonate, and also promotes the dissolution of gaseous carbon dioxide into the CaCl_2 solution, through its conversion to bicarbonate or carbonate. (306) This process is reflected in the jump in supersaturation observed between 10 and 20 minutes (Figure 4-2c). Nucleation of CaCO_3 therefore only occurs after a critical pH/ supersaturation has been reached (at pH ~ 8.5), which marks the partial transformation of bicarbonate to carbonate. As shown in the data, this pH value is coincident with the induction point recorded using turbidity measurements. The pH then continues to increase until it reaches a value of ~ 9.8 , where it remains rather constant ($\text{CO}_3^{2-}/\text{HCO}_3^- \approx 0.38$) until the crystallisation is almost complete. It then decreases very slowly to a constant value of ~ 9.2 after about 20 hours (**Figure 4-4**).

These data therefore indicate that in the ammonia diffusion method, initial ACC nucleation (at the induction point of ~ 15 minutes) occurs above an ACC supersaturation threshold of > 10 . Further, initial crystallisation takes place under an excess of calcium ions, such that the ratio of calcium to carbonate ions is ~ 2.2 . Comparison with alternative CaCO_3 precipitation methods therefore shows that the ADM results in initial ACC precipitation at relatively low supersaturation levels. Indeed, precipitation of ACC using the direct precipitation method, (307) (where 1 M calcium and carbonate solutions are combined and precipitation occurs after an induction period) occurs at $S_{\text{ACC}} > 100$, while supersaturations of $S_{\text{ACC}} > 30$ at pH > 12 are associated with Koga's method, (129) (where calcium and high pH carbonate solutions are combined giving immediate precipitation). These supersaturation values were calculated using Visual MINTEQ (Software to model the chemical equilibrium composition of a solution.) based on experimental parameters provided in these papers. As a further distinction between these different precipitation methods, the direct and Koga's method remove up to 90% of the total precipitation pressure via the initial burst of ACC formation. In contrast, in the ADM, the calcium and reaction profiles tend toward classical S shapes.

Chapter 4: Characterisation of Diffusion Methods

Following the onset of nucleation, the calcium ion profile undergoes an extended linear decrease due to its consumption in CaCO_3 precipitation (Figure 2d), while continued release of fresh ammonium carbonate vapour into the reaction chamber (which continues until equilibrium is reached after ~ 20 hrs) supports an increase in the solution carbonate concentration (Figure 2e). Consequently, the supersaturation continues to increase after the induction point until it peaks at its maximum value of ~ 180 between 60-80 mins under these reaction conditions. The supersaturation then decreases only very slowly, due to the continued introduction of carbonate into the solution. High supersaturation levels, which are well above the critical value for ACC, are therefore maintained even when a significant proportion of Ca^{2+} ions have been consumed. This prolonged period of high supersaturation is a key feature of the ammonia diffusion method and would be expected to support multiple nucleation events.

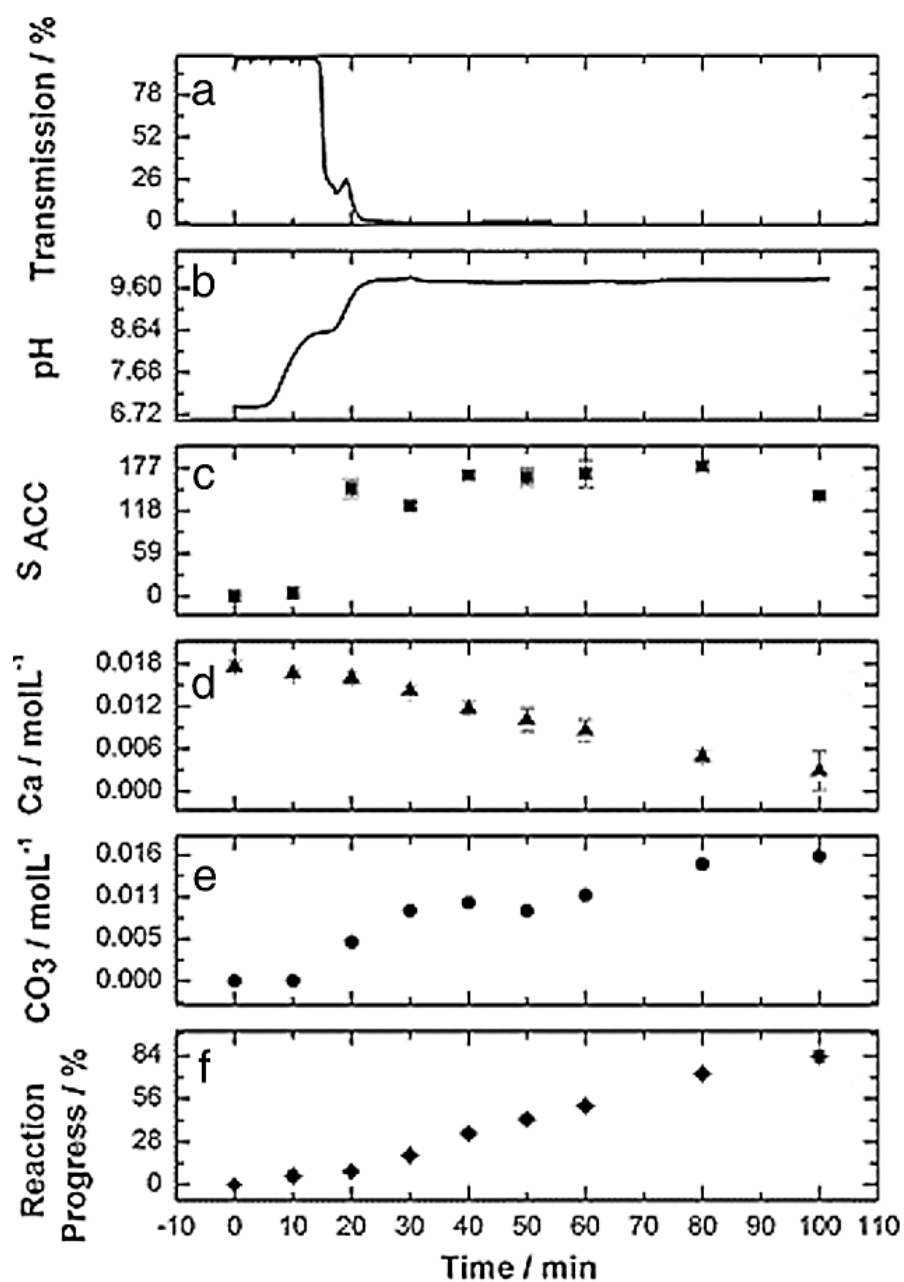


Figure 4 - 2: Time-resolved profiles of calcium carbonate precipitation using the ADM, with reaction conditions: 25 mM CaCl₂, 70 ml, 3 g ammonium carbonate, 2.6 l reaction chamber, no additional diffusion boundaries. The data shown are averages of three experiments, and the error bars show the standard deviation in the values. (a) Transmission, (b) pH, (c) supersaturation, (d) calcium activity, (e) carbonate activity, (f) crystallisation progress.(169).

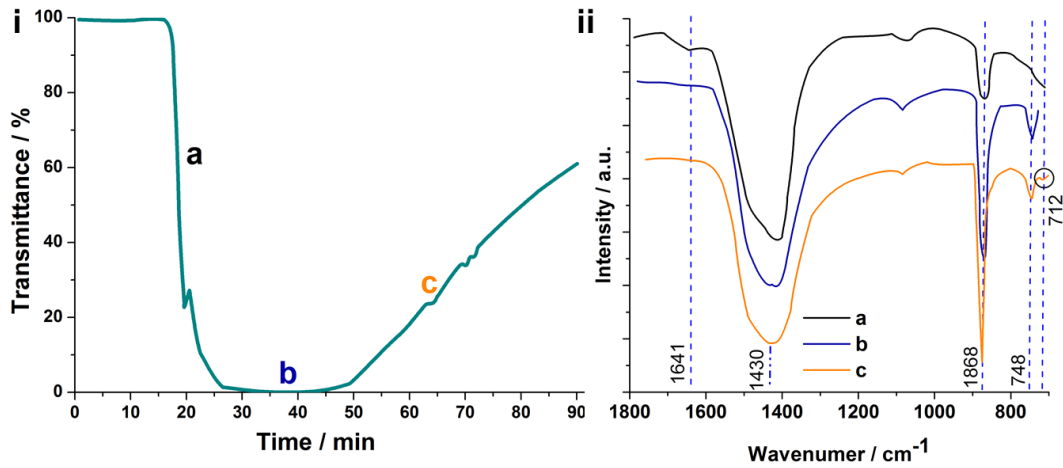


Figure 4 - 3: (i) Time-resolved transmittance profile showing the change in transmittance occurring during CaCO₃ precipitation using the ammonia diffusion method (70 ml, 25 mM CaCl₂, A = 48 cm², 3 g ammonium carbonate, 2.6 l head space, no additional diffusion boundaries). (ii) IR analysis of samples isolated at key times in the reaction were (a) ACC, (b) vaterite and (c) calcite. Here, the peak at 748 cm⁻¹ is a fingerprint for vaterite, while the peak at 712 cm⁻¹ identifies calcite. Image taken from (169).

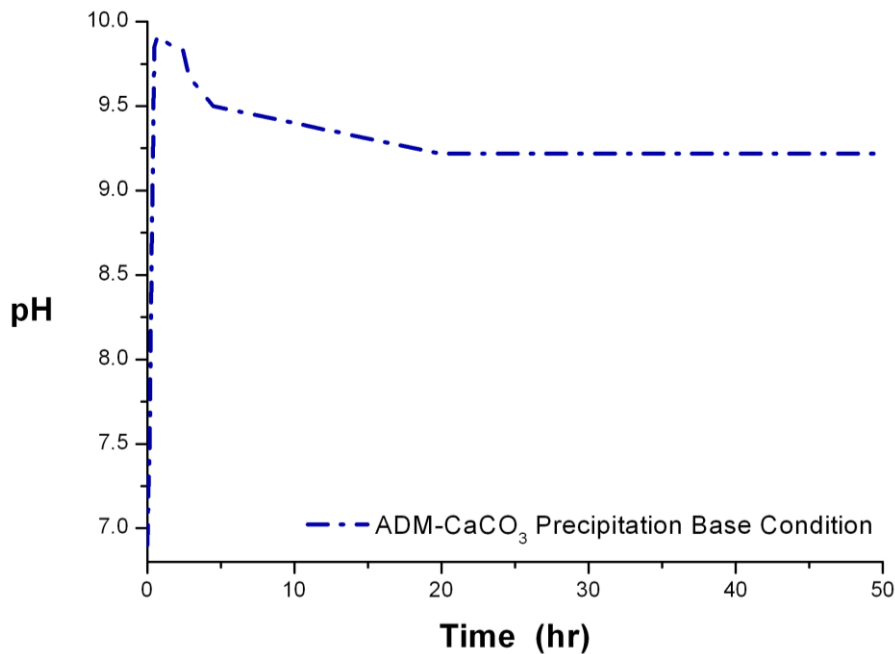


Figure 4 - 4: A typical pH profile for an ADM experiment (70 ml, 25 mM CaCl₂, A = 48 cm², 3 g ammonium carbonate, 2.6 l head space, no additional diffusion boundaries) which shows the establishment of a constant solution pH (9.25) after 20 hours. Image taken from (169).

4.3.2: Experimental

The preceding and following descriptions were made possible given the experimental procedure below. A crystallisation dish with a solution surface area of 13-58 cm² and containing 70 ml of calcium chloride solution (15-50 mM) was placed in a 2.6 L desiccator. A pH electrode, a temperature recorder and a tube through which sample aliquots could be removed were inserted into the crystallisation solution. Solid ammonium carbonate (1.5-5 g), thinly spread in a glass dish, was added to the chamber. This dish was either uncovered, or was covered with Parafilm to provide a diffusion barrier, where the Parafilm was perforated to different degrees to give free surface areas of 0.6, 2 or 4 cm². The chamber was then sealed.

The changes in the reaction solution accompanying precipitation of CaCO₃ were evaluated by taking samples of 0.5 ml from the solution at intervals of 10 min. These were immediately diluted with 19.5 ml ethanol to replace water molecules adsorbed to the calcium carbonate surfaces and to prevent the solid from dissolving.^(101, 103, 104) Next, 10.5 ml of Milli-Q water was added to prevent further precipitation. 5 ml of the obtained mixture was centrifuged at 140 rpm for 90 seconds to separate the solution from the solid matter. The concentrations of aqueous calcium and carbon in the prepared solution were determined using atomic absorption spectroscopy (AA) and Ion chromatography (IC), respectively. The total carbon content in the solution was determined by diluting 0.5 ml of the treated reaction solution with 1 ml of Milli-Q water. The resulting solution was then analysed using a Dionex DX600 Ion chromatograph. The experimental run time was limited to 100 min when no additional diffusion barriers were used and 200 min when further diffusion barriers were in place. The reaction was terminated by opening the reaction chamber, and the remaining solid ammonium carbonate was weighed. The weight loss of the ammonium carbonate ($\Delta(\text{NH}_4)_2\text{CO}_3$) and its molecular weight (MW) were then used in combination with the measured final carbon concentration in solution (C_T), the solution volume (V_L), the carbon concentration in the gas phase (V_{GP}), the expected equilibrium carbon dioxide vapour pressure (P_{CO_2}) and the measured decrease in calcium concentration (ΔCa), to setup a carbon mass balance as a control indicator, Equation 63.

$$\frac{\Delta((\text{NH}_4)_2\text{CO}_3)_s}{\text{MW}_{(\text{NH}_4)_2\text{CO}_3}} = [\Delta\text{Ca} + C_T] * V_L + \frac{P_{\text{CO}_2}}{R * T} * V_{GP} \quad (63)$$

Chapter 4: Characterisation of Diffusion Methods

In a second set of experiments, the above setup was extended to determine the induction point by circulating the crystallizing solution through the beam path of a UV/VIS spectrophotometer in transmission mode set at $\lambda = 500$ nm using a closed flow cell. Liquid transport to and from the flow cell/ desiccator was performed using a double channel peristaltic pump.

The **solution carbonate concentrations** (CO_3^{2-} , HCO_3^- and H_2CO_3) were calculated, based on the total inorganic carbon concentration (C_{TS}) and pH measurements,(168) using a simplified carbon mass balance and carbonic dissociation constants (K_A), as detailed in Chapter 1.4.6 and Appendix C, Equations 64-67. The required activity coefficients were calculated using the Davies equation and were found to be close to unity in diluted samples prior to analyses.(308)

$$[C_{\text{TS}}] = [\text{CO}_3^{2-}] + [\text{HCO}_3^-] + [\text{H}_2\text{CO}_3] \quad (64)$$

$$[\text{CO}_3^{2-}] = \frac{[C_{\text{TS}}] K_{A1} K_{A2}}{[\text{H}^+]^2 + K_{A1} [\text{H}^+] + K_{A1} K_{A2}} \quad (65)$$

$$[\text{HCO}_3^-] = \frac{[C_{\text{TS}}] K_{A1} [\text{H}^+]}{[\text{H}^+]^2 + K_{A1} [\text{H}^+] + K_{A1} K_{A2}} \quad (66)$$

$$[\text{H}_2\text{CO}_3^*] = \frac{[C_{\text{TS}}] [\text{H}^+]}{[\text{H}^+]^2 + K_{A1} [\text{H}^+] + K_{A1} K_{A2}} \quad (67)$$

The **calculated supersaturation (S)** with respect to a specific polymorph (x), is expressed as the ratio of ionic activity product to solubility product (K_{sp}), as presented in Equation 69.

$$K_{\text{sp}_x} = a_{\text{Ca}^{2+}} a_{\text{CO}_3^{2-}} \quad (68)$$

$$S_x = \frac{a_{\text{Ca}^{2+}} a_{\text{CO}_3^{2-}}}{K_{\text{sp}_x}} \quad (69)$$

Calcium concentrations in the mineralizing solution and their ion activities were recalculated from AA measurements of diluted sample aliquots, taking into account all aqueous forms of the calcium ions (e.g. CaOH^+ , CaHCO_3^+) in solution, Figure 1-16, and Appendix C. Carbonate concentrations were similarly recalculated based

Chapter 4: Characterisation of Diffusion Methods

on the C_{TS} concentration determined by IC. For rigour, calcium and carbonate activities were also calculated with respect to calcium chloride ion pairs using Visual MINTEQ.

The **precipitation progress (ξ)** was determined by recording the change in total calcium concentration with progressing precipitation, as described in Equation 70. $[Ca]_0$ was set equal to the initial / starting calcium concentration and $[Ca]_t$ the calcium concentration in solution at experimental time (t)

$$\xi = \left(\frac{[Ca]_0 - [Ca]_t}{[Ca]_0 - [Ca]_{equilibrium}} \right) \quad (70)$$

To provide an appropriate estimate of the precipitation progress, (Equation 46) the final equilibrium solubility of the calcium ions under the given partial pressure of ammonia and carbon dioxide ideally needs to be known.

As established in Chapter 1.4, the equilibrium composition of a calcium carbonate precipitating system is determined by the partial pressure of carbon dioxide alone. In the case of the ADM, this is extended by the two solution terms which describe the conversion of ammonia into ammonium ions, Appendix C – A.7 and A.8. This affects the solution pH and with it the fraction of precipitating carbonate in solution. Unfortunately, it was not possible to measure the partial pressures of the two gases. In the case presented, the final equilibrium calcium concentration used for the calculation of reaction/ crystallisation progress was based on the constant measured pH of 9.25, Figure 4-4, and a fixed total carbon concentration of 250 mM.

Considering the existing knowledge of the given combination of partial pressures, the equilibrium solution composition can be calculated using Equation 71.



Re-writing this using the previously given solubility products, it is then possible to derive the equilibrium concentration of the major solution species, as a function of partial pressures of carbon dioxide and ammonia. An example is shown in **Figure 4-5** in the form of a pH surface plot as a function of $P_{[NH_3]}$ and $P_{[CO_2]}$.

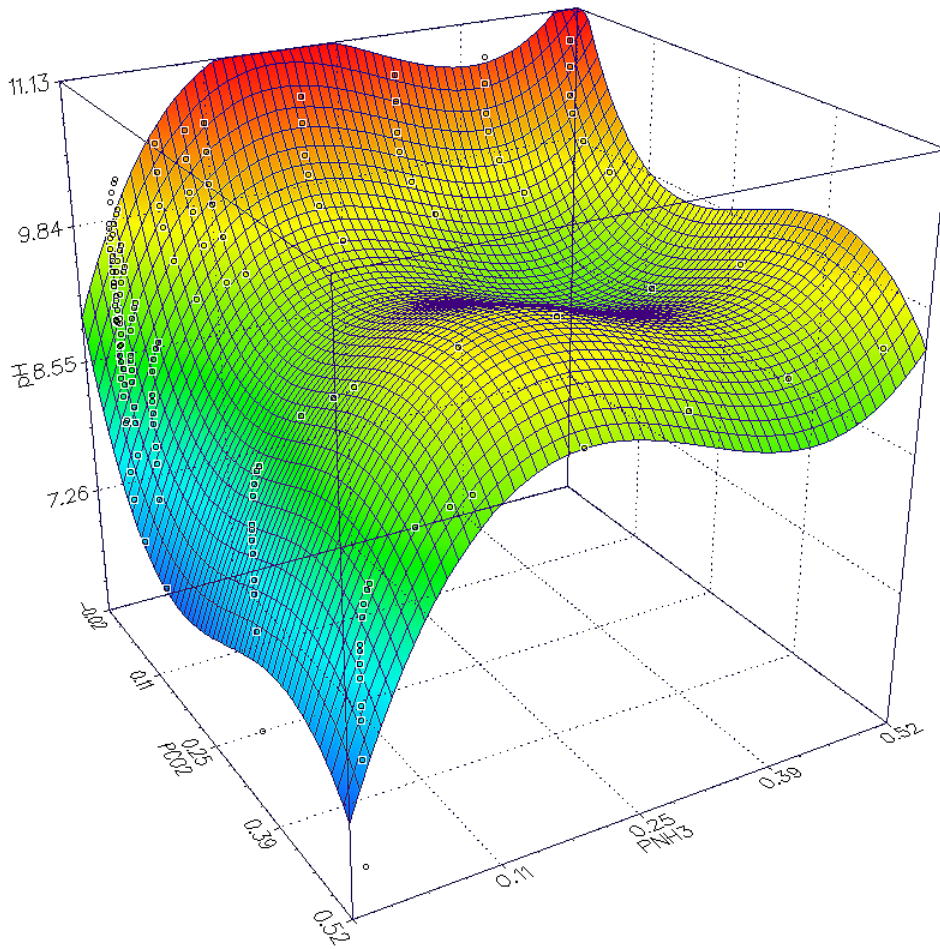


Figure 4 - 5: Surface plot of the equilibrium $\text{pH} = f(P_{\text{NH}_3}, P_{\text{CO}_2})$ in a calcium-carbonate-ammonia system.

4.3.3: Carbonate Addition Rate

Having potentially identified the key features of the ADM, methods were developed to test this hypothesis and to achieve identical results using highly reproducible titration-based methods. This was achieved based on determination of the carbon addition rate (dC_T/dt). Here, C_T corresponds to the total inorganic carbon added to the system ($C_T = [H_2CO_3] + [HCO_3^-] + [CO_3^{2-}]$), which equals the sum of carbon lost to $CaCO_3$ precipitation and the total free inorganic carbon present in the solution (C_{TS}). The total carbon which has been added to the solution at any point in time (C_{Tst}) can be calculated from the reduction in the calcium ion concentration ($\Delta Ca = Ca_0 - Ca_t$), as determined by AA, and from the total carbon content in the solution ($\Delta C_{TS} = C_{Tst} - C_{TS0}$), as measured using IC, Equation 72.

$$C_{T_t} = (C_{T_{s_t}} - C_{T_{s_0}}) + (Ca_0 - Ca_t) \quad (72)$$

The carbon addition rate i.e. the rate at which carbon dioxide diffuses into the solution (dC_T/dt) is then obtained by differentiating Equation 72 with respect to time, Equation 73.

$$\frac{dC_T}{dt} = [C_{Ts} - Ca] \frac{d}{dt} \quad (73)$$

The experimental data (**Figures 4-2 and 6**) shows that at times up to ≈ 100 minutes (when the reaction is almost complete and the Ca concentration depleted) both the Ca and C_{TS} vary linearly with time, and that the pH is almost constant during the region of interest. The change in calcium and carbon concentration in solution can therefore be approximated using first order rate constants, $C_{TS} = k_1 t$, and $Ca = k_2 t$, where t is the experimental time in minutes and k_1 and k_2 are rate constants corresponding to the carbon addition rate and the crystallisation rate respectively. Equation 73 can thus be expressed as Equation 74, where $k_1 = 0.000634 \text{ mol l}^{-1} \text{ min}^{-1}$ and $k_2 = -0.000228 \text{ mol l}^{-1} \text{ min}^{-1}$, based on the data presented in Figure 2.

$$\frac{dC_T}{dt} = k_1 - k_2 \quad (74)$$

Graphs of the experimentally-obtained carbon addition profiles under the given “standard condition” are presented in Figure 4-6, where (a) is the experimentally-obtained addition rate, (b) is theoretical, calculated using the derived rate constants k_1 and k_2 , (Table 6) (c) is theoretical, calculated using k_1 only and (d) is experimental, based on diffusion of ammonium carbonate decomposition products

Chapter 4: Characterisation of Diffusion Methods

into water rather than calcium chloride solution. The curves show that there is indeed a linear increase in the total carbon content until crystallisation is virtually complete (at ≈ 100 minutes). Further, this comparison demonstrates that the analysis made in Equation 74 well-describes the reaction in the first 100 minutes under these standard conditions.

Rate constants and the carbon addition rate are dependent on the given environmental conditions. Modification of these conditions, for example by changing the surface area, the initial calcium concentration, and introducing diffusion barriers, necessarily causes a change in the total carbon addition rate.

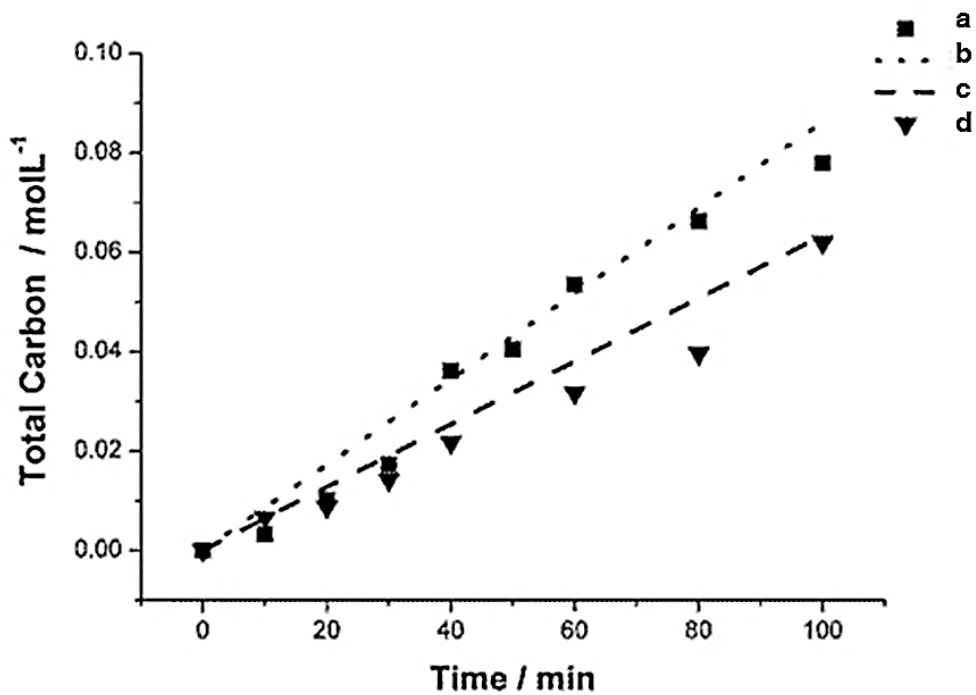


Figure 4 - 6: Comparison of Total Carbon addition rates, (a) experimental, (b) theoretical (c) theoretical k_1 only, (d) experimental pure diffusion no calcium chloride. Image taken from (169).

Chapter 4: Characterisation of Diffusion Methods

Experimental Condition	k_1	k_2	dC_T/dt	dCO_3/dt	t_{ind}	S_{ind}	Polymorph Distribution†	
	[mM/ min]	[mM/ min]	[mM/ min]	[mM/ min]	(min)	[*]	Primary	Secondary
Base Condition*	0.634±0.045	-0.228±0.007	0.849	0.138	15	31	Calcite	Vaterite
Mass (NH ₄) ₂ CO ₃								
5g	0.650±0.012	-0.224±0.038	0.864	0.140	16	30	Calcite	Vaterite
1.5g	0.654±0.095	-0.243±0.012	0.881	0.126	14	32	Calcite	Vaterite
CaCl ₂ Concentration								
50mM	0.554±0.049	-0.464±0.025	1.019	0.090	20	150	Calcite	-
10mM	0.694±0.023	-0.120±0.008	0.814	0.225	10	13	Vaterite	Calcite
Solution Surface Area								
58cm ²	0.685±0.034	-0.320±0.001	1.034	0.176	10	40	Calcite	-
13cm ²	0.139±0.007	-0.072±0.011	0.223	0.050	33	10	Vaterite	Calcite
Sec. Diffusion Barrier								
Free Cross Sectional Area‡								
4cm ²	0.089±0.003	-0.056±0.006	0.156	0.063	35	40	Calcite	Vaterite
2cm ²	0.070±0.014	-0.037±0.005	0.107	0.014	47	50	Calcite	Vaterite
0.6cm ²	0.025±0.006	-0.008±0.002	0.0261	0.008	93	30	Vaterite	Calcite
Agitation								
100 rpm	1.047±0.080	-0.324±0.018	1.261	0.208	15	160	Calcite	Aragonite

*Base Condition (25 mM M CaCl₂, 70 ml, 48 cm², 3g (NH₄)₂CO₃, 2.6 l overhead space, no secondary diffusion boundaries) – Supersaturation in respect to K_{SPACC}

† Primary and Secondary Polymorph Constituent after 100min/ ‡ 200min estimated based on SEM Images, Raman- and IR-Spectra

Table 6: Summary of ADM crystallisation parameters under different experimental conditions, where (k_1) is the carbon accumulation rate in solution, (k_2) is the crystallisation rate, (dC_T/dt) the total carbon addition rate, (dCO_3/dt) the carbonate addition rate, (t_{ind}) the induction time and (S_{ind}) is the supersaturation with respect to ACC at the induction point.(169)

4.3.4: Influence of Reaction Variables

In describing the use of the ammonia diffusion method in the literature, a great weight is placed on precisely defining the crystallisation setup including such variables as the initial amount of solid ammonium carbonate, the starting calcium concentration, the solution surface area, the presence of secondary diffusion barriers and solution agitation. The particular effect each variable has on the precipitation process is rather undefined. As a result, the effect of these variables were investigated by measuring induction time, pH supersaturation, reacting species concentration, total carbon addition rate and reaction progress. This was done taking the above discussed condition as the baseline for evaluation of singular parameter/ variable changes.

4.3.4.1: Initial Mass of Ammonium Carbonate

Initial mass of ammonium carbonate. Provided that the initial amount of solid ammonium carbonate was in excess, the precise mass used in an experiment had no influence on the precipitation profile. This is reflected in the fact that the total carbon addition rates, dC_T/dt , were identical when either 1.5 g, 3 g or 5 g of ammonium carbonate were employed (Table 6 and **Figure 4-7**). This result confirms that a near-constant vapour pressure is present or at least that the decomposition of ammonium carbonate is the fastest reaction step.

Chapter 4: Characterisation of Diffusion Methods

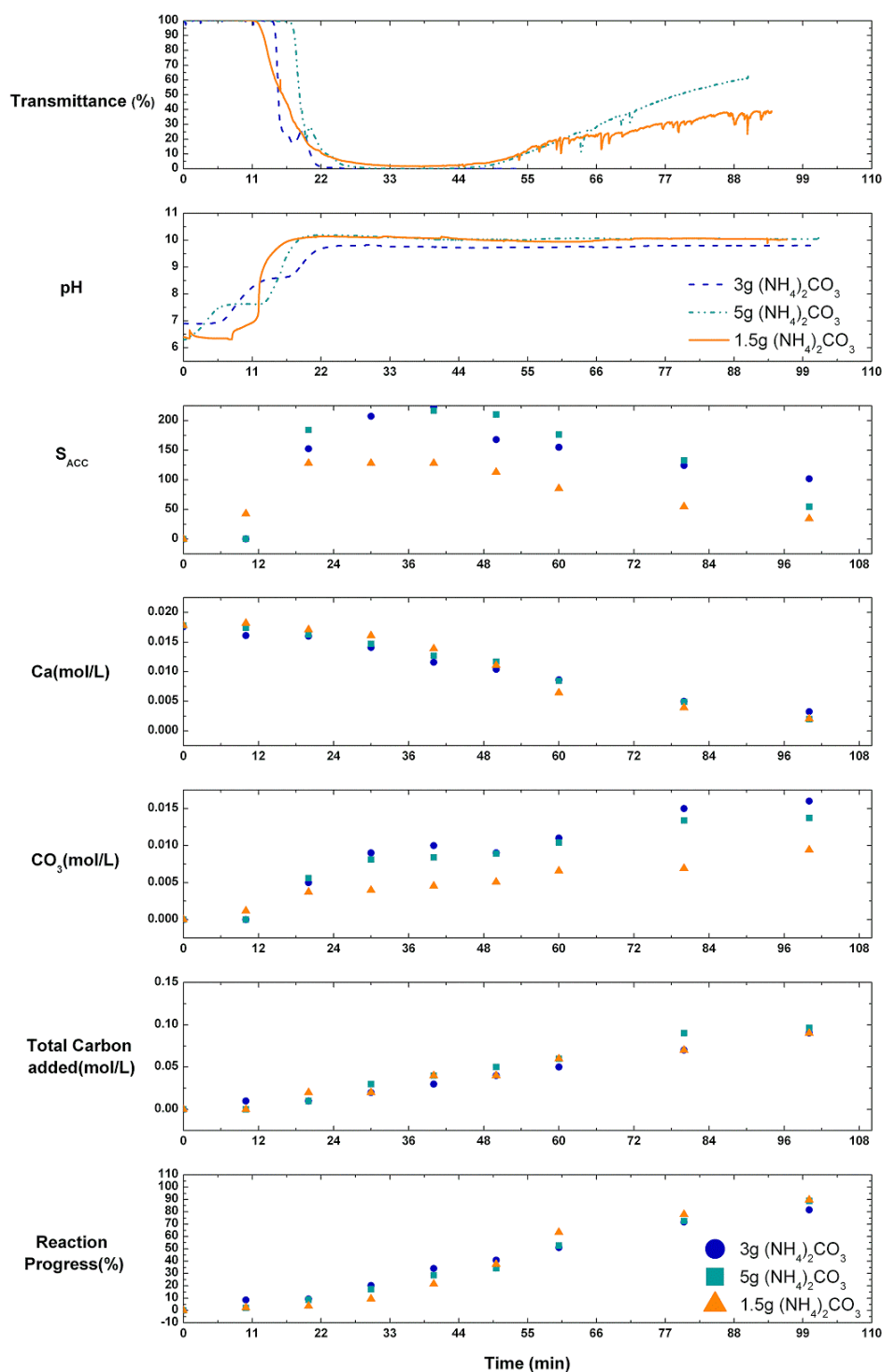


Figure 4 - 7: Time-resolved profiles of calcium carbonate precipitation experiments using the ammonia diffusion method, studying the influence of changes in initial amounts of ammonium carbonate added (1.5g, 3g and 5g). Experimental conditions 70 mL of 25 mM CaCl_2 , 48 cm^2 surface area, 2.6 l head space, no additional diffusion barriers). — 1.5 g, --- 3 g, -.- 5g, ▲ 1.5g, ● 3g, ■ 5g $(\text{NH}_4)_2\text{CO}_3$. Image taken from (169).

4.3.4.2: Calcium Concentration

Altering the **starting calcium concentration** had an effect on the precipitation profile, although the crystallisation progress was little affected. Increasing the initial calcium concentration from 10 mM to 50 mM unexpectedly resulted in shifts in the induction point to longer times, **Figure 4-8**. This can be attributed to the corresponding retardation in pH increase as the initial calcium concentration is increased, which in turn delays the conversion of bicarbonate to carbonate ions. This effect may be founded on the increased association of calcium ions with hydroxide ions, which originate from the ammonia to ammonium ion conversion.

The most significant effect of changing the calcium concentration was on the supersaturation. The supersaturation levels at induction decreased with decreasing calcium concentration due both to the lower calcium concentration and the lower levels of bicarbonate present at induction. On progression of the reaction, significantly higher supersaturation levels of ≈ 230 are reached in the 50 mM solution, as compared with ≈ 75 in the 10 mM solution, which can be associated with a higher nucleation density as the calcium concentration is raised. Characterization of the reaction products sampled after 100 minutes using SEM and Raman spectroscopy showed that the calcium concentration also influenced the polymorph produced, and that a greater proportion of vaterite to calcite was obtained at 10 mM as compared with 50 mM, **Figures 4-9**. The carbon addition rate also increased with the initial calcium concentration due to increased CaCO_3 precipitation, resulting in an extended period of high CO_2 diffusion into the solution, as shown in Table 1.

Chapter 4: Characterisation of Diffusion Methods

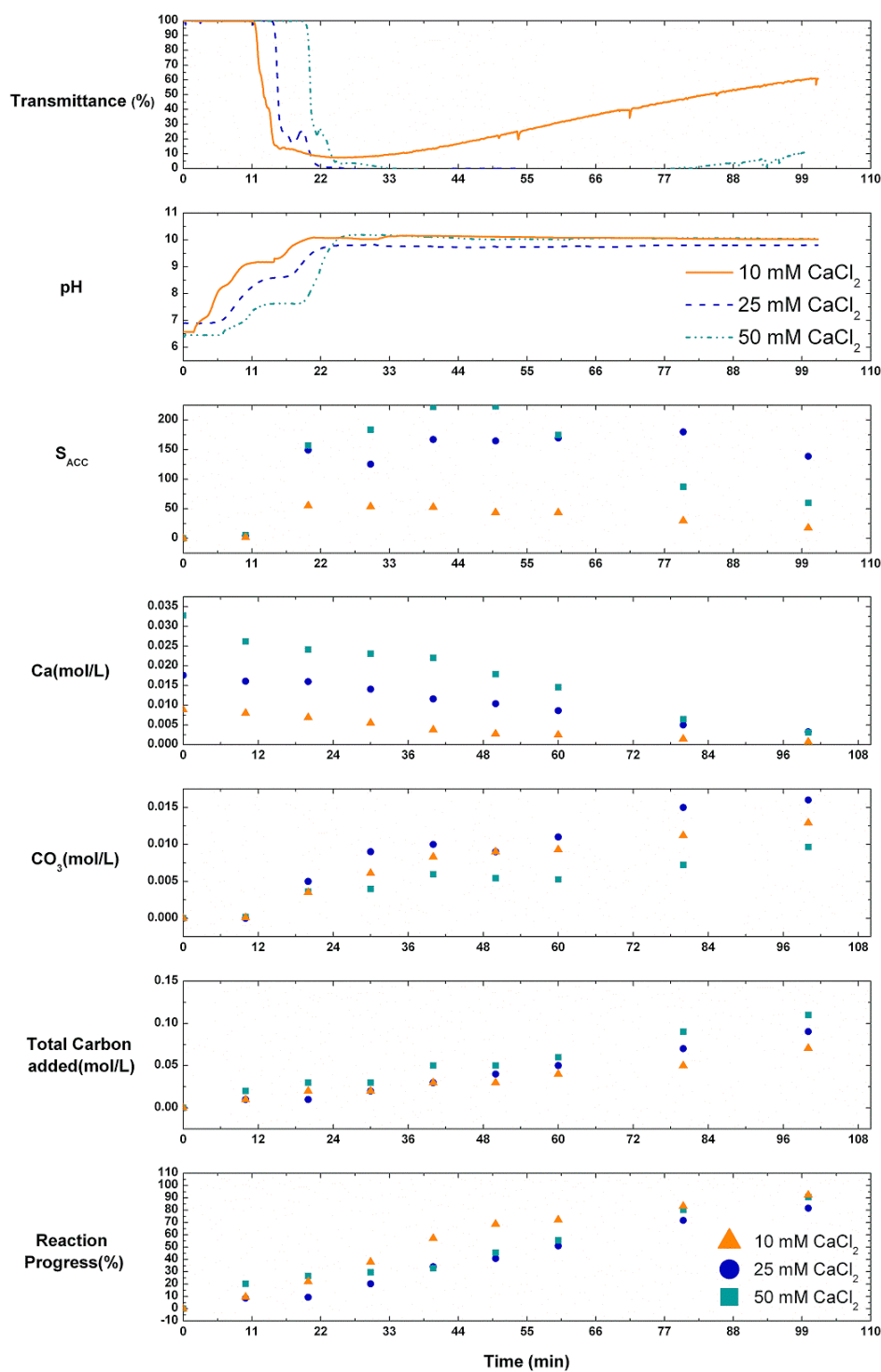


Figure 4 - 8: Time-resolved profiles of calcium carbonate precipitation experiments using the ammonia diffusion method studying the influence of initial CaCl_2 concentration (10 mM, 25 mM and 50 mM). Experimental conditions 70 mL of x mM CaCl_2 , 3 g $(\text{NH}_4)_2\text{CO}_3$, 48 cm^2 surface area, 2.6 l head space, no additional diffusion barriers). —10mM, --- 25mM, -.- 50mM, \blacktriangle 10mM, \bullet 25mM, \blacksquare 50mM CaCl_2 . Image taken from (169).

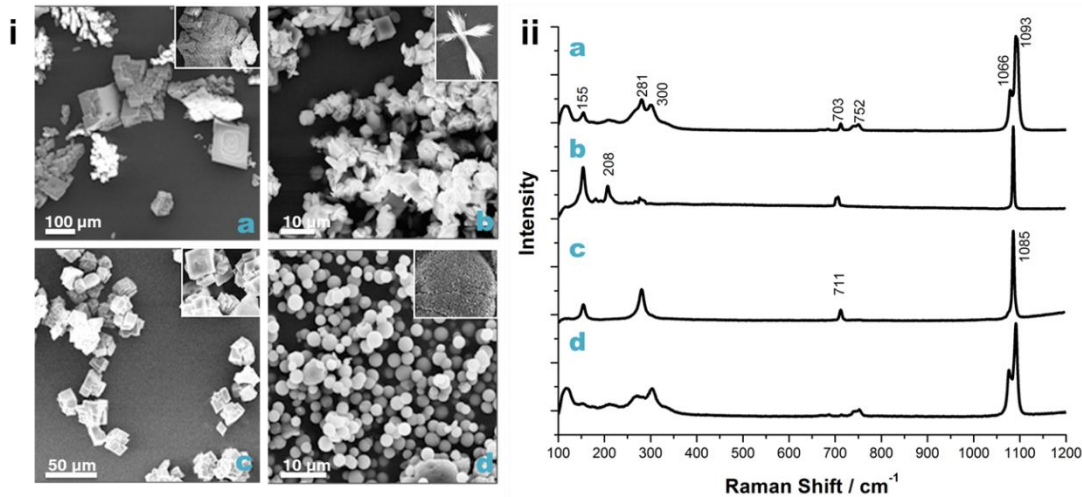


Figure 4 - 9: (i) SEM images and corresponding (ii) Raman spectra of calcium carbonate precipitates obtained via the ADM after 100 minutes under reaction conditions of 70 ml, 3 g ammonium carbonate, 48 cm², 2.6 l head space, no additional diffusion boundaries and (a) 25 mM CaCl₂, no agitation (Calcite+Vaterite), (b) 25 mM CaCl₂ and 100 rpm agitation (Calcite+Aragonite), (c) 50 mM CaCl₂, no agitation (Calcite), (d) 10 mM CaCl₂, no agitation (Vaterite+Calcite). The CaCO₃ polymorphs can be identified based on characteristic peaks, where peaks at 1085, 711, 281 and 155 cm⁻¹ identify calcite, peaks at 1085, 705, 208 and 155 cm⁻¹ aragonite and peaks at 1093, 1066, 753, 713 and 300 cm⁻¹ vaterite. (169, 309)

4.3.4.3: Solution Surface Area

Variation of the **solution surface area**, while maintaining a constant volume, resulted in significant and systematic changes in all of the parameters investigated, indicating that this provides an excellent and straightforward method for controlling the diffusion process, **Figures 4-10**. The induction time of calcium carbonate precipitation decreased when the solution surface area was increased. Similar a more rapid increase in solution pH and nucleation rates were observed at higher surface areas. This is expected due to the more uniform supersaturation profiles in solutions with larger surface areas as the diffusion cross section increases. The total carbon addition profiles given in Figure 4-10 confirm the linearity of this relationship, which is in agreement with Fick's first law,(310) i.e. doubling the surface area leads to a twofold increase in carbon addition rate. Similarly, the reaction progress increased with increasing surface area, and the supersaturation peaked at earlier times in the more rapid (larger surface area) reactions. Therefore, larger surface areas are associated with shorter induction and overall reaction times, higher peak supersaturations, and nucleation rates. In contrast, the lower surface area provides conditions where supersaturations are maintained at constant values for long periods.

Chapter 4: Characterisation of Diffusion Methods

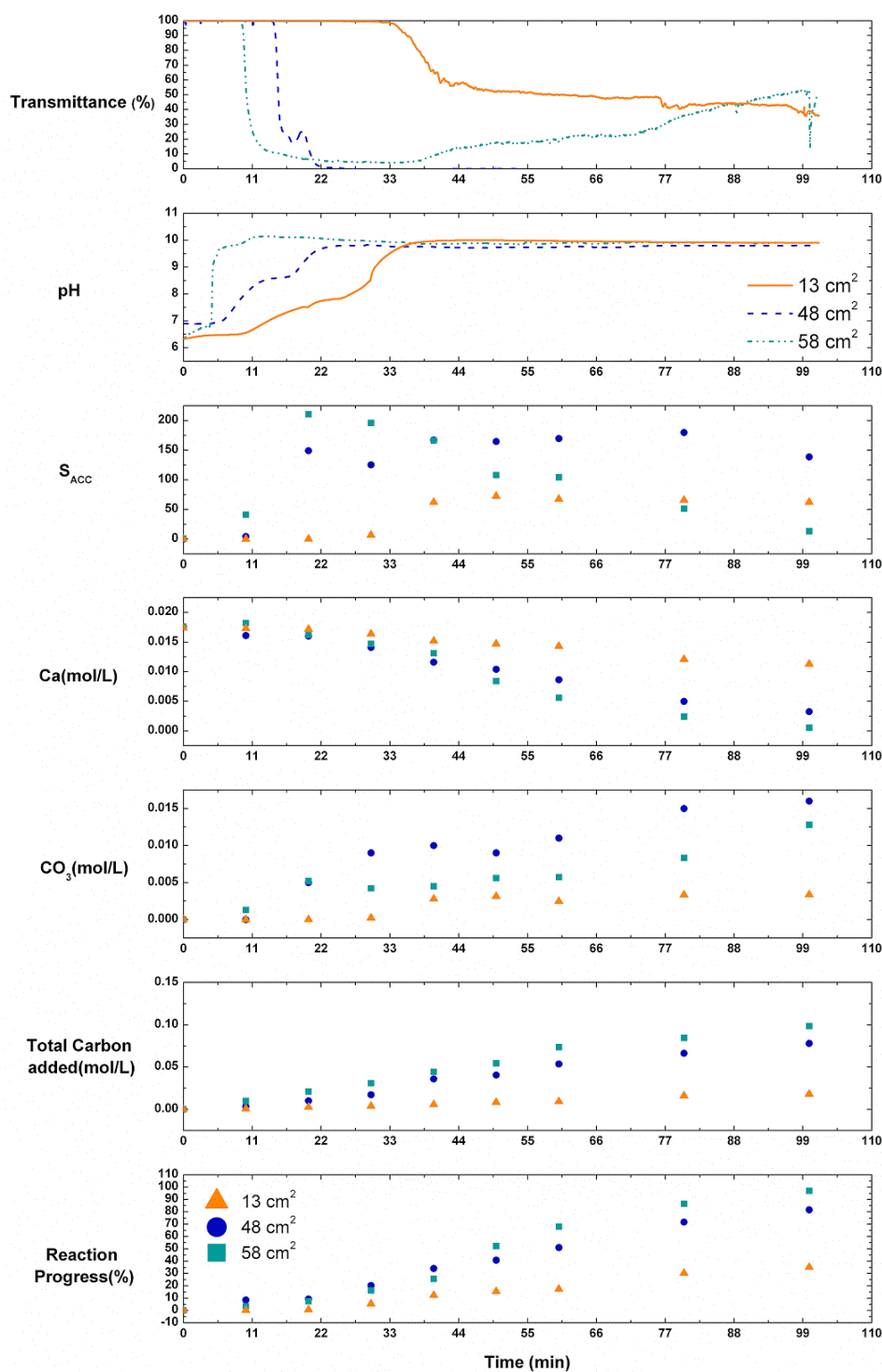


Figure 4 - 10: Time-resolved profiles of calcium carbonate precipitation experiments using the ammonia diffusion method studying the influence of solution surface areas (13 cm², 48 cm², 58 cm²). Experimental conditions 70 ml of 25 mM CaCl₂, 3 g (NH₄)₂CO₃, x cm² surface area, 2.6 L head space, no additional diffusion barriers). —13cm², --- 48cm², -·- 58cm², ▲ 13cm², • 48cm², ■ 58cm². Image after (169).

4.3.4.4: Secondary Diffusion Barrier

Introduction of an **additional diffusion barrier** (typically in the form of Parafilm perforated with needle-holes) is widely used as a method of regulating the ADM. Experiments were therefore conducted where the dish containing the reaction solution was covered with Parafilm punctured with 3, 10 or 20 holes, corresponding to a total free area of 0.6, 2 and 4 cm² respectively. A decrease in the rate of calcium loss and in the reaction progress was observed with a reduction in the free area, and the induction time increased from ~ 15 minutes in the absence of a diffusion barrier to ~ 100 minutes when there was only 0.6 cm² free area. However, in both of these cases, nucleation occurred at supersaturation levels above the ACC solubility limit, (Table 6). The total carbon addition rate was found to exponentially decrease with a decrease in the free area, in contrast to the linear relationship recorded with respect to the liquid surface area. Thus, in common with a reduction in the solution surface area, reduction in the free area through introduction of a diffusion barrier leads to longer reaction times, where supersaturation remains at elevated levels for longer periods.

4.3.4.5: Solution Agitation

The effect of **agitation** on the ADM was studied by addition of a magnetic stirrer to the CaCl_2 solution. An influence on the crystallisation was only observed at stirring rates of 100 rpm and above, where a higher crystallisation rate was recorded as compared with unstirred solutions (**Figure 4-11**). The effect of stirring was more pronounced in the later stages of crystallisation, and no significant change in the induction time was observed, despite there being a more rapid initial increase in the pH. This is consistent with a faster build-up of ammonia and carbonate in the solution, and nucleation occurring at higher supersaturation levels in the stirred solutions. The increase in reaction rate in the later stages of the reaction can be explained by an increase in secondary nucleation events which occurs due to an increased frequency of particle collisions, the generation of additional nucleation sites through attrition processes, and the increased kinetic energy in the system. It is also supported by the presence of aragonite as well as calcite under stirred conditions, while only calcite is present under stagnant conditions (Figure S4). The formation of aragonite due to agitation has been reported elsewhere,⁽³¹¹⁾ and may relate to the increase of kinetic energy in the system.

Chapter 4: Characterisation of Diffusion Methods

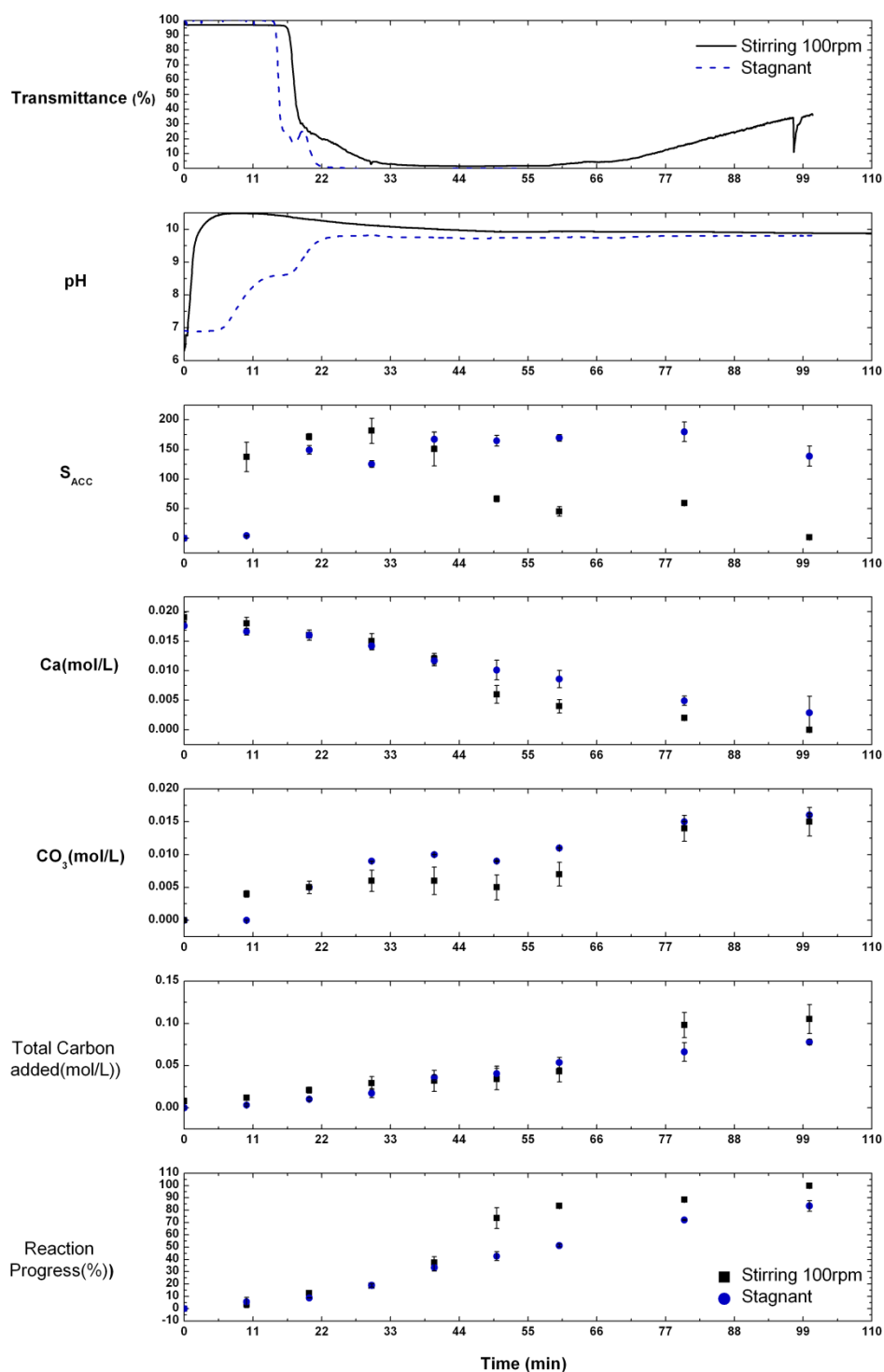


Figure 4 - 11: Time-resolved profiles of calcium carbonate precipitation experiments using the ammonia diffusion method studying the effect of solution agitation (100 rpm). Reaction conditions 70 ml of 25 mM $CaCl_2$, 48 cm^2 surface area, 3g ammonium carbonate, 2.6 liter head space, no additional diffusion barriers). — Stirring 100 rpm, --- Stagnant, ■ Stirring 100 rpm, •Stagnant. Image taken from (169).

4.4: Reproduction of the Ammonia Diffusion Method

Reproducing the ammonia diffusion method using the derived addition rates and supersaturation profiles was necessary not only to validate the obtained results, but also to make products previously limited to diffusion processes available through other methods. This allows the scale up of produced material and in-situ investigations of the formation process.

CaCO₃ mesocrystals formed in the presence of PSS-MA were chosen as the primary model system to test the translation of the obtained reaction conditions.⁽³⁰³⁾ PSS-MA CaCO₃ mesocrystals were chosen due to their distinctive morphologies and properties (in particular their high surface areas of 60-100 m²g⁻¹). CaCO₃ thin film structures associated with a PILP formation process were also reproduced due to their distinct morphological appearance.⁽⁶⁰⁾ Two alternatives were considered in reproducing these products, (i) a mechanically - driven slow addition of a reagent i.e. a titration-based system and (ii) a true one-pot synthesis facilitated by enzymatic hydrolysis of urea. Success in the replication of mesocrystals is important in that it suggests that a prolonged, steady supersaturation promotes the continuous formation of new material, which supports aggregation-based crystallisation.

4.4.1: Mechanically Driven Slow Addition of Reagents

Replication of CaCO₃ PSS-MA mesocrystals was achieved using a slow addition process (schematic given in **Figure 4-12**), in which a carbonate-containing reagent solution (20 ml of either 250 or 175 mM (NH₄)₂CO₃) is added at a rate of 0.0057 ml min⁻¹ to a 80 ml of solution containing 325 ppm PSS-MA and either 5 mM or 1.25 mM CaCl₂, under agitation at 70 rpm. The experimental conditions were selected to mimic the carbon addition rate during the crystallisation zone (the first 100-200 minutes of reaction) of an ammonium carbonate diffusion experiment with the following conditions: 5 mM / 1.25 mM CaCl₂, 325 ppm PSS-MA, 70 ml, 48 cm² and 0.6 cm² diffusion boundary pore surface area. Focus on the early stage was set in agreement with the reaction progress profile. Agitation was required to disperse the highly concentrated ammonium carbonate solution, thereby preventing uncontrolled instantaneous precipitation. The ammonium carbonate solution addition rate (k_s) and concentration ($[C]_{(NH_4)_2CO_3}$) added to a certain volume of calcium solution (V_{Ca})

were determined according to Equation 75 such that they mimicked the carbon addition rate ($d[C]_T/dt$) obtained experimentally from characterization of the ADM.

$$\frac{k_S [C]_{(NH_4)_2CO_3}}{V_{Ca} + k_L t} = \frac{dC_T}{dt} \quad (75)$$

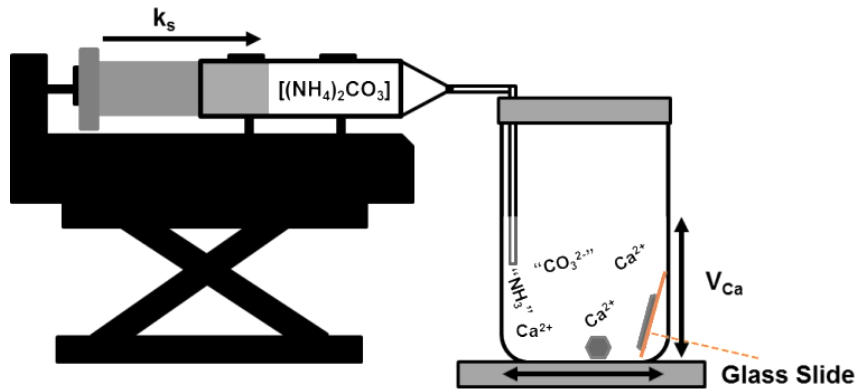


Figure 4 - 12: Schematic of the mechanically driven slow addition setup used for mesocrystal and thin film replication.

Analysis of the product crystals demonstrated that $CaCO_3$ PSS-MA mesocrystals could be obtained by the mechanically-driven slow addition of ammonium carbonate, **Figure 4-13**. These were identical in morphology to $CaCO_3$ mesocrystals produced using the ADM (70 ml of a solution of 1.25 - 5 mM $CaCl_2$, A 48 cm^2 , 0.6 cm^2 of free surface area), as a comparison of electron micrographs demonstrates. Mesocrystal pseudo-octahedral (1.25 mM $CaCl_2$ / 325 ppm PSS-MA) or dodecahedra (5 mM $CaCl_2$ 325 ppm PSS-MA) obtained by the ADM are given in (a) and (c).(303) Mesocrystals obtained by slow addition are shown in (b) and (d). **Figure 4-14**, provides an analysis of pseudo-octahedral mesocrystals produced by slow addition and removed from the reaction solution after 12 hr, by Raman (a) and IR (b) spectroscopy. This demonstrated that the product crystals were calcite with little or no evidence of an amorphous phase.(67) (c) TGA of the “replica” mesocrystals revealed that they comprised 2-4 wt% polymer. Confirmation of mesocrystal structure was obtained by measurement of the surface areas of the crystals prepared. Analysis of pseudo-octahedral mesocrystals produced by slow addition revealed a typical surface areas of $\sim 97 \text{ m}^2\text{g}^{-1}$. This value is consistent with the corresponding crystals produced using the ADM,(303) ($\sim 82 \text{ m}^2\text{g}^{-1}$) and is considerably larger than the $1\text{-}2 \text{ m}^2\text{g}^{-1}$ recorded for rhombohedral calcite crystals of

Chapter 4: Characterisation of Diffusion Methods

comparable sizes. Identical observations were made by adding sodium carbonate as the carbonate solution into a buffered Ca-polymer solution (pH 9 Tris buffer).

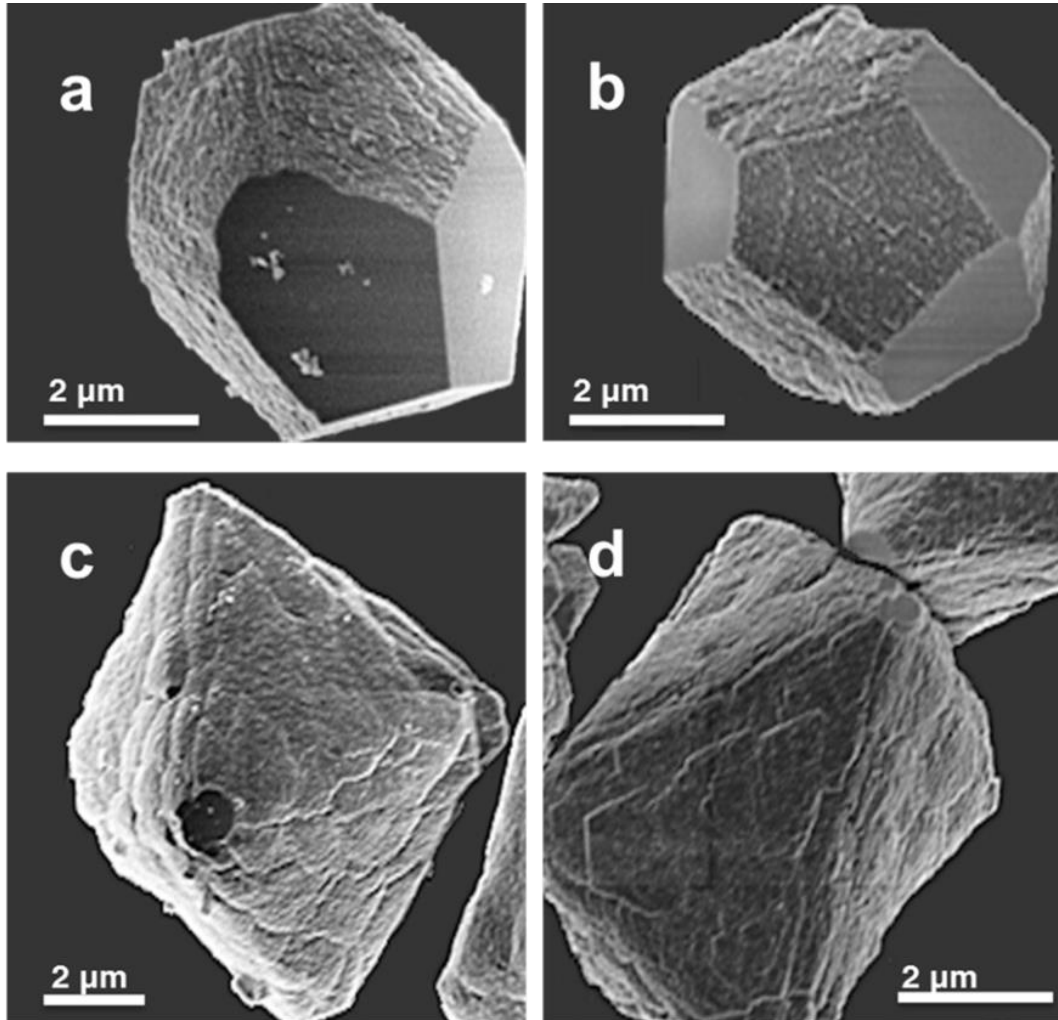


Figure 4 - 13: Electron micrographs of produced mesocrystal. (a) 1.25 mM CaCl_2 ADM, (b) 1.25 mM CaCl_2 Slow Addition, (c) 5 mM CaCl_2 ADM, (d) 5 mM CaCl_2 Slow Addition. Image taken from (169).

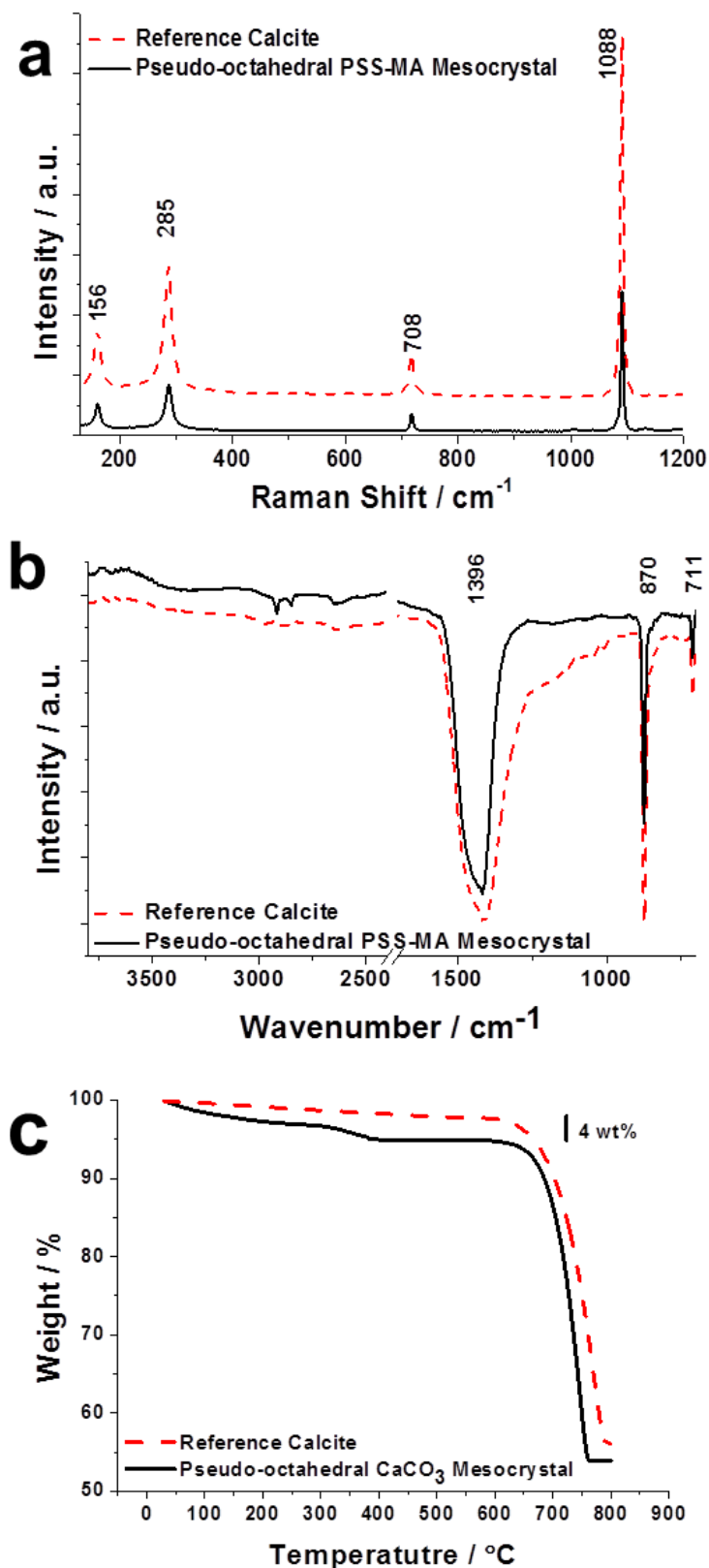


Figure 4 - 14: Characterization data of pseudo-octahedral CaCO_3 mesocrystals obtained in the presence of PSS-MA, and spectra of rhombohedral calcite crystals as reference. (a) Raman and (b) IR spectra. (c) TGA spectra of pseudo-octahedral CaCO_3 mesocrystals produced in the presence of PSS-MA by slow addition of reagents. A heating rate of $5^{\circ}\text{C min}^{-1}$ was applied.(169)

Chapter 4: Characterisation of Diffusion Methods

Replication of CaCO_3 Polymer-Induced-Liquid-Precursor films have also been carried out which focus on the later stages of the carbon addition profile i.e. higher addition rate. Under the presence of PAA it was possible to obtain crystalline films which resemble films obtained using the ammonia diffusion method when PAA is present as an additive. **Figure 4-15** provides a comparison of thin films obtained by the ADM (a) and slow addition (b) after heating to 400°C (300 min).

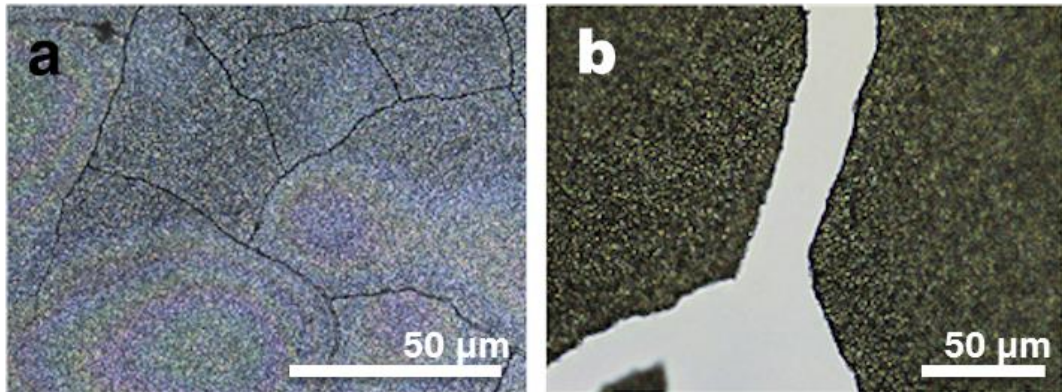
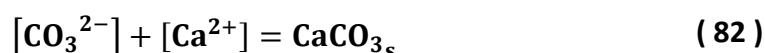
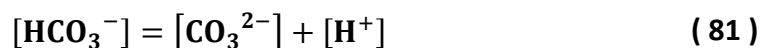
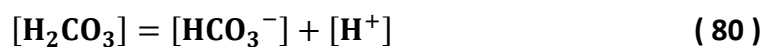
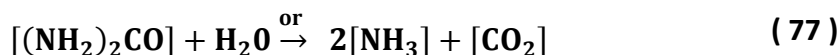


Figure 4 - 15: CaCO_3 thin film formed via (a) ADM (80ml 10 mM CaCl_2 , 50 mgml^{-1} PAA, 48 cm^2 and 0.6 cm^2 diffusion boundary pore surface area.) and via (b) via slow addition (20ml 175 mM $(\text{NH}_4)_2\text{CO}_3$, $0.0148 \text{ mlmin}^{-1}$, 80ml 10 mM CaCl_2 , 50 after heat treatment (400°C , 300min).

4.4.2: Enzymatic Hydrolysis of Urea

As a further development of the slow addition method, a true one-pot CaCO₃-PSS MA mesocrystal synthesis method was realized through the enzymatic hydrolysis of urea by urease in aqueous solution. By variation of substrate (urea) and enzyme (urease) concentrations the rate of carbonate and ammonium produced can be controlled, where this results from the enzymatic hydrolysis of urea released into a solution containing calcium chloride and PSS-MA.(174) The key underlying reactions in precipitating calcium carbonate by urea hydrolysis are given in Equations 76 to 82. The controlled release allows the reproduction of the pH and total carbon concentration profiles, where these are required for the formation of calcium carbonate mesocrystals analogous to those generated using the original ADM. The advantage of a true one pot synthesis method compared to the diffusion(67) and slow addition methods(169) is that it allows the direct observation of the formation process in situ by techniques such as DLS, SAXS and liquid cell TEM without manually interfering with the formation process. It also removes changes which occur due to the presence of a gas-liquid interface.(169) This allows the formation of crystals at a controlled increase in supersaturation, independent of the solution volume, Chapter 5.



In realising the replication of the ADM, a re-evaluation of the **enzymatic activity** of the urease purchased (canavalia ensiformis, subunit molecular weight: ~90.770 kDa) was necessary as precipitation experiments are performed in buffer-free solutions, and variations in urease activity are expected based on the continuous release of ammonia into the solution until an equilibrium between the ammonia and ammonium ions at a pH of ~9.15 is established. Assuming Michaelis Menten

Chapter 4: Characterisation of Diffusion Methods

enzyme kinetics, hydrolysis rates of urea solutions (0-140 mM) at fixed urease concentrations ($22 \mu\text{gml}^{-1}$) were subsequently measured via time resolved conductometry in free pH drift experiments at 24°C .

Conversion of the obtained conductance ($\mu\text{s cm}^{-1}$) to hydrolysed urea (mM) was made possible by measuring the final conductance of urea/ urease solutions with known starting concentrations shown in **Figure 4-16a**. Enzyme-specific parameters given in Table 7 were subsequently obtained following linearization in the form of a Hanes–Wolf plot, (b) \rightarrow (c).⁽³¹²⁾ As is evident from (b) we find a substrate inhibition at urea concentrations above 94 mM in this particular case.

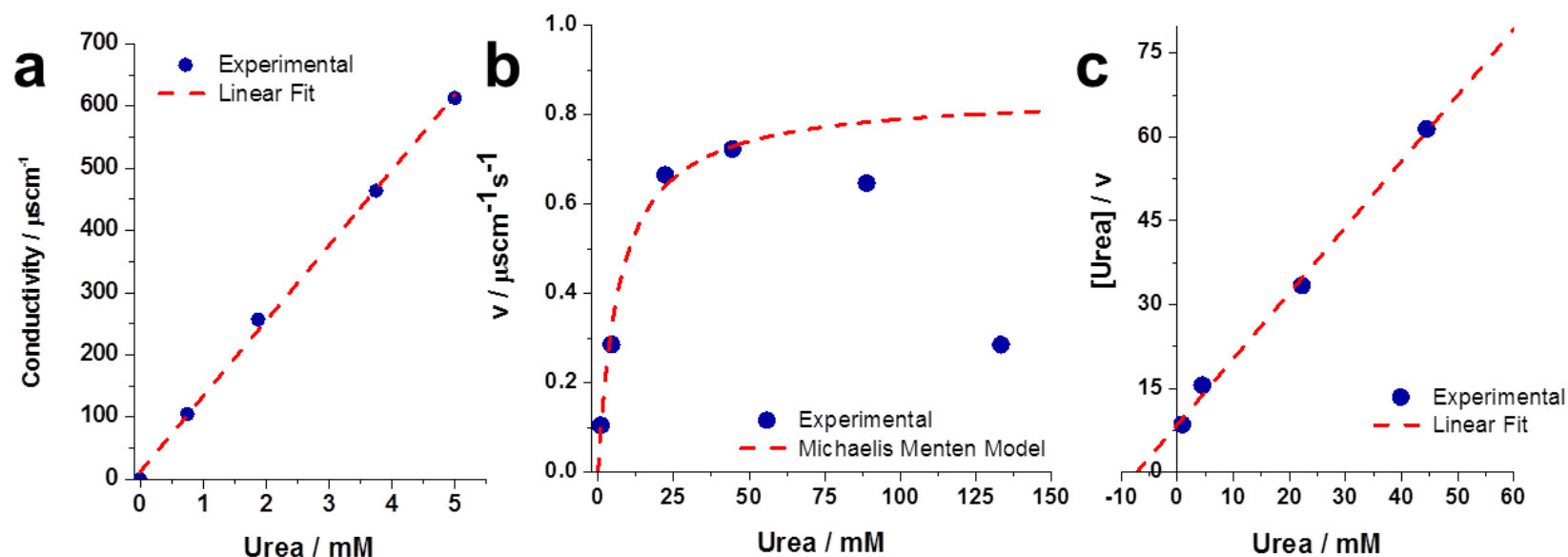


Figure 4 - 16: (a) Typical conductance urea/ urease calibration curve. Stated are final conductance values recorded, a urease/ urea ratio of 0.178 mg/mM was used throughout. (b) Michaelis-Menten and (c) Hanes–Woolf plot of urea/ urease hydrolysis obtained at 24°C a fixed amount of 22 $\mu\text{g ml}^{-1}$ urease was used.

Parameter	Value	Units
V_{\max}	0.0072	mM urea/sec
K_m	0.0607	mM urea
Activity	17.6254	$\mu\text{M urea/min mg urease}$

Table 7: Key enzymatic parameter of urea-urease hydrolysis obtained at 24°C in a free drift pH setup.

Chapter 4: Characterisation of Diffusion Methods

The derived urease activity then allowed the reproduction of the required total carbon and ammonia addition rates stated in Chapter 4.2. and 4.3 to form CaCO_3 -PSS MA mesocrystals by varying the mass of enzyme present, provided that a sufficiently large reservoir of substrate (urea) is present. **Figure 4-17** provides a comparison of the theoretical carbonate addition rates by hydrolysis to the predicted addition rate by slow reagent addition (a). It is evident that in an ideal case the rates can be matched. (b) By comparing the experimental pH – time profile of slow addition with the pH profile obtained from enzymatic hydrolysis, it is evident that the profiles do not completely converge. The observed discrepancy can be seen to arise due to changes in enzyme activity with solution pH and the fact that an average enzyme activity across the whole pH range was used in prediction.

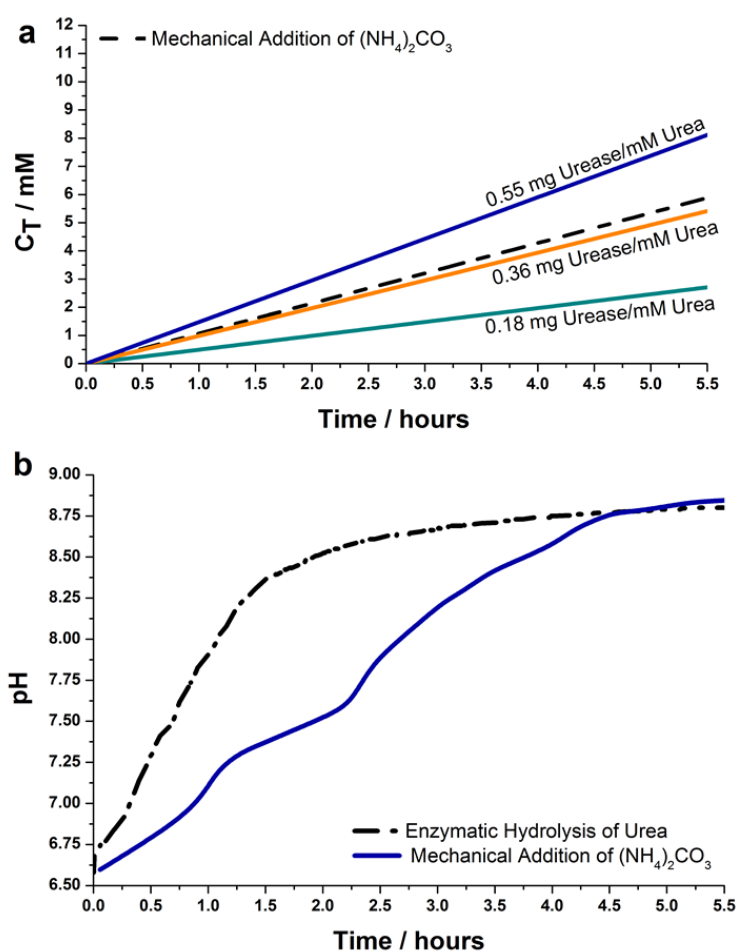


Figure 4 - 17: (a) Theoretical total inorganic carbon (C_T) addition rates required for the production of CaCO_3 -PSS MA mesocrystals based on mechanical reagent addition (---) and C_T addition rates based on enzymatic hydrolysis of urea at 24°C and free pH drift with varying urease/ urea ratios (continuous). (b) Experimentally obtained pH - time profiles of mechanical slow addition -20 ml of 250 mM $(\text{NH}_4)_2\text{CO}_3$ added at 0.0057 ml/min to a 80 ml of solution containing 325 ppm PSS-MA and 5 mM CaCl_2 -, and enzymatic hydrolysis of urea from a 70 ml solution of 5 mM CaCl_2 , 40 mM urea, 1 mg urease and 325 ppm PSS MA.

Chapter 4: Characterisation of Diffusion Methods

Despite the recorded discrepancy in the measured pH profiles, scanning electron micrographs of precipitates prepared by enzymatic hydrolysis were in general morphological agreement with CaCO_3 PSS-MA mesocrystals obtained by the ADM (**Figure 4-18a**). Crystals were retrieved from the solution 48 hours after the urease was added. BET surface area measurements were also performed on the isolated crystals to confirm the formation of mesocrystals. The recorded measurements ($80\text{-}45\text{ m}^2\text{g}^{-1}$) are in fair agreement with the areas reported in the literature. Thermogravimetric analysis confirmed the presence of the block copolymer (~6 wt%) associated with the mesocrystals. Raman (b) and IR spectroscopy (c) showed that only calcite is present as the crystalline phase. The presence or absence of amorphous content in the mesocrystal structure could not be confirmed.

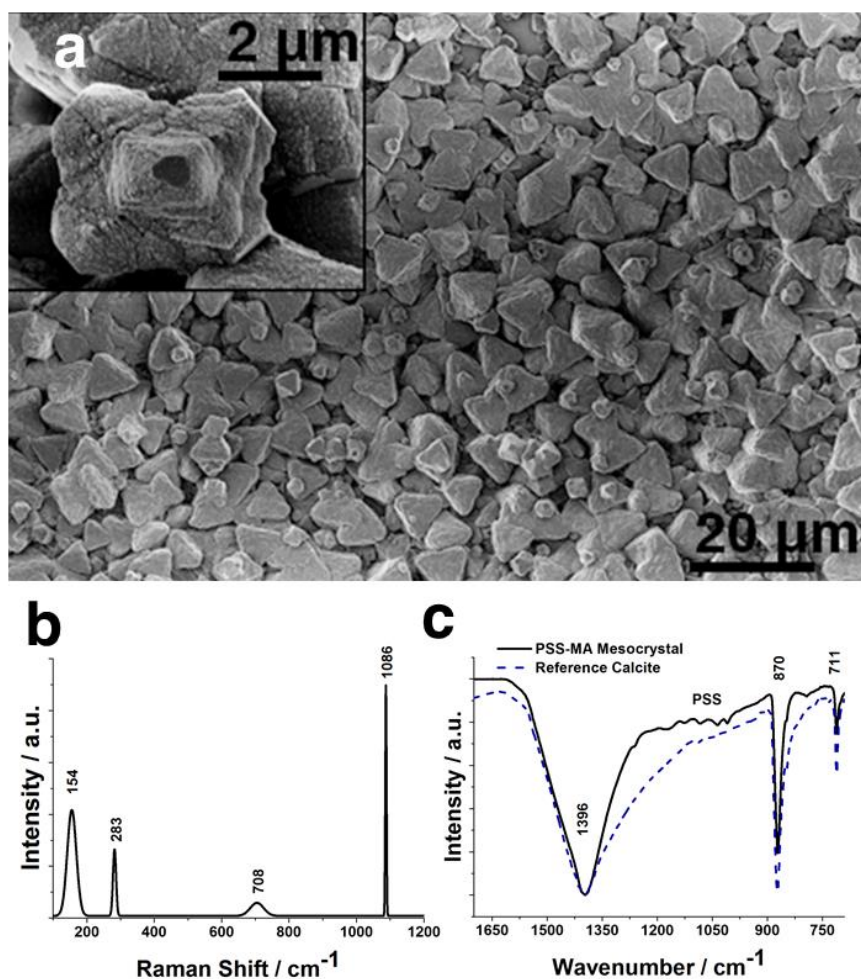


Figure 4 - 18: (a) Scanning electron micrograph of CaCO_3 -PSS MA mesocrystals obtained after 48 hours of incubation from a 70 ml solution of 5 mM CaCl_2 , 40 mM urea, 1 mg urease and 325 ppm PSS MA. (b) Raman and (c) IR-spectra of CaCO_3 -PSS MA mesocrystals obtained by the controlled enzymatic hydrolysis of urea.

4.5: CaCO₃ Mesocrystals

4.5.1: Introduction - What Characterizes a Mesocrystal

Over the recent decades, observations of solution-based crystallisation processes have challenged and are still challenging our understanding of crystal growth.(59, 63, 313) At the core of those observations lies the concept of crystallisation via oriented attachment and its sub-classification of mesocrystals.(66, 314) The term mesocrystal was first used to describe calcite and vaterite crystals with intriguing morphologies, which were precipitated in the presence of polymer additives.(69, 305, 315-319) It is nowadays used to describe a vast number of different crystals, organic and inorganic, which are believed to form by particle-based assembly mechanisms.(294, 303, 304, 320-325)

So what exactly describes a mesocrystal? Initially, the concept was used as an extension of oriented attachment and was applied to the formation of larger, 3D crystals via the oriented assembly of polymer-stabilised crystalline nanoparticles (Chapter 1.3). This was later extended such that the term mesocrystal refers to a structural classification rather than a formation mechanism. The term mesocrystal describes any structure that “comprises a 3D array of iso-oriented single crystal particles of size 1–1000 nm” that behave as one “single crystal”.(67)

A problem in this definition of a mesocrystal is how we classify a crystal as a mesocrystal by means of structural analysis. Two primary identifiers, from the structural analysis of the formed crystals were used in combination in the initial studies to make this separation, of ion-by-ion grown single crystals and mesocrystals. Those primary identifiers are an elevated surface area compared to the surface area expected for an ion-by-ion grown single crystal, and the presence of a crystalline substructure as determined by diffraction. A second, and more subjective identifier, is the morphological appearance of the crystals i.e. they appear to be composed of smaller subunits. The two primary identifiers of mesocrystal structure – surface area and crystalline substructure - were studied here for the case of CaCO₃PSS-MA mesocrystals.

4.5.2: Elevated Surface Area

One of the primary mesocrystal identifiers is the elevated surface area of the mesocrystal as compared to what is measured for a single crystal of equal size. In this respect, the change in surface area of CaCO₃ PSS-MA mesocrystals with increasing incubation time in solution was measured by BET. These studies were initiated based on microscopic observation of an apparently decreasing surface roughness with time spent in solution, **Figure 4-19a**.

For BET analysis, 200 mg of pseudo-octahedral CaCO₃ PSS-MA mesocrystals were prepared by mechanically-driven slow addition, as stated in Chapter 4.4.1. Multiple reactions were set up simultaneously, and were terminated/ transferred for BET analysis after 12 hours to 14 days. The BET determined surface areas were again in fair agreement with the values for calcite mesocrystals reported in the literature.(305, 326) The measured surface area decreased significantly with the time spent in solution. From values of 97 m² g⁻¹ measured 12 hours after the reaction had been initiated, the measured surface area decreased to 22 m² g⁻¹ after 28 days of storage in solution (b). This decrease in surface area was enhanced if the mesocrystals were aged in air for 2 days, when a reduction from 85 m² g⁻¹ to 10 m² g⁻¹ was observed. The faster reduction in air than in solution may be due to stabilization conferred by the residual polymer in the crystallisation solution.

TGA was also performed of CaCO₃ PSS-MA mesocrystals after certain incubation times in solution. This revealed a decrease in polymer “occlusion” from ~ 4 wt% (12 hours) to 1 wt% polymer (28 days) (c). The calculated fractal indices from the absorption measurements made were in agreement with the decrease in surface roughness observed in electron micrographs (d).(186) For a detailed analysis please refer to Kim, Schenk, Ihli, Kulak, Hetherington, Tang, Schmahl, Grieshaber, Hyett and Meldrum (327).

A number of explanations can be given for the measured decrease in surface area with aging in and out of solution. In the first place, mesocrystal theory has suggested that the crystalline subunits can fuse, resulting in a loss of the void space responsible for the enhanced surface area. Secondly, simple Ostwald ripening and associated surface recrystallisation may provide a sufficient decrease in surface roughness to explain the decrease in measured surface area. The latter is proposed under the assumption that surface roughness is the primary factor in determining the measured surface area and not any pre-existing crystallite substructure and associated void space between particles.(327) With no particular

evidence for either of those explanations, this suggests that enhanced surface area is not a definitive indicator of a mesocrystal.

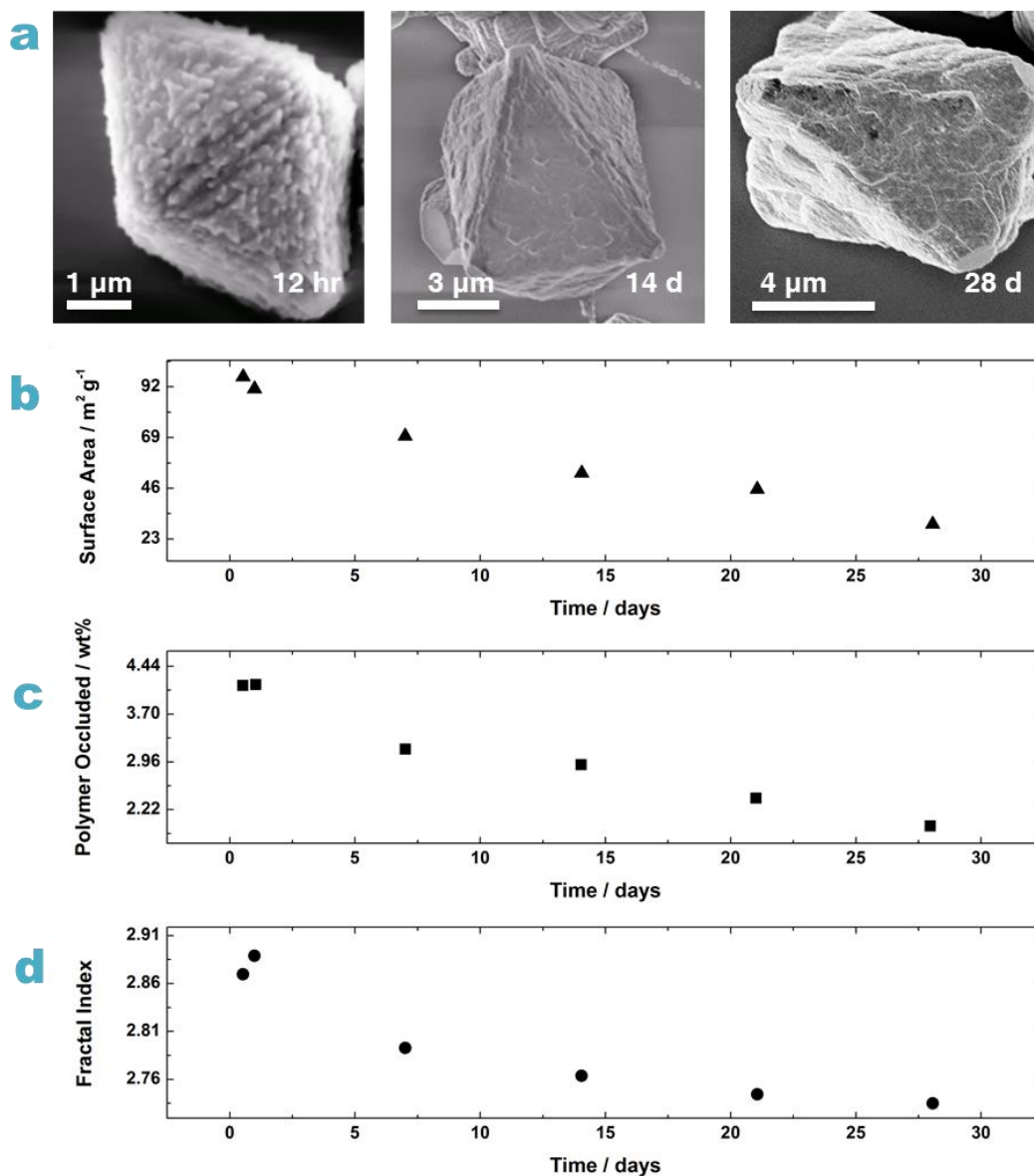


Figure 4 - 19: (a) Scanning electron micrographs of CaCO₃ PSS-MA mesocrystals retrieved from the mineralizing solution after 12 hours, 14 days and 28 days given from left to right. (b) Measured surface area, (c) polymer “occlusion” and (d) fractal index changes with aging in solution. Mesocrystals were prepared by adding a carbonate containing reagent solution (20 ml of either 250 mM (NH₄)₂CO₃) at 0.0057 mlmin⁻¹ to a 80 ml of solution containing 325 ppm PSS-MA and 5 CaCl₂, under agitation at 70 rpm.

4.5.3: Crystallinity

If an elevated surface area cannot be used to reliably identify mesocrystal structures, the identification of an ordered crystalline substructure remains the sole identifier.

Table 8 and 9, describe results extracted from the paper Kim, Schenk, Ihli, Kulak, Hetherington, Tang, Schmahl, Griesshaber, Hyett and Meldrum (327), which show that PXRD is often miss-analysed using the Scherrer equation to demonstrate the sub-structure characteristic of mesocrystals. PXRD data provided in Tables 8 and 9 were collected in a high resolution synchrotron PXRD study of single crystal calcite and “mesocrystal calcite”. The results show that the peak broadening previously associated with the presence of an ordered crystalline substructure alone cannot be used as proof of mesocrystal structure when lattice strain was also present. This is highlighted in the provided tables by the underestimate of apparent crystallite size if strain is disregarded. It is also noted that no analysis gives an average crystallite size that would account for a, “typical” mesocrystal surface area.

Chapter 4: Characterisation of Diffusion Methods

		Control 10 mM	PSS-MA	PSS-MA Seeded	PS-MA
Rietveld (pseudo-voigt)	Size only (nm)	817	380	319	485
	Strain only (%)	0.0010	0.030	0.039	0.022
	Size (nm) and strain (%)	870/0.004	553/0.024	612/0.035	622/0.016
Williamson-Hall plot	Size only (nm)	446.4	141	109	243
	Strain only (%)	0.017	0.057	0.074	0.0325
	Size (nm) and strain (%)	678/0.006	1014/0.049	3228/0.072	647/0.021
Scherrer Eq (104)	Size only (nm)	825	321	278	368
Scherrer Eq (001)	Size only (nm)	798	228	185	435

Table 8: “Strain parameters and coherence lengths derived from line profile analysis of powder synchrotron XRD spectra of calcite crystals.”(327)

		Sample 1		Sample 2		Sample 3	
		Fresh	In situ heating 300 °C	Fresh	Ex situ heating 400 °C	Fresh	Aged in air 24hrs
Rietveld (pseudo-voigt)	Size only (nm)	224	223	388.4	295.2	299.8	322
	Strain only (%)	0.046	0.050	0.029	0.040	0.034	0.032
	Size (nm) and strain (%)	446/0.041	519/0.046	707.9/0.025	1493/0.039	642.5/0.030	666/0.029
Williamson-Hall plot	Size only (nm)	82.6	74	141.2	102.2	112	114
	Strain only (%)	0.099	0.109	0.057	0.079	0.072	0.070
	Size (nm) and strain (%)	2344/0.10	-/0.11	1335/0.051	- /0.084	1011/0.064	1036/0.063
Scherrer Eq (104)	Size only (nm)	224.6	223.2	368	299	319	319
Scherrer Eq (001)	Size only (nm)	191.6	188.6	319.3	257.5	266	266

Table 9: “Strain parameters and coherence lengths derived from line profile analysis of powder synchrotron XRD spectra of three different batches of calcite PSS-MA mesocrystal after *in situ* heating to 300°C, *ex situ* heating to 400°C and aging in air.” (327) Altered after (327)

4.6: Discussion

A number of studies have previously attempted to either modify, or characterize features of the ammonia diffusion method in order to achieve greater reproducibility. These have included substitution of solid ammonium carbonate with a liquid reservoir of ammonium carbonate,(261, 328) or estimation of pH and supersaturation changes (while neglecting precipitation) for precipitation in μL droplets in a so-called crystallisation mushroom.(261) A general comparison of the ammonia diffusion and double diffusion methods has also been made by studying the pH profile.(329) By comparison, we have here provided a very detailed picture of the changes in solution which accompany the precipitation of CaCO_3 using the ADM.

The results presented here demonstrate that the **ADM** can be controlled using a range of variables including the introduction of a diffusion barrier, and change of the solution surface area, which leads to modification of the reaction profile. When conditions are used which lead to a rapid reaction rate, the reaction profile and solution conditions approach those achieved in other techniques. This is characterized by a burst of nucleation which depletes a large proportion of the available calcium ions, followed by a steady drop in the supersaturation as the nuclei grow in solution. In contrast, when the ADM conditions are controlled to give slow growth, a unique profile can be generated where nucleation occurs in an initial burst. This initial burst in nucleation consumes only a relatively small proportion of the available ions. The supersaturation then remains relatively constant, at a level well above the threshold for ACC precipitation, until the calcium ions have been depleted. It is the precipitation of CaCO_3 crystals under the latter conditions that can lead to the generation of unique and often complex crystal morphologies when organic additives such as block copolymers are also present in the reaction solution.

Identification of the solution conditions which lead to these complex crystal structures – which determine the nucleation and growth processes which could feasibly occur – therefore provides a unique insight into the processes which may generate such crystals. As the precipitation occurs under conditions where the supersaturation remains rather constant, but at a level above the ACC threshold for the vast majority of the reaction, it is possible for new nuclei to form throughout the reaction, probably as ACC. This may occur homogeneously or heterogeneously on

Chapter 4: Characterisation of Diffusion Methods

pre-existing precipitates in solution. If further nucleation does not occur, the nuclei formed in the original nucleation event will simply continue to grow.

In the absence of polymer additives, calcite rhombohedra are the typical products of the ADM both under slow and rapid growth regimes. Studies of ACC precipitation in bulk solution (achieved by mixing solutions of calcium and carbonate ions) have shown that ACC particles form in a nucleation burst, and then continue to grow without aggregation.^(220, 243, 330) The mechanism by which they crystallize is less clear. It has been suggested that nucleation of the latter crystalline phases occurs within existing ACC particles,^(218, 331) and there is strong evidence that these crystalline nuclei then grow via dissolution/ reprecipitation of other ACC particles in solution.^(139, 209, 219) Further, an ACC particle cannot start to crystallize until it reaches a critical size.^(137, 160) Crystallisation of ACC to vaterite in bulk solution via a solid state transformation has also been suggested, based on cryo TEM techniques and SAXS/WAXS studies.⁽³⁰⁷⁾ In the latter study the ACC nanoparticles were believed to first dehydrate, then undergo a structural rearrangement to vaterite, and finally aggregate to form micron-scale vaterite particles.

This process will obviously be modified in the presence of polymers. Some studies have attempted to characterize the mechanism of formation of CaCO₃ mesocrystals in the presence of polymer additives. These have analysed the reaction solutions at early times using transmission electron microscopy (TEM), analytical ultracentrifugation and dynamic light scattering,^(305, 318, 332) and have shown the presence of amorphous nanoparticles at early reaction times. As a particular feature of polymer-controlled growth, which distinguishes it from additive-free reactions, these ACC particles rapidly form aggregates, which then ultimately crystallize. Given the challenging nature of these early-time studies, they present only a broad picture of the reaction processes, and little is known about the growth of the aggregates or their crystallisation mechanism.

Our results are therefore fully in keeping with these observations, but importantly also demonstrate that under slow growth in the ADM – which is the regime where mesocrystals are observed – new material is continually produced after the initial nucleation of ACC. This then distinguishes it from rapid growth conditions where there is a single nucleation event, followed by growth. The most probable scenario is therefore that new particles nucleate on the existing polymer-stabilized ACC aggregates, or on crystalline particles at later stages of the reaction, giving rise to more complex morphologies.

Chapter 4: Characterisation of Diffusion Methods

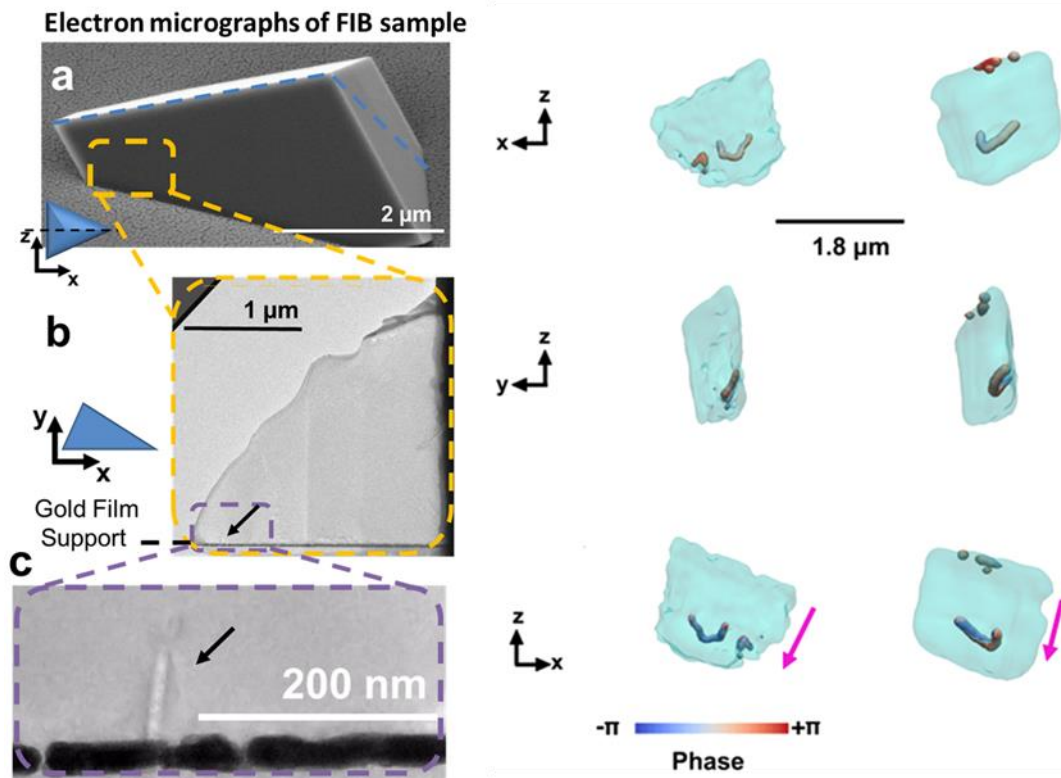
The formation of so-called CaCO_3 “**mesocrystals**” would therefore appear to be based on the crystallisation of an assembly of ACC nanoparticles rather than the oriented assembly of precursor crystalline nanoparticles as was originally suggested.(318) Indeed, nanoparticulate calcite and vaterite are very hard to synthesize due to their rapid growth in solution. In this way, synthetic CaCO_3 mesocrystals would appear to have many similarities to biogenic calcite mesocrystals, where the ultrastructure derives from a memory of the ACC precursor phase.(67, 305) It is also stressed that Ostwald ripening processes are active during CaCO_3 precipitation, such that large crystals grow at the expense of smaller ones. It is also noted that even under the slowest reaction times used here, the reaction is almost complete and the calcium ions depleted after 6-8 hours. Therefore, while a number of articles describe the precipitation of CaCO_3 crystals using the ADM using prolonged incubation periods (days to weeks), any morphological changes reported in crystals after ≈ 12 hours are simply due to Ostwald ripening/ recrystallisation processes. Given that polymer remains in the solution, rough crystal surfaces, as seen in CaCO_3 “mesocrystals”, would be expected. Further, the replication of these “mesocrystals” by the enzymatic hydrolysis of urea, and the inherently homogeneous concentration profile of the reacting species in solution, point to the fact that the formation of mesocrystals and PILP-associated thin films is fundamentally independent of the macroscopic concentration profiles as suggested previously.(333) Rather, local concentration profiles seem to be responsible for aggregation-based crystal growth.

4.7: Conclusion

Despite the wide utilisation of the ADM in precipitating calcium carbonate the method had remained a “black box”. For the first time, this study reports concentration and supersaturation profiles of the precipitation of calcium carbonate using the ADM. Rigorous characterization of the ADM under varying experimental conditions revealed several key aspects which distinguish the method from common direct precipitation methods. These are potentially responsible for the crystal morphologies which are characteristic of diffusion methods. The main difference is that the initial nucleation burst consumes only a relatively small amount of the available calcium ions, and the supersaturation then remains relatively constant, and well above the threshold value for ACC, until the majority of the calcium ions have been consumed. As a result, new material can be generated and deposited throughout the course of the precipitation reaction i.e. multi-nucleation character of the reaction is a possibility, a feature which we believe to be fundamental to the formation of complex, aggregation-based morphologies. The reaction progress profiles show a short phase in which the crystal morphologies would be developed, and also suggest that the often unique calcite morphologies which are produced using the ammonia diffusion method are most likely a result of Oswald ripening or attachment phenomena, rather than being determined by the initial nucleation conditions. This fact was later confirmed by the overgrowth of seed crystals to near identical morphologies.(327)

The obtained reaction profiles were then used to develop a one pot synthesis that can replicate CaCO_3 mesocrystal morphologies. This can enable the scale-up of the process and allow in situ investigations. Lastly, investigation of the characterisation of CaCO_3 mesocrystals puts into question our understanding of how we identify a crystal as a mesocrystal. The primary identifiers used to characterise mesocrystals could either not be confirmed (crystalline sub units) or were time-dependent (elevated surface area).

Chapter 5: Bragg Coherent Diffraction Imaging of Calcite Single Crystals



Chapter 5: Bragg Coherent Diffraction Imaging of Calcite Single Crystals

Chapter 5 is a reproduction of manuscripts accepted or in preparation for publication. Images are provided in reproduction in part or total with the respective source acknowledged. It is stressed that the candidate did not perform the image reconstructions provided in this Chapter. The presented work was executed in collaboration with Jesse N. Clark, performing image reconstruction and in parts their analysis. FEM studies were carried out by Alexander S. Côté. The following discussion focuses particularly on the observations made and their interpretation rather than the underlying reconstruction and phasing procedures. The latter are provided in Appendix D for coherency and are in reproduction of (199).

Clark JN[†], Ihli J[†], Schenk AS, Kim Y-Y, Kulak AN, Campbell JM, Nesbit G, Meldrum FC, Robinson IK. Three-dimensional imaging of dislocation propagation during crystal growth and dissolution. *Nature under review*

Ihli J[†], Clark JN[†], Côté AS, Kim Y-Y, Schenk AS, Kulak AN, Comyn TP, Chammas O, Harder RJ, Duffy DM, Robinson IK, Meldrum FC. The Role of Strain in Controlling Crystallisation at Soft Interfaces. *To be submitted*

5.1: Abstract

The structural organization of a crystalline material, where this includes atomic level defects such as dislocations or the presence of macromolecular occlusions, contribute enormously not only to the physical properties of a material (including hardness and chemical reactivity) but also determines its growth mechanism and ultimately its morphology. Dislocations and the structural organization of materials have therefore been studied extensively using techniques such as XRD, TEM and AFM. However, these techniques have not been able to generate a combined 3D image of a crystal's gross morphology, internal structure, lattice deformations and dislocation network. In this chapter, Bragg Coherent Diffraction Imaging is used to provide exactly this, a combined image of the gross morphology of a single crystal, the 3D strain fields and defects present within it. This directly allows us to visualize the dislocation network present within a single crystal with nanometer resolution. Two case studies are then presented, the first of which provides a demonstration of how the dislocation network and strain within a calcite rhombohedron guides crystal growth and dissolution. The second study addresses how a "soft" organic substrate guides the morphological development of a heterogeneously nucleated calcite crystal due to strain accumulation in the direction of preferred crystal growth.

5.2: Fundamentals of Bragg Coherent Diffraction Imaging

5.2.1: Introduction

Bragg coherent diffraction imaging (BCDI) is a novel form of phase contrast X-ray microscopy in which the common imaging optics are replaced with iterative phase retrieval algorithms.(196, 334) In BCDI, oversampled diffraction patterns collected from an isolated crystal illuminated by a coherent wavefield across a Bragg reflection are inverted into a complex valued 3D image of the specimen illuminated.

The required 3D patterns are acquired under the Shannon constraint i.e. the crystal's Fourier transform is sampled at least twice the Nyquist frequency. The illumination of a crystal that is smaller than the coherence volume of the beam generates a coherent X-ray diffraction (CXD) pattern due to scattering from all parts of the crystal. Both conditions combined with the successful application of phase retrieval algorithms returns a tomographic image of the crystal morphology generated from the intensity of the CXD pattern and the recovered phase.

The reconstructed amplitude contains information about the electron density distribution, $\rho(r)$. Phase shifts $\phi(r)$ in the reconstructed complex amplitude, in turn, arise from strain (internal deformation) in the crystal lattice, where these are apparent in the asymmetric part of the diffraction pattern at each Bragg reflection.

The sensitivity of the returned phase to lattice displacements is due to the fact that the phase is proportional to the projected displacement field, $u(r)$ of the atoms from their ideal lattice points and to the scattering vector \mathbf{Q} via $\phi(r) = \mathbf{Q} \cdot u(r)$. This makes BCDI a unique method for providing combined information on morphology, strain and crystallographic defects in a single crystal with nanometre resolution. Previous applications of BCDI have shown, for example, phonon movement in gold nanoparticles,(197) the evolution of strain with increasing physical load,(335) and the introduction of surface stress by surface absorption of thiols on gold nanocrystals.

Chapter 5: Bragg Coherent Diffraction Imaging of Calcite Single Crystals

A schematic illustration of the “imaging” process from experiment to reconstructed image is presented in **Figure 5-1**. The example presented is of a calcite rhombohedron 1 μm in diameter and nucleated in solution by the ammonia diffusion method. This is used as the reference sample for the subsequent investigations. The 3D far-field diffraction pattern was collected from the off-specular (104) reflection. The given diffraction pattern shown are for demonstration purposes only and do not correspond to the collected 3D patterns.

Reconstructed electron density distributions (amplitude) of the imaged calcite crystals compare well with the common morphology of calcite rhombohedra present in the sample. The projected lattice displacement (phase) is visualized in colour, where the deviation is shown from a homogenous phase condition ranging from $-\pi$ (lattice dilation) to $+\pi$ (lattice contraction). The specimen can be seen to be largely unstrained, with local areas of surface stress accumulated at the crystal edges. It has to be stated that with current experimental facilities available it is not possible to obtain images of one and the same crystal by means of BCDI and for example electron microscopy. This is due to the problems associated with locating a specific crystal across different imaging platforms.

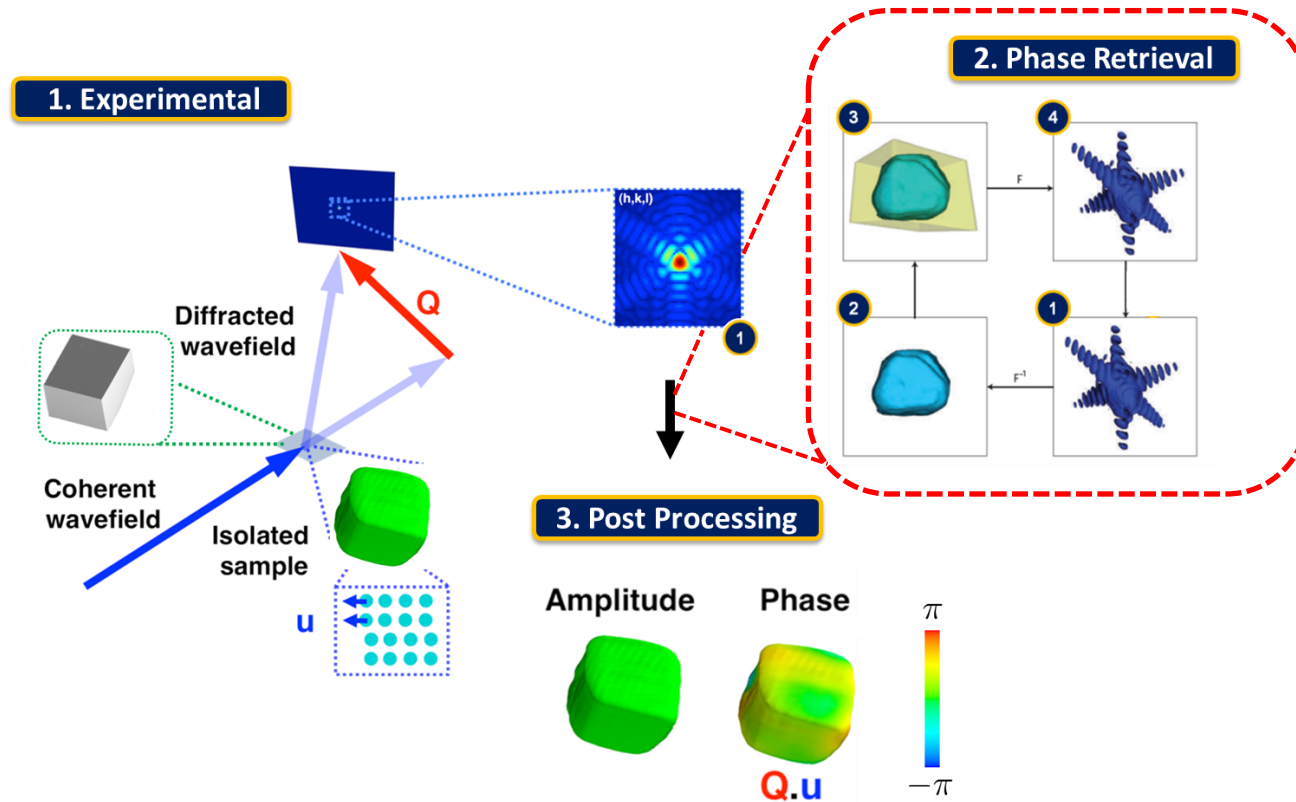


Figure 5 - 1: Principle of Bragg Coherent Diffraction Imaging. 1. Experimental acquisition of coherent 3D diffraction pattern. Diffracted beams (aqua) emitted by an isolated specimen (green) exited by a spatially coherent wave (blue) exceeding the specimen size and undergoing rocking motion are collected by an area detector (2D) and are then stacked (3D). 2. The collected 3D pattern (1) is passed to a phase retrieval algorithm moving between real space and reciprocal space (1 \leftrightarrow 4) till autocorrelation between measured amplitude and retrieved amplitude with an evolving phase is established. This yields a complex function of amplitude (electron density) and phase (lattice displacement) as a product of scattering vector Q (h,k,l) and lattice displacement field u . (3) Fourier transformation of the now known phase and amplitude returns a 3D, tomographic representation of the crystal. An example is shown of a calcite rhombohedron nucleated in solution 1 μ m in diameter. Schematic reproduced and extended after (197) and (196).

5.2.2: Experimental

BCDI measurements were carried out at third generation synchrotron sources (Diamond Light Source DLS and the Advanced Photon Source APS), where these provide x-ray beams with sufficient brightness and coherence for the experiments performed.

In a simple BCDI experiment, a crystalline sample located on a 6 axis diffractometer, aligned with the beam and centred in the selected Bragg condition is illuminated by a spatially coherent beam of X-rays that have been produced by an “undulator device” and monochromatized (Chapter 2.9.2.3). A coherence length greater than the dimensions of the crystal ensures that scattering from all parts of the crystal interfere in the far-field diffraction pattern collected upon illumination. Diffraction patterns are recorded using a charge-coupled area detector, which is positioned at the desired diffraction angle and at a distance far enough from the sample to resolve the finest fringes and speckle patterns. To acquire the full 3D CXD pattern required for BCDI, a rocking curve central to the selected Bragg reflection is performed. For that purpose the crystal is rocked step-wise through its Bragg peak, such that the oversampling constraints are met. Here, the crystal was rocked by 0.3 degrees in total with a step size of 0.003 degree. For each incremental “rocking” step, a two-dimensional slice of the 3D far-field diffraction pattern was recorded. Upon stacking, this yields a complete 3D diffraction pattern, from which real-space images could be reconstructed (Chapter 5.2.3). This stacking of 2D slices collected in the rocking curve yields a 3D representation of the crystal imaged, where this is analogous to electron tomography and is based on the central Fourier section theorem. This states that the Fourier transform of a 2D “slice” of a 3D object is a central section of the 3D Fourier transform of the sample/crystal. A collection of 2D slices through the entirety of the 3D sample/ crystal can then be stacked in reciprocal space to yield the 3D structure in reciprocal space and real space by inverse Fourier transformation.(336)

In this regard, the importance of a coherent illumination source must be stressed. “The beam itself has a point-to-point phase correlation that is preserved throughout the interaction with the sample. The x-rays scattered from different regions of the sample reach a camera with a fixed relative phase to each other and constructively or destructively interfere accordingly.”(337) This enables the imaging of crystals smaller than the coherence length of the illumination source. Subsequently, the

Chapter 5: Bragg Coherent Diffraction Imaging of Calcite Single Crystals

measured squared modulus of the Fourier transform of the sample structure can be transformed back onto the spatial domain by said phase retrieval algorithms.(337)

Examples of CXD patterns collected across a Bragg reflection are given in **Figure 5-1** and **5-2**. These consist of modulated streaks or fringes and airy speckle patterns, which rapidly decline in intensity away from the Bragg centre of the diffraction pattern. Fringes and speckles are a result of the coherent beam illuminating the entirety of the sample; the diffraction spots are strongly modulated by the interference between waves scattered by the crystal surfaces. The modulated fringes are a result of the interference between two major, “fully developed”, opposing facets. The airy speckle pattern in Figure 5-2 originates accordingly from the spherical particle shape. The modulated fringes are then used in the determination of the imaged crystal size. The fringe spacing is inversely proportional to the spacing in real space dimensions.(338)

The real space resolution of a BCDI experiment is determined by the radial cut-off value in detecting X-rays away from the centre. This parameter is limited by the sample, the detection equipment and the brilliance of the X-ray source. A typical real space resolution of 10-50 nm is currently achievable. Experimental details are provided in Chapter 2.9.2.3 and expanded in the case studies discussed below.

5.2.3: Retrieving the phase information from a BCDI pattern

Phasing the acquired 3D CXD pattern correctly is the critical step in BCDI imaging. This is achieved by processing the 3D CXD pattern with iterative phase retrieval algorithms, where these effectively replace the imaging optics in traditional microscopes. The complete knowledge of both the amplitude and phase of the diffracted wavefield eventually allows for a quantitative real-space image to be obtained via an inverse Fourier transform.

The applicability of phase retrieval algorithms and the delivery of unique solutions are founded on multiple imaging and process constraints during the collection of 3D CXD patterns. The applied phase retrieval works on the basis of internal redundancies in the collected patterns. These redundancies are sufficient in quantity as long as the diffraction data meets the oversampling, or **Shannon constraint**.⁽²⁰⁰⁾ That is the “number of measurement points be at least twice the number of unknown density values within this support”⁽¹⁹⁶⁾ or the sample has its Fourier transform sampled at least twice the Nyquist frequency. This is sufficient to determine the unique phase sets in two or three dimensions. The second constraint, the **support constraint**, states that the imaged crystal needs to be isolated or sufficiently separated from others in terms of spatial or orientational distance. This ensures that the recorded diffraction data can be ascribed to only a single crystal in a so-called support volume which contains all of the complex sample density (Chapter 5.2.4.).

Figure 5-2 illustrates a basic phase retrieval process. The procedure begins with a guess for the lost phase information associated with a particular diffraction data set. An inverse Fourier transformation (F^{-1}) is then applied, which yields a first real space estimate of the crystal shape (Fourier transforms connect the generated real space images (left column) with the reciprocal space data sets.). Having ensured that the crystal is indeed isolated (yellow box – indicating the support volume), the generated first estimate of the actual “crystal shape” is Fourier transformed (F) to yield an the three-dimensional diffracted wavefield of this first estimate. A **modulus constraint** is then applied i.e. the differences between the experimentally measured and calculated intensity of the first estimate are minimized. This is achieved by evolving the guessed phase iteratively, i.e. the process is repeated in an iterative round - robin manner with each side repeatedly updated until a self-consistent solution is reached (Chapter 2.9.2.3 and Appendix D).(196)

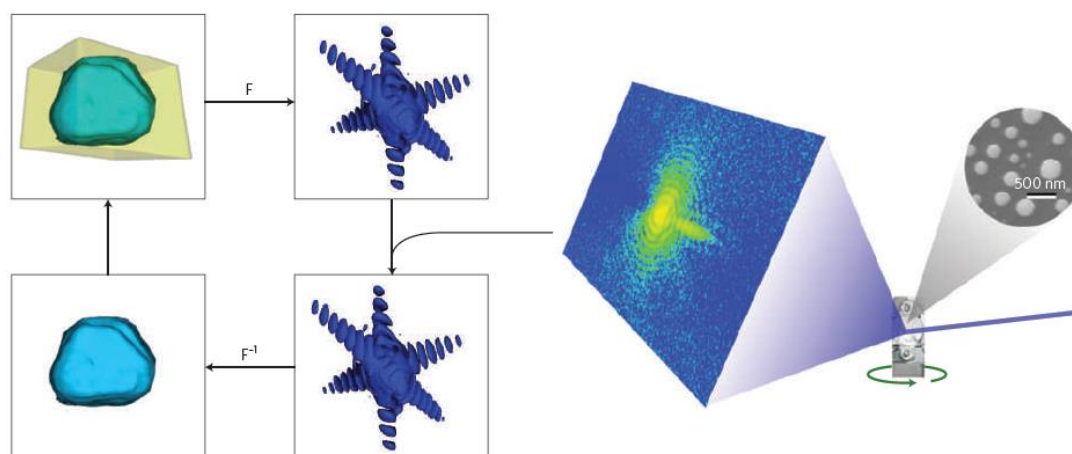


Figure 5 - 2: Illustration of a basic phase retrieval algorithm. This starts from a collected 3D CDX pattern to which a phase is guessed and inverse Fourier transformed (F^{-1}). A support constraint (opaque box) is then applied and a Fourier transformation carried out. A modulus constraint with the measured intensity is enforced next. The process is then repeated under evolution of guessed phase till a self-consistent solution is found. Image taken from (196).

5.2.4: Sensitivity of the Method to Lattice Deformation

A detailed explanation of the origin of lattice deformation sensitivity in BCDI is given in Appendix D. In brief, the lattice displacement present in an imaged crystal results in a distinct asymmetry in the collected CXD pattern. This carryover of information into the recorded coherent 3D diffraction pattern is used in BCDI, and in particular the phase retrieval algorithms, to rebuild the lost phase information and with it the information on lattice displacement. This is analogous to the geometrical phase analysis used in electron microscopy.(197, 339)

Considering the Fourier transform of an ideal crystal – which is finite in dimensions and has a 3D lattice in perfect register - the observable intensity distribution in reciprocal space is periodic and the pattern correlates with the crystal shape as determined by its expressed facets. The intensity distribution is symmetric about the origin of reciprocal space and with it the intensity will be symmetric about the reciprocal lattice points. This ultimately results in a symmetric diffraction intensity pattern when recorded across a Bragg peak. However, since real crystals possess defects the recorded diffraction is generally not symmetric and possesses both a symmetric and anti-symmetric parts.

The symmetric parts can be ascribed to the crystal's electron density distribution, given that these interact with the incoming X-rays. The anti-symmetric part in a CXD pattern can be directly related to variations in the real space phase when measuring under the Bragg condition i.e. coherent scattering conditions. In this case the real space phase changes are a result of local displacements of atoms from their ideal lattice position projected onto the \mathbf{Q} vector of the Bragg peak. In simple terms, the lattice displacement changes locally the scattering condition, which induces a change in phase and therefore a distortion in the collected diffraction pattern. Having reconstructed a 3D CXD pattern due to scattering from all parts of the crystal, the displacement is visualized as a real space phase map at each position in the crystal. This is returned and separated by a phase retrieval algorithm.(196) **Figure 5-3**, illustrates this argument.

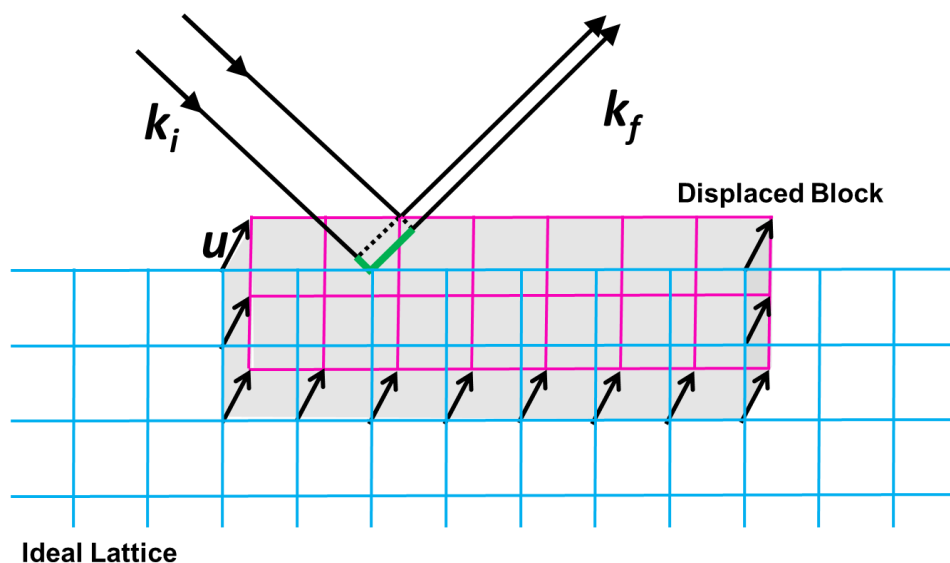


Figure 5 - 3: Illustration highlighting the relationship between the local lattice displacement and the alteration in real space phase carried over into the CXD pattern. Shown is a generic lattice arrangement (blue) in which a block of material is displaced from its ideal position (pink) by a vector or $u(r)$. The phase of X-rays scattered by the displaced block is therefore shifted relative to the material in perfect register (highlighted in green), with the total amount given by $\phi(r) = k_f \cdot u(r) - k_i \cdot u(r) = Q \cdot u(r)$. $\phi(r)$ is equal to the phase. k the incoming and scattered wave vector and Q the scattering vector, set to a Bragg condition. In the Bragg condition every part of the perfect crystal scatters in phase – with areas of displacement and phase shift becoming a region of complex density with the same amplitude as the rest of the crystal but with a phase $\phi(r)$. The scattering vector Q is given by $Q = 4\pi \sin(\theta) / \lambda$. 2θ the angle between the incident wave and the detector. Illustration reproduced after (196, 340).

5.2.5: Data Visualisation

After successful phasing of the 3D CXD patterns and inverse Fourier transformation the data was saved in a VTK format. Data sets were visualised using the Mayavi2 data visualizer.^(341, 342) The obtained complex density can be separated into amplitude and phase. As stated above, this is interpretable as the physical density (electron density distribution) and lattice displacement present in the sample. These are presented either in the form of iso-surfaces and central cut slices through a given electron density representation, or in the form of colour maps projected onto generated iso-surfaces.

5.3: Crystal Growth, Dissolution and Dislocations

5.3.1: Introduction

Dislocations, and the resulting areas of atomic displacement play a significant role in the mechanisms by which crystals grow and dissolve. They also have a significant effect on the properties of crystalline materials,(343, 344) altering the chemical reactivity of rock forming minerals,(345, 346) and the mechanical strength of skeletal and construction materials.(112, 347-350) Our initial knowledge concerning strain and crystallographic defects was primarily derived from indirect observations such as changes in the growth rates and strength of materials. Optical microscopy revealed dislocation pile-ups.(351) With the development of microscopy techniques, it is now possible to directly visualize individual dislocations. AFM has enabled the dynamic study of single dislocations in 2D.(143) TEM, which was initially limited to presenting 2D projections of 3D thin specimens,(352) is nowadays capable of visualizing dislocations and strain fields in 3D with near atomic resolution in vacuum.(339, 353-356) However, due to the inherent shortcomings in these methods, 3D imaging of the formation or movement of dislocations during dynamic processes such as crystal growth and dissolution has still not been achieved.

Utilizing Bragg coherent diffraction imaging (BCDI),(196) we here study the response of individual calcite rhombohedra (CaCO_3 , triclinic) to cycles of crystal growth and dissolution. This work provides a first step in the imaging of the formation and movement of dislocations in 3D. This is rendered possible as BCDI provides combined 3D information regarding morphology and localized lattice deformation of the growing and dissolving calcite rhombohedra at a resolution of ~50 nm.

For the past century, crystal growth and dissolution studies focused on the mechanisms underlying experimental observations.(357) This eventually led to descriptions applicable to both crystal growth and dissolution, Chapter 1.3.2.3.(38) Fundamental to this was the early recognition of crystallographic defects, and most prominently the importance of screw dislocations for crystal growth.(358) The lattice deformation (strain) surrounding a defect not only governs the internal energy of a finite crystalline body,(359) but also locally alters the activation barrier towards external stimuli at a crystal surface. These stimuli include crystal growth, dissolution, catalysis, mechanical impact and charge transport.

Chapter 5: Bragg Coherent Diffraction Imaging of Calcite Single Crystals

The study presented here directly examines the fundamental idea that strain energy and dislocations can alter a crystal's (calcite rhombohedron) response to external stimuli in the form an supersaturated (crystal growth) and undersaturated (dissolution) solution. BCDI allows for a direct visualisation of changes in the localized strain fields associated with dislocations during the growth (and dissolution) of single crystals from the nano- to the micron-scale in their native state. It thus provides a unique insight into these processes, where this is currently not possible using any other means.(197, 360)

5.3.2: Experimental

5.3.2.1: Mineralisation

Calcite crystals to be analysed were **nucleated** by placing 100 μl droplets of a solution containing CaCl_2 , urea and urease on hydroxyl terminated SAMs, supported on gold thin films. The added solution was prepared by combining 350 μl urease (1 mg ml^{-1}) with 1 ml of 5 mM CaCl_2 / 20 mM urea. Details regarding substrate preparation are given in Chapter 2.2.1. Precipitation of calcium carbonate occurs on enzymatic hydrolysis of urea to ammonium and carbonate, Chapter 4.4.2.(174) **Figure 5-4a** illustrates the formation mechanism.

This precipitation procedure was selected for multiple reasons. The enzymatic hydrolysis of urea creates a supersaturation profile similar to that of the ADM (Chapter 4), which results in a large number of majorly unstrained crystals. The use of hydroxyl terminated SAMs ensures that we obtain a population of (104) oriented calcite (Chapter 5.4.2). These two factors, combined with the restricted solution volume used (droplets of 100 μl), limit the final crystal size and generate a sample of predominantly (104) oriented,(361) largely unstrained, calcite rhombohedra with average diameters of $\approx 1.25 \mu\text{m}$ of sufficient density.(219) The prepared crystallisation setup was kept at 100% r.h. to avoid droplet evaporation.

This methodology satisfies four critical constraints for BCDI imaging. Firstly it generates crystals with spatial dimensions smaller than the coherence length of the illumination source. Secondly, the crystals imaged are not overly strained, and thus are suitable for current generation phase retrieval algorithms to handle. Thirdly, a high enough numerical density of crystals on the substrate allows the localisation of a suitable crystal in a timely manner. Finally, nucleation on hydroxyl terminated SAM fixes the crystal in place, which ensures that there is no movement of the imaged crystal during image acquisition.

Overgrowth of deposited calcite rhombohedra was carried out in-situ on samples which had previously been imaged by BCDI and centred into the Bragg condition. Overgrowth was achieved by introducing Kitano solution (Chapter 2.2.2.) and simple solvent evaporation. A 50 μl volume of ≈ 1 mM calcium bicarbonate solution was placed on the still-aligned sample, where evaporation and CO_2 out-gassing results in a supersaturation increase, which induces the deposition of new material. After complete evaporation of the droplet, the selected crystals were then re-imaged, Figure 5-4b. Calcium bicarbonate solutions were prepared by adding 100 mg of CaCO_3 to one litre of Milli-Q water, through which $\text{CO}_{2(g)}$ was bubbled for three hours.

Partial dissolution of BCDI imaged calcite crystals was achieved by depositing 50 μl of 0.1 wt% acetic acid solution onto the aligned substrate, which carried an estimated number density of 0.1 crystals μm^{-2} (Appendix D). The solution was then removed after 60 seconds. This was followed by addition and removal of a drop of ethanol to wash the sample, and a further diffraction pattern was collected. This process was then repeated to obtain successive dissolution stages of the same single crystal, Figure 5-4c.

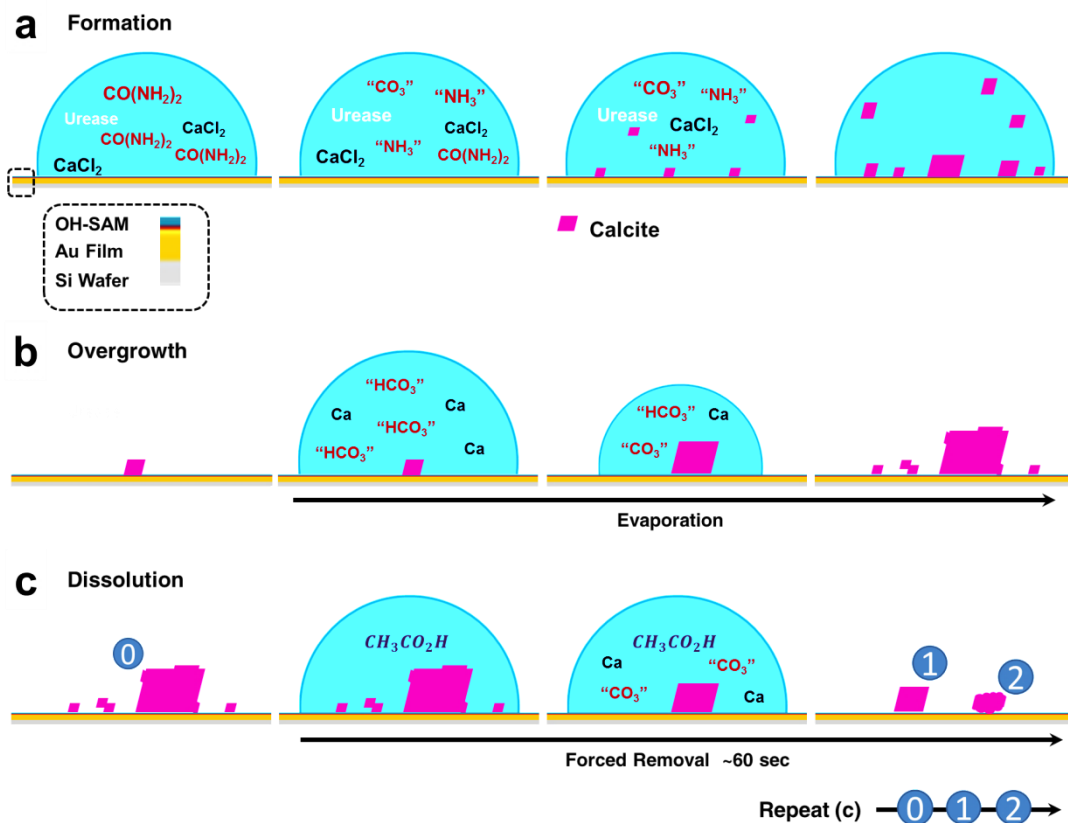


Figure 5 - 4: Schematic illustrating the formation (a), overgrowth (b) and repeated partial dissolution (c) of calcite formed on hydroxyl terminated SAMs. From left to right given in (a) is the urea-urease hydrolysis based nucleation and deposition of calcite rhombohedra. (b) Overgrowth of the formed rhombohedra is achieved by addition of calcium bicarbonate solution and subsequent solvent evaporation. (c) Repeated partial dissolution of the calcite crystals is achieved by the repeated addition of acetic acid solution onto the substrate, followed by its removal and a washing step.

5.3.2.1: Coherent Diffraction Imaging

BCDI experiments were carried out at beamline I16 at the Diamond Light Source. Calcite crystals of sizes 1 - 4 μm were imaged by BCDI at different stages of an applied growth and dissolution cycle. BCDI experiments, phase retrieval and dislocation analysis were performed as outlined in Chapter 2.9.2.3/ Appendix D.

In brief, calcite rhombohedra $< 2 \mu\text{m}$ in diameter were illuminated individually with monochromatic X-rays (8 keV), whose coherence volume is larger than that of the investigated crystal.⁽¹⁹⁸⁾ A series of 2D diffraction patterns, separated by 0.003 degrees under Shannon constraints were then collected, ⁽²⁰⁰⁾ by rocking an isolated calcite crystal through its off-specular (104) reflection.⁽²⁰⁰⁾ The collected coherent 3D diffraction pattern, which was formed by scattering from all parts of the crystal, is then passed to a phase retrieval algorithm to yield a complex-valued 3D image. A novel phase retrieval algorithm was used, which employs a combination of guided phase retrieval with low to high resolution reconstructions.^(201, 202) This allows objects with non-negligible phase to be reconstructed from the now complete knowledge of both amplitude and phase under consideration of partial coherence.⁽¹⁹⁸⁾ This in turn provides a 3D image of the specimen's electron density distribution via the amplitude, and information regarding atomic displacement via the phase. As stated, dissolution was achieved by depositing dilute acetic acid solution on the crystal, while growth was achieved by adding a drop of calcium bicarbonate solution. Alignment of the crystal was maintained throughout, as the X-rays were nominally unfocussed and defined by slits with a square opening of 200 μm placed 0.3 m before the sample.

5.3.3: Results

5.3.3.1: Crystal Growth and Dissolution

Shown in **Figure 5-5** are iso-surface renderings of the reconstructed amplitudes (electron density) (a) and phase (projected displacement) (b) of the initial crystal (i), after growth (ii) along with successive dissolutions steps (iii and iv).

The reconstructed electron density of the initial crystal (i) i.e. as deposited, returned the expected calcite rhombohedra exposing five {104} facets towards the solution. This is in agreement with electron micrographs recorded of the sample prior to analysis, **Figure 5-6**. Crystal overgrowth (i to ii) results in an increase in size and smoothing of solution facing facets, which leads to a more steady state appearance. The face in contact with the SAM remains unaffected. Preferred growth directions are indicated with blue arrows in the figure. It is immediately evident that 2 of the 5 facets grow more rapidly than the other 3. This can only be explained by the presence of more reactive sites at these two facets i.e. a non-uniform distribution of defects. A defect-free rhombohedron would display a completely isotropic growth behaviour of solution-facing facets.

Images of the corresponding projected displacements (strain) are shown in Figure 5-5 b, where this is mapped onto an iso-surface with red and blue representing lattice contraction or expansion respectively by half a lattice spacing. Comparing the projected displacements before (i) and after crystal growth (ii) it is seen that displacements do not grow significantly with the crystal but remain maximal at the edges. This is characteristic of active growth fronts.⁽³⁶²⁾ The projected displacement (strain) is visualized here in colour deviation from a homogenous lattice condition ranging from $-d/2$ (lattice dilation, blue) to $+d/2$ (contraction, red). One colour cycle is equal to the displacement of one unit cell.

Chapter 5: Bragg Coherent Diffraction Imaging of Calcite Single Crystals

Figure 5-5 also displays two crystal dissolution steps (ii to iii and iii to iv). In contrast to the observed crystal growth, dissolution results in a global surface retreat, more strongly in polar crystallographic directions (red arrows) (iii and iv). With the first partial dissolution step (iii) also visible are signs of shape deformation and the onset of etch-pit formation. This ultimately results in an increase in the relative surface area and in particular roughness of the crystal, with pits displaying enhanced degrees of deformation in their direct vicinity. This is expected considering that etch pit formation commonly occurs in the vicinity of crystallographic defects and thus enhanced levels of strain. The second dissolution step (iii to iv) under an effectively enhanced level of undersaturation (the sample mass has decreased, but the amount of acid added remained constant) results in a pronounced change of the overall morphology. The crystal bears no resemblance to its initial form, and now has a porous, spherical appearance.⁽³⁶³⁾ This change in morphology can be explained by the applied undersaturation, which favours the production of a “spherical”, equilibrium shape. The porosity seen can be in part attributed to the removal of defect outcrops at the crystal surface and coincident etch pit formation.^(364, 365) This is confirmed further when examining the lattice deformation (Figure 5-5 b), which reveals an overall reduced deformation on crystal surfaces with progressing dissolution. The “least stable” (strained) regions apparently dissolve first, leaving behind a more stable core region (Supporting Movies 1, Appendix F).⁽³⁶⁶⁾

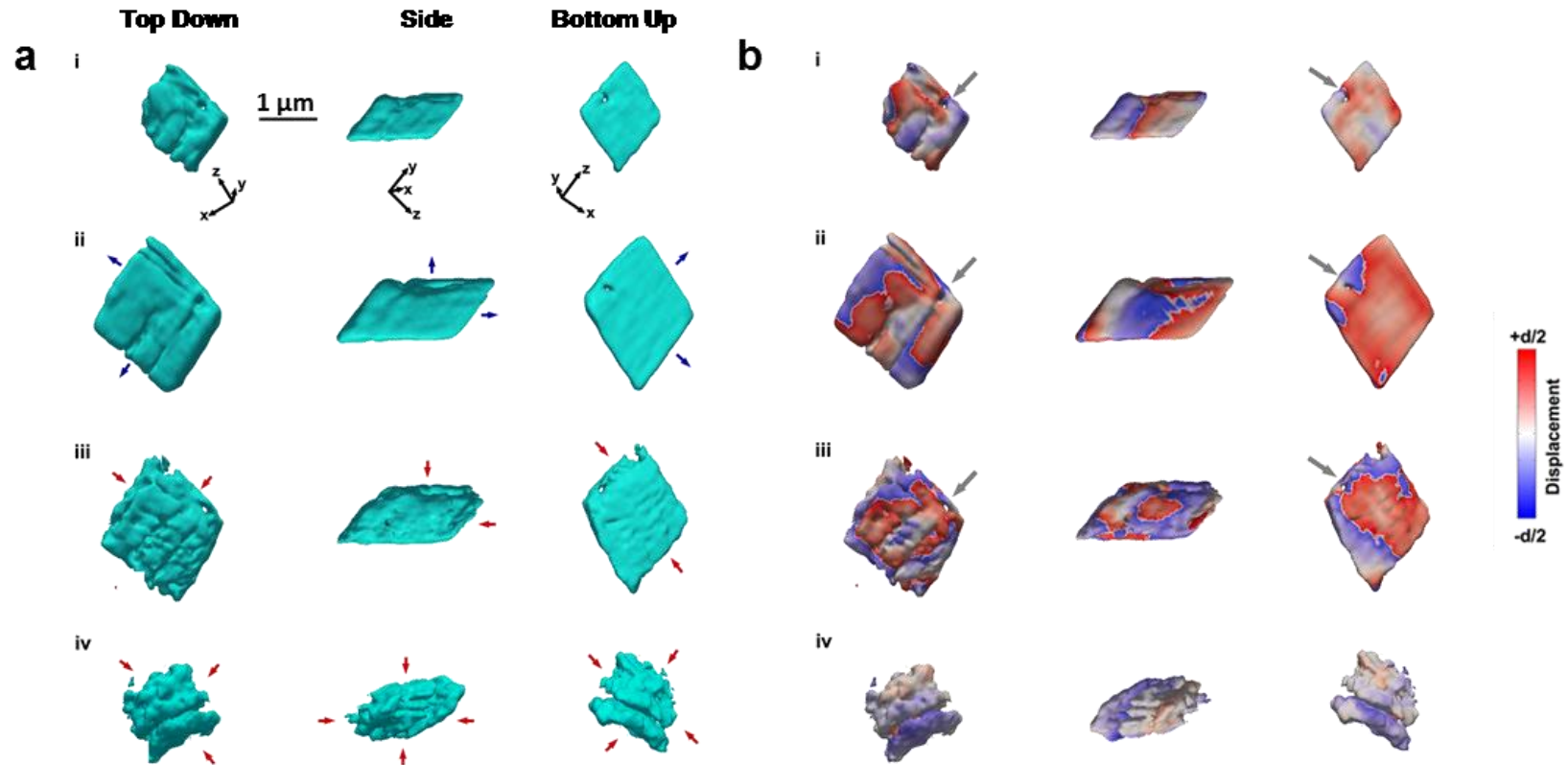


Figure 5 - 5: Summary of BCDI observations. Presented are separately reconstructed images of a calcite rhombohedra sitting on a (104) facet as formed (i), after secondary overgrowth (ii), and (iii & iv) after consecutive dissolution steps. Shown are from left to right, top - down, side and bottom - up perspectives. Given in (a) is the electron density (reconstructed amplitude) and in (b) projected displacement (phase). These highlight the shape transition during growth (prominent surface advance, \rightarrow) towards steady state and equilibrium shape adoption - dissolution (\rightarrow). The primary screw dislocation identified is marked (\rightarrow). The beam enters along the z - axis, with the y axis vertical to z. Crystal and substrate are located at a set scattering angle towards the beam direction (z) and spanned plane (x-z). (199)

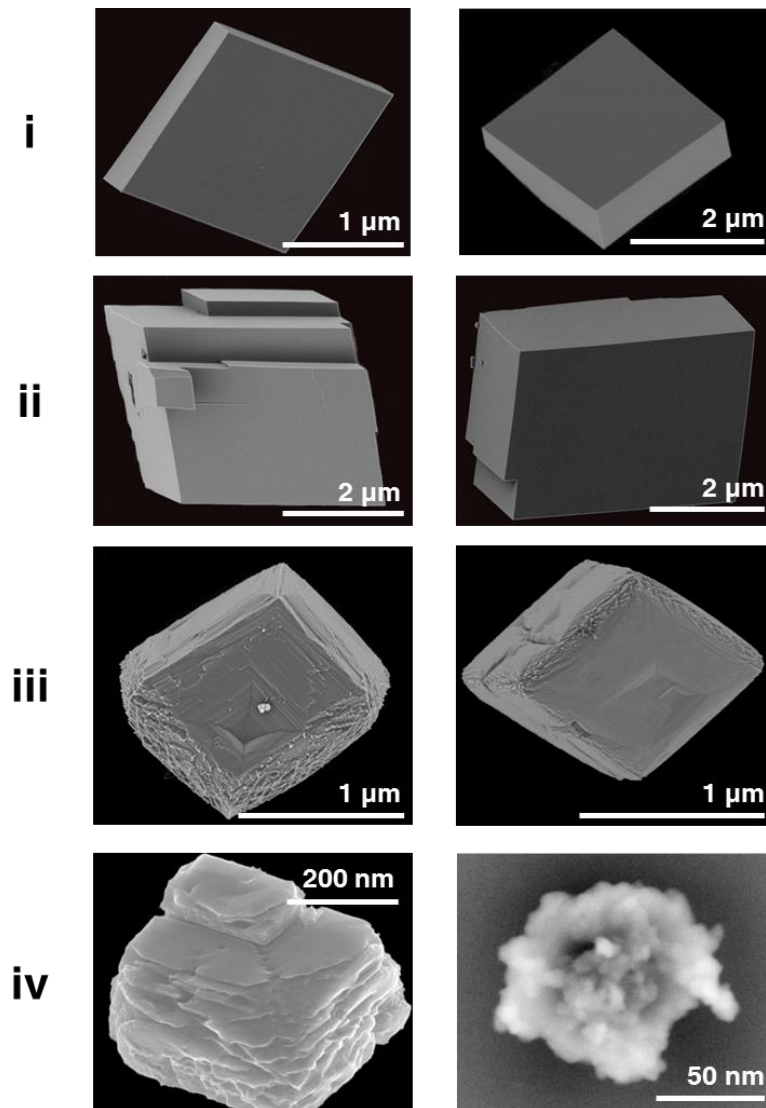


Figure 5 - 6: Electron micrographs of calcite rhombohedra as deposited (i), after secondary overgrowth (ii), and (iii & iv) after consecutive dissolution steps. Evident is the initial increase in particle volume with crystal overgrowth (ii). This is followed by shrinkage, etch pit formation, surface roughening (iii) and a porous “spherical” isometric appearance of the calcite crystal (iv). (199)

5.3.3.2: Screw Dislocations and Dislocation Network

An initial puzzle offered in the data was the nature of a single feature present in both the projected displacement and the electron density, throughout the growth and dissolution cycle (i-iv). This is indicated by the grey arrows in **Figure 5-5**. Closer examination of this region by means of central cut slices through the amplitude and displacement, **Figure 5-7**, revealed the combined presence of a hollow core (white arrows) and a surrounding spiral displacement (arrowed blue circle). In combination, these features are characteristic of a dislocation.(351, 367) It is emphasized that each data set (i-iv) was reconstructed independently and the continued presence of this feature throughout showed that it was not a reconstruction artefact.

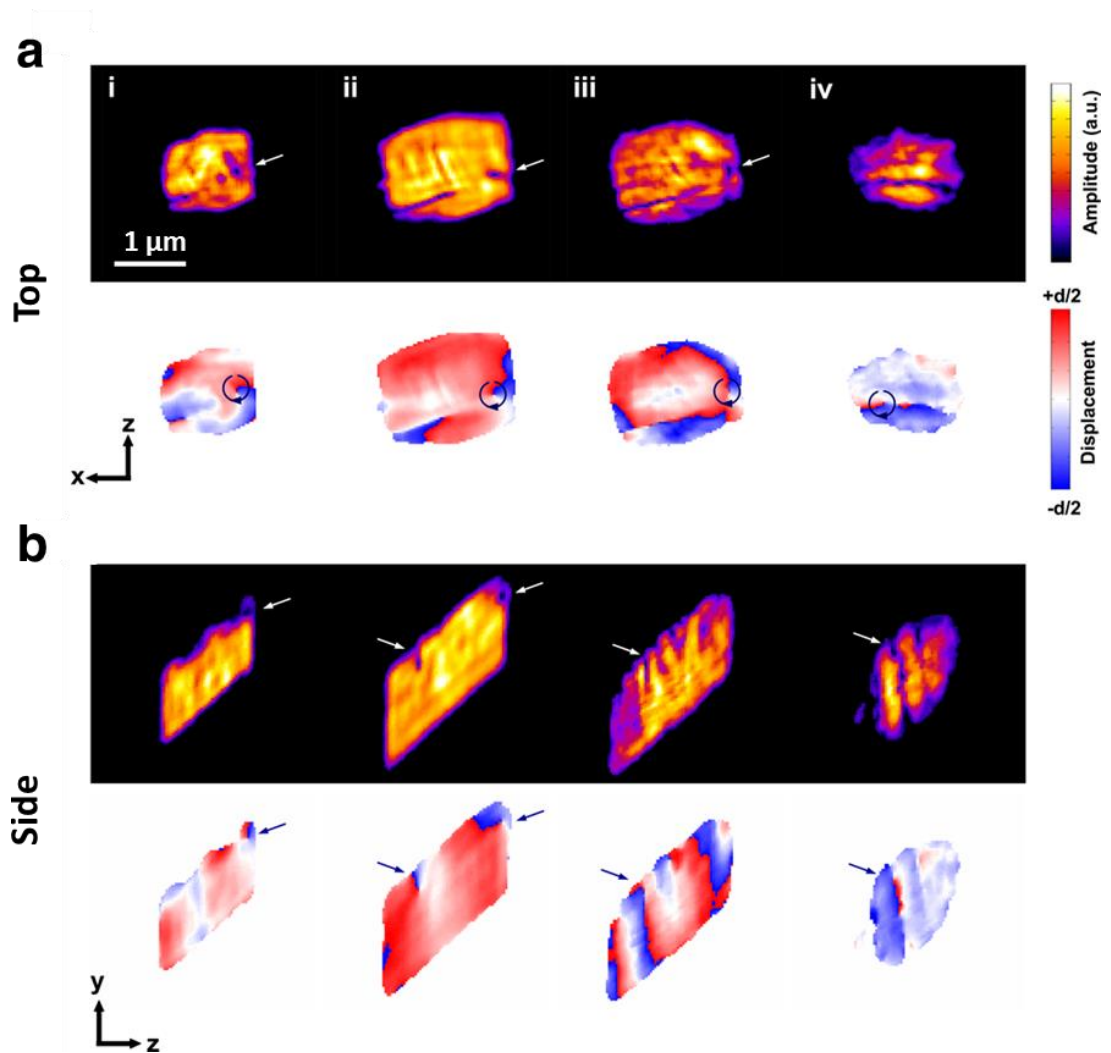


Figure 5 - 7: Central cut slices through the imaged crystal's electron density (amplitude) – top row - and projected displacement – bottom row. Central sections are shown of the initial crystal after growth (ii) and repetitive dissolution steps (iii & iv). Provided are two viewing directions top down (a) and side (b) not corrected for the set scattering angle. Pointed out are the initially detected regions, possessing both a low-amplitude core (white arrows) and spiral deformation (circular blue arrow). (199)

Chapter 5: Bragg Coherent Diffraction Imaging of Calcite Single Crystals

In an effort to confirm the possibility that BCDI can identify individual dislocations, a simulated screw dislocation at atomic resolution was processed by BCDI scripts. Both the hollow core and spiral displacement are retained after BCDI processing the simulated screw dislocation, which indicates that BCDI is truly capable of imaging dislocations, **Figure 5-8**. Details of this procedure are provided in Appendix D.

Figure 5-8 a, presents the simulated screw dislocation. (b) the Fourier transformed and subsequent BCDI processed simulated screw dislocation. The resulting displacement of atoms from their ideal lattice positions is given in (c) for the simulated screw and (d) the BCDI processed screw. Figures 5-4 e, provides a secondary viewing angle of (c) and (d) down the dislocation line. From this perspective it is evident that both the hollow core and spiral displacement were retained after BCDI processing.

Simulation of a screw dislocation at atomic resolution

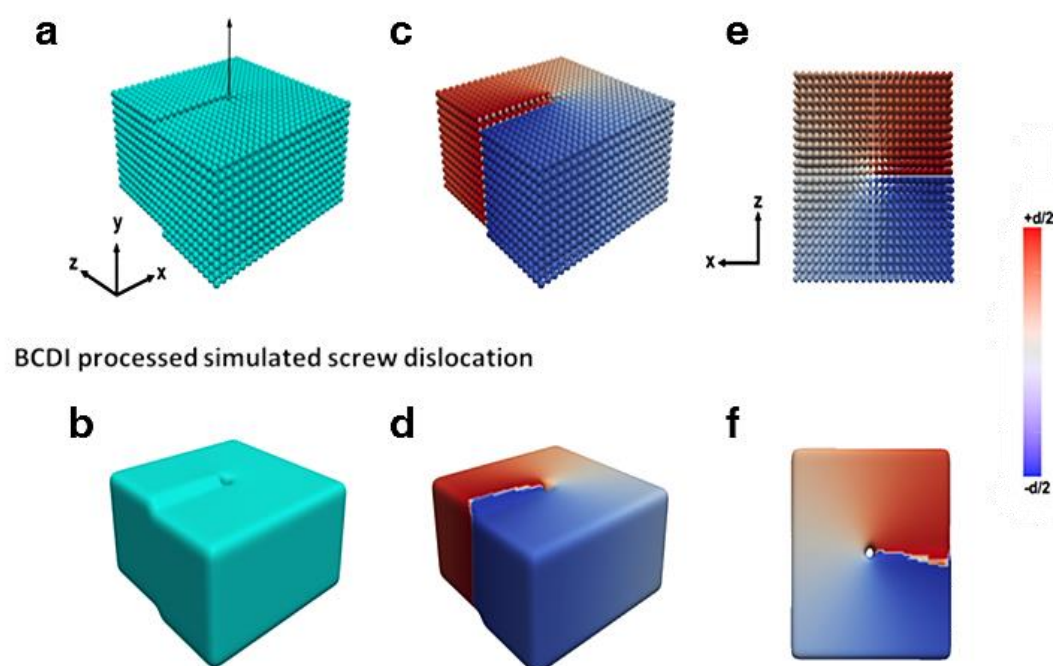


Figure 5 - 8: Provided is a comparison between a simulated screw dislocation at atomic resolution (top) and a simulated screw processed by BCDI scripts applied (bottom). (a) simulated screw, (b) simulated screw Fourier transformed and BCDI processed. (c) and (d) simulated screw with given resulting displacement respectively rendered on top. (e) and (f) secondary viewing angle revealing the retention of both hollow core and spiral displacement after BCDI processing of the simulated screw.(199)

Chapter 5: Bragg Coherent Diffraction Imaging of Calcite Single Crystals

By specifically examining regions that possess a spiral deformation and also have a low-amplitude core, several **additional dislocations** in the imaged crystal can be identified, **Figure 5-9** and Supporting Movies S1 (Appendix D and F).

In simple terms, the crystal is screened for areas that show both of these features by repeatedly taking the gradient of electron density and projected displacement. The gradual decline in electron density towards the dislocation core makes this selective, which results in an increasing gradient value at this point, while declining everywhere else. The procedure can be problematic in that there is a possibility of falsely identifying regions that are just outside of the crystal as dislocations. One of these falsely identified regions is highlighted in Figure 5-9 (orange circle).

The calcite rhombohedra imaged (i) possess several dislocations located close to a crystal surface. The dislocation cores are approximately oriented normal to the expressed 104 facets, and extend to crystal surfaces. Dislocations are preserved during the structural transition (i-iii), and increase in length (ii), commensurate with the overall crystal growth. Crystal growth introduces new dislocations in areas of prominent crystal growth. No information regarding the change in supersaturation during growth and dissolution is available and hence no statement regarding its role in changing the operating growth mechanism can be made.

Following the first dissolution cycle, the dislocations retreat with further etching of the crystal. Prominent etch pits are located on top of the initially present dislocation outcrops. This is consistent with the opening of the dislocation.(38) It is notable that a new dislocation can be identified after the initial dissolution (iii) on the top surface where etch-pit formation is occurring (iv). The origin of this dislocation is as yet unexplained, but it is possible that it was not initially detectable due to the limited resolution of BCDI. The final stage possesses a significantly reduced amount of dislocations. The etch pit profiles end mostly in “sharp tips” or are flat-bottomed, which potentially provides information regarding the type of defect initially present.(365) Loss of faceting and dislocation retreat near the surface supports the postulation given above, such that the least stable regions dissolve first, leaving behind a more stable core.

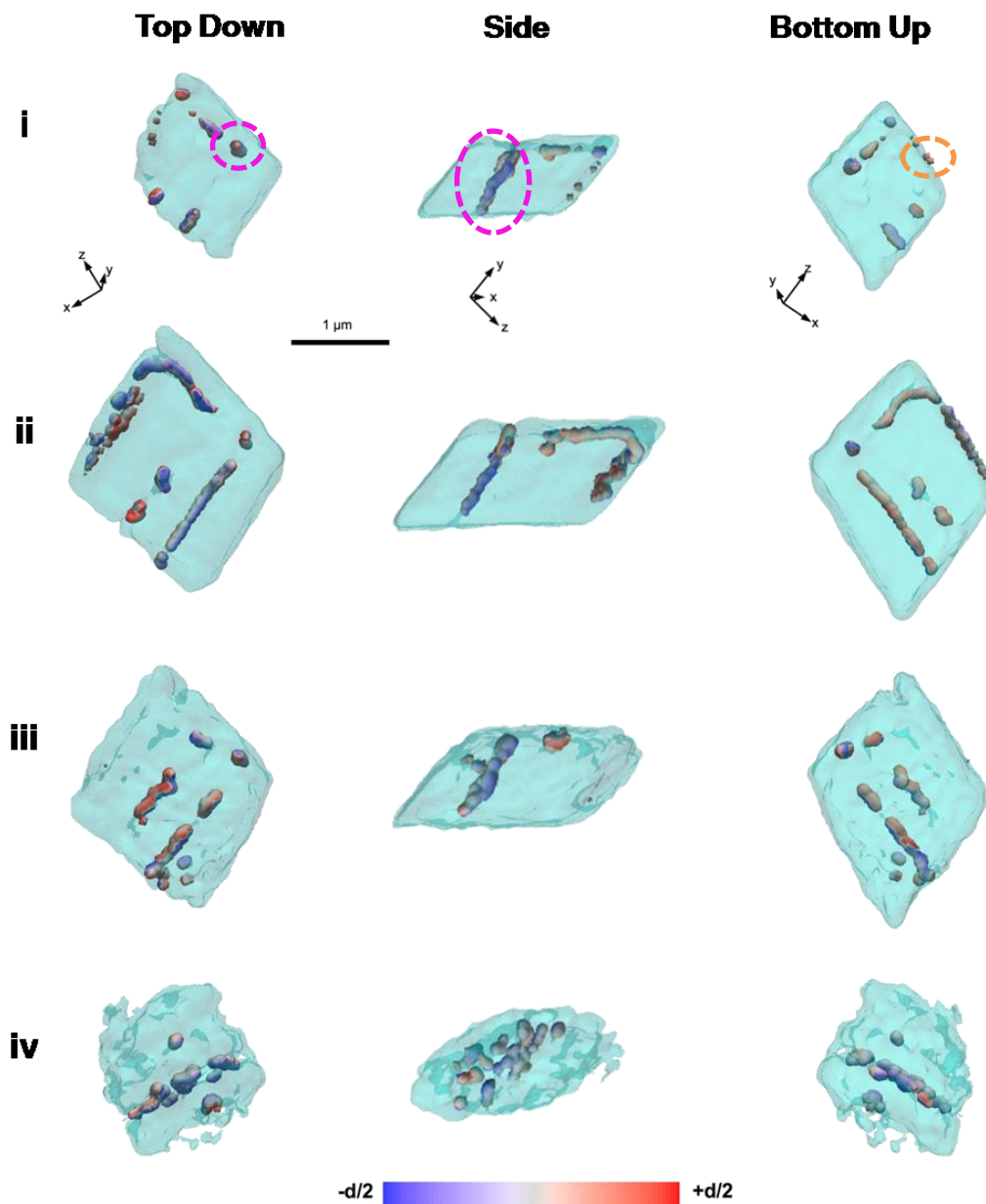


Figure 5 - 9: Given are iso-surface renderings of defects within calcite. Presented are dislocations (hollow core + spiral displacement) identified by BCDI in deposited calcite (i) after growth (i-ii) and dissolution (ii-iv) within overall crystal shape – transparent electron density. From left to right given are top-down, side and bottom up perspectives. Dislocations are primarily identified near crystal surfaces, observed to actively grow in addition to one predominant screw dislocation present. Later being substrate normal present across the whole crystal height (○). Falsely identified dislocation (○).(199)

5.3.3.3: Overall Strain Effect

An assessment of the overall effect of dislocations, and their associated strain fields on the growth/ dissolution behaviour of the crystals was made by determining the root-mean-square (RMS) displacement as a function of fractional crystal size, **Figure 5-10**. The RMS values given were calculated over increasingly larger shells for each reconstruction separately. These start from the centre of the crystal - fractional size 0 – and radiate towards crystal surfaces - fractional size 1.

The crystal as deposited experiences strain which linearly increases with the fractional crystal size, from the centre outwards. This behaviour changes after its overgrowth (ii) revealing a plateau region up to a fractional size of ~ 0.6 , before exponentially increasing. The strain progression that occurs with increasing distance from the core (i.e. edging towards the crystal surfaces) directly implies that (i) is under the effect of surface stress, which propagates almost to the centre of the crystal. The penetration depth of the surface stress then diminishes after crystal growth and the associated increase in size (ii) leading to the observed inner, plateau region. It has to be noted that the presented line plots do not have a common start point in terms of displacement. This is a result of the shift in the centre of mass that occurs as a result of the observed asymmetric growth. the given line plots can therefore only be used to see qualitative data trends. Considering the first dissolution phase (iii) the increased roughness and etch-pit formation that occurs leads to a significantly higher total displacement. The profile of strain progression with fractional size nearly levels out across the whole size regime. This shows that the increased number of surface defects and the associated increase in free surface area, due to etch pit formation, affects the entire crystal, giving rise to the increase in overall displacement. After the final dissolution (iv) and the major removal of dislocations and surface defects, the overall displacement drops significantly, becoming almost horizontal. This is in agreement with the BCDI visualizations given above. It also suggests that the surface effects are less pronounced than after crystal growth, despite the increase in relative surface area to volume.

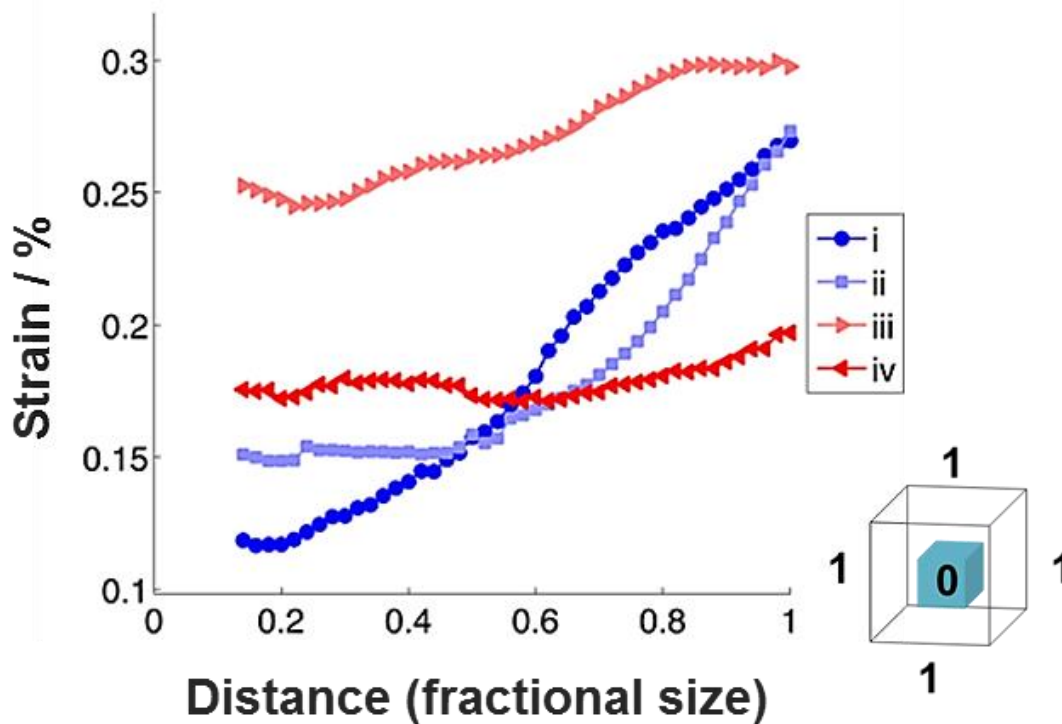


Figure 5 - 10: The total displacement measured over the course of an applied growth/ dissolution cycle (i-iv) vs fractional crystal size is shown. The centre of the crystal is equal to 0 and the crystal surfaces are equal to 1. The total displacement was calculated based on measured mean root means square displacement over increasing shell sizes. The presented line plot highlights the diminishing/ increasing relevance of surface effects with growth and dissolution with respect to the crystal size/ volume. Notable are the unequal starting strain percentages at low fractional sizes (centre of the crystal). These can be explained by the anisotropic growth of the crystal, which induces a shift in the centre of mass i.e. fractional size 0 shifts.(199)

5.3.4: Discussion

With its ability to simultaneously generate 3D images of the strain within a crystal, and of its gross morphology and internal structure, BCDI provides an extremely powerful tool in the visualization of single dislocations or the entire network of dislocations present within an individual crystal. This is particularly impressive when considering the limited real space resolution of BCDI in this case (~50 nm) as compared with the size of crystallographic defects.

The capability of BCDI to do so – visualizing the dislocation network – can be explained when it is recalled that the real-space phase seen in images obtained by BCDI are achieved by mapping the projection of the lattice displacement onto the Bragg peak. As a dislocation is a line defect characterized by a Burgers vector which measures the topological shift of the crystal lattice along the dislocation line, it acts as one entity in the lattice (the hollow core observed here). This means that in order for the crystal to remain uninterrupted at long range, the Burgers vector is usually equal to a lattice vector of the crystal (Chapter 1.3.3).(368) Whenever there is a component of the Burgers vector parallel to the dislocation line, it has a screw dislocation character, which causes the lattice to spiral around the dislocation (In this way growth and dissolution can be facilitated). Because of the lattice potential energy associated with this long-range strain field, line defects are visible to BCDI, “the dislocation/ strain field in its entirety is just bigger than the real space resolution”.

Dislocations, with their hollow cores, are stabilized near free surfaces of crystals, as found in this work. In this way, dislocation motion can be used to transport material (ions, clusters etc.) into and out of crystals from the solution.(369)

Chapter 5: Bragg Coherent Diffraction Imaging of Calcite Single Crystals

The BCDI experiments performed here directly visualize the effect of several fundamental factors governing the growth and dissolution behaviour of a crystal.

The importance of surface energy minimisation is seen in the observed shape transitions towards steady state (growth) and equilibrium shape adoption (dissolution). The minimization of the total surface energy in both cases highlights the effects of relative changes in interfacial energy, where this comes into play here as the crystal is brought into contact with a supersaturated and an undersaturated solution. This drives low energy facet formation during growth while high energy facets are preferentially expressed during dissolution.(363)

The 3D visualization of the dislocation network present within a micron sized single crystal achieved here,(370) is the first identification of the dislocation network present within a mineral crystal under atmospheric conditions (this was previously limited to colloid systems.(371)). What makes this special is that this will now make it possible to image the dynamics of a dislocation network (studies watching dislocation movement in composite crystals are currently pursued.). By applying growth and dissolution we here show the increased reactivity of strained surfaces. Further, the preferential dissolution and etch pit formation on top of/ within receding screw dislocations can be taken as direct evidence of the strain energy stored within dislocations affecting the crystal's response to external stimuli.(366)

The changes seen in RMS displacement upon crystal growth and dissolution are indicative of the decreasing/ increasing significance of surface effects with respect to particle size and volume. This is shown as the imaged crystal transits between sizes of hundreds of nanometres and microns during growth and dissolution.

5.4: Heterogeneous Nucleation on a Soft Interface

5.4.1: Introduction

Biominerals are characterised by unique morphologies, hierarchical ordering and properties unsurpassed by their synthetic equivalents.(23) One key strategy by which organisms create such structures is the use of insoluble organic matrices to regulate crystal nucleation and growth. There, it is widely considered that oriented crystal growth is the product of nucleation on an organized soft substrate whose chemical structure dictates the orientation of a growing crystal.

The default example of this behaviour is Nacre, or mother of pearl. Nacre is an inorganic–organic composite which is present in many molluscs as an iridescent inner shell layer. The inorganic–organic composite matrix consists of thin layers of organic materials, around 30 nm in thickness, sandwiched between hexagonal tablets of aragonite. A particularly intriguing feature of this structure is that each of the aragonite tablets is oriented such that the c-axis of the mineral lattice is tilted about 12° perpendicular to the organic layer. An electron micrograph of this arrangement is provided in **Figure 5-11a and b**. The inner aragonitic layer in combination with the outer calcitic, prismatic layer, which is also highly oriented, provides a hard and fracture resistant protection for the organism. In simple terms, the created brickwork in the aragonitic nacre layer hinders crack propagation in the c-axis direction.(80, 372, 373)

A question that remains unanswered, however, is how the organic, self-assembled matrix is able to dictate not just the morphology of each tablet but also this level of orientational control over thousands of tablets. It is currently believed that it is the chemical functionality of the organic template that provides orientational control while the morphology is confined by the insoluble organic matrix. A schematic illustrating this proposed mechanism of formation of nacre is provided in (c).

Despite a continued emphasis on the use of self-assembly strategies to produce organized materials similar to Nacre, the ability to use soft interfaces to control crystal nucleation and growth is still poorly understood.(374) The manner by which biomineralizing organisms control crystallisation at interfaces has been mimicked by precipitating CaCO₃ on a range of synthetic organic matrices. There, control over nucleation has been attributed to three mechanisms: epitaxy, electrostatic interaction, and stereochemical matching.(42) Organothiol self-assembled

Chapter 5: Bragg Coherent Diffraction Imaging of Calcite Single Crystals

monolayers (SAMs) on coinage metals(171) have been particularly well-studied in this regard and in the case of calcite can select a variation of nucleation planes as a function of chain length,(375) packing geometry/ tilt,(219) the end group of the thiol exposed to the mineral solution,(376) functional group ionization,(377, 378) and metal substrate (Au or Ag).(361, 376) The initial reasoning for the observed substrate-dependent orientation was based on stereochemical matching between a particular crystal “nucleation” plane and the 2D lattice and stern layer of the monolayer.(376) Subsequent studies refined this view and suggested that the dynamic order and flexibility of the interface was a pre-requisite for orientational control.(379) This was postulated based on observations that amorphous precursor deposits of the mineral induced monolayer disorder.(219) This suggests a mutual, cooperative ordering process,(219, 380, 381) which creates local, critically-sized crystalline domains in the monolayer on which nucleation occurs. These then direct subsequent crystal growth(382) such that oriented nuclei form based on charge epitaxy or average charge density in those domains.(383-385)

Here, we use Bragg Coherent Diffraction Imaging (BCDI)(196) to study the growth of calcite crystals on a soft interface (SAM of 11-Mercaptoundecanoic acid on Au (111)/Si (001)). BCDI uniquely allows us to visualize the lattice deformation (strain) present within oriented single crystals at a spatial resolution of 30 nm³, and to observe how this is related to the crystal morphology. This provides the first direct information about how a soft structure can generate lattice deformation in heterogeneously nucleated single crystals and how this strain then informs the growth and final morphologies of the crystal. Patterns extracted from single crystals with a polar nucleation plane exposing alternating Ca²⁺ and CO₃²⁻ layers supported the notion of dynamic surface reorganization as no increased level of strain surrounding the suspected nucleation site could be detected. The accumulation of interfacial strain in the direction of preferred planar growth ultimately results in the formation of stress relief sites in the form of dislocation loops, which cause a morphological instability. This in turn leads to an accelerated shape transition from the initial calcite tetrahedron to thinned calcite rhombohedra.

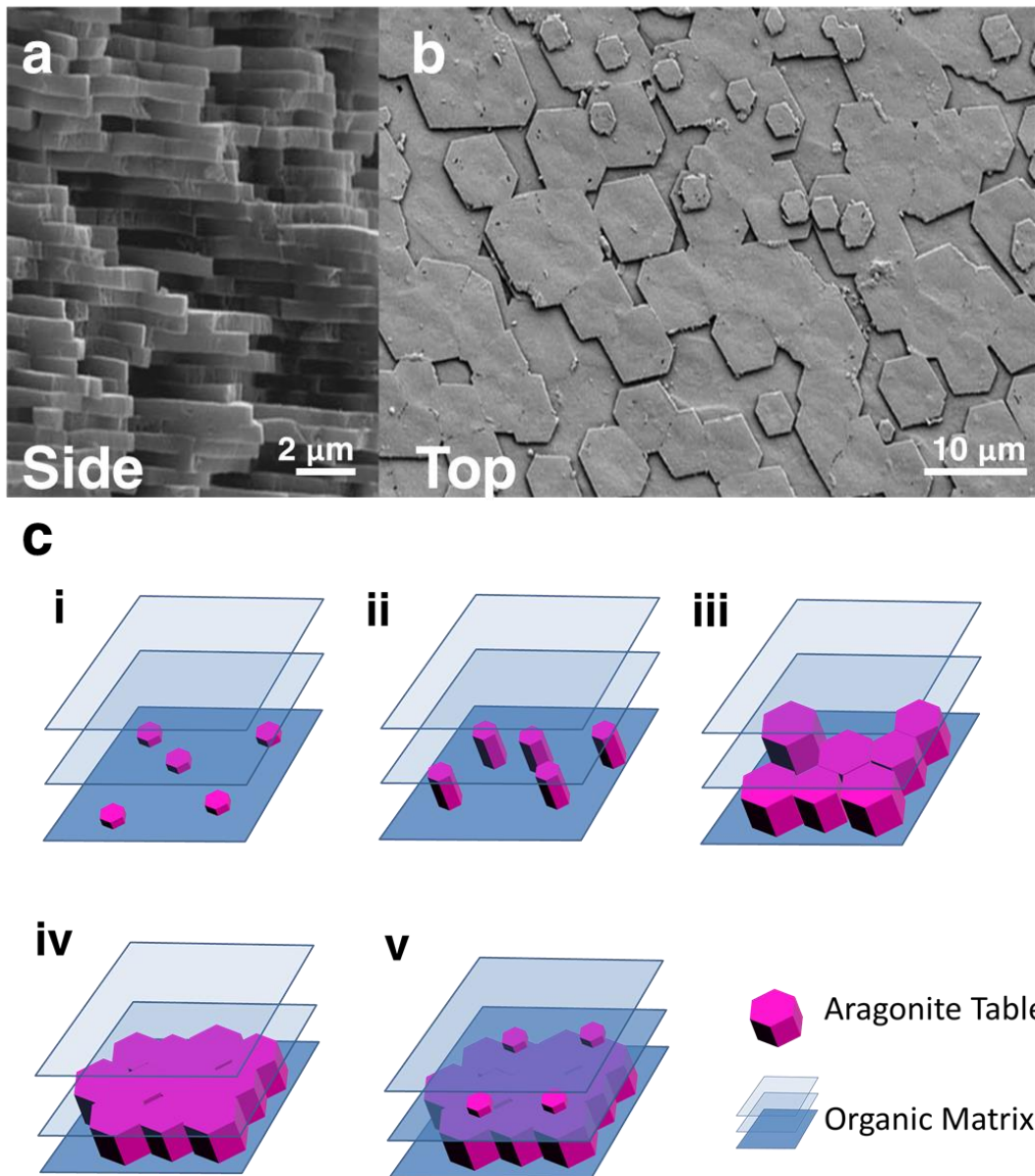


Figure 5 - 11: Electron micrographs of the inner nacreous layer of an *Atrina rigida* mollusc shell. (a) Cross-sectional view of oriented aragonite tablets, (b) top – down view of stacked layers. Images taken from (372). (c) Schematic illustrating the formation of sheet nacre. (i) This starts from the formation of an organic scaffold and initial oriented nucleation of aragonite tablets. (ii) Growth of aragonite tablets is limited in the c-axis direction by secondary layers of organic matrix. (iii) Continued lateral growth of tablets. (iv) Primary nacre layer completion. (v) Nucleation of secondary tablet layer directed by mineral bridges connecting primary and secondary layer. Schematic after (386).

5.4.2: Experimental

Preferentially oriented calcite was obtained by diffusion methods. 200 μl of 5 mM CaCl_2 was deposited on an inverted, functionalized substrate, which was placed in a sealed container (2l) in the presence of $(\text{NH}_4)_2\text{CO}_3(\text{s})$ (2g). The inverted substrate prevented “homogeneously” formed calcite settling onto the surface. $(\text{NH}_4)_2\text{CO}_3(\text{s})$ decomposition into $\text{CO}_2(\text{g})$ and $\text{NH}_3(\text{g})$ created the required supersaturation for CaCO_3 precipitation and provided a gradual increase in supersaturation, which ensures a sufficient number density of single crystals. Samples were removed after < 30 minutes of incubation. Arrays of iso-oriented calcite crystals of 1-4 μm in diameter were obtained.

Functionalized self-assembled monolayers (SAM) were prepared on freshly-deposited noble metal films. Thin films were deposited on silicon wafers using a Mantis Qprep 250 deposition system at a base pressure below 10^{-6} mbar. 2 nm of Cr were initially deposited to promote substrate adhesion, followed by the evaporation of 30-50 nm of Au at $\leq 0.1 \text{ nms}^{-1}$. Monolayer formation on metal substrates was initiated by immersion in 1mM thiol ethanol solution (11-Mercaptoundecanoic acid).

Organothiol self-assembled monolayers on noble metals were chosen as the “soft” substrate due to their reported ability to orient calcite crystals and their ease of preparation.(15) The spontaneous formation of molecular assemblies on noble metals is a result of the strong interaction between the thiol group and the metal substrate and the interaction of neighboring alkyl chains. This introduces a 2D close packing order of the SAM on the substrate. Alkyl thiol SAM units were employed here and have a basic structure of a surface active head group, an alkyl chain and a functionalized tail group, **Figure 5-12a**. The surface active head is a mercapto SH group which interacts strongly with the noble metal substrate. In fact, the reaction is so favorable that all available bonding sites will be utilized. This results in a close packing across the substrate which is further enhanced by the “coalescence” of neighboring alkyl chains via van-der Waals forces (b). This ultimately creates small, defect free areas of a 2 dimensional “crystalline” lattice.(21) In the case of alkyl thiols adsorbed on gold (111), a lattice of $a = 4.97 \text{ \AA}$, $\alpha = 22\text{-}32^\circ$ and $\beta = 50\text{-}55^\circ$ has been reported (c).(387) The size of ordered, potentially defect-free domains is essentially dependent on the quality of the gold substrate used i.e. roughness and gold island size.(388) The functionalized tail group determines the surface properties, and in the case of calcite can select one

or more preferential nucleation planes. A general distinction between “non-polar” (uncharged) functional tail groups (OH), which induce non-polar orientations or nucleation planes (104) and a polar functional tail group (COOH) which induces polar orientations or nucleation planes ((012), (113)) can be made. Why are SAMs considered a soft substrate? SAMs provide a “crystalline” sub lattice - yet they can deform and supposedly absorb a significant amount of stress upon interfacial nucleation and adapt in structure to the nucleating phase.

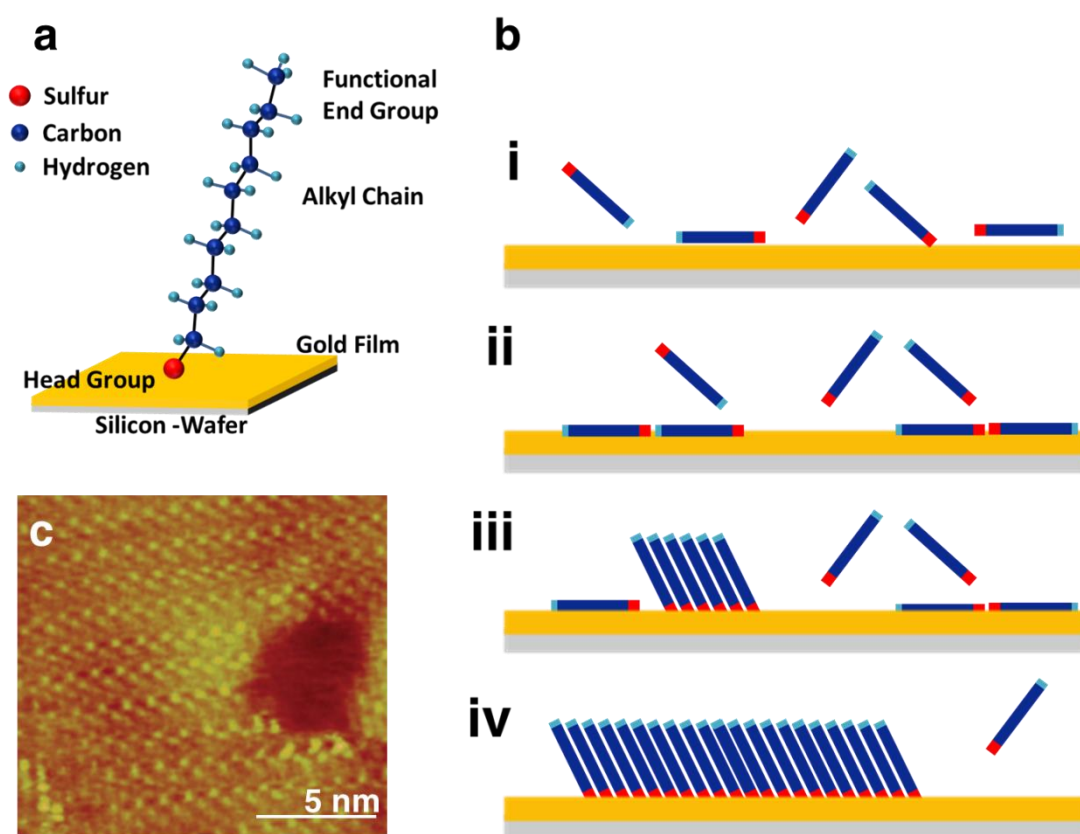


Figure 5 - 12: (a) Schematic showing an Organothiol molecule adsorbed on gold (111) in upright configuration. (b) SAM monolayer formation (i) “physisorption” of Organothiol on gold, (ii) lying down phase, (iii) standing up process, (iv) completed monolayer. Schematics after (387). (c) Scanning tunnelling microscope image of a 2D hexanethiol lattice- SAM on Au. The bright spots indicate the position of the thiol molecules. Image taken from (387).

Chapter 5: Bragg Coherent Diffraction Imaging of Calcite Single Crystals

BCDI experiments, and the subsequent phase retrieval and dislocation analysis were performed as described in Chapter 2.9.2.3/ Appendix D.

The Winterbottom reconstructions shown are of identical volume with stepwise increasing relative surface energies (γ_s ; 0.1 - 0.9). The crystal/ water interfacial energy values used were taken from Duffy.(110) The interfacial energy for the solution-facing {104} facets was kept constant, while the interfacial energy between the suspected nucleation plane (012) and substrate (hard interface) was varied.(111)

Crystal orientation was inferred using a diffractometer in pole configuration, with a step size of 1.5° at 2.5 sec (Psi 0-90, Phi 0-360). Substrates were characterized using atomic force microscopy in tapping mode at a scan rate of 1.98 Hz with pixel dimension of 512 x 512. Images of the internal structure of oriented calcite were obtained using high resolution TEM (HRTEM) imaging of thin sections prepared by Focused Ion Beam Milling (FIB) (Chapter 2).

5.4.3: Results

5.4.3.1: Nucleation and Growth of Calcite on SAMs

Oriented calcite crystals were precipitated on 11-Mercaptoundecanoic acid SAMs on Au (111)/ Si (001) using a hanging drop setup in which 200 μl drops of 5 mM CaCl_2 solution were deposited on the prepared substrate, and then inverted. Samples were then exposed to ammonium carbonate vapour in a sealed environment for 30 minutes.⁽¹⁶⁹⁾ This method was chosen as it limits the crystal size and prevents homogeneously nucleated calcite settling onto the SAM. Characterization of the crystal orientations was achieved using pole measurements, which showed that the majority were oriented with the (012) plane parallel to the SAM, while a minor fraction were (113) oriented, **Figure 5-13**. Investigations regarding the formation and growth of oriented calcite on 11-Mercaptoundecanoic acid are summarized in the schematic presented in **Figure 5-14**. The process starts with the diffusion of CO_2 and NH_3 into hanging droplets of CaCl_2 solution, where this results from the decomposition of ammonium carbonate $((\text{NH}_4)_2\text{CO}_3)$. (a) This causes the formation of amorphous calcium carbonate (ACC), which subsequently deposits onto the substrate. (b) The transformation of ACC yields oriented tetrahedral - pyramidal - calcite with three $\{104\}$ facets in contact with the solution. (c) Further growth of the emerging pyramids leads to the truncation of the long axis vertex and the expression of one additional solution facing $\{104\}$ facet in its place. (d) This culminates in the complete structural transition from initially present tetrahedra to rhombohedra as growth (preferentially normal to substrate) commences.

Electron micrographs of the morphological development of the crystals provide support for this statement, Figure 5-14. These demonstrate that the initial form is roughly pyramidal and appears to comprise an aggregate of smaller particles; this is consistent with growth via an amorphous calcium carbonate (ACC) precursor phase.^(218, 219) These particles then convert to an irregular tetrahedron and eventually truncate on the long axis vertex, generating an additional $\{104\}$ facet. As growth normal to the substrate begins to dominate, the crystals then undergo a morphological transition to rhombohedral morphologies.

The formation of additional facets is readily explained, in terms of surface free energy minimization. As crystal growth continues, the crystal surface-to-volume ratio decreases, and at some point the volume term becomes dominant, which leads to the formation of the energetically more favourable rhombohedral

Chapter 5: Bragg Coherent Diffraction Imaging of Calcite Single Crystals

morphology of calcite. Winterbottom reconstructions, which provide a phenomenological probability of the equilibrium shape of a crystal sitting on a solid substrate, were performed with a fixed crystal volume and orientation of (012). The obtained Winterbottom reconstructions agree with the morphological development of the crystals observed experimentally, when the degree of interaction between the nucleation facet and the substrate was systematically decreased, Figure 5-14. The agreement deviates in the latter growth stages, Winterbottom reconstructions end in regular corner - standing rhombohedra as compared to the thinned, surface elongated calcite rhombohedra found experimentally.(111)

Calcite crystals with sizes 1-4 μm were then investigated at different stages of morphological development using BCDI, where this provides a simultaneous visualization of the crystal morphology and strain. BCDI image reconstructions were performed as outlined in Chapter 2.9.2.3 and Appendix D.

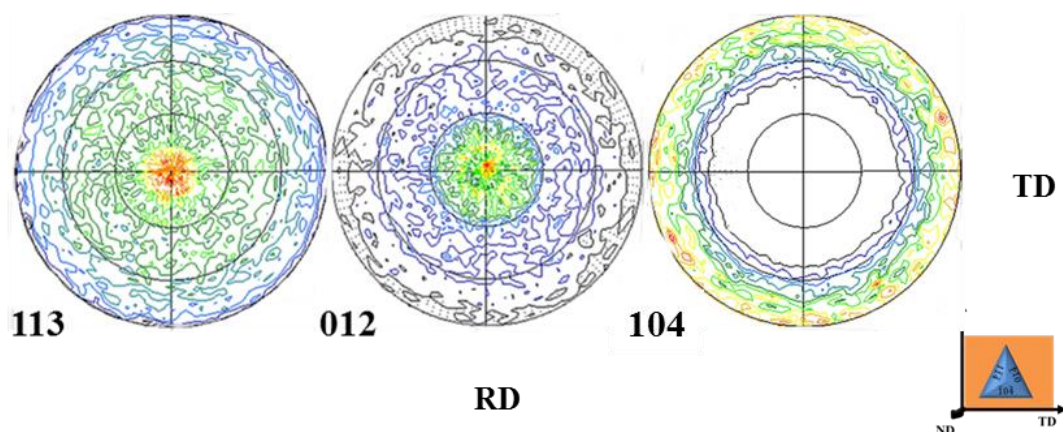


Figure 5 - 13: Texture of calcium carbonate (calcite) precipitated onto carboxylate terminated organothiol SAMs supported on a thin gold film (111) deposited on glass. Presented are pole figures derived from powder diffraction data sets with a (113), (012), and (104) substrate normal (ND - normal direction, RD – rolling direction, TD – transverse direction). Evident is the presence of two highly oriented populations (012) and (113) exposing homoionic substrate facing facets. No signal attributed to crystals oriented with {104} faces parallel to the substrate could be detected. Diffractograms were collected for samples deposited on glass substrates -in contrast to the silicon wafer supported crystals used in BCDI experiments - in order to avoid interference related to silicon or gold scattering .

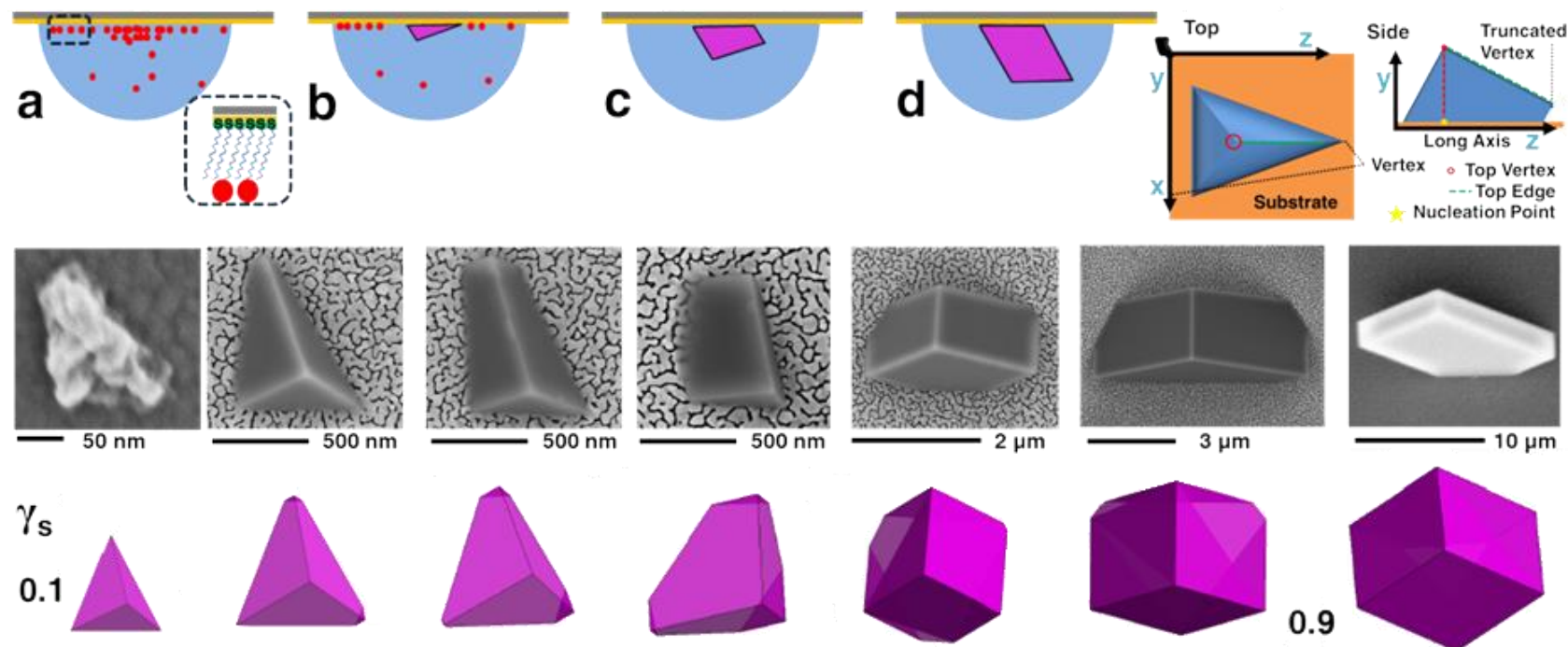


Figure 5 - 14: Morphological progression of calcite nucleated on COOH terminated SAMs. Given are schematic (top), experimental observation – micrographs- (centre) and expected equilibrium morphologies (bottom) depicting the formation of preferentially oriented calcite nucleated on carboxylate-terminated SAM supported by a thin gold film. (a) Diffusion of CO_2 and NH_3 , into $\text{CaCl}_2(\text{aq})$ causes ACC formation (\bullet) and deposition onto the substrate in inverted droplets. (b) Precursor depletion yields oriented tetrahedral calcite exposing three smooth 104 facets. (c) Further growth leads to long axis vertex truncation and development of an additional facet. (d) Further crystal growth, results in the complete transition of calcite tetrahedron to rhombohedral calcite. Winterbottom reconstructions are of identical volume with stepwise increasing relative surface energy (γ_s ; 0.1 - 0.9). Crystal/ water interfacial energy values used were taken from Duffy.(110) Further provided is a geometrical overview of terms used throughout.

5.4.3.2: BCDI Reconstructions of Calcite Nucleated on SAMs

BCDI reconstructions from three different calcite crystals, all of which nucleated from the carboxyl-terminated SAM, are shown in **Figures 5-15 (i-iii)**.

The images shown are top-down and bottom-up projections of the iso-surface renderings of (a) the reconstructed electron densities or gross crystal morphology and (b) the projected atomic displacements (phase). The displacements are represented by a cyclic colour map projected onto the recorded electron density.

The crystal shown in Figure 5-15 (i) is 2.5 μm in diameter, and has a rough appearance. Two explanations for this appearance can be imagined. Remaining residual reaction solution on the sample which crystallized during drying or secondly the crystal was too strained, such that phasing algorithms returned a morphology that is unlikely to reflect the crystals true morphology.

The crystals shown in (ii) and (iii), in contrast, correspond well to the stages in morphological development observed by SEM, with new facets forming, and facets becoming smoother during growth. Crystal (ii) is 1.4 μm in size, and approximately tetrahedral in shape, with three well-defined 104 faces directed into the solution, and one new truncation beginning to form. At 2 μm in diameter, crystal (iii) is at a further stage of development, and has smooth faces and an additional 104 truncation at a vertex. The “top edge” of the crystal has also moved on growth from (ii) to (iii) such that it becomes almost parallel with the substrate.

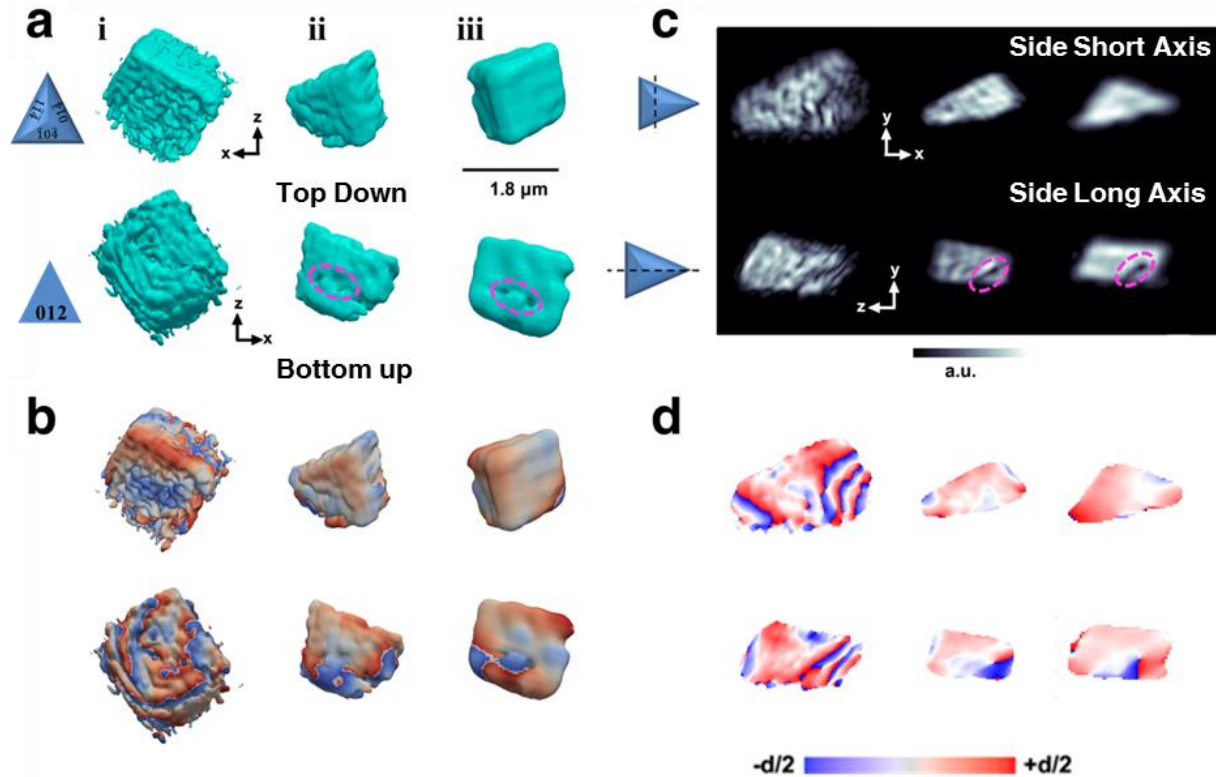



Figure 5 - 15: Summary of BCDI reconstructions. Presented are 3 reconstructions obtained from 3 different crystals of calcite (i-iii) nucleated on a carboxylate-terminated SAM. (a) Reconstructed crystal shapes from BCDI amplitude measurements, and (b) the projected displacements ($-d/2$ blue lattice dilation and $+d/2$ red contraction). Substrate normal central cut slices through retrieved electron density (c) and projected displacement (d). Given are cuts along the short axis (top) and the long axis truncated vertex direction through the isoperimetric point. Surface cusps are highlighted (\circ). The beam direction is along the z - axis, with the y axis oriented vertically. The sample/ substrate is located at a set scattering angle towards the beam direction (z) and plane (x - z).

The BCDI reconstructions also provide a unique opportunity to examine the influence of the SAM on the crystal. In all three crystals, the face adjacent to the SAM exhibits a degree of roughness that is consistent with AFM measurements of the substrate, **Figure 5-16**. While schematic diagrams of SAMs invariably present a SAM/Au substrate as planar, evaporation of Au onto Au or Si actually generates substrates with roughnesses in the order of 1-10 nm.⁽³⁸⁸⁾ That the nucleation face of the calcite crystals are themselves roughened suggests that the crystal grows in a way to preserve interfacial contact.

Closer examination of the nucleation faces of crystals (ii) and (iii) also reveals the presence of two adjacent surface cusp-like cavities of sizes ~70-100 nm on each crystal face. These intriguing features can be seen more clearly in cross sections of the crystals (Figure 5-15 a and c ) , which show that they lie in the same plane, which lies approximately parallel to the truncated vertex. The pair of cusps are also located closely beneath the truncated vertex. Crystal (i), in contrast, shows numerous cusps, where these are particularly concentrated around the “truncated” vertex.

Turning to the strain present in the imaged crystal (as derived from the projected atom displacements), Figure 5-15b shows that lattice deformation/ strain is concentrated at the edges and corners of each of the crystals (i-iii). This becomes centred on the corners as facets develop (ii-iii). The images of the cross sections of the crystals (Figure 5-15d) reveal how far surface stress induced strain penetrates into the crystal. Surface normal penetration depth was measured to be of <200 nm.

Substrate – SAM - facing facets share one common strain feature, namely a highly localized strain field concentrating around the surface cusps (ii & iii). This radiates from the substrate far into the crystal (ii) and subsequently decreases in penetration depth with development (iii). The displacement surrounding the cusps is not evenly distributed around the cusps but is highly concentrated in the direction of the newly forming 104 facets.

Chapter 5: Bragg Coherent Diffraction Imaging of Calcite Single Crystals

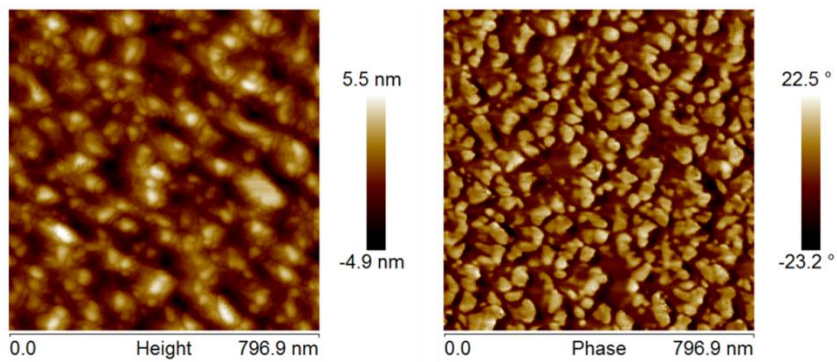


Figure 5 - 16: Atomic force micrographs of gold film deposited on silicon wafer. AFM measurements returned surface roughness of 1.4 nm (Rq) / 6.61 (Rmax).

5.4.3.3: Surface Cusps and Dislocation Loops

Confirmation that the observed cusps correspond to a physical feature in the crystals was obtained by transmission electron microscopy (TEM) of thin sections prepared by focussed ion beam (FIB) milling. Electron micrographs of the prepared section and its location with respect to the original crystal are shown in **Figure 5-17**. Figure 5-17a shows the original crystal with the cut direction highlighted in blue. In Figure 5-17b, the prepared lamella is shown, which was originally located beneath the long axis at the truncated facet, highlight in yellow. An area adjacent to the tip is then thinned for TEM examination (Figure 5-17c). Imaging of this section by TEM clearly shows a linear feature of lateral size 10 - 20 nm (arrowed) whose location is commensurate with the surface cusps observed using BCDI (Figure 5-15 a and c).

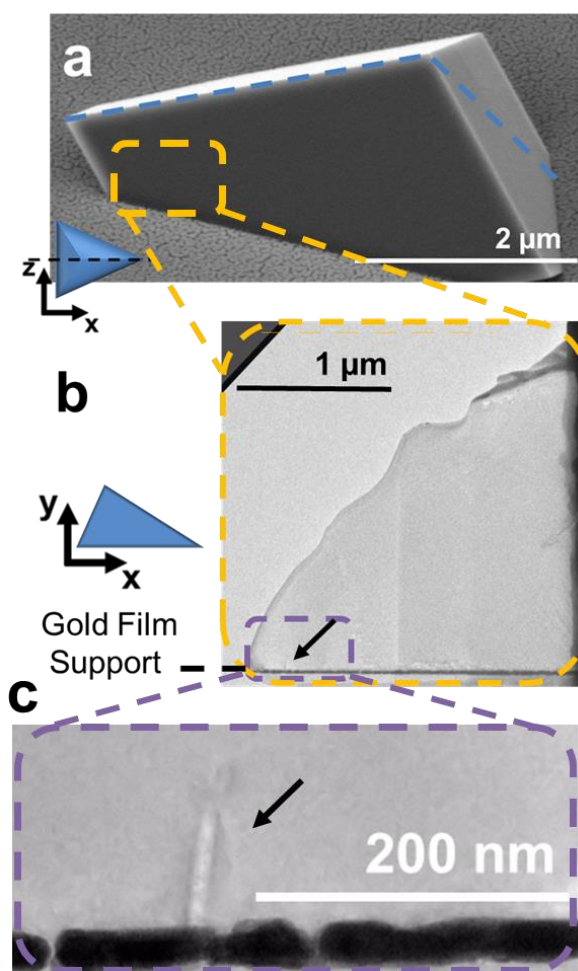


Figure 5 - 17: Electron micrographs of a sample prepared using FIB. (a) SEM of oriented, “tetrahedral” calcite nucleated on a gold film supported SAM eventually cut. (b) Selectively thinned tip of prepared lamella, morphologically originally located central beneath the long axis directly under the truncated vertex onset. (c) Presents a higher magnification of the front end of the tip. Apparent is an area of peculiar phase contrast difference (decreased electron density) $\sim 85 \times 15$ nm.

Chapter 5: Bragg Coherent Diffraction Imaging of Calcite Single Crystals

Having established that the surface cusps visualized within crystals (ii) and (iii) by BCDI are not artefacts, closer examination of BCDI images revealed that each of these cusps are associated with localized strain fields which radiate from the substrate into the crystal. These regions possess both a hollow core and a spiral phase, where this combination of features identifies them as dislocations.(368) Further examination of the strain fields in the vicinity of these cusps then demonstrates that each pair of surface cusps actually form part of a single dislocation loop, **Figure 5-18 ii and iii** and supplementary Movies Appendix F. The cusps are not surface cusps but are the physical expression of the dislocation loop. As shown in Figure 5-15d, the displacements associated with these dislocation loops are not evenly distributed, but are concentrated towards the new “truncation” faces. Identical examination of the first reconstruction (i) revealed an entirely different internal structure. While crystals (ii) and (iii) were each remarkably dislocation-free (with the exception of the single dislocation loops), crystal (i) contained numerous smaller dislocations and two larger helical dislocations. Helical dislocations reach upwards from the centre of substrate facing facet towards the upper active growth front of the truncated vertex. By comparison, crystals (ii & iii) exhibit homogenous strain fields around the centre of the nucleation face.

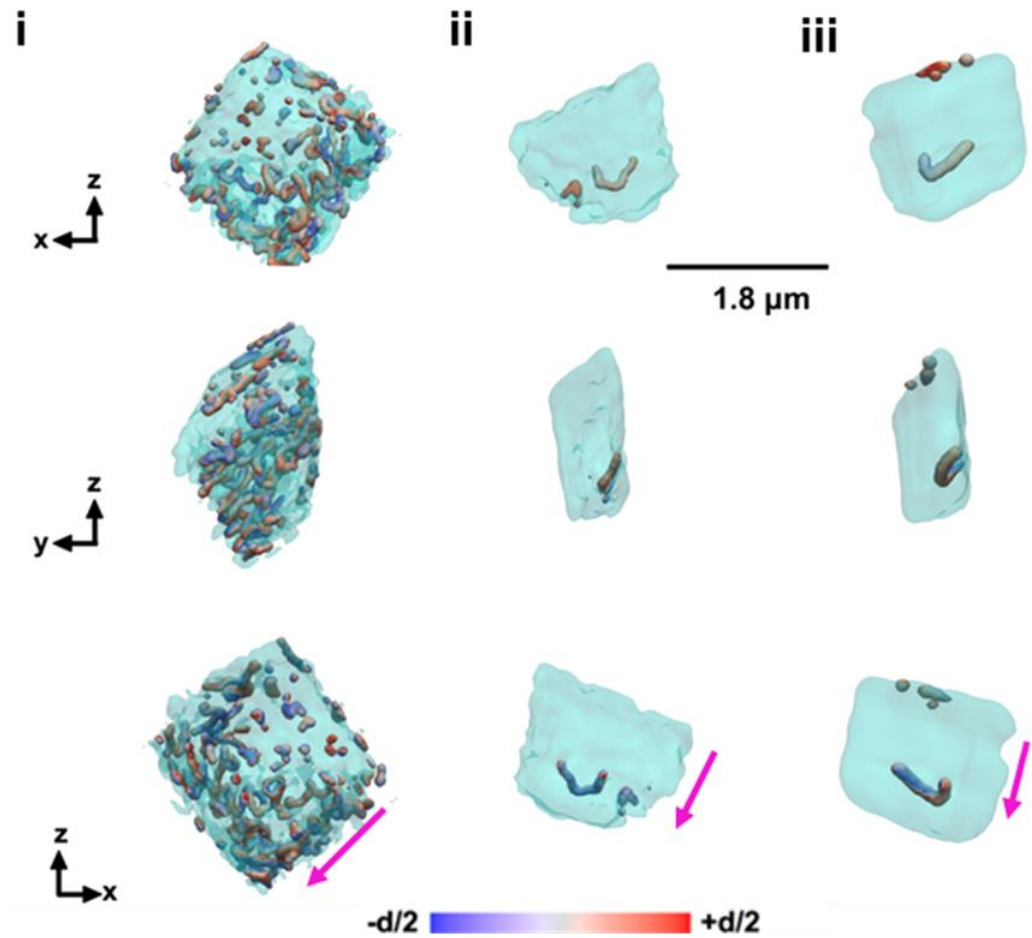


Figure 5 - 18: Iso-surface rendering of defects present within oriented calcite crystals. Highlighted are defects present in oriented calcite which display both a low electron density core and surrounding spiral deformation field. Evident is the defect accumulation (i) and singular dislocation loops (ii & iii) in the direction of the initial, elongated pyramidal axis (\rightarrow).

5.4.3.3: Overall Strain Effect

To further elucidate the effect of the substrate-induced interfacial strain on the growth of the crystal, the displacement present on the nucleation facets was plotted against the fractional crystal size (0-1) for all 3 reconstructions (i-iii), **Figure 5-19**. Plotted is the interfacial projected displacement (50 nm inwards) from the base of the isoperimetric point (highest point of the crystal) (0), past the dislocation outcrops, towards the additional (104) facet (1). The base of the isoperimetric point was considered as potentially reflecting the original nucleation centre. This was done on a purely geometrical basis under the assumption that the smallest crystalline nucleus is present in the form of a tetrahedron. Evident in Figure 5-19 is the general increase in projected displacement with distance away from the isoperimetric base towards the “truncated” crystal facet. Crystal (i) shows an approximately linear increase in the projected displacement, although good correspondence exists between two sections at which there are greater changes in displacement (at ~ 0.3 and 0.5) and the positions of the helical dislocations. Crystal (ii) and (iii) show an increase in the rate of change of the projected displacement at positions 0.8 and 0.5 - 0.6 respectively, where these positions correspond to the positioning of the observed dislocation loops.

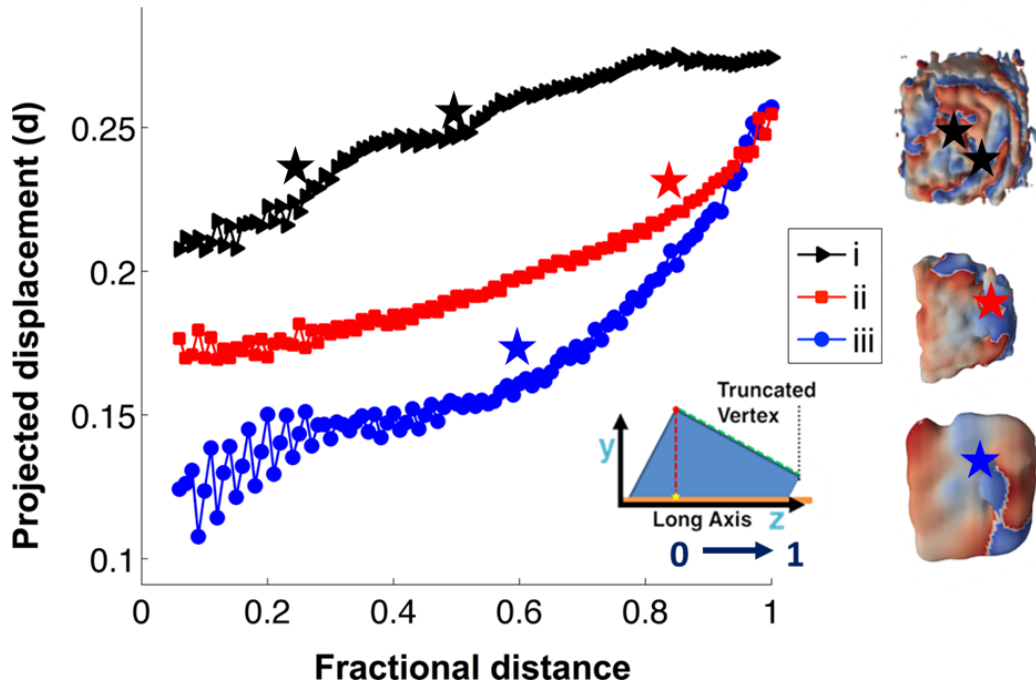


Figure 5 - 19: Projected displacement in the direction of the truncated vertex. Shown is the recorded increase in projected displacement present on the substrate facing facet, with increasing fractional distance away from the suspected nucleation site (0) towards the newly-formed 104 facet (1) i.e. in the direction of the dislocation loop. The recorded increase in projected displacement is shown for all three reconstructions presented previously (i-iii). The stars indicate the approximate location of the major dislocations (helical – black, dislocation loops – red and blue).

5.4.4: Discussion

Putting the observations made here into perspective, several suggestions concerning the mineralization on soft interfaces can be raised. The discernible absence of interfacial strain discontinuities at the base of isoperimetric points (base of the top vertex), combined with the radiating “homogeneous” strain field or plateau shown in Fig. 5-19, can be taken as evidence of reorganization (382) between the monolayer and nucleating mineral on a given gold island. The fact that the measured substrate normal lattice displacement at the base of the isoperimetric points is comparable to that of facets in contact with the solution further supports this. The slightly increased displacement in the substrate-facing facet can be thought to arise from the chemical interaction between the SAM acidic end group and the mineral.(389, 390)

The continued increase in lattice displacement in the direction of the truncated vertices is consistent with the detected dislocations, Fig. 5-18. This is especially obvious in the case of reconstructions (ii) and (iii). There is a gradual to exponential strain accumulation in the direction of the elongated vertices/ truncated vertex. This direction has the highest relative growth rate as is evident by its uniaxial elongation. This can potentially be traced back to an increasingly imperfect alignment between the monolayer and the developing crystal.

Arguments along this line, and based on the unidirectional, preferential lattice matching between a nucleation plane and the 2D-lattice of the SAM has been suggested before.(385) An indirect confirmation of strain build-up was obtained in the referenced work by decreasing the flexibility of the monolayer, (longer backbone chains), which leads to a decreased shape anisotropy of the crystal.(385)

The results obtained here can be seen as a direct confirmation of this. The measured directional increase in lattice displacement culminates in the formation of dislocations at the growth anisotropy edge. The identified dislocation loops can therefore be seen as stress relief sites for the otherwise increasing surface stress and lattice mismatch. This effect is widely reported in thin film epitaxy.(391-393) The detected helical dislocations in (iii), combined with their orientation towards the active growth front, also follow this hypothesis. Helical dislocations may simply present an alternative response to strain accumulation.

Chapter 5: Bragg Coherent Diffraction Imaging of Calcite Single Crystals

The resulting higher lattice “misfit” in this region then has a profound effect on the morphological development of the crystal. The misfit hinders the growth in this direction, which causes a morphological instability. The strain present increases the surface energy and subsequent cost for in-plane growth in this direction. This eventually leads to the expression of an additional (104) facet normal to the substrate, and is followed by preferred growth in perpendicular directions, in an effort to minimize the high energy surface. This is ultimately the reason for the difference in shape, Figure 5-13, between the regular rhombohedra predicted by the Winterbottom reconstructions, and the thinned, surface elongated calcite rhombohedra observed experimentally. A second effect of this strain-induced morphological instability is seen in the maximal size of the tetrahedral calcite size. Oriented calcite grown at the gas/ liquid interface repeatedly shows tetrahedral calcite up to 20 μm in size while here a maximum of $\sim 2 \mu\text{m}$ was observed.(394, 395) A change in equilibrium shape with increasing size of the crystal is common and independent of interfacial strain.(396) The strain present here seemingly accelerates this tendency, which not only causes the deviation from the predicted Wulff shape but also may impose a critical size limit on the tetrahedral calcite as compared with crystals grown on a truly soft interface.

These arguments, of course, are based on the existing literature describing calcium carbonate nucleation on functionalized SAMs. Moving away from these, the premature shape transition and the maximum crystal size observed may simply be explained by a difference in interfacial energy and elasticity between a soft solid support (SAM on thin gold film) and truly soft support (gas/ liquid interface).

Further, the above made casualization of increasing misalignment between the SAM and the crystal, leading to strain accumulation, dislocation loop formation, and eventually “vertex” truncation, can be questioned when abandoning the SAM as a truly soft interface. Yes, the SAM determines the nucleation plane and “forces” the crystal to grow in continuous contact with the substrate, but the truncation and the dislocation loop formation might be independent of each other, and simply present a different response to a common underlying cause. This cause may be the surface roughness/ curvature of the gold islands on the substrate, where an interfacial stress may build when the crystal tries to adapt to this roughness. This could then lead to both shape transition and dislocation loop formation.

5.4.5: Conclusion

In summary, the results shown demonstrate the value of BCDI in generating high-resolution (spatial resolution $\sim 30 \text{ nm}^3$) 3D reconstructions of individual crystals nucleated on interfaces. Unique strain and structural information is obtained which is not accessible using any other technique. Study of calcium carbonate precipitated on carboxylate terminated SAMs identified an in-plane homogenous interfacial strain field surrounding the proposed nucleation site, which may well be in agreement with surface reorganization during nucleation. Increasing misalignment between the crystal and substrate leads to strain accumulation in the preferential growth direction, which causes a premature morphological instability and the formation of dislocation loops. This induces morphologies which differ from the predicted Wulff shape.

The applied methodology can be considered quite general, and can facilitate a greater understanding in the interfacial relationship between a template and supported crystal. This is essential to a variety of processes including biological templating, epitaxial growth and thin film deposition processes.

5.5: Outlook

The case studies presented here clearly demonstrate the unique insight that BCDI can provide of the structural organization and physical properties of single crystals. In contrast to other high resolution imaging techniques such as AFM and TEM, it yields three dimensional structural information while little or no sample preparation is required. Considering that BCDI and indeed general coherent imaging methods are still in their infancy, the current limitations encountered here (i.e. a sample size smaller than 10 μm , spatial resolution of 10-50 nm, maximum strain resolvable) are expected to be overcome rapidly. The continued progress in phasing algorithms, the current construction of dedicated beamline/ End stations with secondary optics (integrated electron microscopy) and spectroscopy equipment support this belief. Further, the emergence of brighter X-ray sources that already allow picosecond observations will enable real-time observations in solution.(196, 197)

In order to analyse inorganic–organic composite materials in particular, additional imaging advances will be required. Current microscopy techniques are suited to the structural analysis of the inorganic host (high electron density) but are rarely able to provide local information regarding the lighter organic guest. They thus provide data dominated by the host. In most cases, this is adequate but fails for example, when considering the composite behaviour under load conditions. Super-resolution microscopy and coupled spectroscopy techniques can potentially provide insight into inorganic-organic composites from the perspective of the organic guest species.(397-399) We are currently anticipating investigations into the distribution and physical state of fluorescent guests – small molecules to nanometre sized occlusions - in inorganic single crystals.

Chapter 6: Conclusions and Outlook

6.1: Conclusions

This thesis investigated the formation and structural evolution of synthetic calcium carbonate in aqueous solution, where the relevance to biomineralization processes was considered.

Chapter 3 followed in detail the amorphous to crystalline transition of ACC either in the presence of additives or under spatial confinement. Observations of the stabilization and transition mechanisms of ACC, both in the solid state and in solution, allowed the primary stabilization factors and the transition mechanism to be determined. The primary factor governing the stability of ACC in solution is the spatial confinement of the ACC particles and the associated limited access to bulk water. Additives play a secondary role in stabilizing the amorphous precursor in solution, inhibiting the nucleation of crystalline calcium carbonate rather than directly stabilizing the ACC. Atmospheric investigations showed that the effect of additives during solid state transition is more subtle. Additives either act as crystallisation promoters or inhibitors based on their molecular weights. In both “confined” solution and atmospheric crystallisation, a common continuous dehydration process in the ACC is observable before crystallisation occurs. In combination with the dehydration activation energies determined for the solid state transformation, this puts the previously stated solid state crystallisation of ACC in solution in question. This indicates that an additional catalysing factor is necessary in solution for ACC to transform to crystalline calcium carbonate by a “solid state” mechanism.

A general method for producing amorphous precursors was also developed, based on the freeze-concentration of “counter-ion free” saturated solutions of the amorphous precursor constituents. The method developed not only allows the production of stable, amorphous precursors of calcium phosphate and calcium carbonate, but also provides a potential way of identifying the presence of amorphous precursor phases in new mineral systems. Initial studies allowed the identification of a previously unknown amorphous calcium oxalate phase which precedes crystalline calcium oxalate in aqueous solution. The existence of this phase was subsequently confirmed by confinement and additive studies, which retard the transformation of the amorphous precursor to crystalline calcium oxalate.

Chapter 4, focused on the characterisation of the ammonia diffusion method used for calcium carbonate precipitation. This was done as the ammonia diffusion method (ADM) was previously the “only” option to obtain calcium carbonate crystals of “extraordinary morphology”. These crystals of “extraordinary morphology” had previously been classified as mesocrystals, inspired by the fact that they appear in images to be composed of amorphous and/ or nano-crystalline units, i.e. they have a crystal “structure” resulting from the oriented attachment of nanoparticles. Characterisation of the ADM was expected to provide insight into the formation mechanisms of crystals with such “extraordinary morphologies”.

The characterisation of the ammonia diffusion method allowed us to identify and quantify factors that govern the method underlying supersaturation/ time profile. Knowledge of the supersaturation/ time profile, that leads to the production of “mesocrystals” in the ammonia diffusion method, enabled the derivation of an enzymatically driven one pot synthesis method. This method will be used for future in-situ investigations on the formation mechanism of “mesocrystals”. The supersaturation/ time profile in itself showed a prolonged increase in supersaturation over the course of mineral formation, which potentially enables the occurrence of multiple nucleation events.

Mesocrystals were first introduced for calcium carbonate, where this structural assignment was primarily made on the basis of their high surface areas and single crystal diffraction. Structural investigations of the validity of these mesocrystal identifiers revealed that both factors are insufficient to distinguish a mesocrystal (array of smaller oriented units) from a single crystal formed by ion-by-ion growth.

Chapter 6: Conclusion and Outlook

Chapter 5, applied BCDI to image the response of calcite to external stimuli such as supersaturation (crystal growth) and undersaturation (dissolution), and the presence of a heterogeneously nucleating substrate. The presented study on the interfacial nucleation of calcite on functionalized self-assembled monolayers supported on thin gold films, revealed that the SAM does indeed guide the selection of a nucleation plane. The actual morphology of the heterogeneously nucleated and growing crystal is defined by the accumulation of strain in a preferential growth direction parallel to the substrate. The accumulation of strain above a certain threshold then causes the formation of stress relief sites in the form of a single dislocation loops and crystal growth preferentially occurs normal to the substrate.

Observations on the growth and dissolution of calcite by BCDI allowed the direct visualization of the 3D dislocation network present within a micron sized single crystal. Future studies will help us to understand how strained surfaces and defects affect crystal growth and dissolution processes.

6.2: Outlook

Amorphous precursor phases. The accumulated knowledge concerning the transformation mechanism of amorphous precursor phases to crystalline phases could potentially be sufficient to start the manufacture of crystals with pre-defined, complex shapes. If we could fulfil the promise of shapeable, amorphous precursors in the formation of single crystalline materials with complex structures and morphologies, this would be amazing.

First steps in this direction are being taken, here and elsewhere. For example, the production of single crystalline lenses of calcium carbonate with concave and convex shapes are currently being trialled.⁽²³⁷⁾ Current challenges include control over crystal orientation and the volume change which occurs on conversion of an amorphous particle to a crystalline one. The latter is particularly problematic as it creates voids in the product crystal or the crystal does not adapt completely to the template that it should entirely fill.⁽⁴⁰⁰⁾ The development and application of 3D templates with a controllable structural elasticity could solve this problem.

The above are relatively minor problems when one wants to manufacture a “big” single crystal out of a lot of smaller amorphous particles, which are inherently metastable and crystallize very fast. The big problem is “how do we induce only one nucleation event?” In an ideal scenario, one even wants to induce nucleation in one particular area and prevent the amorphous particles from nucleating anywhere else. This is a challenging endeavour and we are currently exploring potential solutions to this problem.

Most research on amorphous precursor phases which has been directed at producing crystals with complex shapes is driven by the examples provided by biominerals. Therefore, most studies focus on carbonates, phosphates and silicates, which are not the most interesting choices for new functional materials. To even consider the translation of amorphous precursor based crystallisation to functional material synthesis, we have to ask “do the materials we consider for functional material synthesis even possess an easily accessible amorphous phase which we can utilize?” In view of this, a number of studies will commence trying to identify potential material candidates.

Chapter 6: Conclusion and Outlook

The investigations of **mesocrystals** and oriented attachment crystallisation pathways are, in the author's opinion, only at the beginning. The ammonia diffusion method characterisation and the subsequently developed one pot synthesis method may provide a starting point for an in-depth, in-situ analysis of the formation process of calcium carbonate mesocrystals.

“Bragg” coherent diffraction imaging studies. The inherent potential of coherent diffraction imaging in supplying unique information is impressive. The BCDI applied here which provided localized information about strain and dislocations within a single crystal, is just one of a range of coherent imaging techniques which are currently emerging. Ptychography, which is another coherent imaging technique, is changing the way we address X-ray tomography limitations.

The methodology used in the interfacial nucleation study presented here is easily transferred to any thin film system. More sophisticated crystal growth experiments can be easily accommodated in a BCDI set up as Beamlines become dedicated to coherent diffraction imaging. Given time, coherent imaging techniques will be capable of imaging dynamic processes in any environment, and they will have the possibility of not just providing localized information about strain, dislocations, elemental composition and the structural organization of a single crystal but they will provide information concerning many other physical characteristics. Mapping magnetic domains in relation to lattice displacements and dislocations, and the origin of composite material strength are at the forefront of current investigations.

Word Count: 65,579

List of References

References

1. S. Mann, *Biomaterialization: Principles and concepts in bioinorganic materials chemistry*. (Oxford University Press, Oxford, 2001).
2. Y. Polti, T. Arad, E. Klein, S. Weiner, L. Addadi, Sea Urchin Spine Calcite Forms via a Transient Amorphous Calcium Carbonate Phase. *Science* **306**, 1161 (2004).
3. J. Aizenberg, J. Hanson, T. F. Koetzle, L. Leiserowitz, S. Weiner, L. Addadi, Biologically Induced Reduction in Symmetry: A Study of Crystal Texture of Calcitic Sponge Spicules. *Chem. Eur. J.* **1**, 414 (1995).
4. D. A. Thompson, *On Growth and Form an Abridged Edition*. J. T. Bonner, Ed., (Cambridge University Press Cambridge, 1961), vol. 1, pp. 345.
5. H. A. Lowenstam, S. Weiner, *On Biomaterialization* (Oxford University Press, New York 1989), pp. 324.
6. A. H. Knoll, Biomaterialization and Evolutionary History. *Rev. Mineral. Geochem.* **54**, 329 (2003).
7. A. Sato, S. Nagasaka, K. Furihata, S. Nagata, I. Arai, K. Saruwatari, T. Kogure, S. Sakuda, H. Nagasawa, Glycolytic intermediates induce amorphous calcium carbonate formation in crustaceans. *Nat Chem Biol* **7**, 197 (2011).
8. G. Donnay, D. L. Pawson, X-ray Diffraction Studies of Echinoderm Plates. *Science* **166**, 1147 (1969).
9. S. Mann, *Biomaterialization* (Oxford University Press, New York 2002).
10. J. Aizenberg, A. Tkachenko, S. Weiner, L. Addadi, G. Hendler, Calcitic microlenses as part of the photoreceptor system in brittlestars. *Nature* **412**, 819 (2001).
11. S. Weiner, P. M. Dove, J. J. DeYoreo, Biomaterialization *Rev. Mineral. Geochem.* **54**, (2003).
12. H. Cölfen, M. Antonietti, *Mesocrystals and Nonclassical Crystallization* (Wiley-VCH, Weinheim, 2008).
13. D. Erdemir, A. Y. Lee, A. S. Myerson, Nucleation of Crystals from Solution: Classical and Two-Step Models. *Acc. Chem. Res.* **42**, 621 (2009).
14. L. Addadi, S. Raz, S. Weiner, Taking Advantage of Disorder: Amorphous Calcium Carbonate and its Roles in Biomaterialization *Adv. Mater.* **15**, 959 (2003).
15. J. Aizenberg, A. J. Black, G. M. Whitesides, Oriented Growth of Calcite Controlled by Self-Assembled Monolayers of Functionalized Alkanethiols Supported on Gold and Silver. *J. Am. Chem. Soc.* **121**, 4500 (1999).
16. B. Cantaert, E. Beniash, F. C. Meldrum, The role of poly(aspartic acid) in the precipitation of calcium phosphate in confinement. *J. Mater. Chem. B* **1**, 6586 (2013).
17. J. Aizenberg, G. Lambert, L. Addadi, S. Weiner, Stabilization of amorphous calcium carbonate by specialized macromolecules in biological and synthetic precipitates. *Adv. Mater.* **8**, 222 (1996).

References

18. J. Aizenberg, G. Lambert, S. Weiner, L. Addadi, Factors involved in the formation of amorphous and crystalline calcium carbonate: A study of an ascidian skeleton. *J. Am. Chem. Soc.* **124**, 32 (2002).
19. W. D. Callister, *Materials science and engineering : an introduction*. (John Wiley & Sons, New York, 2007).
20. A. Bravais, Mmoire sur les systmes forms par les points distribus rgulirement sur un plan ou dans l'espace. *J. Ecole Polytech* **19**, 1 (1850).
21. C. J. Stephens, University of Leeds (2010), uk.bl.ethos.534898.
22. Z. H. Stachurski, On Structure and Properties of Amorphous Materials. *Materials* **4**, 1564 (2011).
23. F. C. Meldrum, H. Colfen, Controlling Mineral Morphologies and Structures in Biological and Synthetic Systems. *Chem. Rev.* **108**, 4332 (2008).
24. J. Nývlt, The Ostwald Rule of Stages. *Cryst. Res. Technol.* **30**, 443 (1995).
25. S. E. Wolf, J. Leiterer, V. Pipich, R. Barrea, F. Emmerling, W. Tremel, Strong Stabilization of Amorphous Calcium Carbonate Emulsion by Ovalbumin: Gaining Insight into the Mechanism of 'Polymer-Induced Liquid Precursor' Processes. *J. Am. Chem. Soc.* **133**, 12642 (2011).
26. S. E. Wolf, L. Muller, R. Barrea, C. J. Kampf, J. Leiterer, U. Panne, T. Hoffmann, F. Emmerling, W. Tremel, Carbonate-coordinated metal complexes precede the formation of liquid amorphous mineral emulsions of divalent metal carbonates. *Nanoscale* **3**, 1158 (2011).
27. E. F. Henry, C. B. Adrian, S. S. Philip, Neutron and x-ray diffraction studies of liquids and glasses. *Rep. Prog. Phys.* **69**, 233 (2006).
28. H. Cölfen, S. Mann, Higher-Order Organization by Mesoscale Self-Assembly and Transformation of Hybrid Nanostructures. *Angew. Chem. Int. Ed.* **42**, 2350 (2003).
29. P. Atkins, J. d. Paula, *Atkins' Physical Chemistry* (Oxford University Press, Trento Italy ed. 7, 2002), pp. 1150.
30. A. S. Myerson, *Handbook of Industrial Crystallisation*. (Butterworth Heinemann, United States of America, ed. Second, 2002).
31. A. Putnis, M. Prieto, L. Fernandez-Diaz, Fluid supersaturation and crystallization in porous media *Geol. Mag.* **132**, 13 (1995).
32. J. W. Mullin, *Crystallization*. (Butterworth-Heinemann, Oxford, Great Britian, ed. 4, 2001).
33. A. F. Wallace, L. O. Hedges, A. Fernandez-Martinez, P. Raiteri, J. D. Gale, G. A. Waychunas, S. Whitlam, J. F. Banfield, J. J. De Yoreo, Microscopic Evidence for Liquid-Liquid Separation in Supersaturated CaCO₃ Solutions. *Science* **341**, 885 (2013).
34. M. Volmer, *Kinetic der Phasenbildung* (Steinkoff, Dresden 1931).
35. in *Freeze-drying of Pharmaceuticals and Biopharmaceuticals*. (The Royal Society of Chemistry, 2007), pp. 54-77.
36. J. A. Dirksen, T. A. Ring, Fundamentals of Crystallization : Kinetic Effects on Particle Size Distributions and Morphology *Chem. Eng. Sci.* **46**, 31 (1991).
37. R. Lacmann, A. Herden, C. Mayer, Kinetics of Nucleation and Crystal Growth. *Chem. Eng. Technol.* **22**, 279 (1999).

References

38. P. M. Dove, N. Han, Kinetics of Mineral Dissolution and Growth as Reciprocal Microscopic Surface Processes Across Chemical Driving Force. *AIP Conf. Proc.* **916**, 215 (2007).
39. D. Hull, *Introduction to Dislocations*. W. S. Owen, Ed., International Series on Materials Science and Technology (Pergamon Press, New York, ed. 2, 1975).
40. K. Byrappa, T. Ohachi, *Crystal Growth Technology*. Materials Processing (Springer New York, 2003).
41. G. Wulff, On the question of speed of growth and dissolution of crystal surfaces. *Zeitschrift Fur Krystallographie Und Mineralogie* **34**, 449 (1901).
42. N. A. J. M. Sommerdijk, G. de With, Biomimetic CaCO₃ Mineralization using Designer Molecules and Interfaces. *Chem. Rev.* **108**, 4499 (2008).
43. F. C. Meldrum, S. T. Hyde, Morphological influence of magnesium and organic additives on the precipitation of calcite. *J. Cryst. Growth.* **231**, 544 (2001).
44. D. Ren, Q. Feng, X. Bourrat, Effects of additives and templates on calcium carbonate mineralization in vitro. *Micron* **42**, 228 (2011).
45. K. Naka, S.-C. Huang, Y. Chujo, Formation of Stable Vaterite with Poly(acrylic acid) by the Delayed Addition Method. *Langmuir* **22**, 7760 (2006).
46. R. A. Berner, The role of magnesium in the crystal growth of calcite and aragonite from sea water. *Geochim. Cosmochim. Acta* **39**, 489 (1975).
47. P. Bots, L. G. Benning, R. E. M. Rickaby, S. Shaw, The role of SO₄ in the switch from calcite to aragonite seas. *Geology* **39**, 331 (2011).
48. A. A. Finch, N. Allison, Coordination of Sr and Mg in calcite and aragonite. *Mineral Mag.* **71**, 539 (2007).
49. Y.-Y. Kim, N. B. J. Hetherington, E. H. Noel, R. Kröger, J. M. Charnock, H. K. Christenson, F. C. Meldrum, Capillarity Creates Single-Crystal Calcite Nanowires from Amorphous Calcium Carbonate. *Angew. Chem. Int. Ed.* **50**, 12572 (2012).
50. N. B. J. Hetherington, A. N. Kulak, Y.-Y. Kim, E. H. Noel, D. Snoswell, M. Butler, F. C. Meldrum, Porous Single Crystals of Calcite from Colloidal Crystal Templates: ACC Is Not Required for Nanoscale Templating. *Adv. Funct. Mater.* **21**, 948 (2011).
51. Y. Oaki, H. Imai, Experimental Demonstration for the Morphological Evolution of Crystals Grown in Gel Media. *Cryst. Growth Des.* **3**, 711 (2003).
52. D. W. Oxtoby, Homogenous nucleation: theory and experiment *J. Phys.: Condens. Matter* **4**, 23 (1992).
53. J. W. Cahn, J. E. Hilliard, Free energy of a nonuniform system. I. Interfacial free energy. *J. Chem. Phys.* **31**, 688 (1958).
54. J. D. Gunton, Homogenous Nucleation *J. Stat. Phys.* **95**, 21 (19989).
55. P. G. Vekilov, The two-step mechanism of nucleation of crystals in solution. *Nanoscale* **2**, 2346 (2010).
56. K.-Q. Zhang, X. Y. Liu, In situ observation of colloidal monolayer nucleation driven by an alternating electric field. *Nature* **429**, 739 (2004).

References

57. T. H. Zhang, X. Y. Liu, Effect of Long-Range Attraction on Growth Model. *J. Phys. Chem. C* **111**, 1342 (2006).
58. T. H. Zhang, X. Y. Liu, Multistep Crystal Nucleation: A Kinetic Study Based on Colloidal Crystallization. *J. Phys. Chem. B* **111**, 14001 (2007).
59. D. Gebauer, A. Völkel, H. Cölfen, Stable Prenucleation Calcium Carbonate Clusters. *Science* **322**, 1819 (2008).
60. L. B. Gower, D. J. Odom, Deposition of calcium carbonate films by a polymer-induced liquid-precursor (PILP) process. *J. Cryst. Growth*. **210**, 719 (2000).
61. R. Demichelis, P. Raiteri, J. D. Gale, D. Quigley, D. Gebauer, Stable prenucleation mineral clusters are liquid-like ionic polymers. *Nat. Commun.* **2**, 590 (2011).
62. A. Dey, P. H. H. Bomans, F. A. Muller, J. Will, P. M. Frederik, G. de With, N. Sommerdijk, The role of prenucleation clusters in surface-induced calcium phosphate crystallization. *Nat. Mater.* **9**, 1010 (2010).
63. W. J. E. M. Habraken, J. Tao, L. J. Brylka, H. Friedrich, L. Bertinetti, A. S. Schenk, A. Verch, V. Dmitrovic, P. H. H. Bomans, P. M. Frederik, J. Laven, P. van der Schoot, B. Aichmayer, G. de With, J. J. DeYoreo, N. A. J. M. Sommerdijk, Ion-association complexes unite classical and non-classical theories for the biomimetic nucleation of calcium phosphate. *Nat. Commun.* **4**, 1507 (2013).
64. M. A. Bewernitz, D. Gebauer, J. Long, H. Cölfen, L. B. Gower, A metastable liquid precursor phase of calcium carbonate and its interactions with polyaspartate. *Farad. Discuss.* **159**, 291 (2012).
65. M. Faatz, F. Gröhn, G. Wegner, Amorphous Calcium Carbonate: Synthesis and Potential Intermediate in Biomineralization. *Adv. Mater.* **16**, 996 (2004).
66. J. F. Banfield, S. A. Welch, H. Z. Zhang, T. T. Ebert, R. L. Penn, Aggregation-based crystal growth and microstructure development in natural iron oxyhydroxide biomineralization products. *Science* **289**, 751 (2000).
67. J. Seto, Y. Ma, S. A. Davis, F. Meldrum, A. Gourrier, Y.-Y. Kim, U. Schilde, M. Sztucki, M. Burghammer, S. Maltsev, C. Jäger, H. Cölfen, Structure-property relationships of a biological mesocrystal in the adult sea urchin spine. *Proc. Natl. Acad. Sci. U.S.A.* **109**, 3699 (2012).
68. R. L. Penn, J. F. Banfield, Morphology development and crystal growth in nanocrystalline aggregates under hydrothermal conditions: Insights from titania. *Geochim. Cosmochim. Acta* **63**, 1549 (1999).
69. N. Gehrke, H. Cölfen, N. Pinna, M. Antonietti, N. Nassif, Superstructures of Calcium Carbonate Crystals by Oriented Attachment. *Cryst. Growth Des.* **5**, 1317 (2005).
70. G. Zhang, J. Xu, From colloidal nanoparticles to a single crystal: New insights into the formation of nacre's aragonite tablets. *J. Struct. Biol.* **182**, 36 (2013).
71. D. S. Li, M. H. Nielsen, J. R. I. Lee, C. Frandsen, J. F. Banfield, J. J. De Yoreo, Direction-Specific Interactions Control Crystal Growth by Oriented Attachment. *Science* **336**, 1014 (2012).
72. J. Fang, B. Ding, H. Gleiter, Mesocrystals: Syntheses in metals and applications. *Chem. Soc. Rev.*, (2011).

References

73. G.-T. Zhou, Y.-B. Guan, Q.-Z. Yao, S.-Q. Fu, Biomimetic mineralization of prismatic calcite mesocrystals: Relevance to biomineralization *Chem. Geol.* **279**, 10 (2010).
74. H. Zhai, X. Chu, X. Xu, R. Tang, Controlled formation of calcium-phosphate-based hybrid mesocrystals by organic-inorganic co-assembly *Nanoscale* **2**, 7 (2010).
75. M. Niederberger, H. Colfen, Oriented attachment and mesocrystals: Non-classical crystallization mechanisms based on nanoparticle assembly. *Phys. Chem. Chem. Phys.* **8**, 17 (2006).
76. K. Sawada, N. Abdel-Aal, H. Sekino, K. Satoh, Adsorption of inorganic phosphates and organic polyphosphonate on calcite. *Dalton Trans.*, 342 (2003).
77. M. Atoji, R. Rundle, Neutron Diffraction Study of Gypsum, $\text{CaSO}_4 \cdot 2\text{H}_2\text{O}$. *J. Chem. Phys.* **29**, 1306 (1958).
78. L. B. Gower, Biomimetic Model Systems for Investigating the Amorphous Precursor Pathway and Its Role in Biomineralization. *Chem. Rev.* **108**, 4551 (2008).
79. H. Liu, Y. Zhu, Z. Mao, C. Ning, Nacre-Like Calcium Carbonate Nanoarchitectures. *Nanosci. Nanotechnol. Lett.* **3**, 446 (2011).
80. F. Nudelman, H. H. Chen, H. A. Goldberg, S. Weiner, L. Addadi, Spiers Memorial Lecture Lessons from biomineralization: comparing the growth strategies of mollusc shell prismatic and nacreous layers in *Atrina rigida*. *Farad. Discuss.* **136**, 9 (2007).
81. M. E. Kunitake, S. P. Baker, L. A. Estroff, The effect of magnesium substitution on the hardness of synthetic and biogenic calcite. *MRS Commun.* **2**, 113 (2012).
82. B. Pokroy, A. N. Fitch, F. Marin, M. Kapon, N. Adir, E. Zolotoyabko, Anisotropic lattice distortions in biogenic calcite induced by intracrystalline organic molecules. *J. Struct. Biol.* **155**, 96 (2006).
83. W. Deer, R. Howie, J. Zussman. (Longman Group Ltd., London, 1966).
84. J. H. E. Cartwright, A. G. Checa, J. D. Gale, D. Gebauer, C. I. Sainz-Díaz, Calcium Carbonate Polyamorphism and Its Role in Biomineralization: How Many Amorphous Calcium Carbonates Are There? *Angew. Chem. Int. Ed.* **51**, 11960 (2012).
85. D. Gebauer, P. N. Gunawidjaja, J. Y. P. Ko, Z. Bacsik, B. Aziz, L. J. Liu, Y. F. Hu, L. Bergstrom, C. W. Tai, T. K. Sham, M. Eden, N. Hedin, Proto-Calcite and Proto-Vaterite in Amorphous Calcium Carbonates. *Angew. Chem. Int. Ed.* **49**, 8889 (2011).
86. L. Brecevic, A. E. Nielsen, Solubility of amorphous calcium carbonate. *J. Cryst. Growth.* **98**, 504 (1989).
87. M. Saharay, A. O. Yazaydin, R. J. Kirkpatrick, Dehydration-Induced Amorphous Phases of Calcium Carbonate. *J. Phys. Chem. B* **117**, 3328 (2013).
88. T. Ogino, T. Suzuki, K. Sawada, The formation and transformation mechanism of calcium carbonate in water. *Geochim. Cosmochim. Acta* **51**, 2757 (1987).
89. Z. Nan, Z. Shi, B. Yan, R. Guo, W. Hou, A novel morphology of aragonite and an abnormal polymorph transformation from calcite to aragonite with PAM and CTAB as additives. *J. Colloid Interface Sci.* **317**, 77 (2008).

References

90. M. Donnet, A. aimable, J. Lemaitre, P. Bowen, Contribution of Aggregation to the Growth Mechanism of Seeded Calcium Carbonate Precipitation in the Presence of Polyacrylic Acid *J. Phys. Chem. A* **114**, 10 (2010).
91. A. V. Radha, T. Z. Forbes, C. E. Killian, P. U. P. A. Gilbert, A. Navrotsky, Transformation and crystallization energetics of synthetic and biogenic amorphous calcium carbonate. *Proc. Natl. Acad. Sci. U.S.A.* **107**, (2010).
92. G. Wolf, C. Günther, Thermophysical Investigations of the Polymorphous Phases of Calcium Carbonate. *J. Therm. Anal. Calorim.* **65**, 687 (2001).
93. J. D. Rodriguez-Blanco, S. Shaw, L. G. Benning, The kinetics and mechanisms of amorphous calcium carbonate (ACC) crystallization to calcite, via vaterite. *Nanoscale* **3**, 265 (2011).
94. E. M. Pouget, P. H. H. Bomans, J. Goos, P. M. Frederik, G. de With, N. Sommerdijk, The Initial Stages of Template-Controlled CaCO₃ Formation Revealed by Cryo-TEM. *Science* **323**, 1455 (2009).
95. J. Ihli, W. C. Wong, E. H. Noel, Y.-Y. Kim, A. N. Kulak, H. K. Christenson, M. J. Duer, F. C. Meldrum, Dehydration and crystallization of amorphous calcium carbonate in solution and in air. *Nat. Commun.* **5**, (2014).
96. M. P. Schmidt, A. J. Ilott, B. L. Phillips, R. J. Reeder, Structural Changes upon Dehydration of Amorphous Calcium Carbonate. *Cryst. Growth Des.* **14**, 938 (2014).
97. Y. Politi, R. A. Metzler, M. Abrecht, B. Gilbert, F. H. Wilt, I. Sagi, L. Addadi, S. Weiner, P. U. P. A. Gilbert, Transformation mechanism of amorphous calcium carbonate into calcite in the sea urchin larval spicule. *Proc. Natl. Acad. Sci. U.S.A.* **105**, 17362 (2008).
98. Z. Chen, Z. Nan, Controlling the polymorph and morphology of CaCO₃ crystals using surfactant mixtures. *J. Colloid Interface Sci.* **358**, 416 (2011).
99. G. Yan, L. Wang, J. Huang, The crystallization behavior of calcium carbonate in ethanol/water solution containing mixed nonionic/anionic surfactants. *Powder Technol.* **192**, 58 (2009).
100. N. Koga, Y. Yamane, T. Kimura, Thermally induced transformations of calcium carbonate polymorphs precipitated selectively in ethanol/water solutions. *Thermochim. Acta* **512**, 13 (2011).
101. L. Zhang, L.-H. Yue, F. Wang, Q. Wang, Divisive Effect of Alcohol-Water Mixed Solvents on Growth Morphology of Calcium Carbonate Crystals. *J. Phys. Chem. B* **112**, 10668 (2008).
102. S. R. Dickinson, G. E. Henderson, K. M. McGrath, Controlling the kinetic versus thermodynamic crystallisation of calcium carbonate. *J. Cryst. Growth.* **244**, 369 (2002).
103. D. J. Cooke, R. J. Gray, K. K. Sand, S. L. S. Stipp, J. A. Elliott, Interaction of Ethanol and Water with the {10 $\bar{1}4$ } Surface of Calcite. *Langmuir* **26**, 14520 (2010).
104. K. K. Sand, M. Yang, E. Makovicky, D. J. Cooke, T. Hassenkam, K. Bechgaard, S. L. S. Stipp, Binding of Ethanol on Calcite: The Role of the OH Bond and Its Relevance to Biomineralization. *Langmuir* **26**, 15239 (2010).

References

105. Y. Kitano, K. Park, D. W. Hood, Pure Aragonite Synthesis. *J. Geophys. Res.* **67**, 4873 (1962).
106. R. Beck, J.-P. Andreassen, The onset of spherulitic growth in crystallization of calcium carbonate. *J. Cryst. Growth.* **312**, 2226 (2010).
107. S. K. R. Lam, Dissertation, University of Bristol (2008), uk.bl.ethos.492548.
108. R. J. Reeder, Crystal Chemistry of the Rhombohedral Carbonates *Rev. Mineral. Geochem.* **11**, 1 (1983).
109. F. Lippmann, *Sedimentary Carbonate Minerals*. Minerals, Rocks and Inorganic Materials (Springer, Heidelberg, 1973).
110. D. M. Duffy, J. H. Harding, Simulation of Organic Monolayers as Templates for the Nucleation of Calcite Crystals. *Langmuir* **20**, 7630 (2004).
111. R. Zucker, D. Chatain, U. Dahmen, S. Hagège, W. C. Carter, New software tools for the calculation and display of isolated and attached interfacial-energy minimizing particle shapes. *J. Mater. Sci.* **47**, 8290 (2012).
112. M. E. Kunitake, L. M. Mangano, J. M. Peloquin, S. P. Baker, L. A. Estroff, Evaluation of strengthening mechanisms in calcite single crystals from mollusk shells. *Acta Biomater.* **9**, 5353 (2013).
113. P. Bots, University of Leeds (2011), uk.bl.ethos.557367.
114. M. Prenant, The types of calcium mineral in living beings and the problem of their determination. *Biol Rev Camb Philos Soc* **2**, 365 (1927).
115. Y. Politi, D. R. Batchelor, P. Zaslansky, B. F. Chmelka, J. C. Weaver, I. Sagi, S. Weiner, L. Addadi, Role of Magnesium Ion in the Stabilization of Biogenic Amorphous Calcium Carbonate: A Structure–Function Investigation. *Chem. Mater.* **22**, 161 (2009).
116. Y. Politi, Y. Levi-Kalisman, S. Raz, F. Wilt, L. Addadi, S. Weiner, I. Sagi, Structural Characterization of the Transient Amorphous Calcium Carbonate Precursor Phase in Sea Urchin Embryos. *Adv. Funct. Mater.* **16**, 1289 (2006).
117. S. Weiner, L. Addadi, in *Annual Review of Materials Research, Vol 41*, D. R. Clarke, P. Fratzl, Eds. (Annual Reviews, Palo Alto, 2011), vol. 41, pp. 21-40.
118. Y. U. T. Gong, C. E. Killian, I. C. Olson, N. P. Appathurai, A. L. Amasino, M. C. Martin, L. J. Holt, F. H. Wilt, P. U. P. A. Gilbert, Phase transitions in biogenic amorphous calcium carbonate. *Proc. Natl. Acad. Sci. U.S.A.* **109**, 6088 (2012).
119. C. C. Tester, C.-H. Wu, M. R. Krejci, L. Mueller, A. Park, B. Lai, S. Chen, C. Sun, M. Balasubramanian, D. Joester, Time-Resolved Evolution of Short- and Long-Range Order During the Transformation of Amorphous Calcium Carbonate to Calcite in the Sea Urchin Embryo. *Adv. Funct. Mater.* **23**, 4185 (2013).
120. E. Beniash, J. Aizenberg, L. Addadi, S. Weiner, Amorphous calcium carbonate transforms into calcite during sea urchin larval spicule growth. *Proc. R. Soc. B* **264**, 461 (1997).
121. A. Becker, U. Bismayer, M. Epple, H. Fabritius, B. Hasse, J. Shi, A. Ziegler, Structural characterisation of X-ray amorphous calcium

References

- carbonate (ACC) in sternal deposits of the crustacea *Porcellio scaber*. *Dalton Trans.*, 551 (2003).
122. V. R. Franceschi, P. A. Nakata, Calcium Oxalate in Plants: Formation and Function. *Annu. Rev. Plant Biol.* **56**, 41 (2005).
 123. P. Raiteri, J. D. Gale, Water Is the Key to Nonclassical Nucleation of Amorphous Calcium Carbonate. *J. Am. Chem. Soc.* **132**, 17623 (2010).
 124. M. Faatz, F. Gröhn, G. Wegner, Mineralization of calcium carbonate by controlled release of carbonate in aqueous solution. *Mater. Sci. Eng. C* **25**, 153 (2005).
 125. Y. Levi-Kalisman, S. Raz, S. Weiner, L. Addadi, I. Sagi, Structural Differences Between Biogenic Amorphous Calcium Carbonate Phases Using X-ray Absorption Spectroscopy. *Adv. Funct. Mater.* **12**, 43 (2002).
 126. R. S. K. Lam, J. M. Charnock, A. Lennie, F. C. Meldrum, Synthesis-dependant structural variations in amorphous calcium carbonate. *CrystEngComm* **9**, 1226 (2007).
 127. A. L. Goodwin, F. M. Michel, B. L. Phillips, D. A. Keen, M. T. Dove, R. J. Reeder, Nanoporous Structure and Medium-Range Order in Synthetic Amorphous Calcium Carbonate. *Chem. Mater.* **22**, 3197 (2010).
 128. F. M. Michel, J. MacDonald, J. Feng, B. L. Phillips, L. Ehm, C. Tarabrella, J. B. Parise, R. J. Reeder, Structural Characteristics of Synthetic Amorphous Calcium Carbonate. *Chem. Mater.* **20**, 4720 (2008).
 129. N. Koga, Y. Nakagoe, H. Tanaka, Crystallization of amorphous calcium carbonate. *Thermochim. Acta* **318**, 239 (1998).
 130. M. Huber, W. J. Stark, S. Loher, M. Maciejewski, F. Krumeich, A. Baiker, Flame synthesis of calcium carbonate nanoparticles. *Chem. Commun.*, 648 (2005).
 131. S. Raz, P. C. Hamilton, F. H. Wilt, S. Weiner, L. Addadi, The Transient Phase of Amorphous Calcium Carbonate in Sea Urchin Larval Spicules: The Involvement of Proteins and Magnesium Ions in Its Formation and Stabilization. *Adv. Funct. Mater.* **13**, 480 (2003).
 132. C. Günther, A. Becker, G. Wolf, M. Epple, In vitro Synthesis and Structural Characterization of Amorphous Calcium Carbonate. *Zeitschrift für anorganische und allgemeine Chemie* **631**, 2830 (2005).
 133. R. Gueta, A. Natan, L. Addadi, S. Weiner, K. Refson, L. Kronik, Local Atomic Order and Infrared Spectra of Biogenic Calcite *Angew. Chem., Int. Ed.* **46**, 4 (2007).
 134. R. J. Reeder, A. L. Goodwin, M. Michel, B. L. Phillips, D. A. Keen, M. T. Dove, Structure model of synthetic amorphous calcium carbonate. *Geochim. Cosmochim. Acta* **74**, A855 (2010).
 135. M. Saharay, R. James Kirkpatrick, Onset of Orientational Order in Amorphous Calcium Carbonate (ACC) upon Dehydration. *Chem. Phys. Lett.* **591**, 287 (2014).
 136. E. Loste, R. J. Park, J. Warren, F. C. Meldrum, Precipitation of Calcium Carbonate in Confinement. *Adv. Funct. Mater.* **14**, 1211 (2004).

References

137. F. Nudelman, E. Sonmezler, P. H. H. Bomans, G. de With, N. A. J. M. Sommerdijk, Stabilization of amorphous calcium carbonate by controlling its particle size. *Nanoscale* **2**, 2436 (2010).
138. A. n. Neira-Carrillo, D. F. Acevedo, M. C. Miras, C. A. Barbero, D. Gebauer, H. Cölfen, J. L. Arias, Influence of Conducting Polymers Based on Carboxylated Polyaniline on In Vitro CaCO₃ Crystallization. *Langmuir* **24**, 12496 (2008).
139. T. Y. J. Han, J. Aizenberg, Calcium carbonate storage in amorphous form and its template-induced crystallization. *Chem. Mater.* **20**, 1064 (2008).
140. A. Navrotsky, Energetic clues to pathways to biomineralization: Precursors, clusters, and nanoparticles. *Proc. Natl. Acad. Sci. U.S.A.* **101**, 12096 (2004).
141. A. Baynton, B. D. Chandler, F. Jones, G. Nealon, M. I. Ogden, T. Radomirovic, G. K. H. Shimizu, J. M. Taylor, Phosphonate additives do not always inhibit crystallization. *CrystEngComm* **13**, 1090 (2011).
142. S. Piana, F. Jones, J. D. Gale, Aspartic acid as a crystal growth catalyst. *CrystEngComm* **9**, 1187 (2007).
143. K. J. Davis, P. M. Dove, J. J. De Yoreo, The Role of Mg²⁺ as an Impurity in Calcite Growth. *Science* **290**, 1134 (2000).
144. S. Kerisit, S. C. Parker, Free Energy of Adsorption of Water and Metal Ions on the {1014} Calcite Surface. *J. Am. Chem. Soc.* **126**, 10152 (2004).
145. S. Raz, S. Weiner, L. Addadi, Formation of High-Magnesian Calcites via an Amorphous Precursor Phase: Possible Biological Implications. *Adv. Mater.* **12**, 38 (2000).
146. D. B. Wang, A. F. Wallace, J. J. De Yoreo, P. M. Dove, Carboxylated molecules regulate magnesium content of amorphous calcium carbonates during calcification. *Proc. Natl. Acad. Sci. U.S.A.* **106**, 21511 (2009).
147. E. Loste, R. M. Wilson, R. Seshadri, F. C. Meldrum, The role of magnesium in stabilising amorphous calcium carbonate and controlling calcite morphologies. *J. Cryst. Growth.* **254**, 206 (2003).
148. S. Bentov, S. Weil, L. Glazer, A. Sagi, A. Berman, Stabilization of amorphous calcium carbonate by phosphate rich organic matrix proteins and by single phosphoamino acids. *J. Struct. Biol.* **171**, 207 (2010).
149. R. Lakshminarayanan, X. J. Loh, S. Gayathri, S. Sindhu, Y. Banerjee, R. M. Kini, S. Valiyaveetil, Formation of Transient Amorphous Calcium Carbonate Precursor in Quail Eggshell Mineralization: An In Vitro Study. *Biomacromolecules* **7**, 3202 (2006).
150. T. Ogino, T. Suzuki, K. Sawada, The rate and mechanism of polymorphic transformation of calcium carbonate in water. *J. Cryst. Growth.* **100**, 159 (1990).
151. S. Raz, O. Testeniere, A. Hecker, S. Weiner, G. Luquet, Stable Amorphous Calcium Carbonate Is the Main Component of the Calcium Storage Structures of the Crustacean *Orchestia cavimana*. *Biological Bulletin* **203**, 269 (2002).
152. J. Ihli, Y.-Y. Kim, E. H. Noel, F. C. Meldrum, The Effect of Additives on Amorphous Calcium Carbonate (ACC): Janus Behavior in Solution and the Solid State. *Adv. Funct. Mater.* **23**, 1575 (2013).

References

153. T. Kato, Polymer/Calcium Carbonate Layered Thin-Film Composites. *Adv. Mater.* **12**, 1543 (2000).
154. A. Sugawara, T. Nishimura, Y. Yamamoto, H. Inoue, H. Nagasawa, T. Kato, Self-Organization of Oriented Calcium Carbonate/Polymer Composites: Effects of a Matrix Peptide Isolated from the Exoskeleton of a Crayfish. *Angew. Chem. Int. Ed.* **45**, 2876 (2006).
155. Y. Oaki, S. Kajiyama, T. Nishimura, H. Imai, T. Kato, Nanosegregated Amorphous Composites of Calcium Carbonate and an Organic Polymer. *Adv. Mater.* **20**, 3633 (2008).
156. A. S. Schenk, E. J. Albarracin, Y.-Y. Kim, J. Ihli, F. C. Meldrum, Confinement stabilises single crystal vaterite rods. *Chem. Commun.*, (2014).
157. C. J. Stephens, S. F. Ladden, F. C. Meldrum, H. K. Christenson, Amorphous Calcium Carbonate is Stabilised in Confinement. *Adv. Func. Mater.* **20**, 2108 (2010).
158. Y.-W. Wang, Y.-Y. Kim, H. K. Christenson, F. C. Meldrum, A new precipitation pathway for calcium sulfate dihydrate (gypsum) via amorphous and hemihydrate intermediates. *Chem. Commun.* **48**, 504 (2012).
159. C. J. Stephens, Y.-Y. Kim, S. D. Evans, F. C. Meldrum, H. K. Christenson, Early Stages of Crystallization of Calcium Carbonate Revealed in Picoliter Droplets. *J. Am. Chem. Soc.* **133**, 5210 (2011).
160. C. C. Tester, R. E. Brock, C.-H. Wu, M. R. Krejci, S. Weigand, D. Joester, In vitro synthesis and stabilization of amorphous calcium carbonate (ACC) nanoparticles within liposomes. *Crystengcomm* **13**, 3975 (2011).
161. M. Kellermeier, E. Melero-Garcia, F. Glaab, R. Klein, M. Drechsler, R. Rachel, J. M. Garcia-Ruiz, W. Kunz, Stabilization of Amorphous Calcium Carbonate in Inorganic Silica-Rich Environments. *J. Am. Chem. Soc.* **132**, 17859 (2010).
162. C. Qi, Y.-J. Zhu, B.-Q. Lu, X.-Y. Zhao, J. Zhao, F. Chen, J. Wu, ATP-Stabilized Amorphous Calcium Carbonate Nanospheres and Their Application in Protein Adsorption. *Small*, n/a (2014).
163. M. Donnet, P. Bowen, Lemal, J. tre, A thermodynamic solution model for calcium carbonate: Towards an understanding of multi-equilibria precipitation pathways. *J. Colloid Interface Sci.* **340**, 218 (2009).
164. E. Busenberg, L. N. Plummer, Kinetic and Thermodynamic Factors Controlling the Distribution of SO_4^{2-} and Na^+ in Calcite and Selected Aragonites. *Geochim. Cosmochim. Acta* **49**, 713 (1985).
165. J. Y. Gal, J. C. Bollinger, H. Tolosa, N. Gache, Calcium carbonate solubility: A reappraisal of scale formation and inhibition. *Talanta* **43**, 1497 (1996).
166. L. N. Plummer, E. Busenberg, The solubilities of calcite, aragonite and vaterite in CO_2 - H_2O solutions between 0 and 90°C, and an evaluation of the aqueous model for the system CaCO_3 - CO_2 - H_2O . *Geochim. Cosmochim. Acta* **46**, 1011 (1982).
167. J. Liu, A. Stace-Naughton, X. Jiang, C. J. Brinker, Porous Nanoparticle Supported Lipid Bilayers (Protocells) as Delivery Vehicles. *J. Am. Chem. Soc.* **131**, 1354 (2009).
168. H. L. Bohn, B. McNeal, G. O'Connor, in *Soil Chemistry*. (John Wiley Sons, 1985), pp. 316.

References

169. J. Ihli, P. Bots, A. Kulak, L. G. Benning, F. C. Meldrum, Elucidating Mechanisms of Diffusion-Based Calcium Carbonate Synthesis Leads to Controlled Mesocrystal Formation. *Adv. Funct. Mater.* **23**, 1965 (2013).
170. M. Prieto, A. Putnis, L. Fernandez-Diaz, Factors controlling the kinetics of crystallization: supersaturation evolution in a porous medium. Application to barite crystallization *Geol. Mag.* **127**, 11 (1990).
171. J. C. Love, L. A. Estroff, J. K. Kriebel, R. G. Nuzzo, G. M. Whitesides, Self-Assembled Monolayers of Thiolates on Metals as a Form of Nanotechnology. *Chem. Rev.* **105**, 1103 (2005).
172. J. D. Rodriguez-Blanco, S. Shaw, L. G. Benning, How to make 'stable' ACC: protocol and preliminary structural characterization. *Mineral. Mag.* **72**, 283 (2008).
173. E. E. Ross, S.-W. Mok, S. R. Bugni, Assembly of Lipid Bilayers on Silica and Modified Silica Colloids by Reconstitution of Dried Lipid Films. *Langmuir* **27**, 8634 (2011).
174. A. Antipov, D. Shchukin, Y. Fedutik, I. Zhanaveskina, V. Klechkovskaya, G. Sukhorukov, H. Möhwald, Urease-Catalyzed Carbonate Precipitation inside the Restricted Volume of Polyelectrolyte Capsules. *Macromol. Rapid Commun.* **24**, 274 (2003).
175. J. Ihli, A. N. Kulak, F. C. Meldrum, Freeze-drying yields stable and pure amorphous calcium carbonate (ACC). *Chem. Commun.* **49**, 3134 (2013).
176. E. Abbe, Beiträge zur Theorie des Mikroskops und der mikroskopischen Wahrnehmung. *Archiv für mikroskopische Anatomie* **9**, 413 (1873).
177. D. Semwogerere, E. R. Weeks, in *Encyclopedia of Biomaterials and Biomedical Engineering*. (Taylor & Francis 2005).
178. D. A. Skoog, D. M. West, F. J. Holler, S. R. Crouch, *Fundamentals of Analytical Chemistry* (Thomson, Brooks/Cole, Belmont, ed. 8, 2004).
179. C. A. Schneider, W. S. Rasband, K. W. Eliceiri, NIH Image to ImageJ: 25 years of image analysis. *Nat Meth* **9**, 671 (2012).
180. J. Goldstein, N. D.E., J. D.C., L. C.E., E. P., L. E. S. L., J. R. Michael, *Scanning Electron Microscopy and X-ray Microanalysis*. (Springer, ed. 3, 2003).
181. C. B. C. David B. Williams, *Transmission Electron Microscopy*. (Springer New York, 1996).
182. Peter J. Heaney, Edward P. Vicenzi, Lucille A. Gliannuzzi, K. J. T. Livi, Focused ion beam milling: A method of site-specific sample extraction for microanalysis of Earth and planetary materials. *Am. Mineral.* **86**, 1094 (2001).
183. J. M. Williams, T. P. Beebe, Analysis of fractal surfaces using scanning probe microscopy and multiple-image variography. 1. Some general considerations. *J. Phys. Chem.* **97**, 6249 (1993).
184. R. Pecora, Dynamic Light Scattering Measurement of Nanometer Particles in Liquids. *J. Nanopart. Res.* **2**, 123 (2000).
185. S. Brunauer, P. H. Emmett, E. Teller, Adsorption of Gases in Multimolecular Layers. *J. Am. Chem. Soc.* **60**, 309 (1938).

References

186. A. L. Ahmad, N. N. N. Mustafa, Pore surface fractal analysis of palladium-alumina ceramic membrane using Frenkel–Halsey–Hill (FHH) model. *J. Colloid Interface Sci.* **301**, 575 (2006).
187. A. Patel, A. Pratap, Kinetics of crystallization of $Zr_{52}Cu_{18}Ni_{14}Al_{10}Ti_6$ metallic glass. *J. Therm. Anal. Calorim.* **107**, 159 (2012).
188. B. Adnadevic, Z. Mojovic, A. Abu Rabi, J. Jovanovic, Isoconversional Kinetic Analysis of Isothermal Selective Ethanol Adsorption on Zeolite Type NaZSM-5. *Chem. Eng. Technol.* **30**, 1228 (2007).
189. W. L. Bragg, The diffraction of short electromagnetic waves by a crystal. *Math. Proc. Camb. Phil. Soc.* **17**, 43 (1913).
190. G. Jenö, *X-ray line profile analysis in material science* (IGI Global Hershey USA, ed. 1, 2014).
191. H. M. Rietveld, A profile refinement method for nuclear and magnetic structures. *J. Appl. Crystallogr.* **2**, 65 (1969).
192. E. J. Mittemeijer, U. Welzel, The “state of the art” of the diffraction analysis of crystallite size and lattice strain. *Z. Kristallogr.* **223**, 552 (2008).
193. A. Guinier, *X-ray Diffraction in Crystals, Imperfect Crystals, and Amorphous Bodies*. (Dover Publications, San Francisco, ed. 1, 1963).
194. T. Mitsunaga, X-ray thin-film measurement techniques II. Out-of-plane diffraction measurements. *The Rigaku Journal* **25**, 7 (2009).
195. K. Nagao, E. Kagami, X-ray thin film techniques VII. Pole figure measurement. *The Rigaku Journal* **27**, 6 (2011).
196. I. Robinson, R. Harder, Coherent X-ray diffraction imaging of strain at the nanoscale. *Nat. Mater.* **8**, 291 (2009).
197. J. N. Clark, L. Beitra, G. Xiong, A. Higginbotham, D. M. Fritz, H. T. Lemke, D. Zhu, M. Chollet, G. J. Williams, M. Messerschmidt, B. Abbey, R. J. Harder, A. M. Korsunsky, J. S. Wark, I. K. Robinson, Ultrafast Three-Dimensional Imaging of Lattice Dynamics in Individual Gold Nanocrystals. *Science* **341**, 56 (2013).
198. J. N. Clark, X. Huang, R. Harder, I. K. Robinson, High-resolution three-dimensional partially coherent diffraction imaging. *Nat. Commun.* **3**, 993 (2012).
199. J. N. Clark, Johannes Ihli, A. Schenk, Y. Y. Kim, A. N. Kulak, J. Campbell, G. Nisbet, F. C. Meldrum, I. K. Robinson, Three-dimensional imaging of dislocation propagation during crystal growth and dissolution. *Nature (under review)*, (2014).
200. J. R. Fienup, Phase retrieval algorithms: a comparison. *Appl. Opt.* **21**, 2758 (1982).
201. C.-C. Chen, J. Miao, C. W. Wang, T. K. Lee, Application of optimization technique to noncrystalline x-ray diffraction microscopy: Guided hybrid input-output method. *Phys. Rev. B* **76**, 064113 (2007).
202. B. C. McCallum, R. H. T. Bates, Towards a Strategy for Automatic Phase Retrieval from Noisy Fourier Intensities. *J. Mod. Opt.* **36**, 619 (1989).
203. J. Aizenberg, N. Ilan, S. Weiner, L. Addadi, Intracrystalline macromolecules are involved in the morphogenesis of calcitic sponge spicules. *Conn. Tissue Res.* **35**, 17 (1996).
204. B. A. Gotliv, L. Addadi, S. Weiner, Mollusk shell acidic proteins: In search of individual functions. *ChemBiochem* **4**, 522 (2003).

References

205. A. Gal, S. Weiner, L. Addadi, The Stabilizing Effect of Silicate on Biogenic and Synthetic Amorphous Calcium Carbonate. *J. Am. Chem. Soc.* **132**, 13208 (2010).
206. X. R. Xu, A. H. Cai, R. Liu, H. H. Pan, R. K. Tang, K. W. Cho, The roles of water and polyelectrolytes in the phase transformation of amorphous calcium carbonate. *J. Cryst. Growth* **310**, 3779 (2008).
207. B. Guillemet, M. Faatz, F. Grohn, G. Wegner, Y. Gnanou, Nanosized amorphous calcium carbonate stabilized by poly(ethylene oxide)-b-poly(acrylic acid) block copolymers. *Langmuir* **22**, 1875 (2006).
208. B. Cantaert, Y.-Y. Kim, H. Ludwig, F. Nudelman, N. A. J. M. Sommerdijk, F. C. Meldrum, Think Positive: Phase Separation Enables a Positively Charged Additive to Induce Dramatic Changes in Calcium Carbonate Morphology. *Adv. Func. Mater.* **22**, 907 (2012).
209. K. Sawada, The mechanisms of crystallization and transformation of calcium carbonates. *Pure Appl. Chem.* **69**, 921 (1997).
210. J. Jiang, M.-R. Gao, Y.-H. Qiu, S.-H. Yu, Gram-scale, low-cost, rapid synthesis of highly stable Mg-ACC nanoparticles and their long-term preservation. *Nanoscale* **2**, 2358 (2010).
211. E. Beniash, L. Addadi, S. Weiner, Cellular control over spicule formation in sea urchin embryos: A structural approach. *J. Struct. Biol.* **125**, 50 (1999).
212. H. S. Lee, T. H. Ha, K. Kim, Fabrication of unusually stable amorphous calcium carbonate in an ethanol medium. *Mat. Chem. Phys.* **93**, 376 (2005).
213. O. E. Meiron, E. Bar-David, E. D. Aflalo, A. Shechter, D. Stepensky, A. Berman, A. Sagi, Solubility and Bioavailability of Stabilized Amorphous Calcium Carbonate. *J. Bone. Miner. Res.* **26**, 364 (2011).
214. N. V. Vagenas, A. Gatsouli, C. G. Kontoyannis, Quantitative analysis of synthetic calcium carbonate polymorphs using FT-IR spectroscopy. *Talanta* **59**, 831 (2003).
215. M. M. Tlili, M. B. Amor, C. Gabrielli, S. Joiret, G. Maurin, P. Rousseau, Characterization of CaCO₃ hydrates by micro-Raman spectroscopy. *J. Raman Spec.* **33**, 10 (2002).
216. C. C. Tester, M. L. Whittaker, D. Joester, Controlling nucleation in giant liposomes. *Chem. Commun.* **50**, 5619 (2014).
217. Y. W. Wang, Y. Y. Kim, C. J. Stephens, F. C. Meldrum, H. K. Christenson, In Situ Study of the Precipitation and Crystallization of Amorphous Calcium Carbonate (ACC). *Cryst. Growth Des.* **12**, 1212 (2012).
218. C. J. Stephens, Y. Y. Kim, S. D. Evans, F. C. Meldrum, H. K. Christenson, Early Stages of Crystallization of Calcium Carbonate Revealed in Picoliter Droplets. *J. Am. Chem. Soc.* **133**, 5210 (2011).
219. J. R. I. Lee, T. Y. J. Han, T. M. Willey, D. Wang, R. W. Meulenberg, J. Nilsson, P. M. Dove, L. J. Terminello, T. van Buuren, J. J. De Yoreo, Structural development of mercaptophenol self-assembled monolayers and the overlying mineral phase during templated CaCO₃ crystallization from a transient amorphous film. *J. Am. Chem. Soc.* **129**, 10370 (2007).
220. D. Pontoni, J. Bolze, N. Dingenouts, T. Narayanan, M. Ballauff, Crystallization of calcium carbonate observed in-situ by combined

References

- small- and wide-angle X-ray scattering. *J. Phys. Chem. B* **107**, 5123 (2003).
221. J. W. Morse, R. S. Arvidson, A. Lutge, Calcium carbonate formation and dissolution. *Chem. Revs.* **107**, 342 (2007).
222. M. Avrami, Kinetics of Phase Change. II Transformation-Time Relations for Random Distribution of Nuclei. *J. Chem. Phys.* **8**, 212 (1940).
223. M. M. Reddy, G. H. Nancollas, Crystalization of Calcium-Carbonate 4. Effect of Magnesium, Strontium and Sulfate-Ions. *J. Cryst. Growth.* **35**, 33 (1976).
224. H. J. Meyer, The Influence of Impurities on the Growth Rate of Calcite. *J. Cryst. Growth* **66**, 639 (1984).
225. L. J. Plant, W. A. House, Precipitation of calcite in the presence of inorganic phosphate. *Coll. Surf. A* **203**, 143 (2002).
226. C. A. Orme, A. Noy, A. Wierzbicki, M. T. McBride, M. Grantham, H. H. Teng, P. M. Dove, J. J. DeYoreo, Formation of chiral morphologies through selective binding of amino acids to calcite surface steps. *Nature* **411**, 775 (2001).
227. S. Elhadj, E. A. Salter, A. Wierzbicki, J. J. De Yoreo, N. Han, P. M. Dove, Peptide controls on calcite mineralization: Polyaspartate chain length affects growth kinetics and acts as a stereochemical switch on morphology. *Cryst. Growth Des.* **6**, 197 (2006).
228. A. I. Vavouraki, C. V. Putnis, A. Putnis, P. G. Koutsoukos, An Atomic Force Microscopy study of the growth of calcite in the presence of sodium sulfate. *Chem. Geol.* **253**, 243 (2008).
229. J. Kontrec, D. Kralj, L. Brecevic, G. Falini, S. Fermani, V. Noethig-Laslo, K. Mirosavljevic, Incorporation of inorganic anions in calcite. *Eur. J. Inorg. Chem.*, 4579 (2004).
230. J. J. De Yoreo, A. Wierzbicki, P. M. Dove, New insights into mechanisms of biomolecular control on growth of inorganic crystals. *Crystengcomm* **9**, 1144 (2007).
231. C. Bhugra, M. J. Pikal, Role of thermodynamic, molecular, and kinetic factors in crystallization from the amorphous state. *J. Pharm. Sci.* **97**, 1329 (2008).
232. B. Hasse, H. Ehrenberg, J. C. Marxen, W. Becker, M. Epple, Calcium Carbonate Modifications in the Mineralized Shell of the Freshwater Snail *Biomphalaria glabrata*. *Chem. Eur. J.* **6**, 3679 (2000).
233. J. E. Kreuz, A. Shukhaev, W. Du, S. Druskin, O. Daugulis, R. F. Ismagilov, Evolution of Catalysts Directed by Genetic Algorithms in a Plug-Based Microfluidic Device Tested with Oxidation of Methane by Oxygen. *J. Am. Chem. Soc.* **132**, 3128 (2010).
234. H. Koinuma, I. Takeuchi, Combinatorial solid-state chemistry of inorganic materials. *Nat. Mater.* **3**, 429 (2004).
235. J. Mahamid, A. Sharir, L. Addadi, S. Weiner, Amorphous calcium phosphate is a major component of the forming fin bones of zebrafish: Indications for an amorphous precursor phase. *Proc. Natl. Acad. Sci. U.S.A.* **105**, 12748 (2008).
236. E. Beniash, R. A. Metzler, R. S. K. Lam, P. U. P. A. Gilbert, Transient amorphous calcium phosphate in forming enamel. *J. Struct. Biol.* **166**, 133 (2009).

References

237. K. Lee, W. Wagermaier, A. Masic, K. P. Kommareddy, M. Bennet, I. Manjubala, S.-W. Lee, S. B. Park, H. Cölfen, P. Fratzl, Self-assembly of amorphous calcium carbonate microlens arrays. *Nat. Commun.* **3**, 725 (2012).
238. C. Li, L. M. Qi, Bioinspired fabrication of 3D ordered macroporous single crystals of calcite from a transient amorphous phase. *Angew. Chem. Int. Ed.* **47**, 2388 (2008).
239. A. S. Finemore, M. R. J. Scherer, R. Langford, S. Mahajan, S. Ludwigs, F. C. Meldrum, U. Steiner, Nanostructured Calcite Single Crystals with Gyroid Morphologies. *Adv. Mater.* **21**, 3928 (2009).
240. M. J. Olszta, S. Gajjeraman, M. Kaufman, L. B. Gower, Nanofibrous calcite synthesized via a solution-precursor-solid mechanism. *Chem. Mater.* **16**, 2355 (2004).
241. D. Gebauer, V. Oliynyk, M. Salajkova, J. Sort, Q. Zhou, L. Bergstrom, G. Salazar-Alvarez, A transparent hybrid of nanocrystalline cellulose and amorphous calcium carbonate nanoparticles. *Nanoscale* **3**, 3563 (2011).
242. X. Xu, J. T. Han, D. H. Kim, K. Cho, Two Modes of Transformation of Amorphous Calcium Carbonate Films in Air. *J. Phys. Chem. B* **110**, 2764 (2006).
243. J. Liu, S. Pancera, V. Boyko, A. Shukla, T. Narayanan, K. Huber, Evaluation of the Particle Growth of Amorphous Calcium Carbonate in Water by Means of the Porod Invariant from SAXS. *Langmuir* **26**, 17405 (2010).
244. A. Gal, W. Habraken, D. Gur, P. Fratzl, S. Weiner, L. Addadi, Calcite Crystal Growth by a Solid-State Transformation of Stabilized Amorphous Calcium Carbonate Nanospheres in a Hydrogel. *Angew. Chem. Int. Ed.* **52**, 4867 (2013).
245. W. Pohle, D. R. Gauger, H. Fritzsche, B. Rattay, C. Selle, H. Binder, H. Böhlig, FTIR-spectroscopic characterization of phosphocholine-headgroup model compounds. *J. Mol. Struct.* **563–564**, 463 (2001).
246. C. Huang, J. T. Mason, Geometric packing constraints in egg phosphatidylcholine vesicles. *Proc. Natl. Acad. Sci. U.S.A.* **75**, 308 (1978).
247. A. Khawam, D. R. Flanagan, Solid-State Kinetic Models: Basics and Mathematical Fundamentals. *J. Phys. Chem. B* **110**, 17315 (2006).
248. A. K. Galwey, M. E. Brown, Arrhenius parameters and compensation behaviour in solid-state decompositions. *Thermochim Acta* **300**, 107 (1997).
249. N. Koga, A review of the mutual dependence of Arrhenius parameters evaluated by the thermoanalytical study of solid-state reactions: The kinetic compensation effect. *Thermochim Acta* **244**, 1 (1994).
250. H. Nebel, M. Neumann, C. Mayer, M. Epple, On the Structure of Amorphous Calcium Carbonate A Detailed Study by Solid-State NMR Spectroscopy. *Inorg. Chem.* **47**, 7874 (2008).
251. A. J. Vega, Heteronuclear chemical-shift correlations of silanol groups studied by two-dimensional cross-polarization magic angle spinning NMR. *J. Am. Chem. Soc.* **110**, 1049 (1988).
252. N. H. de Leeuw, S. C. Parker, Surface Structure and Morphology of Calcium Carbonate Polymorphs Calcite, Aragonite, and Vaterite: An Atomistic Approach. *J. Phys. Chem. B* **102**, 2914 (1998).

References

253. H. Zhu, D. J. W. Grant, Dehydration behavior of nedocromil magnesium pentahydrate. *Int. J. Pharm.* **215**, 251 (2001).
254. A. K. Galwey, Structure and Order in Thermal Dehydrations of Crystalline Solids. *Thermochim. Acta* **355**, 181 (2000).
255. C. E. Killian, R. A. Metzler, Y. U. T. Gong, I. C. Olson, J. Aizenberg, Y. Politi, F. H. Wilt, A. Scholl, A. Young, A. Doran, M. Kunz, N. Tamura, S. N. Coppersmith, P. U. P. A. Gilbert, Mechanism of Calcite Co-Orientation in the Sea Urchin Tooth. *J. Am. Chem. Soc.* **131**, 18404 (2009).
256. P. Bots, L. G. Benning, J. D. Rodriguez-Blanco, T. Roncal-Herrero, S. Shaw, Mechanistic Insights into the Crystallization of Amorphous Calcium Carbonate (ACC). *Cryst. Growth Des.* **12**, 3806 (2012).
257. Y. Cudennec, A. Lecerf, The transformation of ferrihydrite into goethite or hematite, revisited. *J. Solid State Chem.* **179**, 716 (2006).
258. K. Yanagisawa, J. Ovenstone, Crystallization of Anatase from Amorphous Titania Using the Hydrothermal Technique: Effects of Starting Material and Temperature. *J. Phys. Chem. B* **103**, 7781 (1999).
259. E. Beniash, Biominerals—hierarchical nanocomposites: the example of bone. *WIREs Nanomed Nanobiotechnol* **3**, 47 (2011).
260. Y. Politi, T. Arad, E. Klein, S. Weiner, L. Addadi, Sea urchin spine calcite forms via a transient amorphous calcium carbonate phase. *Science* **306**, 1161 (2004).
261. J. Gomez-Morales, A. Hernandez-Hernandez, G. Sazaki, J. M. Garcia-Ruiz, Nucleation and Polymorphism of Calcium Carbonate by a Vapor Diffusion Sitting Drop Crystallization Technique. *Cryst. Growth Des.* **10**, 963 (2010).
262. E. L. Himri, M. E. L. Himri, A. Núñez Freeze dried precursor-based synthesis of molybdenum bimetallic nitride. *J. Mater. Environ. Sci.* **2** 6(2011).
263. D. Vie, E. Martínez, F. Sapiña, J.-V. Folgado, A. Beltrán, R. X. Valenzuela, V. Cortés-Corberán, Freeze-Dried Precursor-Based Synthesis of Nanostructured Cobalt–Nickel Molybdates $\text{Co}_{1-x}\text{Ni}_x\text{MoO}_4$. *Chem. Mater.* **16**, 1697 (2004).
264. E. H. Noel, Y.-Y. Kim, J. M. Charnock, F. C. Meldrum, Solid state crystallization of amorphous calcium carbonate nanoparticles leads to polymorph selectivity. *CrystEngComm* **15**, 697 (2013).
265. A. S. Posner, F. Betts, Synthetic amorphous calcium phosphate and its relation to bone mineral structure. *Acc. Chem. Res.* **8**, 273 (1975).
266. T. Tsuji, K. Onuma, A. Yamamoto, M. Iijima, K. Shiba, Direct transformation from amorphous to crystalline calcium phosphate facilitated by motif-programmed artificial proteins. *Proc. Natl. Acad. Sci. U.S.A.* **105**, 16866 (2008).
267. S. Gadaleta, E. Paschalis, F. Betts, R. Mendelsohn, A. Boskey, Fourier transform infrared spectroscopy of the solution-mediated conversion of amorphous calcium phosphate to hydroxyapatite: New correlations between X-ray diffraction and infrared data. *Calcif. Tissue Int.* **58**, 9 (1996).
268. L. Sun, L. C. Chow, S. A. Frukhtbeyn, J. E. Bonevich, Preparation and Properties of Nanoparticles of Calcium Phosphates With Various Ca/P Ratios. *J. Res. Natl. Inst. Stand. Technol.* **115**, 243 (2010).

References

269. J. H. Kim, J. H. Lee, T. Y. Yang, S. Y. Yoon, B. K. Kim, H. C. Park, TBA-based freeze/gel casting of porous hydroxyapatite scaffolds. *Ceram. Int.* **37**, 2317 (2011).
270. S. Deville, E. Saiz, A. P. Tomsia, Freeze casting of hydroxyapatite scaffolds for bone tissue engineering. *Biomaterials* **27**, 5480 (2006).
271. H.-D. Yu, Z.-Y. Zhang, K. Y. Win, J. Chan, S. H. Teoh, M.-Y. Han, Bioinspired fabrication of 3D hierarchical porous nanomicrostructures of calcium carbonate for bone regeneration. *Chem. Commun.* **46**, 6578 (2010).
272. Y.-Y. Kim, L. Ribeiro, F. Maillot, O. Ward, S. J. Eichhorn, F. C. Meldrum, Bio-Inspired Synthesis and Mechanical Properties of Calcite–Polymer Particle Composites. *Adv. Mater.* **22**, 2082 (2010).
273. U. Lins, C. F. Barros, M. da Cunha, F. C. Miguens, Structure, morphology, and composition of silicon biocomposites in the palm tree *Syagrus coronata* (Mart.) Becc. *Protoplasma* **220**, 0089 (2002).
274. I. M. Weiss, N. Tuross, L. Addadi, S. Weiner, Mollusc larval shell formation: amorphous calcium carbonate is a precursor phase for aragonite. *J. Exp. Zool.* **293**, 478 (2002).
275. A. Gal, V. Brumfeld, S. Weiner, L. Addadi, D. Oron, Certain Biominerals in Leaves Function as Light Scatterers. *Adv. Mater.* **24**, OP77 (2012).
276. M. A. Webb, Cell-Mediated Crystallization of Calcium Oxalate in Plants. *Plant Cell* **11**, 751 (1999).
277. H. C. Anderson, Molecular Biology of Matrix Vesicles. *Clin. Orthop. Relat. Res.* **314**, 266 (1995).
278. E. Zindler-Frank, R. Hönow, A. Hesse, Calcium and oxalate content of the leaves of *Phaseolus vulgaris* at different calcium supply in relation to calcium oxalate crystal formation. *Plant Physiol.* **158**, 139 (2001).
279. C. L. Brubaker, H. T. Horner, Development of epidermal crystals in leaflets of *Stylosanthes guianensis* (Leguminosae; Papilionoideae). *Botany* **67**, 1664 (1989).
280. M. Hajir, R. Graf, W. Tremel, Stable amorphous calcium oxalate: Synthesis and potential intermediate in biomineralization. *Chem. Commun.*, (2014).
281. J. Garside, L. Brečević, J. W. Mullin, The effect of temperature on the precipitation of calcium oxalate. *J. Cryst. Growth.* **57**, 233 (1982).
282. K. S. R., Interactions between Stone-Forming Calcific Crystals and Macromolecules. *Urol. Int.* **59**, 59 (1997).
283. J. G. Kleinman, L. J. Alatalo, A. M. Beshensky, J. A. Wesson, Acidic polyanion poly(acrylic acid) prevents calcium oxalate crystal deposition. *Kidney Int.* **74**, 919 (2008).
284. B. Cantaert, E. Beniash, F. C. Meldrum, Nanoscale Confinement Controls the Crystallization of Calcium Phosphate: Relevance to Bone Formation. *Chem. Eur. J.* **19**, 14918 (2013).
285. W. O. S. Doherty, C. M. Fellows, S. Gorjian, E. Senogles, W. H. Cheung, Inhibition of calcium oxalate monohydrate by poly(acrylic acid)s with different end groups. *J. Appl. Polym. Sci.* **91**, 2035 (2004).
286. S. Farmanesh, S. Ramamoorthy, J. Chung, J. R. Asplin, P. Karande, J. D. Rimer, Specificity of Growth Inhibitors and their Cooperative

References

- Effects in Calcium Oxalate Monohydrate Crystallization. *J. Am. Chem. Soc.* **136**, 367 (2013).
287. D. Crawford, Electron microscopy of urinary calculi — Some facts and artefacts. *Urological Research* **12**, 17 (1984).
288. K. J. Kociba, P. K. Gallagher, A study of calcium oxalate monohydrate using dynamic differential scanning calorimetry and other thermoanalytical techniques. *Thermochim. Acta* **283**, 277 (1996).
289. H. T. Horner, Jr., B. L. Wagner, The Association of Druse Crystals with the Developing Stomium of *Capsicum annuum* (Solanaceae) Anthers. *Am. J. Bot.* **67**, 1347 (1980).
290. R. Q. Song, H. Colfen, Additive controlled crystallization. *Crystengcomm* **13**, 1249 (2011).
291. S. H. Yu, H. Colfen, K. Tauer, M. Antonietti, Tectonic arrangement of BaCO₃ nanocrystals into helices induced by a racemic block copolymer. *Nat. Mater.* **4**, 51 (2005).
292. Y. Y. Kim, A. N. Kulak, Y. T. Li, T. Batten, M. Kuball, S. P. Armes, F. C. Meldrum, Substrate-directed formation of calcium carbonate fibres. *J. Mater. Chem.* **19**, 387 (2009).
293. C. Viravaidya, M. Li, S. Mann, Microemulsion-based synthesis of stacked calcium carbonate (calcite) superstructures. *Chem. Commun.*, 2182 (2004).
294. R. Q. Song, H. Colfen, Mesocrystals-Ordered Nanoparticle Superstructures. *Adv. Mater.* **22**, 1301 (2010).
295. Q. Zhang, S. J. Liu, S. H. Yu, Recent advances in oriented attachment growth and synthesis of functional materials: concept, evidence, mechanism, and future. *J. Mater. Chem.* **19**, 191 (2009).
296. V. M. Yuwono, N. D. Burrows, J. A. Soltis, R. L. Penn, Oriented Aggregation: Formation and Transformation of Mesocrystal Intermediates Revealed. *J. Am. Chem. Soc.* **132**, 2163 (2010).
297. P. J. Murphy, A. M. Posner, J. P. Quirk, Characterization of hydrolyzed ferric ion solutions a comparison of the effects of various anions on the solutions. *J. Colloid Interface Sci.* **56**, 312 (1976).
298. R. L. Penn, J. F. Banfield, Imperfect oriented attachment: Dislocation generation in defect-free nanocrystals. *Science* **281**, 969 (1998).
299. A. E. S. Van Driessche, L. G. Benning, J. D. Rodriguez-Blanco, M. Ossorio, P. Bots, J. M. Garcia-Ruiz, The Role and Implications of Bassanite as a Stable Precursor Phase to Gypsum Precipitation. *Science* **336**, 69 (2012).
300. Y. Oaki, A. Kotachi, T. Miura, H. Imai, Bridged Nanocrystals in Biominerals and Their Biomimetics: Classical Yet Modern Crystal Growth on the Nanoscale. *Adv. Funct. Mater.* **16**, 1633 (2006).
301. J. Aizenberg, S. Albeck, S. Weiner, L. Addadi, Crystal-protein interactions studied by overgrowth of calcite on biogenic skeletal elements. *J. Cryst. Growth.* **142**, 156 (1994).
302. S. Albeck, S. Weiner, L. Addadi, Polysaccharides of Intracrystalline Glycoproteins Modulate Calcite Crystal Growth In Vitro. *Chem. Eur. J.* **2**, 278 (1996).
303. R. Q. Song, H. Colfen, A. W. Xu, J. Hartmann, M. Antonietti, Polyelectrolyte-Directed Nanoparticle Aggregation: Systematic Morphogenesis of Calcium Carbonate by Nonclassical Crystallization. *Acs Nano* **3**, 1966 (2009).

References

304. A. N. Kulak, P. Iddon, Y. T. Li, S. P. Armes, H. Colfen, O. Paris, R. M. Wilson, F. C. Meldrum, Continuous structural evolution of calcium carbonate particles: A unifying model of copolymer-mediated crystallization. *J. Am. Chem. Soc.* **129**, 3729 (2007).
305. T. X. Wang, H. Colfen, M. Antonietti, Nonclassical crystallization: Mesocrystals and morphology change of CaCO₃ crystals in the presence of a polyelectrolyte additive. *J. Am. Chem. Soc.* **127**, 3246 (2005).
306. H. V. Tran, L. D. Tran, H. D. Vu, H. Thai, Facile surface modification of nanoprecipitated calcium carbonate by adsorption of sodium stearate in aqueous solution. *Colloids Surf., A* **366**, 95 (2010).
307. P. Bots, L. G. Benning, J.-D. Rodriguez-Blanco, T. Roncal-Herrero, S. Shaw, Mechanistic Insights into the Crystallization of Amorphous Calcium Carbonate (ACC). *Cryst. Growth Des.* **12**, 9 (2012).
308. C. W. Davies. Ion Association (Butterworths, London, 1962), pp. 14.
309. U. Wehrmeister, A. L. Soldati, D. E. Jacob, T. Häger, W. Hofmeister, Raman spectroscopy of synthetic, geological and biological vaterite: a Raman spectroscopic study. *J. Raman Spectrosc.* **41**, 193 (2010).
310. A. Fick, Ueber Diffusion. *Annalen der Physik* **170**, 59 (1855).
311. B. Aziz, D. Gebauer, N. Hedin, Kinetic control of particle-mediated calcium carbonate crystallization. *CrystEngComm* **13**, 4641 (2011).
312. C. S. Hanes, Studies on plant amylases: The effect of starch concentration upon the velocity of hydrolysis by the amylase of germinated barley. *Biochem. J.* **26**, 1406 (1932).
313. R. P. Sear, The non-classical nucleation of crystals: microscopic mechanisms and applications to molecular crystals, ice and calcium carbonate. *Int. Mater. Rev.* **57**, 328 (2012).
314. H. Cölfen, M. Antonietti, Mesocrystals and Nonclassical Crystallization. *Wiley*, (2008).
315. H. Colfen, M. Antonietti, Mesocrystals: Inorganic superstructures made by highly parallel crystallization and controlled alignment. *Angew. Chem. Int. Ed.* **44**, 5576 (2005).
316. S. F. Chen, S. H. Yu, T. X. Wang, J. Jiang, H. Colfen, B. Hu, B. Yu, Polymer-directed formation of unusual CaCO₃ pancakes with controlled surface structures. *Adv. Mater.* **17**, 1461 (2005).
317. T. Miura, A. Kotachi, Y. Oaki, H. Imai, Emergence of acute morphologies consisting of iso-oriented calcite nanobricks in a binary poly(acrylic acid) system. *Cryst. Growth Des.* **6**, 612 (2006).
318. A. W. Xu, M. Antonietti, H. Colfen, Y. P. Fang, Uniform hexagonal plates of vaterite CaCO₃ mesocrystals formed by biomimetic mineralization. *Adv. Func. Mater.* **16**, 903 (2006).
319. T. P. Wang, M. Antonietti, H. Colfen, Calcite mesocrystals: "Morphing" crystals by a polyelectrolyte. *Chem. Eur. J.* **12**, 5722 (2006).
320. A. W. Xu, M. Antonietti, S. H. Yu, H. Colfen, Polymer-mediated mineralization and self-similar mesoscale-organized calcium carbonate with unusual superstructures. *Adv. Mater.* **20**, 1333 (2008).
321. J. J. M. Lenders, A. Dey, P. H. H. Bomans, J. Spielmann, M. Hendrix, G. de With, F. C. Meldrum, S. Harder, N. Sommerdijk, High-Magnesian Calcite Mesocrystals: A Coordination Chemistry Approach. *J. Am. Chem. Soc.* **134**, 1367 (2012).

References

322. Y. Oaki, R. Adachi, H. Imai, Self-organization of hollow-cone carbonate crystals through molecular control with an acid organic polymer. *Polym. J.* **44**, 612 (2012).
323. A. S. Schenk, Y. Y. Kim, A. N. Kulak, F. C. Meldrum, Impurities in pluronic triblock copolymers can induce the formation of calcite mesocrystals. *Chem. Geol.* **294**, 259 (2012).
324. C. You, Q. Zhang, Q. Z. Jiao, Z. D. Fu, Supernet Structures of Calcium Carbonate Mesocrystals Formed in a Blend System of Anionic/Nonionic Surfactants. *Cryst. Growth Des.* **9**, 4720 (2009).
325. G. T. Zhou, Q. Z. Yao, J. Ni, G. Jin, Formation of aragonite mesocrystals and implication for biomineralization. *Am. Mineral.* **94**, 293 (2009).
326. M. Kijima, Y. Oaki, Y. Munekawa, H. Imai, Synthesis and Morphogenesis of Organic and Inorganic Polymers by Means of Biominerals and Biomimetic Materials. *Chem. Eur. J.* **19**, 2284 (2013).
327. Y.-Y. Kim, A. S. Schenk, J. Ihli, A. N. Kulak, N. B. J. Hetherington, C. C. Tang, W. W. Schmahl, E. Griesshaber, G. Hyett, F. C. Meldrum, A critical analysis of calcium carbonate mesocrystals. *Nat. Commun.* **5**, (2014).
328. M. G. Page, H. Cölfen, Improved Control of CaCO₃ Precipitation by Direct Carbon Dioxide Diffusion: Application in Mesocrystal Assembly. *Cryst. Growth Des.* **6**, 1915 (2006).
329. A. Becker, W. Becker, J. C. Marxen, M. Epple, In-vitro Crystallization of Calcium Carbonate in the Presence of Biological Additives — Comparison of the Ammonium Carbonate Method with Double-Diffusion Techniques. *Z. Anorg. Allg. Chem.* **629**, 2305 (2003).
330. J. Bolze, B. Peng, N. Dingenouts, P. Panine, T. Narayanan, M. Ballauff, Formation and growth of amorphous colloidal CaCO₃ precursor particles as detected by time-resolved SAXS. *Langmuir* **18**, 8364 (2002).
331. E. M. Pouget, P. H. H. Bomans, A. Dey, P. M. Frederik, G. de With, N. A. J. M. Sommerdijk, The Development of Morphology and Structure in Hexagonal Vaterite. *J. Am. Chem. Soc.* **132**, 11560 (2010).
332. R. Q. Song, A. W. Xu, M. Antonietti, H. Colfen, Calcite Crystals with Platonic Shapes and Minimal Surfaces. *Angew. Chem. Int. Ed.* **48**, 395 (2009).
333. B. Cantaert, University of Leeds (2013).
334. M. A. Pfeifer, G. J. Williams, I. A. Vartanyants, R. Harder, I. K. Robinson, Three-dimensional mapping of a deformation field inside a nanocrystal. *Nature* **442**, 63 (2006).
335. W. Yang, X. Huang, R. Harder, J. N. Clark, I. K. Robinson, H.-k. Mao, Coherent diffraction imaging of nanoscale strain evolution in a single crystal under high pressure. *Nat. Commun.* **4**, 1680 (2013).
336. J.-J. Fernandez, Computational methods for materials characterization by electron tomography. *Curr. Opin. Solid State Mater. Sci.* **17**, 93 (2013).
337. R. Harder, I. K. Robinson, Coherent X-Ray Diffraction Imaging of Morphology and Strain in Nanomaterials. *JOM* **65**, 1202 (2013).
338. I. Robinson, Nanoparticle Structure by Coherent X-ray Diffraction. *J. Phys. Soc. Jpn.* **82**, 021012 (2012).

References

339. M. J. Hytch, J.-L. Putaux, J.-M. Penisson, Measurement of the displacement field of dislocations to 0.03 Å by electron microscopy. *Nature* **423**, 270 (2003).
340. X. Shi, University College London (2012).
341. P. Ramachandran, G. Varoquaux, Mayavi: 3D Visualization of Scientific Data. *Computing in Science & Engineering* **13**, 40 (2011).
342. S. W.J., M. K., L. W.E., *The Visualization Toolkit: An Object-Oriented Approach to 3D Graphics*. (Kitware, Inc., ed. 3, 2003).
343. A. M. Stoneham, *Theory of Defects in Solids* (Clarendon, Oxford, 1985).
344. C. V. Burton, A theory concerning the constitution of mater *Phil. Mag.* **33**, 191 (1892).
345. A. C. Lasaga, A. Lutge, Variation of Crystal Dissolution Rate Based on a Dissolution Stepwave Model. *Science* **291**, 2400 (2001).
346. J. J. De Yoreo, P. G. Vekilov, Principles of Crystal Nucleation and Growth. *Rev. Mineral. Geochem.* **54**, 57 (2003).
347. E. Ma, T. D. Shen, X. L. Wu, Nanostructured metals: Less is more. *Nat. Mater.* **5**, 515 (2006).
348. I. Sugiyama, N. Shibata, Z. Wang, S. Kobayashi, T. Yamamoto, Y. Ikuhara, Ferromagnetic dislocations in antiferromagnetic NiO. *Nat Nano* **8**, 266 (2013).
349. M.-W. Chu, I. Szafraniak, R. Scholz, C. Harnagea, D. Hesse, M. Alexe, U. Gosele, Impact of misfit dislocations on the polarization instability of epitaxial nanostructured ferroelectric perovskites. *Nat. Mater.* **3**, 87 (2004).
350. Y. Ikuhara, Nanowire design by dislocation technology. *Progress in Materials Science* **54**, 770 (2009).
351. Z. Wang, M. Saito, K. P. McKenna, Y. Ikuhara, Polymorphism of dislocation core structures at the atomic scale. *Nat. Commun.* **5**, (2014).
352. P. Hirsch, D. Cockayne, J. Spence, M. Whelan, 50 Years of TEM of dislocations: Past, present and future. *Philos. Mag.* **86**, 4519 (2006).
353. D. A. Muller, Structure and bonding at the atomic scale by scanning transmission electron microscopy. *Nat. Mater.* **8**, 263 (2009).
354. J. S. Barnard, J. Sharp, J. R. Tong, P. A. Midgley, High-Resolution Three-Dimensional Imaging of Dislocations. *Science* **313**, 319 (2006).
355. C.-C. Chen, C. Zhu, E. R. White, C.-Y. Chiu, M. C. Scott, B. C. Regan, L. D. Marks, Y. Huang, J. Miao, Three-dimensional imaging of dislocations in a nanoparticle at atomic resolution. *Nature* **496**, 74 (2013).
356. J. M. Zuo, I. Vartanyants, M. Gao, R. Zhang, L. A. Nagahara, Atomic Resolution Imaging of a Carbon Nanotube from Diffraction Intensities. *Science* **300**, 1419 (2003).
357. J. D. Weeks, G. H. Gilmer, in *Advances in Chemical Physics*. (John Wiley & Sons, Inc., 2007), pp. 157-228.
358. F. C. Frank, The influence of dislocations on crystal growth. *Farad. Discuss.* **5**, 48 (1949).
359. S. L. Brantley, in *Kinetics of Water-Rock Interaction*, S. L. Brantley, J. D. Kubicki, A. F. White, Eds. (Springer New York, 2008), pp. 151-210.

References

360. W. Cha, N. C. Jeong, S. Song, H.-j. Park, T. C. Thanh Pham, R. Harder, B. Lim, G. Xiong, D. Ahn, I. McNulty, J. Kim, K. B. Yoon, I. K. Robinson, H. Kim, Core-shell strain structure of zeolite microcrystals. *Nat. Mater.* **12**, 729 (2013).
361. M. H. Nielsen, J. R. I. Lee, in *Methods in Enzymology*, J. D. Y. James, Ed. (Academic Press, 2013), vol. Volume 532, pp. 209-224.
362. J. Paquette, R. J. Reeder, Relationship between surface structure, growth mechanism, and trace element incorporation in calcite. *Geochim. Cosmochim. Acta* **59**, 735 (1995).
363. R. C. Snyder, M. F. Doherty, Faceted crystal shape evolution during dissolution or growth. *AIChE Journal* **53**, 1337 (2007).
364. I. N. MacInnis, S. L. Brantley, The role of dislocations and surface morphology in calcite dissolution. *Geochim. Cosmochim. Acta* **56**, 1113 (1992).
365. I. N. MacInnis, S. L. Brantley, Development of etch pit size distributions on dissolving minerals. *Chem. Geol.* **105**, 31 (1993).
366. J. Schott, S. Brantley, D. Crerar, C. Guy, M. Borcsik, C. Willaime, Dissolution kinetics of strained calcite. *Geochim. Cosmochim. Acta* **53**, 373 (1989).
367. C. Woodward, D. R. Trinkle, L. G. Hector, D. L. Olmsted, Prediction of Dislocation Cores in Aluminum from Density Functional Theory. *Phys. Rev. Lett.* **100**, 045507 (2008).
368. J. P. Hirth, J. Lothe, *Theory of Dislocations*. (McGraw-Hill, New York, 1968).
369. G. P. Purja Pun, Y. Mishin, A molecular dynamics study of self-diffusion in the cores of screw and edge dislocations in aluminum. *Acta Mater.* **57**, 5531 (2009).
370. F. Hofmann, B. Abbey, W. Liu, R. Xu, B. F. Usher, E. Balaur, Y. Liu, X-ray micro-beam characterization of lattice rotations and distortions due to an individual dislocation. *Nat. Commun.* **4**, (2013).
371. P. Schall, I. Cohen, D. A. Weitz, F. Spaepen, Visualization of Dislocation Dynamics in Colloidal Crystals. *Science* **305**, 1944 (2004).
372. F. Nudelman, B. A. Gotliv, L. Addadi, S. Weiner, Mollusk shell formation: Mapping the distribution of organic matrix components underlying a single aragonitic tablet in nacre. *J. Struct. Biol.* **153**, 176 (2006).
373. L. Addadi, D. Joester, F. Nudelman, S. Weiner, Mollusk shell formation: A source of new concepts for understanding biomineralization processes. *Chem. Eur. J.* **12**, 981 (2006).
374. A. Ulman, *An Introduction to Ultrathin Organic Films*. (Academic Press, Boston, ed. 1, 1991).
375. E. DiMasi, S.-Y. Kwak, F. F. Amos, M. J. Olszta, D. Lush, L. B. Gower, Complementary Control by Additives of the Kinetics of Amorphous CaCO₃ Mineralization at an Organic Interface: In-Situ Synchrotron X-Ray Observations. *Phys. Rev. Lett.* **97**, 045503 (2006).
376. J. Aizenberg, A. J. Black, G. M. Whitesides, Control of crystal nucleation by patterned self-assembled monolayers. *Nature* **398**, 495 (1999).
377. A. M. Travaille, L. Kaptijn, P. Verwer, B. Hulsken, J. A. A. W. Elemans, R. J. M. Nolte, H. van Kempen, Highly Oriented Self-

References

- Assembled Monolayers as Templates for Epitaxial Calcite Growth. *J. Am. Chem. Soc.* **125**, 11571 (2003).
378. R. Darkins, A. S. Côté, C. L. Freeman, D. M. Duffy, Crystallisation rates of calcite from an amorphous precursor in confinement. *J. Cryst. Growth.* **367**, 110 (2013).
379. P. Calvert, P. Rieke, Biomimetic Mineralization in and on Polymers. *Chem. Mater.* **8**, 1715 (1996).
380. D. J. Ahn, A. Berman, D. Charych, Probing the Dynamics of Template-Directed Calcite Crystallization with in Situ FTIR. *J. Phys. Chem.* **100**, 12455 (1996).
381. J. R. I. Lee, T. Y.-J. Han, T. M. Willey, M. H. Nielsen, L. M. Klivansky, Y. Liu, S. Chung, L. J. Terminello, T. van Buuren, J. J. De Yoreo, Cooperative Reorganization of Mineral and Template during Directed Nucleation of Calcium Carbonate. *J. Phys. Chem. C* **117**, 11076 (2013).
382. D. Quigley, P. M. Rodger, C. L. Freeman, J. H. Harding, D. M. Duffy, Metadynamics simulations of calcite crystallization on self-assembled monolayers. *J. Chem. Phys.* **131**, (2009).
383. D. Volkmer, M. Fricke, D. Vollhardt, S. Siegel, Crystallization of (012) oriented calcite single crystals underneath monolayers of tetra(carboxymethoxy)calix[4]arenes. *Dalton Trans.*, (2002).
384. C. L. Freeman, J. H. Harding, D. M. Duffy, Simulations of Calcite Crystallization on Self-Assembled Monolayers. *Langmuir* **24**, 9607 (2008).
385. B. Pokroy, J. Aizenberg, Calcite shape modulation through the lattice mismatch between the self-assembled monolayer template and the nucleated crystal face. *CrystEngComm* **9**, 1219 (2007).
386. S. N. Coppersmith, P. U. P. A. Gilbert, R. A. Metzler, Theoretical characterization of a model of aragonite crystal orientation in red abalone nacre. *J. Phys. A* **42**, 125101 (2009).
387. C. Vericat, M. E. Vela, G. Benitez, P. Carro, R. C. Salvarezza, Self-assembled monolayers of thiols and dithiols on gold: new challenges for a well-known system. *Chem. Soc. Rev.* **39**, 1805 (2010).
388. S. Borukhin, B. Pokroy, Formation and Elimination of Surface Nanodefects on Ultraflat Metal Surfaces Produced by Template Stripping. *Langmuir* **27**, 13415 (2011).
389. Y.-Y. Kim, K. Ganesan, P. Yang, A. N. Kulak, S. Borukhin, S. Pechook, L. Ribeiro, R. Kröger, S. J. Eichhorn, S. P. Armes, B. Pokroy, F. C. Meldrum, An artificial biomineral formed by incorporation of copolymer micelles in calcite crystals. *Nat. Mater.* **10**, 890 (2011).
390. M. Watari, R. A. McKendry, M. Vögtli, G. Aeppli, Y.-A. Soh, X. Shi, G. Xiong, X. Huang, R. Harder, I. K. Robinson, Differential stress induced by thiol adsorption on faceted nanocrystals. *Nat. Mater.* **10**, 862 (2011).
391. A. G. Cullis, A. J. Pidduck, M. T. Emeny, Misfit Dislocation Sources at Surface Ripple Troughs in Continuous Heteroepitaxial Layers. *Phys. Rev. Lett.* **75**, 2368 (1995).
392. H. Gao, Some general properties of stress-driven surface evolution in a heteroepitaxial thin film structure. *J. Mech. of Physics of Solids* **42**, 741 (1994).

References

393. F. Léonard, J. Tersoff, Competing step instabilities at surfaces under stress. *Appl. Phys. Lett.* **83**, 72 (2003).
394. S. M. Hashmi, H. H. Wickman, D. A. Weitz, Tetrahedral calcite crystals facilitate self-assembly at the air-water interface. *Phys Rev E* **72**, 041605 (2005).
395. E. Loste, E. Díaz-Martí, A. Zorbakhsh, F. C. Meldrum, Study of Calcium Carbonate Precipitation under a Series of Fatty Acid Langmuir Monolayers Using Brewster Angle Microscopy. *Langmuir* **19**, 2830 (2003).
396. R. C. Cammarata, Surface and interface stress effects in thin films. *Progr. Surf. Sci.* **46**, 1 (1994).
397. T. J. Gould, M. S. Gunewardene, M. V. Gudheti, V. V. Verkhusha, S.-R. Yin, J. A. Gosse, S. T. Hess, Nanoscale imaging of molecular positions and anisotropies. *Nat Meth* **5**, 1027 (2008).
398. L. Schermelleh, R. Heintzmann, H. Leonhardt, A guide to super-resolution fluorescence microscopy. *J. Cell Biol.* **190**, 165 (2010).
399. X. Yang, Y. Liu, J. Wang, S. Zhang, H. Xie, X. Chen, P. Xi. (2013), vol. 8845, pp. 88450C-88450C-5.
400. J. Aizenberg, D. A. Muller, J. L. Grazul, D. R. Hamann, Direct Fabrication of Large Micropatterned Single Crystals. *Science* **299**, 1205 (2003).
401. T. Echigo, M. Kimata, A. Kyono, M. Shimizu, T. Hatta, Re-investigation of the crystal structure of whewellite [$\text{Ca}(\text{C}_2\text{O}_4)\cdot\text{H}_2\text{O}$] and the dehydration mechanism of caoxite [$\text{Ca}(\text{C}_2\text{O}_4)\cdot 3\text{H}_2\text{O}$]. *Mineral Mag.* **69**, 77 (2005).
402. A. V. Martin, N. D. Loh, C. Y. Hampton, R. G. Sierra, F. Wang, A. Aquila, S. Bajt, M. Barthelmess, C. Bostedt, J. D. Bozek, N. Coppola, S. W. Epp, B. Erk, H. Fleckenstein, L. Foucar, M. Frank, H. Graafsma, L. Gumprecht, A. Hartmann, R. Hartmann, G. Hauser, H. Hirsemann, P. Holl, S. Kassemeyer, N. Kimmel, M. Liang, L. Lomb, F. R. N. C. Maia, S. Marchesini, K. Nass, E. Pedersoli, C. Reich, D. Rolles, B. Rudek, A. Rudenko, J. Schulz, R. L. Shoeman, H. Soltau, D. Starodub, J. Steinbrener, F. Stellato, L. Strüder, J. Ullrich, G. Weidenspointner, T. A. White, C. B. Wunderer, A. Barty, I. Schlichting, M. J. Bogan, H. N. Chapman, Femtosecond dark-field imaging with an X-ray free electron laser. *Opt. Express* **20**, 13501 (2012).
403. E. V. Blinkova, E. I. Eliseev, Dissolution of Calcium Carbonate in Aqueous Solutions of Acetic Acid. *Russ. J. Appl. Chem.* **78**, 1064 (2005).

Nomenclature

Abbreviations

AA	Atomic Absorption
ACC	Amorphous Calcium Carbonate
ACO	Amorphous Calcium Oxalate
ACP	Amorphous Calcium Phosphate
ACS	Amorphous Calcium Sulphate
ADM	Ammonium Diffusion Method
AFM	Atomic Force Microscopy
AP	Activity Product
APS	Advanced Photon Source
Asp	Aspartic Acid
ATR	Attenuated Total Reflectance
BCDI	Bragg Coherent Diffraction Imaging
BET	Surface Area Measurement Technique
CCD	Charge Coupled Device
CXD	Coherent 3D X-ray Diffraction Pattern
CNT	Classical Nucleation Theory
COD	Calcium Oxalate Dihydrate
COM	Calcium Oxalate Monohydrate
DHP	Dihexadecyl Phosphate
DI	Deionized
DLS	Diamond Light Source
DLS	Dynamic Light Scattering
DOLLOP	Dynamically Ordered Liquid-Like Oxyanion Polymer

Nomenclature

DSC	Differential Scanning Calorimetry
ED	Electron Diffraction
EDX	Energy-dispersive X-ray Spectroscopy
ER	Error Reduction
ER	Error Reduction Phase Retrieval Algorithm
FEG	Field Emission Gun
FIB	Focused Ion Beam (milling)
FT	Fourier Transformation
FTIR	Fourier Transformed Infrared Spectroscopy
FWHM	Full Width Half Maximum
HIO	Hybrid Input Output
HIO	Hybrid Input-Output Phase Retrieval Algorithm
IC	Ion Chromatography
LCP	Liquid Crystalline Phase
LSCM	Laser Scanning Confocal Microscopy
Lys	Lysine
PAA	Polyacrylic Acid
PAH	Poly(allylamine hydrochloride)
PC	Phosphocholine
PEEM	Photo Emission Electron Spectroscopy
PILP	Polymer Induced Liquid Precursor
PNC	Pre Nucleation Cluster
PSS-MA	Polystyrene Sulfonate Maleic Acid
PXRD	Powder X-ray Diffraction
SAED	Selected Area Electron Diffraction
SAM	Self-Assembled Monolayer
SEM	Scanning Electron Microscopy
SSNMR	Solid State Nuclear Magnetic Resonance Spectroscopy

Nomenclature

TEM	Transmission Electron Microscopy
TGA	Thermo Gravimetric Analysis
UV-VIS	Ultraviolet–Visible Spectroscopy
VLM	Visual Light Microscopy
XANES	X-ray Absorption Near Edge Structure
XRD	X-ray Diffraction

Nomenclature

Symbols

α	[/]	Reaction Progress
β	$^{\circ}\text{C}/\text{min}$	Heating Rate
γ	J/m^2	Surface Energy
ε	$\text{l}/\text{mol m}$	Absorption Coefficient
Θ	$^{\circ}$	Scattering Angle
κ	S/m	Conductivity
λ	m	Wavelength
μ	$[10^{-2} \cdot \text{g}/(\text{cm} \cdot \text{s})]$	Dynamic Viscosity
μ	kJ/mole	Chemical Potential
τ	m	Crystallite Size
φ	$^{\circ}$	Sample Rotation
ψ	$^{\circ}$	Sample Tilt
Ω	m^3	Volume of Nucleolus Constituent
A	m^2	Area
A	[/]	Preexponential Factor
A	[/]	Absorbance
A_m	m^2	Gas Molecule Specific Surface Area
B	-	Full Width Half Maximum
c	m/s	Speed of Light
c	[/]	BET Constant
c_i	mol/l	Concentration
c_p	J/K	Heat Capacity
c_T	mol/l	Total Amount of Carbon
c_{Ts}	mol/l	Total Amount of Carbon in Solution
D	[/]	System Coefficient

Nomenclature

d	m	Resolution
d	m	Lattice Plane Spacing
D	cm ² /s	Diffusion Coefficient
d ₀	m	Distance Lens to Sample
D _a	cm ² /s	Diffusion Coefficient Gas Phase
dQ/dt	J/s	Heat Flow
D _s	[/]	Fractal Dimension
D _w	cm ² /s	Diffusion Coefficient Liquid
E	kJ - eV	Energy
e	%	Microstrain
E _A	kJ	Activation Energy
E _{cell}	V	Cell Potential
f	[/]	Volume Fraction Transformed
f	[/]	Activity Coefficient
f	Hz	Frequency
f	m	Focal Depth
F	C/mol	Faradays Constant
G	J/mol	Gibbs Free Energy
h	eV/s	Planck Constant
H	kJ	Heat of Adsorption
I	lux	Light Intensity
I	C/s	Current
I	mol/l	Ionic Strength
J	#/min*ml	Nucleation Rate (nuclei)
j _c	#/L	Cluster Formation Rate
k _B	J/K	Boltzmann Constant
K	[/]	Shape Factor
k _a	(mol/l) ^x	Acid Dissociation Constant

Nomenclature

k_h	l*atm/mol	Henry Constant
k_h'	[/]	Henry Constant
k_{sp}	(mol/l) ^x	Solubility product
k_α	[/]	X-ray Emission Lines
L	cm	Path Length
M	g/mol	Molecular Mass
m	g	Sample Mass
M_v	cm ³ /mol	Molecular Volume
n	[/]	Natural Number
N	[/]	Index of Refraction
N_a	1/mol	Avogadro's Number
N_a	[/]	Numerical Aperture
N_T	mol/l	Total Amount of Nitrogen
P	atm	Pressure (Partial)
P_0	atm	Saturation Pressure
Q	J	Heat
r	m	Radius
R	Ω	Resistance
R	atm*l /K*mol	Gas Constant
S	[/]	Supersaturation (relative)
S_i	m ²	Specific Surface Area
S_T	m ²	Total Surface Area
t	min	Time
T	°C	Temperature
T_P	°C	Peak Temperature
u	[/]	Strain Broadening Factor
U	J/c	Voltage
v	cm/min	Growth Rate Cluster

Nomenclature

V	m^3	Volume
V	cm^3	Adsorbed Gas Quantity
V_m	cm^2	Monolayer Adsorbed Gas
W	[/]	Weight Fraction
w	[/]	Size Broadening Factor
x	nm	Radial Size Increase
x	m	Vertical/horizontal Travel Distance
z		# mol e Transferred (Cell Reaction)
z	e	Electric Charge
Z	[/]	Atomic Number
T	min	Induction Time

Appendix

Appendix A: Reference FTIR- , Raman- and PXRD Spectra

Phase identification of minerals can be achieved based on the presence or absence of polymorph specific peaks in acquired IR-, Raman- and powder X-ray diffraction spectra. Given below is a tabular summary of the most prominent spectral features present in the minerals studied. PXRD peak positions are given with reference to Cu radiation.

Appendix

Principal Peak Positions in FTIR Spectra

		Wavenumber cm ⁻¹					
Water						1641	3350
Ethanol					1680	2962	3300
Silicon dioxide amorphous	SiO ₂	782		1036		1643	
Phosphate	PO ₄					1070	
Calcium Carbonate							
Mineral Name	Composition	V ₄	V ₂		V ₁	V ₃	
ACC	(CaCO ₃ -1H ₂ O)		862 -873		1065 -1075	1396 -1425	1641 3350
Vaterite	(CaCO ₃)	747	868		1085		
Aragonite	(CaCO ₃)	713	866		1090	1430	
Calcite	(CaCO ₃)	712 -714	868 -876			1395 -1420	
Magnesium Calcite	((Ca,Mg) CO ₃)		855 -872	1020 -1160	1084		1801
Calcium Oxalate							
Mineral Name	Composition						
Caoxite	(CaC ₂ O ₄ -3H ₂ O)				775	1313	1600 3476 +3429
Weddellite	(CaC ₂ O ₄ -2H ₂ O)	491	568			1313	1600 3700
Whewellite	(CaC ₂ O ₄ -1H ₂ O)	493	572	649	777	1313	1600 -3100 3018 +3413
Calcium Phosphate							
Mineral Name	Composition						
ACP	(Ca _{1.7} (PO ₄) ₁ OH _{0.4} - 3H ₂ O)		650	950		1050	
Hydroxyl apatite	(Ca ₅ (PO ₄) ₃ OH)	561	602	962	1046 -1032	1084	
Octacalcium phosphate	(Ca ₈ H ₂ (PO ₄) ₆ -5H ₂ O)	560	601	917	1055	1121	1642

Source: [Downs R T \(2006\) The RRUFF Project: an integrated study of the chemistry, crystallography, Raman and infrared spectroscopy of minerals](#). Gueta, Natan, Addadi, Weiner, Refson and Kronik (133), (161), Echigo, Kimata, Kyono, Shimizu and Hatta (401).

Table A. 1: Selected FTIR-spectra peak positions of calcium carbonate, calcium oxalate and calcium phosphate

Appendix

Principle Peak Positions in Raman Spectra

Calcium Carbonate		Raman Shift cm ⁻¹						
Mineral Name	Composition							
ACC	(CaCO ₃ -1H ₂ O)							Single broad peak at 1085
Vaterite	(CaCO ₃)		300	713	752	1066	1093	
Aragonite	(CaCO ₃)	155	208	701	705		1085	
Calcite	(CaCO ₃)	154	281	711			1085	1434
Calcium Oxalate								
Mineral Name	Composition							
Weddellite	(CaC ₂ O ₄ -2H ₂ O)	506		912		1477		1632
Whewellite	(CaC ₂ O ₄ -1H ₂ O)	508	898		1465		1491	1631
Calcium Phosphate								
Mineral Name	Composition							
ACP	(Ca _{1.7} (PO ₄) ₁ OH _{0.4} -3H ₂ O)							Weak shoulder at 952 & broad peak 1040
Hydroxyl apatite	(Ca ₅ (PO ₄) ₃ OH)	433	447	594		961	1046	1076
Octacalcium phosphate	(Ca ₈ H ₂ (PO ₄) ₆ -5H ₂ O)	413	450	591	957	966	1010	1079

Source: [Downs R T \(2006\) The RRUFF Project: an integrated study of the chemistry, crystallography, Raman and infrared spectroscopy of minerals.](#)

Table A. 2: Selected Raman spectra peak positions of calcium carbonate, calcium oxalate and calcium phosphate

Appendix

Principal PXRD Peak Positions

Calcium Carbonate

Mineral Name	Composition	Crystal Symmetry	2theta °/ d spacing			
ACC	(CaCO ₃ -1H ₂ O)	-				
<i>hkl</i>			110	113	116	300
Vaterite	(CaCO ₃)	Hexagonal	24.42	26.64	32.47	42.98
			3.645	3.345	2.757	2.104
<i>hkl</i>			111	012	102	112
Aragonite	(CaCO ₃)	Orthorhombic	26.23	33.16	36.13	37.91
			3.395	2.700	2.484	2.371
<i>hkl</i>			012	104	113	116
Calcite	(CaCO ₃)	Hexagonal	23.07	29.42	39.44	48.54
			3.855	3.035	2.284	1.875

Calcium Oxalate

Mineral Name	Composition	Crystal Symmetry	2theta °/ d spacing			
<i>hkl</i>			001	100	011	210
Caoxite	(CaC ₂ O ₄ -3H ₂ O)	Triclinic	11.25	16.06	16.19	31.49
			7.865	5.519	5.475	2.840
<i>hkl</i>			200	121	130	400
Weddellite	(CaC ₂ O ₄ -2H ₂ O)	Tetragonal	14.32	20.08	22.73	28.87
			6.185	4.421	3.912	3.092
<i>hkl</i>			100	021	040	023
Whewellite	(CaC ₂ O ₄ -1H ₂ O)	Monoclinic	14.94	15.3	24.42	30.68
			5.930	5.792	3.645	2.914

Calcium Phosphate

Mineral Name	Composition	Crystal Symmetry	2theta °/ d spacing			
ACP	(Ca _{1.7} (PO ₄) ₁ OH _{0.4} -3H ₂ O)	-				
<i>hkl</i>			100	002	211	300
Hydroxyapatite	(Ca ₅ (PO ₄) ₃ OH)	Hexagonal	10.81	25.89	31.72	32.72
			8.210	3.442	2.829	2.736

Source: [Downs R T \(2006\) The RRUFF Project: an integrated study of the chemistry, crystallography, Raman and infrared spectroscopy of minerals.](#)

Table A. 3: Selected PXRD spectra peak positions of calcium carbonate, calcium oxalate and calcium phosphate

Appendix

Appendix B: Solution Activity Coefficients

Solution activity coefficients (f) of the ionic species present (i) at concentration (c) were calculated using the Davies equation (A. 1), based on the measured ionic strength (I) (A.2).(308) This is shown here for the dissociation of a simple electrolyte e.g. NaCl.

$$-\log_{10}(f) = 0.5 z_1 z_2 \left(\frac{\sqrt{I}}{1 + \sqrt{I}} - 0.30 I \right) \quad \text{A. 1}$$

$$I = \frac{1}{2} \cdot \sum c_i z_i^2 \quad \text{A. 2}$$

z_i = charge of ionic species considered

Appendix C: CaCO₃ Equilibrium Constants and Solubility Products

CaCO₃ Equilibrium Constants

The solution supersaturation, calcium and carbonate concentrations given in Chapter 3 and 4 were determined using the temperature (T)-dependent equilibrium constants (K), Henry (k_H) and carbonic acid-dissociation constants (K_A) given below. (86, 163-167)

$$K_W = [OH^-][H^+] = 10^{-(0.0261 \cdot (T-273) + 14.583)} \quad \text{A. 3}$$

$$k_{HCO_2} = \frac{P_{CO_2}}{[CO_2]_{(aq)}} = 10^{-\left(108.386 + 0.0198507T - \frac{6919.53}{T} - 40.4515 \log_{10}(T) + \left(\frac{669365}{T^2}\right)\right)} \quad \text{A. 4}$$

$$K_{A1} = \frac{[H^+][HCO_3^-]}{[H_2CO_3^*]} = 10^{\left(\frac{-356.3094 - 0.06091964T + 21834.37}{T} + 126.833 \log_{10}(T) - \frac{1684915}{T^2}\right)} \quad \text{A. 5}$$

$$K_{A2} = \frac{[H^+][CO_3^{2-}]}{[HCO_3^-]} = 10^{\left(-171.9065 - 0.077993T + \frac{2839.319}{T} + 71.595 \log_{10}(T)\right)} \quad \text{A. 6}$$

$$k_{H_{NH_3}} = \frac{P_{NH_3}}{[NH_3]_{(aq)}} = e^{\left(-8.09694 + \left(\frac{3917.507}{T}\right) - 0.00314T\right)} \quad \text{A. 7}$$

$$K_{NH_4} = \frac{[H^+][NH_3]}{[NH_4^+]} = 10^{-\left(14 + \log_{10}\left(e^{-16.97 - \left(\frac{4411.025}{T}\right) - 0.044T}\right)\right)} \quad \text{A. 8}$$

$$K_{CaHCO_3} = \frac{[CaHCO_3^+]}{[Ca^{2+}][HCO_3^-]} = 10^{\left(-1209.12 + 0.31294T - \left(\frac{34765.05}{T}\right) - 478.782 \log_{10}(T)\right)} \quad \text{A. 9}$$

$$K_{CaCO_3_{aq}} = \frac{[Ca^{2+}][CO_3^{2-}]}{[CaCO_3]^0} = 10^{\left(-1228.732 - 0.299444T + \frac{35512.75}{T} + 485.818 \log_{10}(T)\right)} \quad \text{A. 10}$$

$$\log_{10} K_{CaOH} = 25.12 \quad \text{A. 11}$$

$$\log_{10} K_{Ca(OH)_2} = 22.80 \quad \text{A. 12}$$

Temperature-Dependence of the Solubility Products of the CaCO₃ Polymorphs (K_{sp})

Appendix

$$K_{sp\text{Calcite}} = 10^{\left(-171.9065 - 0.077993T + \frac{2839.319}{T} + 71.595 \log_{10}(T)\right)} \quad \mathbf{A. 13}$$

$$K_{sp\text{Aragonite}} = 10^{\left(-171.9773 - 0.0779931T + \frac{2903.293}{T} + 71.595 \log_{10}(T)\right)} \quad \mathbf{A. 14}$$

$$K_{sp\text{Vaterite}} = 10^{\left(-172.1295 - 0.0779933T + \frac{3074}{T} + 71.595 \log_{10}(T)\right)} \quad \mathbf{A. 15}$$

Appendix D: BCDI Image Reconstruction Details

Given below is a detailed description of the image reconstruction methods used in Chapter 5. Detailed descriptions of the phase retrieval procedure used, the pre-processing steps of the diffraction patterns, the sensitivity to lattice deformation, dislocation network identification and screw dislocation simulation are provided. The descriptions given are reproduced from *Clark JN[†], Ihli J[†], Schenk AS, Kim Y-Y, Kulak AN, Campbell JM, Nesbit G, Meldrum FC, Robinson IK. Three-dimensional imaging of dislocation propagation during crystal growth and dissolution.(199)*

Descriptions are provided for completeness. The novel methods employed here were developed by Jesse Clark and are not attributable to the candidate.

Phase Retrieval Procedure

An adjusted guided phase retrieval algorithm was applied to produce the image reconstructions presented in Chapter 5.(201) Guided phase retrieval algorithms are initiated by means of generating an initial population of iterates. Here, random arrays of numbers were used to provide a population of iterates, ρ_n , where n is equal to the count of differing iterates. One by one the iterates are processed by one or a combination of phase retrieval algorithms (error reduction (ER) or hybrid input-output (HIO)) iteratively to enforce agreement with the recorded diffraction intensity (modulus constraint). This is done under the experimental constraint that the sample is isolated i.e. the recorded diffraction pattern is obtained from a “single” crystal (isolation constraint).(200)

Following a pre-set number of iterations, a set of n potential solutions is obtained from which a group of winners or the “best” iterate is selected. A number of selection criteria can be applied to determine the best iterate, where the most common is agreement with the data (Modulus constraint). The best iterate or group of winners is then used to generate a new set of iterates. This is analogous to genetic algorithms in that the winning iterates/ seeds drives all of the subsequently generated iterates/ next generation seeds towards a better solution. Specifically if ρ_α is chosen as the best iterate, then new iterates are generated by $\rho'_n = \sqrt{\rho_n \rho_\alpha}$. The new improved iterate populations are used as inputs to the phase retrieval algorithm, which produce a set of winning iterates which are ideally closer to the desired solution than the previous generation of iterates. The described process (selection of the 'best' iterate, combination/ mutation, iteration) is then repeated a given pre-set number of times or generations.

Appendix

The given procedure runs into one particular problem when applied directly to the reconstruction of objects that have a non-negligible phase i.e. having a highly distorted diffraction pattern. This is not finding the “right” solution. To circumvent this, low-resolution data are used for the first generation of iterates. The resolution is then increased over the successive generations back to the original. The resolution is defined in this particular case as the data’s in reciprocal space. Reducing the resolution is then simply achieved by multiplying the given input data set by a Gaussian G . This means that the given input data I , is transformed to a “low” reduced resolution diffraction pattern I^\dagger by $I^\dagger = IG$. An ideal Gaussian G has the form of $G = H^2$ with H such that it has a Fourier transform that is finite. Since a reduced resolution diffraction pattern has to have a smaller number of solutions, $\rho^\dagger = \rho \otimes h$, where ρ is the original resolution object, h is the inverse Fourier transform of the previously defined H . ρ^\dagger will now have smoother and less pronounced phase features than the original, which becomes easier to reconstruct i.e. finding a right solution for a given low resolution data set is possible. The process is then repeated at increased resolution based on the initially determined low resolution result.(202, 402)

The initial procedure was then modified in terms of how to select the best iterate. Instead of selecting iterates with the best measured data agreement, they were selected as the one that has the smallest value of $\sum |\rho^\dagger|^4$. This gives a better representation of iterates that have a flatter amplitude. A flatter amplitude is advantageous here as objects with non-negligible phase(imaged here) do possess a diffraction pattern that is broader than its real-valued counterpart is in spatial dimension. This is as broadening of a diffraction pattern can also be due to a reduction in size of the object (Chapter 2 peak broadening in PXRD). This false identification would lead to the effect that during the iterative procedure solutions, that are smaller than the original object falsely occur since the broadening in the diffraction pattern can be accommodated this way. This results in potential solutions that are far from the actual solution but that are a good agreement with the data.

In summary, 50 iterates, 3 generations and best iterate selection based on selecting the ‘flattest’ were used to obtain the image reconstructions. During the 3 generations, the input data was masked with a Gaussian that had $\sigma_x = \sigma_y = \sigma_z = 10\%$ of the array size in the first generation, which was increased to $\sigma_x = \sigma_y = \sigma_z = 100\%$ of the array size by generation 3. 1000 iterations were used per

generation, cycling between 10 ER and 90 HIO.

CDX Pattern Pre-Processing

Miss-centering of the data before phase retrieval results in a 'phase ramp' in the real-space reconstruction. This is similar to a uniform expansion/ contraction of the lattice. To avoid this artefact, the phase ramps were removed, leaving just the inhomogeneous deformation (departures from the average lattice) behind in reconstructed images. To remove any real space phase ramp in $\rho(r)$, its Fourier transform, $\hat{\psi}(q)$, needs to be re-centred. This is a simple operation for real - valued objects with negligible phase, as the centre of mass of $|\hat{\psi}(q)|$ is commonly equal to the well-defined central maxima of the collected centro-symmetric diffraction pattern. Non-negligible phase objects do not necessarily possess a centre of mass equal to a defined central maxima (intensity) as $|\hat{\psi}(r)|$ may contain multiple peaks. Here, where we were primarily investigated non-negligible phase objects, any real space phase ramps were removed by centring $\hat{\psi}(r)$ based on the center of mass of $|\hat{\psi}(r)|^4$. Sub pixel shifting of the diffraction pattern was made possible by multiplying $\rho(r)$ by the appropriate phase ramp, as determined from the center of mass.

Origins of Lattice Deformation Sensitivity

BCDI's sensitivity to lattice deformation, and hence the capability to provide projected displacement images, is a result of information regarding the displacement field being carried over into recorded diffraction patterns. Analysis and retrieval of the displacement field is achieved in the derivation of the geometrical phase analysis used in electron microscopy.(197, 339)

In brief; starting from the representation of a sample crystal $\rho(r)$, as the product of an infinite lattice $l(r)$ and a given shape function $s(r)$. The latter defines not only the shape of crystal but further also its dimension as following **A. 16**.

$$\rho(r) = s(r)l(r) \quad \text{A. 16}$$

r is the real space-position vector. The lattice function $l(r)$ can further be expressed in the form of a Fourier series **A. 17**. Where Q is the reciprocal lattice vector giving the location of Bragg peaks and C_Q the complex coefficients.

Appendix

$$l(r) = \sum_Q C_Q \exp [iQ \cdot r] \quad \text{A. 17}$$

Considering a deformed lattice possessing local displacements i.e. atomic displacement from ideal lattice positions (r), the given lattice function $l(r)$ is additionally defined by a displacement field $u(r)$; $r \rightarrow r + u(r)$; $l(r + u(r))$. The describing Fourier series **A. 18** transforms accordingly.

$$l(r + u(r)) = \sum_Q C'_Q \exp [iQ(r + u(r))] \quad \text{A. 18}$$

$$= \sum_Q C'_Q \exp [iQ \cdot u(r)] \exp [iQ \cdot r] \quad \text{A. 19}$$

$$= \sum_Q G_Q(r) \exp [iQ \cdot r] \quad \text{A. 20}$$

The Fourier transform of the deformed lattice, $\hat{L}(q)$, is given by;

$$\hat{L}(q) = \int l(r + u(r)) \exp [-iq \cdot r] dr \quad \text{A. 21}$$

$$= \sum_Q \int G_Q(r) \exp [iQ \cdot r] \exp [-iq \cdot r] dr \quad \text{A. 22}$$

$$= \sum_Q \hat{G}_Q(q) \otimes \delta(q - Q) \quad \text{A. 23}$$

The given Fourier transform shows how the original lattice is altered as a result of the displacement field presence. In considering the experimental parameters used, recording far field diffraction patterns using quasi-monochromatic and spatially coherent X-rays, the diffracted wavefield $\hat{\psi}(q)$ can be described by a Fourier transform of the electron density of the sample crystal. The diffracted wavefield expressed for a crystal with an associated non-negligible displacement field (not considering constant pre-factors) can be described as stated in **A. 24-28**.

$$\hat{\psi}(q) = \int p(r) \exp [-iq \cdot r] dr \quad \text{A. 24}$$

$$= \int s(r) l(r + u(r)) \exp [-iq \cdot r] dr \quad \text{A. 25}$$

$$= \hat{S}(q) \otimes \hat{L}(q) \quad \text{A. 26}$$

Inserting A.28 for the deformed lattice term, $\hat{L}(q)$.

Appendix

$$\hat{\psi}(q) = \hat{S}(q) \otimes \sum_Q \hat{G}_Q(q) \otimes \delta(q - Q) \quad \text{A. 27}$$

$$= \sum_Q \hat{S}(q) \otimes \hat{G}_Q(q) \otimes \delta(q - Q) \quad \text{A. 28}$$

The recorded intensity $I(q)$ from the diffracted wave field $\hat{\psi}(q)$ in the vicinity of a Bragg peak at reciprocal lattice point Q , is then composed of a Fourier transform of the shape function, $\hat{S}(q)$ of the sample, and an additional term $\hat{G}_Q(q)$ as a result of the displacement field present.

$$I(q) = |\hat{\psi}_Q(q)|^2 \quad \text{A. 29}$$

$$= \left| \sum_Q \hat{\psi}_Q(q) \right|^2 \quad \text{A. 30}$$

$$= \left| \sum_Q \hat{S}(q) \otimes \hat{G}_Q(q) \otimes \delta(q - Q) \right|^2 \quad \text{A. 31}$$

Again, this can be simplified in the case of the performed experiments as we are only interested in diffraction centered around one particular reciprocal lattice point Q .

$$I(q) = |\hat{\psi}_Q(q)|^2 \quad \text{A. 32}$$

$$= |\hat{S}(q) \otimes \hat{G}_Q(q) \otimes \delta(q - Q)|^2 \quad \text{A. 33}$$

Particular real space representations of the diffracted wavefield $\hat{\psi}(q)$ - i.e. inverse Fourier transformed- as ultimately given in BCDI image reconstructions and obtained using phase retrieval, is given by

$$\rho_Q(r) = \int \hat{\psi}_Q(q) \exp[iq \cdot r] dq \quad \text{A. 34}$$

$$= \int \hat{S}(q) \otimes \hat{G}_Q(q) \otimes \delta(q - Q) \exp[iq \cdot r] dq \quad \text{A. 35}$$

$$= s(r) C'_Q \exp[iQ \cdot u(r)] \exp[iQ \cdot r] \quad \text{A. 36}$$

$$= |\rho(r)| \exp[i\phi(r)] \quad \text{A. 37}$$

where $\phi(r)$ is the phase of the real space function $\rho_Q(r)$, and is given by

$$\phi(r) = \phi_{c'} + Q \cdot u(r) + Q \cdot r \quad \text{A. 38}$$

$Q \cdot r$ being the phase ramp introduced earlier and removed by setting the average

Appendix

phase across the crystal to 0 and state procedure re-centering, the only component left in the phase will be the $Q \cdot u(r)$ term hence the sensitivity of lattice deformation and following obtained by looking at the phase of the reconstructed quantity in a BCDI experiment.

Identifying the dislocation network

Automated determination of the defect/ dislocation network present within the crystals was achieved by taking the gradient of the phase and then looking at the absolute value. Since dislocations possess a low electron density core the phase has to have a discontinuity at the core. Successive calculations of the gradient results in the values at the core growing in amplitude whereas every other area reduces in value.

The calculation of the discrete gradient of the phase , $\phi(a, b, c)$ ($F(a, b, c) := (F_x(a, b, c), F_y(a, b, c), F_{yz}(a, b, c))$), for a 3D array indexed by pixels a, b and c was achieved by means of **A. 39**, where $g(a, b, c) = \exp(i\phi(a, b, c))$, * denotes complex conjugation and h is a step size. Other constituents follow accordingly and we will denote the calculation of the discrete gradient as given in **A. 40**.

$$F_x(a, b, c) = \left(\frac{1}{h}\right) \arg [g(a + h/2, b, c)g(a - h/2, b, c)^*] \quad \text{A. 39}$$

$$F(a, b, c) = \nabla\phi(a, b, c) \quad \text{A. 40}$$

This calculation A. 45 avoids ambiguities that would arise if the gradient of the phase was calculated directly from taking the difference of the phase when calculated in the usual way of;

$$F_x(a, b, c) = \left(\frac{1}{h}\right) [\tan^{-1} (\exp[i\phi(a + h/2, b, c)]) - \tan^{-1} (\exp[i\phi(a - h/2, b, c)])] \quad \text{A. 41}$$

The ambiguities arise because of the 2π periodicity in the tan function and is a well-known problem ('phase unwrapping'). However, discontinuities will still arise if the phase changes from one pixel to the next by at least π . Equation A. 45 offers a convenient way to begin to determine the locations of defects since in certain directions, the defects will be where the phase changes from one pixel to the next by π (or greater), leaving a large value in F (compared to defect free regions). To isolate the effect of the defects a second step is performed where the gradient is

Appendix

computed again on each component of the original phase gradient to give 9 components given by;

$$K_{x,w}(a, b, c) = \nabla F_x(a, b, c) \quad \mathbf{A. 42}$$

$$K_{y,w}(a, b, c) = \nabla F_y(a, b, c) \quad \mathbf{A. 43}$$

$$K_{z,w}(a, b, c) = \nabla F_z(a, b, c) \quad \mathbf{A. 44}$$

where $w = x, y, z$. This second step helps to suppress the background relative to the defect locations. The following function is formed via;

$$N(a, b, c) = \max_{a,b,c} \left[\prod_w K_x(a, b, c), \prod_w K_y(a, b, c), \prod_w K_z(a, b, c) \right] \quad \mathbf{A. 45}$$

where \prod is the product and $\max_{a,b,c}$ selects the maximum value for each pixel a, b, c from the vector $(A(a, b, c), B(a, b, c), C(a, b, c))$. Although the use of A. 50 eliminates almost all ambiguities related to phase wrapping, defects can be falsely determined if there close to π (or $-\pi$) close to the edge of the crystal (since outside the crystal the phase is zero). However, the presence of false defects near the edge is dependent on a phase offset (ϕ_0 , since an offset will exist that makes the transition smooth), whereas real defects are independent of this (the core always has an abrupt change).

Appendix

Screw dislocation simulation at atomic resolution.

A given displacement field of $u(r) = (u_x(r), u_y(r), u_z(r))$ was used to model the difference in the displacement of atoms from their ideal lattice positions, where r is equal to the real space positioning of a given atom given by $r := (x, y, z)$. For the case of a screw dislocation, which has one non-zero component of the vector displacement field, we set;

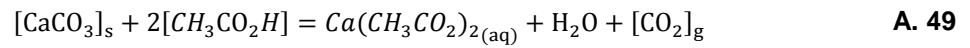
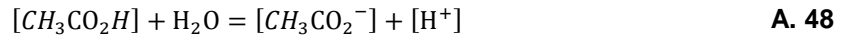
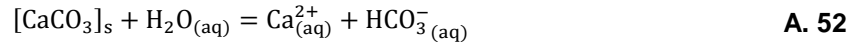
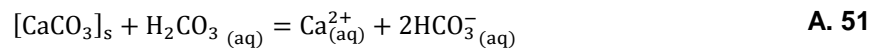
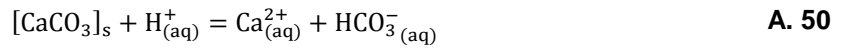
$$u_y(r) = b/2(\pi)\tan^{-1}(z/x) \quad \text{A. 46}$$

$$= b/2(\pi)\tan^{-1}(\theta) \quad \text{A. 47}$$

where b is the Burgers vector. To simulate the defect, a lattice spacing was selected (equal to 4 pixels) and a set of positions was generated (assuming a primitive cubic system) which would make up the ideal 'atom' positions given by C'_Q . These positions were then perturbed by the addition of the term in A. 52 (with b set to one lattice spacing) to give a perturbed lattice, now given as $l(r + u(r))$. The size of the 'crystal' was 96, 96 and 48 pixels for the x , y and z directions respectively and this was embedded into an array of size 128,128 and 64 pixels (x , y and z). A 3D Gaussian ($\sigma_x = \sigma_y = \sigma_z = 0.75$ pixels) was centered at each perturbed lattice position to give the "atoms" and simulate the defect. This 3D array of Gaussians was then Fourier transformed to provide a 3D diffracted wave $\hat{\psi}(q)$, where q is a reciprocal space coordinate. In the BCDI experiment a detector is placed at a Bragg peak and diffraction is recorded in this vicinity. To simulate the BCDI experiment we masked (filtered) the diffracted wave by centring a 3D Gaussian ($\sigma_x = 8$, $\sigma_y = 8$, $\sigma_z = 5.3$ pixels) at the (0 1 0) peak. This masked diffracted wave was then inverse Fourier transformed to provide a real space complex density, as is obtained by BCDI. The amplitude and phase are then related to the projected 'electron' density and projected displacement respectively.

Appendix E: Calcite Dissolution by Acetic Acid

Dissolution by Acetic Acid addition (403)

Undersaturation in H₂O

Appendix F: Supporting Movie Captions

Supplementary Movies Chapter 5.3: The lattice deformation and morphological evolution of a single calcite crystal during growth and successive dissolution is shown. Iso-surface renderings of the reconstructed electron density, projected displacement and iso-surface renderings of defects in the initial crystal, after growth and successive dissolution steps are shown in sequence. The defects which display a low amplitude core and spiral deformation field set in the background of reconstructed electron density are highlighted.

Supporting Movies Chapter 5.4: A sequence of iso-surface renderings of the reconstructed electron density, projected displacement and iso-surface renderings of defects present within a (012) oriented calcite crystal are given. The defect-rich reconstruction and transitional stages of the forming calcite crystals can be seen.

Appendix

Index

ACC CRYSTALLISATION IN THE SOLID STATE	98	AQUEOUS SOLUTION	48
ACC STABILIZATION/ CRYSTALLISATION IN SOLUTION	97	POLYMORPHS.....	34
ADDITIVES.....	24	CALCIUM CARBONATE.....	34
AMORPHOUS CALCIUM CARBONATE	40, 99	CLASSICAL CRYSTALLISATION THEORY.....	16
ACTIVATION ENERGY	148	CONDUCTIVITY	72
ADDITIVES	45, 101, 108	CRYSTAL	7
BIOMINERALS	40	CRYSTALLOGRAPHIC REFERENCE SYSTEM.....	8
CRYSTALLISATION.....	141	INDEXING CRYSTAL FACES AND DIRECTIONS	8
DEHYDRATION	128, 141	POLY.....	10
DEHYDRATION MECHANISM.....	150	SINGLE	9
LIFE-CYCLE	44	CRYSTAL GROWTH	19
LIPID BILAYER COATED	139	CRYSTAL ORIENTATION.....	82
SILICA COATED.....	130	CRYSTALLISATION ACTIVATION ENERGY	76
STRUCTURE	42	DEFECT	22
AMORPHOUS CALCIUM OXALATE	172	DEHYDRATION ACTIVATION ENERGY	77
ADDITIVE	177	DENSITY FLUCTUATION THEORY	27
CONFINEMENT	179	DIFFERENTIAL SCANNING CALORIMETRY	76
AMORPHOUS CALCIUM PHOSPHATE	169	DIFFUSION METHODS	190
AMORPHOUS MATER	11	AMMONIA DIFFUSION METHOD	196
ARAGONITE	36	CARBONATE ADDITION RATE...	205
ATOMIC ABSORPTION.....	68	INFLUENCE OF REACTION VARIABLES.....	208
ATOMIC FORCE MICROSCOPY	65	SUPERSATURATION	199
BIOMINERALIZATION.....	4	DISLOCATION LOOP	283
BRAGG COHERENT DIFFRACTION IMAGING	85, 237	DISLOCATION NETWORK.....	260
EXPERIMENTAL	243	DISSOLUTION.....	21
FUNDAMENTALS.....	240	DYNAMIC LIGHT SCATTERING	73
PHASING	245	EDGE DISLOCATION	22
RECONSTRUCTION ALGORITHM	86	ELECTRON DIFFRACTION	84
SETUP AND DATA ACQUISITION	85	ENERGY-DISPERSIVE X-RAY SPECTROSCOPY	68
CALCITE	38		
CALCIUM CARBONATE			

Index

<p>ENZYMATIC HYDROLYSIS OF UREA 222</p> <p>FLUORESCENCE MICROSCOPY 62</p> <p>FOCUSED ION BEAM MILLING 65</p> <p>FOURIER TRANSFORM INFRARED SPECTROSCOPY 69</p> <p>FRACTAL DIMENSION..... 74</p> <p>FREEZE CONCENTRATION 162</p> <p>GLASSWARE AND SUBSTRATE..... 54</p> <p style="padding-left: 20px;">CLEANING 54</p> <p style="padding-left: 20px;">PREPARATION..... 54</p> <p>HETEROGENEOUS NUCLEATION .. 269</p> <p>ION CHROMATOGRAPHY 72</p> <p>MESOCRYSTAL 32, 227</p> <p style="padding-left: 20px;">CRYSTALLINITY 230</p> <p style="padding-left: 20px;">SURFACE AREA 228</p> <p>MORPHOLOGY..... 25</p> <p>NUCLEATION 16</p> <p>ORIENTED ATTACHMENT 31</p> <p>OSTWALD'S RULE OF STAGES..... 12</p> <p>OSWALD RIPENING..... 21</p> <p>PH 72</p> <p>POLYMER-INDUCED-LIQUID-PRECURSOR 221</p> <p>POLYMORPHISM 10</p> <p>POWDER X-RAY DIFFRACTION 80</p> <p style="padding-left: 20px;">CRYSTALLITE SIZE 80</p> <p style="padding-left: 20px;">POLE FIGURE 82</p> <p>PRECIPITATION METHODS 56</p> <p style="padding-left: 20px;">DIFFUSION 58</p> <p style="padding-left: 20px;">DIRECT 56</p> <p style="padding-left: 20px;">ENZYMATIC HYDROLYSIS 58</p> <p style="padding-left: 20px;">KITANO 57</p>	<p style="padding-left: 20px;">SLOW ADDITION 58</p> <p>PRE-NUCLEATION CLUSTER 28</p> <p>RAMAN SPECTROSCOPY 70</p> <p>ROCKING CURVE 82</p> <p>SCANNING ELECTRON MICROSCOPY 63</p> <p>SCREW DISLOCATION 23, 262</p> <p>SELF-ASSEMBLED MONOLAYER .. 272</p> <p>SOLID-STATE NUCLEAR MAGNETIC RESONANCE SPECTROSCOPY .. 71</p> <p>SOLUTION 13</p> <p style="padding-left: 20px;">METASTABLE..... 13</p> <p style="padding-left: 20px;">SUPERSATURATED..... 14</p> <p style="padding-left: 20px;">UNDERSATURATED 14</p> <p>SPECTROSCOPY..... 67</p> <p>SPINODAL DECOMPOSITION 29</p> <p>STRAIN 81</p> <p style="padding-left: 20px;">GLOBAL UNIFORM 81</p> <p style="padding-left: 20px;">MICRO STRAIN 81</p> <p style="padding-left: 20px;">PARTICLE SIZE 265</p> <p>SURFACE AREA (BET) 74</p> <p>THERMO GRAVIMETRIC ANALYSIS 76</p> <p>TRANSMISSION ELECTRON MICROSCOPY 64</p> <p>UV-VIS..... 67</p> <p>VATERITE..... 36</p> <p>VISIBLE LIGHT MICROSCOPY 61</p> <p>WINTERBOTTOM RECONSTRUCTION 87</p> <p>WULFF'S RULE..... 24</p> <p>X-RAY DIFFRACTION..... 78</p> <p style="padding-left: 20px;">BRAGG'S LAW 78</p>
---	--

